Statistical Machine Learning

for Astronomy

Yuan-Sen Ting

The Ohio State University

June 17, 2025

Version 1.0

To my beloved Popo and my family
who supported my journey with remarkable patience.

Columbus, Ohio

June 17, 2025

Contents

Chapter 1

Preface and Overview

Machine learning has become increasingly prevalent in astronomical research, driven by the unprecedented scale and complexity of modern observational data. From the Sloan Digital Sky Survey to upcoming facilities like the Vera Rubin Observatory and Nancy Grace Roman Space Telescope, astronomers now routinely work with datasets containing billions of objects and petabytes of information. This data revolution has made automated analysis not just useful but essential for extracting scientific insights.

However, discussions about machine learning in astronomy are often complicated by the fact that "machine learning" has become nearly synonymous with neural networks and deep learning due to their recent popularity. This association obscures the fact that machine learning represents a much broader umbrella of techniques with a long history in statistical analysis. The conflation of machine learning with deep learning has made productive discussions about these methods more difficult than they need to be.

Machine learning's growing popularity in astronomy has become a polarizing issue within the research community. This polarization stems largely from misconceptions about what machine learning represents and how it connects to the statistical foundations that astronomers have long relied upon. Too often, machine learning techniques are presented as "black boxes" that somehow circumvent the need for rigorous statistical thinking. This perception has created an unfortunate divide between researchers who embrace these methods and those who view them with suspicion.

The root of this problem lies not in the techniques themselves but in how they are typically presented in research applications. Most existing resources fall into categories

that do not serve the astronomical community well. Classical statistical textbooks provide mathematical rigor but often stop short of modern methods like neural networks. Machine learning textbooks focus on engineering applications and algorithmic implementation while glossing over the statistical foundations that make these methods scientifically valid. There is also a notable lack of astronomy-focused textbooks in this context—when astronomical applications are presented, they are often very practical and application-focused rather than building theoretical understanding.

This gap is particularly problematic in astronomy, where the need for interpretability and uncertainty quantification exceeds that of most other fields. Computer scientists often view statistics and machine learning quite differently than physical scientists do. Unlike commercial applications where predictive power often justifies the means, astronomical research demands understanding not just what our models predict but why they make those predictions and how confident we should be in the results. When we use these techniques to challenge existing physical models or claim new discoveries, we must be clear about what constitutes statistical evidence of discovery.

The consequence of this pedagogical gap has been a fragmented approach to machine learning in astronomy. Researchers often learn specific techniques for particular problems—clustering for galaxy classification, regression for stellar parameter estimation, or neural networks for image analysis—without understanding the underlying statistical principles that connect these methods. This piecemeal approach not only limits the effective application of these techniques but also perpetuates the perception that machine learning is merely a collection of tools without theoretical depth like physics provides.

This textbook aims to bridge that gap by demonstrating that machine learning techniques are natural extensions of the statistical methods astronomers have always used. Rather than presenting these methods as revolutionary departures from traditional approaches, we show how they emerge from the same probability theory and Bayesian inference principles that underlie all scientific data analysis. By building this foundation systematically and providing a helicopter view of the field, we hope to demystify these techniques and enable their more thoughtful and effective application in astronomical research.

What is Machine Learning   At its core, machine learning shares the same goal as traditional scientific modeling: developing a coherent worldview from observed data. Just as Newton developed the law of gravity to predict planetary positions without explicit lookup tables, machine learning attempts to learn general rules that can be applied to new situ-

ations. This perspective reveals that there is no such thing as "pure learning" or "pure modeling"—all approaches fall somewhere on a spectrum between these extremes.

Every machine learning method incorporates what we call inductive bias—the set of assumptions that guide learning when data alone is insufficient to determine a unique solution. When we perform linear regression, we assume relationships follow hyperplanes. When we choose kernel functions for Gaussian Processes, we encode beliefs about function smoothness. When we design convolutional neural network architectures, we assume translation invariance in images. These biases are not limitations but necessities: without them, learning from finite data would be impossible.

The key insight is that stronger assumptions allow more efficient learning from limited data but potentially at the cost of flexibility. This trade-off between modeling (incorporating assumptions) and learning (extracting patterns from data) appears throughout scientific endeavor. Even when developing physical theories, we make implicit assumptions about mathematical forms, symmetries, and which phenomena are relevant. Machine learning makes these assumptions explicit through algorithmic choices, offering a principled framework for balancing prior knowledge with empirical evidence.

Understanding this perspective helps clarify why machine learning is not fundamentally different from traditional astronomical analysis. The choice between a parametric stellar evolution model and a neural network for predicting stellar properties represents different points on the modeling-learning spectrum, not a choice between science and black-box algorithms. Both approaches combine theoretical understanding with data-driven discovery; they simply allocate this combination differently.

What This Book Is—And What It Is Not   This textbook is about statistical machine learning for astronomy, with particular emphasis on building the theoretical foundations necessary to understand and properly apply these methods. While we do include a substantial chapter on neural networks and deep learning, this book is not primarily a deep learning textbook. Instead, we view deep learning as the natural culmination of a progression that begins with basic probability theory and extends through increasingly sophisticated statistical techniques. Understanding the limitations, pros and cons of classical methods helps illuminate why deep learning has become so prevalent in astronomy.

Our approach is deliberately "classical-centric" in the sense that we prioritize understanding the statistical principles that make machine learning methods work. This emphasis

serves several important purposes. First, classical techniques often provide analytical solutions and well-understood uncertainty quantification that remain valuable for many astronomical applications. Second, understanding these foundations illuminates why and when more complex methods like neural networks become necessary. Finally, many supposedly "modern" techniques turn out to be natural extensions of classical ideas—a connection that becomes clear only when both are understood within the same statistical framework.

We do not attempt to provide comprehensive coverage of every machine learning technique or to serve as a handbook of implementations. Instead, we focus on developing conceptual understanding and mathematical intuition that will enable readers to approach new techniques with confidence. Our goal is not to train practitioners who can apply specific algorithms but to develop researchers who can think critically about which methods are appropriate for which problems and why. Although we do provide practical tutorials released on GitHub (https://github.com/tingyuansen/statml), the emphasis here remains on understanding rather than implementation.

This perspective shapes our treatment throughout the book. When we discuss linear regression, for example, we emphasize not just how to fit lines to data but how this connects to maximum likelihood estimation, Bayesian inference, and the treatment of uncertainties. When we introduce Gaussian Processes, we show how they represent both a natural extension of linear methods and a precursor to neural networks. This integrated approach reveals the connections between apparently disparate techniques.

The astronomical focus of this textbook also distinguishes it from general machine learning resources. Astronomical data presents unique challenges—irregular sampling, heteroscedastic uncertainties, physical constraints, and the need for rigorous error propagation—that are rarely addressed in textbooks focused on other domains. Throughout our development, we use astronomical examples not as mere illustrations but as central motivating problems that drive the need for specific techniques.

It is important to emphasize that this textbook does not claim to present new theoretical results or novel algorithmic developments. The mathematical foundations, statistical principles, and machine learning techniques discussed here are well-established in the literature. Rather, our contribution lies in synthesizing this existing knowledge within a coherent framework specifically designed for astronomical applications. While the individual components of our treatment can be found scattered across various specialized texts, research papers, and technical resources, they do not appear to be available elsewhere in the com-

pact, unified form that the astronomical community requires. Our role is thus one of curation and pedagogical organization rather than original research—collecting, connecting, and presenting established results in a way that builds systematic understanding for astronomical researchers.

To support readers in exploring these topics beyond our treatment, we include Further Reading sections at the end of each chapter that highlight seminal works and key references in the relevant areas. These sections focus particularly on the foundational papers and influential texts that have shaped the development of each field. However, given the extraordinary depth and breadth of modern statistical machine learning—spanning statistics, computer science, applied mathematics, and domain-specific applications across numerous scientific disciplines—these reading lists necessarily represent only a tiny selection from a much larger body of literature. Our choices reflect works that we believe provide either historical context for understanding how these methods developed or particularly clear presentations of key concepts, rather than any attempt at comprehensive coverage. We hope these curated selections serve as effective entry points for readers who wish to delve deeper into specific areas, while acknowledging that they represent starting points rather than complete surveys of these rich fields.

The Structure and Philosophy of This Textbook   This textbook follows a designed progression that builds statistical understanding systematically while maintaining clear connections to astronomical applications. The structure reflects our belief that machine learning is best understood as an extension of statistical inference rather than as a separate discipline.

We begin with foundations in probability theory and, more importantly, Bayesian inference (Chapters 2-3). The philosophy behind Bayesian inference as a framework for uncertainty quantification permeates the entire textbook. This investment in theoretical groundwork pays dividends throughout the textbook, as it enables us to show how apparently different methods emerge from the same underlying principles. We then develop these foundations through the lens of summary statistics, showing how finite data constrains our ability to characterize probability distributions and motivating the need for more sophisticated approaches.

The progression through supervised learning (Chapters 4-9) follows a logical sequence that reveals how complexity emerges naturally from limitations of simpler methods. Supervised learning involves mapping inputs to known outputs, learning relationships between variables when we have examples of both. We start with linear regression, showing how

it emerges from maximum likelihood principles and how the Bayesian treatment provides uncertainty quantification. The extension to Bayesian linear regression demonstrates how prior knowledge can be incorporated formally while revealing the connection between regularization and Bayesian priors.

The treatment of input uncertainties in Chapter 6 addresses a challenge that is particularly important in astronomy, where measurement errors in both dependent and independent variables are common. This leads naturally to the iterative optimization methods needed for logistic regression (Chapters 7-8), which in turn motivates the more sophisticated Bayesian treatment of classification problems in Chapter 9.

Our coverage of unsupervised learning (Chapters 10-11) follows a similar philosophy, showing how Principal Component Analysis emerges from constrained optimization and how clustering methods like K-means and Gaussian Mixture Models provide complementary approaches to discovering structure in data. Unsupervised learning seeks to find patterns in data without known target outputs, discovering hidden structure rather than learning input-output relationships. The connection between these methods and their assumptions about data structure becomes clear through this systematic development.

The transition to computational methods (Chapters 12-13) acknowledges that as models become more complex, analytical solutions become unavailable and sampling methods become necessary. Our treatment of Monte Carlo methods and Markov Chain Monte Carlo provides the computational backbone needed for complex probabilistic models while maintaining connections to the Bayesian framework established earlier.

Gaussian Processes (Chapter 14) represent the culmination of our classical approach, combining linear algebra, kernel methods, and Bayesian inference in a framework that provides both flexibility and analytical tractability. The dual perspective on Gaussian Processes—as kernelized linear models and as distributions over functions—illustrates how the same mathematical framework can be understood from multiple viewpoints.

Finally, neural networks (Chapter 15) appear not as a departure from previous methods but as a natural extension that trades some of the mathematical tractability and uncertainty quantification of classical methods for greater computational scalability and flexibility. By this point in the textbook, readers have the background to understand both what neural networks can accomplish and what limitations they inherit from their departure from fully Bayesian approaches.

A Theory-Focused Approach Our pedagogical philosophy emphasizes understanding over application, complementing many existing textbooks. Though we believe that deep understanding ultimately leads to more effective application, we prioritize understanding why these algorithms work, when they are appropriate, and how they connect to broader statistical principles rather than focusing on how to implement specific algorithms.

This approach manifests in several ways throughout the textbook. We consistently derive methods from first principles rather than presenting them as given algorithms. When we introduce maximum likelihood estimation, for example, we show how it emerges from probability theory and how it connects to the method of least squares that readers may know from physics. When we develop the expectation-maximization algorithm, we show how it provides a general framework for dealing with hidden variables that applies to both K-means clustering and Gaussian Mixture Models.

We are unrelenting in our mathematical approach—from discussing the ergodic theorem for MCMC to proving the Bayesian Information Criterion. This might seem excessive, but we believe this mathematical rigor is critical for the motivation of this book. Without understanding the theoretical foundations, it becomes impossible to evaluate when methods are appropriate, how they might fail, or how they connect to the broader framework of statistical inference.

We also emphasize the connections between apparently different techniques. The relationship between ridge regression and Bayesian linear regression with Gaussian priors, for instance, illustrates how regularization techniques can be understood as encoded prior knowledge. The connection between Principal Component Analysis and autoencoders shows how neural networks can extend classical dimension reduction techniques. These connections help readers develop intuition about when different approaches might be appropriate.

Mathematical rigor is balanced with intuitive explanation. While we provide complete derivations for key results, we also use analogies, geometric interpretations, and physical intuitions to help readers understand what the mathematics means. The goal is not mathematical sophistication for its own sake but rather the development of quantitative reasoning skills that enable confident application of these methods to new problems.

Throughout the textbook, we use a musical analogy to frame our approach. Classical machine learning methods are like classical music—they may require more initial investment to appreciate, but this foundation enhances understanding and appreciation of more complex forms. Neural networks and deep learning, by contrast, are like contemporary popular music

or K-pop—immediately accessible and often quite powerful, but best appreciated with some understanding of the underlying compositional principles.

This analogy extends to our treatment of the methods themselves. Just as understanding Bach's compositional techniques illuminates later musical developments, understanding the statistical foundations of classical machine learning enhances the appreciation and effective application of neural networks. Rather than viewing classical and modern methods as competing paradigms, we present them as part of a continuous development of statistical techniques for dealing with increasingly complex data and problems.

Addressing Common Misconceptions   One of the goals of this textbook is to address misconceptions that have created unnecessary controversy around machine learning in astronomy. Chief among these is the characterization of machine learning methods, particularly neural networks, as "black boxes" that somehow avoid the need for statistical understanding.

This characterization is ironic because many machine learning techniques are actually more transparent about their assumptions than traditional approaches. When we engineer features for linear regression, for example, we make implicit assumptions about which transformations of our data are likely to be useful. When we choose a kernel function for Gaussian Process regression, we encode assumptions about the smoothness and structure of the underlying function. Neural networks, by learning these transformations directly from data, often make their representational choices more explicit and interpretable than hand-engineered approaches.

The perception of neural networks as somehow unscientific also reflects a misunderstanding of how scientific progress often works. Throughout history, engineering developments have often preceded theoretical understanding. Steam engines were built and improved for decades before the development of thermodynamics provided a theoretical framework for understanding their operation. Similarly, the empirical success of neural networks has motivated the development of new mathematical frameworks—like neural tangent kernel theory and the study of double descent phenomena—that are advancing our theoretical understanding of these methods.

Another common concern is that machine learning techniques require abandoning the uncertainty quantification that is central to scientific inference. While it is true that neural networks present challenges for full Bayesian treatment, this textbook shows multiple approaches to uncertainty quantification, from the Monte Carlo dropout methods that provide

practical approximations to the rigorous Bayesian treatments available for simpler models. The goal is not to achieve perfect uncertainty quantification in all cases but to understand the trade-offs involved in different approaches.

Perhaps most importantly, we address the concern that using machine learning methods means abandoning physical understanding. Throughout this textbook, we emphasize how physical knowledge can and should inform the choice and application of statistical techniques. The selection of appropriate kernel functions for Gaussian Processes, the design of network architectures that encode relevant symmetries, and the interpretation of latent representations in unsupervised learning all benefit from physical insight. Machine learning is most powerful when it augments rather than replaces scientific understanding.

What You Will Learn   By the end of this textbook, you will have developed a systematic understanding of statistical machine learning that enables confident application of these methods to astronomical research problems. This understanding operates at several levels.

At the conceptual level, you will understand how machine learning techniques emerge from probability theory and Bayesian inference. This foundation will enable you to evaluate new methods critically and to understand their assumptions, limitations, and appropriate domains of application. You will also understand the connections between apparently different techniques and how they represent different solutions to common statistical challenges.

At the mathematical level, you will be comfortable with the derivations and analysis of key algorithms. This includes understanding how maximum likelihood estimation leads to specific loss functions, how regularization emerges from Bayesian priors, and how optimization algorithms like expectation-maximization provide practical solutions to complex inference problems. While mathematical sophistication is not the goal, mathematical understanding provides the foundation for confident application and troubleshooting.

At the practical level, especially with accompanying tutorials, you will understand how to match statistical techniques to astronomical problems. This includes knowing when linear models are sufficient and when more complex approaches are needed, how to incorporate physical knowledge into statistical models, and how to evaluate and compare different approaches to the same problem. You will also understand the computational trade-offs involved in different methods and how to balance statistical rigor against practical constraints.

Perhaps most importantly, you will develop the ability to think statistically about astronomical problems. This means understanding how uncertainty propagates through

analysis pipelines, how to distinguish between different sources of uncertainty, and how to design observational strategies that provide maximum statistical power for addressing specific questions.

The ultimate goal is not mastery of any particular technique but rather the development of statistical reasoning skills that will serve you throughout your research career. As new methods are developed and new data challenges emerge, the foundations developed in this textbook will enable you to evaluate, understand, and apply these developments effectively.

Looking Forward   This textbook represents a snapshot of statistical machine learning as applied to astronomy in the mid-2020s. In a fast-moving field, new theoretical insights and practical techniques appear regularly. However, the foundations developed here—probability theory, Bayesian inference, and the connections between classical and modern statistical methods—provide a stable base for understanding these developments.

As you progress through this textbook, you will likely find that your perspective on both classical and modern statistical methods evolves. Techniques that initially seem complicated often reveal simplicity when understood within the proper framework. Methods that appear unrelated often turn out to share deep mathematical connections. This evolution of understanding is not just a byproduct of the learning process but its primary goal.

The future of astronomical research will undoubtedly involve increasingly sophisticated statistical techniques applied to increasingly complex datasets. Success in this environment will require not just familiarity with specific algorithms but the kind of deep statistical understanding that enables rapid adaptation to new challenges and opportunities. This textbook aims to provide that foundation, ensuring that you can contribute effectively to astronomical research regardless of how the technical landscape continues to evolve.

The journey from basic probability theory to advanced neural networks may seem daunting at the outset. However, by building understanding systematically and maintaining clear connections to the underlying statistical principles, we hope to make this journey not just manageable but enlightening. The goal is not just to understand how these methods work but to appreciate why they work and when they provide the right tools for advancing astronomical knowledge.

Chapter 2

Bayesian Inference

The core of scientific data analysis lies in measuring, quantifying, and reasoning about uncertainty. Throughout this textbook, we will develop machine learning methods that are firmly grounded in Bayesian principles—approaches that provide a principled framework for understanding astronomical phenomena under uncertainty. Before we can apply these methods, however, we must establish the probability theory that underlies the Bayesian approach.

A central insight from Thomas Bayes—one that revolutionized statistical thinking—was that both observations and model parameters should be treated as random variables. This perspective, which we'll explore in depth, forms the mathematical basis for all subsequent chapters. While treating observational data as random variables seems intuitive (our measurements always have uncertainty), extending this treatment to model parameters might initially seem counterintuitive. After all, physical constants like the gravitational constant or the mass of a galaxy should have definite values. Yet our knowledge of these values is inherently uncertain, and Bayesian inference provides a mathematically consistent framework for updating this knowledge as we gather more observations.

This Bayesian perspective is particularly valuable in astronomy, where many phenomena cannot be repeated under controlled conditions. Unlike laboratory experiments where we can run multiple trials, astronomers often study unique events. By treating model parameters as random variables, Bayesian inference allows us to make principled statements about uncertainty even when we have limited data.

In this chapter, we build the mathematical foundation necessary for Bayesian infer-

ence and machine learning. We'll start by distinguishing between deterministic and random variables—a distinction that clarifies why treating model parameters as random variables makes sense. We'll then explore probability distributions commonly encountered in astronomy, establish rules for manipulating probabilities, and contrast frequentist and Bayesian approaches. Through concrete examples, we'll demonstrate how Bayesian inference works in practice, even with minimal data.

This foundation in probability theory will illuminate why methods from linear regression to neural networks can all be understood as extensions of Bayesian principles. Each technique, in its own way, implements the core Bayesian idea of updating our beliefs about model parameters based on observed data. Understanding this connection provides not just practical tools for data analysis but also a deeper appreciation for how machine learning methods relate to the principles of scientific inference.

2.1   Deterministic vs. Random Variables

To understand why scientific inference requires a probabilistic approach, we must first distinguish between two different types of quantities: deterministic and random variables. This distinction forms the conceptual foundation for all statistical methods we'll explore throughout this textbook.

Deterministic Variables are quantities that, given the same conditions, always yield the same value. For example, the orbital period of a planet around a star of known mass at a known distance follows deterministic physical laws. When we say "given the same conditions," we mean that all the relevant physical parameters that could affect the outcome are specified and fixed. Consider Kepler's Third Law for a planet orbiting a star:

$$P^2 = \frac{4\pi^2}{GM}a^3 \tag{2.1}$$

where:

- P is the orbital period

- G is the gravitational constant

- M is the mass of the central star (assuming $M \gg m_{\text{planet}}$)

- a is the semi-major axis of the orbit

The variables P, M, and a are deterministic variables. If we specify M and a, the period P is completely determined—there is no ambiguity or uncertainty in its value. Every time we apply the same values for M and a, we obtain exactly the same period P. This deterministic nature characterizes most quantities from our basic physics and mathematics courses, where solving an equation like:

$$x^2 + 2x - 3 = 0 \tag{2.2}$$

The solutions $x = 1$ or $x = -3$ are deterministic—they are the exact values that satisfy the equation, and they do not change no matter how many times we solve it.

Random Variables, in contrast, are quantities whose values are subject to uncertainty or variation. Even when all known conditions are specified, we can only predict probabilities of different outcomes, not the exact outcome itself. In real astronomical observations, even though the true orbital period of a planet is a deterministic quantity, our measurement of it becomes a random variable. When we measure that orbital period P, we make multiple observations of the star's radial velocity or the planet's transit, and each measurement has some uncertainty due to instrumental noise and atmospheric effects. Our final estimate of P comes with an uncertainty, often expressed as $P \pm \sigma_P$.

This uncertainty does not arise because the true period is random—it is not! Rather, the randomness comes from our imperfect measurement process. The key distinction from deterministic variables is that even when all known conditions are specified, we can only predict probabilities of different outcomes, not the exact outcome itself.

Random variables come in two main forms:

Inherently Random: Some quantities in nature appear to be fundamentally probabilistic, such as quantum phenomena. Examples include:

- The exact time of decay of a radioactive atom

- The spin measurement of an electron in a superposition state

Incomplete Knowledge or Measurement Uncertainty: Many astronomical quantities appear random not because they are inherently probabilistic, but due to practical limitations. Consider again the orbital period example: while Kepler's Third Law tells us the exact period for given values of mass and semi-major axis, our measurements of these quantities

come with uncertainties. The star's mass estimate may have error bars from spectroscopic analysis, and the semi-major axis measurement may be affected by observational limitations. Even though the true orbital period is a fixed, deterministic value, our incomplete knowledge of the input parameters, combined with measurement uncertainties in our period observations themselves, means we can only make probabilistic statements about its value. This transformation of deterministic quantities into random variables due to measurement and parameter uncertainties is a common feature in astronomical analysis.
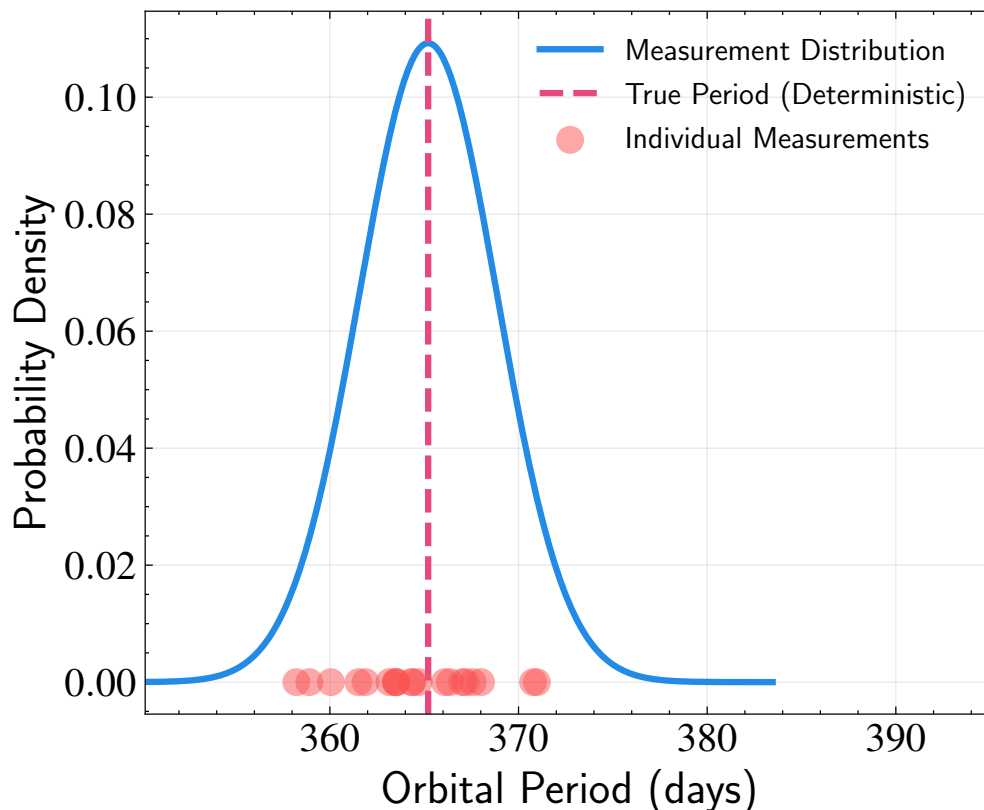
Figure 2.1: Illustration of deterministic versus random variables. The dashed vertical line represents a true (deterministic) value of some quantity. The blue curve shows the probability distribution of measured values when accounting for uncertainties. Individual red dots represent specific measurements, which scatter around the true value due to various sources of uncertainty. This demonstrates how a fundamentally deterministic quantity becomes a random variable when we consider measurement or other uncertainties.

This distinction becomes particularly important when we consider how to analyze physical systems. We often know the physical laws governing these systems (like Kepler's Third Law), but our measurements of the relevant parameters come with uncertainties. This creates an asymmetry in scientific inference: while we can easily predict what observations should result from a given set of parameters (the forward problem), determining the param-

eters from observations (the inverse problem) requires carefully accounting for all sources of uncertainty.

For instance, the mass of a galaxy's central black hole has a definite value in reality. However, our estimate of this mass—based on stellar velocity measurements, gas dynamics, or other observational techniques—comes with uncertainty. We represent this uncertainty through a probability distribution that reflects our current state of knowledge. As we gather more data, this distribution will narrow, becoming more concentrated around the true value, but some uncertainty will always remain.

This perspective of representing our knowledge about physical quantities through probability distributions enables a consistent mathematical framework for scientific inference. It allows us to start with prior knowledge, incorporate new observations, and systematically update our understanding—a process that lies at the heart of all scientific progress.

2.2   Probability Distributions

Having established that many quantities in astronomy can be treated as random variables, we now need a mathematical framework to quantify the uncertainty associated with them. This leads us to probability distributions—mathematical objects that describe how probabilities are distributed across all possible values of a random variable.

When we consider a parameter like the mass of a black hole as a random variable, we're not suggesting the mass itself fluctuates randomly. Rather, the probability distribution represents our state of knowledge about that mass—where the peak indicates our best estimate and the width reflects our uncertainty. Similarly, for observational data, the probability distribution captures both the expected value and the uncertainty in our measurements.

Mathematically, for any event A associated with our random variable X, we denote its probability as $P(A)$, which must satisfy three fundamental axioms:

1. Non-negativity: $P(A) \geq 0$ for any event A

2. Normalization: $P(\Omega) = 1$, where Ω is the sample space (all possible outcomes)

3. Additivity: For mutually exclusive events A and B, $P(A \cup B) = P(A) + P(B)$

While probability gives us a single number for a specific event, a probability distribution describes how probabilities are distributed across all possible values of a random

variable. This concept is central to statistical inference, as it provides a complete description of uncertainty rather than just single-point estimates.

In astronomy, we encounter both discrete and continuous random variables, which are treated differently in probability theory:

Discrete Case: Some astronomical quantities can only take specific, countable values. For instance, when counting the number of photons that hit our detector in a given time interval, or when classifying galaxies into distinct morphological types (e.g., spiral, elliptical, irregular). For a discrete random variable X, we define a probability mass function (PMF) $p(x)$ where:

- $p(x) = P(X = x)$ is the probability of X taking the specific value x

- $\sum_x p(x) = 1$ (normalization)

Continuous Case: Most astronomical measurements are continuous. For these random variables, we define a probability density function (PDF) $p(x)$ where:

- $P(a \leq X \leq b) = \int_a^b p(x)dx$ is the probability of X falling in the interval $[a, b]$

- $\int_{-\infty}^{\infty} p(x)dx = 1$ (normalization)

Since a random variable X does not take a fixed value, but rather follows a certain probability distribution, we write this mathematically as:

$$X \sim P(x) \tag{2.3}$$

This notation expresses concisely that the random variable's behavior is governed by that specific probability distribution.

An important but subtle point about continuous distributions is that the probability of measuring any exact value is actually zero! This might seem counterintuitive, but consider measuring an orbital period: if we could measure with infinite precision, what is the probability of getting exactly 365.256363... days? Since there are infinitely many possible values, the probability of getting any specific one is zero. This is why we can only discuss the probability of measurements falling within intervals (like between 365.2 and 365.3 days) by integrating the PDF. The value of $p(x)$ itself tells us the relative likelihood or density of measurements near x, but we need to integrate over some interval to obtain actual probabilities.

This property of continuous distributions has an important implication for statistical inference with continuous parameters. When we say a probability distribution peaks at a certain parameter value, we're identifying the most likely small range of parameter values, not a specific exact value with non-zero probability. The shape of the distribution around this peak tells us about the uncertainty in our parameter estimates—a narrow peak indicates high confidence, while a broad distribution suggests greater uncertainty.

As we develop statistical methods in subsequent chapters, these probability distributions will provide the mathematical language for expressing uncertainty in both our data and our model parameters. Whether we're performing linear regression, classification, or dimensionality reduction, probability distributions will be our tool for characterizing uncertainty.

2.3 Common Distributions in Astronomy

Several probability distributions appear frequently in astronomical applications. While these distributions can be derived mathematically through the principle of maximum entropy (i.e., finding the least presumptive distribution given certain constraints), we can also understand their origins through physical intuition, which provides deeper insight into when and why they arise in astronomical contexts.

Gaussian Distribution The Gaussian or normal distribution naturally emerges when we only know (or constrain) the mean and variance of a quantity. Physically, it appears when many small, independent effects add together—what we call the Central Limit Theorem. Consider measuring a star's brightness, where the measurement process involves countless sources of uncertainty.

For a single random variable X, we write:

$$X \sim \mathcal{N}(\mu, \sigma^2) \tag{2.4}$$

to denote that it follows a Gaussian distribution with probability density:

$$p(x|\mu, \sigma) = \frac{1}{\sigma\sqrt{2\pi}} \exp\left(-\frac{(x-\mu)^2}{2\sigma^2}\right) \tag{2.5}$$

Here, $p(x|\mu, \sigma)$ is the probability density at value x given parameters μ and σ, where:

- x is the random variable (e.g., the measured brightness)

- μ is the mean or expected value

- σ is the standard deviation, measuring the spread of the distribution

- The factor $\frac{1}{\sigma\sqrt{2\pi}}$ ensures the total probability integrates to 1

To understand why Gaussian distributions are so ubiquitous in astronomical measurements, consider the detailed process of measuring stellar brightness. Each photon's path through the atmosphere is randomly disturbed by countless small air pockets of varying density and temperature, each contributing a tiny deflection. The telescope's optical system introduces minute aberrations from surface imperfections and thermal variations. The detector adds electronic noise from millions of independent electron movements in the CCD. The analog-to-digital conversion process introduces quantization noise. Each of these effects is small and independent, but they all add up. According to the Central Limit Theorem, when many small, independent effects combine additively, the result approaches a Gaussian distribution—regardless of the individual distributions of each effect.

This is why the Gaussian distribution is ubiquitous in nature—it represents the most likely way random effects combine when nothing else is constraining them, making it the natural choice when we know only the mean and variance of a system.

For multivariate data (i.e., many different random variables), we write:

$$\mathbf{X} \sim \mathcal{N}(\boldsymbol{\mu}, \boldsymbol{\Sigma}) \tag{2.6}$$

to denote a multivariate Gaussian distribution with probability density:

$$p(\mathbf{x}|\boldsymbol{\mu}, \boldsymbol{\Sigma}) = \frac{1}{(2\pi)^{n/2}|\boldsymbol{\Sigma}|^{1/2}} \exp\left(-\frac{1}{2}(\mathbf{x} - \boldsymbol{\mu})^T\boldsymbol{\Sigma}^{-1}(\mathbf{x} - \boldsymbol{\mu})\right) \tag{2.7}$$

Here:

- $\mathbf{x}$ is an n-dimensional vector of random variables

- $\boldsymbol{\mu}$ is the mean vector

- $\boldsymbol{\Sigma}$ is the $n \times n$ covariance matrix

- $|\boldsymbol{\Sigma}|$ is the determinant of the covariance matrix
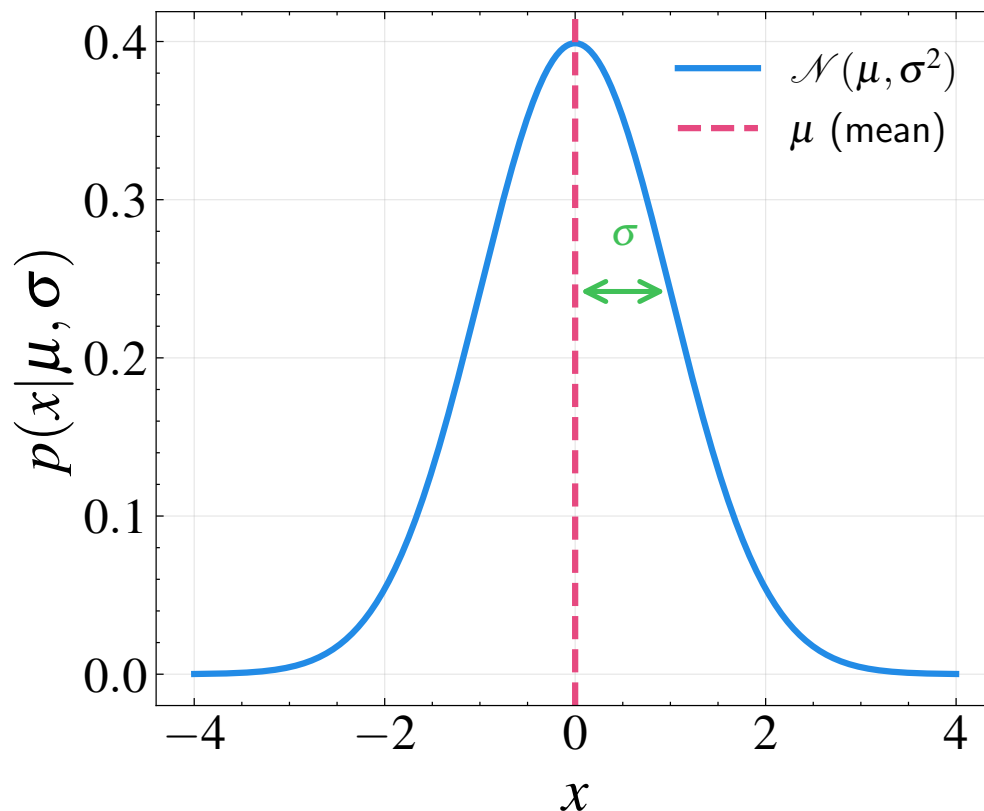
Figure 2.2: Visualization of a standard normal (Gaussian) distribution with mean $\mu = 0$ and standard deviation $\sigma = 1$. The dashed vertical line indicates the mean (μ), which corresponds to the peak of the distribution. The green arrow shows one standard deviation (σ) from the mean, a key measure of the distribution's spread. The Gaussian distribution is symmetric around its mean, with approximately 68% of the probability mass falling within one standard deviation of the mean. This distribution naturally emerges when many small, independent effects combine additively, making it ubiquitous in astronomical measurements due to the Central Limit Theorem.

- $\mathbf{\Sigma}^{-1}$ is the inverse of the covariance matrix

The covariance matrix $\mathbf{\Sigma}$ captures not just the variance of each variable (diagonal elements), but also how pairs of variables are correlated (off-diagonal elements). This becomes particularly important when analyzing multivariate astronomical data, such as the correlation between different spectral lines or between physical properties like mass, age, and metallicity in stellar populations.

Poisson Distribution   The Poisson distribution emerges when we are counting independent events occurring at a constant average rate, with our only constraint being knowledge of the mean rate. This distribution is central to photon detection and many other counting

processes in astronomy:

$$P(X = k|\lambda) = \frac{\lambda^k e^{-\lambda}}{k!} \tag{2.8}$$

To understand how the Poisson distribution arises from physical principles, consider the process of detecting photons from a distant star. Imagine dividing our observation time into infinitesimally small intervals. In each tiny interval, we can expect at most one photon to arrive—the probability of two or more photons arriving in the same infinitesimal interval is negligible. The key physical principles at play involve independence, uniformity, and randomness. The arrival of photons in different time intervals are independent events—whether a photon arrives in one interval has no effect on whether another photon arrives in a different interval. The probability of detecting a photon in any given interval is simply proportional to how long we observe. If we double the observation time (or double the size of our time interval), we double our chances of seeing a photon. Finally, the precise arrival times are truly random. No two photons will arrive at exactly the same instant, and there are no preferred arrival times.

These simple physical assumptions inevitably lead to the Poisson distribution—it is the most natural way to describe random, independent counting events. This is why photon counts, cosmic ray hits, and galaxy counts in small volumes all tend to follow Poisson statistics.

An important property of the Poisson distribution is its relationship to the Gaussian distribution. When the mean rate parameter λ becomes large, the Poisson distribution increasingly resembles a Gaussian distribution with mean $\mu = \lambda$ and variance $\sigma^2 = \lambda$. This convergence is a specific case of the Central Limit Theorem and has practical implications in astronomy: while photon counting fundamentally follows Poisson statistics, we can often approximate these counts with Gaussian distributions when dealing with bright sources where the count rates are high.

Power Law Distribution   Power laws appear when a process has no characteristic scale—that is, when the physics works the same way regardless of size. Consider the mass distribution of stars (the Initial Mass Function):

$$p(x) \propto x^{-\alpha} \tag{2.9}$$

When we have physical limits that constrain the range of x between a minimum value
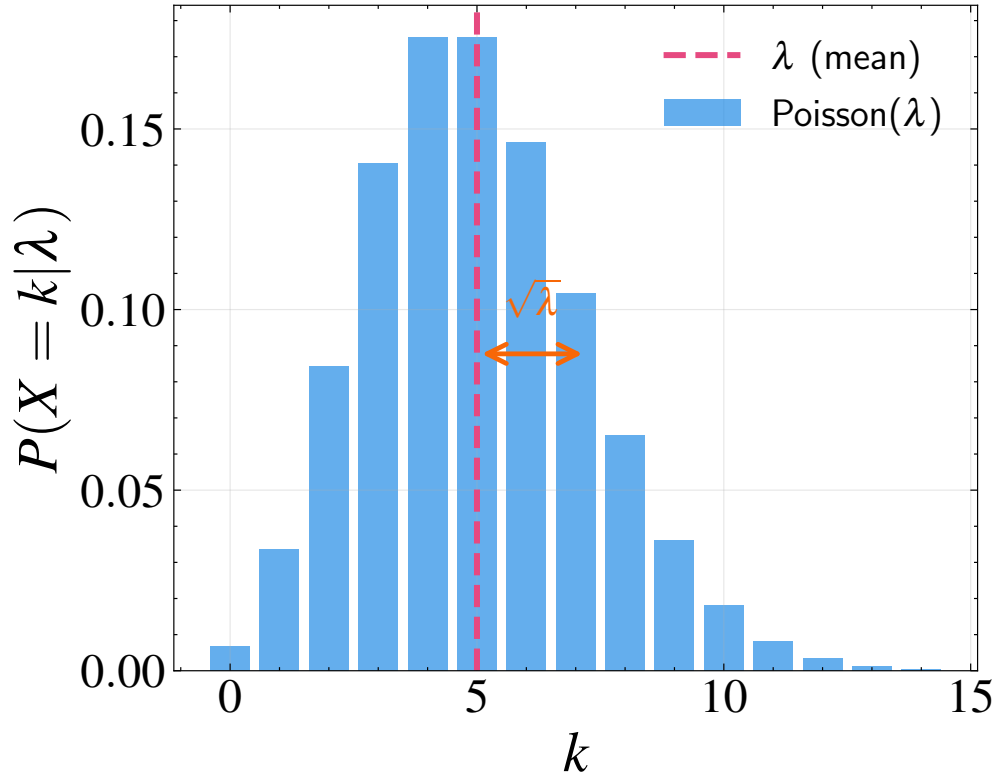
Figure 2.3: Visualization of a Poisson distribution with mean rate parameter $\lambda = 5$. The discrete probability mass function is shown as blue bars, with the mean value indicated by the dashed vertical line. A key property of the Poisson distribution is that its standard deviation equals $\sqrt{\lambda}$ (shown by the orange arrow), making the distribution relatively more spread out for smaller values of λ and more concentrated for larger values. This distribution naturally describes counting processes in astronomy, such as photon arrivals, cosmic ray hits, or galaxy counts in small volumes, where events occur independently at a constant average rate.

$x_{\min}$ and maximum value $x_{\max}$, the normalized form of the power law becomes:

$$p(x) = \frac{1 - \alpha}{x_{\max}^{1-\alpha} - x_{\min}^{1-\alpha}} x^{-\alpha} \tag{2.10}$$

where the prefactor ensures that integrating $p(x)$ from $x_{\min}$ to $x_{\max}$ equals 1.

Why do power laws emerge in star formation? Imagine the process of molecular cloud fragmentation forming stars. As a massive molecular cloud collapses under its own gravity, it becomes unstable and fragments into smaller clouds. Each of these resulting clouds can further break down into even smaller clouds through the same physical processes. The fascinating aspect is that the physics governing this fragmentation process remains remarkably similar regardless of the size scale we are examining.
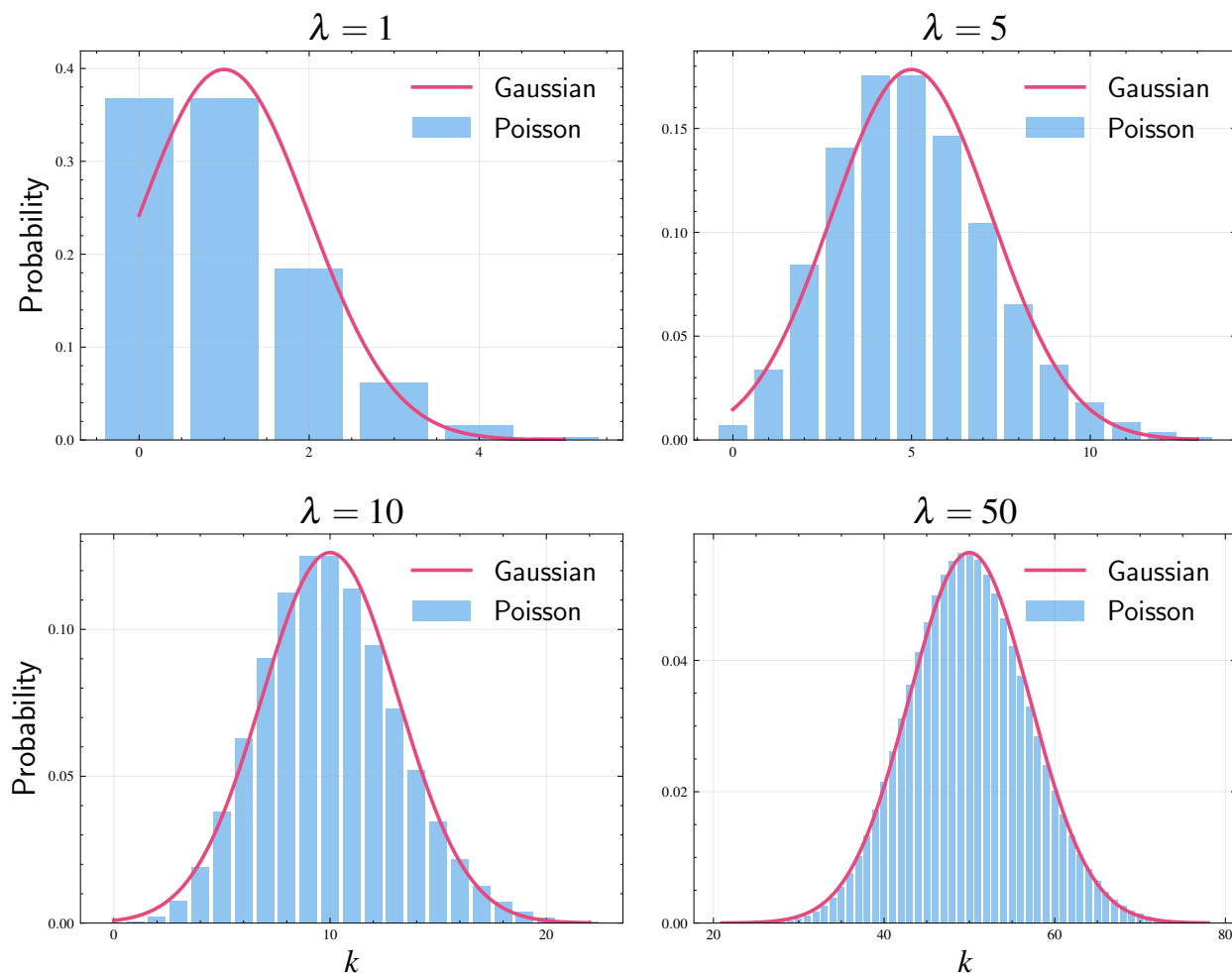
Figure 2.4: Illustration of how the Poisson distribution (blue bars) approaches a Gaussian distribution (red line) as the mean rate parameter λ increases. For small λ (e.g., $\lambda = 1$), the distribution is highly discrete and skewed. As λ increases ($\lambda = 5, 10$), the distribution becomes more symmetric and the discrete nature is less pronounced. By $\lambda = 50$, the Poisson distribution is nearly indistinguishable from a Gaussian distribution with the same mean and variance ($\sigma^2 = \lambda$). This convergence, a consequence of the Central Limit Theorem, explains why photon counting statistics can often be approximated by Gaussian distributions when count rates are high.

Whether we are looking at a massive cloud complex spanning hundreds of parsecs or a small proto-stellar core of 0.01 parsecs, the same physical processes drive the fragmentation: gravitational collapse competes with turbulent pressure, magnetic fields provide additional support, and thermal pressure from heating and cooling processes influences the dynamics. The cloud does not "know" whether it is breaking into 1-parsec or 0.1-parsec sized pieces—the process looks essentially the same at all scales, within the physical limits imposed by the interstellar medium.
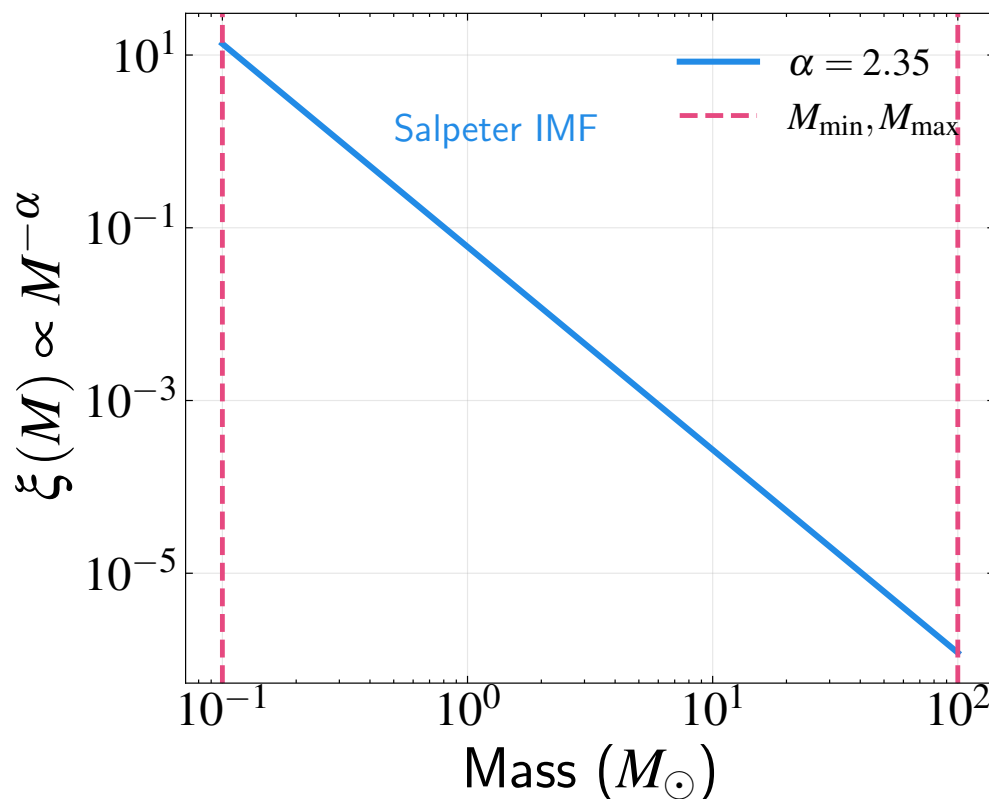
Figure 2.5: Visualization of a power law distribution using the Salpeter Initial Mass Function (IMF) as an example. The Initial Mass Function (IMF) describes the distribution of stellar masses at birth—essentially how many stars of each mass are formed in a given population. The distribution follows $\xi(M) \propto M^{-\alpha}$ with $\alpha = 2.35$ (Salpeter's value), plotted on logarithmic scales. The vertical dashed lines indicate the physical limits of stellar masses ($M_{\min}$ and $M_{\max}$). This power law behavior emerges from the scale-invariant nature of the star formation process, where the same physical mechanisms operate across many orders of magnitude in mass. The negative slope indicates that lower-mass stars are much more numerous than high-mass stars, with the frequency decreasing by a factor of $\sim 10^{2.35} = 222$ for every factor of 10 increase in mass. The distribution is normalized over the finite mass range, though it appears as a simple straight line in log-log space.

Power laws appear across a wide range of astronomical contexts beyond stellar mass distributions. Galaxy luminosity functions, the distribution of cosmic structures, and even the energy distributions of particles in astrophysical plasmas all frequently follow power laws. This prevalence highlights the scale-invariant nature of many astronomical processes, where similar physical mechanisms operate across many orders of magnitude.

2.4   Joint and Conditional Probability

Real astronomical problems inherently involve multiple variables simultaneously. Even in the simplest scenario where we have just one parameter and one observable, we're already dealing with a pair of interrelated random variables that must be analyzed jointly. This multidimensional nature requires us to understand how different random variables relate to each other.

In practice, the dimensionality of astronomical problems tends to be much higher. Consider characterizing a stellar spectrum. We need multiple parameters to describe the physical properties of the star—its effective temperature, surface gravity, metallicity, rotational velocity, and potentially magnetic field strength. Meanwhile, our observational data consists of flux measurements spanning thousands of wavelength points across the spectrum, each with its own uncertainty. This creates a complex web of relationships between many variables that we must carefully untangle through statistical analysis.

This multidimensional nature leads us to need different ways of manipulating these variables. Sometimes we want to know what observations we expect given certain model parameters (forward modeling). Other times, we want to infer model parameters from our observations (inverse problem). To handle these scenarios mathematically, we need to understand joint and conditional probabilities.

Joint Probability   For two random variables x and y, their joint probability distribution $p(x, y)$ describes the probability of both variables taking specific values simultaneously. To understand this concept concretely, we examine how it manifests in both discrete and continuous cases in astronomy.

For discrete variables, joint probability has a straightforward interpretation. Consider classifying galaxies by both morphology (spiral/elliptical) and size (large/small). Here, $p(\text{spiral}, \text{large})$ simply represents the probability of finding a galaxy that is both spiral and large—a direct measure of the frequency of this specific combination in our galaxy population.

The concept extends naturally to continuous variables, though with an important distinction. Take the example of stars characterized by their temperature and luminosity. The joint probability distribution $p(T, L)$ maps out the probability density for finding stars across the temperature-luminosity space, giving rise to the familiar Hertzsprung-Russell

diagram. Here we see that not all combinations are equally likely—stars tend to cluster along the main sequence, reflecting the underlying physics of stellar evolution.

However, with continuous variables, the probability of any exact value pair is zero—just as it is for single continuous variables. To obtain meaningful probabilities, we must integrate over finite regions. For instance, the probability of finding a star with temperature between T_1 and T_2 and luminosity between L_1 and L_2 is given by:

$$P(T_1 \leq T \leq T_2, L_1 \leq L \leq L_2) = \int_{L_1}^{L_2} \int_{T_1}^{T_2} p(T, L) \, dT \, dL \tag{2.11}$$

Conditional Probability Unlike joint distribution, which describes the probability of both events occurring simultaneously, conditional probability addresses a different question: given that we know one event has occurred, what is the probability of another event? We write this conditional probability as $p(x|y)$, which reads as "the probability of x given y."

To make this concrete, consider our stellar example. The joint distribution $p(T, L)$ describes the overall distribution of stars in temperature-luminosity space. But suppose we observe a star and measure its temperature precisely. The conditional probability $p(L|T)$ would then tell us the distribution of possible luminosities for stars at that specific temperature. This "slice" through the joint distribution at a fixed temperature usually gives a much narrower range of likely luminosities than if we had no temperature information at all.

This concept of conditional probability is particularly important in statistical inference. The relationship between forward and inverse problems can be understood through two types of conditional probabilities:

- The forward problem: If we know the model parameters, what observations do we expect? This corresponds to calculating $p(\text{data}|\text{model})$.

- The inverse problem: Given our observations, what can we infer about the underlying model parameters? This corresponds to calculating $p(\text{model}|\text{data})$.

Understanding these two conditional probabilities—and how they relate to each other—is crucial for scientific inference. Our theories naturally predict observables from physical parameters (the forward direction), but we typically observe phenomena and want to infer their physical properties (the inverse direction). In the next section, we'll explore the mathematical rules that connect these different types of probabilities, ultimately leading to a formal
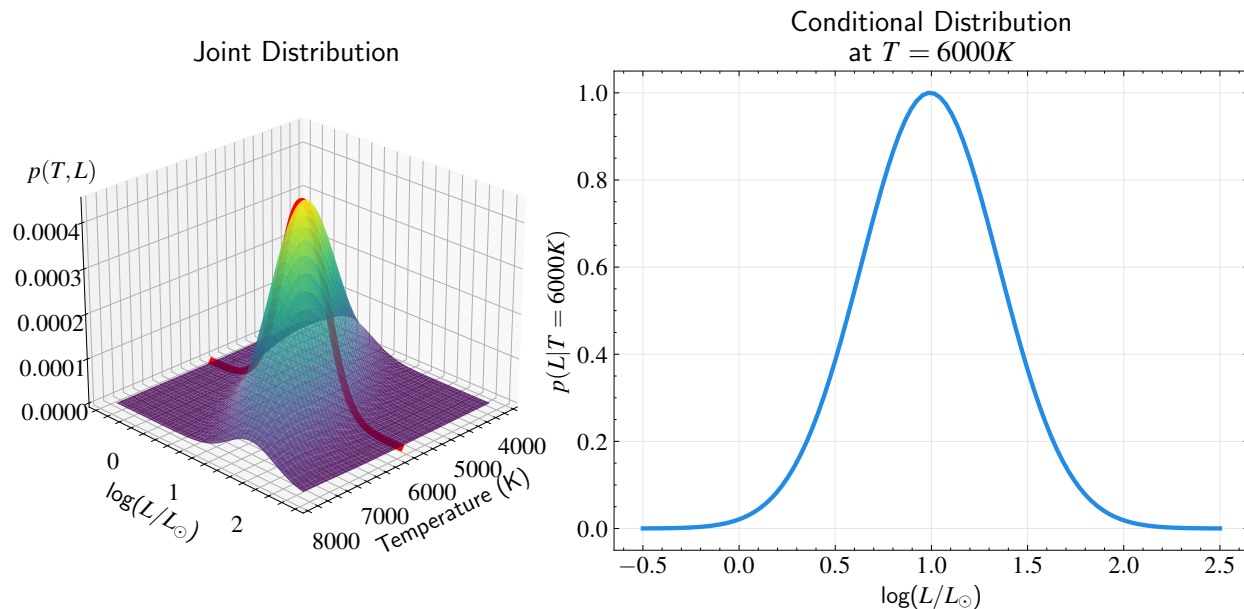
Figure 2.6: Illustration of joint and conditional probability distributions using stellar temperature and luminosity. The left panel shows the joint distribution $p(T, L)$ describing the probability density of finding stars with different combinations of temperature and luminosity. The red plane indicates a slice through the joint distribution at a fixed temperature $T = 6000$K. The right panel shows the corresponding conditional distribution $p(L|T = 6000$K$)$, representing the probability distribution of stellar luminosities for stars with temperature $T = 6000$K.

relationship between forward and inverse problems.

2.5   Probability Rules and Independence

Having introduced joint and conditional distributions, we now explore the mathematical relationships that govern how these probabilities relate to each other. These rules form the foundation for statistical inference and will allow us to derive one of the most important results in probability theory: Bayes' theorem.

The Sum Rule   Often we want to extract information about a single variable from a joint distribution that involves multiple variables. Returning to our stellar example: suppose we have the joint distribution $p(T, L)$ of stellar temperature and luminosity, but we are only interested in the distribution of luminosities, regardless of temperature. How do we obtain this?

This brings us to the concept of marginal distributions and the sum rule. A marginal distribution is what we get when we consider one variable while accounting for all possible

values of the other variables. The sum rule tells us how to compute this mathematically:

For discrete variables, if we want the probability of X taking a specific value x, we sum over all possible values of Y:

$$p(x) = \sum_y p(x, y) \tag{2.12}$$

For continuous variables, like in our stellar example, we integrate over all possible values of the other variable:

$$p(L) = \int p(T, L)\, dT \tag{2.13}$$

Here, $p(L)$ represents the probability of finding a star with luminosity L, taking into account all possible temperatures. We can visualize this as "collapsing" our 2D joint distribution along the temperature axis.

This marginalization process has important implications for analyzing multivariate data. For instance, when studying galaxies, we might have joint distributions of multiple properties—mass, star formation rate, metallicity, etc. The sum rule allows us to extract the distribution of any individual property by integrating over all the others. This capability is crucial when we want to compare our results with previous studies that may have focused on different subsets of properties.

The Product Rule Having understood how to obtain marginal distributions from joint distributions through the sum rule, we now turn to another relationship: the product rule. This rule tells us how joint probabilities relate to conditional probabilities:

$$p(x, y) = p(x|y)p(y) = p(y|x)p(x) \tag{2.14}$$

To understand this intuitively, consider our stellar example. The joint probability $p(T, L)$ of finding a star with both temperature T and luminosity L can be broken down in two equivalent ways:

1. We can first consider the probability $p(T)$ of finding a star with temperature T, and then multiply by the probability $p(L|T)$ of finding luminosity L given that temperature:

$$p(T, L) = p(L|T)p(T) \tag{2.15}$$
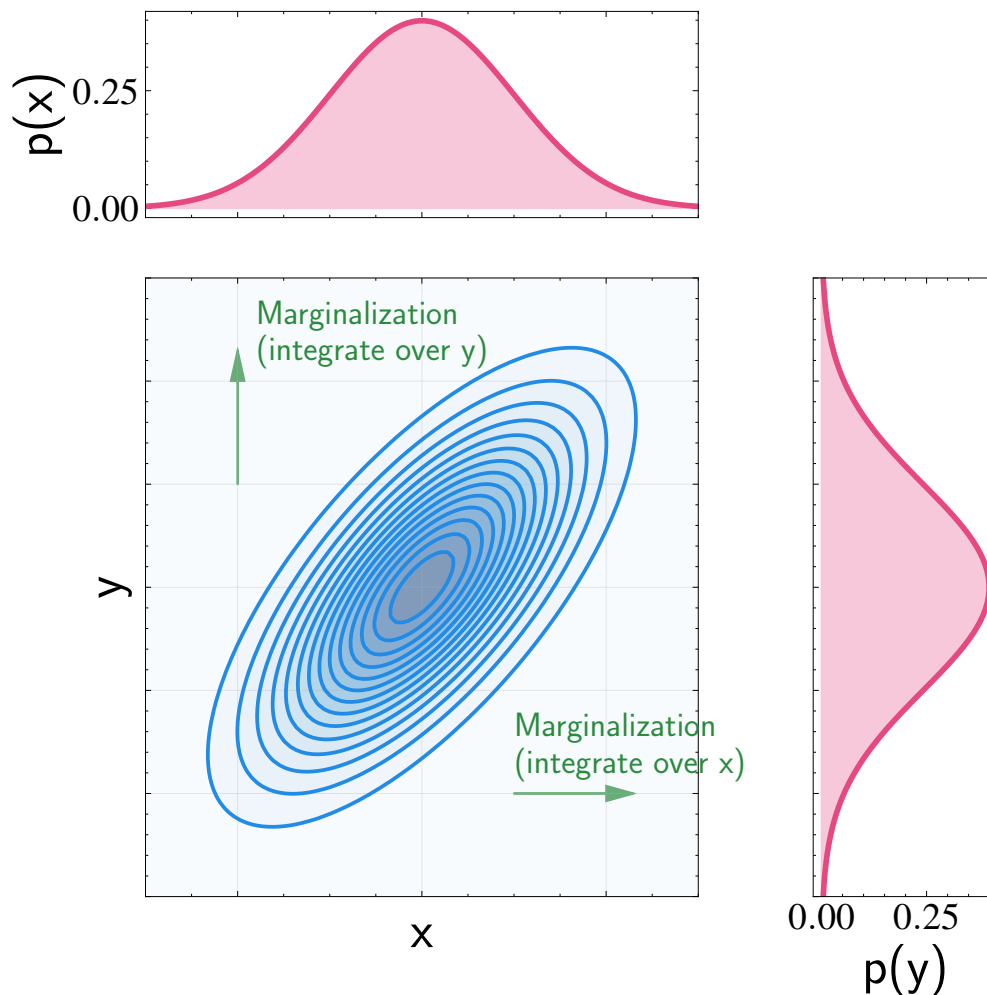
Figure 2.7: Visualization of marginalization for a bivariate Gaussian distribution. The central panel shows contours of a joint probability distribution $p(x, y)$ with positive correlation ($\rho = 0.7$). The top and right panels show the marginal distributions $p(x)$ and $p(y)$ respectively, obtained by integrating the joint distribution over the other variable. The green arrows indicate the marginalization process: integrating over y (vertical arrow) gives the marginal distribution of x (top panel), while integrating over x (horizontal arrow) gives the marginal distribution of y (right panel). This illustrates how marginalization reduces a multivariate distribution to its component distributions by accounting for all possible values of the marginalized variables.

2. Alternatively, we can first consider the probability $p(L)$ of finding a star with luminosity L, and then multiply by the probability $p(T|L)$ of finding temperature T given that luminosity:

$$p(T, L) = p(T|L)p(L) \tag{2.16}$$

The equality of these two expressions $(p(L|T)p(T) = p(T|L)p(L))$ is far more profound

than it might first appear. Consider what it tells us: while stellar evolution naturally gives us the probability of observing certain luminosities given a star's temperature ($p(L|T)$), we might actually want to infer temperature from an observed luminosity ($p(T|L)$). The product rule tells us these viewpoints are intimately connected—we can convert between them if we know the overall distributions of temperature and luminosity in the stellar population.

However, we note that the conditional probabilities $p(L|T)$ and $p(T|L)$ are generally not equal by themselves—knowing the probability of luminosity given temperature does not directly tell us the probability of temperature given luminosity. For example, a star with temperature 6000K might have an 80% chance of having luminosity between 0.5 and 2 solar luminosities, but observing a star with 1 solar luminosity might only give a 30% chance of it having temperature between 5800–6200K.

This asymmetry lies at the heart of scientific inference. Our theories naturally predict observables from physical parameters (forward direction), but we typically observe phenomena and want to infer their physical properties (inverse direction). The product rule, together with the sum rule, provides the mathematical foundation for rigorously connecting these complementary perspectives.

2.5.1   Independence

Having learned about the product rule, before discussing its connection with statistical inference in astronomy, we examine a final useful concept that we will encounter many times in this course. In many cases, when we have many different variables, it is advantageous to know if we can handle them separately without changing the conclusion of the inference. This leads to the concept of independence.

Two random variables X and Y are said to be independent if knowing the value of one variable provides no information about the other. Mathematically, this means that observing Y does not change our probability assessment of X:

$$P(X|Y) = P(X) \quad \text{for all values of } Y \tag{2.17}$$

This definition captures our intuitive notion of independence—if knowing Y tells us nothing new about X, then the probability of X should remain unchanged regardless of what value of Y we observe.

From this definition and the product rule, we can derive another key property of

independent variables. Recall that the product rule gives us:

$$P(X, Y) = P(X|Y)P(Y) \tag{2.18}$$

If X and Y are independent, then $P(X|Y) = P(X)$, so:

$$P(X, Y) = P(X)P(Y) \tag{2.19}$$

This means that for independent variables, the joint probability factorizes into a product of individual probabilities. While this factorization property is often used as the definition of independence, we see here that it follows naturally from our more intuitive definition involving conditional probabilities.

For continuous random variables, these equations still hold but with probability densities rather than probabilities. The interpretation remains the same—independence means knowing one variable tells us nothing about the other:

$$p(x|y) = p(x) \quad \text{leads to} \quad p(x, y) = p(x)p(y) \tag{2.20}$$

Consider a concrete astronomical example: the detection of photons from two widely separated stars. The arrival time of a photon from one star is independent of photon arrivals from the other star—knowing we just detected a photon from the first star tells us nothing about when we might detect one from the second star. Similarly, when counting stars in non-overlapping regions of the sky that are sufficiently far apart, the number of stars in one region is independent of the count in another region—this is why we can analyze different patches of the sky separately when studying stellar populations. In contrast, the temperature and luminosity of a star are not independent—knowing a star's temperature gives us significant information about its likely luminosity.

Independence has important practical implications for statistical analysis. When random variables are independent, we can analyze them separately, which often simplifies our calculations significantly. For example, if we have multiple independent measurements of the same quantity, the joint probability of all measurements is simply the product of the individual probabilities. This property is particularly valuable when dealing with large datasets, as it allows us to break complex problems into simpler, more manageable pieces.

However, we must be careful not to assume independence without justification—many
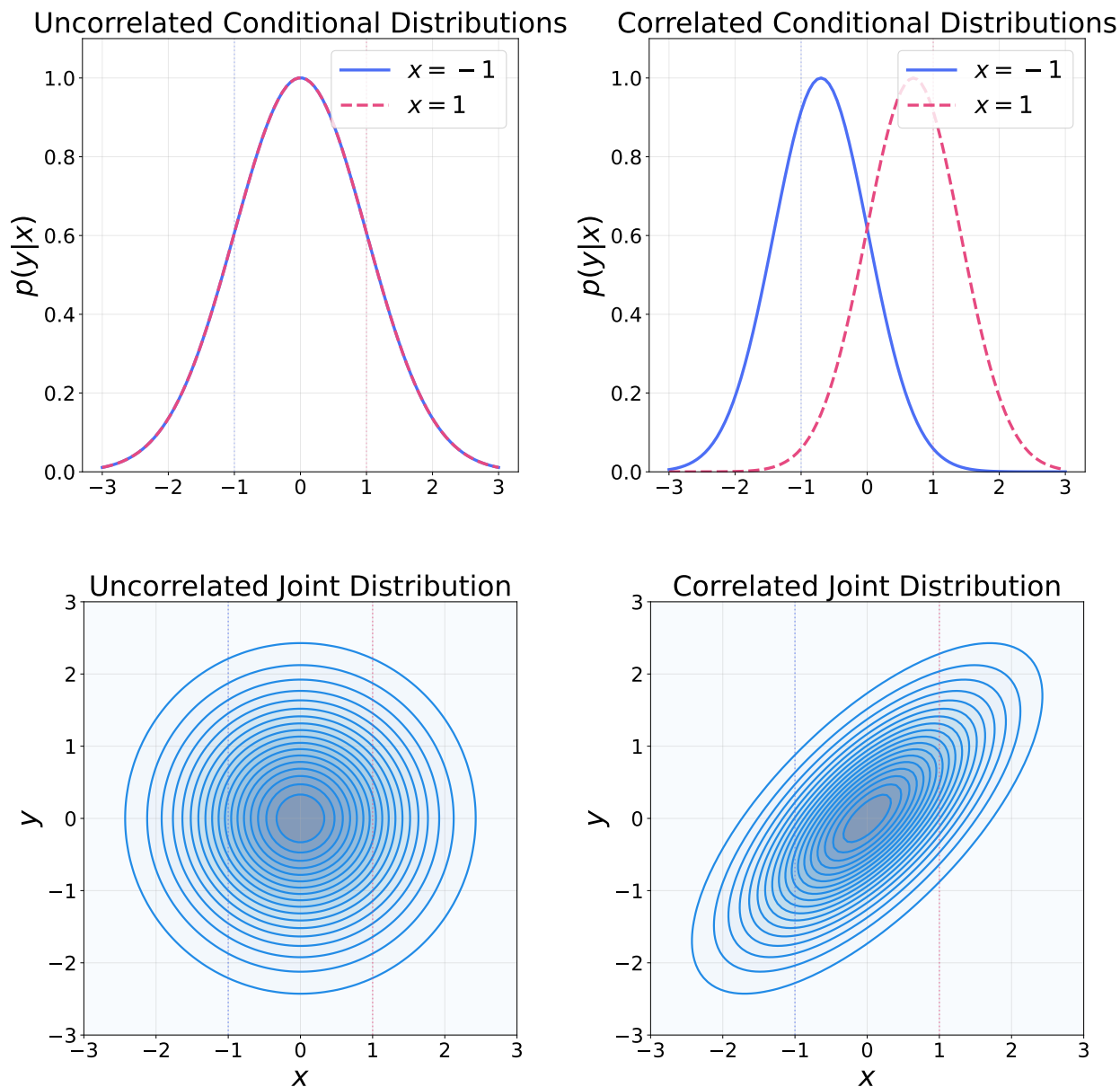
Figure 2.8: Visualization of dependent versus independent variables. Left panels show a case where the variables x and y are independent — note how the conditional distributions $p(y|x)$ remain identical regardless of the value of x. This means knowing x provides no information about y. Right panels show dependent variables where $p(y|x)$ changes with different values of x, demonstrating that knowledge of x informs our expectations about y. Top panels show the conditional distributions for two different values of x (solid blue line: $x = 1$, dashed red line: $x = -1$). Bottom panels show the corresponding joint distributions with vertical lines indicating where the conditional slices were taken.

astronomical properties are correlated in subtle but important ways. For example, in galaxy surveys, the properties of neighboring galaxies are often correlated due to their shared en-

vironment and formation history. Understanding when we can and cannot assume independence is crucial for proper statistical analysis in astronomy.

These rules—the sum rule, product rule, and concept of independence—will become essential tools as we develop statistical inference methods for astronomical data analysis. In the next section, we'll see how these rules lead directly to one of the most powerful tools in statistics: Bayes' theorem.

2.6   Frequentist and Bayesian Approaches

With our probability foundation established, we can now examine two different philosophical approaches to statistical inference: frequentist and Bayesian. Understanding this distinction is crucial because astronomy's unique challenges often necessitate a Bayesian perspective, and this choice affects how we approach machine learning problems in astronomical contexts.

The Frequentist Approach   At its core, the frequentist approach, as the name suggests, defines probability through the concept of repeated experiments (hence frequency). Consider a simple example: determining if a die is fair. A frequentist would roll the die many times and plot the relative frequency of each outcome. As the number of rolls increases, these frequencies should converge to 1/6 for each face if the die is fair. This convergence, known as the law of large numbers, forms the foundation of frequentist probability—given enough trials, the sample average approaches the true population parameter.

This approach is not just mathematically rigorous; it is also intuitive. In many scientific contexts outside astronomical research, particularly in laboratory physics, we can indeed repeat experiments many times under controlled conditions. Each trial is independent, and our statistical uncertainties decrease predictably with the square root of the number of measurements—a direct consequence of the Central Limit Theorem.

One of the clearest demonstrations of the frequentist framework is the confidence interval. A 95% confidence interval means that if we could repeat our experiment many times, about 95% of similarly constructed intervals would contain the true parameter value. Notice how this interpretation relies on the concept of hypothetical repeated experiments—we are making a statement about the procedure's long-run behavior, not about our degree of belief in the parameter value itself.

However, astronomy often presents unique challenges that strain this frequentist framework. The main issue is that in many contexts, we simply cannot repeat the experiment. For example, when we try to constrain cosmological parameters like the densities of dark matter and dark energy, we have only one observable universe. Many astronomical questions involve unique objects or events—the mass of the Milky Way's supermassive black hole, the cause of a particular supernova, or the formation history of our Solar System. In these cases, the concept of "what would happen if we ran this experiment many times" becomes philosophical rather than practical.

These challenges do not mean frequentist methods are never useful in astronomy—they remain valuable tools, particularly when analyzing large surveys where we do have many similar objects, or when characterizing random measurement uncertainties. However, they do explain why astronomers often need additional tools beyond the frequentist framework, particularly when dealing with unique systems or complex systematic uncertainties. This limitation of frequentist statistics in astronomical contexts leads us naturally to consider alternative approaches—the Bayesian approach.

The Bayesian Approach

Core Idea   Bayesian inference asks a different question: given our current knowledge and observations, what can we reasonably infer about the underlying physical system and how should we update these inferences when new data becomes available? Unlike the frequentist approach where there is an inherent asymmetry between observations and the true model—where we aim to approach such truth with larger samples of repeated experiments—the key insight from Thomas Bayes was to treat both the observations and model parameters on equal footing. Both are random variables playing similar roles; they are simply two sides of the same coin.

This treatment of model parameters as uncertain might seem unsettling at first. After all, in physics and astronomy, we believe there are true underlying physical laws governing the universe—the true equation of state of dark energy, the true mass of the Milky Way's supermassive black hole, or the true mechanism driving galaxy evolution. The Bayesian view does not deny the existence of these truths. Rather, it acknowledges that our knowledge of them is inherently uncertain because our observations and theoretical understanding are always incomplete. When we are limited by finite samples (as with our one observable universe) or systematic uncertainties, we can never be absolutely certain about our models.

Our "belief" in our theories should therefore be treated as a random variable itself. This probability distribution representing our state of knowledge will become more sharply peaked as more evidence accumulates, but some uncertainty will always remain. This captures how science progresses: through continuous refinement and updating of our understanding rather than achieving absolute certainty.

In a way, this perspective forms the foundation of modern scientific inquiry itself. Science is not just a collection of facts; it is a process of constantly updating our beliefs and acknowledging the limitations and uncertainties in our models. This is precisely how we make progress—by quantifying our uncertainty and understanding how it changes as we gather new evidence.

Mathematical Formalism   The mathematical framework behind Bayes' theorem is remarkably simple, emerging naturally from the probability rules we established earlier. At its core, Bayes' theorem emerges naturally from the product rule we established earlier. For two random variables $\mathbf{x}$ and $\mathbf{y}$, recall that the product rule gives us two equivalent ways to write their joint probability:

$$p(\mathbf{x}, \mathbf{y}) = p(\mathbf{x}|\mathbf{y})p(\mathbf{y}) = p(\mathbf{y}|\mathbf{x})p(\mathbf{x}) \tag{2.21}$$

This symmetry in the product rule leads directly to Bayes' theorem. Since both expressions equal the joint probability, we can write:

$$p(\mathbf{x}|\mathbf{y})p(\mathbf{y}) = p(\mathbf{y}|\mathbf{x})p(\mathbf{x}) \tag{2.22}$$

And therefore:

$$p(\mathbf{x}|\mathbf{y}) = \frac{p(\mathbf{y}|\mathbf{x})p(\mathbf{x})}{p(\mathbf{y})} \tag{2.23}$$

The beauty of this result lies in its generality—since both $\mathbf{x}$ and $\mathbf{y}$ are treated as random variables, neither plays a privileged role. This symmetry allows us to reverse the direction of conditioning, a capability that proves invaluable in data analysis. To see why, we apply this to astronomical research by denoting our observational data as $\mathcal{D}$ and our model parameters as $\boldsymbol{\theta}$. Despite the simple formula, both can be remarkably complex—$\mathcal{D}$ might contain millions of data points from a large survey, while $\boldsymbol{\theta}$ might encompass hundreds of

parameters describing intricate physical processes. Bayes' theorem then becomes:

$$p(\boldsymbol{\theta}|\mathcal{D}) = \frac{p(\mathcal{D}|\boldsymbol{\theta})p(\boldsymbol{\theta})}{p(\mathcal{D})} \tag{2.24}$$

While this equation might appear to be just algebraic manipulation, its implications run deep. Each term has a specific interpretation in scientific inference:

1. $p(\boldsymbol{\theta}|\mathcal{D})$ is the **posterior distribution**: This represents our updated knowledge about the model parameters after seeing the data. It tells us which combinations of parameters are most likely to explain our observations. The posterior distribution does not just give us the best-fit parameters—it provides a complete picture of our uncertainty about them.

2. $p(\mathcal{D}|\boldsymbol{\theta})$ is the **likelihood function**: This quantifies how well our model explains the observed data. For any specific choice of model parameters, how likely are we to observe the actual data we measured? The likelihood function is our mathematical bridge between model predictions and reality.

3. $p(\boldsymbol{\theta})$ is our **prior distribution**: This encodes what we know about the model parameters before considering the data. This might include knowledge that certain parameter values are physically unreasonable, or that we expect parameters to fall within certain ranges based on previous studies. The prior allows us to formally incorporate existing scientific knowledge.

4. $p(\mathcal{D})$ is the **evidence**: This represents the total probability of observing our data under all possible parameter values. While crucial for model comparison, it acts as a normalization constant when we are focused on parameter estimation.

While we will return to discuss the evidence term $p(\mathcal{D})$ when exploring information criteria and model selection, since this term does not depend on $\boldsymbol{\theta}$, it acts as a constant in parameter estimation. Therefore, throughout this course and in many practical applications, we often work with the proportional form:

$$p(\boldsymbol{\theta}|\mathcal{D}) \propto p(\mathcal{D}|\boldsymbol{\theta})p(\boldsymbol{\theta}) \tag{2.25}$$

To understand how this framework guides scientific inference, imagine we propose a particular set of model parameters $\boldsymbol{\theta}$. We can ask: how likely are we to observe our

actual data $\mathcal{D}$ if these were the true parameter values? Models that maximize $p(\mathcal{D}|\boldsymbol{\theta})$ (high likelihood) become more probable in our posterior distribution $p(\boldsymbol{\theta}|\mathcal{D})$. This mirrors how we evaluate scientific theories more broadly—like understanding that Earth is round because this model better explains observations of ships disappearing hull-first over the horizon or the circular shadow during lunar eclipses.

The Bayesian approach offers several advantages for astronomical inference:

- It provides a complete characterization of parameter uncertainties through the posterior distribution, not just point estimates.

- It naturally incorporates prior knowledge from previous studies or physical constraints.

- It applies consistently regardless of sample size—we can make inferences from a single observation or millions of data points using the same framework.

- It offers a natural way to compare different models through the evidence term $p(\mathcal{D})$.

- It allows for hierarchical modeling, where parameters themselves might depend on higher-level parameters.

These advantages make Bayesian inference particularly well-suited to the challenges of astronomical data analysis, where we often have limited observations of unique phenomena and need to incorporate theoretical constraints with empirical evidence.

2.7   Bayesian Inference in Practice

One of the powerful implications of treating model parameters as random variables is that Bayesian inference can handle scenarios with limited data—even a single observation. This capability is particularly valuable in astronomy where, as we discussed earlier, many phenomena cannot be repeatedly observed under controlled conditions. We explore this through two concrete examples that will bridge our understanding between the theoretical framework and practical applications.

2.7.1   Inference with One Data Point

The Die Example   Consider four competing models for a die's behavior, which we call Fair, Bad, Worse, and Worst. Each model makes specific predictions about the probability of each outcome:

Outcome	Fair	Bad	Worse	Worst
6	1/6	1/8	1/12	1/20
5	1/6	1/8	1/12	1/20
4	1/6	1/6	1/8	1/10
3	1/6	1/6	1/6	1/8
2	1/6	5/24	1/4	1/5
1	1/6	5/24	1/3	1/2

Table 2.1: Probability distributions for different die models. Each column represents a different hypothesis about the die's behavior, with Fair representing an unbiased die and successive models showing increasing bias toward lower numbers.

Under the Fair model, each outcome has equal probability ($p(\mathcal{D} = i|\boldsymbol{\theta} = \text{Fair}) = \frac{1}{6}$ for all i). The Bad model shows slight bias toward lower numbers, while the Worse and Worst models show progressively stronger bias. Note that for each model $\boldsymbol{\theta}$, the probabilities $p(\mathcal{D}|\boldsymbol{\theta})$ must sum to one—this is reflected in how each column in our table sums to unity, ensuring proper normalization of the probability distribution.

Now, imagine we roll the die exactly once and observe a 6. A frequentist approach would struggle with a single data point. However, Bayesian inference provides a natural framework for updating our beliefs. If we begin with equal prior probabilities for each model ($p(\boldsymbol{\theta} = \text{Fair}) = p(\boldsymbol{\theta} = \text{Bad}) = p(\boldsymbol{\theta} = \text{Worse}) = p(\boldsymbol{\theta} = \text{Worst}) = \frac{1}{4}$), Bayes' theorem gives us:

$$p(\boldsymbol{\theta}|\{6\}) \propto p(\{6\}|\boldsymbol{\theta})p(\boldsymbol{\theta}) \tag{2.26}$$

Since we have equal priors $p(\boldsymbol{\theta}) = \text{constant}$, our posterior belief $p(\boldsymbol{\theta}|\mathcal{D} = \{6\})$ is proportional to the likelihood $p(\mathcal{D} = \{6\}|\boldsymbol{\theta})$. This likelihood can be read directly from the first row of our table, as it represents the probability of rolling a 6 under each model. The evidence term $p(\mathcal{D})$ in Bayes' theorem, while not affecting our relative beliefs about different models, serves as a proper normalization constant. In other words, while each column (representing $p(\mathcal{D}|\boldsymbol{\theta})$ for fixed $\boldsymbol{\theta}$) must sum to one, this constraint does not apply to rows. Therefore, to obtain proper posterior probabilities, we must normalize our likelihoods by dividing by their sum across all models.

For our single roll of 6, the likelihoods are:

- Fair: $1/6 = 0.167$

- Bad: $1/8 = 0.125$

- Worse: $1/12 = 0.083$

- Worst: $1/20 = 0.050$

The sum of these likelihoods is 0.425, so our posterior probabilities are:

- $p(\text{Fair}|\{6\}) = 0.167/0.425 = 0.393$

- $p(\text{Bad}|\{6\}) = 0.125/0.425 = 0.294$

- $p(\text{Worse}|\{6\}) = 0.083/0.425 = 0.195$

- $p(\text{Worst}|\{6\}) = 0.050/0.425 = 0.118$

Notice how our beliefs have shifted: we started with equal probability (0.25) for each model, but after observing a single 6, we now favor the Fair model (0.393) and consider the Worst model least likely (0.118). This makes intuitive sense—observing a 6 is most consistent with the Fair model and least consistent with the Worst model, which heavily favors lower numbers.

If we now observe two more outcomes, say 1 and 4, our likelihood becomes $p(\{6, 1, 4\}|\boldsymbol{\theta})$. Since die rolls are independent events (by the definition of independence we discussed earlier), this joint likelihood naturally factorizes:

$$p(\{6, 1, 4\}|\boldsymbol{\theta}) = p(\{6\}|\boldsymbol{\theta})p(\{1\}|\boldsymbol{\theta})p(\{4\}|\boldsymbol{\theta}) \tag{2.27}$$

Calculating this product for each model:

- Fair: $\frac{1}{6} \times \frac{1}{6} \times \frac{1}{6} = \frac{1}{216} \approx 0.0046$

- Bad: $\frac{1}{8} \times \frac{5}{24} \times \frac{1}{6} \approx 0.0043$

- Worse: $\frac{1}{12} \times \frac{1}{3} \times \frac{1}{8} \approx 0.0035$

- Worst: $\frac{1}{20} \times \frac{1}{2} \times \frac{1}{10} = \frac{1}{400} = 0.0025$

Normalizing these values, our updated posterior probabilities become:

- $p(\text{Fair}|\{6, 1, 4\}) \approx 0.31$

- $p(\text{Bad}|\{6, 1, 4\}) \approx 0.29$

- $p(\text{Worse}|\{6, 1, 4\}) \approx 0.23$

- $p(\text{Worst}|\{6, 1, 4\}) \approx 0.17$

The results are now more balanced between the models. While the Fair model still has the highest probability, the difference between models has decreased. This makes sense because we observed a mixture of high (6) and low (1) values, which is somewhat consistent with all the models.

This example illustrates a key strength of Bayesian inference: as long as we can specify the probability of observations under different models (the likelihood), we can update our beliefs even with minimal data. The approach handles any amount of data naturally—from a single observation to thousands of data points—through the same consistent framework.

Fitting a Gaussian with One Data Point   The same principle of performing inference with limited data extends to continuous parameters in astronomy. Consider measuring some astronomical quantity that we believe follows a Gaussian distribution with known standard deviation σ but unknown mean μ. In the frequentist approach, we would take many measurements and use their average as our best estimate. But what if we only have one or two measurements? This is where Bayesian inference becomes particularly valuable.

In this scenario, our model parameter is the unknown mean μ. For simplicity, we'll fix $\sigma = 1$, giving us a standardized Gaussian. Suppose we make a single measurement $x = 6$. Just as with our die example, we can apply Bayes' theorem:

$$p(\mu|\mathcal{D} = \{6\}) \propto p(\mathcal{D} = \{6\}|\mu)p(\mu) \tag{2.28}$$

But instead of having a "look-up" table as we did with the die, the likelihood function $p(\mathcal{D} = \{6\}|\mu)$ in this case is:

$$p(x = 6|\mu) = \frac{1}{\sqrt{2\pi\sigma^2}} \exp\left(-\frac{(6 - \mu)^2}{2\sigma^2}\right) \tag{2.29}$$

That is, if we were to "propose" a value for μ, the probability of observing the value 6 would be the evaluation of the Gaussian PDF with this μ at $x = 6$, following directly from the definition of probability density functions.

In the first figure, we see how different proposed values of μ lead to different prob-
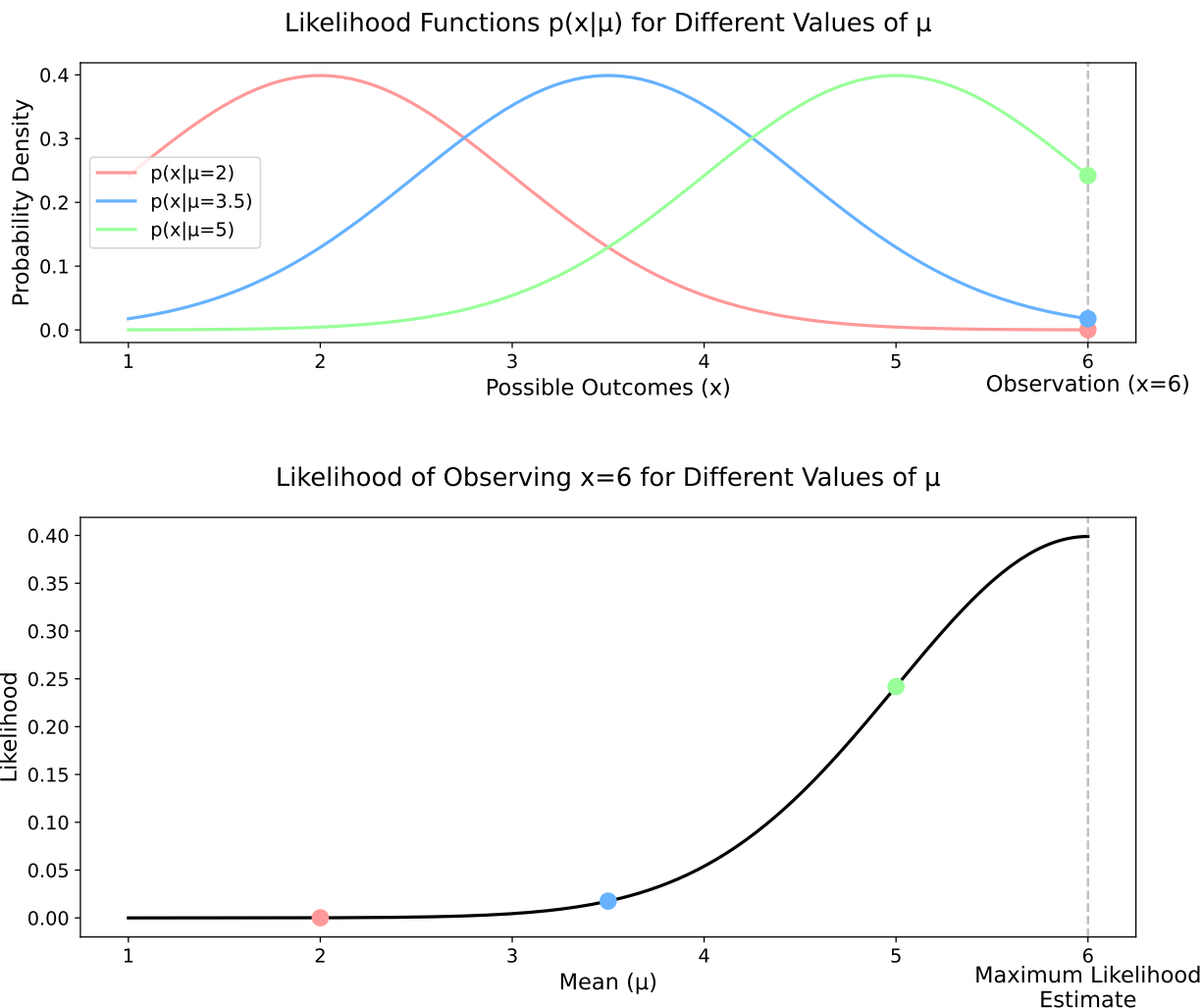
Figure 2.9: Top panel: Likelihood functions $p(x|\mu)$ for different proposed values of μ. When $\mu = 2$ (red curve), the probability of measuring $x = 6$ is very low. When $\mu = 5$ (green curve), this probability is much higher. Bottom panel: The likelihood $p(\{6\}|\mu)$ as a function of μ, showing how likely each proposed mean value is given our single observation. This likelihood is proportional to our posterior distribution (assuming an uninformative prior). The maximum occurs at $\mu = 6$, which makes intuitive sense—with a single measurement and no informative prior, our best estimate for the mean would be exactly what we measured.

abilities of observing our measurement $x = 6$. When $\mu = 2$, the probability of measuring $x = 6$ is very low, as shown by the small value of the red curve at $x = 6$. When $\mu = 5$, the probability is much higher, as shown by the larger value of the green curve at $x = 6$.

The bottom panel shows the likelihood for each proposed value of μ, given our single observation. This is proportional to our posterior distribution (before considering the prior or assuming an uninformative prior). The maximum likelihood estimate occurs at $\mu = 6$,

which makes intuitive sense—with a single measurement and no informative prior, our best estimate for the mean would be exactly what we measured.

We purposely fixed σ here because, given a single data point, the maximum likelihood estimate for σ would tend toward zero—essentially trying to create an infinitely narrow Gaussian centered at 6 (unless we assume a reasonable prior that prevents this degenerate solution).

The scenario becomes more interesting with multiple measurements. Suppose we make a second measurement $x = 4$. Because our measurements are independent (assuming uncorrelated measurement errors), we can multiply the individual likelihoods:

$$p(x_1, x_2|\mu) = p(x_1|\mu)p(x_2|\mu) \tag{2.30}$$

The second figure shows the individual likelihood functions for different values of μ, with vertical lines marking our two observations. The bottom panel shows the joint likelihood—the probability of observing both measurements for each proposed value of μ. Notice how the maximum likelihood estimate has shifted to $\mu = 5$, the average of our two measurements. This illustrates a key principle: as we gather more data, our posterior distribution must account for all available information while becoming more concentrated, reflecting our increasing certainty about the parameter we are trying to estimate.

If we were to add a third measurement, say $x = 5$, our likelihood would become:

$$p(x_1, x_2, x_3|\mu) = p(x_1|\mu)p(x_2|\mu)p(x_3|\mu) \tag{2.31}$$

The maximum likelihood estimate would now be $\mu = 5$, the average of our three measurements (4, 5, and 6). More importantly, the likelihood curve would become narrower, indicating increased confidence in our estimate. This narrowing reflects the principle that uncertainty decreases as we collect more data—a property that emerges naturally from the Bayesian framework.

Implications for Scientific Inference   The examples above illustrate several implications of the Bayesian approach for scientific reasoning. First and foremost, by treating model parameters as random variables, Bayesian inference allows us to handle any amount of data (evidence), regardless of whether we can repeat the experiment—a capability that is particularly valuable in astronomy. While the examples we've explored are deliberately simple,
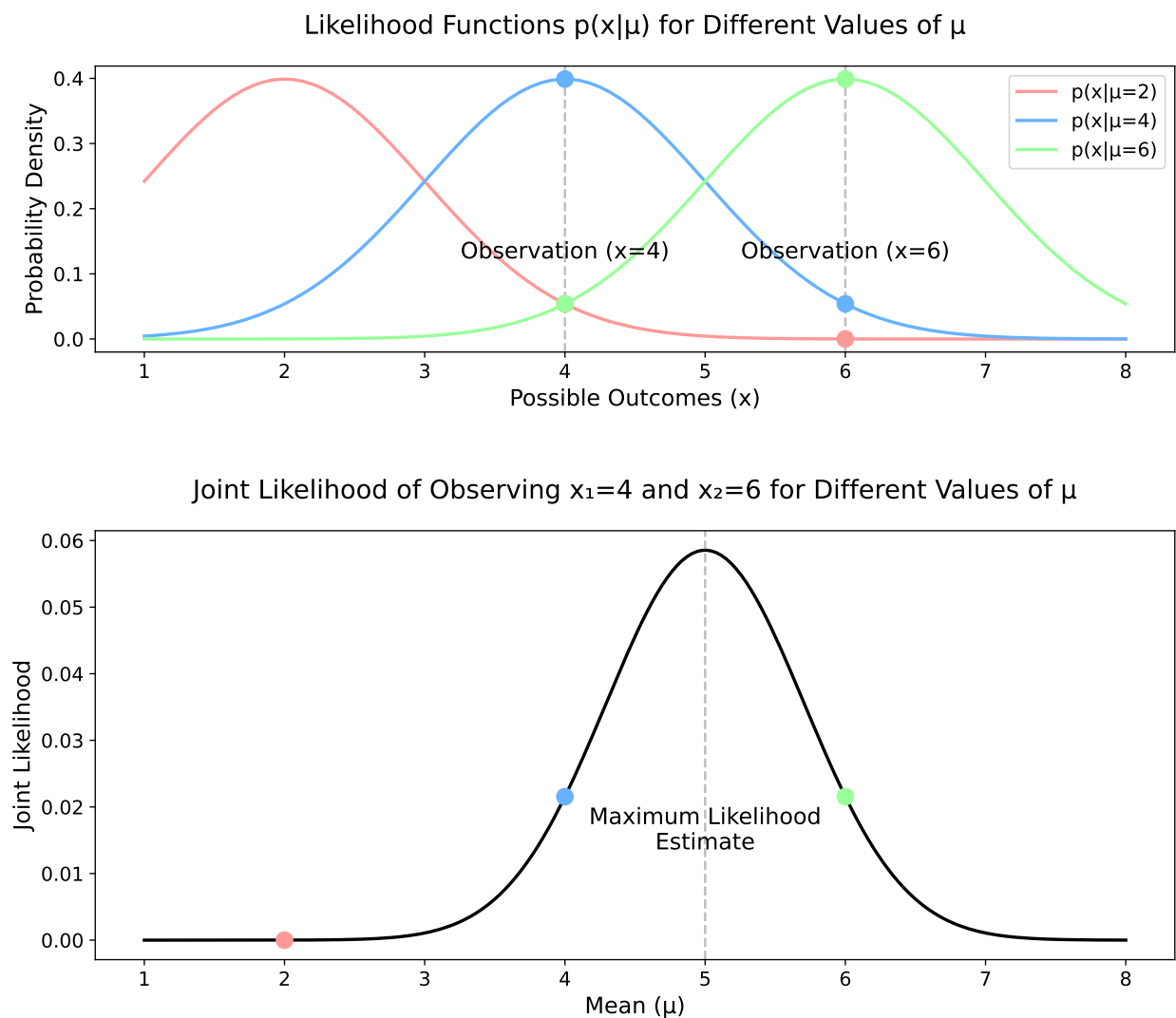
Figure 2.10: Top panel: Individual likelihood functions for different values of μ, with vertical lines marking our two observations at $x = 4$ and $x = 6$. Bottom panel: The joint likelihood—showing how the probability of observing both measurements varies with μ. The maximum likelihood estimate occurs at $\mu = 5$, the average of our two measurements.

the same principles apply to complex models with many parameters, where the posterior distribution becomes a high-dimensional probability distribution over parameter space.

In the die example, we saw how Bayesian inference allows us to rationally update our beliefs about different models as we gather more evidence. Even with a single data point, we could quantify the relative plausibility of each model. With the Gaussian example, we saw how our uncertainty about the mean parameter decreases as we gather more measurements—a natural consequence of the likelihood function becoming more concentrated.

A key advantage of the Bayesian approach is its ability to incorporate prior knowledge. While we used uninformative priors in our examples, we could have specified more informative priors based on previous studies or theoretical constraints. For instance, if previous surveys suggested that our Gaussian mean should be close to 3, we might use a prior like $p(\mu) = \mathcal{N}(\mu|3, 1)$. This would pull our posterior toward 3, especially when we have limited data. As we gather more data, the likelihood would typically dominate the prior, reducing its influence on our final conclusions.

The requirement to specify priors—while sometimes viewed as a limitation—can actually be seen as a strength. The interplay between prior knowledge $p(\boldsymbol{\theta})$ and new evidence $p(\mathcal{D}|\boldsymbol{\theta})$ is particularly relevant for extraordinary claims in science. As Carl Sagan famously noted, "extraordinary claims require extraordinary evidence." In Bayesian terms, this means that overcoming a strong skeptical prior (like our prior against the existence of faster-than-light travel) requires correspondingly strong evidence in the likelihood term $p(\mathcal{D}|\boldsymbol{\theta})$. This formalism thus captures both the open-mindedness and skepticism essential to scientific inquiry.

The examples we have explored—both the die and the Gaussian—represent deliberately simple cases to illustrate the core principles of Bayesian inference. Throughout this textbook, we will see how this mathematical framework provides the foundation for more sophisticated machine learning methods in astronomical data analysis. However, the logic of updating our beliefs about model parameters based on observed data remains analogous to what we have seen here. Despite their simplicity, these examples deserve careful consideration as they embody the core principles that will guide our exploration of more complex methods.

2.8   Summary

This chapter has established the probability theory framework that underlies the Bayesian approach to inference—a foundation that will support all machine learning techniques we explore throughout this textbook.

We began by distinguishing between deterministic and random variables, emphasizing the key Bayesian insight that treating model parameters as random variables provides a principled way to handle uncertainty in scientific inference. While model parameters like a galaxy's mass or a star's temperature may have true, definite values in reality, our knowledge of these values is inherently uncertain. The probability distributions we assign to parameters

represent our state of knowledge, not any inherent randomness in the parameters themselves.

We examined three probability distributions that appear frequently in astronomical applications. The Gaussian distribution emerges when only mean and variance are known, naturally arising from the Central Limit Theorem when many small, independent effects combine. The Poisson distribution describes counting processes with independent events occurring at constant average rates, crucial for modeling photon detection and galaxy counts. Power law distributions appear in scale-invariant processes, exemplified by the stellar Initial Mass Function where the same physical mechanisms operate across many orders of magnitude.

The concepts of joint and conditional probability provide the mathematical foundation for connecting observations with physical models in Bayesian inference. The sum rule enables us to obtain marginal distributions by integrating over unwanted variables—a process essential for analyzing high-dimensional posterior distributions. The product rule reveals the relationship between joint and conditional probabilities and leads directly to Bayes' theorem. The concept of independence, where knowledge of one variable provides no information about another, helps simplify calculations when applicable but must be applied carefully in astronomical contexts where many properties are subtly correlated.

We contrasted frequentist and Bayesian approaches to probability and inference. The frequentist approach defines probability through repeated experiments and relies on the law of large numbers, providing powerful tools when experiments can be replicated under controlled conditions. However, astronomy presents unique challenges where many phenomena cannot be repeated—we have only one observable universe for cosmological studies, and many astronomical objects and events are inherently unique.

The Bayesian approach addresses these limitations by treating both observations and model parameters as random variables. Bayes' theorem, emerging naturally from the product rule, provides a framework for updating our beliefs about model parameters as new evidence becomes available. The posterior distribution represents our updated knowledge, computed from the likelihood (how well our model explains the data) and our prior beliefs. This approach quantifies how extraordinary claims require extraordinary evidence through the interplay between priors and likelihood.

Through concrete examples—from discrete die models to continuous Gaussian parameter estimation—we demonstrated that Bayesian inference can handle any amount of data, even single observations. The posterior distribution provides a complete characterization of

our uncertainty, becoming more concentrated as we gather more evidence. While the requirement to specify priors might seem like a limitation, it actually makes our assumptions explicit and provides a principled way to incorporate existing scientific knowledge.

The probabilistic framework we have developed serves as the foundation for all machine learning methods we will explore in subsequent chapters. In Chapter 3, we will build on these concepts by exploring summary statistics as practical tools for characterizing probability distributions. These summary statistics will prove crucial for understanding how uncertainty propagates through calculations—a key consideration for Bayesian machine learning applications.

As we progress through later chapters on linear regression, classification, clustering, and more advanced techniques, we will see how each method implements the central Bayesian principle of updating our beliefs about model parameters based on observed data. The treatment of parameters as random variables—established in this chapter—will remain the unifying thread throughout our exploration of machine learning for astronomical data analysis.

Further Readings: The development of Bayesian inference has evolved through centuries of mathematical and philosophical contributions, with foundational early work including Bayes' posthumous essay Bayes [1763] on inverse probability. For readers interested in theoretical foundations, Jaynes [2003] presents an influential perspective on probability theory as an extension of logic, exploring connections between Bayesian methods and scientific reasoning. Box and Tiao [1973] offered systematic treatment of applied Bayesian methods, while Gelman et al. [2013] serves as a modern reference connecting theory with practice through examples and computational techniques. The field has seen particular development in astronomical applications: Loredo [1992] helped establish Bayesian methods in modern astronomy through practical demonstrations including supernova analysis, while Gregory [2005] focuses on astronomical applications, comparing frequentist and Bayesian approaches with field-specific examples. For accessible introductions to the subject, Sivia and Skilling [2006] provide a tutorial approach with physical science examples. Trotta [2008] reviews the adoption of Bayesian methods in cosmology, synthesizing theoretical and practical developments across the field. More recent contributions include Eadie et al. on practical implementation aspects in astronomy, and Thrane and Talbot [2019] on Bayesian methods in gravitational-wave astronomy, covering parameter estimation, model selection, and hierarchical models.

Chapter 3

Statistical Foundations and Summary Statistics

In our previous chapter, we explored the concepts of random variables and probability distributions, establishing a mathematical framework for handling uncertainty in data analysis. We examined how treating both our observations and model parameters as random variables naturally leads to Bayesian inference—an approach that has become central to modern research.

However, we left a critical question unanswered: how do we extract meaningful information from probability distributions in practice? The machine learning methods we'll explore in subsequent chapters—from linear regression to Bayesian inference—all depend on our ability to characterize and manipulate probability distributions using finite datasets.

This foundation requires us to address a challenge that directly impacts every machine learning algorithm: how do we reliably extract distributional information from finite, noisy data? Our observations are always limited and uncertain, which means our models and inferences must also carry uncertainty. We never observe the probability distributions we want to characterize—only finite samples drawn from them. When studying any astronomical population, we don't see the theoretical distribution directly, but rather a limited collection of measurements with their own uncertainties.

This sampling limitation becomes particularly acute when we consider the specific demands of machine learning methods. For example, linear regression, which we'll explore in Chapter 4, requires us to estimate means, variances, and covariances from data to determine

optimal model parameters and quantify their uncertainties. When we fit a relationship like the M-σ relation between black hole mass and stellar velocity dispersion, we need to characterize not just the best-fit line, but also our confidence in that fit and our ability to make predictions for new observations.

Bayesian inference, which we'll develop in Chapter 5, further demands that we characterize not just point estimates but complete probability distributions over parameters. This requires robust methods for uncertainty quantification that can distinguish between measurement noise (irreducible randomness in our data) and genuine model uncertainty (our incomplete knowledge of parameters)—a distinction crucial for scientific interpretation and model comparison.

The solution lies in summary statistics—mathematical tools that capture essential characteristics of probability distributions while being reliably estimable from finite samples. Rather than attempting to reconstruct full distributions (often impossible with limited data), we focus on key features that contain the information needed for machine learning: expectations that reveal central tendencies and enable parameter estimation, variances that quantify scatter and measurement precision, and covariances that capture relationships between different observed quantities.

This requires developing a precise mathematical language for discussing these concepts. This chapter develops these statistical foundations systematically, beginning with the expectation operator and moments of distributions. We show how the first moment (expectation) captures central tendencies while higher moments reveal increasingly detailed information about distribution shapes. We then explore how these statistics behave under mathematical transformations, developing the machinery needed for error propagation and uncertainty quantification that will prove essential for linear regression parameter estimation and prediction uncertainties.

The framework culminates in understanding how uncertainties combine when we perform common analytical operations: averaging multiple measurements, combining different datasets, and propagating uncertainties through calculations. Every concept we develop here directly enables the machine learning applications in subsequent chapters. The expectation and variance we study become the mathematical foundation for understanding how linear regression minimizes prediction errors through least-squares optimization. The covariance structures we explore reveal how different measured quantities relate to each other, enabling us to build predictive models and understand their limitations.

3.1 Moments of Distributions

To characterize probability distributions for machine learning applications, we need mathematical tools that capture essential distributional properties. Among the various approaches available, moments of a distribution provide a systematic framework that directly supports the parameter estimation and uncertainty quantification needed for machine learning algorithms.

For a random variable X with probability distribution $p(x)$, we define the kth moment as:

$$\text{Discrete case:} \quad \mu_k = \sum_x x^k p(x), \tag{3.1}$$

$$\text{Continuous case:} \quad \mu_k = \int x^k p(x) dx. \tag{3.2}$$

These expressions are often written in a more compact notation using the expectation operator:

$$\mu_k = \mathbb{E}[x^k], \tag{3.3}$$

where $\mathbb{E}[\cdot]$ denotes the expectation (or average) of a quantity weighted by its probability distribution. This notation represents averaging over the probability distribution of a random variable and will be central to the mathematical framework we develop throughout this chapter.

For discrete variables, we sum over the finite or countably infinite possible values, with $p(x)$ representing the probability mass function. For continuous variables, we integrate over the continuous range of possible values, with $p(x)$ representing the probability density function. This distinction is necessary because continuous variables have zero probability of taking any exact value—we must instead consider probability densities over intervals.

The key intuition behind moments lies in their ability to characterize different aspects of a distribution's shape. Each moment μ_k weights the distribution by increasingly higher powers of x (x^k), with each successive moment emphasizing different features of the distribution.
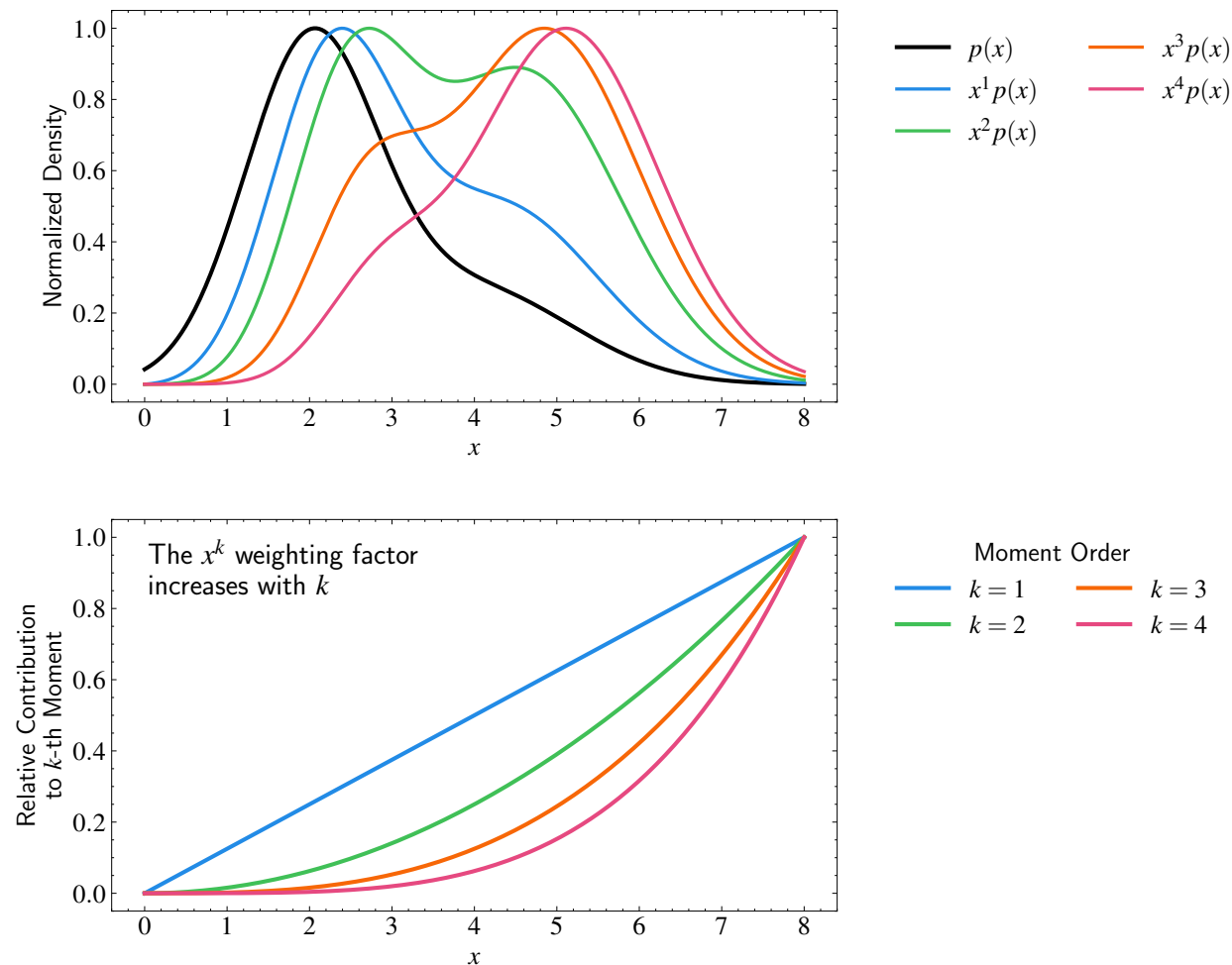
Figure 3.1: Visualization of how different moments weight a probability distribution. Top panel: The black curve shows a normalized probability distribution $p(x)$, while the colored curves show $x^k p(x)$ for different values of k. As k increases, the peaks of $x^k p(x)$ shift toward larger values of x, demonstrating how higher moments become increasingly sensitive to the tails of the distribution. Bottom panel: The relative contribution of different powers of x (x^k) to each moment, showing how higher moments ($k > 1$) give progressively more weight to larger values. This illustrates why higher moments are particularly sensitive to extreme values in a distribution—a feature especially relevant in astronomy where rare, extreme objects often carry important physical information.

The first moment ($k = 1$) is the mean or expected value:

$$\mu_1 = \mathbb{E}[x] = \int x p(x) dx. \tag{3.4}$$

This gives us the distribution's center or typical value, which becomes the basis for parameter estimation in linear regression. To understand why, recall that $p(x)$ represents the probability density—it tells us how likely we are to observe each value x. When we multiply x by $p(x)$

and integrate, we are effectively taking a probability-weighted average of all possible values. This weighting by probability is what makes the first moment a meaningful measure of the distribution's central tendency.

The second moment ($k = 2$) measures the mean squared value:

$$\mu_2 = \mathbb{E}[x^2] = \int x^2 p(x) dx. \tag{3.5}$$

When combined with the first moment, this enables us to calculate variance—the key quantity for uncertainty quantification in machine learning. When the mean is zero, squaring makes both positive and negative deviations from zero contribute positively to the sum, giving us a measure of spread that directly relates to the precision of our parameter estimates.

Higher moments ($k > 2$) become increasingly sensitive to the "tails" of the distribution—the regions far from the center where extreme values occur. This sensitivity arises because, as shown in Figure 3.1, raising values to higher powers (k) amplifies large values much more dramatically than small ones. For instance, if a value is twice the typical scale, its contribution to the kth moment is 2^k times larger—with $k = 3$ it contributes 8 times more, with $k = 4$ it contributes 16 times more, and so on. This exponential amplification means that even if extreme values are rare, they can dominate the higher moments, making these statistics particularly useful for studying rare events in astronomy and for understanding the robustness of our machine learning models to outliers.

In subsequent sections, we will explore how these moments transform under various operations, how they relate to marginal and conditional distributions, and eventually how we can estimate them from observed data. These concepts will provide the foundation for the machine learning methods we'll develop in later chapters, where moments play a crucial role in parameter estimation, uncertainty quantification, and model evaluation.

3.2   Transformation of Random Variables

In our discussion of moments above, we implicitly used what is known as the transformation of random variables. In particular, when computing the kth moment, we transformed the random variable through $x \to x^k$. This seemingly simple operation requires careful consideration that directly impacts how we handle data preprocessing and feature engineering in machine learning applications.

As we established in Chapter 2, x represents an outcome of the random variable X, not merely a deterministic variable. Therefore, x^k naturally represents outcomes of a new random variable X^k. When we apply any function to a random variable, the result is itself a random variable with its own probability distribution. This follows from a basic property: if a quantity has inherent variability, any function of that quantity must also exhibit variability. This understanding becomes critical when we preprocess data for machine learning—transformations like taking logarithms, computing ratios, or standardizing features all create new random variables whose statistical properties need to be understood.

In astronomy and data analysis, we frequently need to transform random variables — whether converting between different units (like parsecs to light-years), applying calibration corrections, or computing derived quantities (like absolute magnitude from apparent magnitude and distance). To formalize how these transformations affect probability distributions, consider a random variable X with probability density function $p_X(x)$. When we apply a function g to create a new variable $Y = g(X)$, we obtain a new random variable Y with its own probability density function $p_Y(y)$. The central question becomes: given the original probability density $p_X(x)$ and transformation function g, how do we determine the transformed probability density $p_Y(y)$?

Let's start with the simplest case relevant to data preprocessing: linear transformations. For a linear transformation of the form:

$$Y = aX + b, \tag{3.6}$$

where a and b are constants, the relationship between the probability densities is:

$$p_Y(y) = p_X\left(\frac{y - b}{a}\right)\frac{1}{|a|}. \tag{3.7}$$

The factor $1/|a|$ appears due to the requirement of probability conservation—a principle that becomes crucial when we standardize or rescale features for machine learning algorithms. Recall that a probability density function represents the chance of an outcome materializing per "unit" of the outcome space. As illustrated in Figure 3.2, when we stretch the distribution by a factor a (e.g., $a = 2$ in the figure), the concept of per "unit" outcome itself changes accordingly. When we scale a variable by a factor a, the probability density must correspondingly scale by $1/|a|$ to maintain this conservation—intuitively, as the units are now a times larger, the probability density per unit must decrease by $1/|a|$ to ensure the
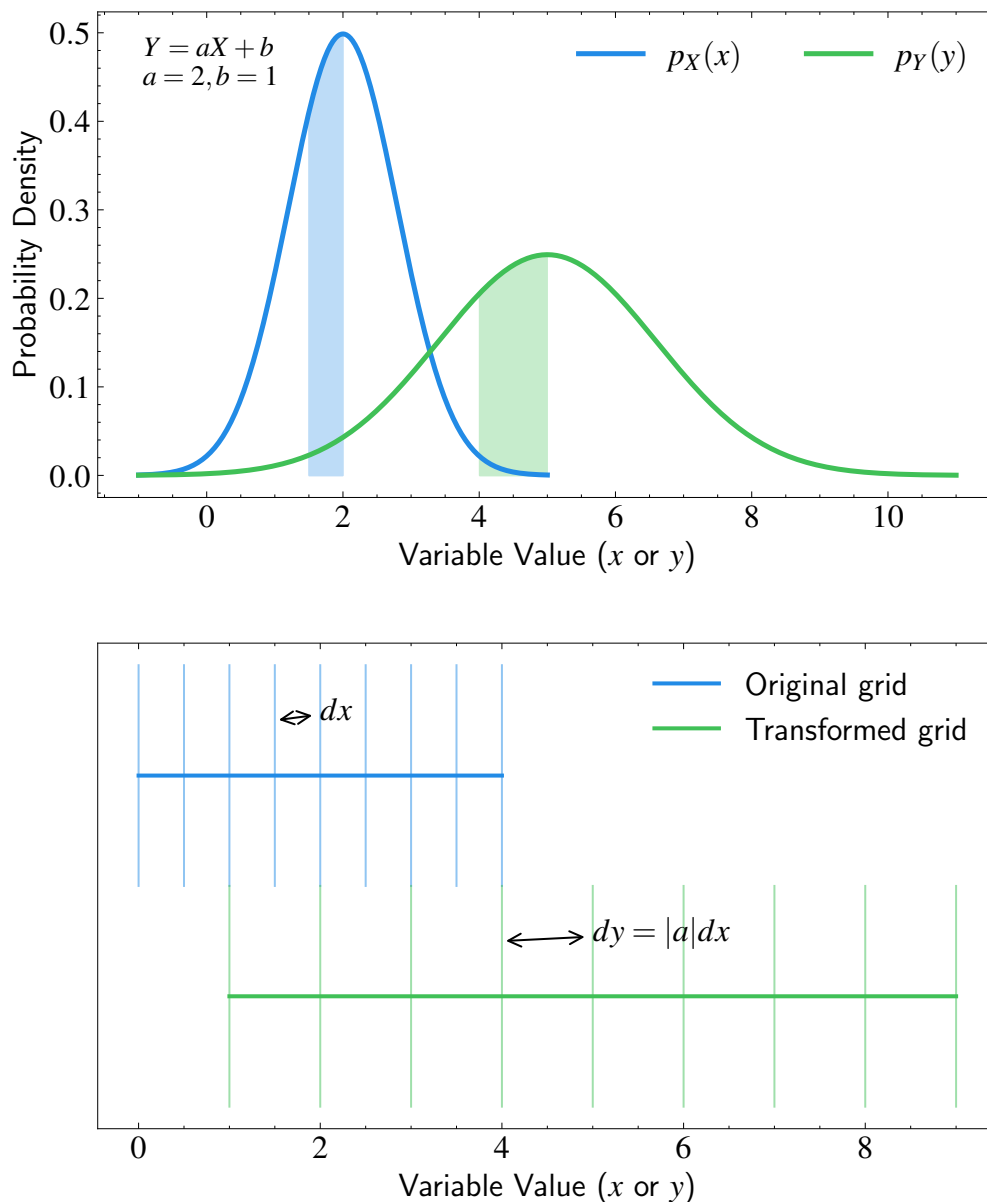
Figure 3.2: Visualization of how probability distributions transform under linear transformations. Top panel: The blue curve shows the original probability distribution $p_X(x)$ and the green curve shows the transformed distribution $p_Y(y)$ under the linear transformation $Y = 2X + 1$. The shaded regions have equal areas, demonstrating probability conservation. Bottom panel: Illustration of how a uniform grid transforms under the same linear transformation. The spacing between grid lines increases by a factor of $|a| = 2$, necessitating a corresponding decrease in probability density by a factor of $1/|a|$ to preserve total probability. This visualization demonstrates why the Jacobian factor $|dx/dy|$ appears in probability transformation formulas.

total probability still integrates to one. This scaling factor representing the change in "unit area" is known as the Jacobian determinant, which appears generally when transforming

between different variables to ensure proper probability conservation.

For a general transformation $Y = g(X)$, where g is a differentiable and monotonic function (either strictly increasing or strictly decreasing), the probability density transforms as:

$$p_Y(y) = p_X(x) \left| \frac{dx}{dy} \right| = p_X(g^{-1}(y)) \left| \frac{d}{dy} g^{-1}(y) \right|. \tag{3.8}$$

The term $|dx/dy|$ is called the Jacobian of the transformation. It accounts for how the transformation stretches or compresses intervals of the random variable, ensuring that probability is conserved. The absolute value ensures that the probability density remains non-negative even when the transformation reverses the orientation (i.e., when g is decreasing). Since probability conservation only needs to be maintained locally at each point, the change of measure through the Jacobian is always well-defined locally, even if the global transformation is complex. This local nature allows us to express the change in measure through calculus as the derivative $|dx/dy|$, which captures how infinitesimal intervals are stretched or compressed at each point.

For multivariate transformations, where we transform multiple random variables simultaneously, the Jacobian becomes a matrix determinant. If we have a vector of random variables $\mathbf{X} = (X_1, ..., X_n)^T$ transforming to $\mathbf{Y} = \mathbf{g}(\mathbf{X})$, then:

$$p_Y(\mathbf{y}) = p_X(\mathbf{g}^{-1}(\mathbf{y})) \left| \det \left(\frac{\partial \mathbf{g}^{-1}}{\partial \mathbf{y}} \right) \right|. \tag{3.9}$$

This multivariate case is particularly relevant for machine learning applications when transforming between different coordinate systems (like equatorial to galactic coordinates) or when dealing with derived astronomical quantities that depend on multiple observables. These transformations become critical when we preprocess multivariate data for linear regression, as the choice of coordinate system can significantly impact the linearity of relationships and the performance of our models.

Another important class of transformations involves combinations of multiple random variables, such as their sum. When we combine random variables, we are effectively creating a new random variable whose outcomes depend on multiple random events. For instance, if we have two random variables X and Y, their sum $Z = X + Y$ represents a new random variable whose probability distribution depends on both the individual distributions of X and Y and their relationship to each other. This type of transformation becomes particularly

relevant in linear regression when we model a response variable as a linear combination of predictors.

In subsequent sections, we will further develop these concepts to understand how transformations affect the moments of distributions and how they apply to common operations in data analysis and machine learning. This framework will provide the foundation for understanding error propagation, uncertainty quantification, and the effects of data preprocessing on model performance.

3.3 Expectation

In our discussion of moments, we introduced the first moment as the mean or expected value of a random variable. This concept is so fundamental to probability theory and machine learning that it deserves deeper exploration. The first moment, which we now refer to more generally as expectation, involves both a weighting process where each possible outcome is weighted by its probability, and in the case of higher moments, a transformation of the random variable $(X \rightarrow X^k)$.

This operation of taking a probability-weighted average is central to machine learning—from parameter estimation to loss function optimization—which is why we give it special notation and terminology. We denote the expectation of a random variable X as $\mathbb{E}[X]$, defined as:

$$\text{Discrete case:} \quad \mathbb{E}[X] = \sum_x x \, p_X(x), \tag{3.10}$$

$$\text{Continuous case:} \quad \mathbb{E}[X] = \int x \, p_X(x) \, dx. \tag{3.11}$$

The argument inside $\mathbb{E}[\cdot]$ represents the random variable whose expectation we are computing. This notation becomes particularly important in machine learning contexts where we need to distinguish between different types of averages. For instance, in linear regression, we'll encounter the expectation over data points, the expectation over noise realizations, and the expectation over parameter distributions—each serving different roles in model fitting and uncertainty quantification.

We note however that the name "expectation" might suggest what we expect to measure, but this can sometimes be misleading. For example, consider the Initial Mass Function

(IMF) for stars. While $\mathbb{E}[M]$ gives us the average stellar mass, most stars actually have masses below this value. This occurs because stellar masses follow a power law that spans several orders of magnitude—from brown dwarfs at about 0.08 solar masses to massive stars exceeding 100 solar masses. The power-law nature of the IMF means we find exponentially more low-mass stars than high-mass stars, but the few high-mass stars pull the average up. For instance, with a Salpeter IMF ($p(M) \propto M^{-2.35}$), we might find thousands of 0.5 solar mass stars for every 50 solar mass star, yet these rare massive stars contribute substantially to the average mass due to their high values.

Having established the foundation of expectation, we now explore how it behaves under the transformations of random variables we discussed in the previous section. These properties, expressed in the compact formalism of expectation values, will prove invaluable for understanding how preprocessing steps affect our machine learning models and for propagating uncertainties through complex calculations.

When working with transformations of random variables, it's important to understand how expectations behave. For a transformation $Y = g(X)$, we can compute its expectation in two equivalent ways:

1. Using the original variable X and its distribution:

$$\mathbb{E}[g(X)] = \int g(x) \, p_X(x) \, dx. \tag{3.12}$$

2. Using the transformed variable Y and its distribution:

$$\mathbb{E}[Y] = \int y \, p_Y(y) \, dy = \int g(x) \, p_X(x) \, dx. \tag{3.13}$$

These expressions are equivalent when we properly account for the transformation of probability densities using $p_Y(y) = p_X(g^{-1}(y))|dg^{-1}/dy|$. This equivalence is particularly useful in machine learning applications where we might transform features before fitting models—we can compute expected values using either the original or transformed representations, provided we handle the probability transformations correctly.

This equivalence explains why we can write our definition of moments either way:

$$\mu_k = \mathbb{E}[X^k] = \mathbb{E}[Y] \text{ where } Y = X^k. \tag{3.14}$$

Let's explore some key properties of expectation that are crucial for machine learning applications. For any constants a and b, expectation exhibits linearity:

$$\mathbb{E}[aX + b] = a\mathbb{E}[X] + b. \tag{3.15}$$

This property is intuitively clear if we think about what scaling and shifting do to a distribution's center, as illustrated in Figure 3.3. When we multiply a random variable by a, we stretch (or compress) all values by that factor, so the center must also stretch by a. Similarly, when we add b, we shift all values by that amount, so the center must shift by b as well. This intuition holds regardless of the distribution's shape—the expectation always transforms linearly because it represents the distribution's center of mass. In machine learning contexts, this linearity property is crucial for understanding how data preprocessing affects model parameters. When we standardize features by subtracting the mean and dividing by the standard deviation, the linearity of expectation tells us exactly how the transformed features will behave.

Formally, we can prove this using the definition of expectation:

$$\mathbb{E}[aX + b] = \int (ax + b)p(x)dx \tag{3.16}$$

$$= a \int xp(x)dx + b \int p(x)dx \tag{3.17}$$

$$= a\mathbb{E}[X] + b, \tag{3.18}$$

where we've used the fact that $\int p(x)dx = 1$ for any probability distribution.

For any two random variables X and Y, expectation is additive:

$$\mathbb{E}_{X,Y}[X + Y] = \mathbb{E}_X[X] + \mathbb{E}_Y[Y]. \tag{3.19}$$

This property tells us that the expectation of a sum is the sum of the expectations, regardless of whether X and Y are independent—a fact that becomes crucial in linear regression where we model the response as a sum of contributions from different predictors.
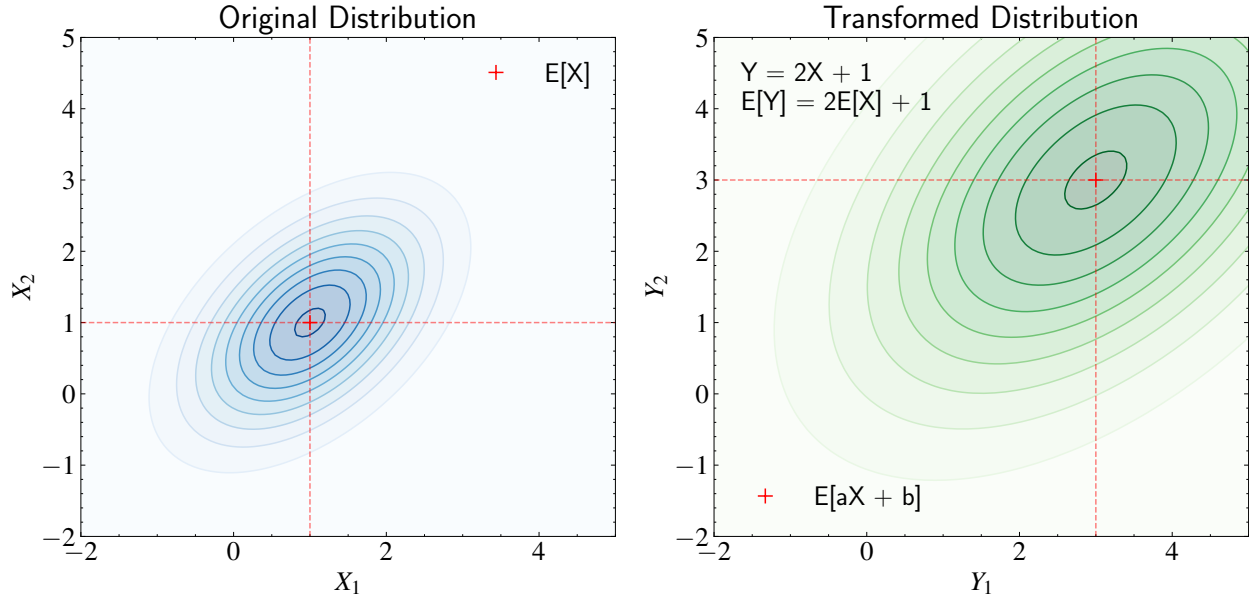
Figure 3.3: Visualization of expectation's linearity property using a bivariate Gaussian distribution. Left panel: Original distribution with expectation $\mathbb{E}[X]$ marked by the red cross. Right panel: The transformed distribution under $Y = 2X + 1$, showing how the expectation transforms linearly: $\mathbb{E}[Y] = 2\mathbb{E}[X] + 1$. The contours represent probability density levels, demonstrating how the entire distribution stretches and shifts while maintaining its shape. The red dashed lines highlight how the center (expectation) transforms according to the same linear rule, regardless of the distribution's specific shape or spread.

This property simply follows from:

$$\mathbb{E}_{X,Y}[X + Y] = \iint (x + y)p(x, y)dxdy \tag{3.20}$$

$$= \iint xp(x, y)dxdy + \iint yp(x, y)dxdy \tag{3.21}$$

$$= \int x \left(\int p(x, y)dy \right) dx + \int y \left(\int p(x, y)dx \right) dy \tag{3.22}$$

$$= \int xp(x)dx + \int yp(y)dy \tag{3.23}$$

$$= \mathbb{E}_X[X] + \mathbb{E}_Y[Y], \tag{3.24}$$

where we've used the fact that integrating the joint distribution $p(x, y)$ over one variable gives us the marginal distribution of the other. For example, if we measure the total light from two stars, the average total luminosity is simply the sum of their average individual luminosities, where each average is taken over all possible values of that star's luminosity.

Having explored expectation in the univariate and bivariate cases, we now extend
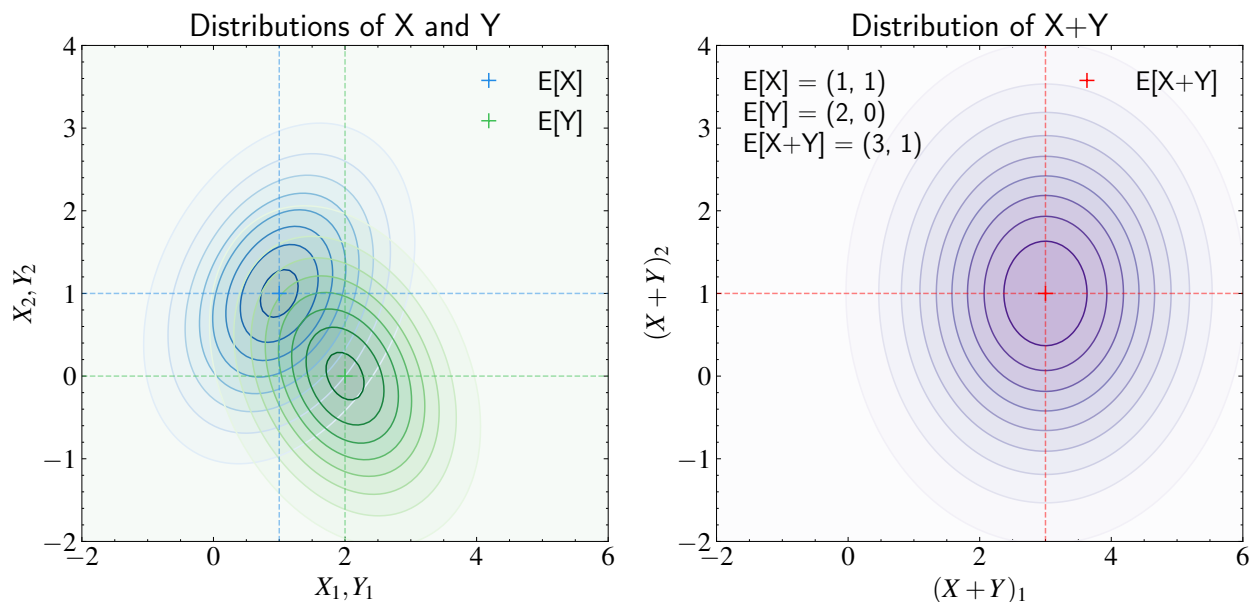
Figure 3.4: Visualization of expectation's additivity property using bivariate Gaussian distributions. Left panel: Original distributions of random variables X (blue contours) and Y (green contours) with their respective expectations $\mathbb{E}[X]$ and $\mathbb{E}[Y]$ marked by colored crosses. The contours represent probability density levels of each distribution, and the dashed lines mark the coordinate positions of the expectations. Right panel: The distribution of the sum $Z = X + Y$ (purple contours) with its expectation $\mathbb{E}[Z] = \mathbb{E}[X + Y]$ marked by the red cross. The figure demonstrates that $\mathbb{E}[X + Y] = \mathbb{E}[X] + \mathbb{E}[Y]$, showing how expectations add component-wise regardless of the correlation structure in the original distributions.

these concepts to the multivariate setting that characterizes most machine learning applications. When dealing with multiple random variables simultaneously, we can represent them as a random vector $\mathbf{X} = (X_1, \ldots, X_n)^T$. The expectation of this random vector, denoted $\mathbb{E}[\mathbf{X}]$, is defined as the vector containing the expectations of each individual component:

$$\mathbb{E}[\mathbf{X}] \equiv \begin{pmatrix} \mathbb{E}[X_1] \\ \vdots \\ \mathbb{E}[X_n] \end{pmatrix}. \tag{3.25}$$

When we apply a linear transformation $\mathbf{A}$, which is an $m \times n$ matrix, to our random vector $\mathbf{X}$, we get a new random vector $\mathbf{Y} = \mathbf{AX} + \mathbf{b}$ of dimension m. By expanding the

matrix multiplication and using the linearity of expectation, we can see that:

$$Y_i = \sum_{j=1}^{n} A_{ij} X_j + b_i, \tag{3.26}$$

$$\mathbb{E}[Y_i] = \sum_{j=1}^{n} A_{ij} \mathbb{E}[X_j] + b_i. \tag{3.27}$$

And hence, in the multivariate case:

$$\mathbb{E}[\mathbf{Y}] = \mathbf{A}\mathbb{E}[\mathbf{X}] + \mathbf{b}, \tag{3.28}$$

where $\mathbf{A}$ is an $m \times n$ transformation matrix and $\mathbf{b}$ is an m-dimensional offset vector.

This linearity property extends beyond simple scaling and shifting operations to more general linear transformations where the components of $\mathbf{X}$ can be mixed together through matrix multiplication. Such transformations effectively rotate our coordinate system or create new variables that are linear combinations of our original variables—operations that are at the heart of linear regression and principal component analysis.

3.4   Law of Total Expectation

Having explored how expectation behaves under transformations, we now turn to another important aspect: how expectation relates to marginal and conditional distributions, which we introduced in Chapter 2. This relationship helps us understand how to calculate expectations when we have partial information or when working with hierarchical probability structures.

For example, suppose we want to estimate a star's mass, but we can only measure its luminosity directly. In this case, we want to make the most of our available data by combining our luminosity measurement with theoretical understanding of how masses tend to be distributed for stars of a given luminosity. This scenario leads us to a powerful principle known as the law of total expectation.

When working with multiple variables, we need to be precise about which variables we're averaging over. For two random variables X and Y, we can write expectations with

subscripts to indicate which variables we're averaging over:

$$\mathbb{E}_{X,Y}[g(X,Y)] = \iint g(x,y)\, p(x,y)\, dx\, dy, \tag{3.29}$$

$$\mathbb{E}_X[g(X,Y)] = \int g(x,y)\, p(x|y)\, dx, \tag{3.30}$$

where in the second equation, we're only averaging over X while treating Y as fixed. This uses the conditional probability $p(x|y)$ since we're considering the distribution of X for a specific value of Y.

The law of total expectation states that we can compute the overall expectation of X in two equivalent ways:

$$\mathbb{E}_X[X] = \mathbb{E}_Y[\mathbb{E}_X[X|Y]]. \tag{3.31}$$

To prove this relationship, let's write out the right-hand side explicitly:

$$\mathbb{E}_Y[\mathbb{E}_X[X|Y]] = \int \mathbb{E}_X[X|Y=y]\, p(y)\, dy \tag{3.32}$$

$$= \int \left(\int x\, p(x|y)\, dx \right) p(y)\, dy \tag{3.33}$$

$$= \int \int x\, p(x|y)\, p(y)\, dx\, dy \tag{3.34}$$

$$= \int \int x\, p(x,y)\, dx\, dy \tag{3.35}$$

$$= \int x \left(\int p(x,y)\, dy \right) dx \tag{3.36}$$

$$= \int x\, p(x)\, dx \tag{3.37}$$

$$= \mathbb{E}_X[X], \tag{3.38}$$

where we've used the product rule that $p(x,y) = p(x|y)p(y)$ and that $p(x) = \int p(x,y)\, dy$ is the marginal distribution.

This mathematical framework proves particularly valuable when dealing with astronomical observations where direct measurements might be challenging or biased. Consider the practical problem of estimating the average stellar mass, illustrated in Figure 3.5. The most straightforward approach would be to directly average all stellar masses:

$$\mathbb{E}_M[M] = \int M\, p(M)\, dM. \tag{3.39}$$
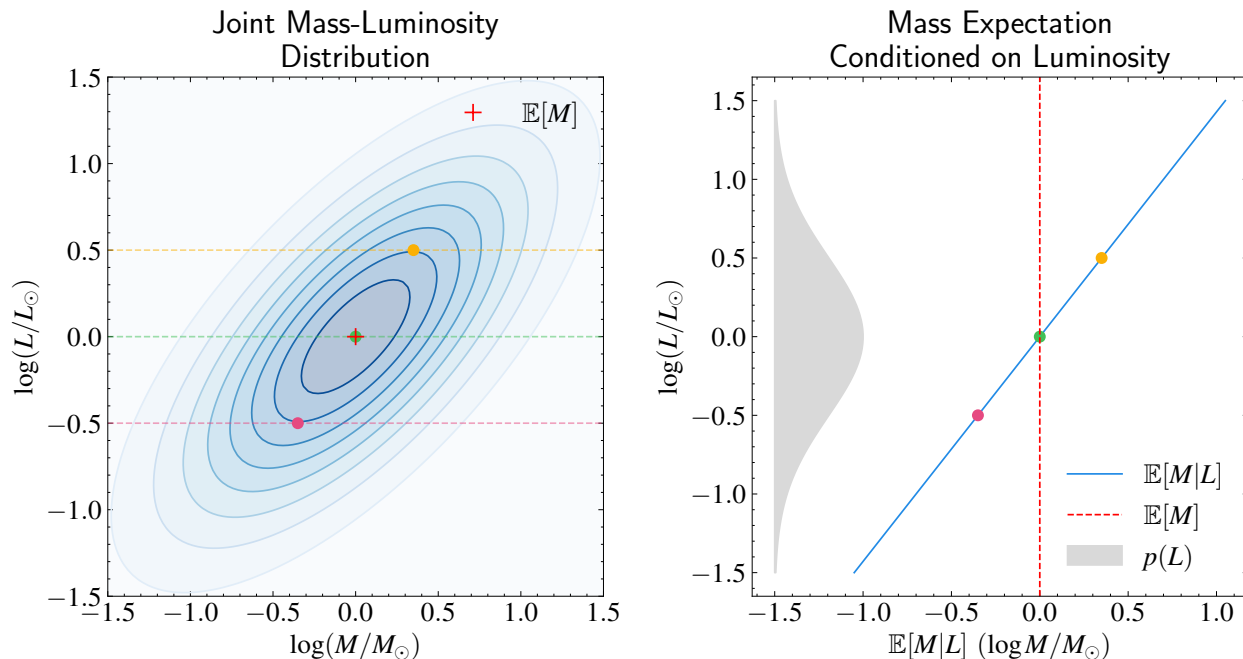
Figure 3.5: Visualization of the law of total expectation using stellar mass-luminosity relationships. Left panel: Joint distribution of stellar mass and luminosity (in solar units and log scale), shown as blue contours. The red cross marks the overall expectation $\mathbb{E}[M]$, while colored circles show conditional expectations $\mathbb{E}[M|L]$ at three different luminosities (marked by dashed lines). Right panel: The conditional expectation $\mathbb{E}[M|L]$ as a function of luminosity (blue line), demonstrating how we can estimate stellar masses given their luminosities. The gray shaded region shows the marginal distribution of luminosity $p(L)$, which accounts for observational selection effects in magnitude-limited surveys. The red dashed line marks the overall expectation $\mathbb{E}[M]$, illustrating how integrating $\mathbb{E}[M|L]$ weighted by $p(L)$ recovers the average stellar mass $\mathbb{E}[M]$, even when direct mass measurements are challenging.

However, we rarely know the true distribution $p(M)$ a priori, and it's particularly difficult to account for observational effects like selection bias. For instance, in a magnitude-limited survey, we preferentially observe brighter, typically more massive stars (as shown by the gray shaded region in the right panel of the figure), making it challenging to directly estimate $p(M)$. The red cross and dashed line in the figure mark this overall expectation $\mathbb{E}_M[M]$, but directly measuring it requires accurately sampling the full mass distribution—something that's often impossible due to observational limitations.

A more powerful approach decomposes the problem using conditional expectations, where we first find the average mass for stars of a specific luminosity, then average over all

possible luminosities:

$$\mathbb{E}_M[M] = \mathbb{E}_L[\mathbb{E}_M[M|L]] = \int \left(\int M \, p(M|L) \, dM \right) p(L) \, dL. \qquad (3.40)$$

As visualized in the figure, this hierarchical decomposition offers several practical advantages. For each luminosity value (shown by horizontal dashed lines in the left panel), we can compute the conditional expectation $\mathbb{E}_M[M|L]$ (marked by colored circles). The blue contours show how mass and luminosity are correlated, with the blue line in the right panel tracing how this conditional expectation varies with luminosity—essentially giving us a regression function that predicts mass from luminosity. These expectations are then weighted by the luminosity distribution $p(L)$, shown by the gray shading in the right panel, which we can measure directly from our magnitude-limited survey.

The power of this approach lies in its ability to handle observational constraints naturally. The luminosity distribution $p(L)$ can be modeled while explicitly accounting for the selection effects of our magnitude-limited survey, as luminosity directly relates to our observational constraints. Meanwhile, the mass distribution at fixed luminosity, $p(M|L)$ (represented by vertical slices through the contours in the left panel), is well-understood from stellar evolution theory and typically has much smaller observational biases.

Just as in the univariate case, the law of total expectation extends naturally to multivariate random variables. For random vectors $\mathbf{X}$ and $\mathbf{Y}$:

$$\mathbb{E}_{\mathbf{X}}[\mathbf{X}] = \mathbb{E}_{\mathbf{Y}}[\mathbb{E}_{\mathbf{X}}[\mathbf{X}|\mathbf{Y}]]. \qquad (3.41)$$

This means that for each component of our random vector, we can compute its expectation by first finding its conditional expectation given $\mathbf{Y}$, and then taking the expectation over all possible values of $\mathbf{Y}$. The proof follows exactly the same steps as in the univariate case, just with additional integration variables—we exchange the order of multiple integrals over the components of $\mathbf{X}$ and $\mathbf{Y}$ using the same chain of probability density relationships.

This principle forms the foundation for calculating predictive distributions in Bayesian modeling. In Bayesian analysis, model parameters (like regression coefficients) are treated as random variables with associated uncertainty. When making predictions, we need to account for this parameter uncertainty. If θ represents our model parameters and y_* a new

observation we want to predict, the law of total expectation allows us to write:

$$\mathbb{E}[y_*] = \mathbb{E}_\theta[\mathbb{E}[y_*|\theta]] \tag{3.42}$$

This means we compute the expected prediction for each possible parameter value θ (the inner expectation), then average these expectations over the posterior distribution of θ (the outer expectation). This process, known as marginalization, properly incorporates parameter uncertainty into our predictions.

3.5   Variance, Covariance, and Correlation

We've seen that the first moment $\mathbb{E}[X]$ characterizes the center of a distribution, providing a foundation for parameter estimation. However, understanding the center alone is insufficient for a complete statistical description. We also need to quantify uncertainty and understand relationships between variables. The second moment $\mathbb{E}[X^2]$ might seem like a natural choice for measuring the spread of a distribution, as it gives more weight to values far from zero. However, there's a subtle but important issue: $\mathbb{E}[X^2]$ only meaningfully measures spread when the distribution is centered at zero. For distributions centered elsewhere, $\mathbb{E}[X^2]$ conflates the spread with the location of the center, making it unsuitable for uncertainty quantification in most practical scenarios.

To isolate the true spread of the distribution, we need to measure deviations from the distribution's center ($\mathbb{E}[X]$), not from zero. This leads us to define the variance of a random variable X, denoted as $\mathrm{Var}[X]$ or σ_X^2:

$$\mathrm{Var}[X] \equiv \mathbb{E}[(X - \mathbb{E}[X])^2]. \tag{3.43}$$

Here we first center the distribution by subtracting $\mathbb{E}[X]$, then compute the average squared deviation from this center. This variance becomes the key quantity for understanding prediction uncertainty and for quantifying the reliability of parameter estimates.

Using the properties of expectation we derived earlier, we can expand this into a more computationally convenient form. Note that while X is a random variable, $\mathbb{E}[X]$ is a

constant (it's just a number), so we can use the linearity property of expectation:

$$\text{Var}[X] = \mathbb{E}[(X - \mathbb{E}[X])^2] \tag{3.44}$$
$$= \mathbb{E}[X^2 - 2X\mathbb{E}[X] + (\mathbb{E}[X])^2] \tag{3.45}$$
$$= \mathbb{E}[X^2] - 2\mathbb{E}[X]\mathbb{E}[X] + \mathbb{E}[(\mathbb{E}[X])^2] \tag{3.46}$$
$$= \mathbb{E}[X^2] - 2(\mathbb{E}[X])^2 + (\mathbb{E}[X])^2 \tag{3.47}$$
$$= \mathbb{E}[X^2] - (\mathbb{E}[X])^2. \tag{3.48}$$

This algebraic manipulation reveals that we can compute the variance simply by calculating the first and second moments of the distribution. Rather than directly computing deviations from the mean, this alternative formulation provides a computationally efficient way to characterize the spread of our data.

The standard deviation σ_X is simply defined as the square root of the variance:

$$\sigma_X = \sqrt{\text{Var}[X]}. \tag{3.49}$$

We define the standard deviation because it has the same units as the original variable. For instance, if we measure stellar masses in solar masses $(M_\odot)$, the variance will be in $(M_\odot)^2$ while the standard deviation is in $M_\odot$. This makes the standard deviation more directly interpretable for uncertainty quantification—when we say the mean stellar mass is $1M_\odot$ with a standard deviation of $0.5M_\odot$, we can immediately understand the scale of the variations.

Having defined variance, we can now examine how it behaves under transformations of random variables. Let's begin with linear transformations, where we scale and shift a random variable. Unlike expectation, which we showed to be a linear operator, variance exhibits a different scaling behavior. For any constants a and b:

$$\text{Var}[aX + b] = a^2\text{Var}[X]. \tag{3.50}$$

We can prove this using the definition of variance and the properties of expectation

we derived earlier:

$$\text{Var}[aX + b] = \mathbb{E}[(aX + b - \mathbb{E}[aX + b])^2] \tag{3.51}$$

$$= \mathbb{E}[(aX + b - (a\mathbb{E}[X] + b))^2] \quad \text{(using linearity of expectation)} \tag{3.52}$$

$$= \mathbb{E}[(aX - a\mathbb{E}[X])^2] \tag{3.53}$$

$$= \mathbb{E}[a^2(X - \mathbb{E}[X])^2] \tag{3.54}$$

$$= a^2\mathbb{E}[(X - \mathbb{E}[X])^2] \tag{3.55}$$

$$= a^2\text{Var}[X]. \tag{3.56}$$
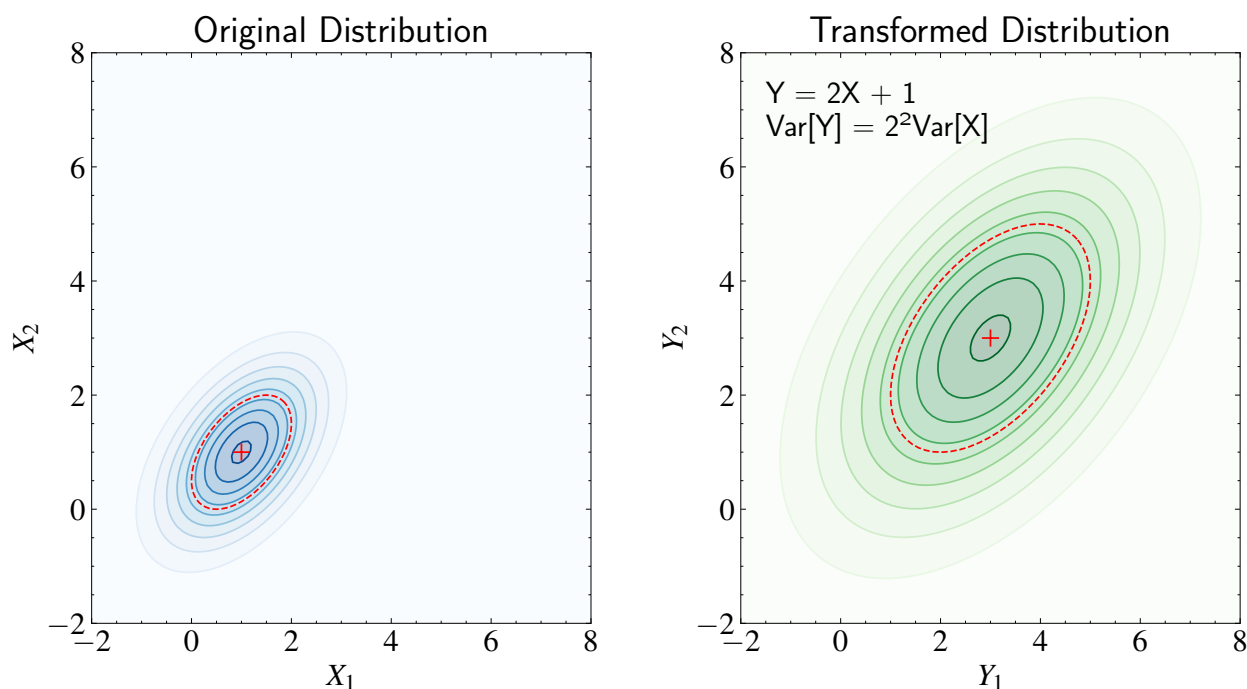
Figure 3.6: Visualization of how variance and standard deviation transform under linear transformations. Left panel: Original bivariate distribution (blue contours) with its expectation marked by the red cross and variance structure indicated by the red dashed ellipse. The ellipse represents a constant probability contour of the distribution, with its shape and orientation determined by the covariance matrix. Right panel: The transformed distribution (green contours) under $Y = 2X + 1$. While the mean shifts by the same linear transformation ($\mathbb{E}[Y] = 2\mathbb{E}[X] + 1$), the standard deviation scales linearly ($\sigma_Y = 2\sigma_X$) while the variance scales quadratically ($\text{Var}[Y] = 4\text{Var}[X]$), as shown by the enlarged red dashed ellipse.

This result has an intuitive interpretation: when we multiply a random variable by a, we stretch (or compress) all deviations from the mean by a factor of a. Since variance measures squared deviations, it scales by a^2. Adding a constant b merely shifts the entire distribution without changing its spread, so it doesn't affect the variance. This behavior

is crucial for understanding how data transformations affect statistical analyses—scaling variables changes the variance of the data, which can impact both interpretation and computational behavior.

Just as we moved from studying single random variables to examining relationships between variables in our discussion of expectation, we can extend our understanding of variance to capture how multiple random variables vary together. This leads us to the concepts of covariance and correlation.

The covariance between two random variables X and Y, denoted as $\mathrm{Cov}(X, Y)$, measures their joint variability:

$$\mathrm{Cov}(X, Y) = \mathbb{E}[(X - \mathbb{E}[X])(Y - \mathbb{E}[Y])]. \tag{3.57}$$

Looking at this definition, we can understand covariance intuitively: it measures whether two variables tend to deviate from their means together. When both variables tend to be simultaneously above or below their means, their deviations multiply to give positive values, resulting in positive covariance. Conversely, when one variable tends to be above its mean while the other is below, we get negative products and thus negative covariance. When there's no systematic relationship between their deviations, positive and negative products cancel out, giving us zero covariance.

This covariance can arise in two distinct ways in astronomical measurements. First, it can reflect inherent physical relationships—for example, more massive stars naturally tend to be more luminous than average, creating a positive covariance between mass and luminosity. Second, it can arise from measurement processes—if our instruments have systematic errors that affect multiple measurements simultaneously, this introduces covariance even when the underlying quantities might be independent.

Using the properties of expectation we derived earlier, we can show that covariance has an alternative, computationally convenient form:

$$\mathrm{Cov}(X, Y) = \mathbb{E}[XY] - \mathbb{E}[X]\mathbb{E}[Y]. \tag{3.58}$$

To prove this:

$$\text{Cov}(X, Y) = \mathbb{E}[(X - \mathbb{E}[X])(Y - \mathbb{E}[Y])] \tag{3.59}$$

$$= \mathbb{E}[XY - X\mathbb{E}[Y] - Y\mathbb{E}[X] + \mathbb{E}[X]\mathbb{E}[Y]] \tag{3.60}$$

$$= \mathbb{E}[XY] - \mathbb{E}[X]\mathbb{E}[Y] - \mathbb{E}[X]\mathbb{E}[Y] + \mathbb{E}[X]\mathbb{E}[Y] \tag{3.61}$$

$$= \mathbb{E}[XY] - \mathbb{E}[X]\mathbb{E}[Y]. \tag{3.62}$$

While covariance effectively measures how variables vary together, it has a limitation that becomes problematic when comparing relationships across different measurement scales: its scale dependence. To see this explicitly, consider what happens when we rescale our variables by constants a and b:

$$\text{Cov}(aX, bY) = \mathbb{E}[(aX - \mathbb{E}[aX])(bY - \mathbb{E}[bY])] \tag{3.63}$$

$$= \mathbb{E}[(aX - a\mathbb{E}[X])(bY - b\mathbb{E}[Y])] \tag{3.64}$$

$$= \mathbb{E}[ab(X - \mathbb{E}[X])(Y - \mathbb{E}[Y])] \tag{3.65}$$

$$= ab\,\text{Cov}(X, Y). \tag{3.66}$$

This means if we change measurement units—for example, converting stellar masses from solar masses to kilograms (multiplying by 2×10^{30})—the covariance scales proportionally. This makes it difficult to compare covariances between different pairs of variables or across different measurement scales.

To address this limitation, it is therefore convenient to define what is known as the correlation coefficient:

$$\rho_{XY} = \frac{\text{Cov}(X, Y)}{\sigma_X \sigma_Y}, \tag{3.67}$$

which is dimensionless and scale independent. This makes it a more useful measure for comparing the strength of relationships between different pairs of variables and for understanding which relationships are strongest in multivariate data.

The scale-invariant properties of correlation can be easily verified. Recall from our earlier discussion that variance scales quadratically: $\text{Var}[aX] = a^2\text{Var}[X]$. By taking the square root on both sides, we have $\sigma_{aX} = |a|\sigma_X$. Using these properties along with our
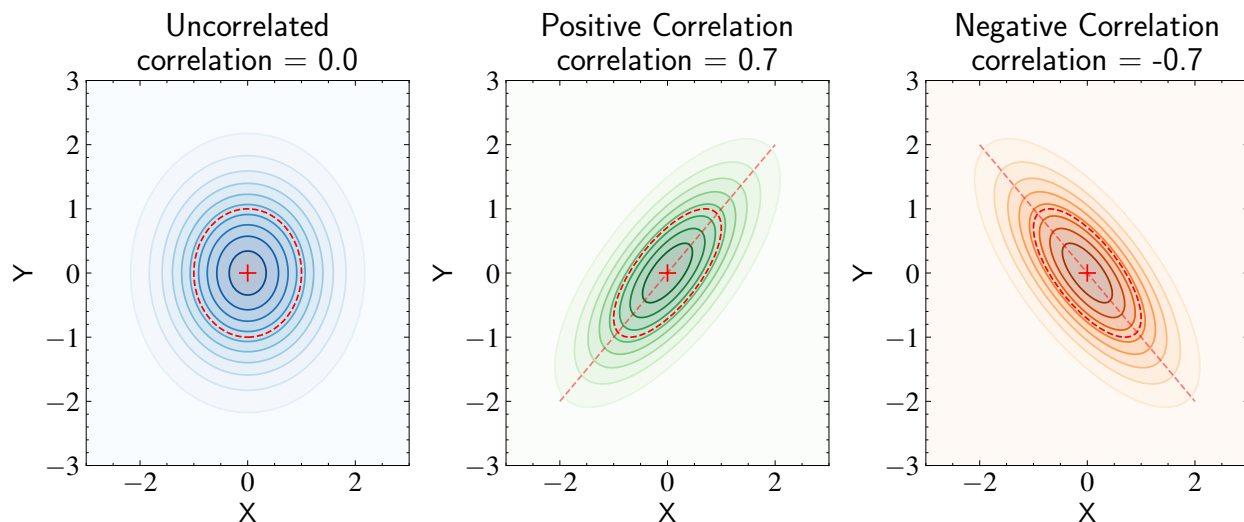
Figure 3.7: Visualization of how correlation shapes bivariate normal distributions. The panels show three distributions with identical marginal variances but different correlation structures. Left panel: Uncorrelated variables ($\rho = 0$) produce circular contours, with the principal axes of the red dashed ellipse aligned with the coordinate axes. Middle panel: Positive correlation ($\rho = 0.7$) stretches the distribution along the diagonal (red dashed line), indicating that higher values of one variable tend to occur with higher values of the other. Right panel: Negative correlation ($\rho = -0.7$) tilts the distribution in the opposite direction, showing that high values of one variable tend to occur with low values of the other. The red dashed ellipses, representing contours of constant probability, rotate and deform based on the correlation strength, while maintaining the same total variance (area). This illustrates how correlation captures the directionality of the relationship between variables without affecting their individual scales.

earlier result about covariance scaling:

$$\rho_{aX,bY} = \frac{\text{Cov}(aX, bY)}{\sigma_{aX}\sigma_{bY}} \tag{3.68}$$

$$= \frac{ab\text{Cov}(X, Y)}{|a|\sigma_X|b|\sigma_Y} \tag{3.69}$$

$$= \text{sign}(ab)\rho_{XY}. \tag{3.70}$$

This result shows that correlation maintains its magnitude under scaling but its sign depends on how we transform our variables. This makes intuitive sense: if we multiply one variable by -1, we reverse the direction of their relationship.

Furthermore, a key property of the correlation coefficient is that it always takes values between -1 and +1. A correlation of +1 indicates perfect positive correlation, meaning

the two variables are linearly related with a positive slope—when one increases, the other increases proportionally. Conversely, a correlation of -1 indicates perfect negative correlation, where one variable decreases proportionally as the other increases. A correlation of zero suggests no linear relationship between the variables. This bounded nature of correlation makes it particularly useful for comparing relationship strengths across different variable pairs.

The fact that correlation must lie between -1 and +1 follows from a mathematical principle known as the Cauchy-Schwarz inequality. For vectors $\mathbf{u}$ and $\mathbf{v}$ in an inner product space, this inequality states that:

$$|\mathbf{u} \cdot \mathbf{v}| \leq \|\mathbf{u}\|\|\mathbf{v}\|, \tag{3.71}$$

where $\|\cdot\|$ denotes the vector norm.

In this framework, for centered random variables (meaning we subtract their means), we can show:

$$|\mathbb{E}[(X - \mathbb{E}[X])(Y - \mathbb{E}[Y])]| \leq \sqrt{\mathbb{E}[(X - \mathbb{E}[X])^2]\mathbb{E}[(Y - \mathbb{E}[Y])^2]}. \tag{3.72}$$

Looking at this inequality more closely, we can see that the left side is the absolute value of the covariance, $|\mathrm{Cov}(X, Y)|$, while the right side is $\sqrt{\mathrm{Var}(X)\mathrm{Var}(Y)} = \sigma_X \sigma_Y$. Therefore, when we divide both sides by $\sigma_X \sigma_Y$, we get the bound on correlation:

$$|\rho_{XY}| = \left|\frac{\mathrm{Cov}(X, Y)}{\sigma_X \sigma_Y}\right| \leq 1. \tag{3.73}$$

In other words, the magnitude of the covariance cannot exceed the product of the standard deviations, which is precisely why correlation must lie between -1 and 1.

This mathematical bound has practical implications for astronomy. When we measure correlations between different astronomical properties, the value tells us not just whether there's a relationship, but how close it is to the theoretical maximum strength possible. The Tully-Fisher relation, for example, shows a strong positive correlation between galaxy luminosity and rotation velocity, remarkably close to perfect correlation. This strong correlation suggests a tight physical relationship between a galaxy's light output and its rotation.

Similarly, the main sequence in the Hertzsprung-Russell diagram shows a very strong

correlation between stellar temperature and luminosity for main sequence stars. This high correlation reflects the physics of stellar structure—stars are not random collections of hot gas but highly ordered systems governed by precise physical laws.

When dealing with multiple random variables simultaneously, it's natural to organize them into a random vector $\mathbf{X} = (X_1, \ldots, X_n)^T$. The variance generalizes to a covariance matrix, typically denoted as $\text{Cov}(\mathbf{X})$ or $\boldsymbol{\Sigma}$:

$$\text{Cov}(\mathbf{X}) = \mathbb{E}[(\mathbf{X} - \mathbb{E}[\mathbf{X}])(\mathbf{X} - \mathbb{E}[\mathbf{X}])^T]. \tag{3.74}$$

The transpose operation here is crucial for dimensional consistency and interpretation. Note that $\mathbf{X} - \mathbb{E}[\mathbf{X}]$ is an $n \times 1$ column vector, while its transpose $(\mathbf{X} - \mathbb{E}[\mathbf{X}])^T$ is a $1 \times n$ row vector. Their multiplication therefore produces an $n \times n$ matrix, where each element (i, j) represents the expected product of deviations in the ith and jth components. This matrix multiplication naturally leads to:

$$\Sigma_{ij} = \mathbb{E}[(X_i - \mathbb{E}[X_i])(X_j - \mathbb{E}[X_j])] = \begin{cases} \text{Var}(X_i) & \text{if } i = j \\ \text{Cov}(X_i, X_j) & \text{if } i \neq j \end{cases}. \tag{3.75}$$

The covariance matrix $\boldsymbol{\Sigma}$ directly encodes all pairwise relationships between variables, making it a central quantity for understanding multivariate data.

Just as variance scales quadratically with scalar transformations ($\text{Var}(aX) = a^2\text{Var}(X)$), the covariance matrix transforms systematically under linear operations. For a linear transformation $\mathbf{Y} = \mathbf{A}\mathbf{X} + \mathbf{b}$, where $\mathbf{A}$ is an $m \times n$ matrix and $\mathbf{b}$ is an m-dimensional vector:

$$\text{Cov}(\mathbf{Y}) = \mathbf{A}\text{Cov}(\mathbf{X})\mathbf{A}^T. \tag{3.76}$$

This "sandwiching" of the covariance matrix between $\mathbf{A}$ and $\mathbf{A}^T$ ensures the dimensions work out correctly: the $n \times n$ covariance matrix of $\mathbf{X}$ is transformed into an $m \times m$ covariance matrix for $\mathbf{Y}$, matching the dimensionality of our transformed random vector.

We can prove this using the same properties of expectation we used in the univariate case:

$$\text{Cov}(\mathbf{Y}) = \mathbb{E}[(\mathbf{Y} - \mathbb{E}[\mathbf{Y}])(\mathbf{Y} - \mathbb{E}[\mathbf{Y}])^T] \tag{3.77}$$

$$= \mathbb{E}[(\mathbf{AX} + \mathbf{b} - (\mathbf{A}\mathbb{E}[\mathbf{X}] + \mathbf{b}))(\mathbf{AX} + \mathbf{b} - (\mathbf{A}\mathbb{E}[\mathbf{X}] + \mathbf{b}))^T] \tag{3.78}$$

$$= \mathbb{E}[\mathbf{A}(\mathbf{X} - \mathbb{E}[\mathbf{X}])(\mathbf{X} - \mathbb{E}[\mathbf{X}])^T \mathbf{A}^T] \tag{3.79}$$

$$= \mathbf{A}\mathbb{E}[(\mathbf{X} - \mathbb{E}[\mathbf{X}])(\mathbf{X} - \mathbb{E}[\mathbf{X}])^T]\mathbf{A}^T \tag{3.80}$$

$$= \mathbf{A}\text{Cov}(\mathbf{X})\mathbf{A}^T. \tag{3.81}$$

This transformation property has important applications in data analysis. When we apply principal component analysis, standardize features, or perform any linear transformation of our data, this formula tells us exactly how the covariance structure will change. These transformations play key roles in many statistical techniques used in astronomy and other fields.

3.6   Sampling Statistics and Uncertainty

Having explored how variance behaves under transformations of individual variables, we now turn to another important question: how does variance behave when we combine different random variables? Just as we did with expectation, we'll begin by examining the variance of sums—a common case that arises frequently in astronomical measurements and statistical applications, from combining multiple observations to understanding how errors propagate through calculations.

For any two random variables X and Y, we have:

$$\text{Var}[X + Y] = \text{Var}[X] + 2\text{Cov}(X, Y) + \text{Var}[Y]. \tag{3.82}$$

We can prove this using our definition of variance:

$$\text{Var}[X + Y] = \mathbb{E}[((X + Y) - \mathbb{E}[X + Y])^2] \tag{3.83}$$

$$= \mathbb{E}[((X - \mathbb{E}[X]) + (Y - \mathbb{E}[Y]))^2] \tag{3.84}$$

$$= \mathbb{E}[(X - \mathbb{E}[X])^2 + 2(X - \mathbb{E}[X])(Y - \mathbb{E}[Y]) + (Y - \mathbb{E}[Y])^2] \tag{3.85}$$

$$= \text{Var}[X] + 2\text{Cov}(X, Y) + \text{Var}[Y]. \tag{3.86}$$

This formula reveals a difference between expectation and variance when combining random variables. While expectations add linearly, variances include an additional covariance term that arises from the squared nature of the calculation. When we expand $(X+Y)^2$, cross-terms of the form XY appear, and their average contribution is precisely the covariance term $2\mathrm{Cov}(X, Y)$. This means that the uncertainty in a sum depends not just on the individual uncertainties, but also on how the variables move together—a crucial principle for error propagation in any scientific measurement or prediction task.

For independent variables, where $\mathrm{Cov}(X, Y) = 0$, the formula simplifies:

$$\mathrm{Var}[X + Y] = \mathrm{Var}[X] + \mathrm{Var}[Y] \quad \text{(for independent variables)}. \tag{3.87}$$

This means that when random variables are independent, their variances add directly. This property underlies much of statistical analysis and has important implications for how uncertainties accumulate in many scientific contexts, from combining multiple measurements to understanding the reliability of aggregate statistics.
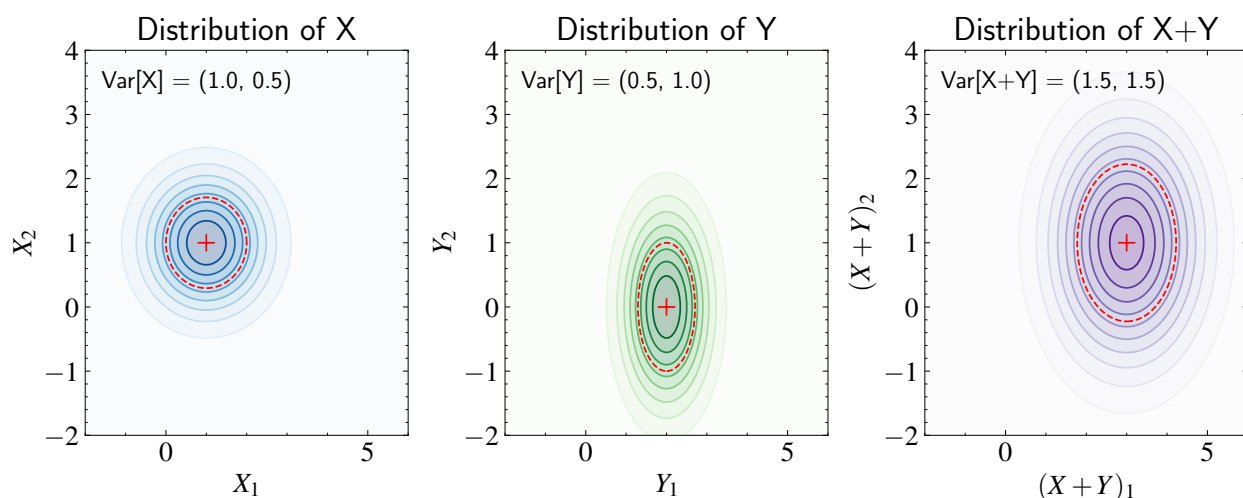
Figure 3.8: Visualization of how variances add for independent random variables. Left panel: Distribution of X (blue contours) with different variances in each dimension (1.0, 0.5). Middle panel: Distribution of Y (green contours) with different variances (0.5, 1.0). Right panel: Distribution of their sum $X + Y$ (purple contours). The red dashed ellipses show the variance structure of each distribution. For independent variables, the variances add component-wise: the variance of the sum in each dimension equals the sum of the individual variances in that dimension. This is evident in the right panel, where $\mathrm{Var}[X+Y] = (1.5, 1.5)$ results from adding the corresponding variances. This increase in variance is intuitive: when we add two independent uncertain quantities, our uncertainty naturally grows since each variable contributes its own source of randomness to the final sum.

This additivity property of variance has a particularly important application: understanding the uncertainty in sample means. When making astronomical measurements, we frequently need to combine multiple observations of the same quantity to improve precision—for instance, multiple measurements of a star's magnitude or repeated spectroscopic observations of a galaxy's redshift. This principle underpins many statistical methods that rely on aggregate information or ensemble behavior.

Let's consider N independent measurements $\{X_1, ..., X_N\}$ of the same quantity. The sample mean, our best estimate of the true value, is defined as:

$$\bar{X} = \frac{1}{N} \sum_{i=1}^{N} X_i. \tag{3.88}$$

Using the variance properties we derived earlier, and assuming the measurements are independent with the same variance σ^2, we can compute:

$$\mathrm{Var}[\bar{X}] = \mathrm{Var} \left[\frac{1}{N} \sum_{i=1}^{N} X_i \right] \tag{3.89}$$

$$= \frac{1}{N^2} \mathrm{Var} \left[\sum_{i=1}^{N} X_i \right] \tag{3.90}$$

$$= \frac{1}{N^2} \sum_{i=1}^{N} \mathrm{Var}[X_i] \quad \text{(all covariances} = 0) \tag{3.91}$$

$$= \frac{1}{N^2} (N\sigma^2) \tag{3.92}$$

$$= \frac{\sigma^2}{N}. \tag{3.93}$$

And hence we recover the well-known result:

$$\mathrm{Var}[\bar{X}] = \frac{\sigma^2}{N}, \tag{3.94}$$

which shows that the variance of the mean decreases inversely with sample size. Taking the square root, the uncertainty decreases as $1/\sqrt{N}$ with sample size. In astronomical terms, this tells us that if each individual measurement of a star's brightness has uncertainty σ, averaging N independent measurements will reduce our uncertainty to $\sigma/\sqrt{N}$. This is why longer exposure times (effectively increasing N) lead to more precise measurements. This same principle explains why larger datasets generally lead to more reliable parameter estimates in

statistical analyses, provided the data are independent and identically distributed.
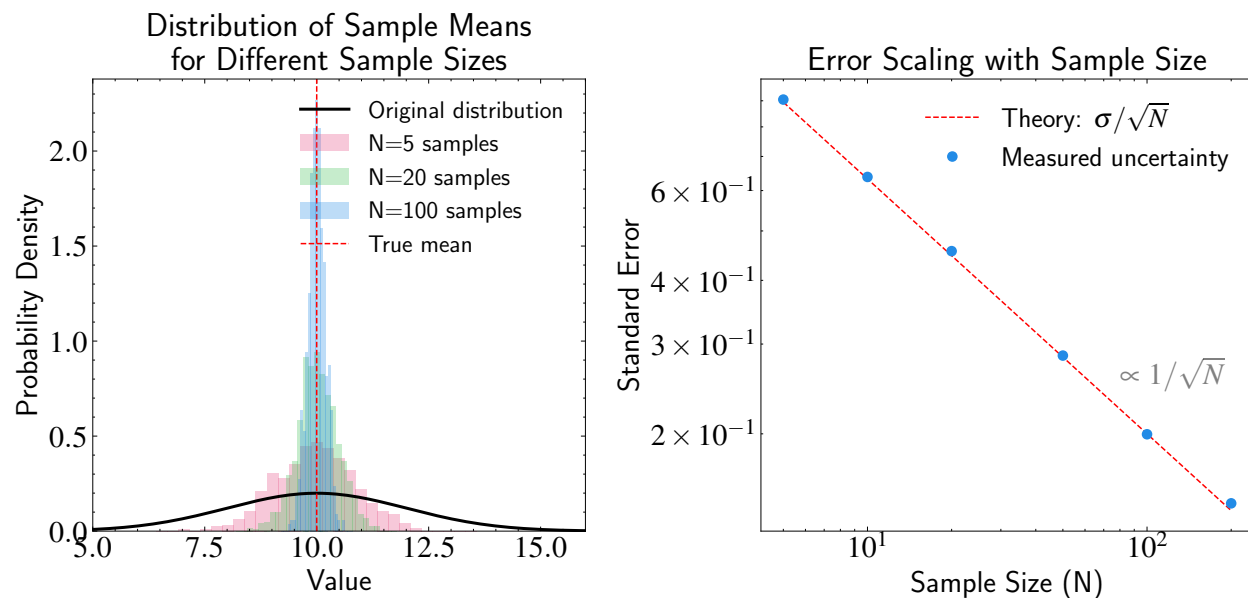
Figure 3.9: Demonstration of how sample mean uncertainty decreases with sample size. Left panel: The black curve shows the original distribution of individual measurements (with true mean shown by red dashed line). The colored histograms show the distributions of sample means for different sample sizes ($N = 5$, 20, and 100). As N increases, the distribution of sample means becomes increasingly concentrated around the true mean, demonstrating how larger samples provide more precise estimates. Right panel: Quantitative analysis of how the standard error (uncertainty in the sample mean) scales with sample size. The red dashed line shows the theoretical prediction $\sigma/\sqrt{N}$, while blue points show the measured uncertainties from numerical simulations.

This discussion of sample mean uncertainty brings us to our original motivation: characterizing probability distributions through summary statistics. When we estimate moments with finite samples, we use sums of the form:

$$\hat{\mu}_k = \frac{1}{N} \sum_{i=1}^{N} x_i^k. \tag{3.95}$$

The hat notation signifies that this is an estimate of the true moment μ_k. This estimate itself exhibits variability known as finite sampling noise—the inherent uncertainty that arises from using a finite number of samples to estimate properties of an infinite population. Understanding this noise is crucial because it determines the reliability of our parameter estimates and the confidence we can place in statistical inferences and predictions based on these estimates.

To understand this noise, consider estimating the moments of the stellar Initial Mass Function (IMF). Even if we could measure stellar masses with perfect precision, our estimate $\hat{\mu}_k$ would still vary if we repeated the measurement with different random samples of stars. This variability occurs because each star's mass is randomly drawn from the underlying IMF distribution, making X^k and consequently $\hat{\mu}_k$ random variables themselves. This same principle applies broadly in statistics: even with perfect measurements, our estimates carry uncertainty because they're based on finite samples from the underlying distribution, and this uncertainty must be properly quantified for reliable statistical inference.

As we established in our analysis of sample means, the precision of such moment estimates improves with larger samples. Specifically, for independent measurements, the variance of our k-th moment estimates scales as $\mathrm{Var}(X^k)/N$, meaning the sampling noise decreases as $1/\sqrt{N}$. This insight explains why modern astronomy has ventured into deep surveys with wide sky coverage. The sheer number of objects in these surveys reduces finite sampling noise, providing increasingly precise estimates of population statistics and thus more stringent constraints on theoretical models. Similarly, in many fields, larger datasets allow for more precise parameter estimation and more reliable statistical inferences.

While the $1/\sqrt{N}$ scaling represents the expected improvement of the moment estimate with sample size, the total uncertainty in moment estimates depends crucially on the variance term $\mathrm{Var}(X^k)$, which grows rapidly with k. To understand this growth, consider expanding a fluctuation around the mean value: if $X = \mu + \delta$ with Taylor's expansion, then

$$X^k = (\mu + \delta)^k \tag{3.96}$$

$$= \mu^k + k\mu^{k-1}\delta + \frac{k(k-1)}{2}\mu^{k-2}\delta^2 + \ldots \tag{3.97}$$

If we only keep the linear term $\mu^k + k\mu^{k-1}\delta$, using the linearity of variance:

$$\mathrm{Var}(X^k) \approx k^2 \mu^{2k-2}\mathrm{Var}(X). \tag{3.98}$$

This shows that the variance of higher moments grows approximately quadratically with k. Just as in our earlier discussion, astronomical distributions often have a few very massive galaxies or extremely bright quasars that can dramatically affect higher-moment estimates, making the estimate of the higher moments inherently noisier compared to lower moment estimates. This phenomenon is not unique to astronomy but appears in many fields where distributions have heavy tails or extreme values.

Yet these higher moments often contain crucial physical information. In cosmology, for instance, the non-Gaussian features in the galaxy distribution—captured only by moments beyond variance—provide key constraints on structure formation theories. This creates a tension: higher moments offer unique physical insights but require substantially larger samples for reliable measurement. This trade-off between information content and estimation precision is a fundamental aspect of statistical analysis that must be carefully navigated when designing studies and analyzing data.

3.7   Bootstrapping

While our discussion above demonstrates the important $\sqrt{N}$ scaling law that governs how uncertainties decrease with sample size, in practice we often need more than just the scaling—we need precise values for these uncertainties to make quantitative statistical inferences. Our analysis above of $\mathrm{Var}(X^k)$ used only the leading-order term in the Taylor expansion to build intuition. The higher-order terms we neglected in our approximation can significantly affect these precise values, especially for small samples or when dealing with highly skewed distributions common in astronomy and many other fields.

Even for simple moment estimates, these higher-order terms in the expansion can become significant, and for multidimensional or nonlinear statistics, analytical expressions may become intractable altogether. This limitation in deriving exact analytical expressions leads us to consider empirical methods for uncertainty estimation that have become increasingly important with the growth of computational statistics.

The bootstrap technique provides a robust way to estimate the variance of estimators when analytical expressions are unavailable. The bootstrap algorithm proceeds as follows: Given an original sample $\{x_1, \ldots, x_N\}$, we:

1. Draw N samples with replacement from this set, creating a "bootstrap sample" $\{x_1^*, \ldots, x_N^*\}$

2. Calculate our statistic of interest (e.g., the k-th moment) on this bootstrap sample:

$$\hat{\mu}_k^* = \frac{1}{N} \sum_{i=1}^{N} (x_i^*)^k \tag{3.99}$$

3. Repeat steps 1–2 many times (typically thousands)

4. Use the variance of these bootstrap estimates to approximate $\text{Var}(\hat{\mu}_k)$
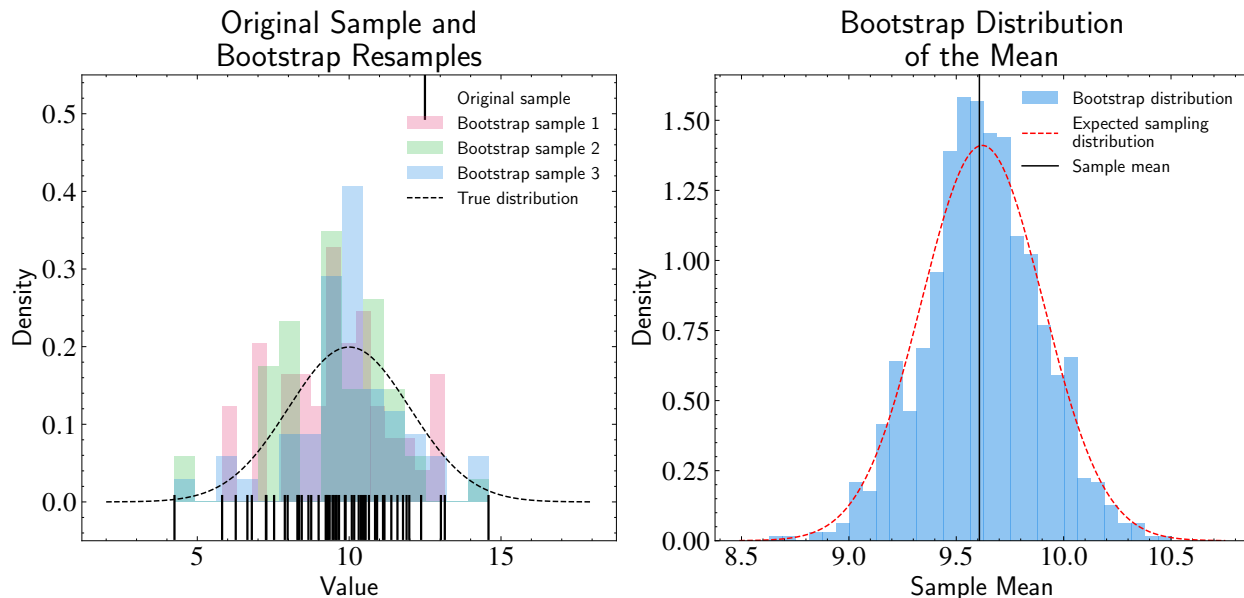
Figure 3.10: Illustration of the bootstrap resampling process and its ability to estimate sampling variance of the first moment. Left panel: Original sample $\{x_1, ..., x_N\}$ (black tick marks) drawn from true distribution $p(x)$ (black dashed curve), with three bootstrap resamples $\{x_1^*, ..., x_N^*\}$ (colored histograms) generated by sampling with replacement. Right panel: Distribution of bootstrap estimates $\hat{\mu}_1^* = \frac{1}{N}\sum_{i=1}^N x_i^*$ from 1000 resamples (blue histogram) compared to theoretical sampling distribution of first moment estimator (red dashed curve). The agreement between bootstrap variance $\text{Var}(\hat{\mu}_1^*)$ and theoretical variance σ^2/N demonstrates bootstrap's accuracy in estimating sampling variance without knowledge of $p(x)$. Black vertical line shows original sample estimate $\hat{\mu}_1 = \frac{1}{N}\sum_{i=1}^N x_i$.

For example, if our original dataset is $\{1, 2, 3\}$, one possible bootstrap sample might be $\{1, 1, 2\}$, another might be $\{2, 3, 3\}$, and so on. Each bootstrap sample maintains the same size as our original dataset, but some values may appear multiple times while others may not appear at all. This resampling process mimics the natural variability that would occur if we could repeatedly collect new datasets of the same size from the same underlying population. The approach is particularly valuable because it provides a computational solution to what is fundamentally a theoretical problem.

The underlying logic of bootstrapping is rooted in how we think about probability distributions and sampling. Recall that our sample $\{x_1, ..., x_N\}$ is drawn from some unknown probability distribution $p(x)$. If we knew $p(x)$ exactly, calculating any moment would simply require integration as discussed earlier. However, we typically only have access to a finite sample. The key insight of bootstrapping is to use this sample itself as a proxy for the underlying distribution, leveraging the information contained in the observed data to estimate

properties of the sampling distribution of our statistics.

When we resample with replacement in bootstrapping, we are effectively treating our observed sample as a discrete approximation to $p(x)$, where each observed value has equal probability $1/N$ of being drawn. This resampling mimics the process that generated our original data: just as our original sample was drawn from the true distribution $p(x)$, our bootstrap samples are drawn from this empirical distribution. If we could draw many new samples from $p(x)$, we could directly study how our statistic $\hat{\mu}_k$ varies across samples, revealing its sampling distribution and hence its uncertainty. Bootstrapping approximates this ideal process using only our available data, providing a powerful tool for uncertainty quantification without requiring additional data collection.

The mathematical justification for this approach relies on the fact that as our sample size N increases, our empirical distribution approaches the true distribution $p(x)$. Consequently, the distribution of statistics computed from bootstrap samples approaches the true sampling distribution we would obtain if we could repeatedly sample from $p(x)$. This convergence explains why bootstrap provides valid estimates of sampling uncertainty and why it has become such a valuable tool for model validation and uncertainty quantification in modern statistical practice.

The power of bootstrapping lies in its generality. Instead of deriving analytical formulas for standard errors—which may be intractable for complex statistics—bootstrapping automatically captures sampling behavior through direct simulation. This is particularly valuable in astronomy where we often need to characterize uncertainty in complex measurements, such as galaxy morphology classifications or stellar parameter estimates from spectroscopy. The method also applies broadly to other fields where complex statistics are used, from economics to ecology, providing uncertainty estimates for quantities ranging from correlation coefficients to diversity indices.

However, understanding bootstrap's logic also reveals its limitations:

First, sample representativeness is crucial. Bootstrap assumes our sample is large enough to reasonably approximate the underlying distribution. If our sample misses important features of $p(x)$ (like rare events), bootstrap will inherit this blindness. This limitation becomes particularly relevant for higher moments, which are sensitive to the distribution's tails, and for applications where the tails of the distribution are of particular interest, such as extreme value analysis or risk assessment.

Second, the basic bootstrap treats observations as independent by resampling individual values. This can produce misleading results when data are correlated, such as in time series or spatial data where neighboring measurements are related. In astronomical contexts, this might occur when studying galaxy clustering or stellar variability. Modified bootstrap techniques like block bootstrapping have been developed to address this limitation, resampling blocks of observations to preserve the correlation structure.

Third, for statistics heavily dependent on extreme values, bootstrap might underestimate uncertainties because it can only resample values present in our original sample. It cannot generate new extreme values that might occur in future datasets, potentially leading to overly optimistic uncertainty estimates for statistics sensitive to outliers. This limitation is particularly relevant in fields like hydrology or finance, where extreme events carry significant importance.

Despite these limitations, bootstrapping remains one of our most valuable tools for uncertainty estimation in practice. Its theoretical foundation in the relationship between samples and populations, combined with its practical simplicity, makes it particularly useful in astronomical applications where we often deal with complex measurements and unknown underlying distributions. The method has been extended in various ways to address its limitations, including parametric bootstrapping, where resamples are drawn from a fitted parametric distribution rather than the empirical distribution, and the jackknife, which systematically leaves out one observation at a time to assess each observation's influence on the statistic of interest.

3.8   Law of Total Variance

Just as the law of total expectation helps us break down expected values in hierarchical problems, the law of total variance provides a framework for decomposing and understanding variability in our data. This decomposition becomes particularly valuable when we want to understand how much of our uncertainty comes from different sources—such as measurement noise versus intrinsic variability, or explainable versus unexplainable variation.

For any two random variables X and Y, the law of total variance states:

$$\mathrm{Var}_X[X] = \mathbb{E}_Y[\mathrm{Var}_X[X|Y]] + \mathrm{Var}_Y[\mathbb{E}_X[X|Y]]. \tag{3.100}$$

This statement says that the total variance of a random variable can be decomposed

into two parts with clear interpretations. The first term, $\mathbb{E}_Y[\mathrm{Var}_X[X|Y]]$, represents the expected value of the conditional variance—the average "unexplained" variability that remains after knowing Y. To understand this term, consider that for each value of Y, we have some spread in possible X values (the conditional variance). We then average these spreads over all possible Y values. For example, even if we know a star's luminosity exactly (Y), there is still some uncertainty in its mass (X) because stars of the same luminosity can have slightly different masses due to factors like age and metallicity—this term quantifies that remaining uncertainty averaged across all luminosities. This represents the irreducible uncertainty that remains even after conditioning on all our available information about Y.

The second term, $\mathrm{Var}_Y[\mathbb{E}_X[X|Y]]$, captures how much of X's variability can be "explained" by knowing Y. This term measures how much the average value of X changes as Y changes. In our stellar example, this represents how much the average stellar mass systematically varies as we look at different luminosities—essentially measuring the strength of the mass-luminosity relation itself. This quantifies how much variance our understanding of the relationship between X and Y can potentially explain.

To prove this relationship, let's write out the total variance and decompose the deviation $(X - \mathbb{E}_X[X])$ into two components: the deviation from the conditional mean $(X - \mathbb{E}_X[X|Y])$, and the deviation of the conditional mean from the overall mean $(\mathbb{E}_X[X|Y] - \mathbb{E}_X[X])$:

$$\mathrm{Var}_X[X] = \mathbb{E}[(X - \mathbb{E}[X])^2] \tag{3.101}$$

$$= \mathbb{E}[((X - \mathbb{E}[X|Y]) + (\mathbb{E}[X|Y] - \mathbb{E}[X]))^2] \tag{3.102}$$

$$= \mathbb{E}[(X - \mathbb{E}[X|Y])^2] + \mathbb{E}[(\mathbb{E}[X|Y] - \mathbb{E}[X])^2] \tag{3.103}$$

$$+ 2\mathbb{E}[(X - \mathbb{E}[X|Y])(\mathbb{E}[X|Y] - \mathbb{E}[X])]. \tag{3.104}$$

The cross-term vanishes because:

$$\mathbb{E}[(X - \mathbb{E}[X|Y])(\mathbb{E}[X|Y] - \mathbb{E}[X])] = \mathbb{E}[\mathbb{E}[(X - \mathbb{E}[X|Y])(\mathbb{E}[X|Y] - \mathbb{E}[X])|Y]] \tag{3.105}$$

$$= \mathbb{E}[(\mathbb{E}[X|Y] - \mathbb{E}[X])\mathbb{E}[(X - \mathbb{E}[X|Y])|Y]] \tag{3.106}$$

$$= \mathbb{E}[(\mathbb{E}[X|Y] - \mathbb{E}[X]) \cdot 0] \tag{3.107}$$

$$= 0, \tag{3.108}$$

where we've used the fact that $\mathbb{E}[X - \mathbb{E}[X|Y]|Y] = 0$ by definition of conditional expectation.

Now looking at the remaining terms:

$$\text{Var}_X[X] = \mathbb{E}[(X - \mathbb{E}[X|Y])^2] + \mathbb{E}[(\mathbb{E}[X|Y] - \mathbb{E}[X])^2] \tag{3.109}$$

$$= \mathbb{E}[\mathbb{E}[(X - \mathbb{E}[X|Y])^2|Y]] + \mathbb{E}[(\mathbb{E}[X|Y] - \mathbb{E}[X])^2] \tag{3.110}$$

$$= \mathbb{E}[\text{Var}[X|Y]] + \text{Var}[\mathbb{E}[X|Y]], \tag{3.111}$$

which is exactly the law of total variance.
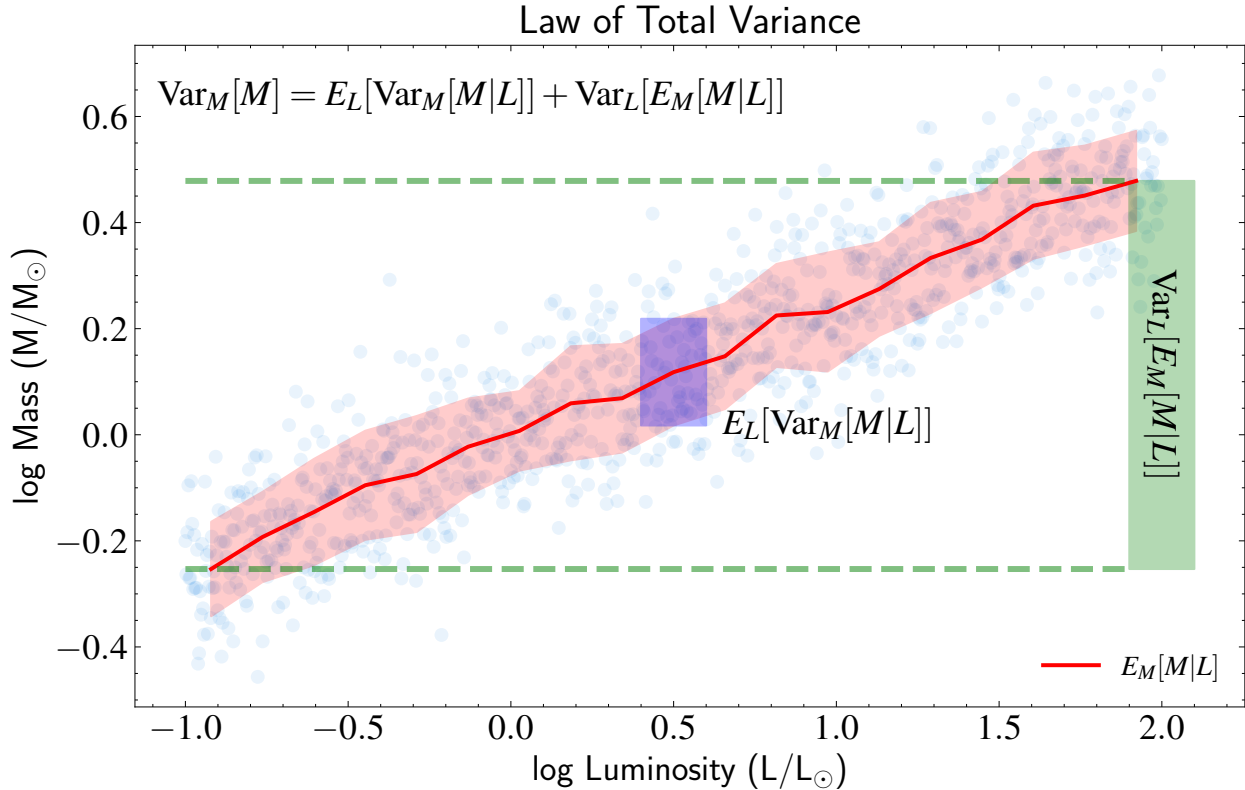
Figure 3.11: Visualization of the law of total variance using the stellar mass-luminosity relationship. The blue points show individual stars, demonstrating the scatter in stellar masses at each luminosity. The red line traces the conditional expectation $\mathbb{E}_M[M|L]$ as a function of luminosity, with the red shaded region showing $\pm 1\sigma$ bounds of the conditional variance. The blue shaded region at $L = 0.5 L_\odot$ highlights $\mathbb{E}_L[\text{Var}_M[M|L]]$, representing the average scatter in mass at fixed luminosity. The green shaded region and dashed lines on the right show the range of conditional expectations, whose variance $\text{Var}_L[\mathbb{E}_M[M|L]]$ captures how the average mass changes with luminosity. The law of total variance states that the total variance in stellar mass equals the sum of these two contributions: the average scatter at fixed luminosity ($\mathbb{E}_L[\text{Var}_M[M|L]]$) plus the variance in the mass-luminosity relationship itself ($\text{Var}_L[\mathbb{E}_M[M|L]]$). This decomposition helps us understand how much of the mass variance comes from intrinsic scatter versus systematic trends with luminosity.

This decomposition is illustrated in Figure 3.11 using the stellar mass-luminosity

relationship. Looking at the figure, we can see individual stars plotted as blue points, showing how stellar masses vary at each luminosity. The red line traces the conditional expectation $\mathbb{E}_M[M|L]$—essentially showing the average mass of stars at each luminosity value. The red shaded region represents the conditional variance at each luminosity, showing how much stellar masses typically deviate from this average. At the specific luminosity $L = 0.5L_\odot$ (highlighted by the blue shaded region), we can see the spread of masses around the conditional mean. When we average these conditional variances across all luminosities, weighted by how common each luminosity is, we get the first term in our decomposition: $\mathbb{E}_L[\mathrm{Var}_M[M|L]]$.

The second term is represented by the green shaded region on the right side of the figure, which shows how much the conditional expectations themselves vary across different luminosities. This variation in $\mathbb{E}_M[M|L]$ (the red line) as L changes represents $\mathrm{Var}_L[\mathbb{E}_M[M|L]]$—capturing how much of the total mass variance can be explained by the systematic relationship between mass and luminosity.

The law of total variance highlights an important principle: improving measurement precision (reducing the first term) might not always substantially reduce our total uncertainty if natural variability (the second term) dominates. For example, in stellar spectroscopy, beyond a certain point, improving our spectral resolution or signal-to-noise ratio won't help us better determine stellar parameters if the remaining variation comes from intrinsic stellar variability or population diversity. This principle has important implications for experimental design and resource allocation in scientific research.

This decomposition also provides insight into when additional variables might be valuable for prediction. If the conditional variance $\mathrm{Var}_X[X|Y]$ is much smaller than the total variance $\mathrm{Var}_X[X]$, then knowing Y substantially reduces our uncertainty about X, suggesting that Y is a valuable predictor. Conversely, if these variances are similar, then Y provides little predictive information about X. This insight helps us assess the potential value of different variables in statistical modeling and prediction tasks.

The law of total variance also generalizes naturally to the multivariate case:

$$\mathrm{Cov}(\mathbf{X}) = \mathbb{E}[\mathrm{Cov}(\mathbf{X}|\mathbf{Y})] + \mathrm{Cov}(\mathbb{E}[\mathbf{X}|\mathbf{Y}]). \tag{3.112}$$

This extension follows from the same proof we developed for the univariate case, as our derivation relied only on properties of expectation that hold equally well for vec-

tors. The interpretation remains similar: the total covariance decomposes into the average of conditional covariances and the covariance of conditional means. This multivariate version becomes particularly useful when analyzing systems with multiple variables, such as multivariate regression problems or complex physical systems with multiple interacting components.

The law of total variance has important applications in Bayesian statistics, particularly for understanding predictive uncertainty. In Bayesian analysis, model parameters (like regression coefficients) are treated as random variables with associated uncertainty. When we want to predict a new outcome y_* while accounting for our parameter uncertainty, the law of total variance allows us to decompose the predictive variance:

$$\text{Var}[y_*] = \mathbb{E}_\theta[\text{Var}[y_*|\theta]] + \text{Var}_\theta[\mathbb{E}[y_*|\theta]] \tag{3.113}$$

The first term represents the average inherent variance of our predictions for each possible parameter value θ (weighted by the posterior distribution of θ), while the second term captures how much our predictions vary due to parameter uncertainty. This decomposition helps distinguish between aleatoric uncertainty (inherent randomness in the data-generating process) and epistemic uncertainty (uncertainty due to our limited knowledge of parameters).

3.9   Summary

In this chapter, we have developed the mathematical machinery needed to characterize probability distributions and extract meaningful information from finite datasets—foundations that prove essential for statistical analysis and the quantitative methods we'll explore in subsequent chapters.

We began with the challenge of extracting reliable information from limited observations, recognizing that we rarely observe probability distributions directly but must instead infer their properties from finite samples with their own uncertainties. This perspective is central to modern statistical thinking, where we explicitly acknowledge the limitations of our data and the uncertainties in our inferences.

Our journey progressed systematically from basic concepts of moments and transformations to more complex ideas like bootstrapping and variance decomposition. We started by exploring moments of distributions, which provide a hierarchical characterization where each successive moment emphasizes different features: the first moment captures central

tendency needed for parameter estimation, the second moment measures spread crucial for uncertainty quantification, and higher moments become increasingly sensitive to extreme values that can significantly impact statistical robustness.

Through the mathematical formalism of expectation, we established key properties including linearity and additivity, extending these concepts naturally to multivariate settings that characterize many real-world problems. The law of total expectation demonstrated how we can decompose complex estimation problems into manageable hierarchical structures—an approach that becomes particularly valuable when dealing with conditional relationships and hierarchical data structures.

Our investigation of transformations of random variables revealed how probability distributions change under mathematical operations, providing the foundation for understanding how uncertainties propagate through calculations. We demonstrated that linear transformations preserve the Gaussian nature of distributions while scaling their variances quadratically, and showed how multivariate transformations require the Jacobian determinant to ensure probability conservation. These insights prove crucial for many statistical applications, from change of variables in integration to understanding how data transformations affect statistical properties.

Our exploration of variance and covariance revealed how uncertainty propagates through combinations of random variables—knowledge that becomes essential for understanding prediction uncertainties and error propagation. We discovered that while expectations add linearly, variances include covariance terms that capture how variables move together, a crucial insight for understanding correlated measurements and their statistical implications. The correlation coefficient provided a scale-invariant measure of relationship strength, bounded between -1 and +1 by the Cauchy-Schwarz inequality, giving us a tool for comparing relationship strengths across different variable pairs and identifying the strongest patterns in multivariate data.

The extension to multivariate settings through covariance matrices demonstrated how these concepts scale to high-dimensional data common in modern scientific applications. We showed how covariance matrices transform under linear operations, knowledge that becomes crucial for understanding how data transformations affect correlation structures and for properly accounting for uncertainties in multivariate analyses.

The study of sampling statistics and uncertainty illuminated how precision improves with sample size through the $1/\sqrt{N}$ scaling law—a relationship that governs the reliability

of statistical estimates across disciplines. We demonstrated how finite sampling noise affects moment estimates differently, with higher moments requiring substantially larger samples for reliable estimation due to their increased sensitivity to rare, extreme events. This analysis revealed a fundamental trade-off: higher moments contain valuable information that can distinguish between different theoretical predictions, but they require significantly larger samples to constrain reliably.

Our exploration of bootstrapping introduced powerful resampling methods that provide practical tools for uncertainty estimation when analytical expressions become intractable. This technique exemplifies how computational approaches can extend our statistical toolkit beyond purely analytical methods, particularly valuable when dealing with complex statistics and unknown underlying distributions. The bootstrap's effectiveness stems from treating our observed sample as an empirical approximation to the underlying distribution, allowing us to simulate the sampling process that generated our data.

The law of total variance provided a framework for decomposing uncertainty into interpretable components, separating "explained" variability from intrinsic scatter. This decomposition proves essential for understanding systems where multiple sources contribute to observed variability, allowing us to systematically separate and quantify different sources of uncertainty. The mathematical framework revealed that total variance decomposes into the expected conditional variance plus the variance of conditional expectations, providing insight into how knowledge of additional variables affects our uncertainty about outcomes and guiding variable selection in statistical modeling.

Chapter 4 will demonstrate how these statistical principles translate directly into the parameter estimation framework of linear regression. We will see how the concept of expectation enables us to derive optimal parameter estimates through maximum likelihood principles, how variance and covariance structures determine the uncertainty in these estimates, and how the sampling theory we developed here helps us understand the reliability of regression models. The mathematical framework for transformations, the understanding of sampling variability, and the tools for uncertainty quantification will all prove essential as we move from characterizing individual distributions to modeling relationships between variables.

Further Reading: The development of statistical theory has been shaped by several foundational contributions, beginning with the influential work of Fisher [1922], which developed concepts of efficiency, sufficiency, and consistency that remain central to statistical infer-

ence. Cramer [1946] provided mathematical treatment connecting probability theory with statistical methods, contributing to a unified framework that became widely adopted in the field. For readers seeking modern treatments of statistical theory, Cox and Hinkley [1974] offer a balance between mathematical rigor and practical insight, while Casella and Berger [2002] serves as a graduate text building statistical inference from probability foundations. Kendall and Stuart [1977] and Stuart and Ord [1994] provide extensive coverage of distribution theory and statistical methods, serving as valuable references for properties of distributions and moments. For practical error analysis in physical sciences, Taylor [1982] offers a widely-used introduction to uncertainty propagation and error estimation. The bootstrap method was developed by Efron [1979], with Davison and Hinkley [1997] providing coverage of bootstrap theory and applications across various contexts. The field has seen particular growth in astronomy-specific applications: Lupton [1993] connects general statistical theory with astronomical practice, while Wall and Jenkins [2003] focus on statistical methods for observational astronomy, covering both frequentist and Bayesian approaches.

Chapter 4

Chapter 4: Linear Regression

In our previous chapters, we developed probability theory and summary statistics, exploring how these frameworks provide natural approaches for astronomical data analysis. We examined why astronomy's unique challenges—from analyzing rare events to confronting systematic uncertainties—often necessitate a Bayesian rather than frequentist perspective. This mathematical groundwork now serves our understanding of various machine learning techniques commonly deployed in astronomy throughout this course.

We begin our exploration of supervised learning techniques by demonstrating the power of Bayesian inference through perhaps one of the simplest yet most elegant techniques in machine learning: linear regression. While conceptually straightforward, we'll discover that even this simple technique reveals surprising mathematical depth when viewed through the lens of Bayesian inference. By treating both our data and model parameters as random variables, we develop a more complete statistical understanding of the fitting process.

Our choice to begin with linear regression serves two key purposes. First, its inherent simplicity provides an ideal context for visualizing and understanding Bayesian inference in action. The concrete nature of line-fitting makes abstract statistical concepts tangible and practical. Second, as we'll see throughout this course, linear regression—both its capabilities and limitations—serves as a natural bridge to many other fundamental concepts in machine learning. The insights we develop here will extend naturally to more sophisticated methods, from logistic regression to Gaussian processes and neural networks in future chapters.

4.1   Linear Regression Fundamentals

Linear regression addresses one of the most fundamental tasks in data analysis: mapping an input variable x to a continuous output variable y through a linear relationship. In its most basic form, this relationship can be expressed as:

$$y = w_0 + w_1 x, \tag{4.1}$$

where w_0 is the intercept and w_1 is the slope. This simple equation embodies a strong inductive bias—an assumption about the nature of the relationship we're trying to model. In this case, we assume the relationship between x and y is linear.

At first glance, this might seem overly restrictive. After all, many astronomical phenomena exhibit complex, nonlinear behaviors. However, linear regression remains a cornerstone technique in astronomical research for several compelling reasons that demonstrate the power of "keeping things simple" while maintaining mathematical rigor.

Expressiveness through transformations   We can make linear regression surprisingly expressive by transforming our input features. For example, consider Kepler's Third Law, which relates orbital period (P) to semi-major axis (a) through the equation:

$$P^2 = \frac{4\pi^2}{GM} a^3. \tag{4.2}$$

This nonlinear relationship becomes linear when we take logarithms of both sides:

$$\log P = \frac{1}{2} \log \left(\frac{4\pi^2}{GM} \right) + \frac{3}{2} \log a. \tag{4.3}$$

The transformation technique becomes particularly powerful when we consider that many fundamental relationships in astronomy follow power laws. As we discussed in Chapter 2, power laws emerge naturally in astronomy when physical processes operate similarly across different scales—when there's no inherent preferred scale in the system. This scale invariance is a common feature in astronomical systems, from stellar masses to galaxy properties, making power-law relationships ubiquitous in our field.

Consider the M-σ relation, which relates the mass of a supermassive black hole (M_{BH})

to the velocity dispersion ($\boldsymbol{\sigma}$) of its host galaxy's bulge:

$$M_{\mathrm{BH}} = \alpha \boldsymbol{\sigma}^{\beta}. \tag{4.4}$$

Similarly, the Kennicutt-Schmidt law describes how the star formation rate surface density ($\boldsymbol{\Sigma}_{SFR}$) relates to the molecular gas surface density ($\boldsymbol{\Sigma}_{mol}$):

$$\boldsymbol{\Sigma}_{SFR} = \alpha \boldsymbol{\Sigma}_{mol}^{\beta}. \tag{4.5}$$

Both of these fundamental astronomical relationships, though nonlinear in their original form, transform into linear relationships in logarithmic space:

$$\log M_{BH} = \log \alpha + \beta \log \boldsymbol{\sigma}, \tag{4.6}$$

$$\log \boldsymbol{\Sigma}_{SFR} = \log \alpha + \beta \log \boldsymbol{\Sigma}_{mol}. \tag{4.7}$$

Physical interpretability These examples illustrate a key advantage of linear regression models: they often provide clearer physical interpretability than more complex approaches. The coefficients (or weights, in modern machine learning terminology) directly correspond to physically meaningful quantities. The slope β in these logarithmic relationships directly represents the power-law index, revealing fundamental aspects of the underlying physics. For instance, in the Kennicutt-Schmidt law, $\beta \approx 1.4$ indicates a superlinear relationship: doubling the gas density leads to more than a doubling of the star formation rate. This superlinearity suggests that star formation becomes increasingly efficient at higher gas densities, possibly due to stronger self-gravity and enhanced molecular cloud collision rates in denser environments.

The intercept terms ($\log \alpha$) also carry physical significance. In the M-$\boldsymbol{\sigma}$ relation, $\log \alpha$ represents the normalization factor that connects stellar dynamics to black hole mass. In the Kennicutt-Schmidt law, $\log \alpha$ quantifies the global efficiency of the star formation process, telling us how effectively a galaxy can convert a given density of molecular gas into new stars.

Mathematical advantages Beyond interpretability, linear regression offers mathematical advantages that emerge from our Bayesian framework. First, for many objective functions derived from Bayesian inference, linear regression yields analytical solutions. This means we can determine the optimal model parameters through direct mathematical calculation,

without requiring computationally expensive iterative optimization procedures. Second, and perhaps more profoundly, linear regression naturally accommodates the Bayesian treatment of model parameters as random variables. This probabilistic approach allows us to quantify not just point estimates of our parameters, but their full probability distributions, enabling rigorous assessment of parameter uncertainties, correlation structures, and confidence intervals—essential tools for robust scientific inference.

This combination of physical interpretability and mathematical tractability explains why linear regression remains a cornerstone technique in astronomical data analysis, even as more sophisticated methods continue to emerge.

4.2   Mathematical Formalism

Having established why linear regression is valuable for astronomy, let's now formalize the mathematical framework that underlies this technique. We assume our output y, a scalar, can be written as a linear combination of our input features. If we have d input features, we can write this out explicitly:

$$y = w_0 + w_1 x_1 + w_2 x_2 + \ldots + w_d x_d + \varepsilon. \tag{4.8}$$

We can express this more compactly using vector notation:

$$y = \mathbf{w}^T \mathbf{x} + \varepsilon. \tag{4.9}$$

Here, w_0 is the intercept term (also known as the bias term), $\mathbf{w}$ is our vector of model parameters (weights), $\mathbf{x}$ is our vector of input features, and ε represents noise or error in our measurements. The intercept/bias term w_0 allows our model to shift the predicted values up or down, independent of the input features.

For example, consider our earlier M-$\boldsymbol{\sigma}$ relation example after taking logarithms. In its simplest form, y would be $\log M_{\mathrm{BH}}$, and x_1 would be $\log \boldsymbol{\sigma}$. However, we can incorporate additional features that might influence black hole mass, such as galaxy morphology indicators or environmental parameters, making $\mathbf{x}$ multidimensional. For instance, we might model:

$$\log M_{\mathrm{BH}} = w_0 + w_1 \log \boldsymbol{\sigma} + w_2 \log R_e + w_3 (B/T) + \varepsilon, \tag{4.10}$$

where R_e is the effective radius of the galaxy and B/T is the bulge-to-total mass ratio. Here,

w_0 serves as the intercept/bias term, representing the baseline black hole mass when all other terms are zero.

While we assume y to be a scalar for simplicity (like a single black hole mass), this framework readily generalizes to vector-valued outputs (like simultaneously predicting multiple galaxy properties). In such cases, we would have a different set of weights $\mathbf{w}_i$ for each output dimension y_i, effectively running multiple parallel regressions.

For mathematical convenience, we can incorporate the intercept/bias term w_0 by augmenting our feature vector with a constant 1:

$$
\begin{pmatrix} y \end{pmatrix} = \begin{pmatrix} w_0 & w_1 & w_2 & \cdots & w_d \end{pmatrix} \cdot \begin{pmatrix} 1 \\ x_1 \\ x_2 \\ \vdots \\ x_d \end{pmatrix} + \varepsilon. \tag{4.11}
$$

By including this constant 1 as our first feature, w_0 becomes part of our weight vector, allowing us to express both the linear transformation and the intercept/bias term in a single, compact dot product $\mathbf{w}^T \mathbf{x}$. This is mathematically equivalent to our earlier formulation but provides a more elegant representation.

As we discussed earlier, we need not limit ourselves to using the raw input features directly. We can apply any mathematical transformation to our inputs, mapping $\mathbf{x}$ to some new feature space through functions $\boldsymbol{\phi}(\mathbf{x})$. This leads to a more general form of linear regression:

$$
y(\mathbf{x}, \mathbf{w}) = \sum_{j=0}^{M-1} w_j \cdot \phi_j(\mathbf{x}) = \mathbf{w}^T \boldsymbol{\phi}(\mathbf{x}), \tag{4.12}
$$

where $\mathbf{w} = (w_0, \ldots, w_{M-1})^T$ is our vector of parameters, $\boldsymbol{\phi}(\mathbf{x}) = (\phi_0(\mathbf{x}), \ldots, \phi_{M-1}(\mathbf{x}))^T$ is our vector of basis functions, and by convention, $\phi_0(\mathbf{x}) = 1$, making w_0 the bias parameter.

The notation $y(\mathbf{x}, \mathbf{w})$ emphasizes that our model represents a function that maps any input $\mathbf{x}$ to a predicted output y, given a specific choice of parameters $\mathbf{w}$. This functional view is crucial because it highlights our ultimate goal in this machine learning model: we want to find parameters $\mathbf{w}$ that not only fit our existing data well but also make accurate predictions for new, unseen data points.

For instance, in our M-$\boldsymbol{\sigma}$ relation example, once we determine suitable parameters $\mathbf{w}$,

we should be able to estimate a black hole mass for any galaxy given its velocity dispersion and other relevant properties. This predictive perspective—transforming data into insight that generalizes beyond our training set—lies at the heart of machine learning.

The basis functions $\phi_j(\mathbf{x})$ can take many forms. For instance, in our earlier power-law examples, $\phi_1(\mathbf{x})$ might be $\log(x)$. Or for polynomial regression, we might use $\phi_j(\mathbf{x}) = x^j$. When we simply take $\boldsymbol{\phi}(\mathbf{x}) = \mathbf{x}$, we recover our original linear regression form.

This mathematical framework provides the foundation for understanding how linear regression connects to the broader machine learning paradigm. The choice of basis functions $\boldsymbol{\phi}(\mathbf{x})$ represents one of the key design decisions in building a linear model, allowing us to encode domain knowledge about the expected relationships in our data while maintaining the mathematical advantages of linearity in the parameters $\mathbf{w}$.

4.3   Maximum Likelihood Estimation

Having defined our model, we now face a crucial question: what makes a set of parameters $\mathbf{w}$ "best" for our purposes? As mentioned earlier, we seek parameters that not only fit our existing data well but also allow our model to generalize effectively to new observations. This balance between fit and generalization can be formalized through Bayesian inference.

Recall from Chapter 2 that in our general Bayesian framework, we use $\boldsymbol{\theta}$ to denote model parameters. For linear regression specifically, we will use $\mathbf{w}$ to represent our weight parameters, following the machine learning convention. The posterior distribution of our parameters is proportional to the product of the likelihood and prior:

$$p(\mathbf{w}|\mathcal{D}) \propto p(\mathcal{D}|\mathbf{w})p(\mathbf{w}). \tag{4.13}$$

Here, $\mathbf{w}$ itself is a random variable, with its probability distribution given by this posterior. This distribution encapsulates our uncertainty about the true parameter values given our data $\mathcal{D}$. The complete posterior distribution provides a full description of our parameter uncertainties, telling us not just the most likely parameter values but also how confident we can be in these estimates.

While having this complete distribution is powerful, for many practical applications, we often want to identify a single "best" set of parameters. One natural approach is to find

the parameters that maximize the posterior probability:

$$\mathbf{w}_{\text{MAP}} = \arg \max_{\mathbf{w}} p(\mathbf{w}|\mathcal{D}). \tag{4.14}$$

This is known as the Maximum A Posteriori (MAP) estimate. However, as a starting point, let's consider an even simpler case where we have minimal prior knowledge about our parameters—what we call an uninformative prior. In this case, we can assume $p(\mathbf{w})$ is approximately constant and independent of $\mathbf{w}$. Under this assumption, maximizing the posterior becomes equivalent to maximizing the likelihood $p(\mathcal{D}|\mathbf{w})$ alone:

$$\mathbf{w}_{\text{ML}} = \arg \max_{\mathbf{w}} p(\mathcal{D}|\mathbf{w}). \tag{4.15}$$

This approach, known as maximum likelihood estimation (MLE), represents the simplest way to determine optimal parameters based purely on how well they explain our observed data.

But what is the likelihood here? Recall that the likelihood $p(\mathcal{D}|\mathbf{w})$ by definition asks: given a proposed set of parameters $\mathbf{w}$ (which we aim to optimize in MLE), how likely are we to observe what we actually observed in our data? In our case, the data consists of pairs $(\mathbf{x}_i, t_i)$, where t_i represents our observed values.

Let's consider how our observations relate to our model predictions. We assume that each observation can be described as:

$$t = y(\mathbf{x}, \mathbf{w}) + \varepsilon, \text{ where } \varepsilon \sim \mathcal{N}(0, \sigma^2). \tag{4.16}$$

Here, we deliberately distinguish between t (our observed values) and $y(\mathbf{x}, \mathbf{w})$ (our model predictions). While $y(\mathbf{x}, \mathbf{w})$ represents our deterministic model prediction for a given input $\mathbf{x}$ and parameters $\mathbf{w}$, the actual observed value t includes measurement noise ε. This noise term ε follows a Gaussian distribution centered at zero with variance σ^2, reflecting our assumption that measurements scatter symmetrically around the true model values due to random uncertainties.

This treatment of uncertainty is not just a mathematical convenience—it's fundamentally necessary for meaningful Bayesian inference. If our data were absolutely certain ($\sigma = 0$), we would expect to know our model parameters with perfect precision—a situation that never occurs in real astronomical observations. As we discussed in Chapter 2, this relationship between data uncertainty and model uncertainty reflects a deeper truth about

scientific knowledge: our understanding of physical systems is fundamentally limited by the precision of our measurements. This is why we needed to develop the rigorous framework of Bayesian statistics—to quantify and reason about these unavoidable uncertainties in a principled way.
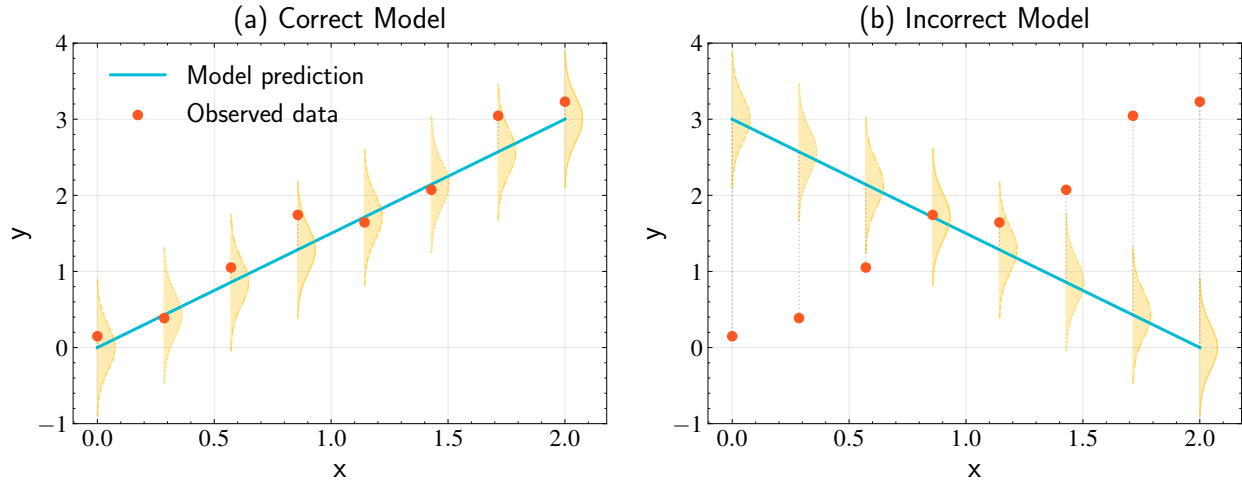
Figure 4.1: Visualization of the likelihood function for linear regression with Gaussian noise. The cyan curves show model predictions $y(\mathbf{x}, \mathbf{w})$ for two different parameter values $\mathbf{w}$. Yellow distributions indicate the Gaussian uncertainty in possible observations at each prediction point, while red dots show actual observations. (a) A model with appropriate linear coefficients, where observations scatter naturally within the expected uncertainty. (b) A model with incorrect coefficients, showing the deviations of the model predictions from the data that cannot be explained by data measurement uncertainty alone.

For a single observation, the likelihood of observing value t given input $\mathbf{x}$ follows directly from our noise model. Since we assumed $t = y(\mathbf{x}, \mathbf{w}) + \varepsilon$ where $\varepsilon \sim \mathcal{N}(0, \sigma^2)$, the observation t must itself follow a Gaussian distribution centered at our model prediction $y(\mathbf{x}, \mathbf{w})$ with variance σ^2. We can write this explicitly using the Gaussian probability density function:

$$
\begin{aligned}
p(t|\mathbf{x}, \mathbf{w}, \sigma^2) &= \frac{1}{\sqrt{2\pi\sigma^2}} \exp\left(-\frac{(t - y(\mathbf{x}, \mathbf{w}))^2}{2\sigma^2}\right) \\
&= \mathcal{N}(t|y(\mathbf{x}, \mathbf{w}), \sigma^2).
\end{aligned}
\tag{4.17}
$$

This equation formalizes our belief about where observations might fall relative to our model predictions. The parameter σ^2 determines how quickly this probability falls off—larger values of σ^2 indicate greater measurement uncertainty and thus a more gradual decrease in probability as we move away from the model prediction. This reflects our level of confidence in the measurements: with small σ^2, for the correct model with the right parameters $\mathbf{w}$, we

expect observations to cluster tightly around our model predictions, while larger σ^2 allows for more scatter in the observations.

With incorrect parameters, we expect systematic deviations where our predictions consistently miss the data points, even accounting for measurement uncertainties. In such cases, the Gaussian distributions centered on our model predictions would fail to capture the actual pattern of observations, indicating that we need to adjust our model parameters.

The figure above illustrates how the likelihood function behaves with good versus poor model parameters. In (a), the model predictions align well with the data within expected uncertainties, while in (b), the predictions systematically miss the observations, indicating poorly chosen parameters. By optimizing MLE, we expect the parameters to converge toward values that produce predictions that best explain our observations, accounting for the known measurement uncertainties.

Having established the likelihood for a single observation, let's consider the more realistic scenario where we have N data points. We'll make a simplifying assumption that our observations are independent. The independence assumption means that knowing the outcome of one measurement tells us nothing about the outcomes of other measurements. For example, in the M-$\boldsymbol{\sigma}$ relation, when measuring velocity dispersions and black hole masses of different galaxies, the measurement of one galaxy's velocity dispersion doesn't influence our measurement of another galaxy. This is often a reasonable assumption in astronomy, where we typically observe different objects with separate observations, each subject to its own set of random measurement uncertainties.

Let's further consider that each measurement may have different uncertainties σ_i^2. The likelihood of observing our entire dataset is the product of the individual likelihoods. This product form follows directly from the definition of independence in probability theory: when events are independent, the probability of all events occurring together equals the product of their individual probabilities. In our case, since the measurements are independent, the probability of obtaining our complete set of measurements is simply the product of the probabilities of each individual measurement. Here, $\mathbf{t}$ represents our vector of all observed target values, and $\mathbf{X}$ is our matrix of input features:

$$p(\mathbf{t}|\mathbf{X}, \mathbf{w}, \{\sigma_i^2\}) = \prod_{n=1}^{N} p(t_n|\mathbf{x}_n, \mathbf{w}, \sigma_i^2) = \prod_{n=1}^{N} \mathcal{N}(t_n|\mathbf{w}^T\boldsymbol{\phi}(\mathbf{x}_n), \sigma_i^2). \tag{4.18}$$

This product form of the likelihood enables us to combine evidence from multiple independent measurements in a mathematically rigorous way, weighting each observation according to its own uncertainty σ_i^2.

To make this product more mathematically tractable, we take the logarithm of both sides. Since the logarithm is a monotonic function—meaning it preserves the order of numbers—maximizing the log-likelihood is equivalent to maximizing the likelihood itself. This transformation is particularly useful because it converts our product of probabilities into a sum, which is much easier to work with:

$$\ln p(\mathbf{t}|\mathbf{X}, \mathbf{w}, \{\sigma_i^2\}) = \sum_{n=1}^{N} \ln \mathcal{N}(t_n|\mathbf{w}^T\boldsymbol{\phi}(\mathbf{x}_n), \sigma_i^2). \tag{4.19}$$

Expanding this using the explicit form of the Gaussian distribution with heterogeneous noise:

$$\ln p(\mathbf{t}|\mathbf{X}, \mathbf{w}, \{\sigma_i^2\}) = -\frac{1}{2}\sum_{n=1}^{N} \ln\left(2\pi\sigma_n^2\right) - \sum_{n=1}^{N} \frac{\left(t_n - \mathbf{w}^T\boldsymbol{\phi}(\mathbf{x}_n)\right)^2}{2\sigma_n^2}. \tag{4.20}$$

When we seek to find the optimal parameters $\mathbf{w}$ that maximize this log-likelihood, we can focus solely on the terms that depend on $\mathbf{w}$. Since the first term doesn't depend on $\mathbf{w}$, we can drop it and focus on minimizing the negative of the second term:

$$\arg\max_{\mathbf{w}} \ln p(\mathbf{t}|\mathbf{X}, \mathbf{w}, \{\sigma_i^2\}) = \arg\min_{\mathbf{w}} \sum_{n=1}^{N} \frac{(t_n - \mathbf{w}^T\boldsymbol{\phi}(\mathbf{x}_n))^2}{2\sigma_n^2}. \tag{4.21}$$

This equation reveals that maximizing the likelihood under our heterogeneous Gaussian noise assumption is mathematically equivalent to minimizing the weighted sum of squared errors. The weights are inversely proportional to the measurement variances, meaning that more precise measurements (smaller σ_n^2) contribute more strongly to determining the optimal parameters. When dealing with varying σ_n^2 (heteroscedastic errors), using standard unweighted least squares would inappropriately give equal weight to all measurements, regardless of their precision.

In the case of homogeneous noise where $\sigma_n = \sigma$ for all n, the equation simplifies to:

$$\arg\min_{\mathbf{w}} \sum_{n=1}^{N} \frac{(t_n - \mathbf{w}^T \boldsymbol{\phi}(\mathbf{x}_n))^2}{2\sigma^2} = \frac{1}{2\sigma^2} \arg\min_{\mathbf{w}} \sum_{n=1}^{N} (t_n - \mathbf{w}^T \boldsymbol{\phi}(\mathbf{x}_n))^2. \tag{4.22}$$

Since $1/2\sigma^2$ is just a constant scaling factor, minimizing this expression is equivalent to minimizing the unweighted sum of squared errors. This explains why standard least squares regression is appropriate when measurement uncertainties are uniform across all observations.

Importantly, in the derivation above, we have seen that weighted least squares emerges naturally from maximum likelihood estimation when we properly account for measurement uncertainties. The weighted sum of squared residuals that we derived, $\sum_{n=1}^{N} \frac{(t_n - \mathbf{w}^T \boldsymbol{\phi}(\mathbf{x}_n))^2}{\sigma_n^2}$, is known in statistics as the chi-square statistic, commonly denoted as χ^2. This statistic measures the goodness of fit between our model predictions and the data, with each squared residual weighted by its measurement uncertainty. While chi-square is commonly used in astronomical model fitting, it is crucial to recognize that this is not an arbitrary choice, but rather a direct mathematical consequence of our probabilistic framework. This connection between chi-square minimization and maximum likelihood estimation demonstrates how seemingly disparate statistical concepts are unified under the framework of probabilistic modeling.

4.4 Analytical Solution

Having established our objective function through maximum likelihood estimation, we now turn to the practical question of finding the optimal parameters $\mathbf{w}$. Our weighted least squares loss function:

$$E(\mathbf{w}) = \sum_{n=1}^{N} \frac{(t_n - \mathbf{w}^T \boldsymbol{\phi}(\mathbf{x}_n))^2}{2\sigma_n^2} \tag{4.23}$$

can be rewritten in matrix form:

$$E(\mathbf{w}) = \frac{1}{2}(\mathbf{t} - \boldsymbol{\Phi}\mathbf{w})^T \mathbf{S}^{-1} (\mathbf{t} - \boldsymbol{\Phi}\mathbf{w}), \tag{4.24}$$

where:

- $\mathbf{t} = (t_1, \ldots, t_N)^T \in \mathbb{R}^{N \times 1}$ is our vector of observed values, where N is the number of data points

- $\mathbf{\Phi} \in \mathbb{R}^{N \times M}$ is our design matrix, a fundamental concept in regression analysis. To understand the design matrix, let's break it down:

  - Each row corresponds to one data point (observation)

  - Each column represents a feature or predictor variable

  - The entry at row i and column j contains the j-th feature evaluated at the i-th data point

  More formally, $\mathbf{\Phi} = [\phi(\mathbf{x}_1), \ldots, \phi(\mathbf{x}_N)]^T$, where $\phi(\mathbf{x})$ represents our feature transformations (also called basis functions) that map each input $\mathbf{x}$ to an M-dimensional feature vector. For example, if we're fitting a quadratic function, $\phi(\mathbf{x})$ might transform a single input x into the vector $(1, x, x^2)$, making $M = 3$

- $\mathbf{S} \in \mathbb{R}^{N \times N}$ is a diagonal matrix of measurement variances: $\mathrm{diag}(\sigma_1^2, \ldots, \sigma_N^2)$, where σ_i^2 represents the variance of the i-th measurement. Since $\mathbf{S}$ is diagonal, its inverse $\mathbf{S}^{-1}$ is also diagonal with elements $1/\sigma_i^2$: $\mathbf{S}^{-1} = \mathrm{diag}(1/\sigma_1^2, \ldots, 1/\sigma_N^2)$

This quadratic form is particularly interesting because it guarantees two important properties, which may be familiar from working with simple quadratic equations like $y = ax^2 + bx + c$:

1. The function is convex (opens upward when $a > 0$), meaning it has a unique global minimum, just as a parabola $y = ax^2 + bx + c$ has exactly one lowest point

2. This minimum can be found analytically through "completing the square"—a technique we learned in basic algebra where we rewrite $ax^2 + bx + c$ as $a(x + \frac{b}{2a})^2 + (c - \frac{b^2}{4a})$ to find the vertex. The same principle applies here, though in higher dimensions

While we could theoretically find the minimum by completing the square, taking derivatives offers a more direct and computationally efficient approach and avoids the need to manipulate large matrices into a perfect square form. Recall that $E(\mathbf{w}) = \frac{1}{2}(\mathbf{t} - \mathbf{\Phi}\mathbf{w})^T \mathbf{S}^{-1}(\mathbf{t} - \mathbf{\Phi}\mathbf{w})$. Expanding this expression:

$$E(\mathbf{w}) = \frac{1}{2}(\mathbf{t}^T \mathbf{S}^{-1}\mathbf{t} - \mathbf{t}^T \mathbf{S}^{-1}\mathbf{\Phi}\mathbf{w} - \mathbf{w}^T \mathbf{\Phi}^T \mathbf{S}^{-1}\mathbf{t} + \mathbf{w}^T \mathbf{\Phi}^T \mathbf{S}^{-1}\mathbf{\Phi}\mathbf{w}). \tag{4.25}$$

Since $\mathbf{t}^T \mathbf{S}^{-1} \boldsymbol{\Phi} \mathbf{w}$ is a scalar, it equals its transpose $\mathbf{w}^T \boldsymbol{\Phi}^T \mathbf{S}^{-1} \mathbf{t}$. Taking the derivative with respect to $\mathbf{w}$ and applying matrix calculus rules:

$$\nabla_{\mathbf{w}} E(\mathbf{w}) = -\boldsymbol{\Phi}^T \mathbf{S}^{-1} \mathbf{t} + \boldsymbol{\Phi}^T \mathbf{S}^{-1} \boldsymbol{\Phi} \mathbf{w} = -\boldsymbol{\Phi}^T \mathbf{S}^{-1} (\mathbf{t} - \boldsymbol{\Phi} \mathbf{w}). \tag{4.26}$$

Here, the nabla symbol $\nabla_{\mathbf{w}}$ represents the gradient operator with respect to the vector $\mathbf{w}$. It produces a vector containing all partial derivatives of $E(\mathbf{w})$ with respect to each component of $\mathbf{w}$. For a vector $\mathbf{w} = (w_1, w_2, \ldots, w_M)^T$, the gradient is defined as:

$$\nabla_{\mathbf{w}} E(\mathbf{w}) = \left(\frac{\partial E}{\partial w_1}, \frac{\partial E}{\partial w_2}, \ldots, \frac{\partial E}{\partial w_M} \right)^T. \tag{4.27}$$

At the minimum of $E(\mathbf{w})$, this gradient must equal zero. Setting $\nabla_{\mathbf{w}} E(\mathbf{w}) = 0$ and solving for $\mathbf{w}$ gives us the maximum likelihood estimate:

$$\mathbf{w}_{\mathrm{ML}} = (\boldsymbol{\Phi}^T \mathbf{S}^{-1} \boldsymbol{\Phi})^{-1} \boldsymbol{\Phi}^T \mathbf{S}^{-1} \mathbf{t}. \tag{4.28}$$

In the special case of homogeneous noise where $\sigma_n = \sigma$ for all n, the covariance matrix $\mathbf{S}$ simplifies to $\sigma^2 \mathbf{I}$, where $\mathbf{I}$ is the identity matrix. Substituting this into our solution:

$$\begin{aligned}
\mathbf{w}_{\mathrm{ML}} &= (\boldsymbol{\Phi}^T (\sigma^2 \mathbf{I})^{-1} \boldsymbol{\Phi})^{-1} \boldsymbol{\Phi}^T (\sigma^2 \mathbf{I})^{-1} \mathbf{t} \\
&= (\boldsymbol{\Phi}^T \frac{1}{\sigma^2} \mathbf{I} \boldsymbol{\Phi})^{-1} \boldsymbol{\Phi}^T \frac{1}{\sigma^2} \mathbf{I} \mathbf{t} \\
&= (\frac{1}{\sigma^2} \boldsymbol{\Phi}^T \boldsymbol{\Phi})^{-1} \frac{1}{\sigma^2} \boldsymbol{\Phi}^T \mathbf{t} \\
&= \sigma^2 (\boldsymbol{\Phi}^T \boldsymbol{\Phi})^{-1} \frac{1}{\sigma^2} \boldsymbol{\Phi}^T \mathbf{t} \\
&= (\boldsymbol{\Phi}^T \boldsymbol{\Phi})^{-1} \boldsymbol{\Phi}^T \mathbf{t}.
\end{aligned} \tag{4.29}$$

This simplified form is the ordinary least squares solution:

$$\mathbf{w}_{\mathrm{ML}} = (\boldsymbol{\Phi}^T \boldsymbol{\Phi})^{-1} \boldsymbol{\Phi}^T \mathbf{t}, \tag{4.30}$$

showing how the general weighted least squares solution reduces to the simpler unweighted case when measurement uncertainties are uniform.

As a concrete example, consider the problem of fitting a straight line $y = mx + b$ to

data points (x_i, y_i). For this linear model:

- $\mathbf{w} = (b, m)^T$ contains the intercept and slope

- $\mathbf{\Phi}$ is an $N \times 2$ matrix where each row is $(1, x_i)$

- $\mathbf{t} = (y_1, \ldots, y_N)^T$ contains the observed y values

For uniform uncertainties, the solution gives the familiar formulas:

$$m = \frac{N \sum x_i y_i - (\sum x_i)(\sum y_i)}{N \sum x_i^2 - (\sum x_i)^2}, \quad b = \frac{\sum y_i - m \sum x_i}{N} \tag{4.31}$$

When measurement uncertainties σ_i vary between points, the weighted least squares solution instead gives:

$$m = \frac{\sum w_i x_i y_i - (\sum w_i x_i)(\sum w_i y_i)/W}{\sum w_i x_i^2 - (\sum w_i x_i)^2/W}, \quad b = \frac{\sum w_i y_i - m \sum w_i x_i}{W} \tag{4.32}$$

where $w_i = 1/\sigma_i^2$ and $W = \sum w_i$. This weights more precise measurements (smaller σ_i) more heavily in determining the fit.

This analytical solution reveals several properties that make linear regression particularly valuable in astronomical applications. First, it provides an exact solution without requiring iterative numerical optimization methods, even in the presence of heterogeneous measurement uncertainties. Second, the solution's mathematical form remains valid regardless of the dimensionality of our feature space. This property proves especially powerful when analyzing high-dimensional astronomical data, such as spectroscopic observations where each spectrum may contain thousands of flux measurements across different wavelengths.

Additionally, the computational cost scales well with the size of the dataset. Let's examine the dimensions of each matrix multiplication: $\mathbf{\Phi}^T$ is $M \times N$, $\mathbf{S}^{-1}$ is $N \times N$, and $\mathbf{\Phi}$ is $N \times M$, resulting in an $M \times M$ matrix that needs to be inverted. The most computationally expensive operation is the matrix inversion of $(\mathbf{\Phi}^T \mathbf{S}^{-1} \mathbf{\Phi})$. However, since this final matrix is only $M \times M$, where M is the number of features, the computation remains tractable even for very large datasets. For instance, with millions of data points but only a few hundred features, the matrix inversion is still computationally feasible since its size depends only on the number of features, not the number of data points.

This favorable scaling with dataset size, combined with the ability to handle high-

dimensional data efficiently, demonstrates why linear regression continues to serve as a foundational tool in modern astronomical research.

4.5   Noise Parameter Estimation

Until now, we've treated the measurement uncertainties σ_i as known quantities. However, in many astronomical applications, these uncertainties themselves need to be estimated from the data. For example, in spectroscopic observations, the quoted instrumental uncertainties might not fully capture systematic effects from sky subtraction or flux calibration. Similarly, in photometric time series, the formal uncertainties often underestimate the true scatter due to unmodeled stellar variability or atmospheric effects.

Moreover, in some cases, the spread in the data reflects physically meaningful variations rather than just measurement error—for instance, the intrinsic dispersion in a mass-metallicity relation could indicate real diversity in galaxy evolution histories, or scatter in a period-luminosity relationship might reveal genuine differences in stellar properties. Understanding and properly modeling this intrinsic scatter can provide valuable physical insights beyond just accounting for measurement uncertainties.

From a maximum likelihood perspective, measurement uncertainties can be naturally incorporated as additional parameters in our model. Formally, if we denote our model parameters as $\mathbf{w}$ and measurement uncertainties as $\boldsymbol{\sigma}$, we seek to maximize $p(\mathbf{t}|\mathbf{X}, \mathbf{w}, \boldsymbol{\sigma})$ with respect to both $\mathbf{w}$ and $\boldsymbol{\sigma}$ simultaneously. This approach acknowledges that both the model parameters and noise characteristics are essential components in describing the observed data distribution.

As shown in the figure above, proper estimation of measurement uncertainties is crucial for maximizing the likelihood. When uncertainties are underestimated (panel a), many data points fall outside the predicted uncertainty bands. Mathematically, this means each point contributes a small likelihood term $\mathcal{N}(t_n|y(\mathbf{x}_n, \mathbf{w}), \sigma^2)$ due to the rapid falloff of the Gaussian distribution, resulting in a low overall likelihood. Conversely, when uncertainties are overestimated (panel c), the Gaussian distributions become very broad, and while more points fall within the expected range, the prefactor $1/\sqrt{2\pi\sigma^2}$ in the likelihood becomes very small, again reducing the overall likelihood. The maximum likelihood estimate of σ^2 (panel b) strikes an optimal balance between these competing effects.

We can treat the uncertainty as another free parameter to optimize in our maximum
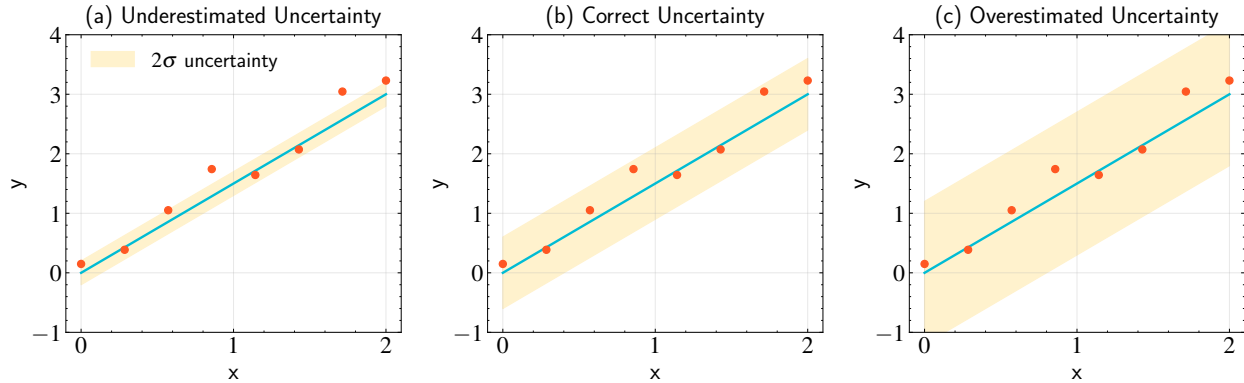
Figure 4.2: Demonstration of how different choices of uncertainty values affect the likelihood in maximum likelihood estimation. Panel (a): With underestimated uncertainties ($\sigma = 0.1$), the narrow Gaussian distributions mean data points far from the model contribute very small likelihood terms, resulting in a low total likelihood. Panel (b): When uncertainties are correctly estimated ($\sigma = 0.3$), we achieve the maximum likelihood—this represents the optimal balance between the width of the Gaussian distributions and their heights. Panel (c): With overestimated uncertainties ($\sigma = 0.6$), while the Gaussian distributions are wide enough to encompass most points, the height of each Gaussian (which scales as $1/\sigma$) becomes smaller, resulting in smaller likelihood values overall.

likelihood framework. However, we need to be careful about how we model these uncertainties. While it may be tempting to allow each data point to have its own independent uncertainty (σ_i), this would introduce as many additional parameters as we have data points. Such an approach would make our model parameters ill-constrained. To understand why, recall that for a Gaussian likelihood, each data point contributes a term $(t_n - y_n)^2/\sigma_n^2$ to χ^2. If we allowed each σ_i to vary independently, we could always achieve $\chi^2 = N$ (where each point contributes exactly 1) by setting $\sigma_i = |t_i - y_i|$ for any set of model parameters, regardless of how well or poorly the model actually fits the data. This would prevent us from meaningfully comparing different model fits and result in a model with no predictive power, as the uncertainties would simply adjust to accommodate any model predictions.

Thus, to make the problem well-defined, we need to parameterize our noise model with fewer parameters than data points. For instance, we might assume the measurement uncertainty varies smoothly with our input features. As an illustrative case, let's consider perhaps the simplest scenario: homogeneous but unknown measurement uncertainty, where all measurements share the same unknown uncertainty σ.

Let's recall our log-likelihood function, written in terms of the precision $\beta = 1/\sigma^2$

(this parameterization will simplify our derivation):

$$\ln p(\mathbf{t}|\mathbf{X}, \mathbf{w}, \beta) = \frac{N}{2}\ln\beta - \frac{N}{2}\ln(2\pi) - \frac{\beta}{2}\sum_{n=1}^{N}(t_n - \mathbf{w}^T\boldsymbol{\phi}(\mathbf{x}_n))^2. \tag{4.33}$$

Previously, we treated σ as a fixed, known quantity while optimizing for $\mathbf{w}$. Now, we recognize that σ can be treated as another parameter of our model, just like $\mathbf{w}$.

To find the optimal value of β, we follow the same approach we used for $\mathbf{w}$: we differentiate the log-likelihood with respect to β and set it to zero:

$$\frac{\partial}{\partial\beta}\ln p(\mathbf{t}|\mathbf{X}, \mathbf{w}, \beta) = \frac{N}{2\beta} - \frac{1}{2}\sum_{n=1}^{N}(t_n - \mathbf{w}^T\boldsymbol{\phi}(\mathbf{x}_n))^2 = 0. \tag{4.34}$$

Solving for β and converting back to σ^2:

$$\frac{1}{\beta_{\text{ML}}} = \sigma_{\text{ML}}^2 = \frac{1}{N}\sum_{n=1}^{N}(t_n - \mathbf{w}^T\boldsymbol{\phi}(\mathbf{x}_n))^2. \tag{4.35}$$

This equation provides us with an intuitive estimate of the measurement variance—it's simply the average of the squared residuals between our observations and model predictions. The logic is straightforward: if our model fits the data well, then any remaining discrepancies between the model predictions and observations should reflect the underlying measurement noise. By averaging these squared residuals, we get a direct estimate of the typical squared deviation (variance) in our measurements. This is analogous to how we might estimate the uncertainty in repeated measurements of the same quantity—we'd look at how much the measurements scatter around their mean value. Here, instead of comparing to a mean, we're comparing to our model predictions, but the principle is the same. If our residuals are typically small, this suggests our measurements are quite precise (small σ^2), while larger residuals indicate more substantial measurement uncertainties (large σ^2).

However, there's a subtle but important point we need to consider: the likelihood function $p(\mathbf{t}|\mathbf{X}, \mathbf{w}, \beta)$ depends jointly on both $\mathbf{w}$ and β. To find the true maximum likelihood solution, we need to maximize with respect to both parameters simultaneously. In

mathematical terms, we seek:

$$(\mathbf{w}_{\mathrm{ML}}, \beta_{\mathrm{ML}}) = \arg\max_{\mathbf{w}, \beta} p(\mathbf{t}|\mathbf{X}, \mathbf{w}, \beta). \tag{4.36}$$

While this might seem challenging, our problem has a special structure that makes it tractable. We've already shown that for any fixed β, we can analytically find $\mathbf{w}_{\mathrm{ML}}(\beta)$. Similarly, for any fixed $\mathbf{w}$, we can analytically find $\beta_{\mathrm{ML}}(\mathbf{w})$. This suggests an iterative approach:
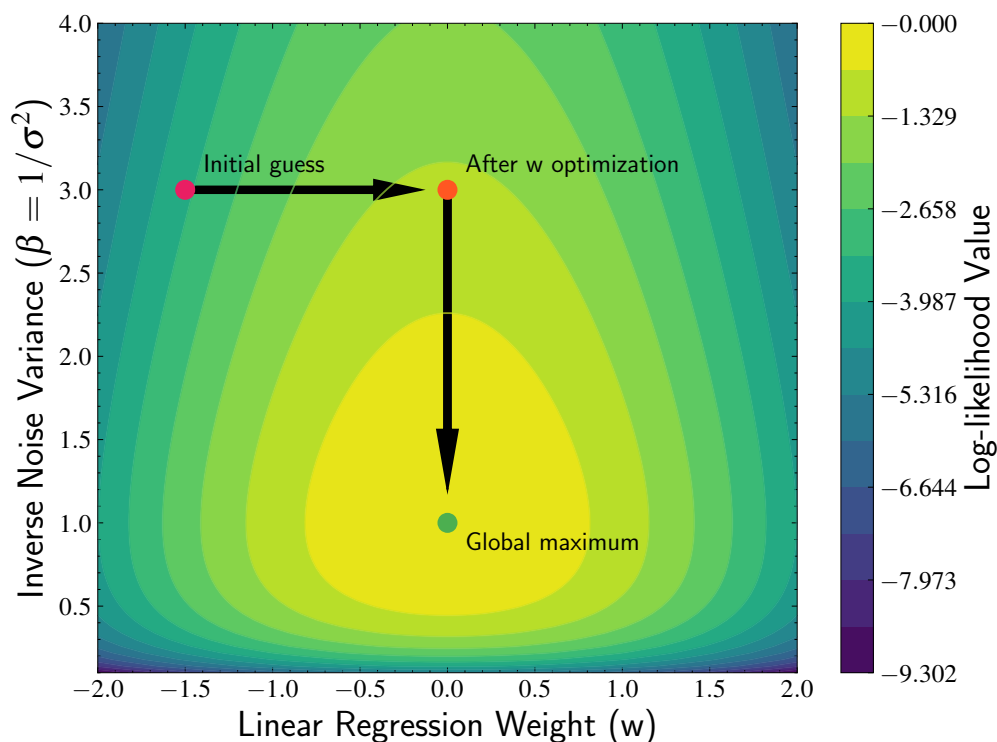
Figure 4.3: Schematic illustration showing the globally convex log-likelihood surface in (w, β) space. The bowl-shaped contours demonstrate why optimization can be achieved in exactly two steps: since the optimal w depends only on relative residual weights (independent of β scale), we can first optimize w for any initial β, then directly find the optimal β using that w. This two-step convergence is guaranteed by the convex geometry, regardless of starting point.

1. Start with an initial guess for β

2. Find $\mathbf{w}_{\mathrm{ML}}(\beta)$ using our weighted least squares solution

3. Use this $\mathbf{w}_{\mathrm{ML}}(\beta)$ to find $\beta_{\mathrm{ML}}(\mathbf{w})$ using our variance estimation formula

4. Repeat steps 2-3 until convergence

Remarkably, in this specific case, the iteration always converges. To understand why, let's examine the structure of our log-likelihood function:

$$\ln p(\mathbf{t}|\mathbf{X}, \mathbf{w}, \beta) = \frac{N}{2}\ln\beta - \frac{N}{2}\ln(2\pi) - \frac{\beta}{2}\sum_{n=1}^{N}(t_n - \mathbf{w}^T\boldsymbol{\phi}(\mathbf{x}_n))^2. \tag{4.37}$$

This function has a special geometric structure that guarantees a unique global maximum. Consider first how the likelihood varies with $\mathbf{w}$ when σ^2 is fixed. The exponential term contains squared distances between predictions and observations, creating a convex "bowl-shaped" surface in parameter space—move too far in any direction and the likelihood drops exponentially.

Similarly, varying σ^2 while holding $\mathbf{w}$ fixed reveals another bowl-shape: very small σ^2 makes the Gaussian distributions too narrow, causing exponentially small likelihoods for points not exactly matching predictions, while very large σ^2 makes the distributions too wide, with the $1/\sqrt{2\pi\sigma^2}$ normalization term driving the likelihood toward zero. The likelihood must peak at an intermediate value where these competing effects balance.

This convexity in all directions ensures a single global maximum. Moreover, because the optimal $\mathbf{w}_{\mathrm{ML}}$ depends only on the relative weighting of squared residuals, which is independent of the scale of β, finding $\mathbf{w}_{\mathrm{ML}}$ for any initial β gives us the correct $\mathbf{w}$ value. We can then use this $\mathbf{w}$ to find the optimal β, converging to the global maximum in exactly two steps, as shown in the figure above.

Combining these insights, we can obtain the maximum likelihood solution through a simple two-step process. First, we estimate $\mathbf{w}_{\mathrm{ML}}$ using the weighted least squares solution:

$$\mathbf{w}_{\mathrm{ML}} = (\boldsymbol{\Phi}^T\boldsymbol{\Phi})^{-1}\boldsymbol{\Phi}^T\mathbf{t}. \tag{4.38}$$

Then, using this $\mathbf{w}_{\mathrm{ML}}$, we can directly compute σ^2_{ML} as:

$$\sigma^2_{\mathrm{ML}} = \frac{1}{N}\sum_{n=1}^{N}(t_n - \mathbf{w}_{\mathrm{ML}}^T\boldsymbol{\phi}(\mathbf{x}_n))^2. \tag{4.39}$$

This estimate of σ^2 represents the average squared deviation between our observa-

tions and the model predictions. It captures the typical magnitude of measurement noise in our data, assuming that any residual differences between the model and observations are primarily due to measurement uncertainties rather than model inadequacies. This assumption is reasonable when we believe our linear model appropriately captures the underlying relationship in the data.

4.6   Limitations of Maximum Likelihood Approach

Throughout this chapter, we've focused on maximum likelihood estimation, demonstrating how it provides a principled framework for finding optimal model parameters and even estimating measurement uncertainties. However, we have made two important simplifications that highlight fundamental limitations of the MLE approach.

First, we assumed no prior knowledge, implicitly treating the data alone as sufficient to determine our model parameters. In astronomy, we often have prior knowledge that could inform our parameter estimates—for instance, we might know physical constraints on possible parameter values or have results from previous studies that suggest likely ranges for parameters.

But perhaps more critically, maximum likelihood estimation focuses solely on finding the best-fit model, which contradicts a fundamental principle of scientific inquiry. In science, we seek not just predictive models, but also a rigorous understanding of our models' limitations and uncertainties. We need to quantify both the uncertainty in our model parameters and in the predictions we make using these models.

MLE provides only single "best" parameter values rather than complete uncertainty distributions. When we compute $\mathbf{w}_{\mathrm{ML}}$, we obtain a single point estimate that represents our best guess for the model parameters. However, this tells us nothing about how confident we should be in these estimates. Are our parameters well-constrained by the data, or might there be a wide range of equally plausible parameter values? Without uncertainty quantification, we cannot answer these essential questions.

Consider our earlier M-$\boldsymbol{\sigma}$ relation example. If we find $\beta = 4.0$ for the power-law index, MLE alone doesn't tell us whether this value is constrained to within ± 0.1 or might reasonably range from 3.0 to 5.0. This uncertainty information is crucial for comparing our results with theoretical predictions or with measurements from other studies.

The MLE approach fundamentally lacks a systematic way to assess parameter un-

certainties. While we can compute residuals and goodness-of-fit statistics, these don't directly translate into confidence intervals or uncertainty estimates for the model parameters themselves. This limitation becomes especially problematic when we need to propagate uncertainties through subsequent calculations or compare models with different numbers of parameters.

A second major limitation is that MLE ignores valuable prior knowledge that often exists in astronomical problems. For example, in stellar astrophysics, we might know that stellar masses must be positive and typically fall within certain ranges based on stellar evolution theory. In cosmology, physical constraints might limit parameter ranges based on nucleosynthesis or structure formation requirements. The MLE framework provides no natural way to incorporate such prior knowledge into our parameter estimation.

Additionally, MLE lacks built-in safeguards against overfitting. Without explicit mechanisms for regularization, it can lead to models that fit the training data well but generalize poorly to new observations. This is particularly problematic when the number of parameters approaches the number of data points, or when our basis functions $\phi(\mathbf{x})$ become very flexible. While the analytical solutions we derived are exact, they don't inherently guard against overfitting—they simply find the parameters that best explain the observed data, regardless of whether this leads to reasonable predictions for future observations.

These limitations highlight why the Bayesian approach becomes essential for rigorous scientific inference. Rather than providing just point estimates like $\mathbf{w}_{\mathrm{ML}}$, Bayesian inference gives us the complete posterior distribution $p(\mathbf{w}|\mathbf{t})$. This comprehensive probabilistic description provides several key advantages for scientific analysis:

Through the posterior distribution, we can quantify uncertainties in our model parameters, enabling us to understand the precision and limitations of our results. The Bayesian framework also allows us to make probabilistic predictions that naturally include uncertainty estimates, giving us a more complete picture of what our models tell us about the phenomena we study. Additionally, it provides a formal and systematic way to incorporate prior knowledge into our analyses, allowing us to build upon previous results and theoretical constraints.

Perhaps most importantly, the Bayesian approach enables us to distinguish between aleatoric and epistemic uncertainties through the posterior predictive distribution, which we will explore in detail in the next chapter. These capabilities make the Bayesian approach particularly valuable for rigorous scientific inference in astronomy, where understanding un-

certainties is often as important as the parameter estimates themselves.

4.7   Summary

In this chapter, we have developed linear regression from first principles, demonstrating how this fundamental technique emerges naturally from the framework of Bayesian inference and maximum likelihood estimation. Our journey began with the recognition that many astronomical relationships, while nonlinear in their original form, become linear through appropriate transformations—particularly the logarithmic transformations that reveal the power-law relationships ubiquitous in astronomy.

We established the mathematical formalism of linear regression, showing how the general model $y(\mathbf{x}, \mathbf{w}) = \mathbf{w}^T \boldsymbol{\phi}(\mathbf{x})$ provides a flexible framework for modeling complex relationships through the choice of basis functions $\boldsymbol{\phi}(\mathbf{x})$. This formulation demonstrates that "linear" regression refers to linearity in the parameters $\mathbf{w}$, not necessarily in the input features themselves.

Through maximum likelihood estimation, we derived the fundamental connection between probabilistic inference and least squares optimization. By modeling observations as $t = y(\mathbf{x}, \mathbf{w}) + \varepsilon$ with Gaussian noise $\varepsilon \sim \mathcal{N}(0, \sigma^2)$, we showed that maximizing the likelihood is mathematically equivalent to minimizing weighted least squares. This connection reveals that the ubiquitous chi-square statistic in astronomical model fitting is not an arbitrary choice, but emerges naturally from rigorous probabilistic principles.

The analytical solution we derived, $\mathbf{w}_{\mathrm{ML}} = (\boldsymbol{\Phi}^T \mathbf{S}^{-1} \boldsymbol{\Phi})^{-1} \boldsymbol{\Phi}^T \mathbf{S}^{-1} \mathbf{t}$, provides several key advantages for astronomical applications. First, it yields exact results without requiring iterative optimization, even in the presence of heterogeneous measurement uncertainties. Second, its computational cost scales favorably with dataset size, depending on the number of features rather than the number of data points—a crucial property for modern astronomical surveys with millions of objects. Third, it naturally accommodates the varying measurement uncertainties that characterize real astronomical observations.

We extended the maximum likelihood framework to estimate measurement uncertainties themselves, showing how both model parameters and noise characteristics can be determined simultaneously through a simple two-step process. The resulting estimate $\sigma_{\mathrm{ML}}^2 = \frac{1}{N} \sum_{n=1}^{N} (t_n - \mathbf{w}_{\mathrm{ML}}^T \boldsymbol{\phi}(\mathbf{x}_n))^2$ provides a principled way to quantify the typical magnitude of measurement noise, whether it represents instrumental uncertainties or intrinsic physical

scatter.

However, our exploration also revealed fundamental limitations of the maximum likelihood approach. Most critically, MLE provides only point estimates rather than complete uncertainty distributions, offering no systematic way to quantify our confidence in parameter estimates. Additionally, MLE provides no framework for incorporating prior knowledge about physically reasonable parameter values, and it offers no inherent protection against overfitting.

These limitations motivate the need for a more complete Bayesian treatment of linear regression. While maximum likelihood estimation asks "what parameter values best explain the observed data?", Bayesian inference addresses the more comprehensive question: "given our data and prior knowledge, what is the complete probability distribution over all possible parameter values?" This shift from point estimates to probability distributions provides the foundation for rigorous uncertainty quantification and scientific inference.

In Chapter 5, we will extend the foundation built here to develop a fully Bayesian treatment of linear regression. We will see how this approach addresses the limitations identified in this chapter by providing complete posterior distributions over parameters, natural incorporation of prior knowledge, and principled uncertainty quantification that distinguishes between different sources of uncertainty. The mathematical framework we have established—from basis functions to likelihood derivation to analytical solutions—will serve as the foundation for this more sophisticated treatment, demonstrating how linear regression serves as a bridge between simple statistical concepts and the rich world of Bayesian machine learning.

4.8   Appendix: Model Evaluation and Cross-Validation

Throughout this chapter, we developed linear regression from maximum likelihood principles, deriving analytical solutions for parameter estimation through our framework of basis functions and design matrices. However, we concluded by identifying fundamental limitations of the maximum likelihood approach: it provides only point estimates without systematic uncertainty quantification, and it offers no inherent protection against overfitting.

While Chapter 5 will address the uncertainty quantification limitation through a full Bayesian treatment, the model selection challenge—determining the appropriate number of basis functions or model complexity—remains important for all approaches. This appendix

introduces cross-validation techniques that provide essential tools for model evaluation and selection, demonstrating these concepts through the linear regression framework we have established.

At the heart of machine learning lies a fundamental question: what constitutes a good model? To explore this question, let's consider polynomial regression as a concrete example. Recall from our discussion of basis functions that we can express any linear regression model as:

$$y(\mathbf{x}, \mathbf{w}) = \sum_{j=0}^{M-1} w_j \cdot \phi_j(\mathbf{x}) = \mathbf{w}^T \boldsymbol{\phi}(\mathbf{x}) \tag{4.40}$$

For polynomial regression, we simply choose polynomial basis functions: $\phi_0(x) = 1$, $\phi_1(x) = x$, $\phi_2(x) = x^2$, and so on. This gives us:

$$y(x, \mathbf{w}) = w_0 + w_1 x + w_2 x^2 + \ldots + w_{M-1} x^{M-1} \tag{4.41}$$

where the weights $\mathbf{w}$ are determined through our maximum likelihood solution $\mathbf{w}_{\text{ML}} = (\boldsymbol{\Phi}^T \boldsymbol{\Phi})^{-1} \boldsymbol{\Phi}^T \mathbf{t}$. This is precisely the linear regression framework we derived, but with polynomial feature engineering applied to transform our input space.

A natural question arises: how many polynomial terms should we include in our basis functions $\boldsymbol{\phi}(\mathbf{x})$? This is a direct application of the feature engineering concepts from this chapter—we are choosing the dimensionality M of our feature space and thus the structure of our design matrix $\boldsymbol{\Phi}$. This question exemplifies the bias-variance tradeoff that underlies all machine learning applications and connects directly to the overfitting concerns we identified as limitations of the maximum likelihood approach.

We can evaluate our model performance using the mean squared error:

$$\text{MSE} = \frac{1}{N} \sum_{i=1}^{N} (t_i - y(\mathbf{x}_i, \mathbf{w}))^2 \tag{4.42}$$

This measures how well our predictions match actual observations—a direct application of the squared-error loss that emerges naturally from our homoscedastic Gaussian noise assumptions in the maximum likelihood framework.

Machine learning fundamentally balances modeling (incorporating prior knowledge and assumptions) with learning (extracting patterns from data). As we increase the number

of polynomial basis functions—effectively increasing the complexity of our feature space—we observe three distinct regimes. First, underfitting occurs when our basis functions are too limited to capture the underlying patterns in the data. A purely linear model applied to clearly nonlinear astronomical relationships exemplifies this regime. Second, we find an optimal balance where our model captures the true underlying relationship without being overly influenced by measurement noise. Finally, overfitting emerges when our feature space becomes so complex that our model begins fitting measurement noise rather than the underlying signal, memorizing peculiarities of our training data rather than learning generalizable patterns.
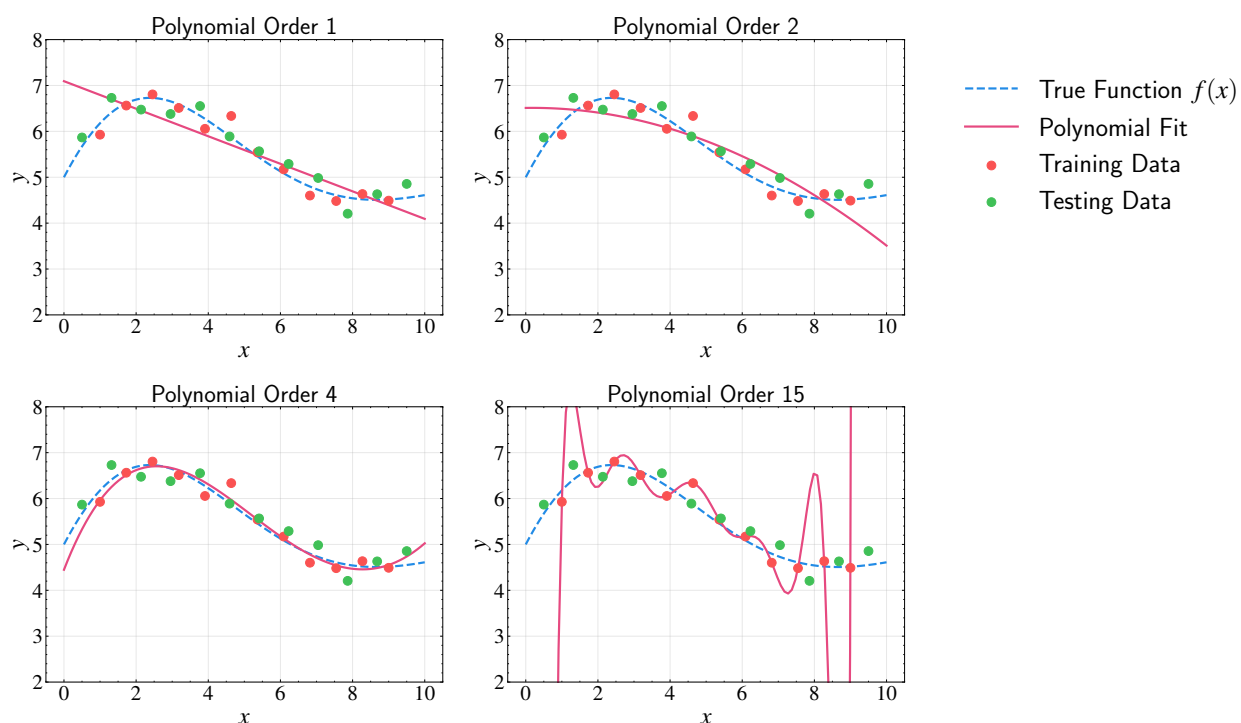
Figure 4.4: Demonstration of polynomial fitting with increasing model complexity. Each panel shows the true underlying function (blue dashed line), training data points (red), test data points (green), and the fitted polynomial (pink) of different orders. As the polynomial order increases from 1 to 15, we observe how the model's flexibility changes. The linear fit (order 1) is too rigid to capture the data's pattern, while the high-order polynomial (order 15) follows the noise in the training data too closely. Intermediate orders provide a better balance between fitting the data and capturing the true underlying pattern.

The key insight for distinguishing between these regimes comes from recognizing that good models should generalize to new observations. This principle is fundamental to scientific inference: our models should make accurate predictions about future data, not merely achieve low residuals on existing measurements.

Training and Test Sets   The solution lies in splitting our dataset into distinct portions. We use a training set to fit model parameters—applying our maximum likelihood solution $\mathbf{w}_{\mathrm{ML}} = (\mathbf{\Phi}^T\mathbf{\Phi})^{-1}\mathbf{\Phi}^T\mathbf{t}$ to determine the optimal weights for each choice of basis functions. Simultaneously, we hold out a test set during training to evaluate generalization performance on data that played no role in parameter estimation.

This approach reveals why the fundamental behavior differs between training and test performance. For the training data, increasing the degrees of freedom (adding more polynomial basis functions) will continuously improve our fit. This occurs because our maximum likelihood solution can always find weights that better explain the training observations — higher-dimensional feature spaces provide more flexibility to minimize training error. However, there's a critical insight: at some point, even though we continue improving our fit on the training data, we begin overfitting to the training set's specific characteristics.

When overfitting occurs, the model starts to memorize noise and peculiarities specific to the training data rather than learning the true underlying relationship. These noise patterns are not fundamental properties of the physical system we're studying—they're artifacts of our particular measurements. As a result, while the model might perform exceptionally well on the training data, it performs poorly when presented with new, unseen data points.

This creates the characteristic learning curve behavior: training error decreases monotonically as we add basis functions, but test error follows a U-shaped curve. For underfitting (too few basis functions), both training and test errors are high because the model lacks sufficient flexibility. In the optimal regime, both errors are minimized as the model captures the true relationship. In the overfitting regime, training error continues to decrease while test error increases, as the model fits training-specific noise that doesn't generalize.

This phenomenon—where more complex models can fit training data better but generalize worse—represents a fundamental tension in machine learning. Interestingly, this classical understanding has been challenged by recent discoveries in neural networks, where the "double descent" phenomenon shows that very highly overparameterized models can sometimes generalize better than expected, a topic we'll explore in Chapter 15. However, for the polynomial regression case and many classical machine learning methods, the U-shaped test error curve remains the standard behavior.

When the model enters the overfitting regime with too many basis functions, it begins fitting noise patterns specific to the training data. These noise patterns do not generalize to new observations, leading to larger errors on the test set. By evaluating our model on held-
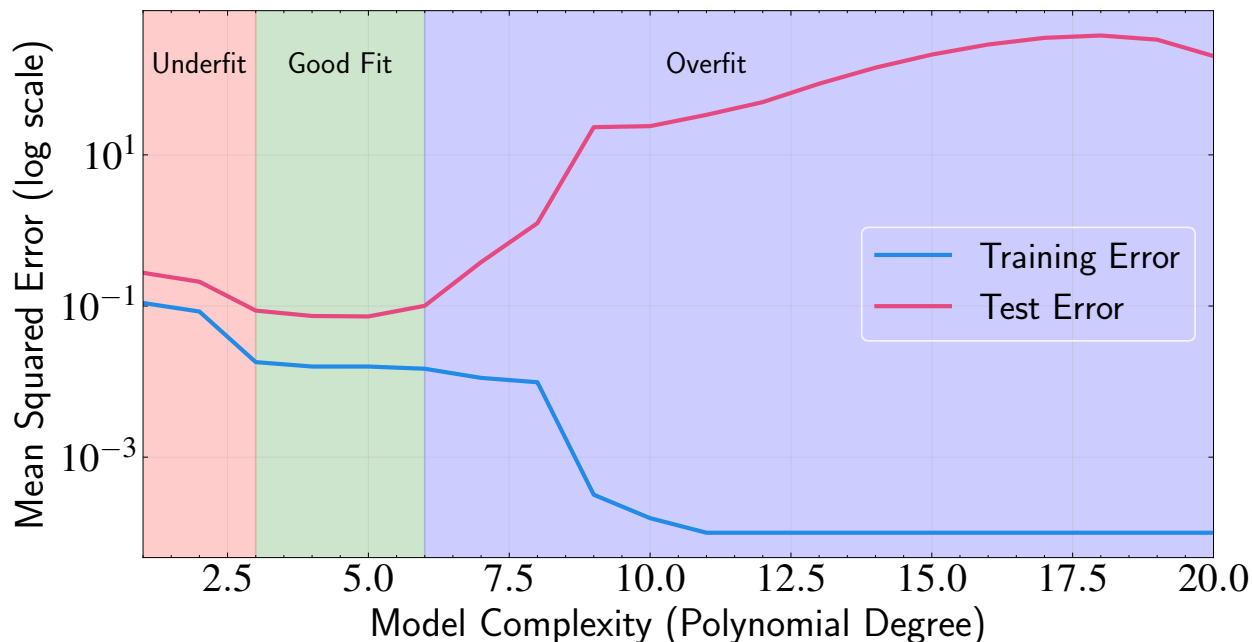
Figure 4.5: Training and test error curves (on log scale) illustrating the three fundamental regimes in model complexity. The underfitting regime (red shading) shows high error on both training and test sets due to insufficient model flexibility. The good fit regime (green shading) represents optimal model complexity where both errors are minimized. The overfitting regime (blue shading) is characterized by very low training error but increasing test error as the model begins to fit noise in the training data. This behavior demonstrates the crucial balance between model complexity and generalization performance.

out test data that never influenced parameter estimation, we obtain an unbiased estimate of how our model will perform on future observations.

Three-Way Data Splitting For methodological rigor, we can implement a three-way data split. The training set applies our maximum likelihood solution for each choice of basis functions, fitting the weight vector $\mathbf{w}$ optimally. The validation set determines the optimal dimensionality of our feature space—how many polynomial terms to include in $\boldsymbol{\phi}(\mathbf{x})$. Finally, the test set provides final evaluation of our chosen model on completely unseen data. This approach ensures that model selection decisions are based on the validation set while the test set provides a truly unbiased assessment of generalization performance.

In practice, particularly in astronomy where data can be scarce, we often work with just training and test sets. While this approach involves some methodological compromise—our model selection still depends on test set performance—it represents a reasonable balance between statistical rigor and practical constraints. There's always tension between

having enough training data for reliable parameter estimation and sufficient validation/test data for trustworthy evaluation. A common split might allocate 60% for training, 20% for validation, and 20% for testing, though these proportions should be adapted based on total dataset size and specific problem characteristics.

Cross-Validation for Limited Data   When datasets are severely limited, cross-validation provides a powerful alternative that makes more efficient use of available data. In Leave-One-Out Cross-Validation (LOOCV), we perform N separate applications of our maximum likelihood solution, each time training on $N - 1$ observations and testing on the remaining observation. We rotate through all observations so each serves as the test set exactly once, then average the test errors to estimate model performance.

This approach maximizes data utilization since nearly all observations are used for training in each iteration, and it provides N independent assessments of generalization performance. However, LOOCV requires training N separate models, which can be computationally expensive. Additionally, since each test set contains only one observation, individual test results can be noisy. The high correlation between training sets—differing by only one observation—may also lead to overly optimistic performance estimates.

K-fold cross-validation offers a practical compromise by dividing data into K folds, training on $K - 1$ folds, and testing on the remaining fold. This reduces computational cost while maintaining many advantages of LOOCV.

Cross-validation in astronomy often requires careful consideration of data structure. For time-series observations, randomly splitting data can lead to information leakage where future information influences past predictions. Time-aware splitting may be more appropriate. When observations are spatially clustered, random splitting might not reflect the challenge of predicting for genuinely new sky regions. Selection effects and systematic uncertainties require careful interpretation of cross-validation results.

Cross-validation provides a practical framework for model evaluation that complements both the maximum likelihood methods developed in this chapter and the Bayesian approaches we'll explore in Chapter 5. While our analytical solutions give principled parameter estimation, and Bayesian methods will provide rigorous uncertainty quantification, cross-validation addresses the fundamental challenge of model selection—determining appropriate complexity levels for any statistical approach. This framework applies broadly across machine learning methods—the fundamental principle of requiring good generalization per-

formance remains central to all effective applications.

As we progress to Bayesian linear regression in Chapter 5, we will see how Bayesian approaches provide powerful tools for uncertainty quantification through posterior distributions. However, the evaluation principles established here prepare us for model selection techniques throughout this textbook, including information criteria for mixture models (Chapter 11) that provide principled alternatives to cross-validation for model comparison. Understanding these evaluation concepts now provides essential groundwork for all subsequent machine learning applications in astronomical research.

Further Readings: The development of linear regression methods traces back to early mathematical contributions from Gauss [1823], who provided exposition of least squares theory and the Gauss-Markov theorem. For practical implementation in astronomical contexts, Bevington and Robinson [1969] offers a widely-used reference for weighted least squares and error analysis in the physical sciences. Linear regression has proven instrumental in revealing astronomical relationships through several scaling relations discovered over the decades: Faber and Jackson [1976] documented how luminosity scales with the fourth power of velocity dispersion for elliptical galaxies, while Tully and Fisher [1977] identified the analogous relation between luminosity and rotation velocity for spiral galaxies. Work on the M-σ relation by Ferrarese and Merritt [2000] and Gebhardt et al. [2000] demonstrated tight correlations between supermassive black hole masses and host galaxy velocity dispersions with small intrinsic scatter. Kennicutt [1998] characterized the star formation law relating gas density to star formation rate. For readers interested in handling challenges specific to astronomical data, Isobe et al. [1990] provided comparison of regression methods addressing measurement errors, while Akritas and Bershady [1996] developed a bivariate estimator that accounts for correlated errors, heteroscedastic uncertainties, and intrinsic scatter. Theoretical foundations for model selection through cross-validation were contributed by Stone [1974], providing methods for assessing predictive performance that have become fundamental to modern machine learning approaches in astronomy.

Chapter 5

Bayesian Linear Regression

In the previous chapter, we explored linear regression through maximum likelihood estimation, demonstrating how this approach provides a framework for fitting linear relationships to astronomical data. We showed that under Gaussian measurement uncertainties, maximizing the likelihood naturally leads to minimizing weighted least squares — connecting rigorous probabilistic principles to the familiar chi-square statistic that pervades astronomical analysis. We discovered that linear regression yields analytical solutions regardless of feature space dimensionality, making it computationally tractable even for high-dimensional astronomical datasets.

In principle, we can obtain uncertainty estimates for these maximum likelihood parameters through bootstrapping, as we explored in Chapter 3. By resampling our data with replacement, we can generate many synthetic datasets, refit our model to each one, and examine the distribution of resulting parameter estimates. This approach has solid theoretical foundations and can work well in many situations, providing a frequentist framework for understanding parameter uncertainties.

However, bootstrapping has practical limitations that become particularly apparent in astronomical applications. It requires sufficient data for reliable resampling - a condition not always met in astronomy where samples may be small or expensive to obtain. The method can also struggle with complex measurement error structures, common in astronomical observations where different measurements may have very different uncertainties. Moreover, bootstrapping provides no natural framework for incorporating prior knowledge from theory or previous observations.
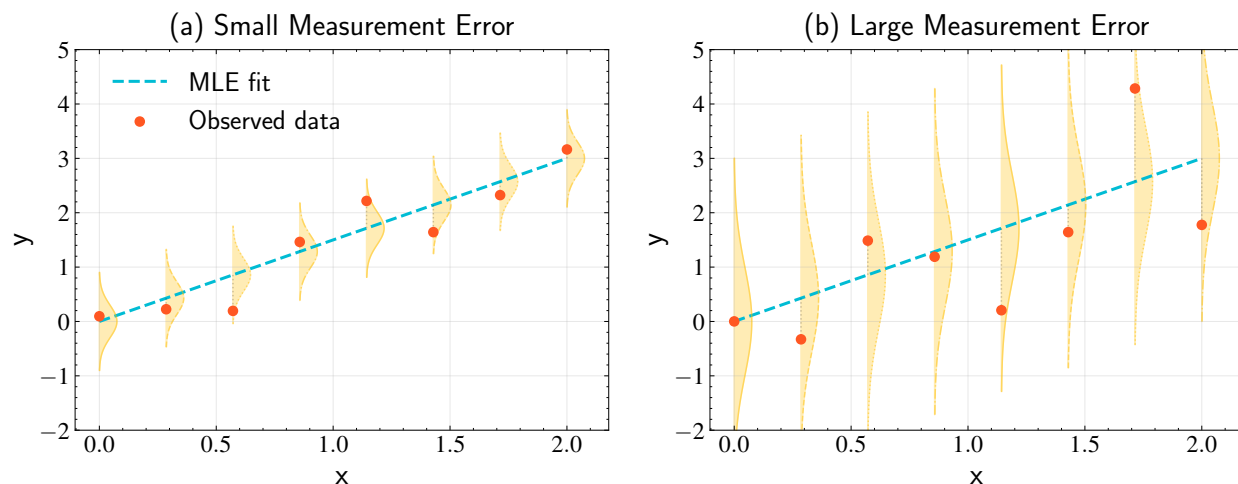
Figure 5.1: Illustration of why we need to go beyond simple maximum likelihood estimation. Both panels show the same underlying relationship (dashed blue line) fitted to observed data (orange points), but with different measurement uncertainties (shown as yellow distributions). Panel (a) shows a case with small measurement errors, where bootstrapped uncertainty estimates are reliable. Panel (b) shows the same fit applied to data with large measurement errors, where bootstrapping may provide misleading uncertainty estimates due to the limited sample size and complex error structure.

The Bayesian approach offers a fundamentally different perspective that addresses these limitations. Rather than treating model parameters as fixed quantities whose sampling distribution we must estimate through resampling, Bayesian inference treats them as random variables with probability distributions. This shift enables us to ask not just "what are the parameter values and their uncertainties?" but "what is the complete probability distribution over all plausible parameter values given our data and prior knowledge?"

This probabilistic treatment provides several crucial advantages for astronomical research. First, it enables full uncertainty quantification without requiring large sample sizes or assumptions about the sampling process. Second, it provides a principled framework for incorporating prior knowledge—whether from previous observations, theoretical constraints, or physical intuition. Third, it naturally prevents overfitting through the connection between priors and regularization, as we will discover.

In this chapter, we will develop a Bayesian framework for linear regression. We begin by exploring conjugate priors, which provide analytical solutions and illuminate the mathematical structure of Bayesian inference. We will see how these concepts extend naturally from simple examples to the full multivariate treatment needed for linear regression. The framework will reveal how Bayesian thinking naturally gives rise to regularization, provides

complete predictive distributions with proper uncertainty propagation, and offers a unified foundation for understanding more sophisticated machine learning methods.

For astronomy, where proper uncertainty handling is critical for robust scientific conclusions, Bayesian linear regression offers particular advantages. Whether we're studying the M-σ relation between black hole mass and stellar velocity dispersion, investigating the Kennicutt-Schmidt law relating gas density to star formation rate, or analyzing any other linear relationship in astronomical data, the ability to quantify both parameter and prediction uncertainties enables more reliable inference and better-informed observational strategies.

5.1 From Maximum Likelihood to Bayesian Inference

To understand why the Bayesian approach represents such a significant advance over traditional frequentist methods, we must first examine what these approaches tell us—and more importantly, what they struggle to tell us.

Consider a concrete astronomical example: fitting the M-σ relation to measure the relationship between black hole mass and stellar velocity dispersion. A frequentist analysis might start with maximum likelihood estimation, then use bootstrapping to estimate uncertainties. While this approach can work well with large, well-sampled datasets, it often struggles with the realities of astronomical data: small sample sizes, heterogeneous measurement errors, and strong prior knowledge from theory or previous observations that cannot be naturally incorporated into the bootstrap framework.

The Bayesian perspective offers a different way to think about this problem. Rather than treating model parameters as fixed quantities whose sampling distribution we must estimate through resampling, Bayesian inference treats them as random variables with probability distributions. This shift asks fundamentally different questions:

- Maximum likelihood asks: "What parameter values best explain my observations?"

- Bayesian inference asks: "Given my observations and prior knowledge, what is the probability distribution over all possible parameter values?"

This distinction is not merely philosophical—it has practical implications for how we interpret and use our results.

The mathematical framework that enables this transformation is Bayes' theorem:

$$p(\mathbf{w}|\mathcal{D}) = \frac{p(\mathcal{D}|\mathbf{w})p(\mathbf{w})}{p(\mathcal{D})}. \tag{5.1}$$

This deceptively simple equation provides a complete recipe for learning from data. Each component has a clear interpretation:

- $p(\mathcal{D}|\mathbf{w})$ is the likelihood—identical to what we used in maximum likelihood estimation. It captures what our data tells us about the parameters.

- $p(\mathbf{w})$ is the prior—our beliefs about the parameters before seeing the data. This allows us to incorporate previous knowledge or physical constraints.

- $p(\mathcal{D})$ is the evidence—a normalization constant that ensures the posterior is a valid probability distribution.

- $p(\mathbf{w}|\mathcal{D})$ is the posterior—our updated beliefs after combining prior knowledge with observed data.

The beauty of this framework lies in how it naturally handles the interplay between different sources of information. When we have strong prior knowledge and weak data, the posterior remains close to the prior. When we have weak priors and strong data, the posterior is dominated by the likelihood. Most importantly, the framework automatically quantifies our confidence: narrow posterior distributions indicate well-constrained parameters, while broad distributions signal high uncertainty.

In contrast to maximum likelihood estimation, which provides a single point estimate $\mathbf{w}_{\mathrm{ML}}$, Bayesian inference yields a complete posterior distribution that captures the full range of parameter values consistent with our observations and prior knowledge. This shift from point estimates to probability distributions enables rigorous uncertainty quantification—a capability essential for robust scientific inference.

To see why this matters, consider again our M-σ relation example. Instead of reporting a slope of 4.0, we might find that the posterior distribution suggests the slope is 4.0 ± 0.3 (at 68% confidence). This uncertainty information is crucial for comparing our results with theoretical predictions, planning follow-up observations, or propagating uncertainties through subsequent calculations.

The Bayesian framework also provides natural protection against overfitting. As we will see later in this chapter, the prior distribution acts as a regularizer, automatically penalizing overly complex models unless they are strongly supported by the data. This regularization emerges naturally from the probabilistic framework rather than being imposed as an ad hoc constraint.

Perhaps most importantly for astronomical applications, the Bayesian approach enables us to make probabilistic predictions that include proper uncertainty estimates. When we use our fitted M-σ relation to predict a black hole mass for a new galaxy, we want to know not just our best estimate, but also how uncertain that prediction is. The Bayesian framework provides exactly this capability through the posterior predictive distribution.

This transformation from point estimates to probability distributions represents more than a technical improvement—it reflects a deeper understanding of how knowledge accumulates in science. Scientific conclusions always carry some degree of uncertainty that should be quantified and propagated through subsequent analyses. The Bayesian approach provides the mathematical tools to do this rigorously and systematically.

5.2 Conjugate Priors

Having established the conceptual framework of Bayesian inference, we now face a practical challenge: how do we actually compute posterior distributions? While Bayes' theorem provides the recipe, the integration required to normalize the posterior and compute expectations can be mathematically intractable for many combinations of priors and likelihoods.

This is where the concept of conjugate priors becomes invaluable. A conjugate prior is a prior distribution that, when combined with a particular likelihood, yields a posterior distribution of the same mathematical family as the prior. This mathematical harmony enables analytical solutions to otherwise complex inference problems.

Let's recall the fundamental equation of Bayesian inference:

$$p(\mathbf{w}|\mathcal{D}) \propto p(\mathcal{D}|\mathbf{w})p(\mathbf{w}). \tag{5.2}$$

The conjugacy property means that if we choose our prior $p(\mathbf{w})$ from the right family of distributions, the posterior $p(\mathbf{w}|\mathcal{D})$ will belong to the same family, just with updated

parameters. This mathematical structure allows us to transform the abstract concept of "updating beliefs" into concrete parameter updates that can be computed analytically.

To build intuition for this concept, let's explore conjugate priors through concrete examples that frequently arise in astronomical data analysis. These examples will reveal the underlying pattern that makes conjugate priors so powerful.

Poisson-Gamma Conjugacy   Consider a fundamental task in observational astronomy: counting stars in different regions of the sky to understand stellar density distributions. Suppose we're conducting a survey where λ represents the expected number of stars in a given region—the true average we would observe if we could survey infinitely many similar regions.

When we observe a single region, the probability of counting exactly n stars follows a Poisson distribution:

$$p(n|\lambda) = \frac{\lambda^n e^{-\lambda}}{n!}. \tag{5.3}$$

This distribution naturally arises when counting rare, independent events—exactly the situation we have with star counts in a given field of view. The Poisson parameter λ encodes both the rate of star formation history and the observational selection effects that determine how many stars we can detect.

Of course, we don't know the true value of λ—that's what we're trying to learn from our observations. Before making any observations, we might have prior beliefs about λ based on previous surveys, theoretical models of stellar formation, or the known properties of the region we're studying.

The Gamma distribution provides a natural way to express these prior beliefs:

$$p(\lambda) = \frac{\beta^\alpha}{\Gamma(\alpha)} \lambda^{\alpha-1} e^{-\beta\lambda}. \tag{5.4}$$

The parameters α and β have intuitive interpretations that connect directly to our prior knowledge. The ratio α/β represents our prior expectation for the star count, while the individual values of α and β determine our confidence in this expectation. We can think of α as the total number of stars we've "effectively observed" in previous similar surveys, and β as the number of regions surveyed. For instance, if previous observations suggest about 5 stars per region and we base this on surveys of 2 regions, we might use $\alpha = 10$ and $\beta = 2$.

The magic of conjugacy reveals itself when we update our beliefs with a new observation. Suppose we count n stars in a new region. Using Bayes' theorem:

$$p(\lambda|n) \propto p(n|\lambda)p(\lambda) \propto \lambda^n e^{-\lambda} \cdot \lambda^{\alpha-1} e^{-\beta\lambda}. \tag{5.5}$$

Combining the terms:

$$p(\lambda|n) \propto \lambda^{(n+\alpha-1)} e^{-(\beta+1)\lambda}. \tag{5.6}$$

This is another Gamma distribution! The posterior has the form $\text{Gamma}(\alpha+n, \beta+1)$, where the parameters update according to simple rules:

- α increases by the number of stars observed (n)

- β increases by 1 (reflecting that we've surveyed one additional region)
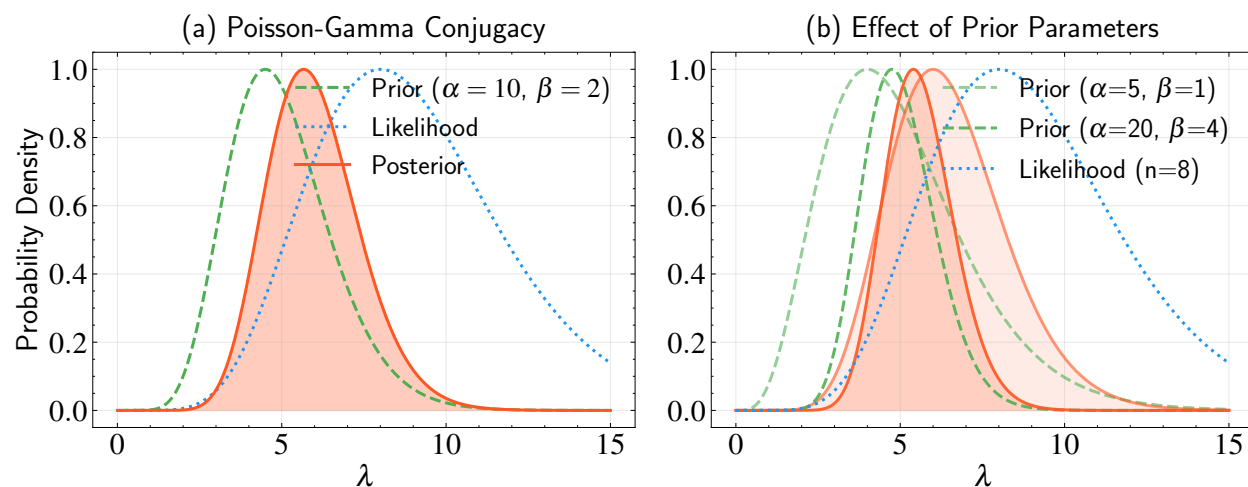
Figure 5.2: Visualization of Poisson-Gamma conjugacy in star count analysis. Panel (a) demonstrates how multiplying the Poisson likelihood (dotted blue line) with a Gamma prior (dashed green line) yields a Gamma posterior (solid red line, with shading). The prior $\text{Gamma}(\alpha = 10, \beta = 2)$ represents previous observations suggesting about 5 stars per region, which is updated by a new observation of 8 stars. Panel (b) shows how different prior parameters affect the posterior distribution, while keeping the same likelihood (8 stars observed). When the prior has higher precision ($\alpha = 20$, $\beta = 4$, darker lines), the posterior stays closer to the prior mean. When the prior has lower precision ($\alpha = 5$, $\beta = 1$, lighter lines), the posterior is more strongly influenced by the likelihood. This illustrates how the relative strength of prior knowledge versus new data shapes our updated beliefs.

This result has beautiful intuitive appeal. If our prior was $\text{Gamma}(10, 2)$ (suggesting

about 5 stars per region based on 2 previous surveys), and we observe 8 stars in a new region, our posterior becomes Gamma$(18, 3)$. This suggests a slightly higher average of about 6 stars per region $(18/3 = 6)$, incorporating both our prior knowledge and the new evidence.

For multiple observations, the updating process extends naturally. If we observe counts $\{n_1, n_2, \ldots, n_k\}$ in k independent regions, the posterior becomes Gamma$(\alpha + \sum n_i, \beta + k)$. This mathematical structure exactly matches our intuitive understanding: our estimate should be influenced by both the total number of stars observed and the number of regions surveyed.

Bernoulli-Beta Conjugacy   Consider another fundamental astronomical task: classifying galaxies as either spiral or elliptical. This binary classification problem illustrates conjugacy in a different but equally illuminating context.

For any individual galaxy, the classification follows a Bernoulli distribution. If θ represents the probability that a randomly selected galaxy is spiral, then:

$$p(x|\theta) = \theta^x (1 - \theta)^{1-x}, \tag{5.7}$$

where $x = 1$ for spiral galaxies and $x = 0$ for elliptical galaxies.

Our prior beliefs about θ—the underlying fraction of spiral galaxies in our survey region—can be expressed using a Beta distribution:

$$p(\theta) = \frac{\Gamma(\alpha + \beta)}{\Gamma(\alpha)\Gamma(\beta)} \theta^{\alpha-1} (1 - \theta)^{\beta-1}. \tag{5.8}$$

Like the Gamma parameters, α and β have intuitive interpretations: if we've previously classified $\alpha + \beta$ galaxies, with α being spiral and β elliptical, this would naturally lead to our Beta prior.

When we observe n new galaxies, with $\sum x_i$ being spiral and $(n - \sum x_i)$ being elliptical, the likelihood is:

$$p(\{x_i\}|\theta) = \theta^{\sum x_i} (1 - \theta)^{n - \sum x_i}. \tag{5.9}$$

The posterior becomes:

$$p(\theta|\{x_i\}) \propto \theta^{\sum x_i} (1 - \theta)^{n - \sum x_i} \cdot \theta^{\alpha-1} (1 - \theta)^{\beta-1} = \theta^{(\alpha + \sum x_i)-1} (1 - \theta)^{(\beta + n - \sum x_i)-1}. \tag{5.10}$$

Once again, we obtain a distribution from the same family: $\text{Beta}(\alpha + \sum x_i, \beta + n - \sum x_i)$. The updating rules are equally intuitive:

- α increases by the number of spiral galaxies observed

- β increases by the number of elliptical galaxies observed

These examples reveal the fundamental pattern that makes conjugate priors so powerful: they allow us to update our beliefs analytically, with parameter updates that have clear interpretations in terms of accumulated evidence. This mathematical elegance will prove essential when we extend these concepts to the more complex setting of linear regression.

5.3 Gaussian-Gaussian Conjugacy in One Dimension

The examples we've explored—Poisson-Gamma and Bernoulli-Beta conjugacy—reveal the power of conjugate priors for discrete problems. However, for linear regression, we need to understand conjugacy for continuous parameters. This leads us naturally to Gaussian-Gaussian conjugacy, which forms the mathematical foundation for Bayesian linear regression.

Let's begin with the simplest possible case: estimating the mean of a Gaussian distribution when the variance is known. While this might seem like an artificial problem, it contains all the essential elements we'll need for the full linear regression treatment, and its simplicity allows us to focus on the key mathematical insights.

Consider a single observation x drawn from a Gaussian distribution with unknown mean μ and known variance σ^2:

$$p(x|\mu) = \mathcal{N}(x|\mu, \sigma^2) = \frac{1}{\sqrt{2\pi\sigma^2}} \exp\left(-\frac{(x-\mu)^2}{2\sigma^2}\right). \tag{5.11}$$

This likelihood function tells us how probable it is to observe the value x for any proposed mean μ. The quadratic term in the exponent means that likelihood decreases rapidly as we move away from $\mu = x$, with the rate of decrease determined by the measurement uncertainty σ^2.

To complete our Bayesian model, we need to specify prior beliefs about μ. A natural

choice is another Gaussian distribution:

$$p(\mu) = \mathcal{N}(\mu|\mu_0, \tau_0^2) = \frac{1}{\sqrt{2\pi\tau_0^2}} \exp\left(-\frac{(\mu - \mu_0)^2}{2\tau_0^2}\right), \tag{5.12}$$

where μ_0 represents our prior belief about the mean and τ_0^2 represents our prior uncertainty.

Why choose a Gaussian prior? Beyond mathematical convenience, this choice reflects a reasonable default assumption: if we're uncertain about a continuous parameter, the Gaussian distribution assigns highest probability to values near our best guess μ_0 and smoothly decreases for values further away. The spread τ_0^2 controls how confident we are in our prior belief.

The magic of Gaussian conjugacy reveals itself when we combine the prior and likelihood. Since both are Gaussian distributions, their product will also be Gaussian—this is the essence of conjugacy. Let's see this explicitly by multiplying the distributions (dropping normalization constants):

$$p(\mu|x) \propto p(x|\mu)p(\mu) \tag{5.13}$$

$$\propto \exp\left(-\frac{(x - \mu)^2}{2\sigma^2}\right) \exp\left(-\frac{(\mu - \mu_0)^2}{2\tau_0^2}\right) \tag{5.14}$$

$$\propto \exp\left(-\frac{1}{2}\left[\frac{(x - \mu)^2}{\sigma^2} + \frac{(\mu - \mu_0)^2}{\tau_0^2}\right]\right). \tag{5.15}$$

To show that this is indeed Gaussian in μ, we need to collect terms and complete the square. Expanding the terms in the exponent:

$$-\frac{1}{2}\left[\frac{(x - \mu)^2}{\sigma^2} + \frac{(\mu - \mu_0)^2}{\tau_0^2}\right] = -\frac{1}{2}\left[\frac{\mu^2 - 2x\mu + x^2}{\sigma^2} + \frac{\mu^2 - 2\mu_0\mu + \mu_0^2}{\tau_0^2}\right] \tag{5.16}$$

$$= -\frac{1}{2}\left[\left(\frac{1}{\sigma^2} + \frac{1}{\tau_0^2}\right)\mu^2 - 2\left(\frac{x}{\sigma^2} + \frac{\mu_0}{\tau_0^2}\right)\mu + \text{const}\right]. \tag{5.17}$$

This quadratic form in μ confirms that the posterior is Gaussian. To identify the parameters of this Gaussian, we can compare with the standard form $\mathcal{N}(\mu|\mu_n, \tau_n^2)$, which has the exponent:

$$-\frac{1}{2\tau_n^2}(\mu - \mu_n)^2 = -\frac{1}{2}\left[\frac{1}{\tau_n^2}\mu^2 - \frac{2\mu_n}{\tau_n^2}\mu + \frac{\mu_n^2}{\tau_n^2}\right]. \tag{5.18}$$

Comparing coefficients, we find:

$$\frac{1}{\tau_n^2} = \frac{1}{\sigma^2} + \frac{1}{\tau_0^2}, \tag{5.19}$$

$$\frac{\mu_n}{\tau_n^2} = \frac{x}{\sigma^2} + \frac{\mu_0}{\tau_0^2}. \tag{5.20}$$

Solving for the posterior parameters:

$$\tau_n^2 = \left(\frac{1}{\sigma^2} + \frac{1}{\tau_0^2} \right)^{-1}, \tag{5.21}$$

$$\mu_n = \tau_n^2 \left(\frac{x}{\sigma^2} + \frac{\mu_0}{\tau_0^2} \right). \tag{5.22}$$

These update equations reveal the beautiful structure of Gaussian conjugacy. The posterior precision (inverse variance) $1/\tau_n^2$ is the sum of the likelihood precision $1/\sigma^2$ and prior precision $1/\tau_0^2$. Our total confidence comes from combining our prior knowledge with what we learn from the data.

The posterior mean μ_n is a weighted average of the observation x and prior mean μ_0, with weights proportional to their respective precisions. More precise information has greater influence on our final estimate—exactly what we would expect intuitively.

To build intuition, consider two extreme cases:

Uninformative prior $(\tau_0^2 \to \infty)$: When we're very uncertain about our prior belief, the posterior becomes:

$$\tau_n^2 \to \sigma^2, \tag{5.23}$$

$$\mu_n \to x. \tag{5.24}$$

The posterior is dominated by the data, with our final estimate essentially equal to the observation and uncertainty equal to the measurement error.
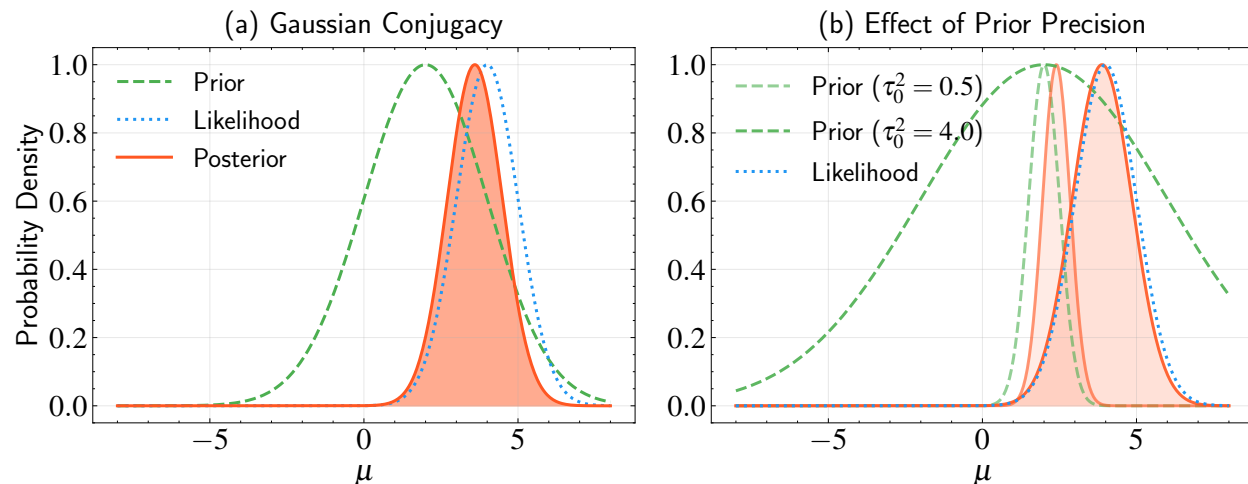
Figure 5.3: Visualization of Gaussian conjugacy. Panel (a) demonstrates how multiplying a Gaussian prior (dashed green line) with a Gaussian likelihood (dotted blue line) yields a Gaussian posterior (solid red line, with shading). Panel (b) shows how different prior precisions affect the posterior distribution, while keeping the same likelihood. When the prior has high precision ($\tau_0^2 = 0.5$, more concentrated), the posterior stays closer to the prior. When the prior has low precision ($\tau_0^2 = 4$, more spread out), the posterior is dominated by the likelihood. This illustrates how the relative precisions of the prior and likelihood determine their influence on the posterior beliefs.

Very uncertain measurement ($\sigma^2 \to \infty$): When our measurement is very noisy, the posterior becomes:

$$\tau_n^2 \to \tau_0^2, \tag{5.25}$$

$$\mu_n \to \mu_0. \tag{5.26}$$

The measurement is so uncertain that we learn almost nothing from it, and the posterior remains close to our prior beliefs.

This one-dimensional example captures the essential logic of Bayesian updating: we combine information sources according to their relative precision, with more reliable information having greater influence on our final conclusions. This same principle will govern the more complex multivariate case needed for linear regression.

The extension to multiple observations follows naturally. If we observe $x_1, x_2, \ldots, x_N$, each observation provides additional information, and the posterior precision grows with the

amount of data. The posterior parameters become:

$$\frac{1}{\tau_n^2} = \frac{1}{\tau_0^2} + \frac{N}{\sigma^2}, \tag{5.27}$$

$$\mu_n = \frac{\frac{\mu_0}{\tau_0^2} + \frac{N\bar{x}}{\sigma^2}}{\frac{1}{\tau_0^2} + \frac{N}{\sigma^2}}, \tag{5.28}$$

where $\bar{x} = \frac{1}{N}\sum_{i=1}^{N} x_i$ is the sample mean.

This framework demonstrates how Bayesian inference systematically balances prior knowledge against observed evidence, with the relative influence determined by their respective uncertainties. The mathematical elegance of this approach, combined with its intuitive appeal, makes Gaussian conjugacy the natural foundation for Bayesian linear regression.

5.4   Multivariate Gaussian Conjugacy

Having established the pattern of Gaussian conjugacy in one dimension, we now face the challenge of extending these insights to multiple dimensions—exactly what we need for linear regression with multiple parameters. The transition from one-dimensional to multivariate Gaussian distributions might seem daunting, but the fundamental principles remain beautifully consistent.

Just as a one-dimensional Gaussian is completely characterized by its mean μ and variance σ^2, a multivariate Gaussian distribution is fully determined by its mean vector $\boldsymbol{\mu}$ and covariance matrix $\boldsymbol{\Sigma}$. The covariance matrix captures not only the individual uncertainties of each parameter (along its diagonal) but also how different parameters covary—a crucial consideration in linear regression where slope and intercept estimates are often correlated.

The multivariate Gaussian probability density function generalizes our familiar one-dimensional form:

$$\mathcal{N}(\mathbf{x}|\boldsymbol{\mu}, \boldsymbol{\Sigma}) = \frac{1}{(2\pi)^{d/2}|\boldsymbol{\Sigma}|^{1/2}} \exp\left(-\frac{1}{2}(\mathbf{x} - \boldsymbol{\mu})^T \boldsymbol{\Sigma}^{-1}(\mathbf{x} - \boldsymbol{\mu})\right), \tag{5.29}$$

where d is the dimensionality of $\mathbf{x}$ and $|\boldsymbol{\Sigma}|$ denotes the determinant of $\boldsymbol{\Sigma}$. The quadratic form $(\mathbf{x} - \boldsymbol{\mu})^T \boldsymbol{\Sigma}^{-1}(\mathbf{x} - \boldsymbol{\mu})$ generalizes the squared distance $(x - \mu)^2/\sigma^2$ from one dimension, but now accounts for correlations between different dimensions.

Most importantly for our purposes, the magical property we discovered in one di-

mension—that multiplying two Gaussians yields another Gaussian—extends seamlessly to multiple dimensions. This preservation of the conjugacy property is what makes Bayesian linear regression analytically tractable.

To demonstrate this crucial result, consider two multivariate Gaussian distributions:

$$p_1(\mathbf{x}) = \mathcal{N}(\mathbf{x}|\boldsymbol{\mu}_1, \boldsymbol{\Sigma}_1), \tag{5.30}$$

$$p_2(\mathbf{x}) = \mathcal{N}(\mathbf{x}|\boldsymbol{\mu}_2, \boldsymbol{\Sigma}_2). \tag{5.31}$$

Following the same approach we used in one dimension, we focus on the exponential terms when multiplying these distributions:

$$p_1(\mathbf{x})p_2(\mathbf{x}) \propto \exp\left(-\frac{1}{2}\left[(\mathbf{x} - \boldsymbol{\mu}_1)^T\boldsymbol{\Sigma}_1^{-1}(\mathbf{x} - \boldsymbol{\mu}_1) + (\mathbf{x} - \boldsymbol{\mu}_2)^T\boldsymbol{\Sigma}_2^{-1}(\mathbf{x} - \boldsymbol{\mu}_2)\right]\right). \tag{5.32}$$

To show this is another Gaussian, we need to demonstrate that the combined exponent has the standard quadratic form. Expanding both quadratic terms and collecting coefficients:

$$-\frac{1}{2}\left[\mathbf{x}^T\boldsymbol{\Sigma}_1^{-1}\mathbf{x} - \boldsymbol{\mu}_1^T\boldsymbol{\Sigma}_1^{-1}\mathbf{x} - \mathbf{x}^T\boldsymbol{\Sigma}_1^{-1}\boldsymbol{\mu}_1 + \boldsymbol{\mu}_1^T\boldsymbol{\Sigma}_1^{-1}\boldsymbol{\mu}_1 \right.$$
$$\left. + \mathbf{x}^T\boldsymbol{\Sigma}_2^{-1}\mathbf{x} - \boldsymbol{\mu}_2^T\boldsymbol{\Sigma}_2^{-1}\mathbf{x} - \mathbf{x}^T\boldsymbol{\Sigma}_2^{-1}\boldsymbol{\mu}_2 + \boldsymbol{\mu}_2^T\boldsymbol{\Sigma}_2^{-1}\boldsymbol{\mu}_2\right]. \tag{5.33}$$

Since the covariance matrices are symmetric, the cross terms $\boldsymbol{\mu}_i^T\boldsymbol{\Sigma}_i^{-1}\mathbf{x}$ and $\mathbf{x}^T\boldsymbol{\Sigma}_i^{-1}\boldsymbol{\mu}_i$ are equal when the result is a scalar. Collecting terms by powers of $\mathbf{x}$:

$$-\frac{1}{2}\left[\mathbf{x}^T(\boldsymbol{\Sigma}_1^{-1} + \boldsymbol{\Sigma}_2^{-1})\mathbf{x} - 2(\boldsymbol{\mu}_1^T\boldsymbol{\Sigma}_1^{-1} + \boldsymbol{\mu}_2^T\boldsymbol{\Sigma}_2^{-1})\mathbf{x} + \text{const}\right]. \tag{5.34}$$

This has exactly the quadratic form of a multivariate Gaussian! Comparing with the standard form, we can identify the parameters of the resulting Gaussian. If the result is $\mathcal{N}(\mathbf{x}|\boldsymbol{\mu}_n, \boldsymbol{\Sigma}_n)$, then by comparing the quadratic and linear terms:

$$\boldsymbol{\Sigma}_n^{-1} = \boldsymbol{\Sigma}_1^{-1} + \boldsymbol{\Sigma}_2^{-1}, \tag{5.35}$$

$$\boldsymbol{\Sigma}_n^{-1}\boldsymbol{\mu}_n = \boldsymbol{\Sigma}_1^{-1}\boldsymbol{\mu}_1 + \boldsymbol{\Sigma}_2^{-1}\boldsymbol{\mu}_2. \tag{5.36}$$

Solving for the parameters of the product distribution:

$$\boldsymbol{\Sigma}_n = (\boldsymbol{\Sigma}_1^{-1} + \boldsymbol{\Sigma}_2^{-1})^{-1}, \tag{5.37}$$

$$\boldsymbol{\mu}_n = \boldsymbol{\Sigma}_n(\boldsymbol{\Sigma}_1^{-1}\boldsymbol{\mu}_1 + \boldsymbol{\Sigma}_2^{-1}\boldsymbol{\mu}_2). \tag{5.38}$$

These expressions beautifully generalize our one-dimensional results. The new precision matrix (inverse covariance) is the sum of the input precision matrices, and the new mean is a precision-weighted average of the input means. The matrix algebra may appear more complex, but the underlying pattern—combining information weighted by its precision—remains identical.
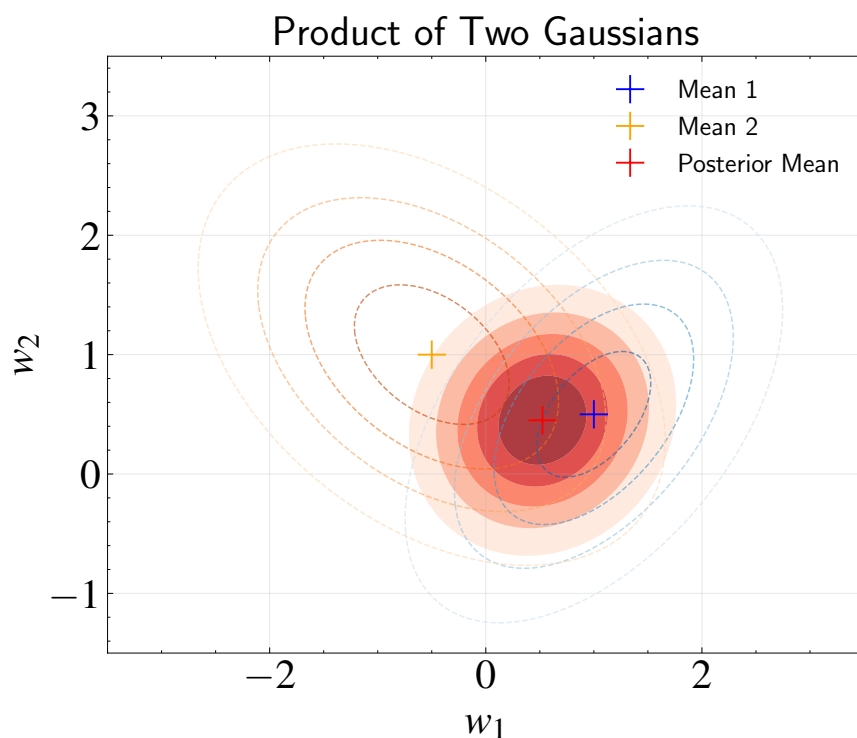
Figure 5.4: Visualization of the product of two 2D Gaussian distributions. The blue and orange dashed contours show the level sets of two original Gaussian distributions, representing our prior beliefs and data-driven information about linear regression parameters. Their means are marked by corresponding colored '+' symbols. The filled red contours show the resulting posterior distribution obtained from their product. The red '+' marks the posterior mean, which is a precision-weighted average of the input means. Note how the posterior distribution is more concentrated than either input distribution, reflecting the combination of information from both sources. The position and shape of the posterior captures how our prior knowledge and observed data combine to yield updated beliefs.

This multivariate conjugacy property is not merely a mathematical curiosity—it pro-

vides the theoretical foundation that makes Bayesian linear regression both analytically tractable and conceptually elegant. When we apply this framework to linear regression, our Gaussian prior on the regression parameters will combine with our Gaussian likelihood to yield a Gaussian posterior, complete with analytical expressions for both the updated parameter estimates and their uncertainties.

The preservation of mathematical structure across dimensions demonstrates the deep consistency of Bayesian inference. Whether we're estimating a single parameter or dozens of regression coefficients, the same principled approach—precision-weighted combination of prior knowledge and observational evidence—governs our updated beliefs. This universality will prove invaluable as we tackle more complex astronomical modeling challenges in subsequent chapters.

5.5 Bayesian Linear Regression: Mathematical Formalism

Having established the mathematical foundations of multivariate Gaussian conjugacy, we can now derive the complete Bayesian solution for linear regression. This represents a fundamental shift from the point estimates we obtained through maximum likelihood estimation to full probability distributions that capture our uncertainty about the model parameters.

Our goal is to find the posterior distribution $p(\mathbf{w}|\mathbf{t}, \mathbf{X}, \mathbf{S})$—the complete probability distribution over possible parameter values given our observed data $\mathbf{t}$, input features $\mathbf{X}$, and measurement uncertainties $\mathbf{S}$. This distribution will tell us not just our best estimates of the regression coefficients, but also how confident we should be in those estimates and how they might correlate with each other.

The foundation of our analysis remains Bayes' theorem:

$$p(\mathbf{w}|\mathbf{t}, \mathbf{X}, \mathbf{S}) \propto p(\mathbf{t}|\mathbf{X}, \mathbf{w}, \mathbf{S})p(\mathbf{w}). \tag{5.39}$$

From Chapter 4, we established that under Gaussian measurement uncertainties, the likelihood takes the form:

$$p(\mathbf{t}|\mathbf{X}, \mathbf{w}, \mathbf{S}) = \mathcal{N}(\mathbf{t}|\mathbf{\Phi}\mathbf{w}, \mathbf{S}), \tag{5.40}$$

where $\mathbf{\Phi}$ is our design matrix containing the basis functions $\phi(\mathbf{x})$ evaluated at each input
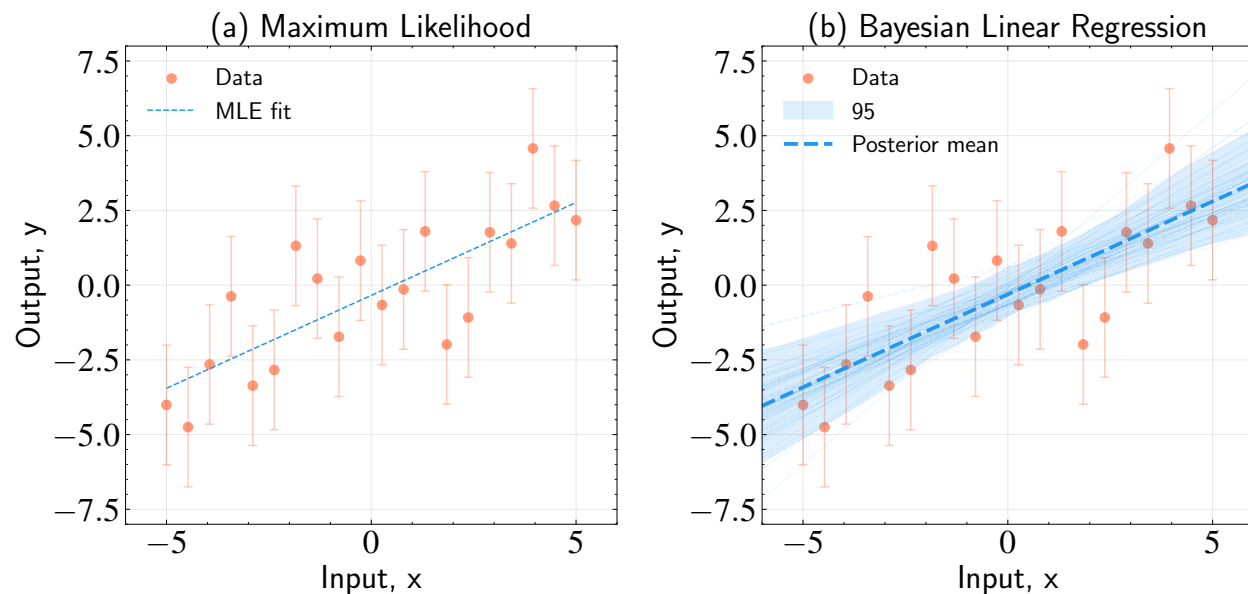
Figure 5.5: Comparison of maximum likelihood and Bayesian approaches to linear regression. Panel (a) shows the maximum likelihood estimate (MLE), which provides a single best-fit line through the data. The error bars on the data points indicate the assumed measurement uncertainty (σ). Panel (b) shows the Bayesian approach with the same data, where the light blue lines represent different possible fits drawn from the posterior distribution over regression parameters. Each line represents a different plausible fit given our data and prior assumptions. The solid blue line shows the posterior mean prediction, and the shaded region represents the 95% credible interval. Both approaches identify the same underlying trend, but the Bayesian approach naturally quantifies our uncertainty in the fit, with credible intervals that widen away from the data points where we have less constraint on the model parameters.

point. For example, in polynomial regression with degree 2, if we have input points x_1 and x_2, then $\boldsymbol{\Phi}$ would be:

$$\boldsymbol{\Phi} = \begin{bmatrix} 1 & x_1 & x_1^2 \\ 1 & x_2 & x_2^2 \end{bmatrix}. \tag{5.41}$$

For our prior, we choose a multivariate Gaussian distribution—the natural conjugate prior for our Gaussian likelihood:

$$p(\mathbf{w}) = \mathcal{N}(\mathbf{w}|\mathbf{m}_0, \mathbf{S}_0). \tag{5.42}$$

Here, $\mathbf{m}_0$ represents our prior beliefs about the most likely parameter values, while $\mathbf{S}_0$ encodes our prior uncertainties and any believed correlations between parameters.

The choice of prior deserves careful consideration in astronomical applications. For

the M-σ relation between black hole mass and stellar velocity dispersion, we might set $\mathbf{m}_0$ based on previous studies, perhaps expecting a slope near 4 and an intercept consistent with theoretical predictions. The covariance matrix $\mathbf{S}_0$ would reflect both our uncertainty in these estimates and any known correlations—for instance, if previous studies show that steeper slopes tend to accompany larger intercepts.

To apply our multivariate conjugacy results, we need to express both the likelihood and prior as Gaussians in the parameter vector $\mathbf{w}$. While our prior is already in the correct form, our likelihood is expressed as a Gaussian in the observations $\mathbf{t}$. We need to rewrite it as a Gaussian in $\mathbf{w}$.

Starting with the likelihood and expanding the quadratic form:

$$p(\mathbf{t}|\mathbf{w}) = \mathcal{N}(\mathbf{t}|\mathbf{\Phi}\mathbf{w}, \mathbf{S}) \propto \exp\left(-\frac{1}{2}(\mathbf{t} - \mathbf{\Phi}\mathbf{w})^T \mathbf{S}^{-1}(\mathbf{t} - \mathbf{\Phi}\mathbf{w})\right). \tag{5.43}$$

Expanding this quadratic form:

$$(\mathbf{t} - \mathbf{\Phi}\mathbf{w})^T \mathbf{S}^{-1}(\mathbf{t} - \mathbf{\Phi}\mathbf{w}) = \mathbf{t}^T \mathbf{S}^{-1}\mathbf{t} - 2\mathbf{t}^T \mathbf{S}^{-1}\mathbf{\Phi}\mathbf{w} + \mathbf{w}^T \mathbf{\Phi}^T \mathbf{S}^{-1}\mathbf{\Phi}\mathbf{w}. \tag{5.44}$$

The first term is constant with respect to $\mathbf{w}$ and can be absorbed into the proportionality. Focusing on the terms that depend on $\mathbf{w}$:

$$p(\mathbf{t}|\mathbf{w}) \propto \exp\left(-\frac{1}{2}\mathbf{w}^T (\mathbf{\Phi}^T \mathbf{S}^{-1}\mathbf{\Phi})\mathbf{w} + \mathbf{w}^T (\mathbf{\Phi}^T \mathbf{S}^{-1}\mathbf{t})\right). \tag{5.45}$$

Comparing this with the standard Gaussian form in $\mathbf{w}$, we can identify this as:

$$p(\mathbf{t}|\mathbf{w}) \propto \mathcal{N}(\mathbf{w}|\boldsymbol{\mu}_1, \boldsymbol{\Sigma}_1), \tag{5.46}$$

where:

$$\boldsymbol{\Sigma}_1^{-1} = \mathbf{\Phi}^T \mathbf{S}^{-1}\mathbf{\Phi}, \tag{5.47}$$

$$\boldsymbol{\Sigma}_1^{-1}\boldsymbol{\mu}_1 = \mathbf{\Phi}^T \mathbf{S}^{-1}\mathbf{t}. \tag{5.48}$$

Solving for the likelihood parameters:

$$\mathbf{\Sigma}_1 = (\mathbf{\Phi}^T \mathbf{S}^{-1} \mathbf{\Phi})^{-1}, \tag{5.49}$$

$$\boldsymbol{\mu}_1 = (\mathbf{\Phi}^T \mathbf{S}^{-1} \mathbf{\Phi})^{-1} \mathbf{\Phi}^T \mathbf{S}^{-1} \mathbf{t}. \tag{5.50}$$

Notice that $\boldsymbol{\mu}_1$ is exactly the maximum likelihood estimate we derived in Chapter 4! This connection reveals that the "mean" of our likelihood function, when viewed as a distribution over parameters, corresponds to the point estimate from maximum likelihood estimation.

Now we can apply our multivariate conjugacy results. The posterior distribution is the product of two Gaussians:

$$p(\mathbf{w}|\mathbf{t}) \propto \mathcal{N}(\mathbf{w}|\boldsymbol{\mu}_1, \mathbf{\Sigma}_1) \mathcal{N}(\mathbf{w}|\mathbf{m}_0, \mathbf{S}_0) = \mathcal{N}(\mathbf{w}|\mathbf{m}_N, \mathbf{S}_N), \tag{5.51}$$

where, using our conjugacy formulas:

$$\mathbf{S}_N^{-1} = \mathbf{\Sigma}_1^{-1} + \mathbf{S}_0^{-1} = \mathbf{\Phi}^T \mathbf{S}^{-1} \mathbf{\Phi} + \mathbf{S}_0^{-1}, \tag{5.52}$$

$$\mathbf{m}_N = \mathbf{S}_N(\mathbf{\Sigma}_1^{-1} \boldsymbol{\mu}_1 + \mathbf{S}_0^{-1} \mathbf{m}_0) = \mathbf{S}_N(\mathbf{\Phi}^T \mathbf{S}^{-1} \mathbf{t} + \mathbf{S}_0^{-1} \mathbf{m}_0). \tag{5.53}$$

Therefore, our complete Bayesian linear regression solution is:

$$p(\mathbf{w}|\mathbf{t}, \mathbf{X}, \mathbf{S}) = \mathcal{N}(\mathbf{w}|\mathbf{m}_N, \mathbf{S}_N), \tag{5.54}$$

where:

$$\mathbf{S}_N = (\mathbf{S}_0^{-1} + \mathbf{\Phi}^T \mathbf{S}^{-1} \mathbf{\Phi})^{-1}, \tag{5.55}$$

$$\mathbf{m}_N = \mathbf{S}_N(\mathbf{S}_0^{-1} \mathbf{m}_0 + \mathbf{\Phi}^T \mathbf{S}^{-1} \mathbf{t}). \tag{5.56}$$

These expressions generalize our one-dimensional intuitions. The posterior precision $\mathbf{S}_N^{-1}$ combines the prior precision $\mathbf{S}_0^{-1}$ with the data precision $\mathbf{\Phi}^T \mathbf{S}^{-1} \mathbf{\Phi}$. The posterior mean $\mathbf{m}_N$ represents a precision-weighted combination of our prior beliefs $\mathbf{m}_0$ and the maximum likelihood estimate embedded in the data term $\mathbf{\Phi}^T \mathbf{S}^{-1} \mathbf{t}$.

Several limiting cases help build intuition about this general solution. When we have minimal prior knowledge, we can take $\mathbf{S}_0 = \eta^2 \mathbf{I}$ with $\eta^2 \to \infty$ and $\mathbf{m}_0 = \mathbf{0}$. In this

uninformative prior limit:

$$\mathbf{S}_N \to (\mathbf{\Phi}^T \mathbf{S}^{-1} \mathbf{\Phi})^{-1}, \tag{5.57}$$

$$\mathbf{m}_N \to (\mathbf{\Phi}^T \mathbf{S}^{-1} \mathbf{\Phi})^{-1} \mathbf{\Phi}^T \mathbf{S}^{-1} \mathbf{t}. \tag{5.58}$$

The posterior mean reduces exactly to the maximum likelihood estimate, confirming the consistency between Bayesian and frequentist approaches when prior knowledge is minimal. However, even with an uninformative prior, we still obtain the covariance matrix $\mathbf{S}_N$, providing crucial uncertainty quantification absent from maximum likelihood methods.

For the common case of uniform measurement uncertainties ($\mathbf{S} = \sigma^2 \mathbf{I}$) and an isotropic prior ($\mathbf{S}_0 = \eta^2 \mathbf{I}$, $\mathbf{m}_0 = \mathbf{0}$), the expressions simplify to:

$$\mathbf{S}_N = \left(\frac{1}{\eta^2} \mathbf{I} + \frac{1}{\sigma^2} \mathbf{\Phi}^T \mathbf{\Phi} \right)^{-1}, \tag{5.59}$$

$$\mathbf{m}_N = \left(\frac{\sigma^2}{\eta^2} \mathbf{I} + \mathbf{\Phi}^T \mathbf{\Phi} \right)^{-1} \mathbf{\Phi}^T \mathbf{t}. \tag{5.60}$$

Compared to the ordinary least squares solution $\mathbf{w}_{OLS} = (\mathbf{\Phi}^T \mathbf{\Phi})^{-1} \mathbf{\Phi}^T \mathbf{t}$, our Bayesian solution includes the regularization term $\frac{\sigma^2}{\eta^2} \mathbf{I}$. This ratio of measurement variance to prior variance naturally controls the trade-off between fitting the data and respecting our prior beliefs.

As the number of observations N grows, the data term $\mathbf{\Phi}^T \mathbf{S}^{-1} \mathbf{\Phi}$ typically scales as N, causing $\mathbf{S}_N$ to shrink roughly as $1/N$. This mathematical behavior reflects the intuitive expectation that parameter uncertainty should decrease as we collect more data. In the limit $N \to \infty$, the posterior becomes increasingly concentrated around the true parameter values, demonstrating how Bayesian inference naturally handles the accumulation of evidence.

This complete analytical solution represents one of the most elegant results in machine learning. Unlike many sophisticated methods that require iterative numerical optimization, Bayesian linear regression provides exact solutions that combine principled uncertainty quantification with computational efficiency. For astronomical applications, where understanding and propagating uncertainties is crucial for scientific inference, this framework offers both theoretical rigor and practical utility.

Consider fitting a mass-luminosity relation for stars, where $L \propto M^\alpha$. When working

in log space ($\log L = \alpha \log M + b$), both the power-law index α and the normalization b carry physical meaning - α tells us how luminosity scales with mass, while b sets the overall luminosity scale. The posterior covariance matrix $\mathbf{S}_N$ reveals these parameters are typically correlated: a slightly steeper slope can be compensated by a lower normalization to fit the same data. Understanding these parameter degeneracies is crucial when using such relations to make predictions or compare with theoretical models.

5.6   Prior as Regularization

The Bayesian framework reveals a connection between statistical inference and machine learning that illuminates why many seemingly ad hoc techniques in modern machine learning actually have deep theoretical foundations. By examining our Bayesian linear regression solution from a different perspective, we'll discover how priors naturally give rise to regularization—one of the most important concepts for preventing overfitting.

Consider two astronomical applications that highlight the range from simple to complex linear regression problems. The M-σ relation we've discussed involves fitting just two parameters (slope and intercept) to relate galaxy properties. In contrast, determining stellar parameters from spectra represents a high-dimensional regression problem: we might use hundreds or thousands of spectral features (absorption line strengths, continuum measurements) as basis functions to estimate quantities like temperature, surface gravity, and chemical abundances. While both problems involve linear regression, the latter's high dimensionality makes it prone to overfitting - much like how a high-degree polynomial can perfectly fit a few data points but perform poorly on new observations. This is where regularization becomes crucial, helping us find simpler solutions that generalize better by preventing the model from placing too much weight on any individual spectral feature.

The key insight emerges when we consider the relationship between maximizing the posterior probability and minimizing a regularized loss function. Rather than working with the full posterior distribution, let's focus on finding the single most probable parameter values—the Maximum A Posteriori (MAP) estimate:

$$\mathbf{w}_{MAP} = \arg \max_{\mathbf{w}} p(\mathbf{w}|\mathbf{t}, \mathbf{X}, \sigma^2). \tag{5.61}$$

Since the logarithm is a monotonic function, maximizing the log-posterior is equivalent

to maximizing the posterior itself. Using Bayes' theorem:

$$\ln p(\mathbf{w}|\mathbf{t}, \mathbf{X}, \sigma^2) = \ln p(\mathbf{t}|\mathbf{w}, \mathbf{X}, \sigma^2) + \ln p(\mathbf{w}) + \text{const.} \tag{5.62}$$

For homogeneous noise ($\mathbf{S} = \sigma^2\mathbf{I}$) and a zero-mean isotropic prior ($p(\mathbf{w}) = \mathcal{N}(\mathbf{w}|\mathbf{0}, \eta^2\mathbf{I})$), let's evaluate each term explicitly.

The likelihood term represents how well our model predictions match the observed data:

$$\ln p(\mathbf{t}|\mathbf{w}, \mathbf{X}, \sigma^2) = \ln \mathcal{N}(\mathbf{t}|\mathbf{\Phi}\mathbf{w}, \sigma^2\mathbf{I}) \tag{5.63}$$

$$= -\frac{1}{2\sigma^2}(\mathbf{t} - \mathbf{\Phi}\mathbf{w})^T(\mathbf{t} - \mathbf{\Phi}\mathbf{w}) + \text{const} \tag{5.64}$$

$$= -\frac{1}{2\sigma^2}\|\mathbf{t} - \mathbf{\Phi}\mathbf{w}\|^2 + \text{const.} \tag{5.65}$$

This is precisely the negative sum of squared residuals that we minimized in maximum likelihood estimation, scaled by the measurement variance.

The prior term captures our belief about parameter values:

$$\ln p(\mathbf{w}) = \ln \mathcal{N}(\mathbf{w}|\mathbf{0}, \eta^2\mathbf{I}) \tag{5.66}$$

$$= -\frac{1}{2\eta^2}\mathbf{w}^T\mathbf{w} + \text{const} \tag{5.67}$$

$$= -\frac{1}{2\eta^2}\|\mathbf{w}\|^2 + \text{const.} \tag{5.68}$$

This zero-mean prior embodies Occam's razor - the principle that among competing hypotheses, we should prefer the one making the fewest assumptions. In the context of linear regression, large coefficients suggest strong dependencies on particular features, while coefficients near zero indicate weak or negligible relationships. When multiple models fit the data equally well, the prior guides us toward solutions that avoid unnecessarily strong feature dependencies unless compelled by evidence.

Combining these terms and defining $\lambda = \sigma^2/\eta^2$:

$$\ln p(\mathbf{w}|\mathbf{t}, \mathbf{X}, \sigma^2) = -\frac{1}{2\sigma^2}\|\mathbf{t} - \boldsymbol{\Phi}\mathbf{w}\|^2 - \frac{1}{2\eta^2}\|\mathbf{w}\|^2 + \text{const} \tag{5.69}$$

$$= -\frac{1}{2\sigma^2}\left[\|\mathbf{t} - \boldsymbol{\Phi}\mathbf{w}\|^2 + \lambda\|\mathbf{w}\|^2\right] + \text{const.} \tag{5.70}$$

Maximizing this log-posterior is equivalent to minimizing the regularized loss function:

$$L(\mathbf{w}) = \|\mathbf{t} - \boldsymbol{\Phi}\mathbf{w}\|^2 + \lambda\|\mathbf{w}\|^2. \tag{5.71}$$

This result reveals the connection between Bayesian inference and regularization. The first term, $\|\mathbf{t} - \boldsymbol{\Phi}\mathbf{w}\|^2$, measures how well our model predictions match the observations. The second term, $\lambda\|\mathbf{w}\|^2$, is the L2 regularization (also known as ridge regression or Tikhonov regularization) that implements our Occam's razor preference: it penalizes strong feature dependencies unless they substantially improve the model's fit to the data.

The regularization parameter $\lambda = \sigma^2/\eta^2$ has a natural interpretation as the ratio of measurement uncertainty to prior uncertainty. When λ is large (noisy measurements or confident prior), the regularization term dominates, forcing the solution toward simpler models with smaller parameter values. When λ is small (precise measurements or uncertain prior), the data-fitting term dominates, allowing more complex fits that closely follow the observations.

This Bayesian perspective provides crucial insights into regularization that extend far beyond linear regression. Rather than treating λ as an arbitrary hyperparameter to be tuned through cross-validation, the Bayesian framework provides a principled interpretation. The optimal regularization strength depends on the relative trustworthiness of our data versus our prior beliefs, encoded in the ratio σ^2/η^2.

Different prior distributions naturally lead to different regularization schemes. For instance, a Laplace prior $p(\mathbf{w}) \propto \exp(-\alpha\|\mathbf{w}\|_1)$ would yield L1 regularization (the lasso), which promotes sparse solutions by driving some coefficients exactly to zero. The corresponding regularized loss function becomes:

$$L(\mathbf{w}) = \|\mathbf{t} - \boldsymbol{\Phi}\mathbf{w}\|^2 + \lambda\|\mathbf{w}\|_1, \tag{5.72}$$

where $\|\mathbf{w}\|_1 = \sum_i |w_i|$ is the L1 norm. This connection reveals that the choice of regulariza-
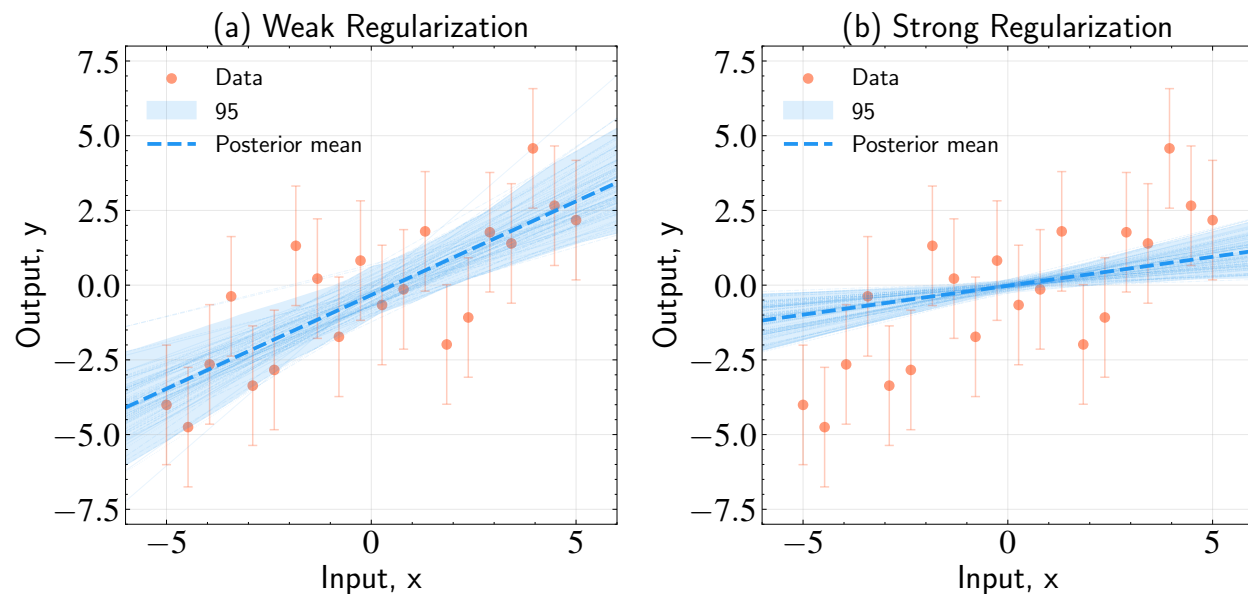
Figure 5.6: Effect of regularization strength ($\lambda = \sigma^2/\eta^2$) in Bayesian linear regression. Panel (a) shows weak regularization (small λ, corresponding to precise measurements or uncertain prior), where the model has more freedom to fit the data, resulting in wider prediction bands that reflect greater parameter uncertainty, especially away from the data points. Panel (b) shows strong regularization (large λ, corresponding to noisy measurements or confident prior), where the prior more strongly constrains the parameters toward smaller values, leading to narrower prediction bands and simpler, more conservative fits. The blue lines show samples from the posterior distribution of possible fits, while the shaded region indicates the 95% credible interval for predictions. This demonstrates how the regularization parameter λ controls the trade-off between model flexibility and constraint—a key mechanism for preventing overfitting.

tion reflects implicit assumptions about the expected structure of good solutions.

While the MAP estimate provides a regularized point solution, the full Bayesian approach offers something more valuable: complete uncertainty quantification. The posterior distribution $p(\mathbf{w}|\mathbf{t})$ captures not just the most likely parameter values but also our confidence in those estimates and their correlations.

For astronomical applications, this distinction is crucial. Consider using the M-σ relation to estimate black hole masses for a sample of galaxies. The MAP estimate might give us a best-fit slope and intercept, but the full posterior tells us how uncertain we should be about these parameters and how they correlate. This uncertainty information is essential when propagating errors through subsequent analyses or when comparing our results with theoretical predictions.

The regularization term naturally prevents overfitting by discouraging overly complex models unless they are strongly supported by the data. This mechanism becomes particularly important when the number of parameters approaches the number of data points, or when using flexible basis functions that could otherwise lead to wild oscillations between observations.

The beauty of this framework lies in how it unifies seemingly disparate concepts. What appears as ad hoc regularization in machine learning emerges naturally from principled Bayesian reasoning. The regularization parameter λ is not an arbitrary tuning parameter but reflects the fundamental balance between trusting our measurements versus trusting our prior knowledge about reasonable parameter values.

This connection extends to virtually all modern machine learning techniques. Neural network weight decay, sparsity constraints in image reconstruction, and smoothness penalties in function approximation all find their theoretical foundation in appropriate choices of prior distributions. The Bayesian perspective provides not just a unifying mathematical framework but also principled guidance for selecting regularization strategies based on domain knowledge and the specific structure we expect in good solutions.

For practitioners, this insight offers a powerful tool for model selection and validation. Rather than relying solely on cross-validation to choose regularization parameters, we can use our understanding of measurement uncertainties and reasonable parameter ranges to make informed choices about λ. This approach proves particularly valuable in astronomy, where physical constraints often provide strong guidance about plausible model parameters.

5.7   Posterior Predictive Distribution

While determining the distribution of model parameters provides valuable insights into our regression coefficients and their uncertainties, the ultimate goal in many applications is making predictions for new observations. When an astronomer measures a galaxy's velocity dispersion and wants to estimate its black hole mass using the M-σ relation, they need more than just parameter estimates—they need a complete characterization of the uncertainty in their prediction.

The Bayesian framework addresses this challenge through the posterior predictive distribution, which naturally incorporates both measurement noise and parameter uncertainty into a single coherent prediction. Rather than making point predictions that ignore uncer-

tainty, we obtain complete probability distributions that capture all sources of uncertainty in our forecasts.

For a new input $\mathbf{x}_*$, the posterior predictive distribution is defined as:

$$p(y_*|\mathbf{x}_*, \mathcal{D}) = \int p(y_*|\mathbf{x}_*, \mathbf{w})p(\mathbf{w}|\mathcal{D})d\mathbf{w}. \tag{5.73}$$

This integral has an elegant interpretation: for each possible set of parameters $\mathbf{w}$ consistent with our data, we compute the predicted distribution of y_* and then average over all possibilities, weighted by how likely each parameter set is given our observations. This process automatically accounts for our uncertainty about the true parameter values when making predictions.
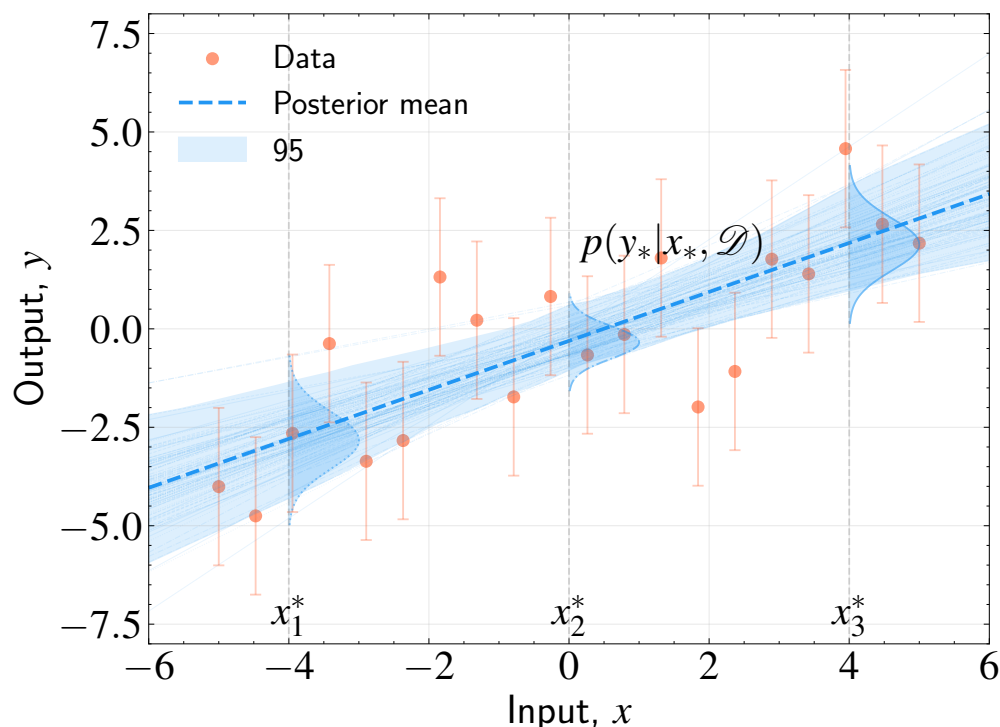
Figure 5.7: Visualization of the posterior predictive distribution in Bayesian linear regression. The red points show observed data with error bars indicating measurement uncertainties. The light blue lines represent individual regression fits sampled from the posterior distribution $p(\mathbf{w}|\mathcal{D})$, illustrating the range of models consistent with our data and prior assumptions. The shaded blue region shows the 95% credible interval for predictions. At three specific input points x_*, we visualize the complete predictive distribution $p(y_*|x_*, \mathcal{D})$ as probability density curves. The mean of each predictive distribution corresponds to our best prediction, while the width reflects our total uncertainty, which increases away from the data points where we have less constraint on the model parameters.

The mathematical structure of our problem—Gaussian likelihood, Gaussian posterior, and linear model—enables analytical evaluation of this integral. Both components under the integral are Gaussian distributions:

- The predictive likelihood $p(y_*|\mathbf{x}_*, \mathbf{w}) = \mathcal{N}(y_*|\phi(\mathbf{x}_*)^T\mathbf{w}, \sigma^2)$

- The posterior $p(\mathbf{w}|\mathcal{D}) = \mathcal{N}(\mathbf{w}|\mathbf{m}_N, \mathbf{S}_N)$

A fundamental property of Gaussian distributions is that when we marginalize (integrate out) some variables from a joint Gaussian distribution, the result is also Gaussian. This means our posterior predictive distribution will be Gaussian, completely characterized by its mean and variance.

To find these moments efficiently, we employ two powerful tools from probability theory that we encountered in Chapter 3. Using the law of total expectation, $\mathbb{E}[y_*] = \mathbb{E}_w[\mathbb{E}[y_*|\mathbf{w}]]$, we find that for any fixed parameter vector $\mathbf{w}$, our model predicts $y_* = \phi(\mathbf{x}_*)^T\mathbf{w}$ (plus measurement noise with zero mean). Taking the expectation over the posterior distribution:

$$\mathbb{E}[y_*] = \mathbb{E}_w[\mathbb{E}[y_*|\mathbf{w}]] \tag{5.74}$$

$$= \mathbb{E}_w[\phi(\mathbf{x}_*)^T\mathbf{w}] \tag{5.75}$$

$$= \phi(\mathbf{x}_*)^T\mathbb{E}_w[\mathbf{w}] \tag{5.76}$$

$$= \phi(\mathbf{x}_*)^T\mathbf{m}_N. \tag{5.77}$$

This result aligns perfectly with intuition: our best prediction at any point $\mathbf{x}_*$ uses our best parameter estimates $\mathbf{m}_N$ with the appropriate basis functions $\phi(\mathbf{x}_*)$.

Using the law of total variance, $\mathrm{Var}[y_*] = \mathbb{E}_w[\mathrm{Var}[y_*|\mathbf{w}]] + \mathrm{Var}_w[\mathbb{E}[y_*|\mathbf{w}]]$, reveals two fundamental sources of uncertainty in our predictions. The first term represents aleatoric uncertainty—the inherent randomness in measurements. Even with perfect knowledge of the model parameters, repeated observations would show scatter due to instrumental noise, photon statistics, and other random effects:

$$\mathbb{E}_w[\mathrm{Var}[y_*|\mathbf{w}]] = \mathbb{E}_w[\sigma^2] = \sigma^2. \tag{5.78}$$

This contribution to uncertainty cannot be reduced by collecting more training data of the same type, as it reflects fundamental limits of the measurement process.

The second term captures epistemic uncertainty—our imperfect knowledge of the true model parameters, which stems from having only finite, potentially noisy training data:

$$\mathrm{Var}_w[\mathbb{E}[y_*|\mathbf{w}]] = \mathrm{Var}_w[\boldsymbol{\phi}(\mathbf{x}_*)^T\mathbf{w}] \tag{5.79}$$

$$= \boldsymbol{\phi}(\mathbf{x}_*)^T\mathrm{Var}_w[\mathbf{w}]\boldsymbol{\phi}(\mathbf{x}_*) \tag{5.80}$$

$$= \boldsymbol{\phi}(\mathbf{x}_*)^T\mathbf{S}_N\boldsymbol{\phi}(\mathbf{x}_*). \tag{5.81}$$

Unlike aleatoric uncertainty, this component decreases as we collect more training data, since additional observations constrain our parameter estimates more tightly.

Combining these contributions, our complete posterior predictive distribution is:

$$p(y_*|\mathbf{x}_*,\mathcal{D}) = \mathcal{N}(y_*|\boldsymbol{\phi}(\mathbf{x}_*)^T\mathbf{m}_N, \sigma^2 + \boldsymbol{\phi}(\mathbf{x}_*)^T\mathbf{S}_N\boldsymbol{\phi}(\mathbf{x}_*)). \tag{5.82}$$

This expression unifies all sources of predictive uncertainty. The mean $\boldsymbol{\phi}(\mathbf{x}_*)^T\mathbf{m}_N$ provides our best estimate, while the variance $\sigma^2 + \boldsymbol{\phi}(\mathbf{x}_*)^T\mathbf{S}_N\boldsymbol{\phi}(\mathbf{x}_*)$ quantifies our total uncertainty by combining both measurement noise and parameter uncertainty.

This decomposition explains several important phenomena observable in predictive uncertainty. The parameter uncertainty term $\boldsymbol{\phi}(\mathbf{x}_*)^T\mathbf{S}_N\boldsymbol{\phi}(\mathbf{x}_*)$ typically grows as we move away from our training data. This reflects the intuitive expectation that extrapolation beyond observed ranges should carry higher uncertainty than interpolation within the data range. For the M-σ relation, this means we should be more cautious about black hole mass predictions for galaxies with velocity dispersions far from our training sample.

The quadratic form $\boldsymbol{\phi}(\mathbf{x}_*)^T\mathbf{S}_N\boldsymbol{\phi}(\mathbf{x}_*)$ depends on both the specific features at the prediction point and the parameter covariance structure. Regions of feature space that are poorly constrained by our training data will exhibit higher predictive uncertainty, providing natural guidance for where additional observations would be most valuable.

When using regression results in subsequent analyses, we can properly account for all uncertainties by sampling from the predictive distribution rather than using point estimates. This capability proves essential in astronomical pipelines where uncertainties must be carefully tracked through multiple processing stages.

The posterior predictive distribution represents one of the most practical advantages of Bayesian methods. It provides a complete, principled framework for making predictions

that honestly reflects all sources of uncertainty. For scientific applications where understanding the reliability of predictions is as important as the predictions themselves, this uncertainty quantification proves invaluable for drawing robust conclusions and planning effective observational strategies.

5.8   Summary

In this chapter, we have developed a Bayesian framework for linear regression that transforms the point estimates of maximum likelihood estimation into complete probability distributions over model parameters and predictions. This transformation addresses fundamental limitations in scientific inference while revealing deep connections between Bayesian thinking and modern machine learning techniques.

Our journey began by establishing why the Bayesian approach represents a fundamental advance over maximum likelihood estimation. While maximum likelihood provides single "best-fit" parameter values, Bayesian inference treats parameters as random variables with probability distributions. This shift enables us to ask not just "what are the best parameter values?" but "what is the complete probability distribution over all plausible parameter values given our data and prior knowledge?" This uncertainty quantification proves essential for robust scientific inference in astronomy, where understanding the reliability of our results is often as important as the results themselves.

The mathematical foundation for this approach rests on conjugate priors, which provide analytical solutions to otherwise intractable Bayesian inference problems. Through concrete examples—Poisson-Gamma conjugacy in star count analysis, Bernoulli-Beta conjugacy in galaxy classification, and Gaussian-Gaussian conjugacy for continuous parameters—we demonstrated how conjugate priors enable tractable updating of beliefs as new data arrives. The pattern that emerges—precision-weighted combination of prior knowledge and observational evidence—remains consistent across all these examples and forms the mathematical backbone of Bayesian linear regression.

The extension to multivariate Gaussian conjugacy preserves these properties while enabling analysis of high-dimensional parameter spaces typical in astronomical applications. We showed that multiplying two multivariate Gaussians yields another Gaussian with precision matrices adding and means becoming precision-weighted averages—a beautiful generalization of one-dimensional intuitions that makes Bayesian linear regression analytically tractable.

The complete Bayesian linear regression solution:

$$p(\mathbf{w}|\mathbf{t}, \mathbf{X}, \mathbf{S}) = \mathcal{N}(\mathbf{w}|\mathbf{m}_N, \mathbf{S}_N), \tag{5.83}$$

where:

$$\mathbf{S}_N = (\mathbf{S}_0^{-1} + \mathbf{\Phi}^T\mathbf{S}^{-1}\mathbf{\Phi})^{-1}, \tag{5.84}$$

$$\mathbf{m}_N = \mathbf{S}_N(\mathbf{S}_0^{-1}\mathbf{m}_0 + \mathbf{\Phi}^T\mathbf{S}^{-1}\mathbf{t}), \tag{5.85}$$

provides a complete analytical characterization of parameter uncertainty. These expressions naturally handle the balance between prior knowledge and observational evidence: when measurements are precise or priors are uncertain, the data dominates; when measurements are noisy or priors are confident, prior beliefs have greater influence.

An insight emerged from examining the connection between priors and regularization. We demonstrated that Bayesian inference with a Gaussian prior naturally leads to the regularized objective function:

$$L(\mathbf{w}) = \|\mathbf{t} - \mathbf{\Phi}\mathbf{w}\|^2 + \lambda\|\mathbf{w}\|^2, \tag{5.86}$$

where $\lambda = \sigma^2/\eta^2$ represents the ratio of measurement variance to prior variance. This connection reveals that what appears as ad hoc regularization in machine learning emerges naturally from principled Bayesian reasoning. The regularization parameter is not arbitrary but reflects the fundamental balance between trusting our measurements versus trusting our prior knowledge about reasonable parameter values.

This insight extends far beyond linear regression, providing theoretical foundations for neural network weight decay, sparsity constraints in image reconstruction, and smoothness penalties in function approximation. The Bayesian perspective offers not just mathematical unification but principled guidance for selecting regularization strategies based on domain knowledge and expected solution structure.

The posterior predictive distribution provides the framework's most practical advantage:

$$p(y_*|\mathbf{x}_*, \mathcal{D}) = \mathcal{N}(y_*|\boldsymbol{\phi}(\mathbf{x}_*)^T\mathbf{m}_N, \sigma^2 + \boldsymbol{\phi}(\mathbf{x}_*)^T\mathbf{S}_N\boldsymbol{\phi}(\mathbf{x}_*)). \tag{5.87}$$

The variance decomposition into aleatoric uncertainty (σ^2, irreducible measurement noise) and epistemic uncertainty ($\boldsymbol{\phi}(\mathbf{x}_*)^T\mathbf{S}_N\boldsymbol{\phi}(\mathbf{x}_*)$, reducible parameter uncertainty) pro-

vides crucial insights for scientific applications. This decomposition explains why prediction bands widen away from observed data, guides where additional observations would be most valuable, and enables proper uncertainty propagation through subsequent analyses.

For astronomical applications, these capabilities prove transformative. Whether studying the M-σ relation between black hole mass and stellar velocity dispersion, investigating the Kennicutt-Schmidt law relating gas density to star formation rate, or analyzing any other linear relationship in astronomical data, the Bayesian framework provides:

1. **Principled uncertainty quantification** that distinguishes between measurement noise and model uncertainty

2. **Natural incorporation of prior knowledge** from previous studies, theoretical constraints, or physical intuition

3. **Automatic regularization** that prevents overfitting without requiring ad hoc parameter tuning

4. **Complete predictive distributions** that enable robust error propagation and scientific inference

The elegance of this framework lies in its unification of seemingly disparate concepts under a single probabilistic umbrella. Least squares fitting, regularization, cross-validation, and uncertainty quantification all emerge as natural consequences of Bayesian reasoning with appropriate priors. This theoretical coherence provides both mathematical beauty and practical guidance for tackling complex inference problems.

Looking ahead, the principles developed in this chapter extend throughout machine learning and statistical inference. The concepts of conjugate priors, regularization through Bayesian thinking, and uncertainty propagation through predictive distributions will recur as we explore more sophisticated methods. Chapter 6 will extend our framework to handle uncertainties in both dependent and independent variables—a critical challenge in astronomical measurements where input uncertainties are often substantial and cannot be ignored.

The Bayesian perspective fundamentally changes how we think about model fitting and prediction. Rather than seeking the single "best" model, we characterize the range of models consistent with our data and prior knowledge. This shift from point estimates to probability distributions provides a more complete and honest representation of our knowledge and its limitations—essential qualities for robust scientific inference in astronomy where

conclusions must be drawn despite inevitable uncertainties in observations and models.

The mathematical tools we have developed—from conjugate priors to predictive distributions—provide both theoretical insight and practical capability. They enable astronomers to extract reliable scientific conclusions from noisy, incomplete data while maintaining rigorous quantification of uncertainties. In an era of increasingly large and complex astronomical datasets, these capabilities prove essential for transforming observations into understanding.

5.9   Appendix: Marginal Distribution of Multivariate Gaussian

Earlier in this chapter, we asserted that the posterior predictive distribution is Gaussian because integrating a product of Gaussians yields another Gaussian. This fundamental property follows from a more general theorem about multivariate Gaussian distributions: any marginal distribution obtained by integrating out some variables from a joint multivariate Gaussian is itself Gaussian.

This result underpins many key calculations in Bayesian inference and deserves careful justification. We will prove that for a joint multivariate Gaussian distribution over partitioned variables, the marginal distribution of any subset maintains the Gaussian form with analytically computable parameters.

Statement of the Result   Consider a joint multivariate Gaussian distribution over partitioned variables:

$$\begin{bmatrix} \mathbf{x}_1 \\ \mathbf{x}_2 \end{bmatrix} \sim \mathcal{N}\left(\begin{bmatrix} \boldsymbol{\mu}_1 \\ \boldsymbol{\mu}_2 \end{bmatrix}, \begin{bmatrix} \boldsymbol{\Sigma}_{11} & \boldsymbol{\Sigma}_{12} \\ \boldsymbol{\Sigma}_{21} & \boldsymbol{\Sigma}_{22} \end{bmatrix} \right), \tag{5.88}$$

where $\mathbf{x}_1 \in \mathbb{R}^m$, $\mathbf{x}_2 \in \mathbb{R}^n$, and the covariance matrix is partitioned accordingly.

We will prove that the marginal distribution of $\mathbf{x}_1$ is:

$$\mathbf{x}_1 \sim \mathcal{N}\left(\boldsymbol{\mu}_1, \boldsymbol{\Sigma}_{11} \right). \tag{5.89}$$

Proof   The joint probability density function is:

$$p(\mathbf{x}_1, \mathbf{x}_2) = \frac{1}{(2\pi)^{(m+n)/2}\sqrt{\det(\boldsymbol{\Sigma})}} \exp\left(-\frac{1}{2} \begin{bmatrix} \mathbf{x}_1 - \boldsymbol{\mu}_1 \\ \mathbf{x}_2 - \boldsymbol{\mu}_2 \end{bmatrix}^T \boldsymbol{\Sigma}^{-1} \begin{bmatrix} \mathbf{x}_1 - \boldsymbol{\mu}_1 \\ \mathbf{x}_2 - \boldsymbol{\mu}_2 \end{bmatrix} \right). \tag{5.90}$$

To find the marginal distribution $p(\mathbf{x}_1)$, we integrate over $\mathbf{x}_2$:

$$p(\mathbf{x}_1) = \int_{\mathbb{R}^n} p(\mathbf{x}_1, \mathbf{x}_2) \, d\mathbf{x}_2. \tag{5.91}$$

Let us define $\mathbf{u} = \mathbf{x}_1 - \boldsymbol{\mu}_1$ and $\mathbf{v} = \mathbf{x}_2 - \boldsymbol{\mu}_2$ for simplicity. The precision matrix $\boldsymbol{\Sigma}^{-1}$ can be partitioned as:

$$\boldsymbol{\Sigma}^{-1} = \begin{bmatrix} \mathbf{P} & \mathbf{Q} \\ \mathbf{R} & \mathbf{S} \end{bmatrix}, \tag{5.92}$$

where the dimensions match the partitioning of $\boldsymbol{\Sigma}$.

The quadratic form in the exponent becomes:

$$\begin{bmatrix} \mathbf{u} \\ \mathbf{v} \end{bmatrix}^T \begin{bmatrix} \mathbf{P} & \mathbf{Q} \\ \mathbf{R} & \mathbf{S} \end{bmatrix} \begin{bmatrix} \mathbf{u} \\ \mathbf{v} \end{bmatrix} = \mathbf{u}^T \mathbf{P} \mathbf{u} + \mathbf{u}^T \mathbf{Q} \mathbf{v} + \mathbf{v}^T \mathbf{R} \mathbf{u} + \mathbf{v}^T \mathbf{S} \mathbf{v}. \tag{5.93}$$

Since $\boldsymbol{\Sigma}^{-1}$ is symmetric (as the inverse of a symmetric matrix), we have $\mathbf{Q} = \mathbf{R}^T$, so:

$$\mathbf{u}^T \mathbf{Q} \mathbf{v} + \mathbf{v}^T \mathbf{R} \mathbf{u} = 2\mathbf{v}^T \mathbf{R} \mathbf{u}. \tag{5.94}$$

The integral becomes:

$$p(\mathbf{x}_1) = \frac{1}{(2\pi)^{(m+n)/2}\sqrt{\det(\boldsymbol{\Sigma})}} \exp\left(-\frac{1}{2}\mathbf{u}^T \mathbf{P} \mathbf{u}\right) \int_{\mathbb{R}^n} \exp\left(-\frac{1}{2}[\mathbf{v}^T \mathbf{S} \mathbf{v} + 2\mathbf{v}^T \mathbf{R} \mathbf{u}]\right) d\mathbf{v}. \tag{5.95}$$

To evaluate the integral, we complete the square in $\mathbf{v}$. Define $\mathbf{b} = \mathbf{R}\mathbf{u}$, so the quadratic form in $\mathbf{v}$ is:

$$\frac{1}{2}\mathbf{v}^T \mathbf{S} \mathbf{v} + \mathbf{b}^T \mathbf{v} = \frac{1}{2}(\mathbf{v} + \mathbf{S}^{-1}\mathbf{b})^T \mathbf{S}(\mathbf{v} + \mathbf{S}^{-1}\mathbf{b}) - \frac{1}{2}\mathbf{b}^T \mathbf{S}^{-1} \mathbf{b}. \tag{5.96}$$

The integral over the completed square is a standard Gaussian integral:

$$\int_{\mathbb{R}^n} \exp\left(-\frac{1}{2}(\mathbf{v} + \mathbf{S}^{-1}\mathbf{b})^T \mathbf{S}(\mathbf{v} + \mathbf{S}^{-1}\mathbf{b})\right) d\mathbf{v} = (2\pi)^{n/2}[\det(\mathbf{S})]^{-1/2}. \tag{5.97}$$

Therefore:

$$p(\mathbf{x}_1) = \frac{(2\pi)^{n/2}}{(2\pi)^{(m+n)/2}\sqrt{\det(\boldsymbol{\Sigma})}} \frac{1}{\sqrt{\det(\mathbf{S})}} \exp\left(-\frac{1}{2}\mathbf{u}^T\mathbf{P}\mathbf{u} + \frac{1}{2}\mathbf{b}^T\mathbf{S}^{-1}\mathbf{b}\right) \tag{5.98}$$

$$= \frac{1}{(2\pi)^{m/2}} \frac{\sqrt{\det(\mathbf{S})}}{\sqrt{\det(\boldsymbol{\Sigma})}} \exp\left(-\frac{1}{2}\mathbf{u}^T[\mathbf{P} - \mathbf{Q}\mathbf{S}^{-1}\mathbf{R}]\mathbf{u}\right). \tag{5.99}$$

From the block matrix inversion formula (Schur complement), we know that:

$$\boldsymbol{\Sigma}_{11} = (\mathbf{P} - \mathbf{Q}\mathbf{S}^{-1}\mathbf{R})^{-1}. \tag{5.100}$$

The determinant relationship for block matrices gives us:

$$\frac{\sqrt{\det(\mathbf{S})}}{\sqrt{\det(\boldsymbol{\Sigma})}} = \frac{1}{\sqrt{\det(\boldsymbol{\Sigma}_{11})}}. \tag{5.101}$$

Substituting these relationships:

$$p(\mathbf{x}_1) = \frac{1}{(2\pi)^{m/2}\sqrt{\det(\boldsymbol{\Sigma}_{11})}} \exp\left(-\frac{1}{2}(\mathbf{x}_1 - \boldsymbol{\mu}_1)^T\boldsymbol{\Sigma}_{11}^{-1}(\mathbf{x}_1 - \boldsymbol{\mu}_1)\right). \tag{5.102}$$

This is precisely the probability density function of $\mathcal{N}(\boldsymbol{\mu}_1, \boldsymbol{\Sigma}_{11})$, completing our proof.

This result has important implications for Bayesian calculations. When we integrate over parameter uncertainty to obtain predictions, the resulting distribution maintains the Gaussian form with analytically computable parameters. The marginal likelihood (evidence) can be computed analytically by integrating over parameter priors, enabling principled model comparison. Complex Bayesian models with multiple levels of uncertainty can often be analyzed analytically by successive marginalization.

The preservation of Gaussian form under marginalization, combined with conjugacy properties, makes many Bayesian calculations tractable that would otherwise require complex numerical integration. This mathematical elegance underlies much of the analytical power of Bayesian linear regression and extends to numerous other problems in statistical inference.

Further Readings: The development of Bayesian linear regression builds upon centuries of advances in probability theory, with early contributions from Laplace [1820] who provided

systematic development of Bayesian methods within a mathematical framework that remains influential today. For readers interested in practical applications of Bayesian methods to regression problems, Zellner [1971] offers treatment focused on econometric applications, while Lindley [1965] provides mathematical foundations including conjugate priors. The concept of conjugate priors, essential for analytical tractability in Bayesian regression, was developed by Raiffa and Schlaifer [1961], with DeGroot [1970] providing treatment of their properties and conditions for existence. The multivariate Gaussian theory underlying Bayesian linear regression is developed in Anderson [1958]. Connections between Bayesian inference and regularization emerged through the work of Tikhonov [1963] on regularization methods and Hoerl and Kennard [1970] who developed ridge regression with discussion of its Bayesian foundations. MacKay [1992] demonstrated how to set regularization parameters using Bayesian evidence, connecting machine learning and Bayesian approaches within a unified framework. For readers interested in model selection and comparison, Kass and Raftery [1995] provide a review of Bayes factors and marginal likelihood computation methods that enable principled model comparison within the Bayesian framework.

Chapter 6

Linear Regression with Input Uncertainties

In the previous two chapters, we developed a framework for linear regression through the lens of Bayesian inference. We demonstrated how this approach allows us to fit linear relationships to data while properly accounting for uncertainties in our dependent variable ($\mathbf{y}$). Through maximum likelihood estimation and Bayesian analysis, we built a foundation for parameter estimation and uncertainty quantification. The Bayesian treatment provided us with a principled way to propagate these uncertainties into our parameter estimates and predictive distributions.

In many real-world machine learning applications, focusing solely on $\mathbf{y}$ uncertainty is often justified. The uncertainty in the independent variables ($\mathbf{x}$) is frequently negligible or challenging to quantify meaningfully. Consider image classification tasks: the input images in real-life applications typically have very high signal-to-noise ratios (SNR) — defined as the ratio between the measured signal and its uncertainty — often exceeding 100 or even 1000. In such cases, the input uncertainty plays a minimal role in our inference.

However, astronomical applications present a different challenge: both our independent ($\mathbf{x}$) and dependent ($\mathbf{y}$) variables often carry substantial uncertainties. Consider astronomical images and spectra, where SNR values frequently hover around 10, and sometimes even approach unity. This means the uncertainty in our input measurements can be as large as 10% or even 100% of the signal itself. This challenge extends beyond raw observational data to derived quantities. In the M-σ relation we've discussed extensively, both the black

hole mass estimates and stellar velocity dispersion measurements carry significant uncertainties, often around 10% of their values relative to the full dynamic range of observations.

As we will demonstrate in this chapter, ignoring input uncertainties — as we have done so far — leads to a systematic effect known as attenuation bias. This phenomenon appears frequently in machine learning applications, extending well beyond linear regression. However, linear regression provides a useful framework for understanding this bias, as it offers both analytical tractability and clear geometric interpretation.
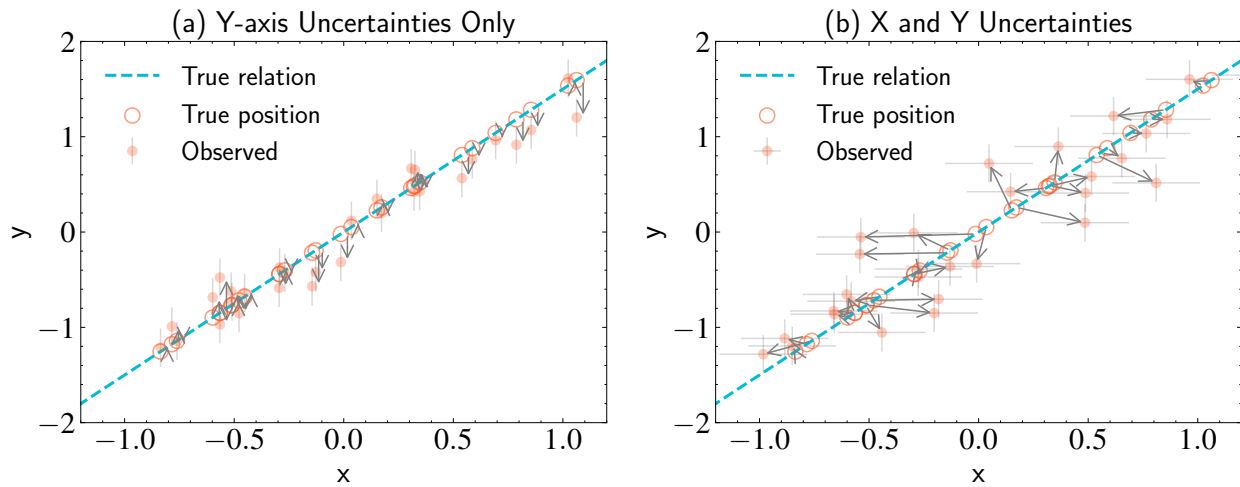
Figure 6.1: Illustration of how measurement uncertainties affect regression. Both panels show the same underlying relationship (dashed blue line) with true positions (hollow circles) and their observed values (solid orange points) connected by gray arrows. Panel (a) shows the case with uncertainties only in the dependent variable (y), where the vertical scatter of observed points around their true positions does not systematically bias our inference. Panel (b) shows what happens when both variables have uncertainties: observed points now scatter in both directions from their true positions, artificially inflating the apparent range of our independent variable (x). This horizontal scatter systematically weakens any relationship we try to measure, leading to attenuation bias. The error bars in both panels represent the measurement uncertainties (σ_y in panel a, σ_x and σ_y in panel b), illustrating how the observed points deviate from their true positions due to measurement noise.

Attenuation bias causes our parameter estimates to be systematically biased toward zero when we ignore input uncertainties. This occurs because treating uncertain x-values as exact effectively introduces additional noise into our predictor variables, artificially weakening (or "attenuating") the relationships we're trying to measure. The magnitude of this bias scales with the ratio of input uncertainty to the true variation in our independent variables.

To understand how input uncertainties affect our inference, we'll proceed in several steps. First, we'll build intuition through concrete astronomical examples, showing how

measurement uncertainties in **x** change the nature of our inference problem. Then, we'll develop a mathematical framework that quantifies this effect precisely. This will bridge statistical rigor with practical astronomical challenges, demonstrating why even small input uncertainties matter for high-precision astronomical measurements.

A key insight we'll explore is the hierarchical perspective: treating the true values of our independent variables as hidden (or latent) variables to be inferred alongside the model parameters. This approach allows us to simultaneously estimate both the underlying relationship and the true positions of our data points, despite the measurement uncertainties that obscure them. This hierarchical approach not only solves the problem at hand but connects to broader themes in modern astronomical data analysis.

Finally, we'll introduce Deming regression as a solution that extends beyond ordinary least squares. This technique properly accounts for uncertainties in both variables, allowing us to recover the true relationships that would otherwise be systematically underestimated. While our focus will be on linear regression, the insights about handling input uncertainties apply broadly across statistical inference in astronomy.

6.1   Attenuation Bias

Let's begin by understanding why input uncertainties matter through a concrete example: the M-σ relation between black hole mass and stellar velocity dispersion. This relationship not only illustrates the challenges of input uncertainties but will serve as our running example throughout this chapter.

Suppose there exists a linear relationship between the logarithm of black hole mass and the logarithm of velocity dispersion. If we could measure velocity dispersion perfectly but had uncertainties in our black hole mass measurements, our data points would scatter vertically around the true relationship. As we demonstrated in previous chapters, when we properly account for these **y**-axis uncertainties through maximum likelihood or Bayesian methods, we can recover the true relationship without bias.

But what happens when we also have uncertainties in our velocity dispersion measurements? Each data point now scatters both horizontally and vertically from its true position. This horizontal scatter has a crucial impact – when we have **x**-axis uncertainties, the dynamic range of our independent variable is artificially inflated. The horizontal scatter makes our distribution of points wider in the **x**-direction without a corresponding increase in the

y-direction. Consider the extreme case: as measurement uncertainties in **x** approach infinity, every **x**-measurement becomes pure noise, completely uncorrelated with its true value. In this limit, any relationship in our data would be completely obscured, and our fitted line would become horizontal – effectively finding no relationship at all.
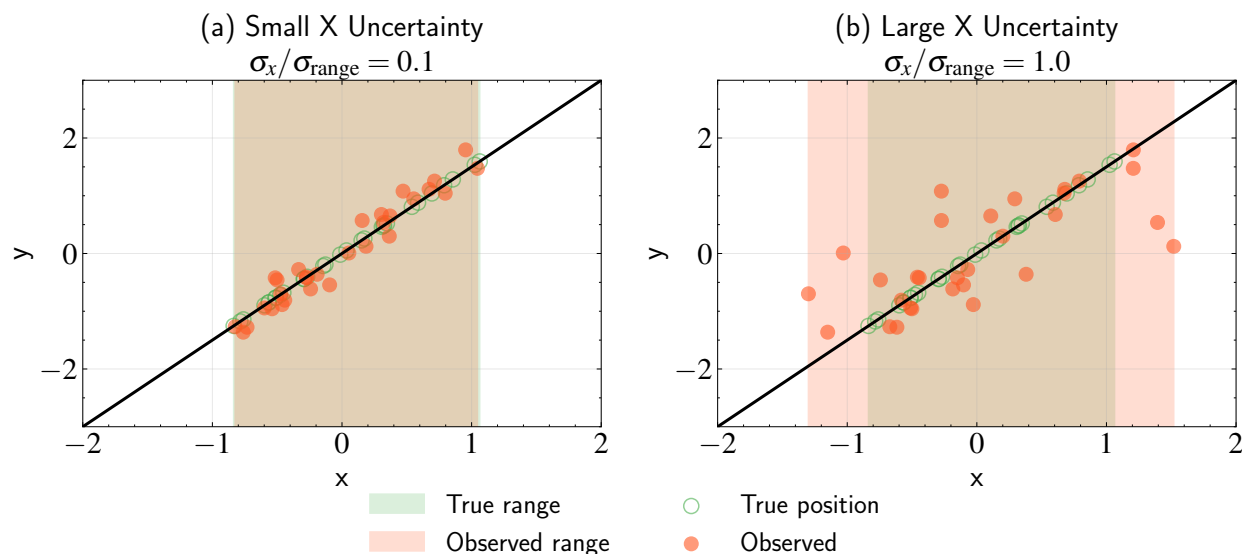
Figure 6.2: Demonstration of how measurement uncertainties affect the apparent dynamic range of our data. Both panels show the same underlying relationship (solid black line) and true data points (hollow green circles) scattered by measurement uncertainties to their observed positions (solid orange circles). The green and orange shaded regions show the true and observed dynamic ranges respectively. Panel (a) shows the case where measurement uncertainty is small compared to the intrinsic spread in x-values ($\sigma_x/\sigma_{\mathrm{range}} = 0.1$), resulting in a modest increase in the observed range. Panel (b) demonstrates the case where measurement uncertainty equals the intrinsic spread ($\sigma_x/\sigma_{\mathrm{range}} = 1.0$), causing an inflation of the observed dynamic range. This artificial expansion of the x-range without a corresponding increase in the y-range directly leads to attenuation bias in our parameter estimates, as the observed distribution appears more stretched horizontally than it truly is.

Why doesn't vertical scatter (**y**-axis uncertainty) cause the same problem? The key lies in the asymmetric roles of **x** and **y** in regression. When fitting a line, we're essentially asking, "Given an **x** value, what **y** value do we expect?" Uncertainty in **y** simply adds noise to this prediction, which averages out with enough data. But uncertainty in **x** changes the very question we're asking – we're now attempting to predict **y** based on a noisy version of **x**, which systematically weakens any relationship we find.

This weakening of relationships due to input uncertainties is known as attenuation bias or regression dilution. The effect is to systematically underestimate the strength of relationships (i.e., slopes in linear regression). Importantly, this bias doesn't diminish with

more data – even with infinite sample size, the bias persists as long as there are measurement uncertainties in our independent variables.

To illustrate this effect mathematically, consider a simple linear relationship with a slope of β, where both variables have measurement uncertainties:

$$\mathbf{x}_{\text{obs}} = \mathbf{x}_{\text{true}} + \delta_x \tag{6.1}$$

$$\mathbf{y}_{\text{obs}} = \mathbf{y}_{\text{true}} + \delta_y = \beta\mathbf{x}_{\text{true}} + \delta_y \tag{6.2}$$

As we'll show in the next section, the standard linear regression estimator will recover a slope that is attenuated by a factor λ:

$$\mathbb{E}[\hat{\beta}] = \beta \cdot \lambda \tag{6.3}$$

where $\lambda < 1$. This means our estimated slope systematically underestimates the true slope. This bias isn't a quirk of specific datasets – it's a direct mathematical consequence of input uncertainties that affects all regression analyses where independent variables have measurement error.

6.2   Mathematical Framework

Our M-σ thought experiment revealed that input uncertainties can systematically weaken the relationships we observe. To make this precise, let's develop a mathematical framework that captures both the true relationship we're trying to measure and how measurement uncertainties affect our observations.

For clarity, we'll start with the simplest possible case: univariate linear regression where both variables have homogeneous measurement uncertainties. While this might seem restrictive, it will allow us to derive analytical results that provide insight into the nature of attenuation bias. Later, we can extend these insights to more complex scenarios with multiple variables and heterogeneous uncertainties.

Let's start with the true underlying relationship we're trying to measure:

$$\mathbf{y}_{\text{true}} = \beta\mathbf{x}_{\text{true}}, \tag{6.4}$$

where β represents the true slope. For our M-σ example, $\mathbf{x}_{\text{true}}$ would be the logarithm of the

true velocity dispersion, and $\mathbf{y}_{\text{true}}$ would be the logarithm of the true black hole mass.

In real observations, we never measure these true values directly. Instead, our measurements contain uncertainties:

$$\mathbf{x}_{\text{obs}} = \mathbf{x}_{\text{true}} + \delta_x \tag{6.5}$$

$$\mathbf{y}_{\text{obs}} = \mathbf{y}_{\text{true}} + \delta_y = \beta\mathbf{x}_{\text{true}} + \delta_y \tag{6.6}$$

To analyze this mathematically, we need to make some assumptions about these uncertainties.

1. The uncertainties are unbiased:

$$\mathbb{E}[\delta_x] = 0 \tag{6.7}$$

$$\mathbb{E}[\delta_y] = 0 \tag{6.8}$$

This means our measurements don't systematically over- or under-estimate the true values. In astronomy, most measurement procedures are designed specifically to ensure this property - we carefully calibrate our instruments and correct for known systematic effects.

2. The uncertainties have homogeneous variances:

$$\text{Var}(\delta_x) = \sigma_x^2 \tag{6.9}$$

$$\text{Var}(\delta_y) = \sigma_y^2 \tag{6.10}$$

For simplicity, we'll assume all measurements have the same uncertainty (homogeneous noise).

3. The uncertainties are independent of the true values and of each other:

- δ_x doesn't depend on $\mathbf{x}_{\text{true}}$ or $\mathbf{y}_{\text{true}}$

- δ_y doesn't depend on $\mathbf{x}_{\text{true}}$ or $\mathbf{y}_{\text{true}}$

- δ_x and δ_y don't depend on each other

This is often approximately true in astronomy. For instance, photon noise in different measurements is typically independent, and instrumental effects usually don't depend

strongly on the signal being measured.

These assumptions capture the essential features of many astronomical measurements and allow us to derive analytical results that provide insight into how measurement uncertainties affect our inference.

One additional simplification that will prove useful is to work with centered variables - that is, variables that have been shifted to have zero mean. We can redefine our observed variables by subtracting their means:

$$\mathbf{x}_{\text{obs}} \leftarrow \mathbf{x}_{\text{obs}} - E[\mathbf{x}_{\text{obs}}] \tag{6.11}$$

$$\mathbf{y}_{\text{obs}} \leftarrow \mathbf{y}_{\text{obs}} - E[\mathbf{y}_{\text{obs}}] \tag{6.12}$$

Working with centered variables not only simplifies our mathematics but also helps us focus on what we're really interested in: how changes in $\mathbf{x}$ relate to changes in $\mathbf{y}$. This will become particularly useful when we examine how measurement uncertainties affect our parameter estimates.

6.3 Maximum Likelihood with Input Uncertainties

Having established our framework, let's connect it to our previous work on maximum likelihood estimation. In Chapter 4, we showed that for homogeneous noise, the maximum likelihood estimator takes the matrix form:

$$\mathbf{w}_{\text{ML}} = (\mathbf{\Phi}^T \mathbf{\Phi})^{-1} \mathbf{\Phi}^T \mathbf{y}_{\text{obs}} \tag{6.13}$$

Our current case - simple linear regression with one input variable - is just a special case of this general formula. Since we're working with centered variables, we only need to estimate the slope parameter (the bias term becomes zero). The design matrix $\mathbf{\Phi}$ becomes simply a vector of our observed x values:

$$\mathbf{\Phi} = \begin{bmatrix} x_{\text{obs},1} & x_{\text{obs},2} & \cdots & x_{\text{obs},N} \end{bmatrix}^T \tag{6.14}$$

Let's work through the matrix multiplication step by step:

$$\mathbf{\Phi}^T\mathbf{\Phi} = \begin{bmatrix} x_{\text{obs},1} & x_{\text{obs},2} & \cdots & x_{\text{obs},N} \end{bmatrix} \begin{bmatrix} x_{\text{obs},1} \\ x_{\text{obs},2} \\ \vdots \\ x_{\text{obs},N} \end{bmatrix} = \sum_{i=1}^{N} x_{\text{obs},i}^2 \qquad (6.15)$$

$$\mathbf{\Phi}^T\mathbf{y}_{\text{obs}} = \begin{bmatrix} x_{\text{obs},1} & x_{\text{obs},2} & \cdots & x_{\text{obs},N} \end{bmatrix} \begin{bmatrix} y_{\text{obs},1} \\ y_{\text{obs},2} \\ \vdots \\ y_{\text{obs},N} \end{bmatrix} = \sum_{i=1}^{N} x_{\text{obs},i} y_{\text{obs},i} \qquad (6.16)$$

Therefore, our matrix equation reduces to the scalar form for the slope estimate:

$$\hat{\beta} = \frac{\sum_{i=1}^{N} x_{\text{obs},i} y_{\text{obs},i}}{\sum_{i=1}^{N} x_{\text{obs},i}^2} \qquad (6.17)$$

Our maximum likelihood solution can be written in terms of statistical quantities that capture the essential relationship between our measurements:

$$\hat{\beta} = \frac{\text{Cov}(\mathbf{x}_{\text{obs}}, \mathbf{y}_{\text{obs}})}{\text{Var}(\mathbf{x}_{\text{obs}})} \qquad (6.18)$$

This form provides insight into what a slope actually means. The numerator (covariance) measures how much $\mathbf{y}$ changes as $\mathbf{x}$ varies across its range - in other words, the total change in $\mathbf{y}$ that corresponds to the full spread of $\mathbf{x}$ values. When we divide this by the denominator (variance), which represents the total spread of $\mathbf{x}$ values, we get the change in $\mathbf{y}$ per unit change in $\mathbf{x}$ - exactly what we mean by slope!

However, note that while this interpretation is accurate when $\text{Var}(\mathbf{x}_{\text{obs}})$ represents the true variance in $\mathbf{x}$, it becomes problematic when $\mathbf{x}_{\text{obs}}$ contains measurement uncertainties. In this case, the variance in the denominator becomes inflated by the uncertainty, making it larger than it should be and consequently diluting (attenuating) our slope estimate.

To understand exactly how these uncertainties quantitatively affect our parameter estimates, let's analyze each component separately. We'll start with the numerator - the

covariance between our observed quantities. Using our expressions for centered variables:

$$\text{Cov}(\mathbf{x}_{\text{obs}}, \mathbf{y}_{\text{obs}}) = \text{Cov}(\mathbf{x}_{\text{true}} + \delta_x, \beta\mathbf{x}_{\text{true}} + \delta_y) \tag{6.19}$$

$$= \beta\,\text{Cov}(\mathbf{x}_{\text{true}} + \delta_x, \mathbf{x}_{\text{true}}) + \text{Cov}(\mathbf{x}_{\text{true}} + \delta_x, \delta_y) \tag{6.20}$$

$$= \beta[\text{Cov}(\mathbf{x}_{\text{true}}, \mathbf{x}_{\text{true}}) + \text{Cov}(\delta_x, \mathbf{x}_{\text{true}})] + [\text{Cov}(\mathbf{x}_{\text{true}}, \delta_y) + \text{Cov}(\delta_x, \delta_y)] \tag{6.21}$$

$$= \beta[\text{Var}(\mathbf{x}_{\text{true}}) + 0] + [0 + 0] \tag{6.22}$$

$$= \beta\,\text{Var}(\mathbf{x}_{\text{true}}) \tag{6.23}$$

The expansion in the third line reveals four distinct contributions to the covariance:

- $\text{Cov}(\mathbf{x}_{\text{true}}, \mathbf{x}_{\text{true}})$: The intrinsic spread in true values (this is $\text{Var}(\mathbf{x}_{\text{true}})$)

- $\text{Cov}(\delta_x, \mathbf{x}_{\text{true}})$: The relationship between measurement errors and true values

- $\text{Cov}(\mathbf{x}_{\text{true}}, \delta_y)$: How y-errors relate to true x values

- $\text{Cov}(\delta_x, \delta_y)$: The relationship between x and y measurement errors

Our independence assumptions tell us that the last three terms are zero - measurement errors don't depend on true values or on each other. Therefore:

$$\text{Cov}(\mathbf{x}_{\text{obs}}, \mathbf{y}_{\text{obs}}) = \beta\,\text{Var}(\mathbf{x}_{\text{true}}) \equiv \beta\sigma_{\text{range}}^2 \tag{6.24}$$

Here, σ_{range}^2 represents the intrinsic variance of the true velocity dispersions in our M-σ example - the actual spread of galaxy properties in our dataset.

For the denominator, we're looking at the variance of our observed x values:

$$\text{Var}(\mathbf{x}_{\text{obs}}) = \text{Var}(\mathbf{x}_{\text{true}} + \delta_x) \tag{6.25}$$

$$= \text{Var}(\mathbf{x}_{\text{true}}) + \text{Var}(\delta_x) \tag{6.26}$$

$$= \sigma_{\text{range}}^2 + \sigma_x^2 \tag{6.27}$$

The second line follows directly from our assumption that $\mathbf{x}_{\text{true}}$ and δ_x are independent - when we add independent random variables, their variances add.

To understand whether our estimator is systematically biased, we need to examine its expected value - what value it will converge to on average. Combining our results for the

numerator and denominator:

$$\mathbb{E}[\hat{\beta}] = \beta \frac{\sigma_{\text{range}}^2}{\sigma_{\text{range}}^2 + \sigma_x^2} = \beta \frac{1}{1 + (\sigma_x/\sigma_{\text{range}})^2} \tag{6.28}$$

This is our key result. Our estimate $\hat{\beta}$ is related to the true slope β through an attenuation factor:

$$\lambda \equiv \frac{1}{1 + (\sigma_x/\sigma_{\text{range}})^2} \tag{6.29}$$
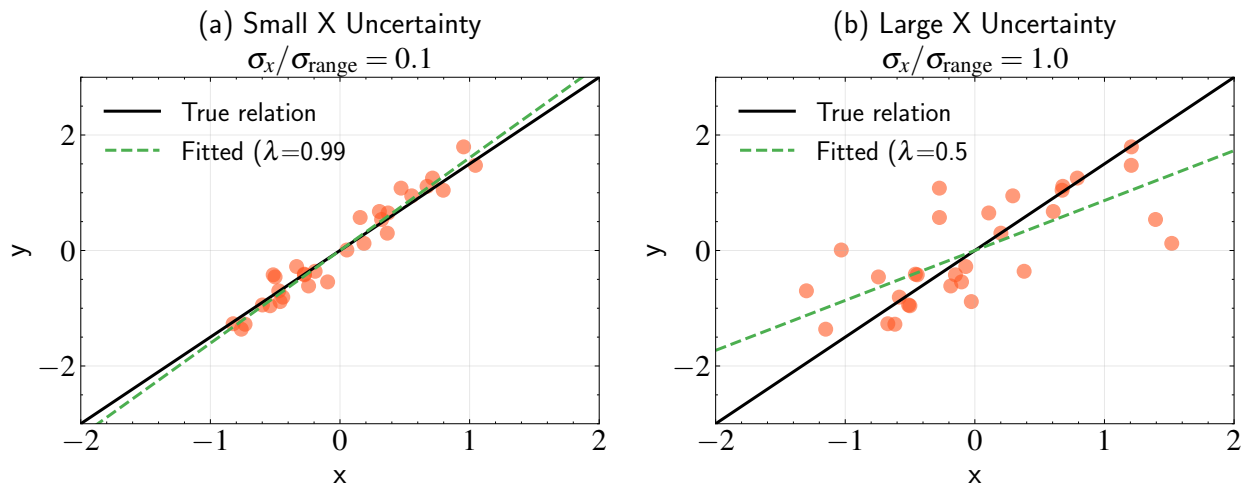
Figure 6.3: Demonstration of attenuation bias in parameter estimation. Both panels show the same underlying relationship (solid black line) with observed data points (orange circles) and their fitted relationships (dashed green lines). Panel (a) shows the case of small measurement uncertainty ($\sigma_x/\sigma_{\text{range}} = 0.1$), where the fitted slope is only slightly attenuated ($\lambda \approx 0.99$). Panel (b) shows the case of large measurement uncertainty ($\sigma_x/\sigma_{\text{range}} = 1.0$), where the attenuation becomes severe ($\lambda \approx 0.50$). The attenuation factor λ, shown in the legend of each panel, quantifies how much the observed slope underestimates the true slope. This demonstrates that when measurement uncertainties become comparable to the intrinsic spread in our independent variable, our ability to recover the true relationship is compromised.

This attenuation factor reveals how measurement uncertainties in the input variable affect our inference. Note that σ_x here refers specifically to uncertainty in our input measurements - this explains why in Chapters 4 and 5, where we assumed $\mathbf{x}$ was measured perfectly, we were able to recover the true slope. More generally, λ is always less than one unless we have perfect measurements ($\sigma_x = 0$). When our measurements are perfect, $\lambda = 1$ and we recover the true slope exactly. But as our measurement uncertainty increases, λ decreases, systematically weakening our estimated relationship.

In the extreme case where measurement uncertainties become infinitely large ($\sigma_x \to \infty$), λ approaches zero, completely obscuring any relationship in our data. This makes intuitive sense because when our measurements are dominated by noise, the observed values become essentially random numbers that bear no relationship to the true underlying values, making it impossible to detect any real correlation in the data.

The mathematical form of λ shows that what matters is not the absolute size of our measurement errors, but rather how large they are compared to the true spread in our data - the ratio $\sigma_x/\sigma_{\text{range}}$. This makes intuitive sense: when our measurement uncertainty σ_x becomes comparable to the true range σ_{range}, we're effectively doubling the apparent spread in our x values without any corresponding increase in y.

In our M-σ example, if the true velocity dispersions span 100 km/s (σ_{range}) and our measurement uncertainty is also 100 km/s (σ_x), then our observed distribution of velocity dispersions appears twice as wide as it truly is. This artificial widening of the x-distribution without a corresponding widening in y naturally leads to a shallower slope - we're literally "diluting" the relationship by spreading out our x values.

Most importantly, since λ depends only on this ratio of measurement uncertainty to true spread, and not on sample size, this bias persists no matter how much data we collect. Even with infinite data, if our measurements have uncertainty, we will systematically underestimate the true relationship. This is different from random errors that can be averaged out with more data - measurement uncertainties in x create a systematic bias that more data cannot resolve.

The independence of λ from y-uncertainties reveals an asymmetry in regression. In our M-σ example, uncertainties in black hole mass measurements (y) can be properly accounted for through weighted fitting, as we saw in Chapters 4 and 5. However, uncertainties in velocity dispersion measurements (x) inevitably bias our slope estimates when using standard regression techniques.

6.4   Practical Implications of Attenuation Bias

Having derived the mathematical form of attenuation bias, let's examine its practical implications for astronomical measurements. Our attenuation factor $\lambda = 1/(1+(\sigma_x/\sigma_{\text{range}})^2)$ provides a precise way to quantify how measurement uncertainties affect our parameter estimates. The key question becomes: what values of $\sigma_x/\sigma_{\text{range}}$ do we typically encounter in
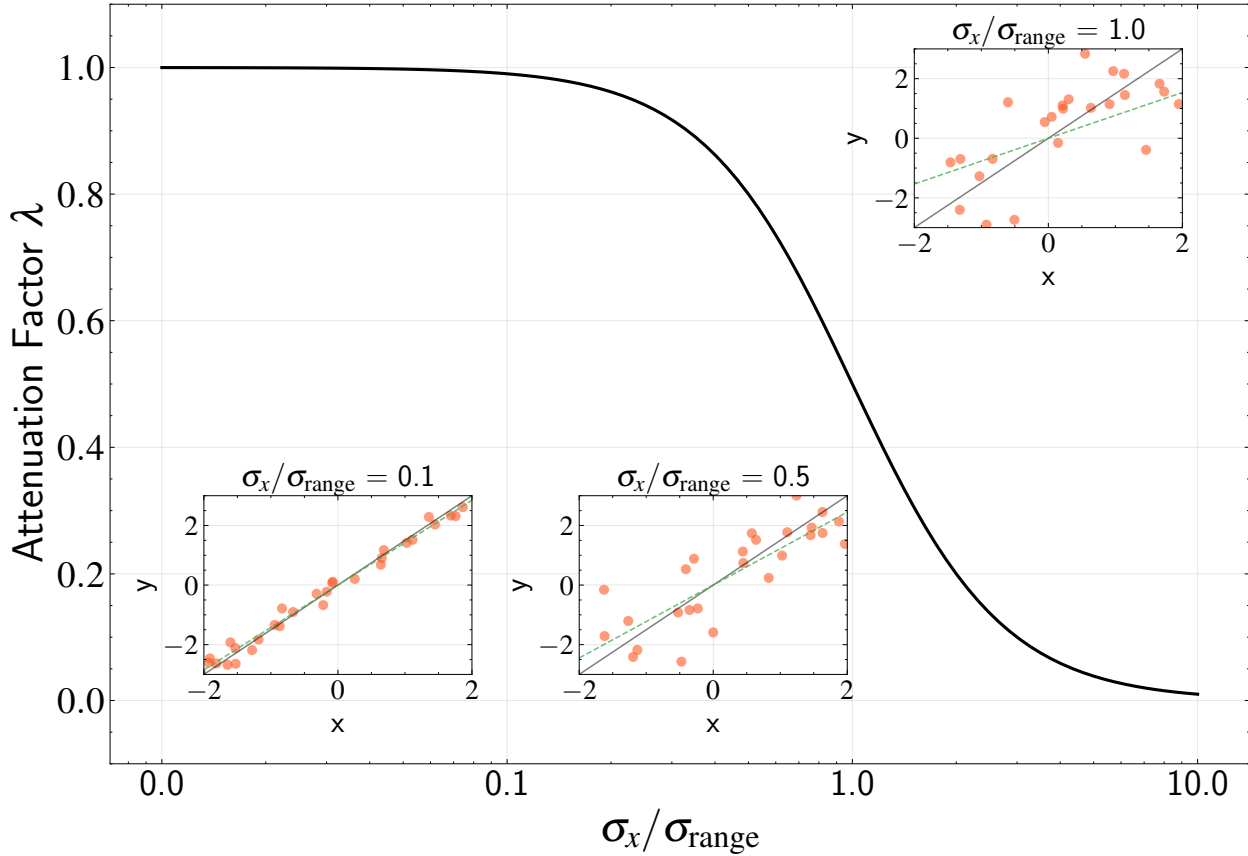
Figure 6.4: Demonstration of how measurement uncertainties affect parameter estimation through attenuation bias. The main plot shows how the attenuation factor λ depends on the ratio of measurement uncertainty to intrinsic spread ($\sigma_x/\sigma_{\mathrm{range}}$). The solid black line shows the theoretical prediction $\lambda = 1/(1 + (\sigma_x/\sigma_{\mathrm{range}})^2)$. Three inset panels demonstrate the effect for different uncertainty ratios: small ($\sigma_x/\sigma_{\mathrm{range}} = 0.1$), moderate ($\sigma_x/\sigma_{\mathrm{range}} = 0.5$), and large ($\sigma_x/\sigma_{\mathrm{range}} = 1.0$). In each inset, the solid black line shows the true relationship, orange points show observed data (with both x and y uncertainties), and the dashed green line shows the attenuated relationship recovered from the data. This illustrates how measurement uncertainties comparable to or larger than the intrinsic spread lead to systematically shallower slopes in our parameter estimates.

astronomy, and how much bias do they introduce?

Returning to our M-σ example, suppose we have velocity dispersion measurements with 10% uncertainty relative to the full range of velocities in our sample. This corresponds to $\sigma_x/\sigma_{\mathrm{range}} = 0.1$, yielding $\lambda = 0.99$ - a 1% bias in our slope estimate. While this might seem small, this 1% bias can be quite important for many astronomical applications. Modern astronomy often operates in a regime where our individual measurements have uncertainties around 10%, but we aim to leverage large statistical samples to achieve percent-level precision

in our final inference.

Consider cosmological studies: while photometric redshift measurements for individual galaxies might have 10% uncertainties, we aim to constrain cosmological parameters like the Hubble constant or dark energy equation of state to percent-level precision. Similarly, in stellar population studies, while individual stellar age measurements might be uncertain at the gigayear level, we hope to determine the star formation history of galaxies with much higher precision through statistical analysis of large samples. Even a 1% systematic bias can impact these precision measurements, potentially affecting our model inference.

This challenge appears consistently across many astronomical measurements:

Stellar Ages   Except for the select few stars with precise asteroseismic measurements, typical age uncertainties are around 1 Gyr - approximately 10% of the Hubble time. This places our measurements in the regime where attenuation bias becomes significant when studying age-dependent relationships.

Chemical Abundances   Even the most careful spectroscopic analyses achieve precisions of 0.05-0.1 dex, which represents about 10% of the full metallicity range we observe in our Galaxy. For studies examining how various properties depend on metallicity, this level of uncertainty can systematically dilute the true relationships.

Black Hole Masses   Measurements of supermassive black hole masses typically carry uncertainties of 0.3-0.5 dex, even when studying relationships that span 3-5 orders of magnitude in mass. The resulting attenuation can significantly impact our understanding of black hole scaling relations.

Stellar and Gas Masses   Measurements of stellar mass and gas mass typically carry uncertainties of 0.1-0.2 dex. When these quantities are used as independent variables in scaling relations (e.g., studying how star formation efficiency depends on gas mass), the resulting attenuation bias can lead to systematic underestimation of the true relationships.

This tension between individual measurement precision and desired statistical inference precision makes attenuation bias a challenge in modern astronomy. It's not just a technical issue - it's a systematic effect that must be understood and accounted for as we push toward ever more precise measurements of physical parameters.

The particularly problematic aspect of attenuation bias is that it cannot be elimi-

nated simply by collecting more data. Unlike random errors that average out with larger samples, this bias is a direct consequence of measurement uncertainties in our independent variables. Even with infinite data, if our velocity dispersion measurements have 10% uncertainty relative to the range, we'll still underestimate the slope of the M-σ relation by 1%. This highlights the need for methods that can properly account for uncertainties in both variables, which we'll explore in the remainder of this chapter.

6.5 Latent Variable Formalism

Our analysis of attenuation bias has revealed a challenge in astronomical measurements: when we ignore uncertainties in our independent variable, we systematically underestimate the strength of relationships in our data. This raises an important question: can we modify our inference framework to properly account for uncertainties in both variables?

The answer lies in extending our maximum likelihood approach from Chapters 4 and 5. Previously, we treated our **x**-measurements as fixed, known quantities and only modeled the probability of observing **y**-values. Now we need to take a step back and consider the joint probability of observing both **x** and **y**, given their true underlying values and our model parameters.

This shift in perspective - from modeling just **y** to modeling both **x** and **y** - is subtle but important. Instead of asking "what is the probability of observing this **y**-value given our **x**-measurement?", we now ask "what is the probability of observing both this **x**-value and this **y**-value given our model?" While this makes our mathematics slightly more complex, it allows us to properly account for the reality of astronomical measurements where both variables carry significant uncertainties.

To address uncertainties in both variables, we need to carefully think about how our measurements relate to the true underlying values. First, recall our model: there exists a true linear relationship between the black hole mass and velocity dispersion of galaxies:

$$\mathbf{y}_{\mathrm{true}} = \beta \mathbf{x}_{\mathrm{true}} \tag{6.30}$$

However, we never observe these true values directly. Instead, our measurements

contain errors:

$$\mathbf{x}_{\text{obs}} = \mathbf{x}_{\text{true}} + \delta_x \tag{6.31}$$

$$\mathbf{y}_{\text{obs}} = \mathbf{y}_{\text{true}} + \delta_y \tag{6.32}$$

$$= \beta\mathbf{x}_{\text{true}} + \delta_y \tag{6.33}$$

These measurement errors follow normal distributions:

$$\delta_x \sim \mathcal{N}(0, \sigma_x^2) \tag{6.34}$$

$$\delta_y \sim \mathcal{N}(0, \sigma_y^2) \tag{6.35}$$

Now comes a crucial insight: while $\mathbf{x}_{\text{obs}}$ and $\mathbf{y}_{\text{obs}}$ are related (that's the whole point of our analysis!), their measurement errors δ_x and δ_y are independent. Think about our M-σ example: the instrumental noise that affects our velocity dispersion measurement has nothing to do with the uncertainties in our black hole mass estimation.

This independence of measurement errors has an important consequence: if we know the true velocity dispersion $\mathbf{x}_{\text{true}}$, then:

1. Any deviation of $\mathbf{x}_{\text{obs}}$ from $\mathbf{x}_{\text{true}}$ is purely due to δ_x

2. Any deviation of $\mathbf{y}_{\text{obs}}$ from $\beta\mathbf{x}_{\text{true}}$ is purely due to δ_y

3. Since δ_x and δ_y are independent, these deviations don't affect each other

Therefore, when we condition on $\mathbf{x}_{\text{true}}$:

- $\mathbf{x}_{\text{obs}}$ follows a normal distribution centered at $\mathbf{x}_{\text{true}}$ with variance σ_x^2

- $\mathbf{y}_{\text{obs}}$ follows a normal distribution centered at $\beta\mathbf{x}_{\text{true}}$ with variance σ_y^2

- These distributions are independent

This allows us to write the joint probability as a product:

$$p(\mathbf{x}_{\text{obs}}, \mathbf{y}_{\text{obs}} \mid \mathbf{x}_{\text{true}}, \beta) = \mathcal{N}(\mathbf{x}_{\text{obs}} \mid \mathbf{x}_{\text{true}}, \sigma_x^2)\,\mathcal{N}(\mathbf{y}_{\text{obs}} \mid \beta\mathbf{x}_{\text{true}}, \sigma_y^2) \tag{6.36}$$

The first term represents how our measured velocity dispersion scatters around its

true value due to instrumental noise, while the second term represents how our measured black hole mass scatters around its predicted value due to measurement uncertainties. While both $\mathbf{x}$ and $\mathbf{y}$ are linked through the M-σ relation, their measurement errors arise from independent sources, allowing us to multiply their probabilities when we condition on the true value.

However, there's a catch in our likelihood formulation: we've conditioned everything on $\mathbf{x}_{\text{true}}$, but we don't actually know these true values! If we did, we'd be back to the simpler case from Chapters 4 and 5 where we only had to deal with $\mathbf{y}$-uncertainties. This might seem like a problem, but the Bayesian framework treats all unknowns - whether they're model parameters or hidden true values - as random variables to be inferred.

In this context, we need to estimate not just our model parameter β, but also the set of true values $\{\mathbf{x}_{\text{true},i}\}$ for each observation. Our full likelihood becomes:

$$\mathcal{L}(\beta, \{\mathbf{x}_{\text{true},i}\}) = \prod_{i=1}^{N} \mathcal{N}(\mathbf{x}_{\text{obs},i} \mid \mathbf{x}_{\text{true},i}, \sigma_x^2)\,\mathcal{N}(\mathbf{y}_{\text{obs},i} \mid \beta\mathbf{x}_{\text{true},i}, \sigma_y^2) \tag{6.37}$$

This formulation has an intuitive interpretation: we're simultaneously trying to:

1. Estimate the true velocity dispersion of each galaxy ($\mathbf{x}_{\text{true},i}$)

2. Find the slope of the M-σ relation (β) that best explains these true values

At first glance, this might seem like a challenging task - we've added N new parameters (one $\mathbf{x}_{\text{true}}$ for each galaxy) to our inference problem! In many statistical problems, adding parameters like this would make the problem intractable, leading to overfitting or computational challenges. However, linear regression has a special property: the linear relationship between variables provides enough structure to make this inference possible.

This approach of treating unknown true values as parameters to be inferred is an example of hierarchical modeling. The structure of our inference follows a hierarchical pattern, where at the top level we have our model parameter β, followed by the true values $\mathbf{x}_{\text{true}}$ for each observation at the next level, and finally our actual measurements $(\mathbf{x}_{\text{obs}}, \mathbf{y}_{\text{obs}})$ at the bottom level.

The importance of this hierarchical approach continues to grow in modern astronomy and machine learning. Consider stellar population studies, where astronomers must simul-

taneously infer both individual stellar parameters and the relationships that govern entire populations. Similarly, in cosmological analyses, researchers frequently tackle the challenge of estimating individual galaxy properties while also understanding large-scale structure parameters.
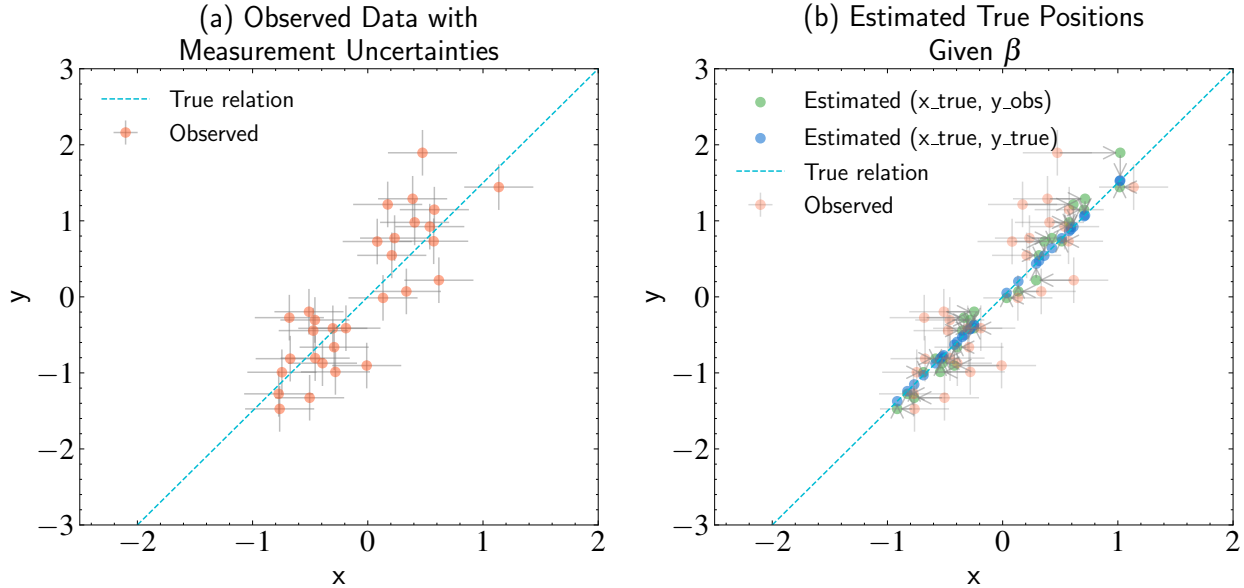
Figure 6.5: Demonstration of how we estimate true positions in a hierarchical model. Both panels show the same underlying relationship (dashed blue line) and observed data points with measurement uncertainties (error bars). Panel (a) shows the raw observed data, where both x and y measurements carry uncertainties. Panel (b) visualizes our inference process: for each observation, we estimate both its true x-position (blue points) and corresponding model-predicted y-value. Gray arrows show the two-step correction: first a horizontal shift from the observed x to its estimated true value, then a vertical shift to the model prediction. The magnitude of these corrections depends on the measurement uncertainties (σ_x and σ_y) and the model parameter (β). The estimated true positions (blue points) lie exactly on the model line because they represent our complete model prediction ($\mathbf{x}_{\text{true}}, \beta\mathbf{x}_{\text{true}}$), while the intermediate points (green) show the state after x-correction but before y-correction. This hierarchical estimation process, updating both $\mathbf{x}_{\text{true}}$ values and β, forms the basis of Deming regression.

6.6   Deming Regression

Now that we have set up the full likelihood, let's solve for both $\mathbf{x}_{\text{true}}$ and β. Our likelihood across all observations is:

$$\mathcal{L}(\beta, \{\mathbf{x}_{\text{true},i}\}) = \prod_{i=1}^{N} \mathcal{N}(\mathbf{x}_{\text{obs},i} \mid \mathbf{x}_{\text{true},i}, \sigma_x^2)\, \mathcal{N}(\mathbf{y}_{\text{obs},i} \mid \beta\mathbf{x}_{\text{true},i}, \sigma_y^2) \qquad (6.38)$$

Expanding the normal distributions:

$$
\mathcal{L}(\beta, \{\mathbf{x}_{\text{true},i}\}) = \prod_{i=1}^{N} \frac{1}{\sqrt{2\pi\sigma_x^2}} \exp\left(-\frac{(\mathbf{x}_{\text{obs},i} - \mathbf{x}_{\text{true},i})^2}{2\sigma_x^2}\right) \frac{1}{\sqrt{2\pi\sigma_y^2}} \exp\left(-\frac{(\mathbf{y}_{\text{obs},i} - \beta\mathbf{x}_{\text{true},i})^2}{2\sigma_y^2}\right)
$$

$$(6.39)$$

Taking the logarithm of the likelihood and dropping constant terms, we obtain the negative log-likelihood:

$$
E(\{\mathbf{x}_{\text{true},i}\}, \beta) = \sum_{i=1}^{N} \left[\frac{(\mathbf{x}_{\text{obs},i} - \mathbf{x}_{\text{true},i})^2}{2\sigma_x^2} + \frac{(\mathbf{y}_{\text{obs},i} - \beta\mathbf{x}_{\text{true},i})^2}{2\sigma_y^2} \right]
$$

$$(6.40)$$

The structure of this expression reveals something important: while β appears in every term as a global parameter, each $\mathbf{x}_{\text{true},i}$ only appears in the ith term. This separable structure suggests a logical optimization approach: we can optimize each $\mathbf{x}_{\text{true},i}$ independently while holding β fixed, then use those optimized values to update β itself.

For a single observation i:

$$
E(\mathbf{x}_{\text{true},i}, \beta) = \frac{(\mathbf{x}_{\text{obs},i} - \mathbf{x}_{\text{true},i})^2}{2\sigma_x^2} + \frac{(\mathbf{y}_{\text{obs},i} - \beta\mathbf{x}_{\text{true},i})^2}{2\sigma_y^2}
$$

$$(6.41)$$

To find the optimal $\mathbf{x}_{\text{true},i}$, we take the derivative with respect to $\mathbf{x}_{\text{true},i}$ and set it to zero:

$$
\frac{\partial E}{\partial \mathbf{x}_{\text{true},i}} = -\frac{(\mathbf{x}_{\text{obs},i} - \mathbf{x}_{\text{true},i})}{\sigma_x^2} - \frac{\beta(\mathbf{y}_{\text{obs},i} - \beta\mathbf{x}_{\text{true},i})}{\sigma_y^2} = 0
$$

$$(6.42)$$

Rearranging terms:

$$
\frac{\mathbf{x}_{\text{true},i}}{\sigma_x^2} + \frac{\beta^2\mathbf{x}_{\text{true},i}}{\sigma_y^2} = \frac{\mathbf{x}_{\text{obs},i}}{\sigma_x^2} + \frac{\beta\mathbf{y}_{\text{obs},i}}{\sigma_y^2}
$$

$$(6.43)$$

$$
\mathbf{x}_{\text{true},i}\left(\frac{1}{\sigma_x^2} + \frac{\beta^2}{\sigma_y^2}\right) = \frac{\mathbf{x}_{\text{obs},i}}{\sigma_x^2} + \frac{\beta\mathbf{y}_{\text{obs},i}}{\sigma_y^2}
$$

$$(6.44)$$

Multiplying both sides by $\sigma_x^2\sigma_y^2$:

$$
\mathbf{x}_{\text{true},i}(\sigma_y^2 + \beta^2\sigma_x^2) = \sigma_y^2\mathbf{x}_{\text{obs},i} + \beta\sigma_x^2\mathbf{y}_{\text{obs},i}
$$

$$(6.45)$$

Using $\lambda = \sigma_y^2 / \sigma_x^2$ and dividing both sides by $\sigma_x^2(\lambda + \beta^2)$:

$$\mathbf{x}_{\text{true},i} = \frac{\lambda \mathbf{x}_{\text{obs},i} + \beta \mathbf{y}_{\text{obs},i}}{\lambda + \beta^2} \tag{6.46}$$

This expression provides insight into how we estimate the true x-positions. The estimate is a weighted average between the observed $\mathbf{x}$-value ($\mathbf{x}_{\text{obs},i}$) and what we would predict from the $\mathbf{y}$-measurement ($\mathbf{y}_{\text{obs},i}/\beta$). The weights depend on the relative uncertainties (λ). Two limiting cases are particularly illuminating:

- When $\lambda \gg 1$ (i.e., when x-measurements are much more precise than $\mathbf{y}$-measurements relative to the slope), we have $\mathbf{x}_{\text{true},i} \approx \mathbf{x}_{\text{obs},i}$ - we trust our $\mathbf{x}$-measurements almost completely.

- When $\lambda \ll 1$ (i.e., when $\mathbf{y}$-measurements are more precise), we have $\mathbf{x}_{\text{true},i} \approx \mathbf{y}_{\text{obs},i}/\beta$ - we rely more heavily on inferring x-positions from our $\mathbf{y}$-measurements and the model.

This formula quantifies precisely how we should balance our direct measurements against our model predictions when estimating the true underlying values. In essence, we're using the linear relationship between $\mathbf{x}$ and $\mathbf{y}$ to constrain our estimates of the true values in both dimensions simultaneously.

Understanding how this estimation works requires careful attention to the weighting. The formula can be rewritten as:

$$\mathbf{x}_{\text{true},i} = w_x \mathbf{x}_{\text{obs},i} + w_y \frac{\mathbf{y}_{\text{obs},i}}{\beta} \tag{6.47}$$

where $w_x = \frac{\lambda}{\lambda + \beta^2}$ and $w_y = \frac{\beta^2}{\lambda + \beta^2}$ are weights that sum to 1.

These weights are determined by the relative uncertainties in our measurements, properly scaled by the relationship between $\mathbf{x}$ and $\mathbf{y}$. If our $\mathbf{x}$-measurements are very precise (small σ_x, large λ), the weight w_x approaches 1, and we rely more on direct $\mathbf{x}$-measurements. Conversely, if our $\mathbf{y}$-measurements are very precise (small σ_y, small λ), the weight w_y approaches 1, and we rely more on inferring $\mathbf{x}$ from $\mathbf{y}$ using our model.

This optimal weighting is what allows Deming regression to correct for attenuation bias. By appropriately balancing our direct measurements against the constraints imposed by our model, we can recover estimates of both the true parameter values and the true

underlying data points.

6.7 Analytical Solution

To complete our optimization, we now need to find β given our estimates of $\mathbf{x}_{\text{true},i}$. Let's revisit our negative log-likelihood:

$$E(\{\mathbf{x}_{\text{true},i}\}, \beta) = \sum_{i=1}^{N} \left[\frac{(\mathbf{x}_{\text{obs},i} - \mathbf{x}_{\text{true},i})^2}{2\sigma_x^2} + \frac{(\mathbf{y}_{\text{obs},i} - \beta\mathbf{x}_{\text{true},i})^2}{2\sigma_y^2} \right] \tag{6.48}$$

Taking the derivative with respect to β and setting it to zero:

$$\frac{\partial E}{\partial \beta} = -\sum_{i=1}^{N} \frac{\mathbf{x}_{\text{true},i}(\mathbf{y}_{\text{obs},i} - \beta\mathbf{x}_{\text{true},i})}{\sigma_y^2} = 0 \tag{6.49}$$

Substituting our expression for $\mathbf{x}_{\text{true},i}$:

$$-\sum_{i=1}^{N} \frac{1}{\sigma_y^2} \left(\frac{\lambda\mathbf{x}_{\text{obs},i} + \beta\mathbf{y}_{\text{obs},i}}{\lambda + \beta^2} \right) (\mathbf{y}_{\text{obs},i} - \beta\mathbf{x}_{\text{obs},i}) = 0 \tag{6.50}$$

Multiplying through by $(\lambda + \beta^2)$ (since it's always positive):

$$\sum_{i=1}^{N} (\lambda\mathbf{x}_{\text{obs},i} + \beta\mathbf{y}_{\text{obs},i})(\mathbf{y}_{\text{obs},i} - \beta\mathbf{x}_{\text{obs},i}) = 0 \tag{6.51}$$

Expanding this expression:

$$\sum_{i=1}^{N} [\lambda\mathbf{x}_{\text{obs},i}\mathbf{y}_{\text{obs},i} - \lambda\beta\mathbf{x}_{\text{obs},i}^2 + \beta\mathbf{y}_{\text{obs},i}^2 - \beta^2\mathbf{x}_{\text{obs},i}\mathbf{y}_{\text{obs},i}] = 0 \tag{6.52}$$

From Chapter 3, we know that for any dataset, we can compute summary statistics that capture the essential relationships between variables. These summary statistics are

defined by:

$$S_{xx} = \sum_{i=1}^{N}(\mathbf{x}_{\mathrm{obs},i} - E[\mathbf{x}_{\mathrm{obs}}])^2 \tag{6.53}$$

$$S_{yy} = \sum_{i=1}^{N}(\mathbf{y}_{\mathrm{obs},i} - E[\mathbf{y}_{\mathrm{obs}}])^2 \tag{6.54}$$

$$S_{xy} = \sum_{i=1}^{N}(\mathbf{x}_{\mathrm{obs},i} - E[\mathbf{x}_{\mathrm{obs}}])(\mathbf{y}_{\mathrm{obs},i} - E[\mathbf{y}_{\mathrm{obs}}]) \tag{6.55}$$

These statistics are closely related to, but not identical to, the variance and covariance. Specifically, they differ by a factor of N:

$$\mathrm{Var}(\mathbf{x}_{\mathrm{obs}}) = \frac{1}{N}S_{xx} \tag{6.56}$$

$$\mathrm{Var}(\mathbf{y}_{\mathrm{obs}}) = \frac{1}{N}S_{yy} \tag{6.57}$$

$$\mathrm{Cov}(\mathbf{x}_{\mathrm{obs}}, \mathbf{y}_{\mathrm{obs}}) = \frac{1}{N}S_{xy} \tag{6.58}$$

For centered variables, where $E[\mathbf{x}_{\mathrm{obs}}] = E[\mathbf{y}_{\mathrm{obs}}] = 0$, these expressions simplify to:

$$S_{xx} = \sum_{i=1}^{N}\mathbf{x}_{\mathrm{obs},i}^2 \tag{6.59}$$

$$S_{yy} = \sum_{i=1}^{N}\mathbf{y}_{\mathrm{obs},i}^2 \tag{6.60}$$

$$S_{xy} = \sum_{i=1}^{N}\mathbf{x}_{\mathrm{obs},i}\mathbf{y}_{\mathrm{obs},i} \tag{6.61}$$

Using these summary statistics, we can rewrite our equation in a more compact form:

$$\lambda S_{xy} - \lambda\beta S_{xx} + \beta S_{yy} - \beta^2 S_{xy} = 0 \tag{6.62}$$

Rearranging into standard quadratic form:

$$\beta^2 S_{xy} - \beta(S_{yy} - \lambda S_{xx}) - \lambda S_{xy} = 0 \tag{6.63}$$

This is a standard quadratic equation of the form $ax^2 + bx + c = 0$, with solution $x = \frac{-b \pm \sqrt{b^2 - 4ac}}{2a}$. In our case, $a = S_{xy}$, $b = -(S_{yy} - \lambda S_{xx})$, and $c = -\lambda S_{xy}$. The solution to this quadratic equation gives us the Deming regression estimator:

$$\hat{\beta} = \frac{S_{yy} - \lambda S_{xx} \pm \sqrt{(S_{yy} - \lambda S_{xx})^2 + 4\lambda S_{xy}^2}}{2S_{xy}} \tag{6.64}$$

We take only the positive branch of this quadratic solution for two important reasons. First, only the positive branch yields the correct limiting behavior when $\sigma_x \to 0$, where we recover the maximum likelihood estimator for the case with no $\mathbf{x}$ uncertainties (as we will show below). Second, the positive branch ensures that $\hat{\beta}$ has the same sign as S_{xy}, which is physically necessary - a positive correlation between $\mathbf{x}$ and $\mathbf{y}$ ($S_{xy} > 0$) should yield a positive slope, while a negative correlation ($S_{xy} < 0$) should yield a negative slope.

An interesting aspect of our derivation is that we obtain a direct solution rather than requiring an iterative procedure, despite dealing with both unknown true values $\mathbf{x}_{\text{true},i}$ and an unknown slope β.

The key to understanding this lies in how the problem naturally decomposes:

1. For any fixed β, the negative log-likelihood is quadratic (and thus convex) in each $\mathbf{x}_{\text{true},i}$, allowing us to find their optimal values analytically:

$$\mathbf{x}_{\text{true},i} = \frac{\mathbf{x}_{\text{obs},i}/\sigma_x^2 + \beta \mathbf{y}_{\text{obs},i}/\sigma_y^2}{1/\sigma_x^2 + \beta^2/\sigma_y^2} \tag{6.65}$$

2. When we substitute these optimal $\mathbf{x}_{\text{true},i}$ values back into the derivative of the negative log-likelihood with respect to β, we obtain a quadratic equation that yields our Deming regression estimator.

As in Chapter 4, while the overall problem is not globally convex in all variables simultaneously, it has a special bi-convex structure: it is convex when we fix either β or the set of $\mathbf{x}_{\text{true},i}$ values. This bi-convexity, combined with our ability to find closed-form solutions for each part, enables us to reach the global optimum in a single step rather than through iteration.

We can verify that Deming regression converges to ordinary least squares when $\sigma_x \to 0$ (or equivalently when $\lambda = \sigma_y^2/\sigma_x^2 \to \infty$). Let's examine what happens to our formula in this
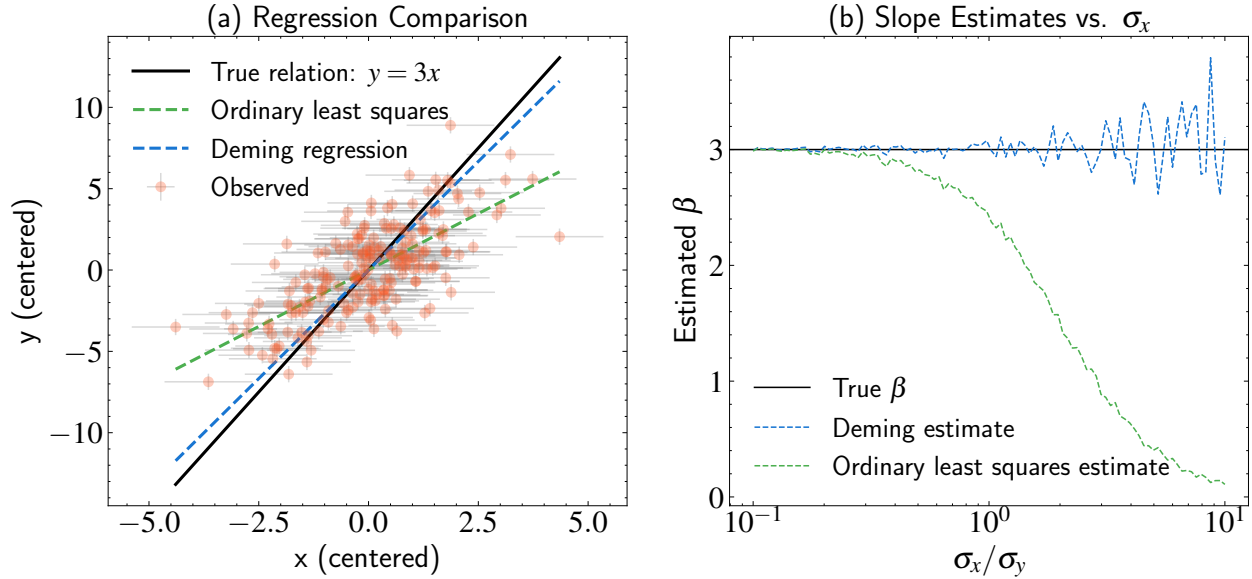
Figure 6.6: Demonstration of how Deming regression corrects for attenuation bias compared to ordinary least squares (OLS, also known as the maximum likelihood solution when there is no x-uncertainty). Panel (a) shows simulated data (orange points with error bars) from a true linear relationship $y = 3x$ (solid black line) with measurement uncertainties $\sigma_x = 1.0$ and $\sigma_y = 0.5$. The OLS fit (green dashed line) systematically underestimates the true slope due to attenuation bias, while Deming regression (blue dashed line) better recovers the true relationship by properly accounting for measurement uncertainties in both variables. Panel (b) demonstrates how these estimators behave as the relative measurement uncertainty (σ_x/σ_y) varies: OLS estimates become increasingly attenuated as x-uncertainty grows, while Deming regression maintains better accuracy by appropriately weighting the uncertainties. When x-uncertainty is small compared to y-uncertainty $(\sigma_x \ll \sigma_y)$, both methods converge to the true slope as standard regression assumptions become valid.

limit.

First, we note that:

$$S_{yy} - \lambda S_{xx} = \lambda \left(\frac{S_{yy}}{\lambda} - S_{xx} \right) \tag{6.66}$$

The square root term can be rewritten as:

$$\sqrt{(S_{yy} - \lambda S_{xx})^2 + 4\lambda S_{xy}^2} = \sqrt{\lambda^2 \left(\frac{S_{yy}}{\lambda} - S_{xx} \right)^2 + 4\lambda S_{xy}^2} \tag{6.67}$$

Factoring out λ from under the square root:

$$\sqrt{(S_{yy} - \lambda S_{xx})^2 + 4\lambda S_{xy}^2} = \lambda\sqrt{\left(\frac{S_{yy}}{\lambda} - S_{xx}\right)^2 + \frac{4S_{xy}^2}{\lambda}} \qquad (6.68)$$

This allows us to express $\hat{\beta}$ as:

$$\hat{\beta} = \frac{S_{yy} - \lambda S_{xx} + \sqrt{(S_{yy} - \lambda S_{xx})^2 + 4\lambda S_{xy}^2}}{2S_{xy}} \qquad (6.69)$$

$$\hat{\beta} = \frac{\lambda\left(\frac{S_{yy}}{\lambda} - S_{xx} + \sqrt{\left(\frac{S_{yy}}{\lambda} - S_{xx}\right)^2 + \frac{4S_{xy}^2}{\lambda}}\right)}{2S_{xy}} \qquad (6.70)$$

For large λ, we can expand the square root using:

$$\sqrt{1 + \epsilon} \approx 1 + \frac{\epsilon}{2} \qquad (6.71)$$

where ϵ is a small term. In our case, we can rewrite the term under the square root as:

$$\left(S_{xx} - \frac{S_{yy}}{\lambda}\right)^2 + \frac{4S_{xy}^2}{\lambda} = S_{xx}^2\left(1 + \left(-\frac{2S_{yy}}{\lambda S_{xx}} + \frac{S_{yy}^2}{\lambda^2 S_{xx}^2} + \frac{4S_{xy}^2}{\lambda S_{xx}^2}\right)\right) \qquad (6.72)$$

As $\lambda \to \infty$, the terms $\frac{S_{yy}}{\lambda S_{xx}}$ and $\frac{S_{yy}^2}{\lambda^2 S_{xx}^2}$ approach zero. Therefore,

$$\epsilon = -\frac{2S_{yy}}{\lambda S_{xx}} + \frac{S_{yy}^2}{\lambda^2 S_{xx}^2} + \frac{4S_{xy}^2}{\lambda S_{xx}^2} \approx \frac{4S_{xy}^2}{\lambda S_{xx}^2} \qquad (6.73)$$

which becomes small as λ becomes large. This gives us:

$$\sqrt{\left(S_{xx} - \frac{S_{yy}}{\lambda}\right)^2 + \frac{4S_{xy}^2}{\lambda}} \approx S_{xx} - \frac{S_{yy}}{\lambda} + \frac{2S_{xy}^2}{\lambda S_{xx}} \qquad (6.74)$$

Substituting back:

$$\hat{\beta} = \frac{\lambda\left[-S_{xx} + \frac{S_{yy}}{\lambda} + \left(S_{xx} - \frac{S_{yy}}{\lambda} + \frac{2S_{xy}^2}{\lambda S_{xx}}\right)\right]}{2S_{xy}} \qquad (6.75)$$

The S_{xx} terms and S_{yy}/λ terms cancel, leaving:

$$\hat{\beta} = \frac{\lambda \left(\frac{2S_{xy}^2}{\lambda S_{xx}} \right)}{2S_{xy}} = \frac{S_{xy}}{S_{xx}} = \frac{\text{Cov}(\mathbf{x}_{\text{obs}}, \mathbf{y}_{\text{obs}})}{\text{Var}(\mathbf{x}_{\text{obs}})} \tag{6.76}$$

Thus, we've shown that in the limit where $\lambda \to \infty$ (equivalently, when $\sigma_x \to 0$), the Deming regression slope converges to $\frac{S_{xy}}{S_{xx}} = \frac{\text{Cov}(\mathbf{x}_{\text{obs}}, \mathbf{y}_{\text{obs}})}{\text{Var}(\mathbf{x}_{\text{obs}})}$. This confirms our expectation that when measurement errors in $\mathbf{x}$ become negligible, the Deming regression naturally reduces to the maximum likelihood estimator we derived earlier for the case with uncertainty only in $\mathbf{y}$.

6.8 Extension to Heteroscedastic Uncertainties

So far, we've assumed that measurement uncertainties are homogeneous - that is, σ_x and σ_y are constant across all observations. While this simplification helped us build intuition and derive analytical results, real astronomical measurements often have uncertainties that vary from point to point. For instance, in our M-σ example, velocity dispersion measurements might be more precise for brighter galaxies, while black hole mass uncertainties could vary based on the specific measurement technique used.

Extending our framework to handle heteroscedastic uncertainties (where $\sigma_{x,i}$ and $\sigma_{y,i}$ vary with i) follows naturally from our previous derivation. Just as before, we start with the likelihood function, but now each data point has its own uncertainties:

$$\mathcal{L}(\beta, \{\mathbf{x}_{\text{true},i}\}) = \prod_{i=1}^{N} \mathcal{N}(\mathbf{x}_{\text{obs},i} \mid \mathbf{x}_{\text{true},i}, \sigma_{x,i}^2) \, \mathcal{N}(\mathbf{y}_{\text{obs},i} \mid \beta \mathbf{x}_{\text{true},i}, \sigma_{y,i}^2) \tag{6.77}$$

Taking the logarithm and dropping constant terms gives us the negative log-likelihood:

$$E(\{\mathbf{x}_{\text{true},i}\}, \beta) = \sum_{i=1}^{N} \left[\frac{(\mathbf{x}_{\text{obs},i} - \mathbf{x}_{\text{true},i})^2}{2\sigma_{x,i}^2} + \frac{(\mathbf{y}_{\text{obs},i} - \beta \mathbf{x}_{\text{true},i})^2}{2\sigma_{y,i}^2} \right] \tag{6.78}$$

Following our earlier approach of maximizing this likelihood, we first solve for each

$\mathbf{x}_{\mathrm{true},i}$ by taking the derivative with respect to $\mathbf{x}_{\mathrm{true},i}$ and setting it to zero:

$$\frac{\partial E}{\partial \mathbf{x}_{\mathrm{true},i}} = -\frac{(\mathbf{x}_{\mathrm{obs},i} - \mathbf{x}_{\mathrm{true},i})}{\sigma_{x,i}^2} - \frac{\beta(\mathbf{y}_{\mathrm{obs},i} - \beta\mathbf{x}_{\mathrm{true},i})}{\sigma_{y,i}^2} = 0 \tag{6.79}$$

Rearranging:

$$\frac{\mathbf{x}_{\mathrm{true},i}}{\sigma_{x,i}^2} + \frac{\beta^2 \mathbf{x}_{\mathrm{true},i}}{\sigma_{y,i}^2} = \frac{\mathbf{x}_{\mathrm{obs},i}}{\sigma_{x,i}^2} + \frac{\beta\mathbf{y}_{\mathrm{obs},i}}{\sigma_{y,i}^2} \tag{6.80}$$

$$\mathbf{x}_{\mathrm{true},i}\left(\frac{1}{\sigma_{x,i}^2} + \frac{\beta^2}{\sigma_{y,i}^2}\right) = \frac{\mathbf{x}_{\mathrm{obs},i}}{\sigma_{x,i}^2} + \frac{\beta\mathbf{y}_{\mathrm{obs},i}}{\sigma_{y,i}^2} \tag{6.81}$$

Solving for $\mathbf{x}_{\mathrm{true},i}$:

$$\mathbf{x}_{\mathrm{true},i} = \frac{\sigma_{y,i}^2 \mathbf{x}_{\mathrm{obs},i} + \beta\sigma_{x,i}^2 \mathbf{y}_{\mathrm{obs},i}}{\sigma_{y,i}^2 + \beta^2 \sigma_{x,i}^2} \tag{6.82}$$

This expression is analogous to our homoscedastic result, but now the weighting depends on the individual uncertainties $\sigma_{x,i}$ and $\sigma_{y,i}$. We can interpret this as a weighted average between the direct measurement $\mathbf{x}_{\mathrm{obs},i}$ (weighted by $\sigma_{y,i}^2$) and the model-inferred value $\mathbf{y}_{\mathrm{obs},i}/\beta$ (weighted by $\sigma_{x,i}^2$). This weighting scheme ensures that when a measurement has a large uncertainty in one dimension, the solution relies more heavily on information from the other dimension.

When we substitute these optimal $\mathbf{x}_{\mathrm{true},i}$ values back into our likelihood and differentiate with respect to β, we get:

$$\frac{\partial E}{\partial \beta} = -\sum_{i=1}^{N} \frac{\mathbf{x}_{\mathrm{true},i}(\mathbf{y}_{\mathrm{obs},i} - \beta\mathbf{x}_{\mathrm{true},i})}{\sigma_{y,i}^2} = 0 \tag{6.83}$$

Substituting our expression for $\mathbf{x}_{\mathrm{true},i}$:

$$-\sum_{i=1}^{N} \frac{1}{\sigma_{y,i}^2}\left(\frac{\sigma_{y,i}^2 \mathbf{x}_{\mathrm{obs},i} + \beta\sigma_{x,i}^2 \mathbf{y}_{\mathrm{obs},i}}{\sigma_{y,i}^2 + \beta^2 \sigma_{x,i}^2}\right)(\mathbf{y}_{\mathrm{obs},i} - \beta\mathbf{x}_{\mathrm{obs},i}) = 0 \tag{6.84}$$

This can be simplified to:

$$F(\beta) = \sum_{i=1}^{N} \frac{\sigma_{y,i}^2 \mathbf{x}_{\text{obs},i} + \beta \sigma_{x,i}^2 \mathbf{y}_{\text{obs},i}}{\sigma_{y,i}^2 + \beta^2 \sigma_{x,i}^2} (\mathbf{y}_{\text{obs},i} - \beta \mathbf{x}_{\text{obs},i}) = 0 \qquad (6.85)$$

Unlike our homoscedastic case where we found a neat quadratic equation for β, this equation (which we define as our objective function $F(\beta)$) is more complex and generally doesn't have a simple closed-form solution. This is because each term in the sum has a different weighting factor that depends on both β and the individual uncertainties. However, we can solve this numerically through several approaches:

Grid Search   The simplest approach is a grid search, where we evaluate $F(\beta)$ for a range of β values and find where it crosses zero. While computationally inefficient, this method is robust and easy to implement.

Newton's Method   For faster convergence, Newton's method uses the derivative of $F(\beta)$ to iteratively approach the solution:

$$\beta_{n+1} = \beta_n - \frac{F(\beta_n)}{F'(\beta_n)} \qquad (6.86)$$

This converges quadratically near the solution but requires computing the derivative of our complex objective function.

Root-Finding Algorithms   Standard numerical libraries provide robust root-finding algorithms like Brent's method, which combines bisection, secant, and inverse quadratic interpolation. These methods offer good convergence properties without requiring derivatives.

The heteroscedastic solution maintains all the key insights we developed in the homoscedastic case while adding important nuances. It still corrects for attenuation bias, but now the correction is specific to each data point based on its uncertainties. Data points with smaller uncertainties naturally carry more weight in determining β, which is exactly what we want in our parameter inference. When all $\sigma_{x,i}$ approach zero, we recover ordinary least squares, just as we showed analytically for the homoscedastic case. Throughout, the solution represents a careful balance between the direct measurements and the constraints imposed by our linear model.

This extension to heteroscedastic uncertainties is particularly important in astron-
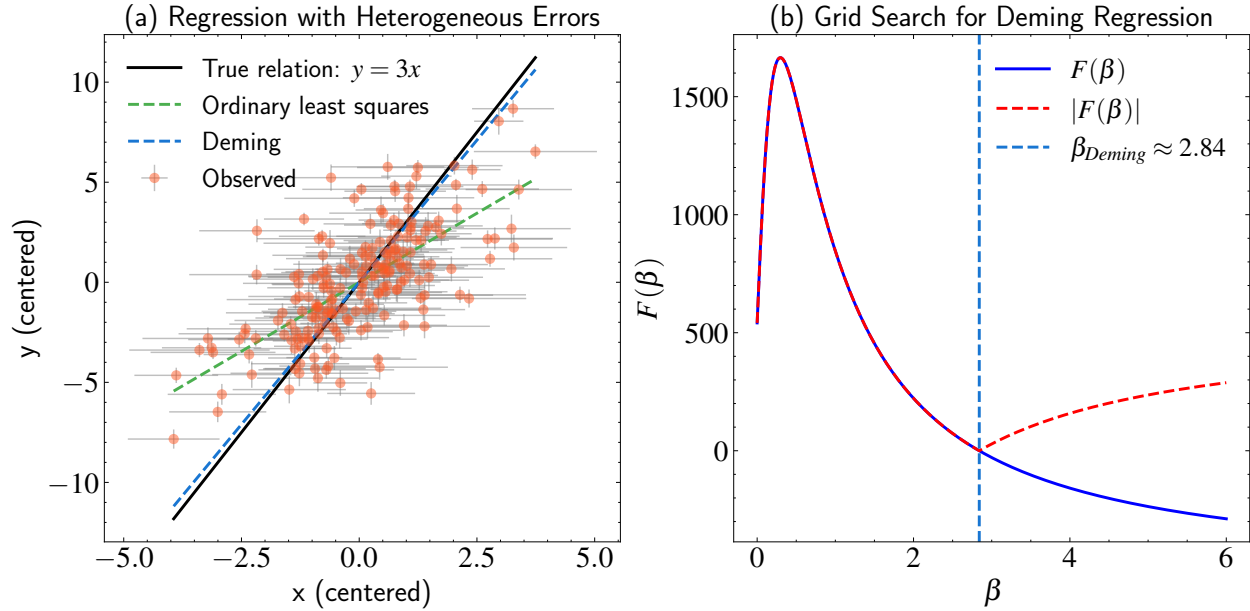
Figure 6.7: Demonstration of heteroscedastic Deming regression and its numerical solution. Panel (a) shows simulated data (orange points) with heterogeneous measurement uncertainties (gray error bars) drawn from uniform distributions: $\sigma_x \sim U(0.5, 1.5)$ and $\sigma_y \sim U(0.3, 0.7)$. The true relationship $y = 3x$ (solid black line) is compared with ordinary least squares (green dashed line) and heteroscedastic Deming regression (blue dashed line). Panel (b) illustrates the numerical solution method: the objective function $F(\beta)$ (solid blue line) and its absolute value $|F(\beta)|$ (dashed red line) are plotted against candidate slope values. The Deming regression slope is found where $F(\beta)$ crosses zero, or equivalently where $|F(\beta)|$ reaches its minimum.

omy, where measurement uncertainties often vary by orders of magnitude within a single dataset. For example, in the M-σ relation, nearby galaxies typically have much more precise measurements than distant ones. The same pattern appears in many other astronomical contexts: brighter objects generally have more precise measurements than fainter ones, and different measurement techniques often have systematically different uncertainties. By properly accounting for these varying uncertainties, we can make optimal use of all our data while ensuring that more precise measurements appropriately dominate our parameter inference.

6.9   Summary

In this chapter, we have focused on a critical challenge in astronomical inference: accounting for uncertainties in both dependent and independent variables. We identified attenuation bias (or regression dilution) as a systematic effect that leads to underestimation of relationship strengths when input uncertainties are ignored.

This bias becomes significant even in linear regression when input uncertainties reach just 10% of the data's range - a common scenario in astronomical measurements. Unlike random errors that average out with more data, attenuation bias persists regardless of sample size. The attenuation factor $\lambda = 1/(1 + (\sigma_x/\sigma_{\mathrm{range}})^2)$ provides a precise quantification of how measurement uncertainties dilute our parameter estimates.

We demonstrated that this issue affects all regression analyses in astronomy, from stellar age-metallicity relations to black hole scaling relations, stellar population studies, and cosmological parameter estimation. The tension between individual measurement precision (often around 10%) and desired statistical inference precision (at the percent level) makes proper treatment of input uncertainties essential for robust astronomical inference.

To address this challenge, we developed a hierarchical framework where the true values of our independent variables are treated as latent variables to be inferred alongside model parameters. This approach led us to Deming regression, which extends ordinary least squares by properly accounting for uncertainties in both variables.

The key insights from our analysis include:

1. The optimal estimate of the true position $\mathbf{x}_{\mathrm{true},i}$ is a weighted average between the direct measurement and the value inferred from the model, with weights determined by the relative uncertainties. This represents a principled approach to combining information from multiple sources based on their reliability.

2. The slope estimator has a closed-form solution in the homoscedastic case, providing a direct correction for attenuation bias. This analytical solution makes Deming regression computationally tractable even for large datasets.

3. The method generalizes naturally to heteroscedastic uncertainties, though numerical methods are required for the optimal slope. This extension is crucial for astronomical applications where measurement uncertainties often vary by orders of magnitude.

4. When uncertainties in $\mathbf{x}$ approach zero, Deming regression converges to ordinary least squares, maintaining consistency with our earlier work. This ensures that we can apply these methods across the full spectrum of measurement uncertainty scenarios.

The hierarchical perspective introduced in this chapter extends beyond linear regression with input uncertainties. This approach - where we simultaneously infer both model parameters and latent variables - is becoming increasingly important across astronomy and

machine learning. Moreover, the hierarchical perspective will return in more advanced topics like mixture models and Bayesian networks, highlighting the broad applicability of the principles we've explored here.

In the next chapter, we will shift our focus from regression (modeling continuous outputs) to classification (modeling discrete outputs). While classification presents new challenges, it builds on the same statistical foundations we've established here. The concepts of likelihood maximization, uncertainty quantification, and hierarchical modeling all transfer directly to the classification domain. The proper treatment of input uncertainties continues to be essential, especially in astronomical applications where measurement errors are substantial.

Further Readings: The development of methods for handling measurement errors in both variables has evolved through several historical contributions, beginning with early work by Adcock [1878] who developed methods that would later be called orthogonal regression, and Pearson [1901] who developed geometric frameworks for finding lines of closest fit when both variables contain errors. Deming [1943] contributed a practical solution known as Deming regression, providing a weighted least squares approach that accounts for known error variance ratios. The computational foundations were later advanced by Golub and Van Loan [1980] who analyzed the total least squares problem using singular value decomposition, with Van Huffel and Vandewalle [1991] providing treatment of computational aspects and numerical stability considerations. For readers interested in theoretical foundations of measurement error models, Fuller [1987] covers estimation, identifiability, and asymptotic properties, while Carroll et al. [2006] extends these methods to nonlinear models and modern applications including semiparametric regression and survival analysis. The field has benefited from astronomical applications that contributed to methodological development: Isobe et al. [1990] provided comparison of various regression methods for astronomical data with measurement errors, while Kelly [2007] developed Bayesian approaches that handle heteroscedastic errors, intrinsic scatter, and selection effects. Connections to structural equation modeling were explored by Bentler and Weeks [1980], demonstrating how latent variable methods provide a unified framework for complex error structures. For practical guidance on implementation, Carroll and Ruppert [1996] examined the use and misuse of orthogonal regression, highlighting concerns about inappropriate applications when error variance ratios are unknown or variable.

Chapter 7

Classification and Logistic Regression

In the previous chapters, we explored linear regression, where we built a linear model to make inferences on continuous variable labels. We saw how linear regression emerged naturally from probabilistic principles, allowing us to predict quantities like stellar masses, luminosities, or temperatures from observable features. Now we turn to another major category of supervised learning: classification.

Classification differs from regression in a key way. Rather than predicting continuous values, we aim to categorize objects into discrete classes. When observing a celestial object, we might want to determine whether it's a star or a galaxy, classify a galaxy as spiral or elliptical, or identify a variable star as a Cepheid or RR Lyrae. In each case, we assign discrete class labels rather than continuous values.

This discrete nature creates a mathematical challenge. In linear regression, our model could predict any real-valued output. But classification requires our model to output class probabilities, which must lie between 0 and 1. This constraint means we cannot simply apply linear regression techniques directly to classification problems. If we did, our model might predict probabilities greater than 1 or less than 0, which would be meaningless.

Figure 7.1 illustrates the classification process. In this example, we have data points representing stars (blue) and galaxies (red) plotted in a two-dimensional feature space. These features might be photometric colors, morphological parameters, or astrometric measurements. Logistic regression learns a decision boundary (green dashed line) that separates the two classes. When a new object (yellow star) is observed, its position relative to this boundary determines how the model classifies it. The further an object is from the boundary, the
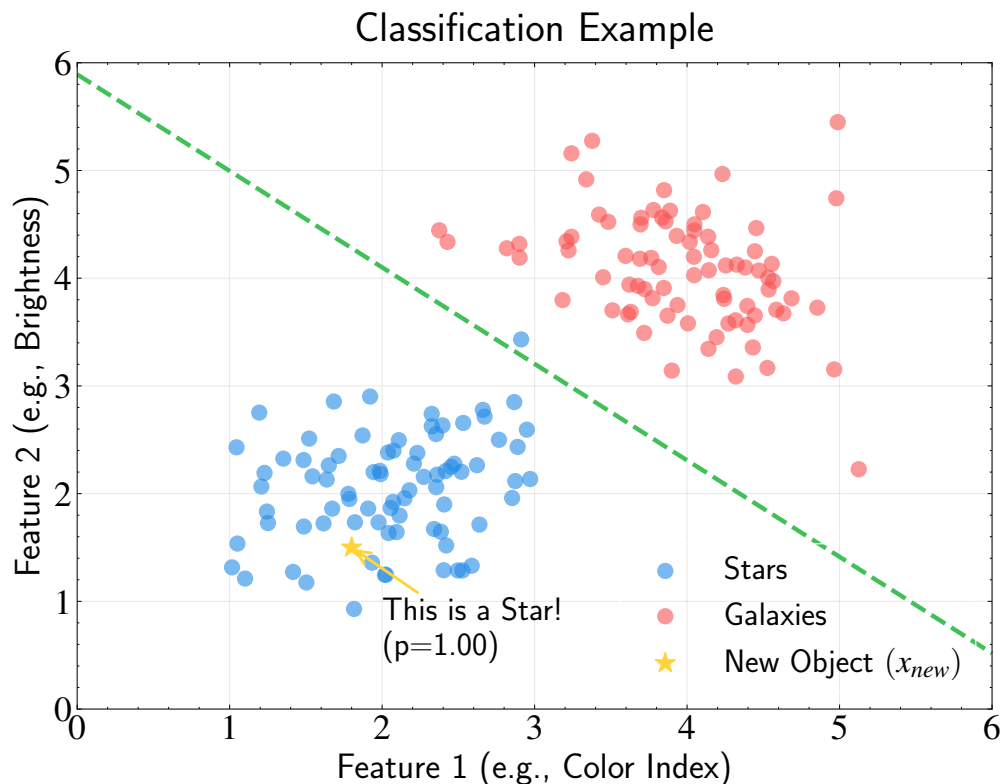
Figure 7.1: Demonstration of binary classification in a two-dimensional feature space. Stars (blue) and galaxies (red) form distinct clusters based on two observable features. The dashed green line shows the decision boundary learned by logistic regression, which separates the two classes. A new object (yellow star) is classified based on its position relative to this boundary, with the model assigning probabilities to each class membership. This illustrates how classification algorithms learn to partition the feature space and make predictions for new observations. The logistic regression—a linear classifier—assumes a linear decision boundary as shown. The features could represent various astronomical measurements that help distinguish stars from galaxies, such as photometric colors, morphological parameters (comparing PSF vs model magnitudes), or astrometric measurements from missions like Gaia (proper motions and parallaxes).

more confident the classification.

Logistic regression addresses the challenge of classification by introducing a transformation that maps unconstrained linear predictions to valid probabilities. Despite its name, logistic regression is actually a classification technique, not a regression method. The "regression" part refers to the linear combination of inputs, while "logistic" refers to the transformation that ensures outputs are valid probabilities.

The need for classification methods is particularly acute in modern astronomy. With large-scale surveys like Gaia, SDSS, and the upcoming Vera C. Rubin Observatory collecting

data on billions of objects, automated classification has become essential. Astronomers cannot manually examine every object, and telescope time for follow-up observations is limited and expensive. Classification algorithms help prioritize targets efficiently.

For instance, when searching for rare metal-poor stars, we need to identify promising candidates from photometric data before investing in high-resolution spectroscopy. Similarly, identifying quasar candidates from millions of point sources requires effective classification using features like photometric colors and variability patterns. In time-domain astronomy, automatically classifying variable stars and transient events by their light curves is crucial for timely follow-up of scientifically valuable phenomena.

In this chapter, we will develop logistic regression from first principles, following a similar path to our treatment of linear regression. We'll see how the method emerges naturally from a probabilistic perspective, discover why the sigmoid function arises as a key component, and derive the cross-entropy loss function as a consequence of maximum likelihood estimation. We'll also explore two complementary approaches to classification: discriminative models, which directly learn to separate classes, and generative models, which learn how to generate data from each class.

Through this exploration, we'll gain both practical tools for astronomical classification tasks and deeper insights into the probabilistic foundations of machine learning. Logistic regression will serve as our entry point into classification, providing a foundation for more complex techniques we'll encounter in later chapters.

7.1 Binary Classification Fundamentals

We begin our exploration of classification by addressing a fundamental question: how do we mathematically represent categorical class labels? Unlike regression problems where our labels are naturally numeric (stellar mass in solar masses, luminosity in ergs per second, or temperature in Kelvin), classification deals with categories that don't inherently have numerical values. For instance, galaxy morphology (spiral, elliptical, irregular), stellar spectral types (O, B, A, F, G, K, M), or object types (star, galaxy, quasar) are categories without natural numerical representations.

For binary classification—where we sort objects into one of two possible categories—the standard approach is to encode our classes as 0 and 1. For example:

- Star (0) vs. Galaxy (1)

- Non-variable (0) vs. Variable star (1)

- Non-transient (0) vs. Transient event (1)

This encoding is purely conventional—we could just as easily swap the assignments. By convention, we typically assign 0 to what we might consider the "background" or "default" class, and 1 to the "target" or "positive" class of interest. In a transient detection system, for instance, assigning 1 to the rare transient events aligns with our focus on finding these unusual objects among the vastly more common non-transient sources.

The binary encoding has a useful mathematical symmetry: if we swap our labels (turning all 0s to 1s and vice versa), we can recover equivalent predictions by simply taking 1 minus our original prediction probability. For example, if our original model predicts a 0.8 probability of class 1 (transient), a model with swapped labels would predict a 0.2 probability of class 0 (non-transient), since $1 - 0.8 = 0.2$. This symmetry means that whether we frame our question as "what's the probability this is a transient?" or "what's the probability this is not a transient?" we're dealing with mathematically equivalent problems.

With our labels encoded as 0 and 1, a classification algorithm's task is to predict the probability that a given object belongs to class 1, which we denote as $P(C_1|\mathbf{x})$, where $\mathbf{x}$ represents the object's features (like colors, morphology, or astrometric measurements). Since probabilities for all classes must sum to 1, we automatically know that $P(C_0|\mathbf{x}) = 1 - P(C_1|\mathbf{x})$ in binary classification. The decision boundary—the surface in feature space that separates the two classes—occurs where $P(C_1|\mathbf{x}) = P(C_0|\mathbf{x}) = 0.5$.

Now that we've established how to represent class labels mathematically, the next question is: how do we build a model that predicts these class probabilities? There are two fundamental approaches to this problem, which we'll explore in the next section.

7.2 Discriminative vs. Generative Models

When we perform classification, we ultimately want to determine the probability that an object belongs to a particular class given its observed features—mathematically, we want to model $P(C_k|\mathbf{x})$. But there are two distinct paths to modeling this probability, both connected through Bayes' theorem:

$$P(C_k|\mathbf{x}) = \frac{P(\mathbf{x}|C_k) \cdot P(C_k)}{P(\mathbf{x})} \tag{7.1}$$

This equation reveals two different approaches to classification, each with its own perspective on the problem.

Discriminative approach   The discriminative approach directly models $P(C_k|\mathbf{x})$—exactly what we need for classification. This approach focuses on learning the boundary between classes, essentially answering the question: "Given these features, what's the probability this object belongs to class k?"

When classifying stars versus galaxies, a discriminative model takes our input features $\mathbf{x}$ (which might include dozens of measurements of the object) and directly outputs the probability that the object belongs to each class—for example, "this object has an 80% chance of being a galaxy." The model learns to map from complex input data to these class probabilities without explicitly modeling how the features are distributed within each class.
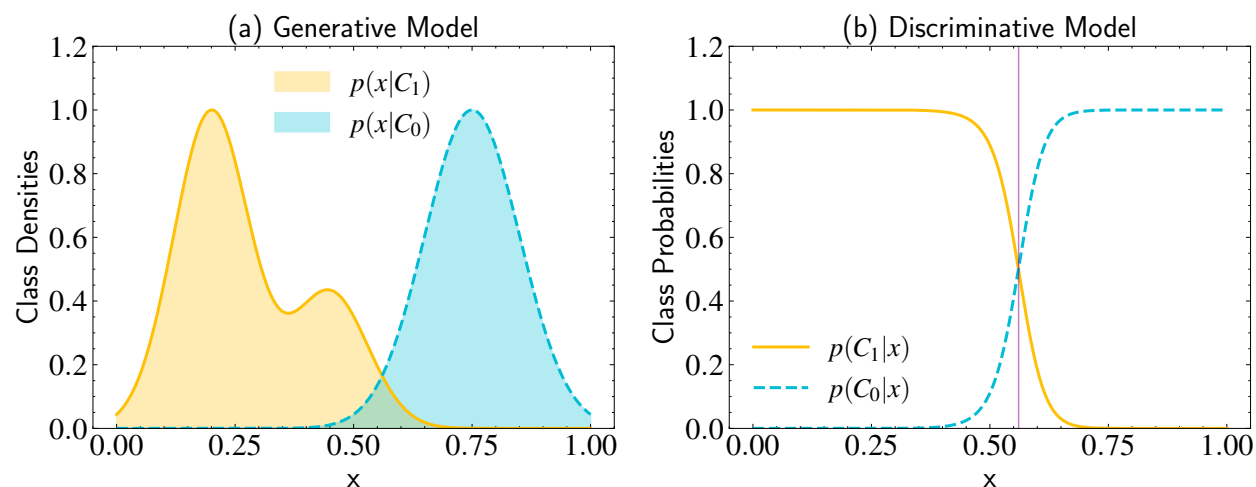
Figure 7.2: Visualization of generative versus discriminative approaches in classification. Panel (a) shows the generative model perspective: learning the class-conditional densities $p(x|C_k)$ for each class separately. This illustrates how generative models capture the full complexity of feature distributions within each class, enabling tasks beyond classification like anomaly detection (e.g., identifying quasars that don't match either stellar or galactic distributions) and synthetic data generation. Panel (b) shows the discriminative model perspective: directly learning the posterior probabilities $p(C_k|x)$ of class membership. The vertical purple line indicates the decision boundary where the probabilities of both classes are equal ($p(C_1|x) = p(C_0|x) = 0.5$). While simpler to learn, the discriminative approach focuses solely on classification, potentially missing valuable information about the underlying physical distributions that generative models preserve.

Generative Approach   The generative approach takes the alternative path through Bayes' theorem. Instead of directly modeling $P(C_k|\mathbf{x})$, it models the components needed to compute

it indirectly:

1. $P(\mathbf{x}|C_k)$ — the probability distribution of features for each class (likelihood)

2. $P(C_k)$ — the prior probability of each class

Then, through Bayes' theorem, we can compute $P(C_k|\mathbf{x})$ by combining these components and normalizing by $P(\mathbf{x})$.

The generative approach gets its name because it models enough about each class to theoretically generate new examples from them. For stars versus galaxies, this means learning separately what stars look like (their colors, their point-like appearance, their proper motions) and what galaxies look like (their extended shapes, their color distributions, their lack of proper motion).

To understand the difference between these approaches, consider an analogy of language identification. A discriminative approach to distinguishing German from Portuguese would focus on specific distinguishing features—perhaps noting that German has more harsh consonants while Portuguese has more nasal sounds. It learns just enough to tell the languages apart.

A generative approach, in contrast, would involve learning to speak both languages — understanding their grammar, vocabulary, and pronunciation rules. This is much more challenging, but also more powerful. Someone who speaks both languages can not only distinguish between them but can also generate new sentences, recognize dialects, and understand why certain sound combinations are valid in one language but not the other.

One key advantage of generative models is their ability to detect outliers or novel classes. Someone who only knows how to distinguish German from Portuguese (discriminative model) might confidently misclassify Spanish as one or the other. However, someone who speaks both languages fluently (generative model) would immediately recognize that Spanish follows different patterns—mathematically, they would find that both $P(\mathbf{x}|\text{German})$ and $P(\mathbf{x}|\text{Portuguese})$ are small, indicating this example doesn't fit either known class.

In astronomy, this capability is particularly valuable. A discriminative model trained only on stars and galaxies might confidently but incorrectly classify a quasar as one or the other. A generative model would recognize that the quasar's features don't follow the expected patterns of either known class, flagging it as something potentially new and interesting.

Having established these two approaches to classification—both connected through Bayes' theorem—we now turn to logistic regression, which takes the discriminative approach. We'll see that despite taking this direct path, logistic regression has a precise corresponding generative model, providing a concrete example of how these two perspectives relate.

7.3   Logistic Regression and The Sigmoid Function

Logistic regression is a discriminative classification method that directly models $P(C_1|\mathbf{x})$. Given our experience with linear regression, a natural first attempt might be to model this probability as a linear function of our features:

$$P(C_1|\mathbf{x}) = \mathbf{w}^T\mathbf{x} \qquad (7.2)$$

where $\mathbf{w}$ is our vector of model parameters and $\mathbf{x}$ is our vector of input features (with a constant 1 appended to account for the bias term).

However, this straightforward approach encounters two critical problems:

First, linear models produce unbounded outputs. Our predicted value could be any real number, taking values like -2.7 or 5.3, but probabilities must be confined to the range $[0, 1]$. This mismatch causes conceptual and practical problems—a prediction of 1.5 cannot be interpreted as a probability.

Second, treating classification as regression misrepresents the nature of our problem. In regression, a prediction of 10.2 when the true value is 10.0 represents a small error. But in classification, predicting a probability of 1.2 for a positive example isn't just slightly wrong—it's fundamentally meaningless in a probabilistic framework.

Moreover, this unbounded behavior creates a serious problem for finding the optimal decision boundary. Consider data points from class 1 that are far from the boundary—the linear model might predict values like $y = 2$ for these points. When we try to minimize prediction error (say, using least squares), these large deviations from the target value of 1 would dominate our error calculation. The model would focus more on reducing these large errors far from the boundary rather than getting the boundary location correct, potentially skewing the decision boundary away from its optimal position.

What we need is a "tapering" function—a mathematical transformation that takes our linear predictor $\mathbf{w}^T\mathbf{x}$ and "squashes" it into the proper range for probabilities, while
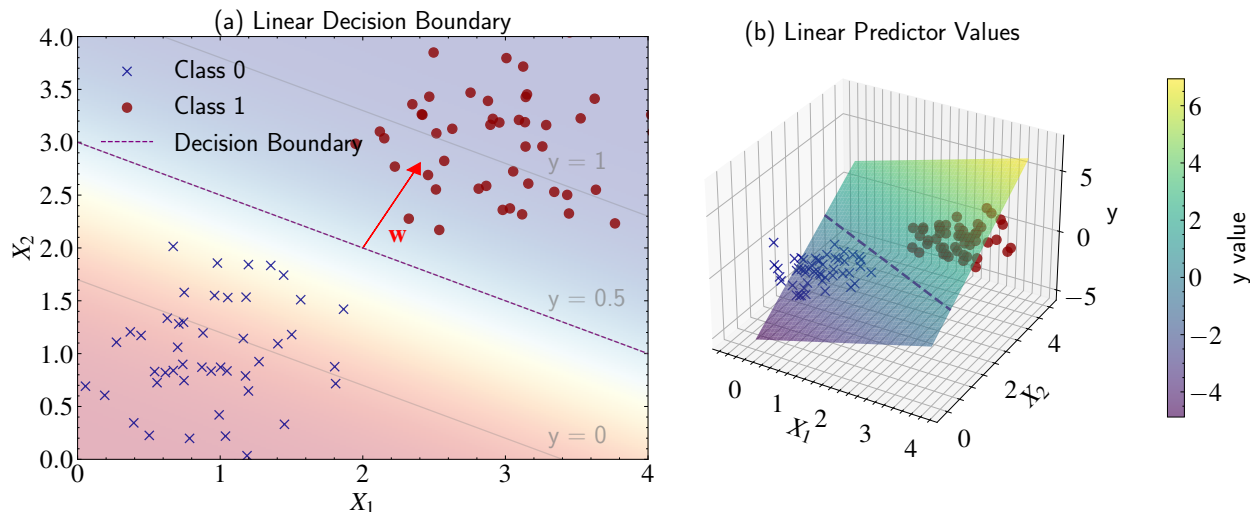
Figure 7.3: Illustration of the problem of simply treating classification as regression. Panel (a) shows the 2D feature space with two classes (cyan and yellow) and the linear decision boundary (purple dashed line) where $y = 0.5$. The weight vector $\mathbf{w}$ (red arrow) is perpendicular to the decision boundary, determining its orientation. Gray lines show contours of constant y values (-1, 0, 1, 2), demonstrating how the linear predictor continues to grow indefinitely as we move away from the boundary. Panel (b) shows the same scenario in 3D, where the vertical axis represents the raw output $y = \mathbf{w}^T\mathbf{x}$ of the linear model. While the decision boundary at $y = 0.5$ appears reasonable, the unbounded nature of y means that points far from the boundary receive predictions well outside the valid probability range of [0,1], leading to potential issues in model fitting.

maintaining the linear nature of our decision boundary. The sigmoid function provides exactly this transformation:

$$\sigma(z) = \frac{1}{1 + e^{-z}} \tag{7.3}$$

This S-shaped curve maps any real number to the range $[0, 1]$, making it suitable for representing probabilities. When z is very negative, $\sigma(z)$ approaches 0; when z is very positive, $\sigma(z)$ approaches 1; and when $z = 0$, $\sigma(z) = 0.5$, marking the decision boundary.

But the sigmoid function isn't just a convenient mathematical solution—it emerges naturally from probabilistic reasoning. To understand why, let's consider how we might quantify our relative belief between two classes. For binary classification, the odds ratio provides a natural measure:

$$\text{odds} = \frac{P(C_1|\mathbf{x})}{P(C_0|\mathbf{x})} = \frac{P(C_1|\mathbf{x})}{1 - P(C_1|\mathbf{x})} \tag{7.4}$$
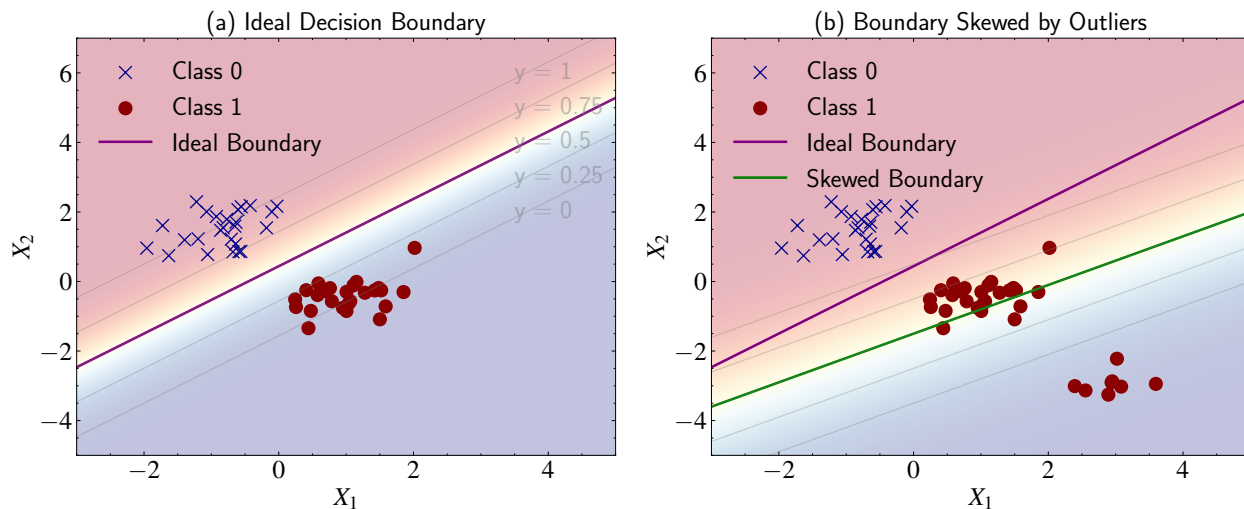
Figure 7.4: Illustration of how direct linear regression can lead to suboptimal decision boundaries in classification. Panel (a) shows the ideal decision boundary (purple line) that correctly separates two classes when considering only the main clusters, with gray lines showing contours of constant y values from the linear predictor $\mathbf{w}^T\mathbf{x}$. Panel (b) demonstrates how the boundary can be skewed (green line) when attempting direct linear regression with outliers: because the linear predictor grows unboundedly, outlying points produce very large errors ($y \gg 1$) that dominate the least squares optimization. The model shifts the boundary to reduce these large errors, even though this compromises the classification of the main clusters. This illustrates why we need a tapering function like the sigmoid to ensure predictions remain bounded between 0 and 1, preventing outliers from having undue influence on the boundary placement.

This odds ratio is useful because while probabilities are bounded between 0 and 1, the odds can range from 0 to infinity. Taking the logarithm of these odds—called the "logit" transformation—extends the range further to the entire real line:

$$\text{logit}(P(C_1|\mathbf{x})) = \ln\left(\frac{P(C_1|\mathbf{x})}{1 - P(C_1|\mathbf{x})}\right) \tag{7.5}$$

This suggests that instead of modeling probabilities directly with our linear function, we should model the logit:

$$\text{logit}(P(C_1|\mathbf{x})) = \mathbf{w}^T\mathbf{x} \tag{7.6}$$

This approach makes sense because both our linear predictor $\mathbf{w}^T\mathbf{x}$ and the logit can take any real value. To find the actual probability, we need to reverse the logit transformation:
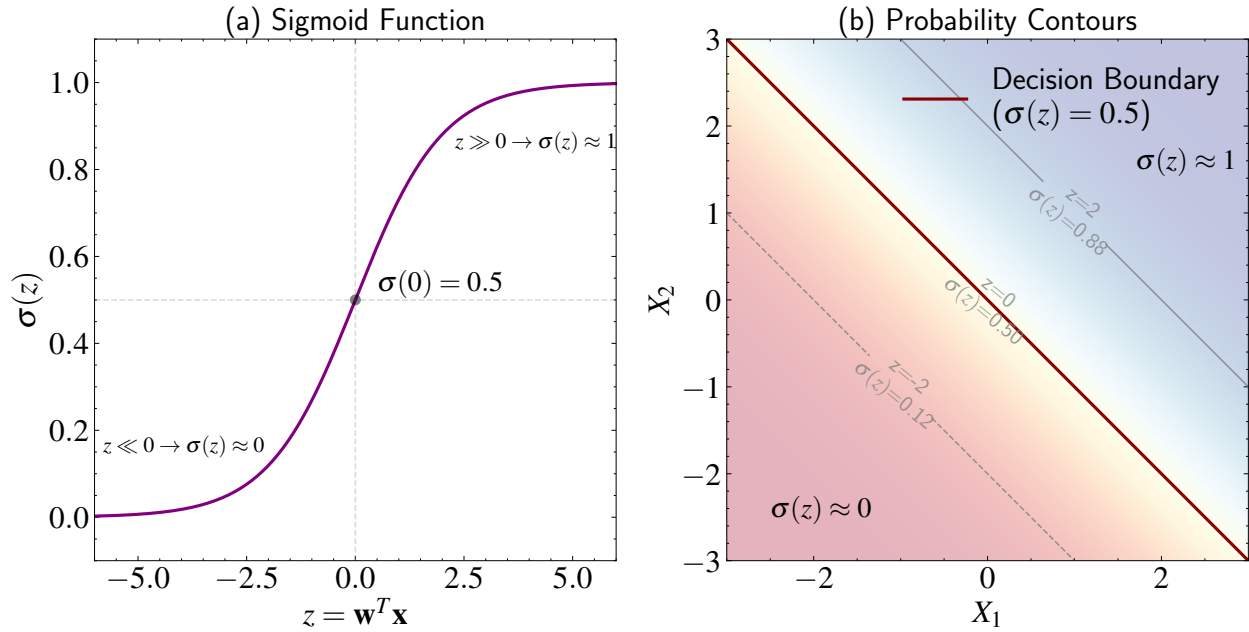
Figure 7.5: The sigmoid function and its role in logistic regression. Panel (a) shows the sigmoid function $\sigma(z) = 1/(1 + e^{-z})$, which "squashes" any real number into the range [0,1]. When $z \ll 0$, the function approaches 0; when $z \gg 0$, it approaches 1; and at $z = 0$, it takes the value 0.5. Panel (b) shows how this creates probability contours in feature space: the decision boundary (purple line) corresponds to $\sigma(z) = 0.5$, while the gray contour lines show both the linear predictor z values and their corresponding sigmoid probabilities $\sigma(z)$. This demonstrates how the sigmoid function ensures predictions remain bounded between 0 and 1 regardless of distance from the decision boundary.

Starting with the logit equation and applying algebraic manipulations:

$$\ln\left(\frac{P(C_1|\mathbf{x})}{1 - P(C_1|\mathbf{x})}\right) = \mathbf{w}^T\mathbf{x} \tag{7.7}$$

$$\frac{P(C_1|\mathbf{x})}{1 - P(C_1|\mathbf{x})} = e^{\mathbf{w}^T\mathbf{x}} \tag{7.8}$$

$$P(C_1|\mathbf{x}) = e^{\mathbf{w}^T\mathbf{x}}(1 - P(C_1|\mathbf{x})) \tag{7.9}$$

$$P(C_1|\mathbf{x}) = e^{\mathbf{w}^T\mathbf{x}} - e^{\mathbf{w}^T\mathbf{x}}P(C_1|\mathbf{x}) \tag{7.10}$$

$$P(C_1|\mathbf{x})(1 + e^{\mathbf{w}^T\mathbf{x}}) = e^{\mathbf{w}^T\mathbf{x}} \tag{7.11}$$

$$P(C_1|\mathbf{x}) = \frac{e^{\mathbf{w}^T\mathbf{x}}}{1 + e^{\mathbf{w}^T\mathbf{x}}} = \frac{1}{1 + e^{-\mathbf{w}^T\mathbf{x}}} = \sigma(\mathbf{w}^T\mathbf{x}) \tag{7.12}$$

This derivation reveals that the sigmoid function emerges naturally when we model log-odds using a linear function. The name "logistic regression" now makes sense: we're performing linear regression in the log-odds (logit) space, which transforms to probabilities

through the sigmoid function.
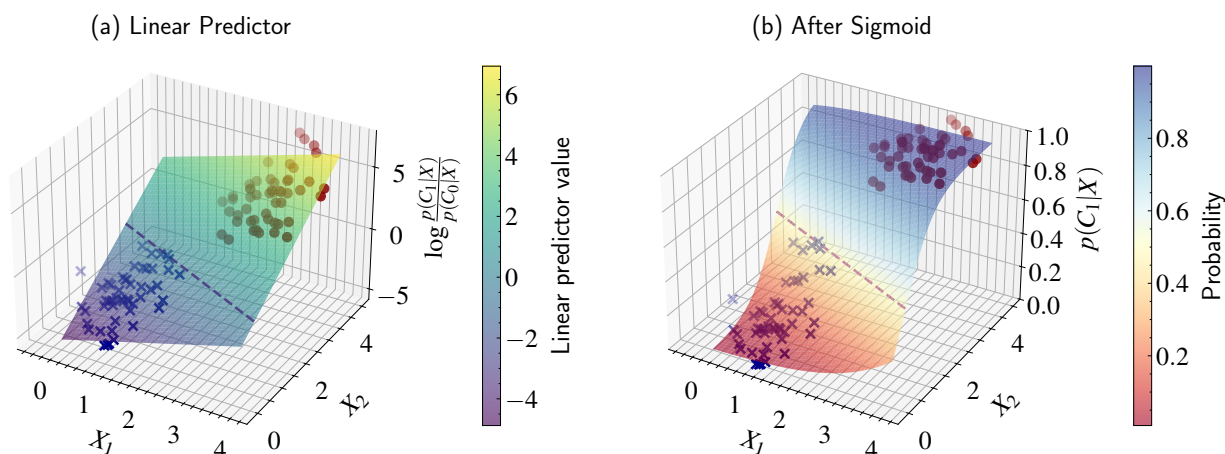
Figure 7.6: Visualization of how logistic regression transforms unbounded linear predictions into probabilities. Panel (a) shows the linear predictor $\log(p(C_1|X)/p(C_0|X)) = \mathbf{w}^T\mathbf{x} + b$ in feature space, where the surface extends infinitely in the vertical direction. The purple dashed line indicates the decision boundary where the log-odds ratio equals zero. Panel (b) shows the same predictor after applying the sigmoid function, transforming the unbounded log-odds into probabilities $p(C_1|X)$ bounded between 0 and 1. The sigmoid function "squashes" the linear predictor while preserving the location of the decision boundary (where $p(C_1|X) = 0.5$). Blue crosses and red circles represent two classes of data points, demonstrating how points far from the boundary receive probability predictions close to 0 or 1, while points near the boundary receive intermediate probabilities.

The linear decision boundary is preserved in this approach. The boundary occurs where $P(C_1|\mathbf{x}) = 0.5$, which corresponds to $\sigma(\mathbf{w}^T\mathbf{x}) = 0.5$, which happens precisely when $\mathbf{w}^T\mathbf{x} = 0$. This gives us a linear boundary in feature space, just as we wanted.

In astronomical terms, our linear predictor $\mathbf{w}^T\mathbf{x}$ now has a clear interpretation: it represents the log-odds of an object belonging to one class versus another. For star-galaxy classification, a log-odds of 2 means an object is $e^2 \approx 7.4$ times more likely to be a star than a galaxy. The sigmoid function converts these log-odds into probabilities that we can use for decision-making.

It's worth noting that while we've formulated logistic regression as a discriminative model that directly predicts $P(C_1|\mathbf{x})$, it has a precise corresponding generative model. In the next section, we'll explore this connection, showing that logistic regression with a linear boundary emerges naturally when we assume our features follow Gaussian distributions with equal covariance matrices across classes. This connection will provide deeper insight into the strengths and limitations of logistic regression.

7.4   From Discriminative to Generative

Our discussion thus far has focused on the discriminative approach to classification, where we directly model $P(C_k|\mathbf{x})$ through logistic regression. However, as we noted earlier, Bayes' theorem connects this discriminative perspective to its generative counterpart. In this section, we'll explore this connection in detail, showing how specific assumptions about the underlying data distributions in a generative model can lead precisely to logistic regression.

Let's start with what we know about logistic regression. In this discriminative approach, we made a key assumption: that the log-odds can be written as a linear function $\mathbf{w}^T\mathbf{x}$. This creates a hyperplane decision boundary in our feature space (a line in 2D, a plane in 3D, etc.), where points on one side (where $\mathbf{w}^T\mathbf{x} > 0$) are classified as class 1, and points on the other side (where $\mathbf{w}^T\mathbf{x} < 0$) are classified as class 0. The vector $\mathbf{w}$ determines the orientation of this boundary, acting perpendicular to the dividing hyperplane.

This naturally leads to a key question: what assumptions about the underlying feature distributions $P(\mathbf{x}|C_k)$ would give rise to such a linear boundary? In other words, if we were to work backwards from our linear boundary to a generative model, what would the feature distributions need to look like within each class?

It turns out that the linear boundary of logistic regression emerges naturally when we assume our features follow multivariate Gaussian distributions with equal covariance matrices across classes.

In mathematical terms, we assume that for each class k, the features follow a multivariate Gaussian distribution:

$$P(\mathbf{x}|C_k) = \frac{1}{(2\pi)^{D/2}|\Sigma|^{1/2}} \exp\left(-\frac{1}{2}(\mathbf{x} - \mu_k)^T \Sigma^{-1} (\mathbf{x} - \mu_k) \right) \tag{7.13}$$

The dimensionality D represents how many features we're working with. Each class has its own mean vector μ_k, and the covariance matrix Σ. Here's where we make a further crucial assumption: we use the same Σ for all classes. This means that while different classes can have different centers (means), they must have the same shape and orientation in feature space.

Geometrically, this assumption means that each class forms a "cloud" of points in our feature space, with these clouds having the same shape and orientation but centered at different locations. While this may seem like a strong assumption—in our star-galaxy

classification example, galaxies likely show more varied color distributions than stars due to their more complex nature—it turns out to be mathematically necessary. As we will see in the derivation below, having equal covariance matrices is crucial because it allows the quadratic terms in our features to cancel out, leading to the linear decision boundary that characterizes logistic regression.
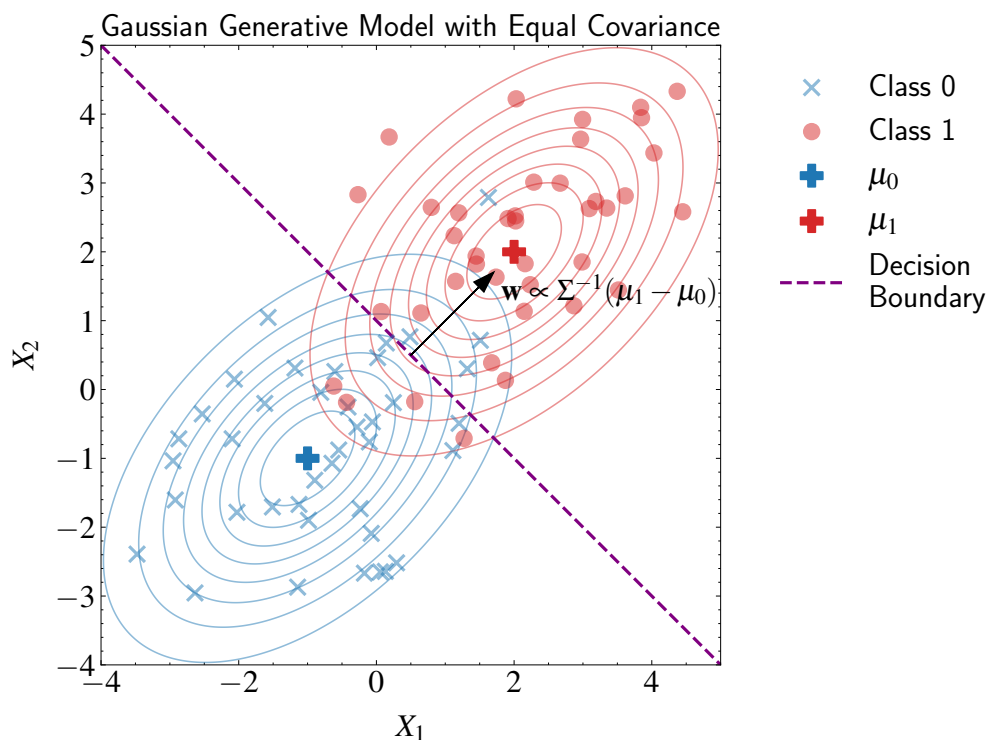
Figure 7.7: Illustration of how Gaussian generative models with equal covariance matrices naturally lead to linear decision boundaries. The contour lines show the probability density of two Gaussian distributions with means μ_0 and μ_1 (shown as larger markers) sharing the same covariance matrix Σ. Sample points (crosses and circles) are drawn from each distribution. The optimal decision boundary (purple dashed line) emerges naturally from the equality of the covariance matrices and is perpendicular to the direction $\mathbf{w} \propto \Sigma^{-1}(\mu_1 - \mu_0)$. This demonstrates how our assumptions about the generative model's covariance structure directly determine the form of the optimal classifier.

Let's now show that if we assume the features follow multivariate Gaussian distributions with equal covariance matrices, the log-odds ratio will indeed be linear in the features. Starting with Bayes' theorem:

$$\ln\left(\frac{P(C_1|\mathbf{x})}{P(C_0|\mathbf{x})}\right) = \ln\left(\frac{P(\mathbf{x}|C_1)P(C_1)}{P(\mathbf{x}|C_0)P(C_0)}\right) \tag{7.14}$$

Notice how the denominator $P(\mathbf{x})$ from Bayes' theorem cancels out in the ratio. Now,

we can substitute our Gaussian assumption for $P(\mathbf{x}|C_k)$. The equation gets a bit lengthy, but let's break it down piece by piece:

$$\ln\left(\frac{P(C_1|\mathbf{x})}{P(C_0|\mathbf{x})}\right) = \ln\left(\frac{P(C_1)}{P(C_0)}\right) + \ln\left(\frac{\exp(-\frac{1}{2}(\mathbf{x}-\mu_1)^T\Sigma^{-1}(\mathbf{x}-\mu_1))}{\exp(-\frac{1}{2}(\mathbf{x}-\mu_0)^T\Sigma^{-1}(\mathbf{x}-\mu_0))}\right) \tag{7.15}$$

The first term, $\ln(P(C_1)/P(C_0))$, represents our prior beliefs about the relative frequencies of the classes. And the second term compares how well our features $\mathbf{x}$ match the Gaussian distribution of each class.

Here's where the equal covariance assumption shows its necessity. We begin with the logarithm of the ratio of the Gaussian distributions:

$$\ln\left(\frac{\exp(-\frac{1}{2}(\mathbf{x}-\mu_1)^T\Sigma^{-1}(\mathbf{x}-\mu_1))}{\exp(-\frac{1}{2}(\mathbf{x}-\mu_0)^T\Sigma^{-1}(\mathbf{x}-\mu_0))}\right) \tag{7.16}$$

Using the properties of logarithms, this becomes a difference rather than a ratio:

$$-\frac{1}{2}(\mathbf{x}-\mu_1)^T\Sigma^{-1}(\mathbf{x}-\mu_1) + \frac{1}{2}(\mathbf{x}-\mu_0)^T\Sigma^{-1}(\mathbf{x}-\mu_0) \tag{7.17}$$

Let's expand each quadratic form. For the first term:

$$(\mathbf{x}-\mu_1)^T\Sigma^{-1}(\mathbf{x}-\mu_1) = \mathbf{x}^T\Sigma^{-1}\mathbf{x} - \mathbf{x}^T\Sigma^{-1}\mu_1 - \mu_1^T\Sigma^{-1}\mathbf{x} + \mu_1^T\Sigma^{-1}\mu_1 \tag{7.18}$$

Note that $\mathbf{x}^T\Sigma^{-1}\mu_1$ is a scalar, so it equals its transpose $\mu_1^T\Sigma^{-1}\mathbf{x}$. Similarly for the second term. Substituting these expansions back into our difference equation:

$$\begin{aligned}
-\frac{1}{2}(\mathbf{x}^T\Sigma^{-1}\mathbf{x} - 2\mu_1^T\Sigma^{-1}\mathbf{x} + \mu_1^T\Sigma^{-1}\mu_1) \\
+ \frac{1}{2}(\mathbf{x}^T\Sigma^{-1}\mathbf{x} - 2\mu_0^T\Sigma^{-1}\mathbf{x} + \mu_0^T\Sigma^{-1}\mu_0)
\end{aligned} \tag{7.19}$$

The terms with $\mathbf{x}^T\Sigma^{-1}\mathbf{x}$ cancel out because they appear with opposite signs! This cancellation is crucial—it eliminates the quadratic terms in $\mathbf{x}$ that would have prevented us from getting a linear boundary. After the cancellation:

$$\mu_1^T\Sigma^{-1}\mathbf{x} - \mu_0^T\Sigma^{-1}\mathbf{x} - \frac{1}{2}\mu_1^T\Sigma^{-1}\mu_1 + \frac{1}{2}\mu_0^T\Sigma^{-1}\mu_0 \tag{7.20}$$
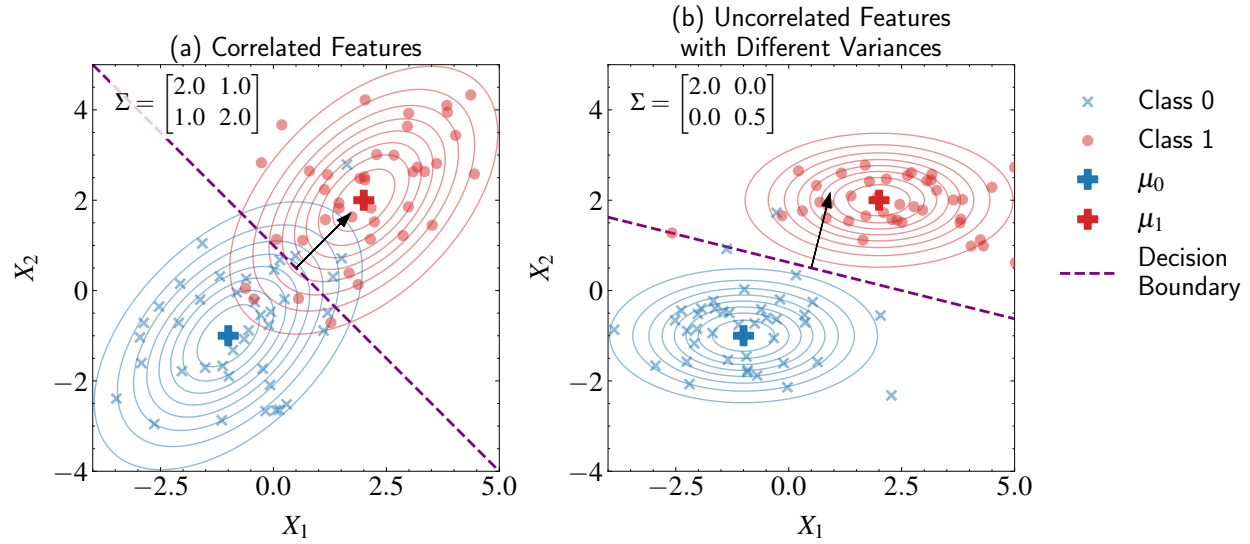
Figure 7.8: Illustration of how the covariance structure affects the optimal decision boundary in Gaussian generative models. Both panels share the same class means μ_0 and μ_1 but have different covariance matrices Σ. Panel (a) shows the case of correlated features, where off-diagonal terms in Σ create tilted elliptical contours, resulting in a decision boundary that accounts for this correlation. Panel (b) demonstrates uncorrelated features with different variances in each direction, producing axis-aligned elliptical contours of varying spread. In each case, the weight vector $\mathbf{w} \propto \Sigma^{-1}(\mu_1 - \mu_0)$ (black arrows) points in different directions because Σ^{-1} transforms the mean difference vector according to the feature covariance structure. The shape of the contours directly visualizes the role of Σ in determining how the features vary, while the decision boundaries (purple dashed lines) show how Σ^{-1} affects the optimal classification rule.

We can factor out $\Sigma^{-1}\mathbf{x}$:

$$(\mu_1 - \mu_0)^T\Sigma^{-1}\mathbf{x} - \frac{1}{2}(\mu_1^T\Sigma^{-1}\mu_1 - \mu_0^T\Sigma^{-1}\mu_0) \tag{7.21}$$

This gives us our final form:

$$\ln\left(\frac{P(C_1|\mathbf{x})}{P(C_0|\mathbf{x})}\right) = \mathbf{w}^T\mathbf{x} + b \tag{7.22}$$

where:

$$\mathbf{w} = \Sigma^{-1}(\mu_1 - \mu_0) \tag{7.23}$$

$$b = \ln\left(\frac{P(C_1)}{P(C_0)}\right) - \frac{1}{2}(\mu_1^T\Sigma^{-1}\mu_1 - \mu_0^T\Sigma^{-1}\mu_0) \tag{7.24}$$

The weight vector $\mathbf{w} = \Sigma^{-1}(\mu_1 - \mu_0)$ has a clear geometric interpretation. Intuitively,
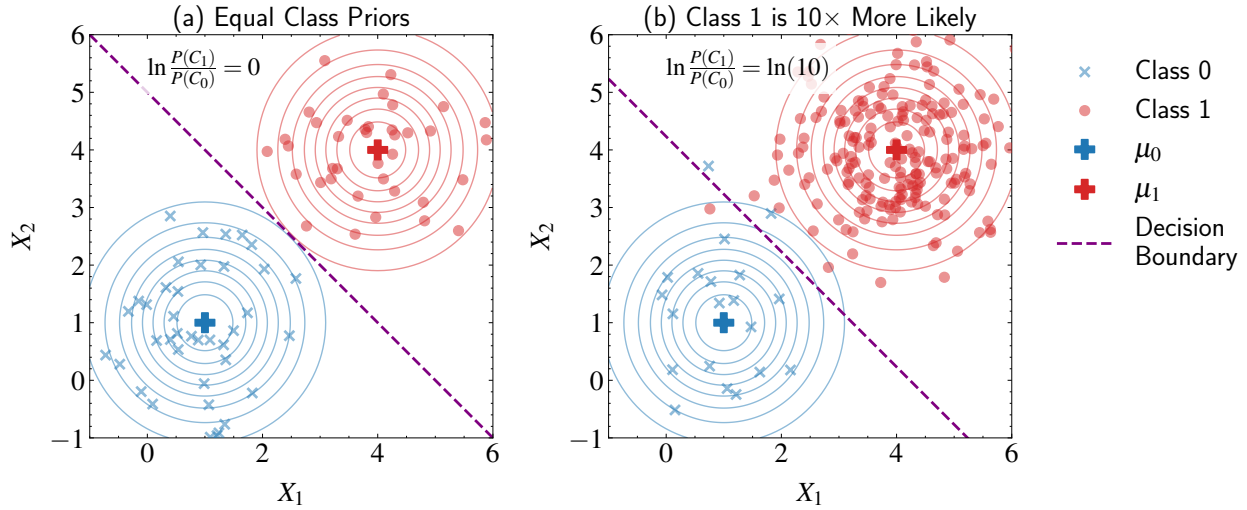
Figure 7.9: Demonstration of how class priors affect the decision boundary in logistic regression. Both panels show the same feature distributions (Gaussian contours) and weight vector orientation (determined by $\mathbf{w} = \Sigma^{-1}(\mu_1 - \mu_0)$), but with different class priors. Panel (a) shows the case of equal class priors ($\ln(P(C_1)/P(C_0)) = 0$), where the decision boundary (purple dashed line) is placed solely based on the feature distributions. Panel (b) shows the effect when Class 1 is ten times more likely than Class 0 ($\ln(P(C_1)/P(C_0)) = \ln(10)$), causing the boundary to shift towards Class 0 to reflect this prior knowledge. The number of sample points (crosses for Class 0, circles for Class 1) also reflects this class imbalance. This illustrates how the prior term in the intercept b can independently shift the decision boundary without affecting its orientation, allowing the classifier to account for known class imbalances in the training data.

we expect the decision boundary to lie somewhere between the two class centers, which explains why $(\mu_1 - \mu_0)$ forms the basis of our weight vector. However, this raw direction alone isn't enough—we need to account for how our data is distributed in feature space.

This is where Σ^{-1} comes in. It acts as a transformation matrix that adjusts the direction of $(\mu_1 - \mu_0)$ based on the covariance structure of our features. The exact effect of this transformation depends on the relationship between the covariance structure and the mean difference vector—in some cases preserving the original direction, in others rotating it to better account for the natural variations in our data. This ensures our decision boundary optimally separates the classes while accounting for their underlying distribution patterns.

Now let's examine the bias term b more carefully. Including back the prior term that we had temporarily set aside in our derivation, we see it has two distinct components:

$$b = \ln\left(\frac{P(C_1)}{P(C_0)}\right) - \frac{1}{2}(\mu_1^T \Sigma^{-1} \mu_1 - \mu_0^T \Sigma^{-1} \mu_0) \tag{7.25}$$

The first term, $\ln(P(C_1)/P(C_0))$, accounts for any class imbalance in our data. For instance, if stars are ten times more common than galaxies in our survey, this term would be $\ln(10)$, shifting our decision boundary to account for this prior knowledge. The second term, $-\frac{1}{2}(\mu_1^T \Sigma^{-1} \mu_1 - \mu_0^T \Sigma^{-1} \mu_0)$, works in conjunction with the weight vector $\mathbf{w} = \Sigma^{-1}(\mu_1 - \mu_0)$ to define the decision boundary. When Σ changes, both $\mathbf{w}$ and b change in a coordinated way to maintain the optimal decision boundary that accounts for both the feature covariance structure and the class means.

Having derived the log-odds ratio $\ln(P(C_1|\mathbf{x})/P(C_0|\mathbf{x})) = \mathbf{w}^T\mathbf{x}+b$ from our generative model assumptions, we can now convert this back to actual class probabilities. Since we know that $P(C_1|\mathbf{x}) + P(C_0|\mathbf{x}) = 1$ (the probabilities must sum to 1), and defining $z = \mathbf{w}^T\mathbf{x} + b$, we can solve:

$$\ln\left(\frac{P(C_1|\mathbf{x})}{1 - P(C_1|\mathbf{x})}\right) = z \tag{7.26}$$

This gives us:

$$P(C_1|\mathbf{x}) = \sigma(z) = \frac{1}{1 + e^{-z}} = \frac{1}{1 + e^{-(\mathbf{w}^T\mathbf{x}+b)}} \tag{7.27}$$

where $\sigma(z)$ is the sigmoid function. This transformation ensures our output is always between 0 and 1, as required for probabilities.

This derivation reveals the deep connection between generative and discriminative approaches to classification. Starting from a simple assumption about how our features are generated within each class (Gaussian distributions with equal covariance), we have arrived exactly at the logistic regression model with a linear discriminant boundary which we previously motivated from a discriminative perspective.

In other words, while logistic regression is typically presented as a discriminative model that directly predicts $P(C_1|\mathbf{x})$, we've now shown that it has a precise corresponding generative model: one where the features in each class follow Gaussian distributions with different means but the same covariance matrix. This connection provides deeper insight into why logistic regression works well in some situations but may struggle in others—if our data's true generative process differs significantly from these assumptions, logistic regression might not be the optimal choice.

The connection also helps us interpret the parameters of logistic regression in terms of the underlying data distributions. The weight vector $\mathbf{w}$ reflects both the difference between class means and how features covary, while the bias term b accounts for both class priors and the positions of class centers. This interpretation enriches our understanding of what logistic

regression is actually modeling when we apply it to astronomical classification problems.

7.5   Limitations of Logistic Regression

The mathematical bridge we've built between generative and discriminative approaches reveals several key insights about logistic regression and its inductive bias — the core assumptions that shape how the model learns and generalizes. When our features approximately follow Gaussian distributions with similar covariance structures, logistic regression emerges naturally as the optimal classifier. This isn't just mathematical convenience, but rather represents the model's inductive bias: it assumes our data classes can be separated by a linear boundary in feature space, which is precisely what we get when our features follow these Gaussian patterns.

The success of any machine learning method depends critically on how well its inductive bias matches the true structure of our data. The model parameters ($\mathbf{w}$ and b) have clear probabilistic interpretations tied to the means, covariances, and prior probabilities of our classes—they aren't arbitrary fitting parameters, but rather encode this Gaussian inductive bias into the model's structure. Understanding this bias helps us anticipate when logistic regression will succeed (when our data approximately follows these Gaussian assumptions) and when it might fail (when our data exhibits more complex, non-linear class boundaries).

However, we must ask: how realistic are these assumptions? In astronomy, different classes often exhibit quite different covariance structures. When classifying galaxies by morphology, spiral galaxies might show greater variance in certain color indices compared to elliptical galaxies due to their more complex star formation histories. Similarly, in star-galaxy separation, the spread of features for galaxies (with their diverse morphologies and redshifts) typically differs from the tighter distribution of stellar features. Poor performance with a linear boundary often indicates our features aren't following these Gaussian patterns.

Another limitation becomes apparent when classes aren't linearly separable in feature space. Consider trying to separate type Ia supernovae from other transients using light curve features. If the relationship between rise time, decay time, and supernova type forms a complex nonlinear boundary, logistic regression with raw features will struggle regardless of how much data we provide.

Despite these apparent limitations, logistic regression remains a powerful tool, largely due to our ability to transform our input features. Just as we saw with linear regression,

we're not constrained to work with raw features X—we can apply transformations $\phi(X)$ to create new features that better satisfy our assumptions. Consider a concrete example from astronomy. Imagine trying to separate stars from galaxies using apparent magnitude (m) and surface brightness (μ). A linear boundary in these raw features might perform poorly because their distributions aren't Gaussian. However, if we transform to $\log(m)$ and $\log(\mu)$, the distributions often become more Gaussian-like, making logistic regression more appropriate. Similarly, when classifying objects that form circular or spiral patterns in feature space, transforming from Cartesian to polar coordinates can often make the classes linearly separable, even though they weren't in the original space.
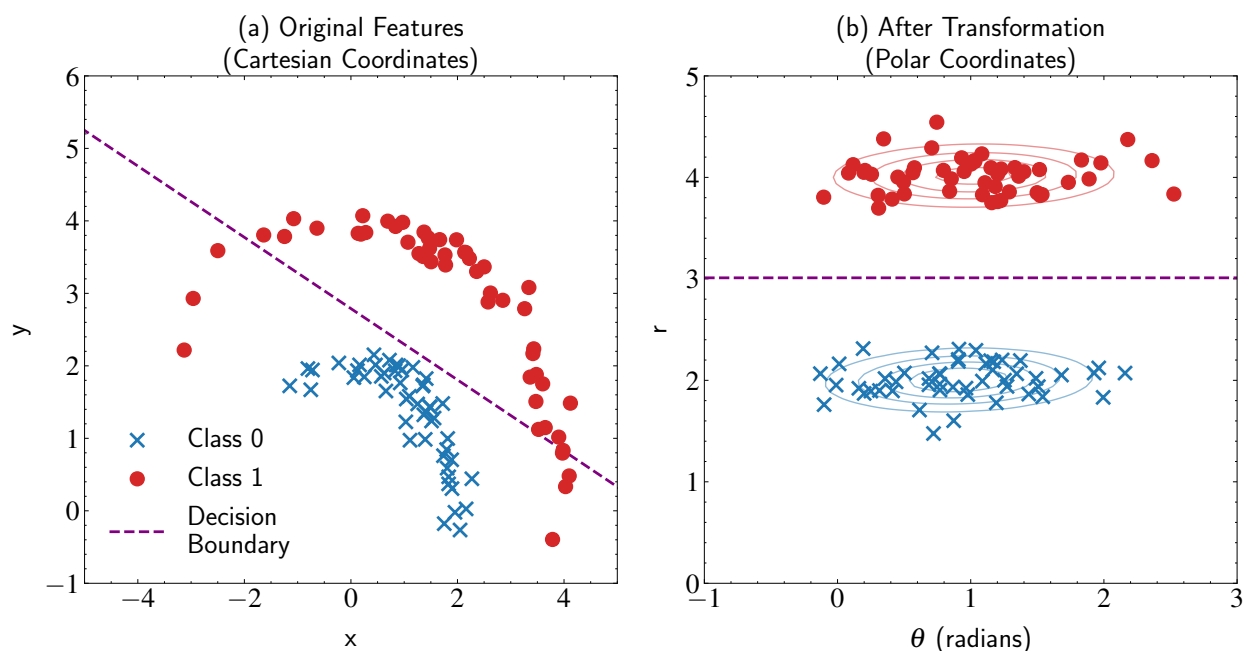
Figure 7.10: Demonstration of how feature transformations can improve classification performance. Panel (a) shows the original data in Cartesian coordinates, where two classes (blue crosses for Class 0, red circles for Class 1) form curved, non-linearly separable patterns. The purple dashed line shows the best linear decision boundary, which poorly separates the classes. Panel (b) shows the same data transformed into polar coordinates (θ-r space), where the classes become linearly separable. The contours show the Gaussian distributions fit to each class in this transformed space, and the purple dashed line shows the optimal linear decision boundary. This illustrates how appropriate feature transformations can make logistic regression's linear boundary assumption more valid by reshaping the data distribution.

This process of creating new, more informative features—known as feature engineering—has historically been crucial in astronomical classification. Common transformations include taking logarithms of fluxes to work with magnitudes, computing color indices from raw fluxes, creating concentration indices from different aperture measurements, and calcu-

lating various morphological parameters. Each of these transformations represents domain knowledge about what features might better separate our classes. When we write $\mathbf{w}^T\phi(\mathbf{x})$ instead of $\mathbf{w}^T\mathbf{x}$, we're essentially encoding our astronomical understanding into the model.

For instance, in photometric classification of quasars, simple color cuts in $(u - g)$ vs. $(g - r)$ space can effectively separate quasars from stars at certain redshifts. This works because these specific color combinations trace the distinctive spectral energy distributions of quasars. The transformation from flux measurements to colors creates a feature space where the classes become more separable.

One of logistic regression's key advantages is its interpretability. Its linear form $\mathbf{w}^T\phi(\mathbf{x})$ provides immediate insight into how each feature contributes to the classification decision. The weight vector $\mathbf{w}$ directly tells us the relative importance of each feature—a larger absolute weight indicates that feature plays a more crucial role in the classification. For instance, in star-galaxy separation using photometric features, if the weight for the $g - r$ color is larger than for $r - i$, we immediately understand that $g - r$ is more important for the classification. This transparency is particularly valuable in astronomy where we need to verify that our model's decisions align with physical understanding.

Moreover, because the decision boundary is linear, we can easily visualize and understand how the model makes its decisions. In a two-feature space, we can literally draw the line that separates our classes. Even in higher dimensions, we can project onto the most important feature directions to understand the model's behavior. This geometric interpretability means we can verify whether the model is using physically sensible criteria for its classifications. For example, if we're using concentration index and color to separate stars from galaxies, we can directly verify that our model is placing the decision boundary where we expect based on physical principles—stars being more point-like and following stellar locus colors.

Understanding these limitations and extensions of logistic regression proves crucial in practice. When our classes can be reasonably separated by a linear boundary in some feature space, logistic regression offers an excellent combination of performance, interpretability, and computational efficiency. When they cannot, we must either find better feature transformations or consider more flexible models. This understanding of inductive bias—what our model assumes about the data—forms the foundation for making informed choices about classification approaches in astronomy.

7.6 Maximum Likelihood and Cross-Entropy Loss

Having established how logistic regression emerges naturally from our probabilistic assumptions, we now turn to a crucial question: how do we actually find the optimal parameters $\mathbf{w}$ and b for our model? In our earlier derivation of the generative approach, we saw that when our data truly follows Gaussian distributions with equal covariance matrices, the optimal parameters have an elegant form: $\mathbf{w} = \Sigma^{-1}(\mu_1 - \mu_0)$ and $b = \ln(P(C_1)/P(C_0)) - (1/2)(\mu_1^T \Sigma^{-1} \mu_1 - \mu_0^T \Sigma^{-1} \mu_0)$.

However, this solution becomes problematic in practice. Real astronomical data rarely follows exactly Gaussian distributions with equal covariances—consider how the spread of features for spiral galaxies might differ dramatically from ellipticals. While these generative models provide valuable intuition and help us understand the limitations of logistic regression, they shouldn't constrain our approach. Even when the Gaussian assumptions fail, we can still seek the best linear decision boundary directly through discriminative modeling, letting the data itself guide us to the optimal separation between classes.

Just as we did with linear regression, we'll approach this through the lens of maximum likelihood estimation—we want to find the parameters that maximize the probability of observing our actual training data. This principle of maximizing the likelihood of our observations underpins most optimization problems in machine learning.

Following the notation in linear regression, in our probabilistic framework, each observation $(\mathbf{x}_i, t_i)$ represents a data point with features $\mathbf{x}_i$ and a binary label $t_i \in \{0, 1\}$. Recall from our extensive derivation above that our model predicts the probability of class membership through the sigmoid function:

$$P(C_1|\mathbf{x}_i, \mathbf{w}) = y_i = \sigma(\mathbf{w}^T \mathbf{x}_i) \tag{7.28}$$

where, as in linear regression, we've absorbed the bias term b into $\mathbf{w}$ by augmenting our feature vector with a constant 1. Following our earlier astronomical example, y_i might represent the probability that the ith object is a star rather than a galaxy.

The likelihood function represents the probability of observing our entire dataset under our model. Assuming our observations are independent (a standard assumption, though not always valid in astronomy where spatial and temporal correlations often exist),

we can write the likelihood as a product:

$$L(\mathbf{w}) = \prod_{i=1}^{N} P(t_i|\mathbf{x}_i, \mathbf{w}) \tag{7.29}$$

For each observation, the contribution to this product depends on its true class:

- If $t_i = 1$ (e.g., the object is actually a star), we want $P(C_1|\mathbf{x}_i, \mathbf{w}) = y_i$

- If $t_i = 0$ (e.g., the object is actually a galaxy), we want $P(C_0|\mathbf{x}_i, \mathbf{w}) = 1 - y_i$

We can combine these cases into a single expression:

$$L(\mathbf{w}) = \prod_{i=1}^{N} y_i^{t_i}(1 - y_i)^{1-t_i} \tag{7.30}$$

This compact form handles both classes through the exponents t_i and $(1 - t_i)$. For stars $(t_i = 1)$, the second term becomes $(1 - y_i)^0 = 1$, leaving just y_i. For galaxies $(t_i = 0)$, the first term becomes $y_i^0 = 1$, leaving $(1 - y_i)$.

This likelihood looks familiar—it's precisely the Bernoulli likelihood we encountered when discussing conjugate priors. However, there's a crucial difference: while in the Bernoulli case we directly optimized the probability parameter, now that parameter is determined by our linear model through the sigmoid transformation:

$$y_i = \sigma(\mathbf{w}^T\mathbf{x}_i) = \frac{1}{1 + e^{-\mathbf{w}^T\mathbf{x}_i}} \tag{7.31}$$

While the foundational principle remains the same—maximizing the likelihood of our observations.

Just as in linear regression, we'll work with the negative log-likelihood to convert our product into a sum and improve numerical stability. We take the negative here because most optimization algorithms are designed to minimize rather than maximize. This transformation serves multiple practical purposes: it converts products into sums which are computationally easier to handle, prevents numerical underflow from multiplying many small probabilities, and frames our problem as minimizing a loss:

$$E(\mathbf{w}) = -\ln L(\mathbf{w}) = -\sum_{i=1}^{N}[t_i \ln y_i + (1 - t_i)\ln(1 - y_i)] \tag{7.32}$$

To ensure that our loss function scales appropriately with the size of our dataset, we typically divide by the number of samples N:

$$E(\mathbf{w}) = -\frac{1}{N} \sum_{i=1}^{N} [t_i \ln y_i + (1 - t_i) \ln(1 - y_i)] \tag{7.33}$$

This normalization is important because it ensures that the magnitude of the loss remains roughly the same regardless of how many data points we have, which facilitates optimization by keeping gradients at a consistent scale. Without this normalization, adding more data would artificially inflate the loss value and potentially require adjustments to optimization parameters like the learning rate.

This expression is known as the cross-entropy loss function, a name that comes from information theory. The term "cross-entropy" arises because we're measuring the difference between two probability distributions: our model's predictions (y_i) and the true labels (t_i). In information theory, entropy measures the average information content or "surprise" in a probability distribution, and cross-entropy measures how different two distributions are.

To understand why this is such a natural measure for classification, let's examine what happens for a single data point:

- For a star ($t_i = 1$), if we correctly predict $y_i \approx 1$, then $\ln y_i \approx 0$, implying little penalty

- But if we incorrectly predict $y_i \approx 0$, then $\ln y_i \to -\infty$, implying severe penalty

- Similarly for galaxies ($t_i = 0$), predicting $y_i \approx 0$ gives small loss, while $y_i \approx 1$ is heavily penalized

This behavior makes cross-entropy loss particularly effective for classification tasks—it naturally enforces a strong penalty for confident but wrong predictions, while rewarding accurate predictions with minimal loss. The asymmetric nature of the penalty (approaching infinity for severe mistakes) helps push the model toward making careful predictions.

Writing out the full optimization problem we need to solve:

$$\mathbf{w}^* = \operatorname{argmin}_{\mathbf{w}} \left\{ -\frac{1}{N} \sum_{i=1}^{N} \left[t_i \ln \sigma(\mathbf{w}^T \mathbf{x}_i) + (1 - t_i) \ln(1 - \sigma(\mathbf{w}^T \mathbf{x}_i)) \right] \right\} \tag{7.34}$$

Here, $\operatorname{argmin}_{\mathbf{w}}$ means we want to find the value of $\mathbf{w}$ that minimizes the expression.

Unlike linear regression, this optimization problem doesn't have a closed-form solution. The nonlinearity introduced by the sigmoid function prevents us from solving for $\mathbf{w}$ analytically by setting the derivatives to zero. Instead, we need computational optimization techniques, particularly gradient descent, to iteratively find the optimal parameter values. This marks an important transition in our exploration of machine learning methods—from problems with analytical solutions to those requiring numerical optimization, a theme that will continue as we explore more complex models in later chapters.

7.7   Gradient Descent for Logistic Regression

Having derived our cross-entropy loss function, we now face a challenge: how do we find the weights $\mathbf{w}$ that minimize this loss? Unlike linear regression, we can't solve this analytically by setting derivatives to zero. Instead, we need to explore the loss landscape and find its minimum through an iterative process.

The intuition behind gradient descent is straightforward. Imagine our loss function $E(\mathbf{w})$ creates a landscape in the space of possible weight vectors $\mathbf{w}$. Each point in this landscape represents a particular choice of weights, and the height at that point represents the loss value—how poorly our model performs with those weights. Our goal is to find the lowest point in this landscape, where our model performs best.

Think of yourself standing somewhere on this weight-space landscape, trying to reach the valley. Your natural strategy would be to feel the steepness and direction of the slope, take a step downhill proportional to how steep it is, and repeat this process until you reach a flat spot, which hopefully corresponds to optimal weights.

This physical intuition translates into mathematics. The slope we feel at any point $\mathbf{w}$ is the gradient $\nabla E(\mathbf{w})$—a vector pointing in the direction of steepest ascent in weight space. Since we want to go downhill, we move in the negative gradient direction. The size of our step is controlled by a parameter η, called the learning rate:

$$\mathbf{w}^{(new)} = \mathbf{w}^{(old)} - \eta \nabla E(\mathbf{w}) \tag{7.35}$$

To use this approach, we need to compute the gradient of our cross-entropy loss with respect to the weights. Let's break down this calculation step by step.

First, let's understand the nonlinearity in our model: the sigmoid function. Its deriva-
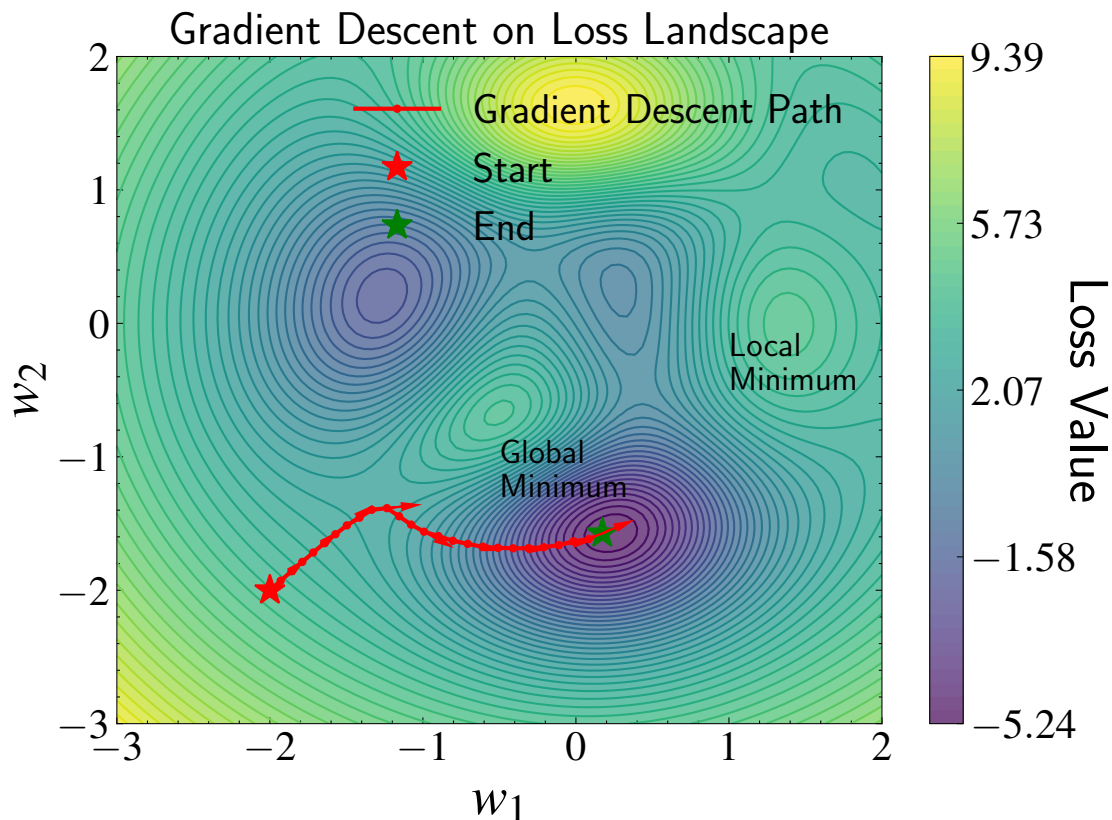
Figure 7.11: Visualization of gradient descent optimization in weight space. The contours represent the loss landscape $E(\mathbf{w})$, with darker colors indicating higher loss values. The red path shows the trajectory of gradient descent starting from a high-loss region (red star), with arrows indicating the negative gradient direction $-\nabla E(\mathbf{w})$ at each step. The learning rate η determines the step size along this path. The landscape illustrates common optimization challenges: multiple local minima that could trap the optimization, varying gradient magnitudes across the space, and plateau regions where gradients become small. The global minimum (annotated) represents the optimal weight configuration, while local minima demonstrate potential convergence points that may not be globally optimal.

tive turns out to have a simple form:

$$\frac{d\sigma(z)}{dz} = \sigma(z)(1 - \sigma(z)) \tag{7.36}$$

We can derive this directly. Recall that $\sigma(z) = \frac{1}{1+e^{-z}}$. Using the chain rule:

$$
\begin{aligned}
\frac{d\sigma(z)}{dz} &= \frac{d}{dz}\left(\frac{1}{1+e^{-z}}\right) \\
&= -(1+e^{-z})^{-2} \cdot \frac{d}{dz}(1+e^{-z}) \\
&= -(1+e^{-z})^{-2} \cdot (-e^{-z}) \\
&= \frac{e^{-z}}{(1+e^{-z})^2} \\
&= \frac{1}{1+e^{-z}} \cdot \frac{e^{-z}}{1+e^{-z}} \\
&= \frac{1}{1+e^{-z}} \cdot \left(1 - \frac{1}{1+e^{-z}}\right) \\
&= \sigma(z)(1 - \sigma(z))
\end{aligned}
$$

This simple form of the sigmoid derivative is convenient. For any given weight vector $\mathbf{w}$ and input $\mathbf{x}$, when we compute $z = \mathbf{w}^T\mathbf{x}$ and evaluate $\sigma(z)$, we can simultaneously evaluate the gradient by simply plugging the same $\sigma(z)$ value into the derivative formula $\sigma(z)(1 - \sigma(z))$. This computational efficiency becomes crucial during optimization.

With the gradient of the sigmoid function, we are now set to tackle the gradient of our loss function. Recall that the cross-entropy loss is:

$$
E(\mathbf{w}) = -\frac{1}{N}\sum_{i=1}^{N}[t_i \ln y_i + (1 - t_i)\ln(1 - y_i)] \tag{7.37}
$$

where $y_i = \sigma(\mathbf{w}^T\mathbf{x}_i)$. To find $\partial E/\partial w_j$, we need to carefully apply the chain rule. Let's break this down step by step:

First, consider how y_i depends on w_j:

$$
\frac{\partial y_i}{\partial w_j} = \frac{\partial}{\partial w_j}\sigma(\mathbf{w}^T\mathbf{x}_i) = \sigma(\mathbf{w}^T\mathbf{x}_i)(1 - \sigma(\mathbf{w}^T\mathbf{x}_i))x_{ij} = y_i(1 - y_i)x_{ij} \tag{7.38}
$$

Now, taking the derivative of our loss with respect to w_j:

$$\frac{\partial E}{\partial w_j} = -\frac{1}{N} \sum_{i=1}^{N} \left[t_i \frac{\partial}{\partial w_j} \ln y_i + (1-t_i) \frac{\partial}{\partial w_j} \ln(1-y_i) \right]$$

$$= -\frac{1}{N} \sum_{i=1}^{N} \left[t_i \frac{1}{y_i} \frac{\partial y_i}{\partial w_j} + (1-t_i) \frac{1}{1-y_i} \frac{\partial(1-y_i)}{\partial w_j} \right]$$

$$= -\frac{1}{N} \sum_{i=1}^{N} \left[t_i \frac{1}{y_i} \frac{\partial y_i}{\partial w_j} - (1-t_i) \frac{1}{1-y_i} \frac{\partial y_i}{\partial w_j} \right]$$

Substituting our expression for $\partial y_i / \partial w_j$:

$$\frac{\partial E}{\partial w_j} = -\frac{1}{N} \sum_{i=1}^{N} \left[t_i \frac{1}{y_i} - (1-t_i) \frac{1}{1-y_i} \right] y_i(1-y_i) x_{ij}$$

$$= -\frac{1}{N} \sum_{i=1}^{N} \left[t_i(1-y_i) - (1-t_i)y_i \right] x_{ij}$$

$$= -\frac{1}{N} \sum_{i=1}^{N} (t_i - y_i) x_{ij}$$

Therefore, the gradient vector is:

$$\nabla E(\mathbf{w}) = -\frac{1}{N} \sum_{i=1}^{N} (t_i - y_i)\mathbf{x}_i = \frac{1}{N} \sum_{i=1}^{N} (y_i - t_i)\mathbf{x}_i \tag{7.39}$$

This gradient expression is insightful both in its mathematical compactness and its interpretation. After the calculus manipulation, we arrive at a compact form that reveals the learning mechanism of our model. Note that in the formalism above, we have absorbed the bias term into the weight vector by augmenting our feature vectors with a constant term.

The gradient is driven entirely by the prediction error $(y_i - t_i)$, scaled by the features $\mathbf{x}_i$ that led to that prediction. Let's understand why this makes intuitive sense. When our prediction matches the true label $(y_i = t_i)$, that sample contributes nothing to the gradient. This is exactly what we want—there's no need to adjust weights that are already giving correct predictions. But when we predict incorrectly $(y_i \neq t_i)$, the model updates its weights in a very specific way. The magnitude of the update depends on two factors: how wrong we were (the size of $y_i - t_i$), and the strength of the features that led to that mistake ($\mathbf{x}_i$).
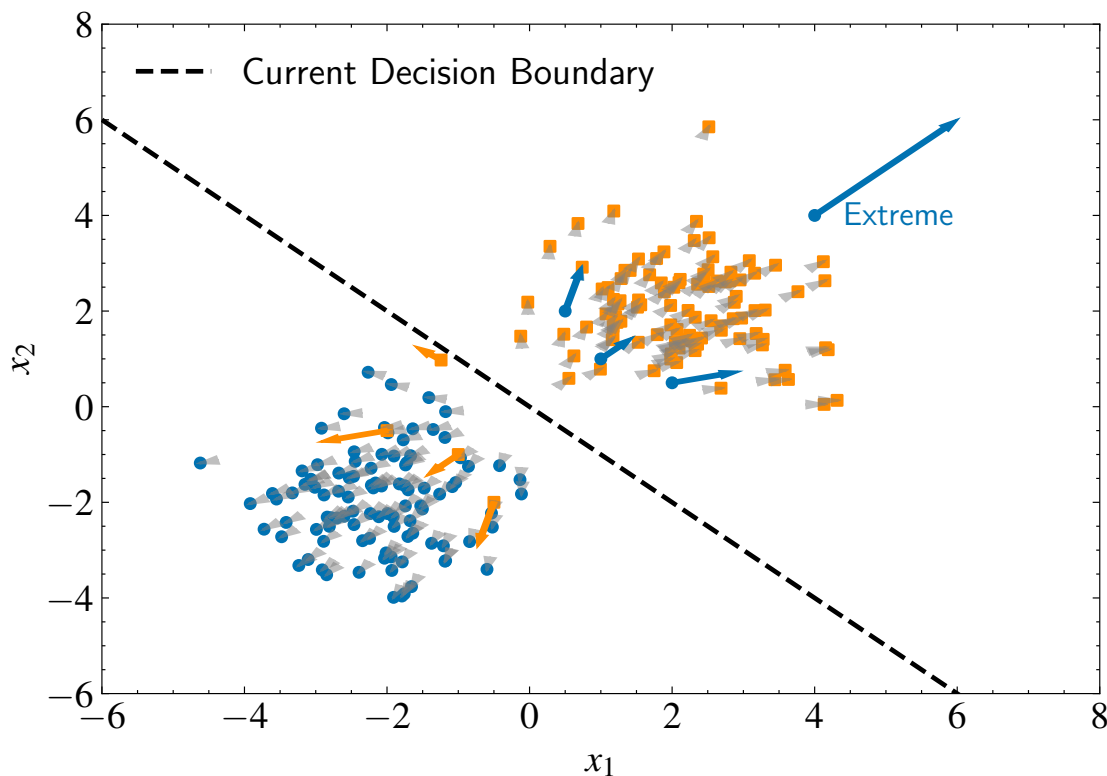
Figure 7.12: Visualization of gradient contributions in logistic regression. The plot shows data points from two classes (blue circles for class 0, orange squares for class 1) along with their gradient vectors. The dashed line represents the current decision boundary. Each point's gradient is represented by an arrow, with length proportional to both the prediction error and feature magnitude. Correctly classified points have shorter, grey arrows, while misclassified points have longer, colored arrows in their respective class colors. Note how the "Extreme" point, being far from the decision boundary, contributes a large gradient due to both its high prediction error and large feature magnitude. This visualization demonstrates two key properties of logistic regression gradients: (1) misclassified points contribute larger gradients than correctly classified ones, and (2) points with larger feature magnitudes generate proportionally larger gradients, as evidenced by the arrow lengths.

Consider classifying stars versus galaxies. If we misclassify an object that has very clear stellar features (large values in the relevant components of $\mathbf{x}_i$), the gradient will push for a larger correction than if we misclassify an ambiguous object with weak features. Similarly, a confident wrong prediction (e.g., predicting $y_i = 0.9$ for a galaxy) generates a larger gradient than an uncertain wrong prediction (e.g., predicting $y_i = 0.6$). The model automatically prioritizes fixing its most egregious errors while being more cautious about borderline cases.

The computational efficiency of this gradient expression becomes crucial in practice. At each step, we only need to:

1. Compute current predictions $y_i = \sigma(\mathbf{w}^T \mathbf{x}_i)$

2. Calculate prediction errors $(y_i - t_i)$

3. Scale our features by these errors

With this gradient in hand, we can now fully understand our gradient descent algorithm. At each iteration t, we update our weights according to:

$$\mathbf{w}^{(t+1)} = \mathbf{w}^{(t)} - \eta \frac{1}{N} \sum_{i=1}^{N} (y_i^{(t)} - t_i)\mathbf{x}_i \tag{7.40}$$

This update rule embodies the core principle of gradient descent—by taking steps in the direction opposite to the gradient, we systematically descend the loss surface toward a minimum.

7.7.1 Stochastic Gradient Descent

While the gradient expression is computationally straightforward, calculating it over large astronomical datasets becomes impractical. Here, N represents the size of our training set—the number of labeled examples we use to train our model. In modern astronomical surveys, N can range from millions of objects to billions of measurements. Each weight update requires a sum over all N training examples, making the computational cost per iteration $\mathcal{O}(N)$.

The key insight of Stochastic Gradient Descent (SGD) is that we don't need the exact gradient—an approximation might be good enough. Just as we can estimate population statistics using random samples, we can approximate the gradient using a small random subset of data:

$$\nabla E(\mathbf{w}) \approx \frac{1}{M} \sum_{i=1}^{M} (y_i - t_i)\mathbf{x}_i \tag{7.41}$$

where M is our batch size (typically 32-128 samples), much smaller than N. This approximation works because, if our training examples are drawn from the same underlying distribution, a random sample provides an unbiased estimate of the full gradient's direction.

Think of it like taking a survey of galaxy properties. While measuring every galaxy would give us the most accurate statistics, we can get reasonably good estimates from a random sample, and we can take many such samples in the time it would take to measure

the full population. Similarly, SGD lets us make rapid progress by taking many steps in approximately the right direction, rather than fewer steps in exactly the right direction.

Like in bootstrapping discussed in Chapter 3, larger samples give us lower variance estimates, but the key trade-off is different here. While our mini-batch gradients are noisier than the full gradient, they allow us to make many more parameter updates for the same computational cost.
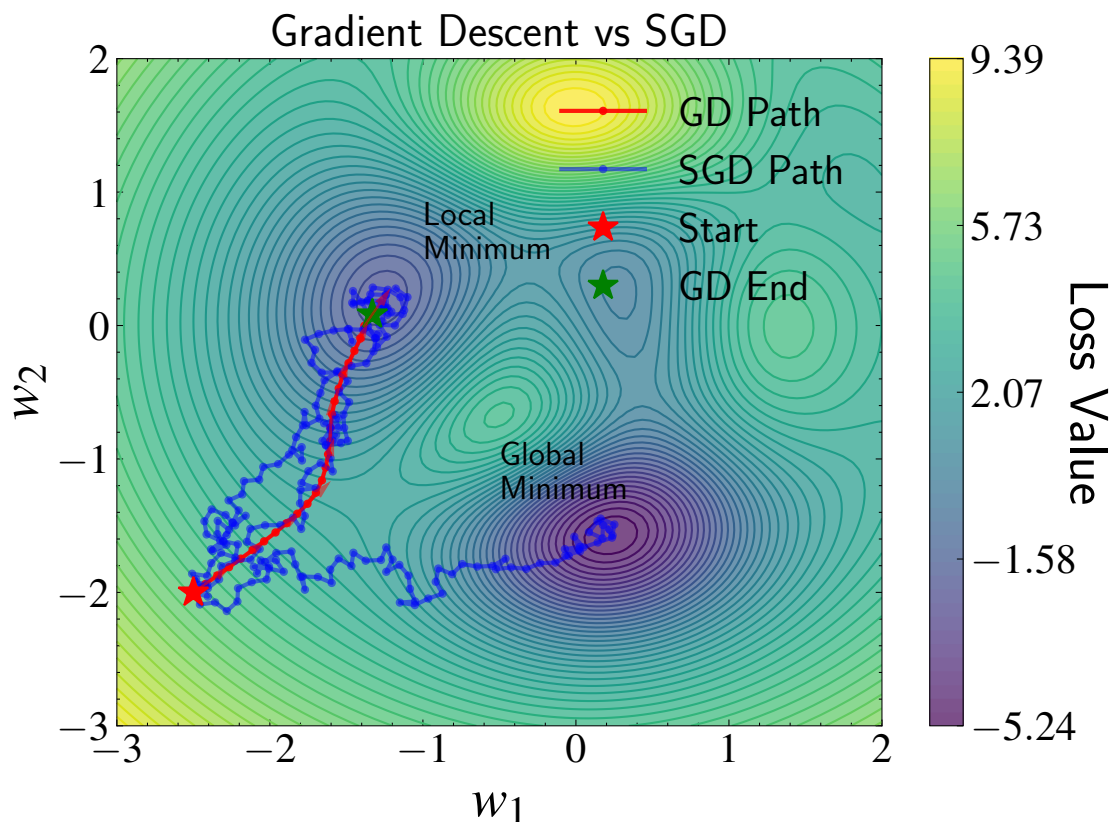
Figure 7.13: Comparison of Gradient Descent (GD) and Stochastic Gradient Descent trajectories in weight space. The contour plot shows the loss landscape $E(\mathbf{w})$, with darker colors indicating lower loss values. The red path shows the deterministic GD trajectory, which follows the exact gradient at each step. The blue paths demonstrate multiple possible SGD trajectories, illustrating its stochastic nature. While GD follows a direct path toward a local minimum, SGD's added noise allows it to explore more of the parameter space and potentially escape local minima. Starting from the same point (red star), GD converges to a local minimum (green star), while SGD paths show more exploration and can potentially find the global minimum.

An interesting and often beneficial aspect of SGD is that its inherent noise enables broader exploration of the parameter space. While GD moves deterministically along the steepest descent direction, SGD's stochastic behavior can help avoid convergence to poor

local minima, which is particularly important in non-convex optimization problems common in machine learning. The trade-off between exploitation (following the gradient) and exploration (random perturbations) is controlled by the noise magnitude in the gradient estimates, which in practice is determined by the batch size—smaller batches typically introduce more variance in the gradient estimates.

This stochastic approach thus transforms our update rule from processing the entire dataset to working with mini-batches:

$$\mathbf{w}^{(t+1)} = \mathbf{w}^{(t)} - \eta \cdot \frac{1}{M} \sum_{i=1}^{M} (y_i - t_i)\mathbf{x}_i \tag{7.42}$$

The benefits of SGD go beyond just computational efficiency. As we saw earlier, the stochastic nature of mini-batch sampling provides a form of regularization and exploration that can help avoid poor local minima. The frequent parameter updates also allow the model to make rapid progress early in training when the initial parameters are far from optimal.

7.8   Hyperparameters and Regularization

Besides the mini-batch sampling discussed above which could help us navigate the loss landscape more efficiently, equally crucial is how large a step we take in our chosen direction. This is controlled by the learning rate η.

Learning rate considerations.   Think of the learning rate like the size of a wheel rolling down our loss landscape. A large wheel (large η) can roll over small bumps and valleys, potentially helping escape local minima, but might also bounce erratically down steep slopes and miss deeper valleys entirely. A small wheel (small η) follows the terrain more precisely and can dig deep when needed to find better minima, but might get stuck in every minor depression. In astronomical terms, it's like the difference between slewing a telescope with coarse or fine adjustments:

- Large η is like using coarse slewing—you can cover large distances quickly but might overshoot your target

- Small η is like using fine adjustment knobs—precise but painfully slow for large movements

Both the learning rate η and batch size M are what we call hyperparameters—parameters that control the learning process itself rather than being learned from the data. Unlike our weights $\mathbf{w}$ which are optimized by gradient descent, hyperparameters must be chosen before training begins. Their choice is particularly challenging because we typically don't know the shape of our loss landscape a priori—it's like trying to choose the right wheel size for navigating terrain we can't fully see.

For simple problems, we might use a grid search to find good hyperparameter values. We typically search learning rates on a logarithmic scale (e.g., $\{10^{-4}, 10^{-3}, 10^{-2}, 10^{-1}\}$) to efficiently explore a wide dynamic range of values. This allows us to test learning rates that differ by orders of magnitude with relatively few trials. Similarly, we might try batch sizes that are powers of 2 (e.g., $\{32, 64, 128, 256\}$). While for our simple logistic regression implementation this choice is not crucial, in more complex models trained on GPUs, powers of 2 are preferred because GPU memory and compute architectures are optimized for such sizes. While more sophisticated approaches exist for hyperparameter tuning, a simple grid search often suffices for logistic regression.

Learning rate schedules.   Using a fixed learning rate throughout training isn't always optimal. For more complex problems, we often want to start with larger steps to quickly reach approximately the right region of parameter space, then gradually take smaller steps to refine our solution. A simple but effective learning rate schedule that achieves this balance, known as inverse time decay, is:

$$\eta^{(t)} = \frac{\eta_0}{1 + \gamma t} \tag{7.43}$$

where η_0 is our initial learning rate and γ is the decay rate that controls how quickly the learning rate diminishes over time.

This schedule has an intuitive analogy to our earlier wheel metaphor: initially, with a large learning rate ($\eta \approx \eta_0$), we use a big wheel that can roll quickly across the loss landscape. As training progresses (t increases), the denominator grows and η shrinks, effectively switching to a smaller wheel that can navigate the terrain more precisely. The decay parameter γ determines this transition—larger values favor quick refinement, while smaller values maintain exploration longer.

Building on this concept of dynamic learning rates, more sophisticated approaches like cosine annealing with warm-up have emerged. Drawing inspiration from metallurgy, where careful heating and cooling creates stronger materials, we start by warming up the
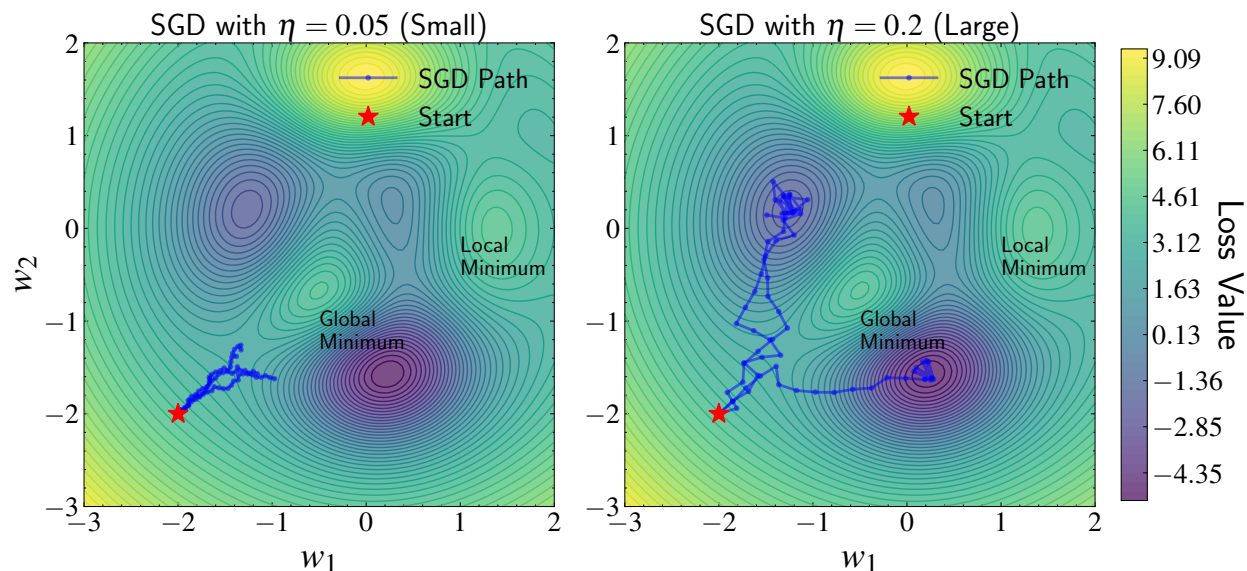
Figure 7.14: Comparison of Stochastic Gradient Descent behavior with different learning rates η. Both panels show the same loss landscape $E(\mathbf{w})$ with contours indicating level sets of the loss function, where darker colors represent lower loss values. **Left:** With a small learning rate ($\eta = 0.05$), the trajectories show more conservative exploration, following the gradient more closely but potentially getting trapped in local minima. **Right:** With a larger learning rate ($\eta = 0.2$), the paths exhibit more extensive exploration of the parameter space, potentially escaping local minima but risking overshooting optimal points. Multiple SGD paths (blue) starting from the same initialization point (red star) demonstrate how the combination of stochastic gradients and learning rate affects the optimization dynamics. In both cases, we observe the characteristic "noisy" trajectories of SGD compared to standard gradient descent, arising from the stochastic gradient estimates. This visualization highlights the crucial role of learning rate selection in balancing between exploitation and exploration.

learning rate from a small value to η_0, then follow a cosine schedule:

$$\eta^{(t)} = \eta_{\min} + \frac{1}{2}(\eta_0 - \eta_{\min})\left(1 + \cos\left(\frac{t\pi}{T}\right)\right) \tag{7.44}$$

where T is the total number of steps. Like the controlled cooling process in metallurgy that allows atoms to find their optimal arrangement, this creates a smooth transition from high to low learning rates.

In practice, we often run this schedule for only a quarter of the period ($T/4$) before restarting back at η_0. This cyclic pattern of exploration (high learning rate) followed by exploitation (low learning rate) helps the model escape local minima while still allowing for precise optimization—similar to how repeated heating and cooling cycles in metallurgy can progressively refine a metal's structure.
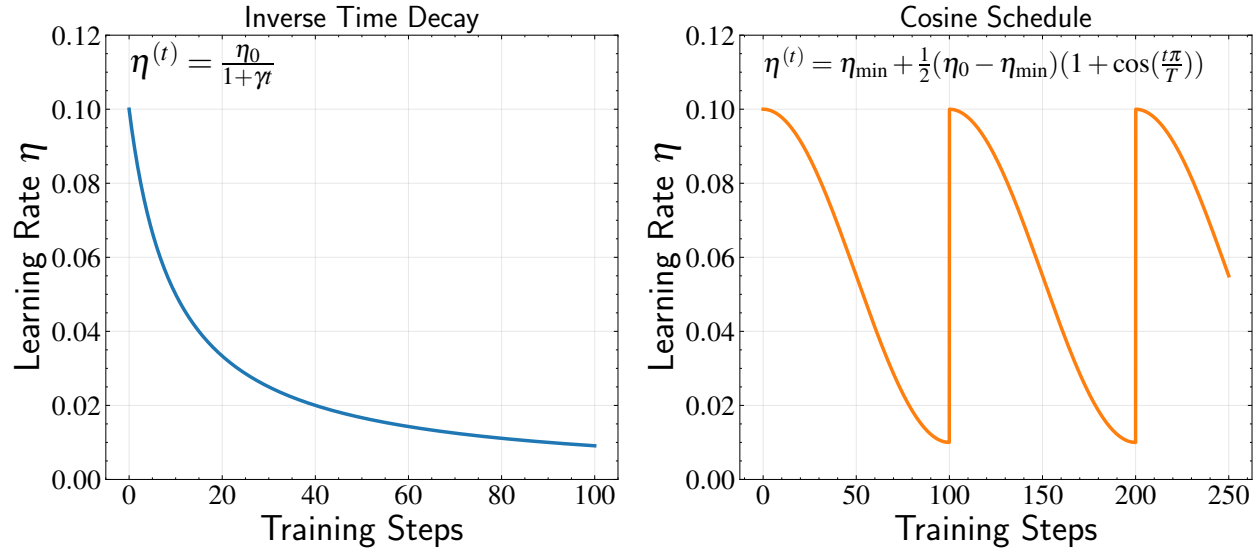
Figure 7.15: Comparison of two learning rate scheduling strategies. **Left:** Inverse time decay schedule with $\eta^{(t)} = \frac{\eta_0}{1+\gamma t}$, showing a monotonic decrease in learning rate that starts rapid and becomes increasingly gradual. This schedule embodies the intuition that large steps are most beneficial early in training, with progressively finer adjustments needed as we approach convergence. **Right:** Cosine annealing schedule with restarts, where $\eta^{(t)} = \eta_{\min} + \frac{1}{2}(\eta_0 - \eta_{\min})(1 + \cos(t\pi/T))$. The cyclic nature of this schedule allows periodic returns to higher learning rates, potentially helping escape local minima. Each cycle begins with a phase of exploration (high learning rate) and ends with exploitation (low learning rate), similar to the repeated heating and cooling cycles in metallurgical annealing processes.

Regularization.   As we've seen in previous chapters, gradient descent alone doesn't protect against overfitting. Especially with high-dimensional feature spaces common in astronomy, our model can easily fit noise in the training data rather than real patterns. Regularization addresses this problem by adding a penalty for complex models to our loss function.

The standard approach, called L2 regularization or weight decay, adds a penalty proportional to the squared norm of the weight vector:

$$E_{\text{reg}}(\mathbf{w}) = E(\mathbf{w}) + \lambda \|\mathbf{w}\|^2 = -\frac{1}{N} \sum_{i=1}^{N} [t_i \ln y_i + (1 - t_i) \ln(1 - y_i)] + \lambda \sum_{j=1}^{D} w_j^2 \qquad (7.45)$$

where λ is the regularization strength and D is the number of features. This modification changes our gradient descent update:

$$\nabla E_{\text{reg}}(\mathbf{w}) = \nabla E(\mathbf{w}) + 2\lambda \mathbf{w} = \frac{1}{N} \sum_{i=1}^{N} (y_i - t_i)\mathbf{x}_i + 2\lambda \mathbf{w} \qquad (7.46)$$

This new term $2\lambda\mathbf{w}$ in the gradient continuously pulls weights toward zero during optimization, with strength proportional to λ. Intuitively, this prevents any single weight from becoming excessively large, which would indicate that the model is overrelying on a specific feature—a classic sign of overfitting.

From a Bayesian perspective, this regularization is equivalent to assuming a Gaussian prior on the weights, just as we saw in linear regression. Recall that in the Bayesian framework, the posterior distribution is proportional to the product of the likelihood and the prior:

$$p(\mathbf{w}|\mathcal{D}) \propto p(\mathcal{D}|\mathbf{w})p(\mathbf{w}) \tag{7.47}$$

When we assume a Gaussian prior on the weights with zero mean and variance $1/2\lambda$:

$$p(\mathbf{w}) \propto \exp\left(-\lambda\|\mathbf{w}\|^2\right) \tag{7.48}$$

maximizing the posterior becomes equivalent to minimizing the negative log-posterior:

$$-\ln p(\mathbf{w}|\mathcal{D}) = -\ln p(\mathcal{D}|\mathbf{w}) - \ln p(\mathbf{w}) = E(\mathbf{w}) + \lambda\|\mathbf{w}\|^2 + \text{const.} \tag{7.49}$$

This Bayesian interpretation helps us understand regularization as a way of navigating the bias-variance tradeoff. Without regularization, our model might fit training data perfectly but fail to generalize to new observations (high variance). With very strong regularization, our model might not even fit training data well (high bias). The optimal λ gives us the right balance, and in a Bayesian framework, it corresponds to the correct strength of our prior beliefs.

In practical astronomical applications, proper regularization is particularly important when dealing with high-dimensional data like spectra, where the number of features can exceed the number of training examples. For instance, when classifying stellar types based on spectral features, regularization helps prevent the model from fitting to noise in specific wavelengths, instead encouraging it to identify broader, more robust patterns across the spectrum.

7.9   Implementation Considerations

We now turn to several practical considerations that can make or break our training process. Even with well-chosen learning rates and batch sizes, several pitfalls can derail our optimization. The logistic regression implementation needs safeguards against various numerical issues that can corrupt our results.

Numerical stability.   The most fundamental challenge arises in computing our cross-entropy loss:

$$E(\mathbf{w}) = -\frac{1}{M} \sum_{i=1}^{M} [t_i \ln y_i + (1 - t_i) \ln(1 - y_i)] \tag{7.50}$$

This expression becomes problematic when our predictions y_i approach 0 or 1, as the logarithm can lead to numerical overflow. To understand why, consider what happens when $y_i \approx 0$: $\ln(y_i)$ approaches negative infinity, potentially exceeding our computer's numerical limits. A simple but effective solution is to add a small constant ϵ (typically 10^{-7}) to prevent taking the logarithm of zero:

$$E(\mathbf{w}) = -\frac{1}{M} \sum_{i=1}^{M} [t_i \ln(y_i + \epsilon) + (1 - t_i) \ln(1 - y_i + \epsilon)] \tag{7.51}$$

Similarly, we need a numerically stable implementation of the sigmoid function itself:

$$\sigma(z) = \begin{cases} \frac{1}{1+e^{-z}} & \text{if } z \geq 0 \\ \frac{e^z}{1+e^z} & \text{if } z < 0 \end{cases} \tag{7.52}$$

This piecewise implementation avoids computing large exponentials that could overflow. When z is large and positive, computing e^{-z} is safer than e^z, and vice versa for negative z.

Optimization pathologies.   Beyond numerical stability, the training process can encounter two major pathologies. First, vanishing gradients occur when $\|\nabla E(\mathbf{w})\|$ becomes very small early in training, causing optimization to stall. This is particularly relevant with sigmoid functions because their derivatives approach zero for large inputs.

To see why, recall that the derivative of the sigmoid is:

$$\frac{d\sigma}{dz} = \sigma(z)(1 - \sigma(z)) \tag{7.53}$$

When $|z|$ is large, $\sigma(z)$ approaches either 0 or 1, making this derivative vanishingly small. This means that even if our model is making poor predictions, the gradient provides little guidance for improvement. While we're stuck with sigmoid for logistic regression (it's baked into our probabilistic model), we'll see in neural networks how alternative activation functions can help avoid this issue.

Second, exploding gradients can manifest when we encounter a "bad" batch of data containing outliers, causing weights to grow uncontrollably large and leading to numerical overflow. This is a common concern in astronomical applications where outliers frequently arise from instrumental artifacts, cosmic rays, or rare astrophysical phenomena. Gradient clipping has thus become standard practice, both for simpler models and when optimizing more complex models like neural networks.

We can detect potential explosions by monitoring $\max(|\mathbf{w}|)$ during training. When we observe weights growing beyond reasonable bounds (say, 10^4), we can implement gradient clipping—scaling down large gradients while preserving their direction:

$$\nabla E_{\text{clipped}} = \min\left(1, \frac{\text{threshold}}{\|\nabla E\|}\right) \nabla E \qquad (7.54)$$

This acts like a safety valve, allowing optimization to continue even when gradients temporarily become very large due to outliers or other numerical instabilities that are more common in complex models beyond logistic regression.

Monitoring and early stopping.   Unlike linear regression which has a closed-form solution, logistic regression's iterative optimization requires us to decide when to stop training. Monitoring performance on a validation set provides our best defense against overfitting. Rather than training for a fixed number of iterations, we should track model performance on held-out test data after each epoch (a complete pass through the training data). When validation performance stops improving, we've likely reached the limit of what can be learned from our data. This "early stopping" strategy often proves more effective than fixed iteration counts or gradient magnitude thresholds.

Several other practices can improve training robustness. Randomly shuffling data between epochs prevents the model from learning spurious patterns based on data order and helps ensure each batch represents the overall data distribution. This is particularly important when dealing with astronomical data, where objects may be ordered by position, brightness, or observation time. Without shuffling, the model could learn these ordering pat-

terns rather than the true underlying relationships. Additionally, shuffling helps prevent the model from getting stuck in local minima by introducing randomness into the optimization process.

Class imbalance in astronomy.   A critical issue in astronomical classification tasks is severe class imbalance. Consider the challenge of detecting rare transient events like supernovae or finding high-redshift quasars—the target class might represent less than 0.1% of all objects. With such imbalance, a model that simply predicts "not a transient" for every object would achieve 99.9% accuracy while completely failing at its primary task. This problem is particularly acute in survey astronomy, where we often search for rare objects among millions of background sources.

To address class imbalance, we can modify our cross-entropy loss function to weight the minority class more heavily:

$$E_{\text{weighted}}(\mathbf{w}) = -\frac{1}{N} \sum_{i=1}^{N} [w_1 t_i \ln y_i + w_0 (1 - t_i) \ln(1 - y_i)] \qquad (7.55)$$

where w_1 and w_0 are class weights. A common approach sets weights inversely proportional to class frequencies. For example, if transients comprise only 1% of our dataset, we might set $w_1 = 0.99$ and $w_0 = 0.01$, effectively making each transient count 99 times more than each non-transient. This ensures that the rare class contributes meaningfully to the gradient despite its scarcity.

7.10   Summary

In this chapter, we've introduced logistic regression—one of the most widely used classification methods. Starting from the fundamental differences between classification and regression, we discovered how the requirement for bounded outputs (probabilities) naturally led us to a key insight: rather than linearly predicting probabilities directly, we should predict log-odds (logit) between classes. This approach effectively imposes a linear decision boundary in feature space, which we transform to probabilities through the sigmoid function.

A valuable aspect of our development has been the duality between generative and discriminative approaches to classification. We discovered that the linear decision boundary of logistic regression emerges naturally when we assume our features follow Gaussian distributions with equal covariance structures for both classes. This connection not only provides

deeper insight into why logistic regression works but also helps us understand its inductive bias and limitations. When our data violates these Gaussian assumptions, as often happens in astronomical applications, we can anticipate where and how the model might fail.

Throughout our exploration of implementation details, we've seen how theoretical understanding meets practical challenges. The cross-entropy loss function, while mathematically natural, requires careful numerical treatment to avoid overflow. Despite the nonlinearity introduced by the sigmoid function, we found that the gradient takes a simple form. This mathematical convenience, combined with the sigmoid's natural probabilistic interpretation, helps explain why logistic regression has remained a cornerstone of classification even in the era of deep learning.

The simplicity of this gradient expression enabled us to explore gradient descent—a fundamental optimization technique that would later become crucial for training modern neural networks. By approximating gradients using small random batches of data, stochastic gradient descent allows us to make rapid progress in optimization while managing computational constraints. We discovered how careful choice of learning rates and batch sizes, far from being mere technical details, controls how we explore the loss landscape. The development of adaptive learning rates and principled scheduling strategies further showcases how practical challenges drive technical innovations.

Despite its apparent simplicity, logistic regression required us to address several implementation challenges, from numerical stability issues to class imbalance—a particular concern in astronomy where we often search for rare objects among vast datasets. These practical considerations highlight the gap between mathematical formulation and real-world application that exists with all machine learning methods.

For all its advantages, logistic regression comes with a key limitation: it assumes classes are linearly separable in feature space. However, as we've seen, we can often overcome this limitation through feature transformations. Just as we transformed our probability space using the sigmoid function, we can transform our input features using domain-specific knowledge to create more linearly separable representations. This technique has proven particularly valuable in astronomy, where physical understanding guides our feature engineering.

In the next chapter, we'll extend our framework to handle multi-class classification, essential for many astronomical applications where binary classification is insufficient. We'll see how concepts from information theory, particularly mutual information, provide deeper insight into classification performance.

Further Readings: The development of classification methods emerged from parallel advances in biostatistics and discriminant analysis, with several foundational contributions shaping modern approaches. Fisher [1936] developed linear discriminant analysis, contributing theoretical foundations for classification problems, while Bliss [1934] developed probit analysis for binary responses, with this work later expanded by Finney [1947]. The logistic approach was advanced through Berkson [1944] who developed logistic regression for binary data, and Cox [1958] who extended this framework to handle multiple covariates. Information-theoretic perspectives were contributed by Shannon [1948] through his development of entropy theory, and Kullback and Leibler [1951] who connected information theory to statistical inference through the KL divergence. For readers interested in theoretical comparisons between classification approaches, Efron [1975] analyzed the efficiency of logistic regression versus discriminant analysis, Rubinstein and Hastie [1997] examined discriminative versus informative learning trade-offs, and Ng and Jordan [2001] provided modern comparison of discriminative and generative classifiers. The optimization foundations underlying these methods trace to work by Cauchy [1847] who described gradient descent mathematically, Curry [1944] who studied convergence properties for non-linear problems, and Robbins and Monro [1951] who developed the stochastic approximation framework that underlies modern stochastic gradient descent methods.

Chapter 8

Multi-Class Classification

In the previous chapter, we explored binary logistic regression as a classification technique. We learned that despite its name, logistic regression is fundamentally a classification method that transforms probabilities through the log-odds (logit) function to create an unbounded range suitable for linear modeling. The sigmoid function then converts these values back to probabilities. Through maximizing the joint likelihood of the Bernoulli distribution, we derived the cross-entropy loss function for binary classification. Now, we extend these concepts to tackle the more general challenge of multi-class classification.

Real-world classification problems often involve distinguishing between multiple categories rather than just two. In astronomy, for example, we frequently need to classify celestial objects into various subtypes - not simply choosing between "star" or "galaxy". We might need to classify galaxies into categories like "elliptical galaxy," "spiral galaxy," "irregular galaxy," or "quasar." Similarly, we might classify stars into spectral types such as "O-type," "B-type," "red giant," or "white dwarf." This natural extension raises an important question: how can we best adapt our binary classification framework to handle multiple classes?

A seemingly straightforward approach would be to apply binary classification multiple times, comparing each class against all others. However, this intuitive solution has limitations that we'll explore in detail. Understanding why this approach falls short will help us develop the intuition needed for a more robust framework. We'll see how properly formulating the problem through maximum likelihood leads to a natural generalization of both the cross-entropy loss function for multiple classes and the sigmoid function - what we call the softmax

function - to convert multiple log-odds into their respective probabilities.

Additionally, we'll discuss how to implement multi-class classification efficiently using Stochastic Gradient Descent, addressing some of the subtle implementation challenges that arise when extending optimization techniques from binary to multi-class scenarios. These practical considerations are crucial for developing scalable classification systems that can handle the complexity of real-world astronomical data.

We'll also explore some connections between our classification framework and concepts from information theory. The cross-entropy loss we'll derive has ties to information-theoretic measures like entropy, which helps us understand why this loss function is appropriate for classification tasks. These concepts appear in various astronomical applications, such as determining which observations might best distinguish between competing models. This connection between classification methods and information theory provides context for our approach and helps explain why the same mathematical framework used in relatively simple classification tasks also serves as the foundation for more complex applications like large language models, which can be viewed as sophisticated multi-class classifiers operating over very large vocabularies.

8.1 Multi-Class Classification vs. Binary Classification

Building on our understanding of binary classification, let's explore why extending binary classification methods to multi-class problems requires careful consideration. The key challenge is extending the binary framework to handle multiple categories simultaneously in a mathematically consistent way. A seemingly intuitive first approach would be to decompose the multi-class problem into multiple binary classifications, but as we'll see, this creates issues.

One-vs-Rest Limitations One common strategy for handling multi-class problems is the One-vs-Rest (OvR) approach. In this approach, for each class C_k, we train a binary classifier to distinguish between "class C_k" and "not class C_k" (all other classes combined).

However, this approach can lead to logical inconsistencies. Let's examine this with a concrete example in a three-class problem with classes C_1, C_2, and C_3. One might think we could simply train two binary classifiers: one separating C_1 from everything else (C_2 and C_3 combined), and another separating C_2 from everything else (C_1 and C_3 combined). Then, we would assign points to C_3 when both classifiers predict their negative class. Each classifier
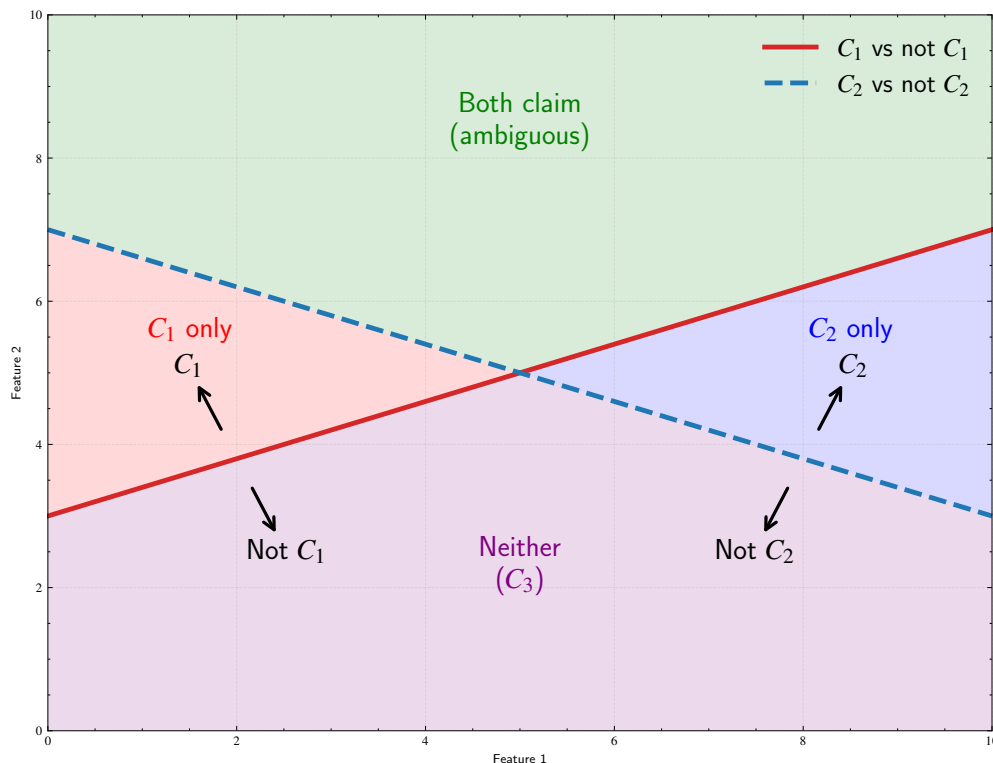
Figure 8.1: Illustration of pathological cases in One-vs-Rest (OvR) multi-class classification. The plot shows two binary decision boundaries: a solid red line separating class C_1 from "not C_1" and a dashed blue line separating class C_2 from "not C_2". These boundaries create four distinct regions: a green region where both classifiers claim the point (both predict their positive class), a purple region where neither classifier claims the point (both predict their negative class, implying C_3 by default), a red region where only C_1 is predicted, and a blue region where only C_2 is predicted. The ambiguous green region, where both classifiers simultaneously predict their respective classes with high confidence, demonstrates a fundamental limitation of the OvR approach and motivates the need for a unified multi-class classification framework that ensures unambiguous class assignments.

establishes its own linear decision boundary, dividing the feature space into regions.

While the case where neither classifier claims a point is clearly resolved (it belongs to C_3), we can still have problematic regions in the feature space where the classifiers give contradictory results. Consider a point where the C_1 vs Rest classifier predicts it belongs to C_1 with high confidence, while simultaneously the C_2 vs Rest classifier predicts it belongs to C_2 with high confidence. This creates a logical contradiction: how can a point belong to both class C_1 and class C_2 simultaneously?

The problem here shows that we are treating the questions as two distinct classifications without interdependent relationships between them. This will be solved with a more

probabilistic and unified framework later in this chapter.

One-vs-One Limitations   One might think we could resolve the ambiguity by using a One-vs-One (OvO) approach - where we train a separate binary classifier for each possible pair of classes. For a problem with K classes, this approach requires training $K(K-1)/2$ binary classifiers - one for each possible pair. For example, in our three-class problem, we would need three binary classifiers: one comparing C_1 vs C_2, another comparing C_2 vs C_3, and a third comparing C_1 vs C_3. While this approach might seem more natural since it directly compares classes against each other rather than against aggregated groups, it actually introduces its own set of problems.
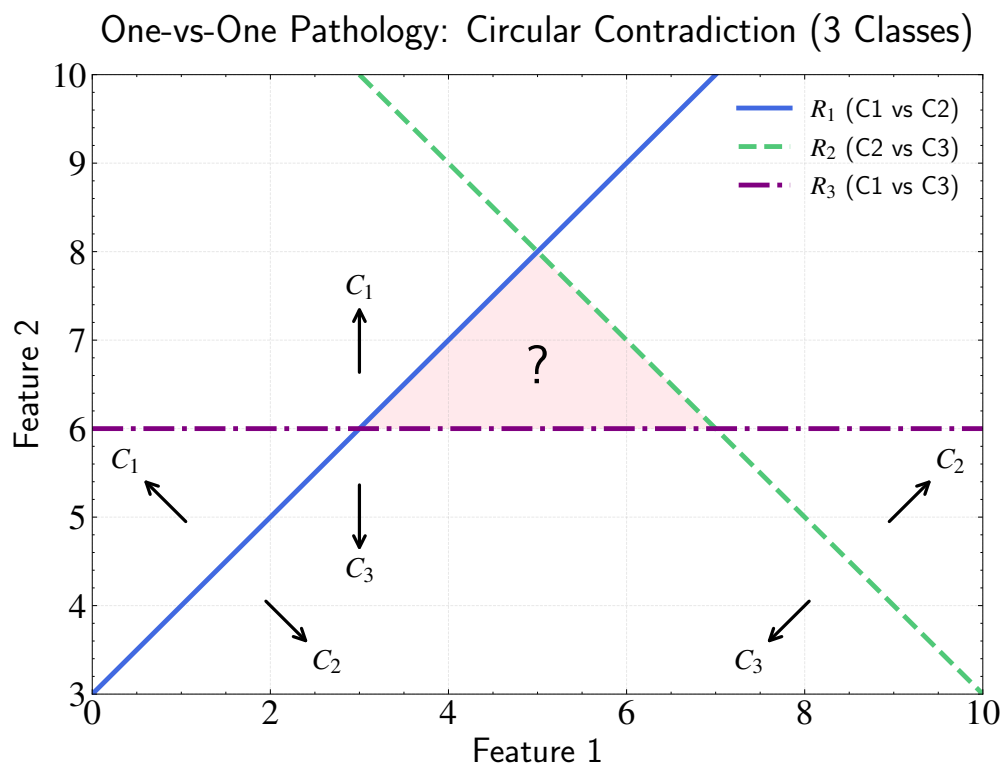
Figure 8.2: Illustration of the circular contradiction problem in One-vs-One classification with three classes. The plot shows three decision boundaries: R_1 (solid blue line) separating C_1 from C_2, R_2 (dashed green line) separating C_2 from C_3, and R_3 (dash-dotted purple line) separating C_1 from C_3. The pink shaded region highlights where the binary decisions create a circular contradiction: points in this region are classified as C_2 over C_1 by R_1, as C_3 over C_2 by R_2, but then as C_1 over C_3 by R_3. This cyclic inconsistency ($C_1 \rightarrow C_2 \rightarrow C_3 \rightarrow C_1$) demonstrates why decomposing multi-class problems into independent binary decisions is problematic. The perpendicular arrows on each boundary indicate the direction of classification decisions, showing how the circular contradiction arises from the interaction of these independent binary classifications.

The key issue with the OvO approach is that it can lead to circular contradictions in the classification decisions. Since each classifier makes its decision independently, we can encounter situations where the binary decisions form an inconsistent chain. To understand this intuitively, imagine three different experts each tasked with comparing only two classes at a time. The first expert, looking at C_1 and C_2, decides a point belongs to class C_2. The second expert, examining C_2 and C_3, assigns that same point to class C_3. But when the third expert compares C_1 and C_3, they assign it to class C_1. This creates a logical impossibility - following the chain of decisions, we have C_1 losing to C_2, C_2 losing to C_3, but then C_3 losing to C_1, forming an irreconcilable loop of preferences where each class is simultaneously preferred and not preferred over the others.

These logical contradictions are not merely theoretical concerns. In practical applications, they create regions where classification becomes arbitrary or dependent on implementation details rather than meaningful patterns in the data. We need a more coherent approach that considers all classes simultaneously.

The core insight from examining these naive approaches is that a principled multi-class classification framework must treat all classes simultaneously, rather than through independent binary decisions. This unified approach is particularly important for astronomical applications, where consistent and physically meaningful classification is essential. For example, in galaxy morphology classification, stellar type identification, or exoplanet categorization, we need frameworks that provide coherent predictions without the contradictions inherent in decomposed binary approaches.

8.2 One-Hot Encoding for Multi-Class Problems

Having seen the limitations of decomposing multi-class problems into binary classifications, we need a more principled approach that treats all classes simultaneously. The first step is to fundamentally rethink how we represent class labels in multi-class problems. While binary classification could use a simple scalar label (typically 0 or 1), this representation breaks down when we move beyond two classes.

Let's consider common astronomical classification tasks. In galaxy morphology classification, we need to categorize galaxies into several types: elliptical, spiral, irregular, and so on. Similarly, stellar classification distinguishes between different spectral types (O, B, A, F, G, K, M), each representing stars with distinct physical properties. Coming from binary classification, our first instinct might be to simply use consecutive integers: 0 for elliptical

galaxies, 1 for spiral, 2 for irregular, or 0 for O-type stars, 1 for B-type, and so forth.

However, this integer encoding introduces a fundamental flaw: it imposes an artificial ordering on our classes. The numerical sequence 0, 1, 2 suggests that spiral galaxies (class 1) are somehow "between" elliptical (class 0) and irregular (class 2) galaxies in terms of their properties. In reality, these are simply different categories with no inherent ordering. The numerical differences between these integers ($1 - 0 = 1$, $2 - 1 = 1$) also falsely suggest equal "distances" between classes. Furthermore, unlike binary classification where we could simply take 1 minus the prediction probability to swap classes, there's no simple mathematical operation that would let us arbitrarily reorder multiple classes while preserving the model's predictions.

To address these issues, we need an encoding scheme that treats all classes equally without suggesting any ordering or distance relationships. The solution lies in one-hot encoding, where we represent each class as a vector rather than a single number. Instead of trying to encode class identity in a single dimension, we use multiple dimensions to represent class membership, ensuring each class has equal status in our mathematical framework.

In one-hot encoding, we create a vector with as many dimensions as we have classes (K), where each position in the vector corresponds to one class. To represent a particular class, we put a 1 in the position corresponding to that class and 0s everywhere else. For example, in a problem with K classes, our encoding vectors will have K dimensions:

- Class 1 (e.g., elliptical galaxy): $[1, 0, 0, \ldots, 0]$,

- Class 2 (e.g., spiral galaxy): $[0, 1, 0, \ldots, 0]$,

- Class 3 (e.g., irregular galaxy): $[0, 0, 1, \ldots, 0]$,

and so on.

Consider how this one-hot encoding treats our classes symmetrically. In the vector space we've created, each class is represented by a unit vector pointing in a different coordinate direction. For example, in our three-class galaxy problem, elliptical galaxies might be $[1, 0, 0]$, spirals $[0, 1, 0]$, and irregulars $[0, 0, 1]$. This equal distance property reflects the reality that in pure classification, no class is inherently "closer" to another.

From a geometric perspective, one-hot encoding represents each class as a point at the corner of a K-dimensional hypercube. These points are equidistant from each other, all

with the same Euclidean distance of $\sqrt{2}$ between any pair. This symmetry ensures that our encoding doesn't artificially suggest relationships between classes that don't exist in reality.

This multi-class probabilistic framework we've developed for astronomical classification extends far beyond astronomy - it forms the mathematical foundation for modern large language models. In these models, the task of predicting the next word in a sequence is fundamentally a massive multi-class classification problem. Instead of classifying galaxies into a few morphological types, these models classify each position in the text into one of tens or hundreds of thousands of possible words in their vocabulary. The principles remain the same: each word in the vocabulary corresponds to a one-hot encoded vector, and the model must predict a probability distribution over this entire vocabulary at each position in the text sequence.

8.3   Multi-Class Logistic Regression

Having established one-hot encoding as our way to represent class labels as vectors rather than scalars, we must now develop a model that can output vectors rather than scalar values. This key difference from binary classification requires careful consideration - our model needs to predict a probability for each class simultaneously, producing a vector output that matches the dimensionality of our one-hot encoded labels.

Specifically, while our training labels are one-hot encoded vectors (containing only 0s and 1s, with exactly one 1 indicating the true class), our model will output probability vectors $\mathbf{p} = [p_1, p_2, ..., p_K]$, where each p_i represents the probability of belonging to class i. These probabilities must satisfy two key constraints:

- each p_i must lie between 0 and 1 ($p_i \in [0, 1]$)

- they must sum to 1 ($\sum_{i=1}^{K} p_i = 1$)

To make this concrete, consider our galaxy classification example. While a training label might be a strict one-hot vector like $[1, 0, 0]$ (indicating an elliptical galaxy), our model might output $\mathbf{p} = [0.70, 0.25, 0.05]$, representing probabilities of 70% elliptical, 25% spiral, and 5% irregular. The key challenge is designing a model that can learn to map input features to these probability vectors while respecting both their vector nature and the constraints on probabilities.

This probabilistic framework proves particularly valuable in astronomy, where clas-

sification confidence often varies with data quality. A bright, well-resolved galaxy might receive a high-confidence classification like $\mathbf{p} = [0.95, 0.04, 0.01]$, where the 0.95 probability strongly indicates an elliptical galaxy. In contrast, a faint or poorly-resolved galaxy might get a more uncertain classification $\mathbf{p} = [0.45, 0.40, 0.15]$, where the similar probabilities reflect genuine uncertainty between elliptical and spiral classifications. Even more importantly, this framework can naturally represent truly ambiguous cases - a galaxy showing both spiral and irregular features might receive probabilities like $\mathbf{p} = [0.10, 0.45, 0.45]$, where the equal probabilities capture its intermediate nature.

So how do we construct such a model? Recall that in binary classification, we couldn't directly apply linear regression to probabilities because they're bounded between 0 and 1, while linear functions are unbounded. We solved this through a transformation - taking the ratio of probabilities and its logarithm (the log-odds), which mapped our bounded probabilities to an unbounded space where linear modeling made sense. We expressed this using vector notation $\mathbf{w}^T\mathbf{x}$, where we absorbed the bias term into $\mathbf{w}$ by augmenting $\mathbf{x}$ with a 1, making our equations more compact.

In the multi-class setting, we face a similar but more complex challenge. We need to transform our vector of probabilities $\mathbf{p}(\mathbf{x}) = [p_1(\mathbf{x}), p_2(\mathbf{x}), ..., p_K(\mathbf{x})]$ in a way that preserves the relationships between classes while allowing for linear modeling. Earlier, we saw that naive approaches like One-vs-One or One-vs-Rest led to inconsistencies because they treated each binary decision independently. Instead, we need a transformation that handles all classes simultaneously while maintaining their interdependence.

The key insight is that we can create a coherent framework by comparing all classes to a single reference class. Just as in binary classification where we express probabilities as a ratio relative to class 0, we can extend this idea to multiple classes by choosing one class as our reference. This choice reflects a fundamental property of probability normalization - since probabilities must sum to one, we effectively reduce our degrees of freedom by one, allowing us to express all probabilities relative to a single reference class. While this reference class could be any of our classes - analogous to choosing an origin in a coordinate system - the actual relationships between classes and our final predictions remain invariant to this choice.

Let's develop this mathematically. For K classes, we can construct $K-1$ probability

ratios by comparing each class to a reference class (which we'll arbitrarily label as class K):

$$\frac{P(C_k|\mathbf{x})}{P(C_K|\mathbf{x})} = \frac{P(\mathbf{x}|C_k)P(C_k)}{P(\mathbf{x}|C_K)P(C_K)} \text{ for } k = 1, ..., K - 1 \tag{8.1}$$

Just as in binary classification, the log of these ratios can take any real value from $-\infty$ to ∞, making them suitable targets for linear modeling. Following our approach from binary classification, and using the same augmented vector notation, we model each log-ratio as:

$$\ln\left(\frac{P(C_k|\mathbf{x})}{P(C_K|\mathbf{x})}\right) = \mathbf{w}_k^T \mathbf{x} \tag{8.2}$$

This formulation introduces $K - 1$ weight vectors $\mathbf{w}_k$, one for each non-reference class, which must be optimized simultaneously due to their interconnected nature through the shared reference class. Unlike in OvR where each binary classifier operates independently, when we adjust the weights $\mathbf{w}_1$ for class 1 versus the reference class, we're implicitly affecting the relationship between class 1 and all other classes through their common reference. This coupling enables our model to discover complex decision boundaries that couldn't be found by independent binary classifiers.

For example, in our galaxy classification problem, adjusting the weights that distinguish elliptical galaxies from the reference class automatically influences how the model distinguishes between elliptical and spiral galaxies, even without explicitly training a binary classifier between these classes. This interconnected optimization ensures our model learns a single, coherent decision boundary structure rather than multiple independent binary boundaries, thereby avoiding the contradictions we encountered in OvO and OvR approaches.

Having modeled our class relationships through log-ratios, we now face the same challenge we encountered in binary classification: how do we convert these predictions in the unbounded space back into probabilities? The multi-class setting makes this even more challenging. While in binary classification we only needed to predict one probability (since the second was determined by their sum equaling 1), we now need to recover K probabilities from $K - 1$ log-ratios, while maintaining the relative relationships between all classes that we've carefully modeled. This challenge will be addressed in the next section with the softmax function.

8.4   The Softmax Function

In binary classification, we solved the conversion problem using the sigmoid function - the inverse of our log-odds (logit) transformation. This sigmoid function emerged naturally from our probabilistic framework. Given a linear prediction $\mathbf{w}^T\mathbf{x}$ representing the log-odds, the probability of class 1 was given by:

$$P(C_1|\mathbf{x}) = \frac{1}{1 + \exp(-\mathbf{w}^T\mathbf{x})} \tag{8.3}$$

The sigmoid function ensures our output is a valid probability between 0 and 1, and since probabilities must sum to 1, we automatically have the probability of the reference class $P(C_0|\mathbf{x}) = 1 - P(C_1|\mathbf{x})$.

In our multi-class setting, we need an analogous transformation that can convert our $K - 1$ linear predictions back into K valid probabilities. This generalization of the sigmoid function to multiple classes is what we call the softmax function. Let's derive it following the same logic as our binary case.

We've modeled the log-ratios of probabilities as linear functions:

$$\ln\left(\frac{P(C_k|\mathbf{x})}{P(C_K|\mathbf{x})}\right) = \mathbf{w}_k^T\mathbf{x} \text{ for } k = 1, ..., K - 1 \tag{8.4}$$

Now we need to solve for the individual probabilities. From our log-ratio equations:

$$\frac{P(C_k|\mathbf{x})}{P(C_K|\mathbf{x})} = \exp(\mathbf{w}_k^T\mathbf{x}) \tag{8.5}$$

Therefore:

$$P(C_k|\mathbf{x}) = P(C_K|\mathbf{x})\exp(\mathbf{w}_k^T\mathbf{x}) \tag{8.6}$$

Using our constraint that probabilities must sum to one:

$$\sum_{k=1}^{K} P(C_k|\mathbf{x}) = 1 \tag{8.7}$$

Substituting our expressions:

$$P(C_K|\mathbf{x}) + \sum_{k=1}^{K-1} P(C_K|\mathbf{x})\exp(\mathbf{w}_k^T\mathbf{x}) = 1 \tag{8.8}$$

$$P(C_K|\mathbf{x}) \left(1 + \sum_{k=1}^{K-1} \exp(\mathbf{w}_k^T \mathbf{x}) \right) = 1 \tag{8.9}$$

Solving for $P(C_K|\mathbf{x})$:

$$P(C_K|\mathbf{x}) = \frac{1}{1 + \sum_{k=1}^{K-1} \exp(\mathbf{w}_k^T \mathbf{x})} \tag{8.10}$$

And consequently, for any class $k \neq K$:

$$P(C_k|\mathbf{x}) = \frac{\exp(\mathbf{w}_k^T \mathbf{x})}{1 + \sum_{j=1}^{K-1} \exp(\mathbf{w}_j^T \mathbf{x})} \tag{8.11}$$

We can derive a more compact and symmetric form by introducing a weight vector $\mathbf{w}_K = \mathbf{0}$ for our reference class. This isn't a parameter we optimize - it's a fixed constraint that reflects our choice of reference class. With this definition, we can rewrite the probability for the reference class as:

$$P(C_K|\mathbf{x}) = \frac{1}{1 + \sum_{j=1}^{K-1} \exp(\mathbf{w}_j^T \mathbf{x})} \tag{8.12}$$

$$= \frac{\exp(0)}{1 + \sum_{j=1}^{K-1} \exp(\mathbf{w}_j^T \mathbf{x})} \tag{8.13}$$

$$= \frac{\exp(\mathbf{w}_K^T \mathbf{x})}{1 + \sum_{j=1}^{K-1} \exp(\mathbf{w}_j^T \mathbf{x})} \tag{8.14}$$

Now we can rewrite the denominator in a more symmetric form:

$$1 + \sum_{j=1}^{K-1} \exp(\mathbf{w}_j^T \mathbf{x}) = \exp(\mathbf{w}_K^T \mathbf{x}) + \sum_{j=1}^{K-1} \exp(\mathbf{w}_j^T \mathbf{x}) \tag{8.15}$$

$$= \sum_{j=1}^{K} \exp(\mathbf{w}_j^T \mathbf{x}) \tag{8.16}$$

This gives us a more symmetric form for all classes $k = 1, 2, \ldots, K$:

$$P(C_k|\mathbf{x}) = \frac{\exp(\mathbf{w}_k^T \mathbf{x})}{\sum_{j=1}^{K} \exp(\mathbf{w}_j^T \mathbf{x})} \tag{8.17}$$

This function, which transforms a set of K linear predictors into a proper probability distribution over K classes, is called the softmax function. It's important to emphasize that

we only optimize $K - 1$ weight vectors, with $\mathbf{w}_K = \mathbf{0}$ fixed by our choice of reference class. This constraint reflects the fact that with probabilities summing to one, we only need $K - 1$ independent parameters to fully specify a K-class probability distribution.

While this may seem similar to the sigmoid function $\sigma(z) = 1/(1+e^{-z})$ we encountered in binary classification, there's an important distinction: the sigmoid function maps a single real number to a probability between 0 and 1, suitable for binary outcomes, while softmax generalizes this to map a vector of real numbers to a probability distribution over multiple classes.

To see how the binary case is a special case of our more general formulation, let's substitute $K = 2$ into our compact softmax formula. With two classes, we have:

$$P(C_1|\mathbf{x}) = \frac{\exp(\mathbf{w}_1^T\mathbf{x})}{\exp(\mathbf{w}_1^T\mathbf{x}) + \exp(\mathbf{w}_2^T\mathbf{x})} \tag{8.18}$$

Since we've defined $\mathbf{w}_2 = \mathbf{0}$ for our reference class, this becomes:

$$P(C_1|\mathbf{x}) = \frac{\exp(\mathbf{w}_1^T\mathbf{x})}{\exp(\mathbf{w}_1^T\mathbf{x}) + 1} \tag{8.19}$$

$$= \frac{1}{1 + \exp(-\mathbf{w}_1^T\mathbf{x})} \tag{8.20}$$

This is exactly the sigmoid function we used in binary classification. Similarly, for the reference class:

$$P(C_0|\mathbf{x}) = \frac{\exp(\mathbf{w}_2^T\mathbf{x})}{\exp(\mathbf{w}_1^T\mathbf{x}) + \exp(\mathbf{w}_2^T\mathbf{x})} \tag{8.21}$$

$$= \frac{1}{\exp(\mathbf{w}_1^T\mathbf{x}) + 1} \tag{8.22}$$

$$= 1 - P(C_1|\mathbf{x}) \tag{8.23}$$

Thus, our compact softmax formulation naturally reduces to the familiar sigmoid when we have only two classes, confirming that multi-class logistic regression is indeed a proper generalization of binary logistic regression.

Let's understand the geometric interpretation of our model - specifically, how it divides the feature space into regions for different classes. The boundaries between classes occur

where the model is equally uncertain between two classes - that is, where their probabilities are equal:

$$P(C_j|\mathbf{x}) = P(C_k|\mathbf{x}) \tag{8.24}$$

Substituting our expressions in terms of the reference class K:

$$\frac{P(C_j|\mathbf{x})}{P(C_K|\mathbf{x})} = \frac{P(C_k|\mathbf{x})}{P(C_K|\mathbf{x})} \tag{8.25}$$

Since we model these ratios as:

$$\frac{P(C_j|\mathbf{x})}{P(C_K|\mathbf{x})} = \exp(\mathbf{w}_j^T \mathbf{x}) \tag{8.26}$$

We get:

$$\exp(\mathbf{w}_j^T \mathbf{x}) = \exp(\mathbf{w}_k^T \mathbf{x}) \tag{8.27}$$

Taking logarithms:

$$\mathbf{w}_j^T \mathbf{x} = \mathbf{w}_k^T \mathbf{x} \tag{8.28}$$

This equation defines a hyperplane in feature space where classes j and k are equally likely. For any K classes, we have $\binom{K}{2}$ such hyperplanes - one for each possible pair of classes. Each hyperplane $\mathbf{w}_j^T \mathbf{x} = \mathbf{w}_k^T \mathbf{x}$ divides the space into two regions: one where class j is more likely than k ($\mathbf{w}_j^T \mathbf{x} > \mathbf{w}_k^T \mathbf{x}$), and another where class k is more likely than j ($\mathbf{w}_j^T \mathbf{x} < \mathbf{w}_k^T \mathbf{x}$). The hyperplane itself is characterized by the difference vector $(\mathbf{w}_j - \mathbf{w}_k)$, which determines both its orientation and position in feature space. The normal vector to this hyperplane is parallel to this difference vector, meaning the boundary will be perpendicular to the direction in which the difference between the linear predictors $\mathbf{w}_j^T \mathbf{x}$ and $\mathbf{w}_k^T \mathbf{x}$ changes most rapidly.

While this geometric interpretation might seem similar to the One-vs-One approach we criticized earlier, there's a crucial difference. Our multi-class model provides two complementary ways to understand the classification: First, at any point $\mathbf{x}$ in feature space, we can compute the complete probability distribution over all K classes using the softmax function. For any class k (including the reference class), we can write:

$$P(C_k|\mathbf{x}) = \frac{\exp(\mathbf{w}_k^T \mathbf{x})}{\sum_{j=1}^{K} \exp(\mathbf{w}_j^T \mathbf{x})} \tag{8.29}$$

This gives us the probability for every class at any point in feature space.
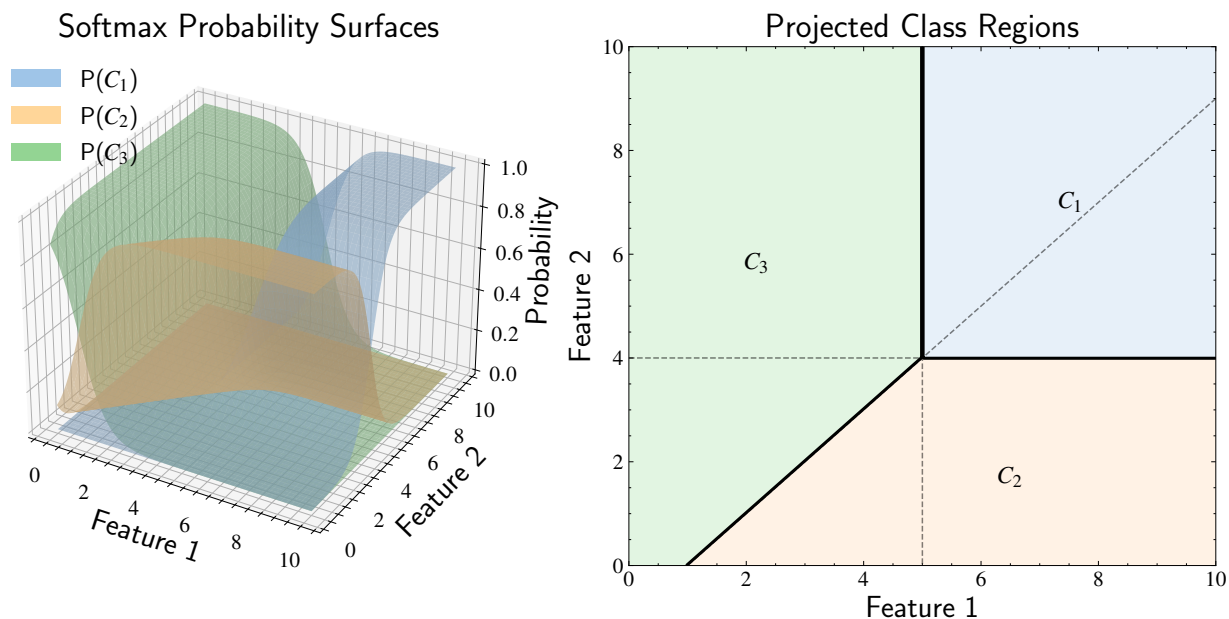
Figure 8.3: Visualization of how softmax-based multi-class classification ensures consistent decisions without ambiguity. The left panel shows the probability surfaces $P(C_k|\mathbf{x})$ for each class k, demonstrating how the softmax function transforms linear predictions $\mathbf{w}_k^T\mathbf{x}$ into proper probability distributions that sum to 1 at every point in feature space. The right panel projects these surfaces onto the feature plane, where colored regions indicate the dominant class (highest probability), solid lines mark decision boundaries where the highest probability changes from one class to another, and dashed lines show where any two classes have equal probabilities. Unlike the One-vs-One approach in Figure 2, there can be no ambiguity because every point has a well-defined probability distribution over all classes through the shared softmax denominator, with decision boundaries emerging naturally from comparing these interdependent probabilities rather than from independent binary classifications.

Second, the $\binom{K}{2}$ boundaries tell us precisely where any two classes are equally likely, partitioning the space into regions where different classes dominate. To determine the predicted class at any point, we simply take

$$\mathrm{argmax}_k P(C_k|\mathbf{x}) \tag{8.30}$$

This operation returns the class k that has the highest probability $P(C_k|\mathbf{x})$ at that point. While this gives us a definitive classification, we don't have to discard the probability information - we can use the full probability distribution to express our uncertainty about the classification. For example, if two classes have similar probabilities, this tells us the model is uncertain between those classes, even though argmax would still pick one of them.

The softmax function transforms a vector of K linear predictors into a probability
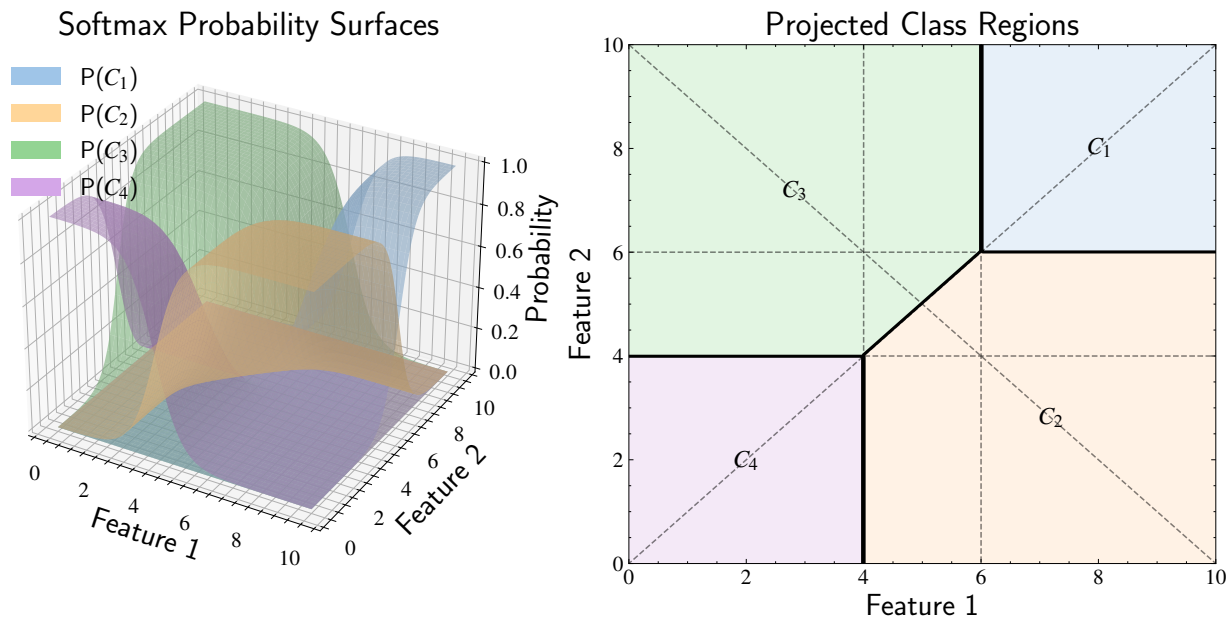
Figure 8.4: Extension of the softmax visualization to four classes, demonstrating how the framework naturally scales to higher dimensions. The left panel shows four probability surfaces $P(C_k|\mathbf{x})$ that sum to 1 at every point, while the right panel reveals the resulting decision structure with $\binom{4}{2} = 6$ pairwise boundaries. Solid lines mark the actual decision boundaries where the highest probability changes between classes, while dashed lines indicate where pairs of classes have equal probabilities. The colored regions show where each class achieves the highest probability. Despite the increased complexity with four classes, the softmax function still ensures a consistent probability distribution everywhere in feature space, eliminating any possibility of contradictory classifications. This window-pane pattern of boundaries emerges naturally from comparing probabilities in our unified framework, rather than from independent binary decisions.

distribution over K classes:

$$P(C_k|\mathbf{x}) = \frac{\exp(\mathbf{w}_k^T\mathbf{x})}{\sum_{j=1}^K \exp(\mathbf{w}_j^T\mathbf{x})} \tag{8.31}$$

This formulation smoothly approximates the maximum operation - when one linear prediction $\mathbf{w}_m^T\mathbf{x}$ is significantly larger than others, the exponential term $\exp(\mathbf{w}_m^T\mathbf{x})$ dominates both numerator and denominator, causing $P(C_m|\mathbf{x})$ to approach 1 while all other probabilities approach 0. This is why it's called "softmax" - it's a smooth, differentiable version of the maximum function.

These perspectives work together harmoniously - the boundaries emerge naturally from comparing the probabilities, and crossing a boundary between classes j and k corresponds exactly to the point where their probabilities become equal. When several linear predictions $\mathbf{w}_k^T\mathbf{x}$ are similar in value, the softmax function expresses this uncertainty by

distributing probability mass across the corresponding classes. This is fundamentally different from OvO, where independent binary classifiers can lead to contradictory predictions because they lack this unified probabilistic framework.

In two dimensions, where $\mathbf{x}$ represents points in a plane, each hyperplane becomes a line. For three classes (say A, B, and C), we get three boundary lines: one separating A from B, another separating B from C, and a third separating A from C. These three lines create regions where one class has the highest probability, and because all probabilities come from the same probability expressions relative to our reference class, these regions never lead to the ambiguous or contradictory classifications we saw with OvO. When the classes are well-separated, these lines often form a pattern reminiscent of a Mercedes-Benz logo, with three regions radiating from a central point where all three lines intersect.

With four classes, the geometry becomes richer still. We now have six boundary lines (as $\binom{4}{2} = 6$), which can create patterns resembling a window pane as they partition the space into regions for each class. The beauty of this framework is that despite the potentially complex patterns of these boundaries, each point in space is assigned a well-defined probability distribution over all classes through the softmax function, ensuring consistent and meaningful classifications.

8.5 Multi-Class Cross-Entropy Loss

Now that we've derived the softmax function to convert our linear predictions into proper probabilities, we need to determine how to find the optimal weight vectors $\{\mathbf{w}_k\}_{k=1}^{K-1}$. Just as in binary classification, we'll use maximum likelihood estimation - choosing the weights that make our observed data most probable under our model.

The key difference here is that unlike binary classification, where the likelihood is depicted by the Bernoulli distribution (as we only had two possible outcomes), we now need to handle K possible outcomes. Let's denote our true labels as $\mathbf{t}$, a one-hot encoded vector where $t_k = 1$ if the example belongs to class k and 0 otherwise. For a single training example, the likelihood - that is, the probability of observing this particular class label given our model's predictions and parameters - is:

$$L = \prod_{k=1}^{K} P(C_k|\mathbf{x}, \{\mathbf{w}_k\}_{k=1}^{K-1})^{t_k} \tag{8.32}$$

Since $\mathbf{t}$ is one-hot encoded, only one term in this product will be non-zero - the term corresponding to the true class. For example, if an object belongs to class 2, then $t_2 = 1$ and all other $t_k = 0$, so the likelihood for this single datum is $L = P(C_2|\mathbf{x}, \{\mathbf{w}_k\}_{k=1}^{K-1})$. This matches our intuition - the likelihood of observing this particular instance of class 2 under our model is exactly the probability our model assigned to class 2.

For our full dataset of N examples, assuming independence between observations, the joint likelihood is the product of individual likelihoods:

$$L = \prod_{i=1}^{N}\prod_{k=1}^{K} P(C_k|\mathbf{x}_i, \{\mathbf{w}_k\}_{k=1}^{K-1})^{t_{ik}} \tag{8.33}$$

where i indexes over the N training examples and k indexes over the K possible classes. The term t_{ik} is the (i, k) element of our one-hot encoded label matrix - it equals 1 if the ith example belongs to class k, and 0 otherwise. Taking the negative logarithm of this joint likelihood for numerical stability (just as we did in binary classification) and normalizing by N to ensure consistent scale across different dataset sizes:

$$E(\{\mathbf{w}_k\}_{k=1}^{K-1}) = -\frac{1}{N}\ln L = -\frac{1}{N}\sum_{i=1}^{N}\sum_{k=1}^{K} t_{ik}\ln P(C_k|\mathbf{x}_i, \{\mathbf{w}_k\}_{k=1}^{K-1}) \tag{8.34}$$

This multi-class cross-entropy loss naturally generalizes our binary cross-entropy. To see this connection explicitly, let's first examine what happens when $K = 2$:

$$E = -\frac{1}{N}\sum_{i=1}^{N}\sum_{k=1}^{2} t_{ik}\ln P(C_k|\mathbf{x}_i, \{\mathbf{w}_k\}_{k=1}^{1}) \tag{8.35}$$

$$= -\frac{1}{N}\sum_{i=1}^{N}\left[t_{i1}\ln\frac{\exp(\mathbf{w}_1^T\mathbf{x}_i)}{1 + \exp(\mathbf{w}_1^T\mathbf{x}_i)} + t_{i2}\ln\frac{1}{1 + \exp(\mathbf{w}_1^T\mathbf{x}_i)}\right] \tag{8.36}$$

Since each example belongs to exactly one class, $t_{i1} + t_{i2} = 1$. Using $t_i = t_{i1}$ (so $t_{i2} = 1 - t_i$), this simplifies to:

$$E = -\frac{1}{N}\sum_{i=1}^{N}[t_i\ln y_i + (1 - t_i)\ln(1 - y_i)] \tag{8.37}$$

where

$$y_i = \frac{\exp(\mathbf{w}^T\mathbf{x}_i)}{1 + \exp(\mathbf{w}^T\mathbf{x}_i)} \tag{8.38}$$

is our predicted probability for class 1 - exactly the binary cross-entropy loss from Chapter

7.

In our current multi-class setting with K classes, we can express our cross-entropy loss more compactly. Using the softmax function to compute our predicted probabilities:

$$y_{ik} = P(C_k|\mathbf{x}_i) = \frac{\exp(\mathbf{w}_k^T \mathbf{x}_i)}{\sum_{j=1}^{K} \exp(\mathbf{w}_j^T \mathbf{x}_i)} \tag{8.39}$$

where we set $\mathbf{w}_K = \mathbf{0}$ for the reference class. It's important to note that this additional weight vector for the reference class is fixed at zero and is not optimized during training. With this convention, our loss function becomes:

$$E(\{\mathbf{w}_k\}_{k=1}^{K-1}) = -\frac{1}{N} \sum_{i=1}^{N} \sum_{k=1}^{K} t_{ik} \ln y_{ik} \tag{8.40}$$

To find the optimal weight vectors $\{\mathbf{w}_k\}_{k=1}^{K-1}$, we will need to use gradient descent, carefully considering how changes in each weight vector affect not just its own class probabilities but all others through the normalization term. We'll explore these optimization details in Section 7. However, the form of our loss function - particularly terms like $t_{ik} \ln y_{ik}$ - might remind you of expressions from information theory, such as entropy. This is not a coincidence.

There are connections between our classification framework and fundamental concepts from information theory that help explain why this loss function works well. Before diving into the technical details of optimization, we'll explore these connections in the next section, which will provide valuable insight into why cross-entropy is a natural choice for our loss function.

8.6   Information Theory and Cross-Entropy

The cross-entropy loss we derived for multi-class logistic regression has connections to information theory that go beyond mere mathematical coincidence, which is why the loss is called cross-entropy in the first place. A successful classification model should serve as a useful compression of the data - if we have learned a good set of weights, we can predict class labels from features without storing all the true labels. This connection between compression, prediction, and information leads us to the concept of mutual information. Let's explore these relationships systematically.

For any two random variables X and Y, their mutual information $I(X;Y)$ quantifies how much knowing one tells us about the other:

$$I(X;Y) = \sum_{x \in \mathcal{X}} \sum_{y \in \mathcal{Y}} P(X = x, Y = y) \log_2 \left[\frac{P(X = x, Y = y)}{P(X = x)P(Y = y)} \right] \tag{8.41}$$

The ratio $\frac{P(X,Y)}{P(X)P(Y)}$ compares the joint probability $P(X,Y)$ to what we'd expect if X and Y were independent ($P(X)P(Y)$). When X and Y are truly independent, this ratio equals 1 and thus $\log_2(1) = 0$. However, when the variables are dependent, this ratio exceeds 1 in regions where they share information. Taking the logarithm converts this multiplicative relationship to an additive one, and weighting by $P(X,Y)$ ensures we average over the actual joint distribution of the variables.

The output is measured in bits because we use logarithm base 2 in the formula, where each bit represents a binary decision that halves the uncertainty about one variable given knowledge of the other. This choice of base 2 aligns with information theory's fundamental unit of binary digits (bits), making the measure directly interpretable in terms of the minimum number of yes/no questions needed to specify one variable.

One of the key advantages of mutual information is that it provides a more robust measure of dependence than correlation by examining the full joint probability distribution rather than just linear relationships. To understand this distinction, let's first recall how correlation measures relationships between variables.

From Chapter 3, recall that the correlation coefficient measures linear relationships through:

$$\rho_{XY} = \frac{\text{Cov}(X,Y)}{\sigma_X \sigma_Y} = \frac{E[(X - \mu_X)(Y - \mu_Y)]}{\sigma_X \sigma_Y} \tag{8.42}$$

where μ_X and μ_Y are the means of X and Y respectively, and σ_X and σ_Y are their standard deviations. This formula shows how correlation only captures linear trends through the average product of deviations from the mean.

In contrast, mutual information measures general statistical dependence:

$$I(X;Y) = \sum_{x,y} p(x,y) \log \left(\frac{p(x,y)}{p(x)p(y)} \right) \tag{8.43}$$

To illustrate this difference, consider a circular relationship where points lie roughly

on a circle centered at the origin. Despite the clear geometric pattern, the correlation coefficient is near zero because the relationship isn't linear - when we move right on the circle, sometimes Y increases and sometimes it decreases, averaging out in the correlation calculation. However, knowing X clearly provides information about Y - for any given X value, Y is constrained to be approximately $\pm\sqrt{1 - X^2}$ on the unit circle. Mutual information captures this structure by detecting that knowing X constrains the possible values of Y to specific regions, making their joint distribution $p(x, y)$ significantly different from the product of their marginals $p(x)p(y)$.
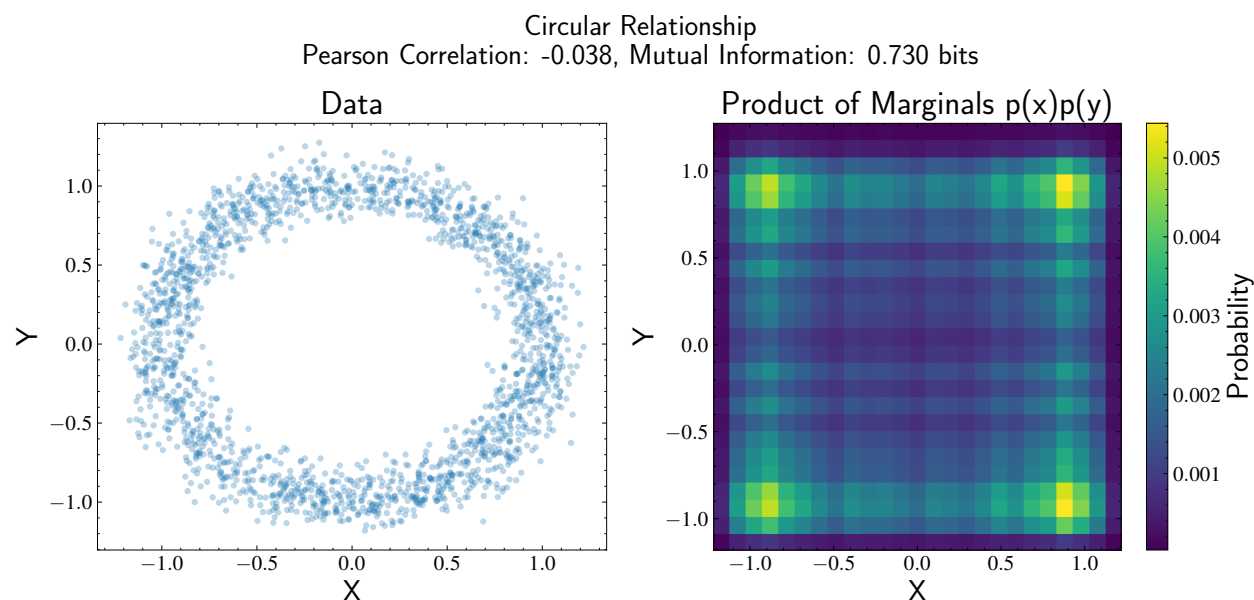
Figure 8.5: Comparison of (Pearson) correlation and mutual information for detecting statistical dependence. Left panel: Scatter plot showing data points arranged in a circular pattern. Despite the clear geometric structure, the correlation is nearly zero ($\rho \approx 0$) because the relationship is not linear - as X increases, Y sometimes increases and sometimes decreases, averaging out in the correlation calculation. Right panel: The product of marginal distributions $p(x)p(y)$ shows what we would expect if X and Y were independent. The significant difference between this independent model and the actual circular pattern in the data (left panel) leads to high mutual information ($I(X; Y) \approx 1$ bit), correctly identifying the strong statistical dependence between the variables. This example illustrates how mutual information can detect nonlinear relationships that correlation misses.

This example highlights why mutual information often serves as a better measure of statistical dependence in machine learning applications. While correlation only detects linear trends, mutual information can identify any systematic relationship where knowing one variable provides information about the other, regardless of the relationship's shape.

To better understand how mutual information is calculated in practice, let's work

through a concrete example. Suppose Y is a uniformly distributed number between 1 and 16, and X tells us whether Y is in the first half (1-8) or second half (9-16) of its range. The probabilities are:

- $P(Y = y) = 1/16$ for each y (uniform distribution)

- $P(X = \text{first}) = P(X = \text{second}) = 1/2$

- $P(Y|X = \text{first}) = 1/8$ for y in 1-8, 0 otherwise

- $P(Y|X = \text{second}) = 1/8$ for y in 9-16, 0 otherwise

The key insight comes from rewriting the ratio inside the logarithm:

$$\frac{P(X,Y)}{P(X)P(Y)} = \frac{P(Y|X)}{P(Y)} \tag{8.44}$$

This ratio compares our knowledge of Y before and after knowing X. Initially, $P(Y) = 1/16$ for any value. After knowing X, $P(Y|X) = 1/8$ for values in the correct half and 0 otherwise. When $P(Y|X) > P(Y)$, the logarithm becomes positive, indicating we've gained information:

$$I(X;Y) = \sum_{x,y} P(X,Y) \log_2 \left[\frac{P(Y|X)}{P(Y)} \right] \tag{8.45}$$

$$= 16 \cdot \frac{1}{16} \log_2 \left[\frac{1/8}{1/16} \right] \tag{8.46}$$

$$= \log_2(2) = 1 \text{ bit} \tag{8.47}$$

The ratio $\frac{1/8}{1/16} = 2$ inside the logarithm shows that knowing X doubles our certainty about Y (halves our uncertainty), corresponding to one bit of information gained. To fully specify Y, we would need three additional bits to narrow down which of the eight remaining values is correct, but X only provides us with that first bit of information.

Note that the factor $P(X,Y)$ in the summation serves to average this information gain over all possible combinations of X and Y values according to their joint probability distribution. In our case, since all valid combinations are equally likely (with probability $1/16$), this averaging simply gives us the typical information gain of one bit.

Now that we understand how mutual information quantifies the information shared

between variables in a simple numeric example, let's see how this concept applies to our classification problem. In our classification task, X represents input features (like a galaxy's concentration index or asymmetry) and Y represents class labels (such as elliptical, spiral, or irregular). The mutual information $I(X;Y)$ quantifies how much our features tell us about the class labels.

To make this connection precise, let's first rewrite mutual information using conditional probabilities. Starting from our earlier formula:

$$I(\mathbf{x};\mathbf{y}) = \sum_{\mathbf{x},\mathbf{y}} p(\mathbf{x},\mathbf{y}) \log \left[\frac{p(\mathbf{y}|\mathbf{x})}{p(\mathbf{y})} \right] \tag{8.48}$$

Here, $p(\mathbf{y}|\mathbf{x})$ represents the probability of class $\mathbf{y}$ given features $\mathbf{x}$. In our classifier, this conditional probability is exactly what the softmax function computes when we write $P(C_k|\mathbf{x})$.

Now let's examine our cross-entropy loss for multi-class classification averaged over N training examples:

$$E(\{\mathbf{w}_k\}) = -\sum_{i=1}^{N} \sum_{k=1}^{K} \frac{t_{ik}}{N} \log P(C_k|\mathbf{x}_i) \tag{8.49}$$

The term t_{ik}/N represents the empirical probability of observing class k with feature vector $\mathbf{x}_i$ in our training data. Therefore, this sum can be rewritten as an expectation over the empirical joint distribution $p(\mathbf{x},\mathbf{y})$ of our training data:

$$E(\{\mathbf{w}_k\}) = -\sum_{\mathbf{x},\mathbf{y}} p(\mathbf{x},\mathbf{y}) \log p(\mathbf{y}|\mathbf{x}) \tag{8.50}$$

Looking at these equations side by side, let's expand the mutual information:

$$I(\mathbf{x};\mathbf{y}) = \sum_{\mathbf{x},\mathbf{y}} p(\mathbf{x},\mathbf{y}) \log p(\mathbf{y}|\mathbf{x}) - \sum_{\mathbf{x},\mathbf{y}} p(\mathbf{x},\mathbf{y}) \log p(\mathbf{y}) \tag{8.51}$$

$$= -E(\{\mathbf{w}_k\}) - \sum_{\mathbf{y}} p(\mathbf{y}) \log p(\mathbf{y}) \tag{8.52}$$

The second term, $-\sum_{\mathbf{y}} p(\mathbf{y}) \log p(\mathbf{y})$, is the information entropy of our class distribution $H(\mathbf{y})$, which depends only on the frequencies of different classes in our dataset. Since this

term is independent of our model parameters $\{\mathbf{w}_k\}$, we have a fundamental relationship:

$$E(\{\mathbf{w}_k\}) = H(\mathbf{y}) - I(\mathbf{x}; \mathbf{y}; \{\mathbf{w}_k\}) \tag{8.53}$$

Thus, minimizing cross-entropy loss is equivalent to maximizing the mutual information between our predictions and class labels! When we train our classifier by minimizing cross-entropy loss, we're actually finding the optimal linear combination of input features that produces predictions sharing maximum mutual information with the true class labels.

Combinations of features that work well for classification must have high mutual information with class labels. For galaxy classification, morphological features like concentration index work well because they share significant mutual information with galaxy type - knowing a galaxy's concentration index tells us a lot about its morphological class. Conversely, a feature like absolute sky position typically has low mutual information with morphology.

Finally, let's examine the entropy term $H(\mathbf{y})$ that appeared in our derivation. While this term doesn't affect our optimization of weights, it reveals some insights about our classification task. Recall that our cross-entropy loss is:

$$E(\{\mathbf{w}_k\}) = -\sum_{i=1}^{N} \sum_{k=1}^{K} \frac{t_{ik}}{N} \log P(C_k|\mathbf{x}_i) = H(\mathbf{y}) - I(\mathbf{x}; \mathbf{y}) \tag{8.54}$$

If we achieve perfect prediction where $P(C_k|\mathbf{x}_i) = 1$ exactly when $t_{ik} = 1$ for all data points (meaning our model predicts probability 1 for the correct class and 0 for all others), then $E(\{\mathbf{w}_k\}) = 0$. This implies $H(\mathbf{y}) = I(\mathbf{x}; \mathbf{y})$, meaning we've extracted all possible information from our features about the class labels. Hence, optimizing cross-entropy loss can be viewed as trying to get $I(\mathbf{x}; \mathbf{y})$ as close as possible to $H(\mathbf{y})$. The remaining gap represents the uncertainty in mapping features to class labels with our model.

In information theory, entropy quantifies uncertainty - specifically, how many bits we need on average to encode different possibilities. For any random variable with probability distribution $p(\mathbf{y})$, its entropy is:

$$H(\mathbf{y}) = -\sum_{\mathbf{y}} p(\mathbf{y}) \log p(\mathbf{y}) \tag{8.55}$$

To understand this concretely, imagine encoding different galaxy types in a catalog.

If we have three types (elliptical, spiral, irregular) appearing with equal frequency, then $p(\mathbf{y}) = 1/3$ for each type, giving us:

$$H(\mathbf{y}) = -3 \cdot \frac{1}{3} \log \frac{1}{3} = \log 3 \approx 1.58 \text{ bits} \tag{8.56}$$

This means we need about 1.58 bits per galaxy to encode its type in this idealized case. To understand why we can do better than 2 bits, consider a simpler example: encoding the letters 'e' and 'z' in English text. While we could use 1 bit per letter (0 for 'e', 1 for 'z'), this ignores that 'e' appears much more frequently in English. By using a shorter code for 'e' (say 0) and a longer code for 'z' (say 110), we can achieve an average bits-per-letter lower than 1 when encoding lots of text. Similarly, if certain galaxy types appear more frequently than others, we can use shorter codes for common types and longer codes for rare types, achieving the theoretical minimum of 1.58 bits per galaxy on average.

In our case, spiral galaxies are more common than irregulars, so we need fewer bits on average by using shorter codes for spirals. This is exactly what entropy captures - it's minimized when one class dominates (requiring fewer bits since most instances belong to the same class) and maximized when classes are balanced (requiring more bits since we have maximum uncertainty about class membership).

In our classifier, this entropy term comes from the empirical distribution of our training data:

$$H(\mathbf{y}) = -\sum_{\mathbf{y}} \frac{N_k}{N} \log \frac{N_k}{N} \tag{8.57}$$

where N_k is the number of examples of class k in our N total examples. This term is completely determined by our class distribution - no amount of clever feature engineering or weight optimization can change it.

Mathematically, if we achieved perfect prediction where features completely determined class labels, we would have $I(\mathbf{x}; \mathbf{y}) = H(\mathbf{y})$ and thus zero loss. This would mean our model's predicted probabilities exactly match the true class indicators: $P(C_k|\mathbf{x}_i) = t_{ik}$ for all examples.

When our loss approaches zero, it indicates our classifier is approaching the best theoretically possible performance, extracting nearly all available information from the features. At this point, we only need $H(\mathbf{y})$ bits to encode the output class, as we can safely ignore other information due to perfect prediction. The gap between our actual loss and zero tells

us how far we are from this theoretical ideal. A large gap suggests room for improvement, either in our choice of features or how to combine them.

8.7 Gradient Descent for Multi-Class Classification

Now that we've established the cross-entropy loss function for multi-class classification, let's extend our optimization approach to the multi-class setting. We'll see how the principles of gradient descent generalize to handle multiple classes, with some important considerations specific to this more complex scenario.

Recall that our multi-class cross-entropy loss function is:

$$E(\{\mathbf{w}_k\}_{k=1}^{K-1}) = -\frac{1}{N} \sum_{i=1}^{N} \sum_{k=1}^{K} t_{ik} \ln y_{ik} \tag{8.58}$$

where y_{ik} is the predicted probability that the i-th example belongs to class k, and t_{ik} is the corresponding element of the one-hot encoded true label.

To optimize this loss function using gradient descent, we need to compute the gradient with respect to each weight vector $\mathbf{w}_j$ for $j = 1, 2, \ldots, K - 1$. This is more complex than the binary case because changes in any weight vector affect the predicted probabilities for all classes through the normalization term in the softmax function.

Let's derive the gradients step by step. First, recall that we've simplified our softmax expressions by setting $\mathbf{w}_K = \mathbf{0}$ for the reference class, giving us:

$$y_{ik} = \frac{\exp(\mathbf{w}_k^T \mathbf{x}_i)}{\sum_{j=1}^{K} \exp(\mathbf{w}_j^T \mathbf{x}_i)} \quad \text{for } k = 1, 2, \ldots, K \tag{8.59}$$

where $\mathbf{w}_K = \mathbf{0}$ implies $\exp(\mathbf{w}_K^T \mathbf{x}_i) = 1$.

We need to compute $\partial E / \partial \mathbf{w}_j$ for each $j \in \{1, 2, \ldots, K - 1\}$. Using the chain rule:

$$\frac{\partial E}{\partial \mathbf{w}_j} = -\frac{1}{N} \sum_{i=1}^{N} \sum_{k=1}^{K} t_{ik} \frac{\partial \ln y_{ik}}{\partial \mathbf{w}_j} \tag{8.60}$$

The key challenge is determining how changes in $\mathbf{w}_j$ affect each y_{ik}. There are two cases to consider:

1. How changes in $\mathbf{w}_j$ affect the probability of class j itself (y_{ij})

2. How changes in $\mathbf{w}_j$ affect the probabilities of other classes (y_{ik} for $k \neq j$)

Let's start by examining the derivatives of y_{ik} with respect to the dot product $z_{ij} = \mathbf{w}_j^T \mathbf{x}_i$. The key insight is that when $k = j$, both the numerator and denominator of the softmax function depend on $\mathbf{w}_j$, requiring the quotient rule. When $k \neq j$, only the denominator depends on $\mathbf{w}_j$.

For $k = j$ (the same class as the weight vector we're differentiating with respect to):

$$\frac{\partial y_{ij}}{\partial z_{ij}} = \frac{\partial}{\partial z_{ij}} \frac{e^{z_{ij}}}{\sum_{l=1}^{K} e^{z_{il}}} \tag{8.61}$$

Here we need to apply the quotient rule

$$\frac{d}{dx}\left(\frac{f(x)}{g(x)}\right) = \frac{f'(x)g(x) - f(x)g'(x)}{g(x)^2} \tag{8.62}$$

where:

$$f(z_{ij}) = e^{z_{ij}} \quad \Rightarrow \quad f'(z_{ij}) = e^{z_{ij}} \tag{8.63}$$

$$g(z_{ij}) = \sum_{l=1}^{K} e^{z_{il}} \quad \Rightarrow \quad g'(z_{ij}) = e^{z_{ij}} \tag{8.64}$$

Applying the quotient rule:

$$\frac{\partial y_{ij}}{\partial z_{ij}} = \frac{e^{z_{ij}} \cdot \sum_{l=1}^{K} e^{z_{il}} - e^{z_{ij}} \cdot e^{z_{ij}}}{(\sum_{l=1}^{K} e^{z_{il}})^2} \tag{8.65}$$

$$= \frac{e^{z_{ij}} \cdot (\sum_{l=1}^{K} e^{z_{il}} - e^{z_{ij}})}{(\sum_{l=1}^{K} e^{z_{il}})^2} \tag{8.66}$$

$$= \frac{e^{z_{ij}}}{\sum_{l=1}^{K} e^{z_{il}}} \cdot \frac{\sum_{l=1}^{K} e^{z_{il}} - e^{z_{ij}}}{\sum_{l=1}^{K} e^{z_{il}}} \tag{8.67}$$

$$= y_{ij} \cdot \left(1 - \frac{e^{z_{ij}}}{\sum_{l=1}^{K} e^{z_{il}}}\right) \tag{8.68}$$

$$= y_{ij} \cdot (1 - y_{ij}) \tag{8.69}$$

For $k \neq j$ (different class), the numerator $e^{z_{ik}}$ is constant with respect to z_{ij} (since $k \neq j$), so we only need to consider how the denominator changes:

$$\frac{\partial y_{ik}}{\partial z_{ij}} = \frac{\partial}{\partial z_{ij}} \frac{e^{z_{ik}}}{\sum_{l=1}^{K} e^{z_{il}}} \tag{8.70}$$

$$= e^{z_{ik}} \cdot \frac{\partial}{\partial z_{ij}} \left(\frac{1}{\sum_{l=1}^{K} e^{z_{il}}} \right) \tag{8.71}$$

$$= e^{z_{ik}} \cdot \frac{-e^{z_{ij}}}{\left(\sum_{l=1}^{K} e^{z_{il}} \right)^2} \tag{8.72}$$

$$= -\frac{e^{z_{ik}} \cdot e^{z_{ij}}}{\left(\sum_{l=1}^{K} e^{z_{il}} \right)^2} \tag{8.73}$$

$$= -\frac{e^{z_{ik}}}{\sum_{l=1}^{K} e^{z_{il}}} \cdot \frac{e^{z_{ij}}}{\sum_{l=1}^{K} e^{z_{il}}} \tag{8.74}$$

$$= -y_{ik} \cdot y_{ij} \tag{8.75}$$

Now, using the chain rule to compute $\partial \ln y_{ik}/\partial \mathbf{w}_j$, we need to recognize that y_{ik} depends on all logits z_{il} for $l = 1, 2, \ldots, K$. Therefore, we should apply the chain rule across all these dependencies:

$$\frac{\partial \ln y_{ik}}{\partial \mathbf{w}_j} = \sum_{l=1}^{K-1} \frac{\partial \ln y_{ik}}{\partial z_{il}} \cdot \frac{\partial z_{il}}{\partial \mathbf{w}_j} \tag{8.76}$$

However, only one term in this sum is non-zero: $\partial z_{il}/\partial \mathbf{w}_j = \mathbf{x}_i$ when $l = j$, and $\partial z_{il}/\partial \mathbf{w}_j = 0$ when $l \neq j$. This simplifies our calculation to:

$$\frac{\partial \ln y_{ik}}{\partial \mathbf{w}_j} = \frac{\partial \ln y_{ik}}{\partial z_{ij}} \cdot \frac{\partial z_{ij}}{\partial \mathbf{w}_j} \tag{8.77}$$

$$= \frac{\partial \ln y_{ik}}{\partial z_{ij}} \cdot \mathbf{x}_i \tag{8.78}$$

For $k = j$ (same class):

$$\frac{\partial \ln y_{ij}}{\partial \mathbf{w}_j} = \frac{\partial \ln y_{ij}}{\partial z_{ij}} \cdot \mathbf{x}_i \tag{8.79}$$

$$= \frac{1}{y_{ij}} \cdot \frac{\partial y_{ij}}{\partial z_{ij}} \cdot \mathbf{x}_i \tag{8.80}$$

$$= \frac{1}{y_{ij}} \cdot y_{ij} \cdot (1 - y_{ij}) \cdot \mathbf{x}_i \tag{8.81}$$

$$= (1 - y_{ij}) \cdot \mathbf{x}_i \tag{8.82}$$

For $k \neq j$ (different class):

$$\frac{\partial \ln y_{ik}}{\partial \mathbf{w}_j} = \frac{\partial \ln y_{ik}}{\partial z_{ij}} \cdot \mathbf{x}_i \tag{8.83}$$

$$= \frac{1}{y_{ik}} \cdot \frac{\partial y_{ik}}{\partial z_{ij}} \cdot \mathbf{x}_i \tag{8.84}$$

$$= \frac{1}{y_{ik}} \cdot (-y_{ik} \cdot y_{ij}) \cdot \mathbf{x}_i \tag{8.85}$$

$$= -y_{ij} \cdot \mathbf{x}_i \tag{8.86}$$

Now we can substitute these results back into our gradient expression:

$$\frac{\partial E}{\partial \mathbf{w}_j} = -\frac{1}{N} \sum_{i=1}^{N} \left[t_{ij} \cdot (1 - y_{ij}) \cdot \mathbf{x}_i - \sum_{k \neq j} t_{ik} \cdot y_{ij} \cdot \mathbf{x}_i \right] \tag{8.87}$$

$$= -\frac{1}{N} \sum_{i=1}^{N} \left[t_{ij} - t_{ij} \cdot y_{ij} - y_{ij} \cdot \sum_{k \neq j} t_{ik} \right] \mathbf{x}_i \tag{8.88}$$

Since $\mathbf{t}_i$ is a one-hot encoded vector, $\sum_{k=1}^{K} t_{ik} = 1$, and $\sum_{k \neq j} t_{ik} = 1 - t_{ij}$. Therefore:

$$\frac{\partial E}{\partial \mathbf{w}_j} = -\frac{1}{N} \sum_{i=1}^{N} [t_{ij} - t_{ij} \cdot y_{ij} - y_{ij} \cdot (1 - t_{ij})] \mathbf{x}_i \tag{8.89}$$

$$= -\frac{1}{N} \sum_{i=1}^{N} [t_{ij} - t_{ij} \cdot y_{ij} - y_{ij} + t_{ij} \cdot y_{ij}] \mathbf{x}_i \tag{8.90}$$

$$= -\frac{1}{N} \sum_{i=1}^{N} (t_{ij} - y_{ij}) \mathbf{x}_i \tag{8.91}$$

$$= \frac{1}{N} \sum_{i=1}^{N} (y_{ij} - t_{ij}) \mathbf{x}_i \tag{8.92}$$

This gives us the final gradient formula:

$$\frac{\partial E}{\partial \mathbf{w}_j} = \frac{1}{N} \sum_{i=1}^{N} (y_{ij} - t_{ij}) \mathbf{x}_i \tag{8.93}$$

The gradient for each weight vector $\mathbf{w}_j$ is determined by the difference between the predicted probability y_{ij} and the true label t_{ij} for class j, scaled by the feature vector $\mathbf{x}_i$. This is exactly analogous to the binary case, with the key difference being that we now have $K - 1$ separate weight vectors to update, one for each non-reference class.

The gradient formula reveals important insights into how multi-class logistic regression learns from data. While superficially similar to the binary case, the multi-class gradient introduces a different correction mechanism. In binary classification, when an example is misclassified, there's a single correction that moves the decision boundary in the appropriate direction. In multi-class classification, a single misclassified example simultaneously affects multiple decision boundaries through a coordinated push-pull dynamic.

Consider a galaxy that truly belongs to class j but is incorrectly assigned high probability for class k. For the true class j, the term $(y_{ij} - t_{ij})$ becomes $(y_{ij} - 1)$, which is negative since $y_{ij} < 1$. When multiplied by $-\eta$ in the gradient descent update, this results in adding a positive multiple of $\mathbf{x}_i$ to $\mathbf{w}_j$, effectively increasing the weight vector in the direction of the galaxy's features. Simultaneously, for the incorrect class k, the term $(y_{ik} - t_{ik})$ becomes $(y_{ik} - 0) = y_{ik} > 0$, which leads to a subtraction from $\mathbf{w}_k$. This coordinated push-pull dynamic, where multiple weight vectors are adjusted concurrently in response to a single misclassification, creates significantly more complex learning behavior than in the binary

classification case.

The magnitude of these corrections also differs meaningfully. In binary classification, the largest corrections occur for high-confidence mistakes. In multi-class settings, the correction magnitude depends on how the probability mass is distributed across all classes. Mathematically, if $y_{ij} \approx 0$ for the true class j, the update magnitude $|y_{ij} - 1| \approx 1$ is at its maximum. If this missing probability mass is concentrated in a single incorrect class k such that $y_{ik} \approx 1$, then $|y_{ik} - 0| \approx 1$ also approaches its maximum value, resulting in large updates to both weight vectors. However, if the probability is spread across many incorrect classes, each with small y_{ik} values, the individual updates to each incorrect class's weight vector will be smaller, though their cumulative effect remains significant.

This interdependence of updates has implications for the optimization landscape. The complex loss surface requires SGD to navigate by systematically adjusting multiple decision boundaries in a coordinated manner, with each update propagating effects throughout the entire model structure.

Extending SGD to Multi-Class Problems   Having derived the gradients for multi-class logistic regression and understood their geometric interpretation, we can now extend our SGD approach from the binary case. The core principle remains the same: we approximate the full gradient using mini-batches and update the parameters iteratively.

For multi-class classification, the SGD update rule is:

$$\mathbf{w}_j^{(t+1)} = \mathbf{w}_j^{(t)} - \eta \cdot \frac{1}{M} \sum_{i=1}^{M} (y_{ij}^{(t)} - t_{ij})\mathbf{x}_i \quad \text{for } j = 1, 2, \ldots, K - 1 \tag{8.94}$$

The key difference from binary classification is that we're now updating $K - 1$ weight vectors simultaneously rather than a single weight vector. This parallel updating of multiple weight vectors is crucial for maintaining consistency among the class probability estimates, which must sum to 1 across all classes.

Many of the techniques discussed for binary classification—like mini-batching, learning rate scheduling, and regularization—apply directly to the multi-class case with minimal modification. For example, we can still implement weight decay by adding the term $-\lambda\mathbf{w}_j$ to each update, or use adaptive learning rates. The fundamental principles remain the same, though the implementation must account for the additional weight vectors.

It's important to note that we only update the first $K - 1$ weight vectors, keeping $\mathbf{w}_K = \mathbf{0}$ fixed throughout training as our reference class. This constraint reflects our parameterization choice and ensures that our model remains properly specified with the correct degrees of freedom.

8.8 Implementation Considerations

The mathematical formulation of multi-class logistic regression with softmax is straightforward in theory, but several practical considerations become important when implementing these models for real-world applications. These considerations can significantly impact model performance, training stability, and computational efficiency.

Numerical Stability The softmax function involves exponentials, which can easily cause overflow or underflow. While the binary logistic regression also uses an exponential function in the sigmoid ($\sigma(z) = 1/(1 + e^{-z})$), the multi-class case is more susceptible to numerical issues because we're computing multiple exponentials across K classes. With more weight vectors $\mathbf{w}_j$, there's a higher chance that some logit values $\mathbf{w}_j^T \mathbf{x}_i$ will be extremely large or small, potentially causing numerical instability.

A standard practice to prevent numerical issues is to subtract the maximum logit value before exponentiation:

$$y_{ik} = \frac{\exp(\mathbf{w}_k^T \mathbf{x}_i - \max_j \mathbf{w}_j^T \mathbf{x}_i)}{\sum_{j=1}^K \exp(\mathbf{w}_j^T \mathbf{x}_i - \max_j \mathbf{w}_j^T \mathbf{x}_i)} \tag{8.95}$$

This normalization doesn't change the resulting probabilities because the constant factor $\exp(-\max_j \mathbf{w}_j^T \mathbf{x}_i)$ appears in both numerator and denominator and cancels out:

$$y_{ik} = \frac{\exp(\mathbf{w}_k^T \mathbf{x}_i - \max_j \mathbf{w}_j^T \mathbf{x}_i)}{\sum_{j=1}^K \exp(\mathbf{w}_j^T \mathbf{x}_i - \max_j \mathbf{w}_j^T \mathbf{x}_i)} \tag{8.96}$$

$$= \frac{\exp(\mathbf{w}_k^T \mathbf{x}_i) \cdot \exp(-\max_j \mathbf{w}_j^T \mathbf{x}_i)}{\sum_{j=1}^K \exp(\mathbf{w}_j^T \mathbf{x}_i) \cdot \exp(-\max_j \mathbf{w}_j^T \mathbf{x}_i)} \tag{8.97}$$

$$= \frac{\exp(\mathbf{w}_k^T \mathbf{x}_i)}{\sum_{j=1}^K \exp(\mathbf{w}_j^T \mathbf{x}_i)} \tag{8.98}$$

While mathematically equivalent, the normalized version prevents numerical issues by ensuring the largest exponent is always 0, keeping all values in a manageable range.

Parameter Initialization   Parameter initialization plays a crucial role in multi-class settings. A common approach is to initialize each weight vector with small random values drawn from a multidimensional normal or uniform distribution, with the same dimensionality as the feature space. This is particularly advantageous because both normal and uniform distributions allow us to easily generate random values regardless of the dimensionality of the feature space, making them practical choices even when dealing with high-dimensional astronomical data.

This initialization strategy serves a vital purpose: it breaks the symmetry between different weight vectors and ensures that they diverge during training to learn distinct patterns. Without this random initialization, weight vectors might update identically and fail to differentiate between classes, essentially defeating the purpose of having multiple classifiers. The small magnitude of these initial values is also significant as it prevents the softmax function from saturating at the beginning of training, allowing gradients to flow effectively and enabling the model to learn more efficiently from early training examples.

Unlike binary logistic regression, which has a convex optimization landscape, multiclass logistic regression does not necessarily present a convex optimization problem. This non-convexity means that different initializations can lead to different local minima, potentially resulting in varying model performance. For this reason, employing multiple random initializations and selecting the best-performing model based on validation performance becomes a critical practice in multi-class settings.

This random restart approach can be implemented through the following steps:

1. Initialize R different models with random weight matrices $\mathbf{W}^{(1)}, \mathbf{W}^{(2)}, \ldots, \mathbf{W}^{(R)}$, where each $\mathbf{W}^{(r)} \in \mathbb{R}^{K \times d}$. Here, K represents the total number of classes in our classification problem, and d is the dimensionality of our feature space (i.e., the number of features or predictors in our dataset). For each initialization, ensure that the last row $\mathbf{w}_K$ is set to zero, as this corresponds to our reference class. This constraint maintains consistency with our mathematical formulation where we defined the reference class to have zero weights.

2. For each initialization $r = 1, 2, \ldots, R$:

(a) Train the model using SGD with the update rule:

$$\mathbf{w}_j^{(t+1)} = \mathbf{w}_j^{(t)} - \eta \cdot \frac{1}{M} \sum_{i=1}^{M} (y_{ij}^{(t)} - t_{ij}) \mathbf{x}_i \quad \text{for } j = 1, 2, \ldots, K-1 \tag{8.99}$$

where M is the mini-batch size. Note that we only update the first $K-1$ weight vectors, keeping $\mathbf{w}_K = \mathbf{0}$ fixed throughout training as our reference class.

(b) Evaluate the trained model on a validation set to obtain a performance metric $S^{(r)}$ (e.g., accuracy, F1-score, or cross-entropy loss).

3. Select the best model r^* according to:

$$r^* = \arg\max_r S^{(r)} \tag{8.100}$$

This identifies the index r^* of the model that achieved the highest performance after training.

4. Use the selected model $\mathbf{W}^{(r^*)}$ for final evaluation on the test set. Here, $\mathbf{W}^{(r^*)}$ represents the fully trained weight matrix that performed best on the validation set, containing all the optimized weight vectors $\mathbf{w}_j$ for $j = 1, 2, \ldots, K-1$ that define our optimal multi-class logistic regression model.

The computational cost of this approach scales linearly with the number of initializations R, but the benefits often outweigh this cost. In astronomical applications where classification accuracy directly impacts scientific conclusions (such as galaxy morphology classification or stellar type identification), this additional computational effort to find optimal initializations is well justified by the improved classification performance. For example, when classifying rare astronomical phenomena that may constitute only a small fraction of the dataset, finding the optimal decision boundaries through multiple initializations can significantly improve the detection rate of these important but infrequent objects.

Matrix Formulation for Efficiency For efficient implementation, we can organize the weight vectors as rows of a matrix $\mathbf{W} \in \mathbb{R}^{K \times d}$ (where d is the feature dimension). This matrix formulation enables vectorized computation across all classes and examples simultaneously, with the understanding that the last row $\mathbf{w}_K$ is constrained to be zero:

1. Let $\mathbf{X} \in \mathbb{R}^{N \times d}$ be the data matrix containing N examples, each with d features.

2. The matrix multiplication $\mathbf{Z} = \mathbf{X}\mathbf{W}^T \in \mathbb{R}^{N \times K}$ computes all logits for all examples in a single operation. Each element z_{ij} represents the logit for example i and class j where $j = 1, 2, \ldots, K$.

3. We ensure that $\mathbf{w}_K = \mathbf{0}$, which means the logits for the reference class K are always zero: $z_{iK} = 0$ for all i.

4. The softmax operation is then applied to compute all class probabilities:

$$y_{ik} = \frac{\exp(z_{ik})}{\sum_{j=1}^{K} \exp(z_{ij})} \tag{8.101}$$

5. For numerical stability, we subtract the maximum logit in each row:

$$y_{ik} = \frac{\exp(z_{ik} - \max_j z_{ij})}{\sum_{j=1}^{K} \exp(z_{ij} - \max_j z_{ij})} \tag{8.102}$$

This matrix formulation is particularly advantageous for mini-batch processing. If $\mathbf{X}_{\text{batch}} \in \mathbb{R}^{M \times d}$ represents a mini-batch of M examples, we can compute all logits for this batch as $\mathbf{Z}_{\text{batch}} = \mathbf{X}_{\text{batch}}\mathbf{W}^T \in \mathbb{R}^{M \times K}$. Modern linear algebra libraries are highly optimized for such matrix operations. These libraries leverage parallel processing to achieve orders of magnitude speedup compared to iterative implementations, making the matrix approach both mathematically elegant and computationally efficient.

The gradient computation can also be expressed in matrix form. If $\mathbf{Y} \in \mathbb{R}^{N \times K}$ contains the predicted probabilities and $\mathbf{T} \in \mathbb{R}^{N \times K}$ contains the one-hot encoded true labels, the gradient matrix is:

$$\nabla_{\mathbf{W}_{1:K-1}} E = \frac{1}{N}(\mathbf{Y}_{1:K-1} - \mathbf{T}_{1:K-1})^T \mathbf{X} \tag{8.103}$$

where $\mathbf{W}_{1:K-1}$ represents the first $K - 1$ rows of $\mathbf{W}$, and $\mathbf{Y}_{1:K-1}$ and $\mathbf{T}_{1:K-1}$ denote the first $K - 1$ columns of $\mathbf{Y}$ and $\mathbf{T}$ respectively. This gradient matrix contains all the partial derivatives $\partial E / \partial \mathbf{w}_j$ for $j = 1, 2, \ldots, K - 1$ as its rows. During the update step, we only modify the first $K - 1$ rows of $\mathbf{W}$, keeping the last row $\mathbf{w}_K$ fixed at zero throughout training.

The application of multi-class logistic regression to astronomical data requires balancing theoretical considerations with practical implementation concerns. By addressing the issues of numerical stability, parameter initialization, computational efficiency, and domain-

specific challenges, we can develop robust classification models that provide reliable insights into astronomical phenomena.

8.9   Summary

In this chapter, we've explored the extension of logistic regression from binary to multi-class classification problems. We began by examining the limitations of one-vs-rest and one-vs-one approaches, highlighting the potential inconsistencies that can arise. We then introduced the multinomial logistic regression model, which provides a framework for directly handling multiple classes.

The progression from binary to multi-class classification followed a natural path. We first established the need for one-hot encoding to represent class labels without imposing artificial ordering. Building on this representation, we extended our mathematical framework by comparing each class to a reference class through log-ratios. This led to the softmax function—a generalization of the sigmoid function—which transforms linear predictions into proper probability distributions across all classes. We demonstrated that when $K = 2$, our multi-class formulation reduces precisely to binary logistic regression, confirming that our approach is a proper generalization.

A key strength of the multi-class logistic regression framework is its coherent probabilistic interpretation. The model assigns a probability distribution over all classes, allowing it to express both high-confidence predictions and genuine uncertainty. This property is particularly valuable in astronomy, where measurement quality varies substantially and many objects exhibit genuinely intermediate characteristics between established classes. The principled nature of this approach ensures that our decision boundaries remain consistent and well-defined throughout the feature space, avoiding the contradictions that plagued the naive decomposition approaches.

The cross-entropy loss function emerged naturally from maximum likelihood estimation, just as in the binary case. However, our information-theoretic analysis revealed a deeper insight: minimizing cross-entropy loss is mathematically equivalent to maximizing the mutual information between our predictions and the true class labels. This perspective explains why cross-entropy works well—it's finding the combination of features that shares maximum information with the classification target. Furthermore, we saw how entropy quantifies the inherent uncertainty in our classification task, setting a theoretical limit on how well any model can perform given the available features.

The mathematics of multi-class logistic regression showed consistency with the binary case. The gradient of the cross-entropy loss with respect to the weight vectors takes a simple form: the difference between predicted probabilities and true labels, scaled by the feature vectors. This pattern extends directly from binary classification, despite the increased complexity of the multi-class setting. The simplicity of this gradient enables efficient optimization through stochastic gradient descent, with each update adjusting multiple decision boundaries in a coordinated manner.

Beyond the theoretical formulation, we addressed practical implementation considerations essential for applying these methods to real astronomical data. These included techniques for numerical stability, parameter initialization strategies, and efficient matrix implementations. These practical aspects are crucial for developing robust classification systems that can reliably analyze the massive datasets modern astronomy produces.

The multi-class framework we've developed has enhanced expressive power compared to binary classification. With K classes, the model creates $\binom{K}{2}$ distinct hyperplanes that partition the feature space into regions for each class. This structure can model complex decision boundaries that binary methods cannot, making it suitable for the nuanced classification tasks astronomers face when categorizing celestial objects.

While we've established a framework for multi-class classification, we've focused only on the maximum likelihood solution. In Chapter 9, we'll build upon these foundations to explore Bayesian treatments of logistic regression, which will allow us to quantify uncertainty in our classifications. This extension is essential for scientific applications where understanding confidence and error rates is crucial for drawing robust conclusions. The Bayesian approach will require new techniques beyond those used for regression, as the non-Gaussian likelihood introduced by the sigmoid/softmax function creates mathematical challenges not present in linear regression.

As we move forward, the concepts from this chapter—particularly the information-theoretic perspective and the probabilistic framework—will continue to inform our understanding of more advanced machine learning methods. The principles we've established for multi-class classification serve as a foundation for sophisticated approaches to extract meaningful patterns from astronomical data.

Further Readings: The development of multi-class classification methods represents an important extension beyond binary approaches, with several key contributions shaping the

field. Dietterich and Bakiri [1991] developed error-correcting output codes for multi-class learning, with their treatment in Dietterich and Bakiri [1995] providing detailed theoretical and practical guidance. The various decomposition methods, including One-vs-Rest and One-vs-One approaches, were later unified by Allwein et al. [2001] who demonstrated their connections within a margin-based framework. Fürnkranz [2002] contributed analysis of the round robin approach, examining both computational and theoretical properties of pairwise classification strategies. The theoretical foundations underlying the softmax function trace to work by Luce [1959], whose choice axiom provided the probabilistic basis for modeling multiple alternatives. McFadden [1973] made connections to econometric choice models, contributing to the development of multinomial logistic regression, while Theil [1969] offered alternative mathematical development of these concepts. For readers interested in optimization approaches for these multi-class models, Dennis and Schnabel [1983] developed numerical methods for the unconstrained optimization problems that arise, and Polyak and Juditsky [1992] demonstrated how averaging in stochastic gradient methods could accelerate convergence—work that proves particularly relevant for the large-scale multi-class problems encountered in astronomical surveys.

Chapter 9

Bayesian Logistic Regression

In previous chapters, we explored logistic regression for binary classification, learning how to assign discrete class labels to astronomical objects. We discovered that the likelihood function naturally transforms into cross-entropy loss, which we can optimize through stochastic gradient descent to find maximum likelihood estimates of our model parameters.

This approach gives us a set of weights that convert input features into logits, which in turn yield probabilities for class membership. These weights determine linear decision boundaries between classes—for instance, separating stars from galaxies based on their photometric and morphological properties.

However, this maximum likelihood approach has a limitation that becomes particularly problematic in astronomical applications. When we find the single "best" set of weights, we're assuming this decision boundary is optimal everywhere in feature space. But consider what happens when two groups in our training data are well separated: based solely on this training data, we could place the boundary anywhere in the gap between groups and achieve similar performance on our training set.

This presents a serious issue when we encounter new objects that fall into these sparsely sampled regions. The maximum likelihood solution might confidently classify an unusual object, even though we have little evidence to support such confidence. In astronomy, where we frequently encounter objects unlike anything in our training data, this overconfidence can lead to systematic errors and missed discoveries.

The problem becomes more acute due to two constraints common in astronomical

applications. First, we often have limited labeled data—obtaining spectroscopic classifications or detailed morphological labels requires expensive telescope time and expert analysis. Second, our labeled data typically comes from biased sampling: astronomers naturally label objects that are easier to classify or more scientifically interesting, leaving gaps in our coverage of transitional or unusual objects.

What we need is a classification method that expresses appropriate uncertainty when it encounters data unlike what it was trained on. Rather than forcing confident predictions in regions far from training examples, our model should indicate when it lacks sufficient evidence for classification. This is where Bayesian logistic regression provides value.
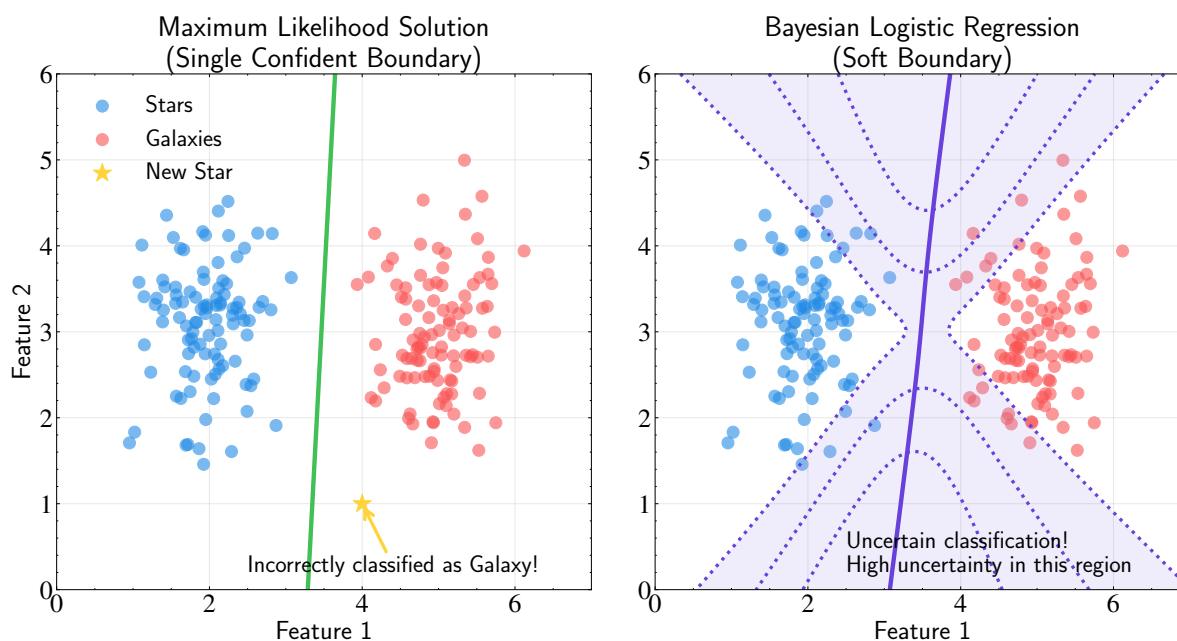
Figure 9.1: Comparison between standard and Bayesian approaches to logistic regression. **Left panel:** The maximum likelihood solution produces a single confident decision boundary that can lead to incorrect classifications in regions with sparse or no training data. The yellow star indicates an object that is incorrectly classified with high confidence despite being in a region without training examples. **Right panel:** The Bayesian approach acknowledges uncertainty in the decision boundary, particularly in regions far from training data. The purple contour lines show the predictive uncertainty (standard deviation), with higher values in areas where the model should be less confident. This illustrates how Bayesian logistic regression naturally expresses uncertainty in regions of feature space that are poorly sampled by training data, avoiding overconfident but incorrect classifications for novel objects. This property is especially valuable in astronomical classification tasks where we frequently encounter objects unlike anything in our training set.

The key insight is that instead of finding a single decision boundary, we should characterize our uncertainty about where the boundary should be placed. This naturally leads

to the Bayesian approach: rather than seeking point estimates of our model parameters, we derive their full posterior distribution given the observed data.

You've seen this approach before in Chapter 5 with Bayesian linear regression. There, we derived the posterior distribution of weights $p(\mathbf{w}|\mathcal{D})$ given the data $\mathcal{D}$, which naturally led to prediction uncertainties that grew larger for inputs far from our training data. The same principle applies to classification: by sampling different decision boundaries from our posterior, we can see how much our predictions vary in different regions of feature space.

However, Bayesian logistic regression presents new mathematical challenges that we didn't face in the linear case. The likelihood function involves the sigmoid transformation of linear combinations of features, which creates a non-Gaussian posterior distribution. This breaks the convenient conjugacy we enjoyed in Bayesian linear regression, where Gaussian priors and likelihoods led to Gaussian posteriors with closed-form solutions.

We'll address these challenges through a series of approximations that make the problem tractable while maintaining accuracy. First, we'll use the Laplace approximation to represent the complex posterior as a Gaussian distribution centered at the maximum a posteriori (MAP) estimate. Second, we'll employ the probit approximation to compute predictive distributions analytically. While these might sound technical, we'll develop them step by step, showing how each approximation emerges naturally from the mathematical structure of the problem.

The result is a classification framework that not only makes predictions but also quantifies confidence in those predictions. This capability proves particularly valuable in astronomical surveys, where understanding when our models are uncertain can be as important as the classifications themselves.

9.1   Bayesian Logistic Regression: Mathematical Formalism

To keep our mathematical development manageable, we'll focus exclusively on binary classification in this chapter. This allows us to build the core techniques and intuition without the additional complexity of multi-class scenarios, which require more advanced methods like Monte Carlo sampling that we'll explore in later chapters.

Let's begin by revisiting the standard binary logistic regression model, then see how

the Bayesian perspective changes our approach.

Standard logistic regression review   In binary logistic regression, we model the probability of class membership through the sigmoid function:

$$p(C_1|\mathbf{x}, \mathbf{w}) = y = \sigma(\mathbf{w}^T\mathbf{x}) = \frac{1}{1 + e^{-\mathbf{w}^T\mathbf{x}}}. \tag{9.1}$$

The probability of the reference class follows automatically:

$$p(C_0|\mathbf{x}, \mathbf{w}) = 1 - p(C_1|\mathbf{x}, \mathbf{w}) = 1 - \sigma(\mathbf{w}^T\mathbf{x}) = \frac{e^{-\mathbf{w}^T\mathbf{x}}}{1 + e^{-\mathbf{w}^T\mathbf{x}}}. \tag{9.2}$$

Our likelihood function comes from the Bernoulli distribution:

$$p(\mathbf{t}|\mathbf{w}, \mathbf{X}) = \prod_{n=1}^{N} y_n^{t_n}(1 - y_n)^{(1-t_n)}, \tag{9.3}$$

where t_n represents the true class label (0 or 1) for data point n, and $y_n = \sigma(\mathbf{w}^T\mathbf{x}_n)$ is our model's predicted probability.

In maximum likelihood estimation, we find the weights $\mathbf{w}$ that maximize this likelihood, typically by minimizing the cross-entropy loss through gradient descent. This gives us a single "best" set of weights that defines our decision boundary.

The Bayesian perspective   The Bayesian approach fundamentally changes how we think about the model parameters. Instead of seeking a single best model, we acknowledge that given finite data, multiple decision boundaries could reasonably explain our observations. Some boundaries might fit the training data slightly better, others slightly worse, but many could be plausible given the evidence we have.

Consider an astronomical example: if our training data contains well-separated clusters of stars and galaxies, many different linear boundaries could separate these clusters perfectly. The maximum likelihood approach arbitrarily picks one, but the Bayesian approach asks: what's the probability distribution over all reasonable boundaries?

This uncertainty in model parameters naturally propagates to our predictions. When classifying a new object, rather than using a single boundary to make a confident prediction, we should consider all plausible boundaries and see how much they agree. If they largely agree, we can be confident in our classification. If they disagree, we should express

uncertainty.

The mathematics of Bayesian inference provides a principled way to capture this reasoning. We start by expressing our prior beliefs about the model parameters, update these beliefs based on observed data, and use the resulting posterior distribution to make predictions that appropriately reflect our uncertainty.

Prior specification   To implement the Bayesian approach, we need to specify our prior beliefs about the weights before seeing any data. A natural choice is a Gaussian prior:

$$p(\mathbf{w}) = \mathcal{N}(\mathbf{w}|\mathbf{m}_0, \mathbf{S}_0), \tag{9.4}$$

where $\mathbf{m}_0$ represents our prior belief about the most likely weight values, and $\mathbf{S}_0$ captures our uncertainty in those beliefs.

This choice is mathematically convenient and often reasonable in practice. If we have no strong prior knowledge about which features should be important, we might set $\mathbf{m}_0 = \mathbf{0}$, expressing no preference for any particular decision boundary orientation. The covariance matrix $\mathbf{S}_0$ then controls how strongly we believe in this neutrality—larger diagonal elements indicate greater prior uncertainty about the corresponding weight values.

Posterior derivation   Using Bayes' theorem, we can compute the posterior distribution:

$$p(\mathbf{w}|\mathbf{t}, \mathbf{X}) \propto p(\mathbf{w}) \cdot p(\mathbf{t}|\mathbf{w}, \mathbf{X}), \tag{9.5}$$

which expands to:

$$p(\mathbf{w}|\mathbf{t}, \mathbf{X}) \propto \mathcal{N}(\mathbf{w}|\mathbf{m}_0, \mathbf{S}_0) \cdot \prod_{n=1}^{N} y_n^{t_n}(1 - y_n)^{(1-t_n)}. \tag{9.6}$$

Here we encounter our first major challenge. In Bayesian linear regression, both the prior and likelihood were Gaussian, leading to a Gaussian posterior with a closed-form solution. But in logistic regression, the likelihood involves the sigmoid function, which destroys this convenient mathematical structure.

The sigmoid function's non-linear nature means our posterior is no longer Gaussian. We can't write down a simple formula for it, and we can't easily sample from it or compute predictions analytically. This is the price we pay for moving from regression (where outputs

can be any real number) to classification (where outputs must be probabilities between 0 and 1).

Why the sigmoid breaks conjugacy   To understand why this creates such a problem, let's compare the mathematical forms. In Bayesian linear regression, our posterior was proportional to:

$$p(\mathbf{w}|\mathbf{y}, \mathbf{X}) \propto \exp\left(-\frac{1}{2}(\mathbf{w} - \mathbf{m}_0)^T \mathbf{S}_0^{-1}(\mathbf{w} - \mathbf{m}_0)\right) \cdot \exp\left(-\frac{1}{2\sigma^2}(\mathbf{y} - \mathbf{X}\mathbf{w})^T(\mathbf{y} - \mathbf{X}\mathbf{w})\right). \quad (9.7)$$

Both terms are exponentials of quadratic forms in $\mathbf{w}$, so their product is also an exponential of a quadratic form—another Gaussian.

In logistic regression, our posterior is proportional to:

$$p(\mathbf{w}|\mathbf{t}, \mathbf{X}) \propto \exp\left(-\frac{1}{2}(\mathbf{w} - \mathbf{m}_0)^T \mathbf{S}_0^{-1}(\mathbf{w} - \mathbf{m}_0)\right) \cdot \prod_{n=1}^{N} \sigma(\mathbf{w}^T \mathbf{x}_n)^{t_n}(1 - \sigma(\mathbf{w}^T \mathbf{x}_n))^{1-t_n}. \quad (9.8)$$

The first term is still a quadratic form, but the second term involves products of sigmoid functions—a much more complex expression that doesn't reduce to any standard distribution.

This mathematical complexity is the central challenge of Bayesian logistic regression. In the next section, we'll see how the Laplace approximation provides a practical solution by approximating this complex posterior with a Gaussian distribution.

9.2   Laplace Approximation: Intuition

The central insight of the Laplace approximation is surprisingly simple: near its peak, any smooth probability distribution can be well-approximated by a Gaussian distribution. This approximation becomes increasingly accurate as we gather more data, making it particularly valuable for Bayesian inference with moderate to large datasets.

Let's build some intuition for why this works. Consider our complex posterior distribution $p(\mathbf{w}|\mathbf{t}, \mathbf{X})$ with a peak at some location $\mathbf{w}_0$. If we zoom in closely enough around this peak, the shape of the distribution begins to resemble a parabola in the log domain—or equivalently, a Gaussian in the original domain.

A Gaussian distribution is completely characterized by its mean and covariance. In the Laplace approximation, the mode of our posterior serves as the mean of our approximating
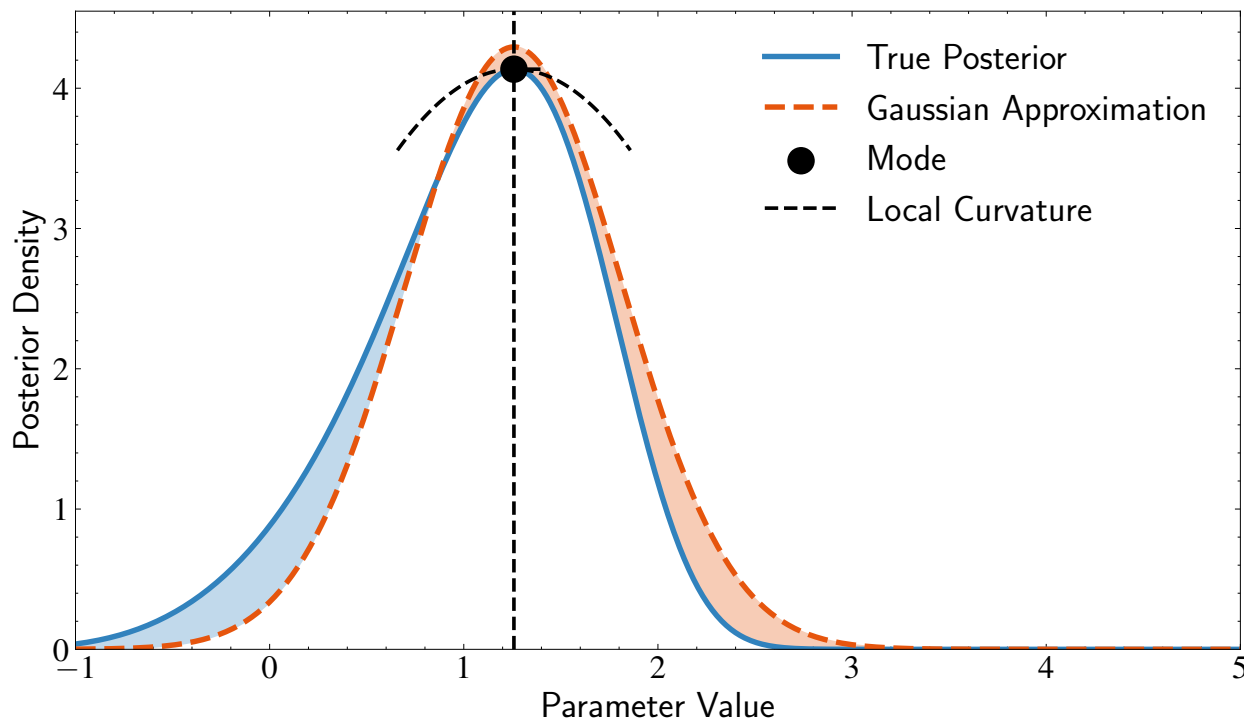
Figure 9.2: Visualization of the Laplace approximation principle. The true posterior distribution (blue solid line) is non-Gaussian with asymmetric tails, which is typical for posteriors in logistic regression with limited data. The Laplace approximation (orange dashed line) produces a Gaussian that matches the true distribution at its mode (black dot) and captures the local curvature around this peak. The approximation is determined by two key properties: (1) the location of the mode, which becomes the mean of the approximating Gaussian, and (2) the curvature at the mode (second derivative of the log posterior), which determines the variance of the Gaussian. This approach provides an excellent approximation near the mode where most probability mass is concentrated, especially as the sample size increases and the posterior becomes more concentrated.

Gaussian. The covariance is determined by the curvature at the peak—specifically, how quickly the probability density falls off as we move away from the mode.

This curvature is measured by the second derivatives of the log posterior with respect to the parameters. The sharper the peak (steeper curvature), the narrower our approximating Gaussian will be. These two quantities—the location of the peak and the curvature at that peak—fully capture the essential characteristics of our distribution near its maximum.

This approach works particularly well when two conditions are met:

- The true distribution has a single dominant mode (unimodal)

- Most of the probability mass is concentrated near this mode

In the context of Bayesian logistic regression with a Gaussian prior, both conditions are typically satisfied, especially as our dataset grows. With limited data, our posterior might be quite diffuse, reflecting high uncertainty about model parameters. However, as we gather more observations, the likelihood term representing our data increasingly dominates the prior, causing our posterior to concentrate more tightly around its mode.

Consider how this applies to astronomical classification. With just a few observed objects, many different decision boundaries could reasonably fit our data, resulting in a spread-out posterior distribution. But with hundreds or thousands of classified objects, the range of plausible boundaries narrows considerably. Our posterior becomes more concentrated and more Gaussian-like, making the Laplace approximation increasingly accurate.

Bernstein-von Mises Theorem   This concentration effect reflects a deeper mathematical principle known as the Bernstein-von Mises theorem. This result states that under mild conditions, posteriors tend toward Gaussian distributions as sample size increases, regardless of the chosen prior.

The theorem is closely related to the Central Limit Theorem. Just as the Central Limit Theorem tells us that the sum of many independent random variables tends toward a Gaussian distribution, the Bernstein-von Mises theorem shows that as we accumulate posterior contributions from many data points, the resulting posterior distribution approaches a Gaussian form centered at the true parameter value.

Each observation contributes information to our posterior, and the aggregate effect of many observations produces a distribution that becomes increasingly Gaussian-shaped. This property makes the Laplace approximation not just a mathematical convenience, but a theoretically justified approach for Bayesian inference problems with substantial data.

The practical implication is encouraging: the more data we have, the more we can trust our Laplace approximation. In astronomical surveys where we might have thousands or millions of classified objects, this approximation becomes quite reliable. Even when our data doesn't perfectly follow the Gaussian assumptions we discussed in Chapter 7, the Laplace approximation can still provide accurate uncertainty estimates for our classification boundaries.

This sets up our approach for the remainder of the chapter. We'll use the Laplace
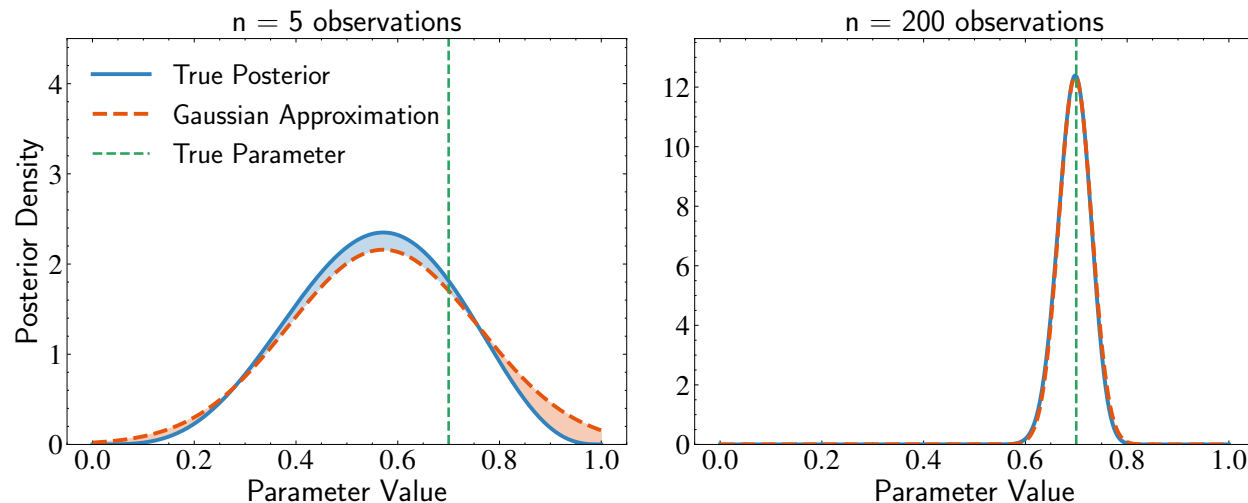
Figure 9.3: Visualization of the Bernstein-von Mises theorem, demonstrating why Laplace approximation becomes increasingly accurate with larger sample sizes. **Left panel:** With only 5 observations, the posterior distribution (blue) is noticeably asymmetric, and the Gaussian approximation (orange dashed line) provides a poor fit, particularly in the tails. **Right panel:** With 200 observations, the posterior becomes nearly indistinguishable from a Gaussian distribution, making the Laplace approximation highly accurate. The vertical green dashed line indicates the true parameter value. This convergence to normality occurs regardless of the prior distribution, and extends to multivariate posteriors in models like logistic regression.

approximation to convert our complex, non-Gaussian posterior into a tractable Gaussian form. This will allow us to compute predictive distributions and quantify uncertainty in our classifications, giving us the tools we need for responsible astronomical classification.

9.3   Laplace Approximation: Mathematical Formalism

Now let's formalize our intuition mathematically. We'll first develop the Laplace approximation in general terms, then apply it specifically to our Bayesian logistic regression problem.

Suppose we have a probability distribution $p(z)$ that is complex and non-Gaussian, but has a clear peak (mode). In Bayesian inference, we often encounter situations where we only know this distribution up to a normalization constant:

$$p(z) = \frac{f(z)}{Z}, \tag{9.9}$$

where $f(z)$ is the unnormalized density and $Z = \int f(z)dz$ is the normalization constant.

This is particularly common in Bayesian statistics where, by Bayes' theorem:

$$p(z|\text{data}) = \frac{p(\text{data}|z)p(z)}{p(\text{data})}. \tag{9.10}$$

The denominator $p(\text{data})$, also known as the evidence, is often difficult or impossible to compute analytically. The Laplace approximation allows us to work directly with the unnormalized density $f(z) = p(\text{data}|z)p(z)$, bypassing the need to calculate this normalization constant.

The strategy is to approximate $f(z)$ near its peak using a quadratic function in the log domain. Since the logarithm of a Gaussian distribution has exactly this quadratic form, our approximation will correspond to a Gaussian when we exponentiate back to the original scale.

Finding the mode   We begin by locating the mode of our distribution—the point where the probability density reaches its maximum value. Mathematically, this is where the derivative of our function $f(z)$ equals zero:

$$\frac{d}{dz}f(z)\bigg|_{z=z_0} = 0. \tag{9.11}$$

This is equivalent to finding where the derivative of the log-density equals zero:

$$\frac{d}{dz}\ln f(z)\bigg|_{z=z_0} = 0. \tag{9.12}$$

Working with the logarithm is often more convenient, as it transforms products into sums and simplifies our calculations.

Analyzing local behavior   Once we've identified the mode z_0, we want to understand how the distribution behaves in its vicinity. The key insight is that near its peak, almost any smooth function can be well-approximated by a quadratic function.

To formalize this, we use a second-order Taylor expansion of the log-density around the mode:

$$\ln f(z) \approx \ln f(z_0) + \frac{d}{dz}\ln f(z)\bigg|_{z=z_0}(z - z_0) + \frac{1}{2}\frac{d^2}{dz^2}\ln f(z)\bigg|_{z=z_0}(z - z_0)^2. \tag{9.13}$$

Since z_0 is a maximum, the first derivative term equals zero, simplifying our expression to:

$$\ln f(z) \approx \ln f(z_0) + \frac{1}{2} \frac{d^2}{dz^2} \ln f(z) \bigg|_{z=z_0} (z - z_0)^2. \tag{9.14}$$

At a maximum, the second derivative is negative, indicating the downward curvature of our function. For convenience, we define:

$$A = - \frac{d^2}{dz^2} \ln f(z) \bigg|_{z=z_0}. \tag{9.15}$$

This positive value A represents the sharpness of the peak. With this definition, our approximation becomes:

$$\ln f(z) \approx \ln f(z_0) - \frac{1}{2} A(z - z_0)^2. \tag{9.16}$$

Constructing the Gaussian approximation When we compare our quadratic approximation with the log of a Gaussian distribution, we notice that they have the same structure. The correspondence becomes clear:

- The mode z_0 corresponds to the Gaussian mean μ

- The curvature parameter A corresponds to the Gaussian precision $1/\sigma^2$

To convert our log-density approximation back to a density function, we exponentiate both sides:

$$f(z) \approx f(z_0) \exp\left(-\frac{1}{2} A(z - z_0)^2 \right). \tag{9.17}$$

This expression has the form of an unnormalized Gaussian distribution. The constant factor $f(z_0)$ does not affect the shape of the distribution—it only scales the overall height. When we normalize to obtain a proper probability distribution, this constant factor gets absorbed into the normalization constant.

After normalization, we obtain:

$$q(z) = \mathcal{N}(z|z_0, A^{-1}) = \sqrt{\frac{A}{2\pi}} \exp\left(-\frac{1}{2} A(z - z_0)^2 \right). \tag{9.18}$$

To summarize the Laplace approximation procedure:

1. Find the mode z_0 of the distribution (where the first derivative equals zero)

2. Calculate the second derivative at the mode to determine $A = -\left.\frac{d^2}{dz^2} \ln f(z)\right|_{z=z_0}$

3. Construct a Gaussian approximation with mean z_0 and variance A^{-1}

Multivariate Extension   For our Bayesian logistic regression problem where we have multiple weight parameters, we need to extend this approach to multiple dimensions. The procedure remains conceptually the same, with vectors and matrices replacing scalars.

We begin by finding the mode $\mathbf{z}_0$ where the gradient of the log density vanishes:

$$\nabla \ln f(\mathbf{z})\Big|_{\mathbf{z}=\mathbf{z}_0} = \mathbf{0}. \tag{9.19}$$

Next, we approximate the log density around the mode using a second-order Taylor expansion:

$$\ln f(\mathbf{z}) \approx \ln f(\mathbf{z}_0) + (\mathbf{z} - \mathbf{z}_0)^T \nabla \ln f(\mathbf{z})\Big|_{\mathbf{z}=\mathbf{z}_0} + \frac{1}{2}(\mathbf{z} - \mathbf{z}_0)^T \nabla\nabla \ln f(\mathbf{z})\Big|_{\mathbf{z}=\mathbf{z}_0} (\mathbf{z} - \mathbf{z}_0). \tag{9.20}$$

Since $\mathbf{z}_0$ is the mode, the gradient term vanishes, leaving us with:

$$\ln f(\mathbf{z}) \approx \ln f(\mathbf{z}_0) + \frac{1}{2}(\mathbf{z} - \mathbf{z}_0)^T \mathbf{H}(\mathbf{z} - \mathbf{z}_0). \tag{9.21}$$

The matrix $\mathbf{H}$ is the Hessian matrix of second derivatives:

$$\mathbf{H} = \nabla\nabla \ln f(\mathbf{z})\Big|_{\mathbf{z}=\mathbf{z}_0}, \tag{9.22}$$

where each element is:

$$H_{ij} = \left.\frac{\partial^2 \ln f(\mathbf{z})}{\partial z_i \partial z_j}\right|_{\mathbf{z}=\mathbf{z}_0}. \tag{9.23}$$

This matrix captures the curvature of the log density in all directions. Since we're at a maximum, this Hessian matrix is negative definite, meaning the curvature is downward in all directions.

Following our univariate approach, we define $\mathbf{A} = -\mathbf{H}$ (the negative Hessian), which

is positive definite at a maximum. Our approximation becomes:

$$\ln f(\mathbf{z}) \approx \ln f(\mathbf{z}_0) - \frac{1}{2}(\mathbf{z} - \mathbf{z}_0)^T \mathbf{A}(\mathbf{z} - \mathbf{z}_0). \tag{9.24}$$

Exponentiating both sides:

$$f(\mathbf{z}) \approx f(\mathbf{z}_0) \exp\left(-\frac{1}{2}(\mathbf{z} - \mathbf{z}_0)^T \mathbf{A}(\mathbf{z} - \mathbf{z}_0)\right). \tag{9.25}$$

This is an unnormalized multivariate Gaussian. The complete normalized approximation becomes:

$$q(\mathbf{z}) = \frac{|\mathbf{A}|^{1/2}}{(2\pi)^{d/2}} \exp\left(-\frac{1}{2}(\mathbf{z} - \mathbf{z}_0)^T \mathbf{A}(\mathbf{z} - \mathbf{z}_0)\right) = \mathcal{N}(\mathbf{z}|\mathbf{z}_0, \mathbf{A}^{-1}), \tag{9.26}$$

where $|\mathbf{A}|$ is the determinant of $\mathbf{A}$ and d is the dimensionality of $\mathbf{z}$.

The normalization constant ensures that the probability density integrates to one over the entire parameter space, with the determinant term accounting for how the precision matrix $\mathbf{A}$ scales volumes in this space.

Now that we have the general mathematical framework, we can apply it specifically to our Bayesian logistic regression problem, which we'll tackle in the next section.

9.4   Applying Laplace Approximation to Bayesian Logistic Regression

Now that we've established the general framework for Laplace approximation, let's apply it specifically to our Bayesian logistic regression problem. This application will allow us to quantify uncertainty in our classification boundaries—a crucial capability when working with astronomical data where observations may be sparse or unevenly distributed across parameter space.

Setting up the correspondence   We need to map our general Laplace approximation framework to the specific case of logistic regression. The correspondences are:

- $\mathbf{z}$ corresponds to our weight vector $\mathbf{w}$

- $f(\mathbf{z})$ corresponds to our unnormalized posterior $p(\mathbf{w}) \cdot p(\mathbf{t}|\mathbf{w}, \mathbf{X})$

- $\mathbf{z}_0$ corresponds to the maximum a posteriori (MAP) estimate $\mathbf{w}_{\mathrm{MAP}}$

Before proceeding, let's clarify what we mean by the MAP estimate. MAP stands for Maximum A Posteriori, which extends the familiar concept of Maximum Likelihood Estimation (MLE) by incorporating prior beliefs about the parameters. While MLE finds the parameter values that maximize the likelihood function $p(\mathcal{D}|\mathbf{w})$, MAP finds the parameter values that maximize the posterior probability:

$$\mathbf{w}_{\mathrm{MAP}} = \arg\max_{\mathbf{w}} p(\mathbf{w}|\mathcal{D}) = \arg\max_{\mathbf{w}}\{p(\mathcal{D}|\mathbf{w})p(\mathbf{w})\}. \tag{9.27}$$

In other words, MAP balances the information from our data with our prior knowledge. When the prior is uniform (expressing no preference for particular parameter values), the MAP estimate reduces exactly to the MLE. However, with informative priors, MAP can be particularly valuable when working with limited datasets.

Components of our posterior Our unnormalized posterior combines the prior and likelihood terms. For the prior, we assume a multivariate Gaussian distribution:

$$p(\mathbf{w}) = \mathcal{N}(\mathbf{w}|\mathbf{m}_0, \mathbf{S}_0) = \frac{1}{(2\pi)^{d/2}|\mathbf{S}_0|^{1/2}} \exp\left(-\frac{1}{2}(\mathbf{w} - \mathbf{m}_0)^T \mathbf{S}_0^{-1}(\mathbf{w} - \mathbf{m}_0)\right). \tag{9.28}$$

The likelihood from our binary classification model is:

$$p(\mathbf{t}|\mathbf{w}, \mathbf{X}) = \prod_{n=1}^{N} \sigma(\mathbf{w}^T\mathbf{x}_n)^{t_n}(1 - \sigma(\mathbf{w}^T\mathbf{x}_n))^{1-t_n}. \tag{9.29}$$

Taking the logarithm of the posterior, we get:

$$\ln p(\mathbf{w}|\mathbf{t}, \mathbf{X}) = \ln p(\mathbf{w}) + \ln p(\mathbf{t}|\mathbf{w}, \mathbf{X}) \tag{9.30}$$

$$= -\frac{1}{2}(\mathbf{w} - \mathbf{m}_0)^T \mathbf{S}_0^{-1}(\mathbf{w} - \mathbf{m}_0) + \sum_{n=1}^{N}[t_n \ln \sigma(\mathbf{w}^T\mathbf{x}_n) + (1 - t_n)\ln(1 - \sigma(\mathbf{w}^T\mathbf{x}_n))]. \tag{9.31}$$

Here $\mathbf{m}_0$ represents our prior belief about the most likely weight values, and $\mathbf{S}_0$ cap-

tures our uncertainty in those beliefs before seeing any data. The second term is the familiar cross-entropy term we encountered in maximum likelihood estimation.

Finding the MAP estimate   Following our Laplace approximation procedure, we first need to find $\mathbf{w}_{\mathrm{MAP}}$, the weight vector that maximizes this log posterior. We compute the gradient of the log posterior with respect to $\mathbf{w}$ and set it to zero.

The gradient combines contributions from the prior and likelihood:

$$\nabla \ln p(\mathbf{w}|\mathbf{t}, \mathbf{X}) = \nabla \ln p(\mathbf{w}) + \nabla \ln p(\mathbf{t}|\mathbf{w}, \mathbf{X}). \tag{9.32}$$

For the Gaussian prior, the gradient is:

$$\nabla \ln p(\mathbf{w}) = \nabla \left[-\frac{1}{2}(\mathbf{w} - \mathbf{m}_0)^T \mathbf{S}_0^{-1}(\mathbf{w} - \mathbf{m}_0) \right] \tag{9.33}$$

$$= -\mathbf{S}_0^{-1}(\mathbf{w} - \mathbf{m}_0). \tag{9.34}$$

For the log likelihood, we can use our result from Chapter 7:

$$\nabla \ln p(\mathbf{t}|\mathbf{w}, \mathbf{X}) = \sum_{n=1}^{N} (t_n - \sigma(\mathbf{w}^T \mathbf{x}_n)) \mathbf{x}_n. \tag{9.35}$$

This is precisely the gradient we used in stochastic gradient descent for logistic regression, where $(t_n - \sigma(\mathbf{w}^T \mathbf{x}_n))$ represents the prediction error for each data point.

Combining these terms and setting the gradient to zero:

$$\nabla \ln p(\mathbf{w}|\mathbf{t}, \mathbf{X}) = -\mathbf{S}_0^{-1}(\mathbf{w} - \mathbf{m}_0) + \sum_{n=1}^{N} (t_n - \sigma(\mathbf{w}^T \mathbf{x}_n)) \mathbf{x}_n = \mathbf{0}. \tag{9.36}$$

This equation has an interesting interpretation. The left-hand side represents the "pull" of the prior—how strongly our prior beliefs encourage the weights to stay close to $\mathbf{m}_0$. The right-hand side represents the "pull" of the data, with each data point contributing based on the prediction error $(t_n - \sigma(\mathbf{w}^T \mathbf{x}_n))$ and its feature vector $\mathbf{x}_n$.

Unlike the linear regression case, this equation doesn't have a closed-form solution due to the nonlinearity introduced by the sigmoid function. We need to use gradient descent

to find $\mathbf{w}_{\text{MAP}}$:

$$\mathbf{w}^{(t+1)} = \mathbf{w}^{(t)} + \eta \nabla \ln p(\mathbf{w}^{(t)}|\mathbf{t}, \mathbf{X}) \tag{9.37}$$

where η is the learning rate. Note the positive sign before the gradient term, since we're climbing up the posterior distribution to find its maximum, rather than descending to find a minimum.

Computing the Hessian   Once we've found $\mathbf{w}_{\text{MAP}}$ through gradient descent, we can proceed with the Laplace approximation. This requires us to characterize the curvature of the log posterior at this maximum point by computing the Hessian matrix.

The Hessian is the matrix of second derivatives with respect to the weights:

$$\mathbf{H} = \nabla\nabla \ln p(\mathbf{w}|\mathbf{t}, \mathbf{X}) \tag{9.38}$$

$$= \nabla\nabla \ln p(\mathbf{w}) + \nabla\nabla \ln p(\mathbf{t}|\mathbf{w}, \mathbf{X}). \tag{9.39}$$

For the prior term, the second derivative is straightforward:

$$\nabla\nabla \ln p(\mathbf{w}) = \nabla\nabla \left[-\frac{1}{2}(\mathbf{w} - \mathbf{m}_0)^T \mathbf{S}_0^{-1}(\mathbf{w} - \mathbf{m}_0) \right] \tag{9.40}$$

$$= -\mathbf{S}_0^{-1}. \tag{9.41}$$

For the likelihood term, we need to compute the second derivative of:

$$\nabla \ln p(\mathbf{t}|\mathbf{w}, \mathbf{X}) = \sum_{n=1}^{N} (t_n - \sigma(\mathbf{w}^T\mathbf{x}_n))\mathbf{x}_n. \tag{9.42}$$

Taking the derivative with respect to $\mathbf{w}$ again:

$$\nabla\nabla \ln p(\mathbf{t}|\mathbf{w}, \mathbf{X}) = \sum_{n=1}^{N} \left[-\frac{d\sigma(\mathbf{w}^T\mathbf{x}_n)}{d(\mathbf{w}^T\mathbf{x}_n)} \frac{d(\mathbf{w}^T\mathbf{x}_n)}{d\mathbf{w}} \mathbf{x}_n \right] \tag{9.43}$$

$$= \sum_{n=1}^{N} \left[-\sigma(\mathbf{w}^T\mathbf{x}_n)(1 - \sigma(\mathbf{w}^T\mathbf{x}_n))\mathbf{x}_n\mathbf{x}_n^T \right] \tag{9.44}$$

$$= -\sum_{n=1}^{N} \sigma(\mathbf{w}^T\mathbf{x}_n)(1 - \sigma(\mathbf{w}^T\mathbf{x}_n))\mathbf{x}_n\mathbf{x}_n^T. \tag{9.45}$$

Combining the prior and likelihood terms, the Hessian of the log posterior is:

$$\mathbf{H} = -\mathbf{S}_0^{-1} - \sum_{n=1}^{N} \sigma(\mathbf{w}^T \mathbf{x}_n)(1 - \sigma(\mathbf{w}^T \mathbf{x}_n))\mathbf{x}_n \mathbf{x}_n^T. \tag{9.46}$$

For the Laplace approximation, we need the negative of the Hessian evaluated at $\mathbf{w}_{\mathrm{MAP}}$:

$$\mathbf{A} = -\mathbf{H}|_{\mathbf{w}=\mathbf{w}_{\mathrm{MAP}}} = \mathbf{S}_0^{-1} + \sum_{n=1}^{N} \sigma(\mathbf{w}_{\mathrm{MAP}}^T \mathbf{x}_n)(1 - \sigma(\mathbf{w}_{\mathrm{MAP}}^T \mathbf{x}_n))\mathbf{x}_n \mathbf{x}_n^T. \tag{9.47}$$

Interpreting the precision matrix This matrix $\mathbf{A}$ represents the precision (inverse covariance) of our Gaussian approximation to the posterior. It consists of two terms: the prior precision matrix $\mathbf{S}_0^{-1}$, which represents our uncertainty before seeing any data, and a data-dependent term that incorporates information from our observations.

Looking at the data-dependent term more closely, each data point contributes based on its features $\mathbf{x}_n$ and the term $\sigma(\mathbf{w}_{\mathrm{MAP}}^T \mathbf{x}_n)(1 - \sigma(\mathbf{w}_{\mathrm{MAP}}^T \mathbf{x}_n))$. This term has a maximum value of 0.25 when $\sigma(\mathbf{w}_{\mathrm{MAP}}^T \mathbf{x}_n) = 0.5$—precisely at the decision boundary where the model is most uncertain about the classification.

This makes intuitive sense: points near the boundary provide the most information about where exactly the boundary should be placed. Even small shifts in the boundary would affect the classification of these points. In contrast, points far from the boundary contribute little to pinpointing the exact boundary location—shifting the boundary slightly wouldn't change their classification.

The final approximation With $\mathbf{w}_{\mathrm{MAP}}$ and $\mathbf{A}$ determined, our Gaussian approximation to the posterior becomes:

$$q(\mathbf{w}) = \mathcal{N}(\mathbf{w}|\mathbf{w}_{\mathrm{MAP}}, \mathbf{A}^{-1}). \tag{9.48}$$

This approximation gives us a tractable representation of the distribution over possible decision boundaries. The covariance matrix $\mathbf{A}^{-1}$ encodes our uncertainty about the weights—larger values along the diagonal indicate greater uncertainty in the corresponding parameters, while off-diagonal elements capture parameter correlations.

The magnitude of $\mathbf{A}$ reflects our overall confidence in the model parameters. As we collect more data points near the decision boundary, the magnitude of $\mathbf{A}$ increases,
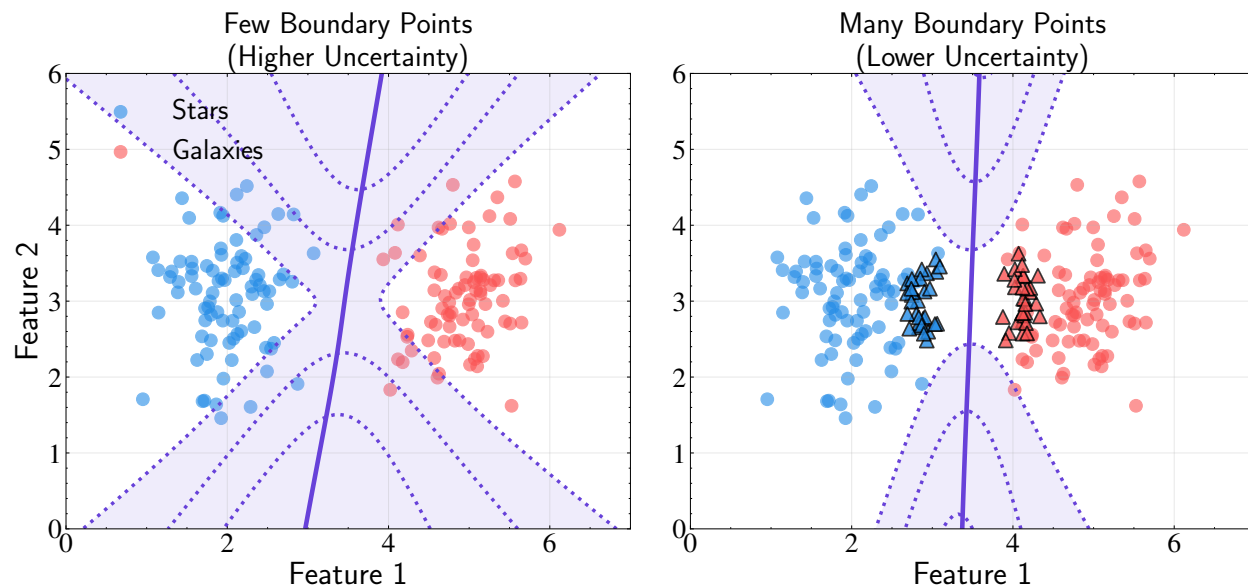
Figure 9.4: Illustration of how boundary points affect uncertainty in Bayesian logistic regression. **Left panel:** With only the original data points, there is significant uncertainty in the decision boundary, shown by the wide purple uncertainty region and the spread of possible boundaries. **Right panel:** After adding data points specifically near the decision boundary (triangular markers), the uncertainty region narrows significantly, and possible boundaries become more tightly clustered. This demonstrates why points near the decision boundary provide the most information about model parameters. The information value of a data point is proportional to $\sigma(\mathbf{w}_{\mathrm{MAP}}^T \mathbf{x}_n)(1 - \sigma(\mathbf{w}^T \mathbf{x}_n))$, which is maximized when $\sigma(\mathbf{w}_{\mathrm{MAP}}^T \mathbf{x}_n) = 0.5$ (exactly at the boundary) and approaches zero for points far from the boundary.

corresponding to a smaller covariance matrix $\mathbf{A}^{-1}$ and less uncertainty in our parameters. This relationship aligns with our intuition: the more informative data points we have, the more confident we should be about our model parameters.

However, even with many data points, if they are all far from the boundary, we might still have considerable uncertainty about the exact boundary location. This is why a well-designed training set for astronomical classification should ideally include objects spanning the full range of feature space, including those near potential boundaries between classes.

With our Gaussian approximation of the posterior in hand, we can now tackle the final challenge: computing predictions that account for parameter uncertainty. This leads us to the predictive distribution, which we'll explore in the next section.

9.5 Predictive Distribution of Bayesian Regression

In the previous section, we developed the Laplace approximation for Bayesian logistic regression, which allowed us to approximate the posterior distribution over our weights with a Gaussian:

$$q(\mathbf{w}) = \mathcal{N}(\mathbf{w}|\mathbf{w}_{\mathrm{MAP}}, \mathbf{A}^{-1}). \tag{9.49}$$

This posterior distribution represents a key advantage of the Bayesian approach: rather than committing to a single decision boundary as in traditional logistic regression, we now have a distribution over possible boundaries. Each set of weights $\mathbf{w}$ sampled from this posterior corresponds to a different decision boundary, and each will assign a different probability to a new object belonging to a particular class.

Consider classifying a new astronomical object: one boundary might assign it a 70% probability of being a star, while another might assign only 40%. This variation reflects our uncertainty in the true decision boundary, especially in regions of feature space with sparse training data. While we could examine the full distribution of these probability assignments, our goal is usually to make a single prediction that accounts for this uncertainty.

Predictive distribution formulation   This leads us to the predictive distribution—the probability of a class label for a new input point, obtained by integrating over all possible model parameters weighted by their posterior probability. Rather than arbitrarily selecting one boundary, we consider all plausible boundaries simultaneously, with each contributing according to its posterior probability.

For a new input $\mathbf{x}^*$, the predictive distribution for class 1 is given by:

$$p(y^* = 1|\mathbf{x}^*, \mathcal{D}) = \int p(y^* = 1|\mathbf{x}^*, \mathbf{w})p(\mathbf{w}|\mathcal{D})d\mathbf{w}. \tag{9.50}$$

This integral represents a weighted average over all possible model parameters, with each model's prediction weighted by its posterior probability. The term $p(y^* = 1|\mathbf{x}^*, \mathbf{w})$ is our sigmoid function $\sigma(\mathbf{w}^T\mathbf{x}^*)$, while $p(\mathbf{w}|\mathcal{D})$ is our posterior distribution over weights.

Using our Gaussian approximation to the posterior, we get:

$$p(y^* = 1|\mathbf{x}^*, \mathcal{D}) \approx \int \sigma(\mathbf{w}^T\mathbf{x}^*)\mathcal{N}(\mathbf{w}|\mathbf{w}_{\mathrm{MAP}}, \mathbf{A}^{-1})d\mathbf{w}. \tag{9.51}$$
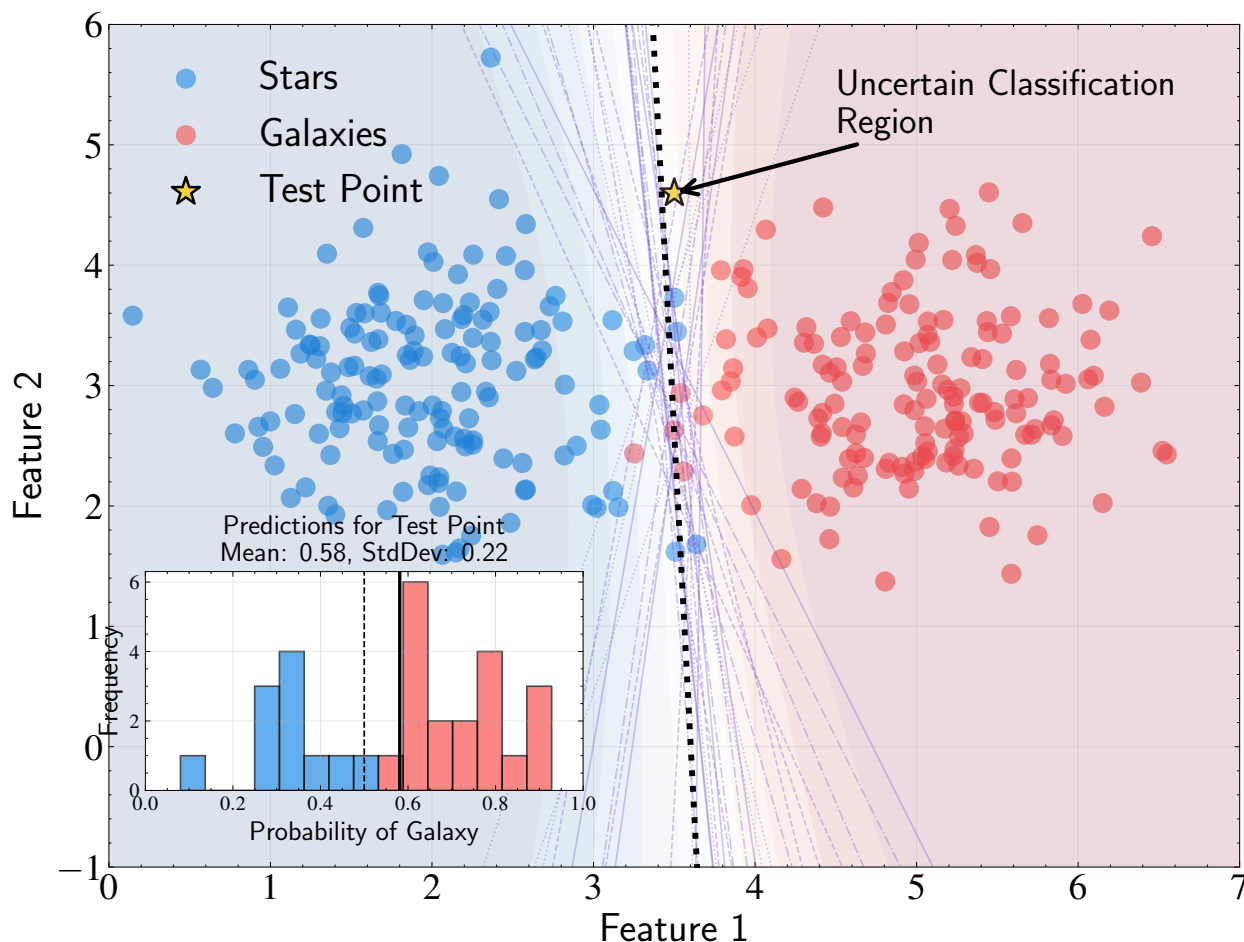
Figure 9.5: Bayesian logistic regression illustrated through multiple decision boundaries sampled from the posterior distribution. Each purple line represents a possible decision boundary according to the posterior, while the bold black line shows the MAP estimate. The yellow star indicates a test point in an uncertain region, with the inset histogram displaying the distribution of predictions from all sampled models. Unlike standard logistic regression which produces a single confident boundary, the Bayesian approach naturally quantifies uncertainty through this distribution of predictions. Note how predictions span both classes (blue for Stars, red for Galaxies), reflecting genuine ambiguity in regions far from training data.

Let's understand what this integral represents. For a new input point $\mathbf{x}^*$, we want to predict its probability of belonging to class 1. This probability depends on the sigmoid function $\sigma(\mathbf{w}^T\mathbf{x}^*)$, which maps the linear combination of features and weights to a probability

between 0 and 1.

Since we're uncertain about the true weights $\mathbf{w}$, we need to average this probability over all possible weights, weighted by how likely each set of weights is according to our posterior distribution. This averaging process is exactly what the integral accomplishes—it's a weighted average of the sigmoid function over all possible weight values from the posterior.

While we've made progress by approximating the posterior with a Gaussian, we now face another challenge: this integral still doesn't have a closed-form solution. The difficulty arises from the sigmoid function $\sigma(\mathbf{w}^T\mathbf{x}^*)$—its nonlinear form doesn't combine with Gaussians in a way that allows direct analytical integration.

However, there's a strategy we can take. We can make this integral tractable by first reducing its dimensionality, then approximating the sigmoid function with a closely related function that does allow for analytical integration with Gaussians.

Dimensional reduction   The predictive distribution requires integrating over the entire high-dimensional weight space, but do we actually need all that information? For classification, what truly matters is the logit value $a = \mathbf{w}^T\mathbf{x}^*$. This single number determines the class probability through the sigmoid function and represents the signed distance from the point to the decision boundary.

Here's the key insight: many different weight vectors $\mathbf{w}$ can produce exactly the same logit value a for a given input $\mathbf{x}^*$. Specifically, if we add any vector perpendicular to $\mathbf{x}^*$ to our weight vector, the logit value doesn't change:

$$(\mathbf{w} + \mathbf{w}_\perp)^T\mathbf{x}^* = \mathbf{w}^T\mathbf{x}^* + \mathbf{w}_\perp^T\mathbf{x}^* = \mathbf{w}^T\mathbf{x}^* = a, \tag{9.52}$$

where $\mathbf{w}_\perp^T\mathbf{x}^* = 0$ by definition.

This means that weight vectors forming a hyperplane perpendicular to $\mathbf{x}^*$ all map to the same logit value a. Since $\mathbf{w}$ follows a Gaussian distribution, and $a = \mathbf{w}^T\mathbf{x}^*$ is a linear combination of the components of $\mathbf{w}$, we know that a also follows a Gaussian distribution.

The mean and variance of this Gaussian distribution for a are:

$$\mu_a = \mathbf{w}_{\text{MAP}}^T\mathbf{x}^*, \tag{9.53}$$

$$\sigma_a^2 = \mathbf{x}^{*T}\mathbf{A}^{-1}\mathbf{x}^*. \tag{9.54}$$
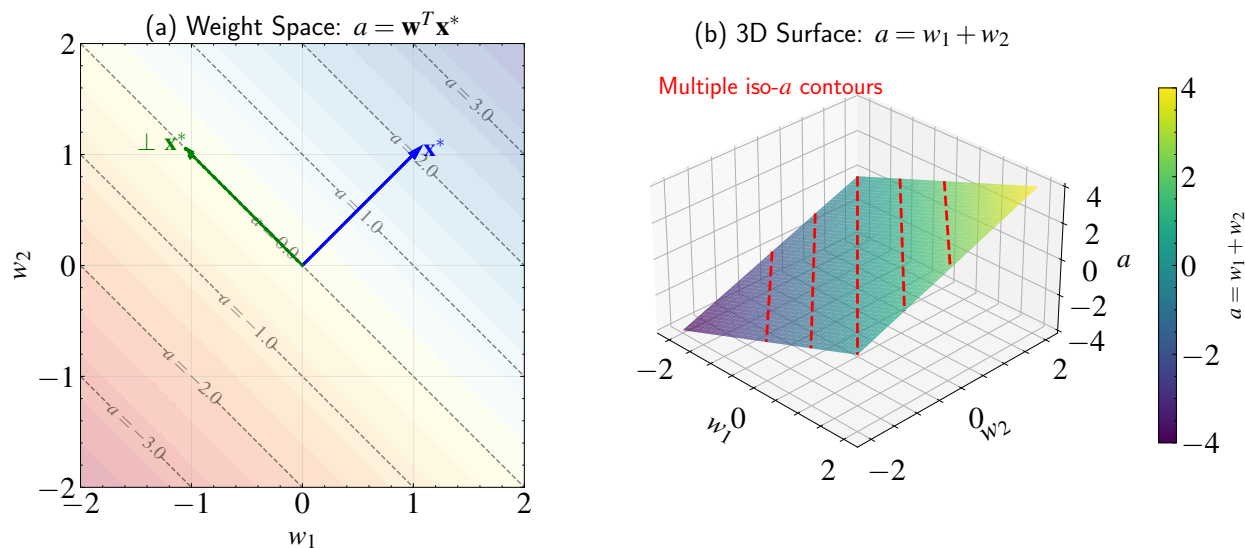
Figure 9.6: Visualization of the dimensionality reduction from weight space to logit space in Bayesian logistic regression. **Panel (a)** shows the 2D weight space where each point represents a possible weight vector $\mathbf{w}$. The blue arrow indicates the direction of the test point $\mathbf{x}^*$, while the green dashed arrow shows the direction perpendicular to $\mathbf{x}^*$. The dashed lines represent iso-a contours, where all weight vectors along a given contour yield the same value of $a = \mathbf{w}^T\mathbf{x}^*$. **Panel (b)** presents the same relationship as a 3D surface, where the height corresponds to the value of a, with red dashed lines highlighting constant-a contours. This geometric perspective explains why we can simplify the integration from the high-dimensional weight space to a one-dimensional integral over a: many different weight vectors map to the same scalar a value, and for logistic regression, the prediction depends only on this scalar. This insight enables the mathematical transformation $\int \sigma(\mathbf{w}^T\mathbf{x}^*)p(\mathbf{w}|\mathcal{D})d\mathbf{w} = \int \sigma(a)p(a)da$, dramatically simplifying the computation of the predictive distribution.

Therefore, $a \sim \mathcal{N}(\mu_a, \sigma_a^2)$.

This is a powerful result: although $\mathbf{w}$ is a complex, high-dimensional Gaussian random variable, the single quantity $a = \mathbf{w}^T\mathbf{x}^*$ that determines our prediction follows a simple one-dimensional Gaussian distribution.

Our original predictive distribution integral becomes:

$$p(y^* = 1|\mathbf{x}^*, \mathcal{D}) \approx \int \sigma(a)\mathcal{N}(a|\mu_a, \sigma_a^2)da. \tag{9.55}$$

This simplification is remarkable—we've reduced a potentially very high-dimensional integral to a one-dimensional integral! The mean $\mu_a = \mathbf{w}_{\text{MAP}}^T\mathbf{x}^*$ represents our best estimate of the logit value, while the variance $\sigma_a^2 = \mathbf{x}^{*T}\mathbf{A}^{-1}\mathbf{x}^*$ quantifies our uncertainty about this

estimate.

In practical applications, weight vectors might have hundreds or thousands of dimensions, making direct integration over the weight space computationally infeasible. By reducing to a one-dimensional integral, we've made the problem tractable while preserving all the information relevant for classification.

The remaining challenge Despite this dramatic simplification, we still face a challenge because the sigmoid function $\sigma(a)$ doesn't combine with the Gaussian in a way that permits analytical integration. Our remaining one-dimensional integral:

$$p(y^* = 1|\mathbf{x}^*, \mathcal{D}) \approx \int \sigma(a)\mathcal{N}(a|\mu_a, \sigma_a^2)da \qquad (9.56)$$

represents our final computational hurdle.

If we can solve this integral, we'll have a complete solution for the predictive distribution in Bayesian logistic regression, allowing us to make predictions that properly account for parameter uncertainty. The key insight, which we'll explore in the next section, is to replace the sigmoid function with a closely related function that does allow for analytical integration with Gaussians: the probit function.

9.6 The Probit Approximation

In the previous section, we simplified our predictive distribution integral to a one-dimensional form:

$$p(y^* = 1|\mathbf{x}^*, \mathcal{D}) \approx \int \sigma(a)\mathcal{N}(a|\mu_a, \sigma_a^2)da. \qquad (9.57)$$

Despite this simplification, we still face a challenge: there is no analytical solution for this integral. The sigmoid function $\sigma(a)$ and the Gaussian distribution don't combine in a way that allows for direct integration. We need a creative approach to make further progress.

The key insight is to replace the sigmoid function with a similar function that does allow for analytical integration with a Gaussian. This function is the probit function, denoted as $\Phi(x)$, which is the cumulative distribution function (CDF) of the standard Gaussian distribution.

Understanding the probit function While we typically work with probability density functions (PDFs) that describe the relative likelihood of different values, the CDF gives us the probability of observing a value less than or equal to x. The probit function is obtained by integrating the standard normal PDF:

$$\Phi(x) = \int_{-\infty}^{x} \mathcal{N}(t|0, 1)dt. \tag{9.58}$$

We can scale this function with a parameter λ, giving us $\Phi(\lambda x)$:

$$\Phi(\lambda x) = \int_{-\infty}^{\lambda x} \mathcal{N}(t|0, 1)dt. \tag{9.59}$$

This scaling is equivalent to working with a random variable $Z \sim \mathcal{N}(0, 1/\lambda^2)$, since:

$$P(Z < x) = P(X < \lambda x) = \Phi(\lambda x) \tag{9.60}$$

where $X \sim \mathcal{N}(0, 1)$ and $Z = X/\lambda$.
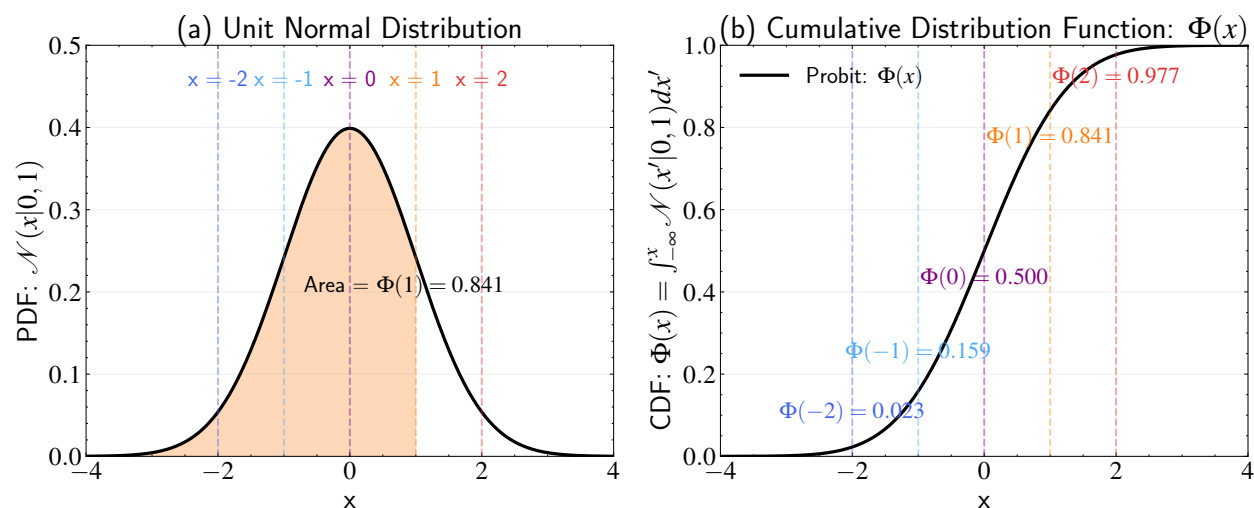
Figure 9.7: The probit function as the cumulative distribution function (CDF) of the standard normal distribution. **Panel (a)** shows the unit normal probability density function (PDF) $\mathcal{N}(x|0, 1)$. The shaded orange area represents the cumulative probability up to $x = 1$, which equals $\Phi(1) = 0.841$. **Panel (b)** displays the probit function $\Phi(x)$, which is the CDF of the standard normal distribution. For any value x, the probit function $\Phi(x)$ gives the probability mass contained in the normal distribution up to that point.

The probit function shares several important properties with the sigmoid: both map the real line to the interval $(0, 1)$, both are monotonically increasing with an S-shaped curve,

and both approach 0 as $x \to -\infty$ and 1 as $x \to \infty$. Visually, they appear quite similar, which suggests one might serve as a good approximation for the other.

Key mathematical property   What makes the probit function particularly valuable for our problem is a mathematical property: when multiplied by a Gaussian and integrated, it yields another probit function:

$$\int \Phi(\lambda a)\mathcal{N}(a|\mu, \sigma^2)da = \Phi\left(\frac{\lambda\mu}{\sqrt{1 + \lambda^2\sigma^2}}\right). \tag{9.61}$$

This result is exactly what we need to solve our predictive distribution integral.

Let's understand where this identity comes from through an approach that uses properties of random variables. Consider two independent random variables:

- $X \sim \mathcal{N}(0, 1/\lambda^2)$ (a scaled standard normal distribution)

- $Y \sim \mathcal{N}(\mu, \sigma^2)$ (our Gaussian from the integral)

We can express the identity in terms of the probability that X is less than Y. This probability can be calculated in two different ways, which must give the same result.

First approach: We compute $P(X < Y)$ by looking at their difference $X - Y$. Since X and Y are independent Gaussian random variables, their difference is also Gaussian:

- The mean of the difference is: $E[X - Y] = 0 - \mu = -\mu$

- The variance of the difference is: $\text{Var}[X - Y] = 1/\lambda^2 + \sigma^2$

Therefore:

$$X - Y \sim \mathcal{N}(-\mu, 1/\lambda^2 + \sigma^2). \tag{9.62}$$

The probability that $X - Y < 0$ is:

$$P(X - Y < 0) = P(X < Y) \tag{9.63}$$

$$= \Phi\left(\frac{\mu}{\sqrt{1/\lambda^2 + \sigma^2}}\right) \tag{9.64}$$

$$= \Phi\left(\frac{\lambda\mu}{\sqrt{1 + \lambda^2\sigma^2}}\right). \tag{9.65}$$

Second approach: We calculate the same probability by conditioning on the value of Y. For each possible value y that Y could take:

- The probability that $X < y$ is $\Phi(\lambda y)$

- We weight this by the probability density of Y being equal to y

- We integrate over all possible values of y

This gives us:

$$P(X < Y) = \int_{-\infty}^{\infty} \Phi(\lambda y)\mathcal{N}(y|\mu, \sigma^2)dy. \tag{9.66}$$

Since both approaches must yield the same probability, we can equate them:

$$\int \Phi(\lambda a)\mathcal{N}(a|\mu, \sigma^2)da = \Phi\left(\frac{\lambda\mu}{\sqrt{1 + \lambda^2\sigma^2}}\right). \tag{9.67}$$

Sigmoid approximation   Now that we have this powerful identity for integrating probit functions with Gaussians, we can use it to solve our predictive distribution integral. However, we first need to approximate the sigmoid function using a scaled probit function:

$$\sigma(a) \approx \Phi(\lambda a). \tag{9.68}$$

To determine the optimal value of λ, we can match the derivatives of the sigmoid and probit functions at $a = 0$. The sigmoid function's derivative is:

$$\frac{d}{da}\sigma(a) = \sigma(a)(1 - \sigma(a)) = \frac{e^{-a}}{(1 + e^{-a})^2}. \tag{9.69}$$

At $a = 0$, this equals $1/4$. For the probit function:

$$\frac{d}{da}\Phi(\lambda a) = \lambda\phi(\lambda a) = \frac{\lambda}{\sqrt{2\pi}}e^{-\lambda^2 a^2/2}. \tag{9.70}$$

where $\phi(x)$ is the standard normal probability density function. At $a = 0$, this equals $\lambda/\sqrt{2\pi}$. Equating these derivatives:

$$\frac{1}{4} = \frac{\lambda}{\sqrt{2\pi}} \implies \lambda = \sqrt{\frac{\pi}{8}}. \tag{9.71}$$

This value of λ ensures that both functions have identical slopes at the decision bound-

ary ($a = 0$), providing optimal local approximation where it matters most for classification.
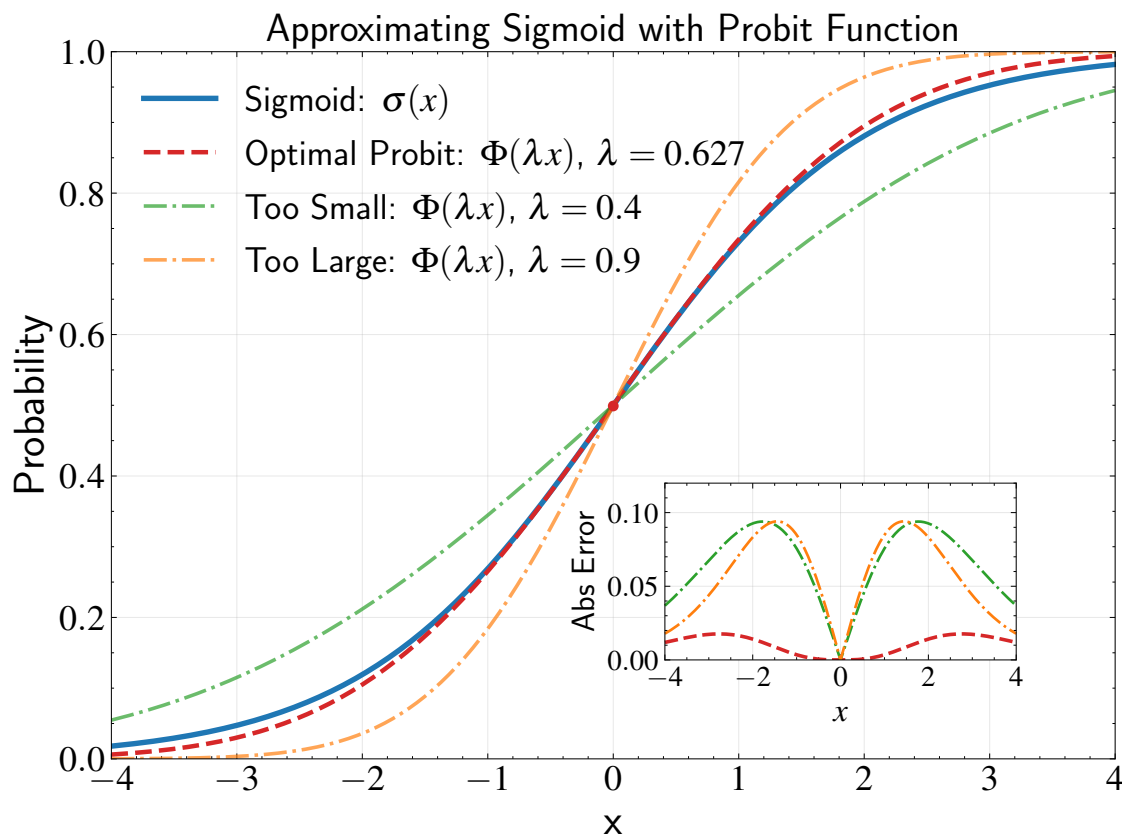
Figure 9.8: Comparison of the sigmoid function $\sigma(x)$ with different scaled probit functions $\Phi(\lambda x)$. The optimal scaling factor $\lambda = \sqrt{\pi/8} \approx 0.63$ (red dashed line) provides the best overall approximation to the sigmoid function (blue solid line). This scaling factor is derived by matching the derivatives of both functions at $x = 0$, where they cross the probability value of 0.5. The inset shows the absolute error for each approximation across the input range, demonstrating that the optimal scaling minimizes the maximum error. Alternative scaling factors that are either too small ($\lambda = 0.4$, green) or too large ($\lambda = 0.9$, orange) produce poorer approximations. This optimal approximation enables us to transform the intractable sigmoid-Gaussian integral in the predictive distribution into an analytically solvable probit-Gaussian integral while maintaining high accuracy, particularly near the decision boundary.

The resulting approximation is:

$$\sigma(a) \approx \Phi\left(\sqrt{\frac{\pi}{8}}a\right). \tag{9.72}$$

Solving the predictive distribution With our probit approximation in hand, we can now tackle the predictive distribution integral. We substitute our scaled probit function for

the sigmoid:

$$p(y^* = 1|\mathbf{x}^*, \mathcal{D}) \approx \int \Phi\left(\sqrt{\frac{\pi}{8}}a\right) \mathcal{N}(a|\mu_a, \sigma_a^2)da. \tag{9.73}$$

We can directly apply our integration formula with $\lambda = \sqrt{\pi/8}$:

$$\int \Phi\left(\sqrt{\frac{\pi}{8}}a\right) \mathcal{N}(a|\mu_a, \sigma_a^2)da = \Phi\left(\frac{\sqrt{\pi/8} \cdot \mu_a}{\sqrt{1 + (\pi/8)\sigma_a^2}}\right). \tag{9.74}$$

To maintain consistency with our original framework, we can convert this result back to the sigmoid function. Using our approximation in reverse:

$$\Phi\left(\frac{\sqrt{\pi/8} \cdot \mu_a}{\sqrt{1 + (\pi/8)\sigma_a^2}}\right) \approx \sigma\left(\frac{\mu_a}{\sqrt{1 + \pi\sigma_a^2/8}}\right). \tag{9.75}$$

This gives us our final expression for the predictive distribution:

$$p(y^* = 1|\mathbf{x}^*, \mathcal{D}) \approx \sigma\left(\frac{\mu_a}{\sqrt{1 + \pi\sigma_a^2/8}}\right). \tag{9.76}$$

The uncertainty factor   To make this expression more intuitive, let's define an "uncertainty factor" $\kappa(\sigma_a^2) = (1 + \pi\sigma_a^2/8)^{-1/2}$. This allows us to write:

$$p(y^* = 1|\mathbf{x}^*, \mathcal{D}) \approx \sigma(\kappa(\sigma_a^2) \cdot \mu_a). \tag{9.77}$$

Substituting our original expressions for μ_a and σ_a^2:

$$p(y^* = 1|\mathbf{x}^*, \mathcal{D}) \approx \sigma\left(\kappa(\mathbf{x}^{*T}\mathbf{A}^{-1}\mathbf{x}^*) \cdot \mathbf{w}_{\text{MAP}}^T\mathbf{x}^*\right). \tag{9.78}$$

This formula contains the key insight of Bayesian logistic regression. Compared to standard logistic regression, which predicts $\sigma(\mathbf{w}_{\text{MAP}}^T\mathbf{x}^*)$, the Bayesian approach introduces the uncertainty factor $\kappa(\sigma_a^2)$ that modifies our prediction based on how uncertain we are about the model parameters.

Since $\kappa(\sigma_a^2)$ is always between 0 and 1, it dampens the logit value before applying the sigmoid function. When our uncertainty σ_a^2 is small (we're confident about our parameters),

$\kappa(\sigma_a^2) \approx 1$ and we recover the standard logistic regression prediction. When our uncertainty is large, $\kappa(\sigma_a^2)$ becomes small, pushing our prediction toward 0.5 (maximum uncertainty).

This uncertainty factor provides exactly what we wanted: a principled way to express less confidence when classifying objects in regions of feature space where we have little training data. In the next section, we'll explore the properties and implications of this result for astronomical classification tasks.

9.7 Properties of Bayesian Logistic Regression

Now that we have derived the predictive distribution for Bayesian logistic regression, let's explore its properties and implications for astronomical applications. The formula we derived provides a principled way to incorporate parameter uncertainty into our classifications, leading to more calibrated probability estimates.

Comparison with standard logistic regression Let's begin by comparing our Bayesian predictive distribution with standard logistic regression. In standard logistic regression, our prediction is simply:

$$p(y^* = 1|\mathbf{x}^*, \mathbf{w}_{\text{MAP}}) = \sigma(\mathbf{w}_{\text{MAP}}^T \mathbf{x}^*). \tag{9.79}$$

This gives a single prediction based on our best estimate of the model parameters.

In contrast, our Bayesian approach gives:

$$p(y^* = 1|\mathbf{x}^*, \mathcal{D}) \approx \sigma(\kappa(\sigma_a^2) \cdot \mathbf{w}_{\text{MAP}}^T \mathbf{x}^*), \tag{9.80}$$

where $\kappa(\sigma_a^2) = (1 + \pi\sigma_a^2/8)^{-1/2}$ and $\sigma_a^2 = \mathbf{x}^{*T} \mathbf{A}^{-1} \mathbf{x}^*$.

The key difference is the uncertainty factor $\kappa(\sigma_a^2)$, which modulates our prediction based on our uncertainty about the model parameters. This seemingly small addition has important implications for classification tasks.

Properties of the uncertainty factor Let's examine the behavior of this uncertainty factor:

First, $\kappa(\sigma_a^2)$ is always between 0 and 1. Since σ_a^2 is a variance term, it is always non-negative, making the denominator always greater than or equal to 1. When $\sigma_a^2 = 0$ (no uncertainty), $\kappa(0) = 1$, and our Bayesian prediction reduces exactly to the standard logistic

regression prediction. As σ_a^2 increases, $\kappa(\sigma_a^2)$ decreases toward 0.

Second, the uncertainty factor decreases monotonically as our uncertainty increases. This makes intuitive sense—the less certain we are about our model parameters, the more we should temper our predictions.

Third, when $\kappa(\sigma_a^2)$ multiplies the logit value before applying the sigmoid function, it pushes predictions toward 0.5 (maximum uncertainty). For example:

- If $\mathbf{w}_{\text{MAP}}^T \mathbf{x}^* = 2$ (strong positive prediction), then $\sigma(2) \approx 0.88$

- With $\kappa(\sigma_a^2) = 0.5$, we get $\sigma(0.5 \cdot 2) = \sigma(1) \approx 0.73$

- With $\kappa(\sigma_a^2) = 0.2$, we get $\sigma(0.2 \cdot 2) = \sigma(0.4) \approx 0.60$

As $\kappa(\sigma_a^2)$ approaches 0, our prediction approaches 0.5, reflecting maximum uncertainty.

This behavior is symmetric: if $\mathbf{w}_{\text{MAP}}^T \mathbf{x}^*$ is negative (favoring class 0), the uncertainty factor will push the prediction upward toward 0.5. This ensures that uncertainty always moves predictions toward the middle, regardless of which class is initially favored.

Geometric interpretation　What determines the value of $\sigma_a^2 = \mathbf{x}^{*T} \mathbf{A}^{-1} \mathbf{x}^*$? Recall that $\mathbf{A}$ is the precision matrix of our approximate posterior:

$$\mathbf{A} = \mathbf{S}_0^{-1} + \sum_{n=1}^{N} \sigma(\mathbf{w}_{\text{MAP}}^T \mathbf{x}_n)(1 - \sigma(\mathbf{w}_{\text{MAP}}^T \mathbf{x}_n)) \mathbf{x}_n \mathbf{x}_n^T. \tag{9.81}$$

The term $\sigma(\mathbf{w}_{\text{MAP}}^T \mathbf{x}_n)(1 - \sigma(\mathbf{w}_{\text{MAP}}^T \mathbf{x}_n))$ reaches its maximum of 0.25 when the predicted probability is 0.5, which occurs near the decision boundary. Therefore, training points near the boundary contribute more strongly to $\mathbf{A}$.

For a new point $\mathbf{x}^*$, the value σ_a^2 represents a quadratic form with $\mathbf{A}^{-1}$. When $\mathbf{x}^*$ is far from the training data, it will have low similarity (as measured by inner products) with the training points $\mathbf{x}_n$. Consequently, the contributions to $\mathbf{A}$ in the direction of $\mathbf{x}^*$ will be small, making the corresponding elements of $\mathbf{A}^{-1}$ large. This results in a larger value of σ_a^2, reflecting increased uncertainty in regions distant from training data.

Consider what this means geometrically. In a two-dimensional feature space with separated clusters of training points, standard logistic regression gives us a linear decision
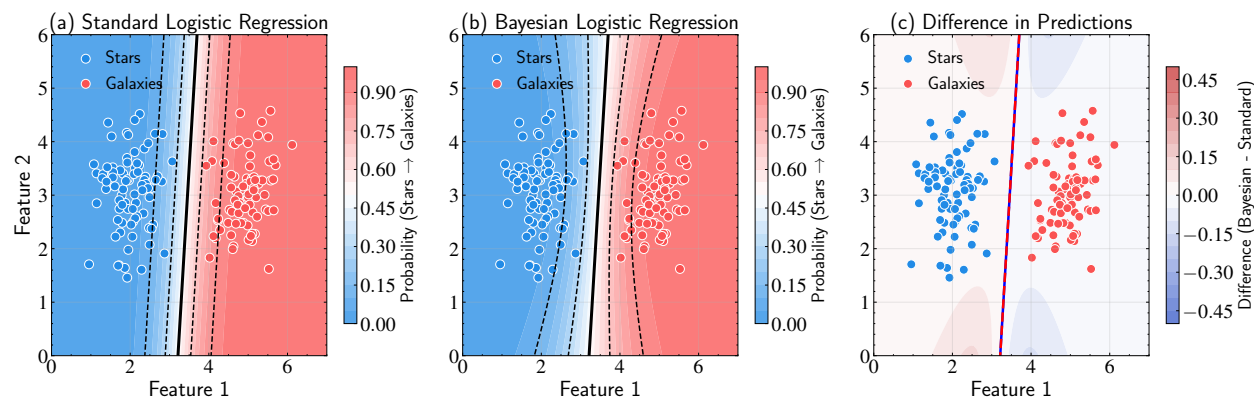
Figure 9.9: Comparison of standard and Bayesian logistic regression predictions. **Panel (a)** shows the standard logistic regression probability contours with a sharp decision boundary and increasing confidence away from the boundary regardless of data density. **Panel (b)** shows Bayesian logistic regression probability contours, which feature a more gradual transition between classes in regions far from training data. **Panel (c)** visualizes the difference between Bayesian and standard predictions, with blue regions indicating where Bayesian predicts lower probabilities (more likely to be stars) and red regions indicating higher probabilities (more likely to be galaxies) compared to standard logistic regression. The white regions in the center show where predictions are pulled toward 0.5 (maximum uncertainty). This occurs in the sparse regions between and away from the training clusters, illustrating how the uncertainty factor $\kappa(\sigma_a^2)$ naturally provides a measure of confidence that depends on the distribution of training data. The decision boundary in Bayesian logistic regression (red dashed line) is essentially identical to the standard approach (blue solid line) where data is plentiful, but the confidence in predictions away from data is appropriately reduced.

boundary. As we move away from this boundary in either direction, our confidence increases monotonically—even in regions far from any training data where such confidence is unjustified.

Bayesian logistic regression behaves differently. Near the training data, where σ_a^2 is small, predictions closely resemble standard logistic regression. But as we venture into regions with little or no training data, σ_a^2 increases, causing $\kappa(\sigma_a^2)$ to decrease. This pushes our predictions toward 0.5, appropriately reflecting our growing uncertainty.

The result is a more nuanced decision boundary that becomes increasingly "soft" as we move away from the training data. Rather than a sharp boundary extending indefinitely into unexplored regions of feature space, we have a boundary that acknowledges our uncertainty about regions where evidence is scarce.

Astronomical applications This behavior of Bayesian logistic regression proves particularly valuable in astronomical classification tasks, where we frequently encounter objects outside the parameter ranges represented in our training data. Consider classifying galaxies as either spiral or elliptical based on morphological features.

In traditional logistic regression, if our training set consists primarily of typical spiral and elliptical galaxies, the model might assign high confidence to classifications of unusual or intermediate objects, even though such confidence is unwarranted. A model might classify a peculiar galaxy with 99% confidence, even if nothing remotely similar appeared in the training data.

Bayesian logistic regression naturally avoids this pitfall. When presented with a galaxy unlike any in the training set, the model's uncertainty will increase, reflected in a prediction closer to 0.5. This uncertainty signal is valuable for astronomers, as it highlights objects that merit closer inspection or might represent new or transitional types.

Beyond identifying unusual objects, this approach offers several advantages for astronomical applications:

First, it prevents overconfident classifications for novel objects. This is crucial in survey science, where we often need to classify millions of objects automatically. Overconfidence can lead to systematic biases in derived statistics or hide interesting outliers. By expressing appropriate uncertainty for novel objects, Bayesian logistic regression helps astronomers identify where manual follow-up is needed versus where automated classification is reliable.

Second, it helps identify boundary cases that may represent transitional or new object types. Many astronomical discoveries occur at the boundaries between established categories—galaxies in transformation, stars in unusual evolutionary states, or entirely new classes of objects. By highlighting regions of parameter space with high uncertainty, Bayesian logistic regression can help identify these scientifically valuable boundary cases.

Third, it provides a principled way to handle class overlap. In many astronomical classification problems, categories aren't strictly separable—there may be genuine overlap or ambiguity. Rather than forcing hard classifications in these regions, Bayesian logistic regression expresses the inherent uncertainty, which more accurately reflects the underlying physical reality.

This approach aligns with the scientific principle that uncertainty quantification is

as important as the predictions themselves. In astronomy, understanding the limitations of our knowledge is crucial for drawing valid scientific conclusions. Bayesian logistic regression provides a framework where uncertainty is an integral part of the classification process, rather than an afterthought.

Practical implications The uncertainty factor provides exactly what we sought at the beginning of this chapter: a method that expresses appropriate uncertainty when encountering data unlike what it was trained on. This capability proves especially valuable in astronomical surveys where:

- Training data is often limited and expensive to obtain

- The labeled data comes from biased sampling (easier or more interesting objects)

- We frequently encounter objects in unexplored regions of parameter space

- Overconfident misclassifications can lead to missed discoveries

By naturally detecting and highlighting regions of feature space that are poorly sampled by training data, Bayesian logistic regression not only makes better predictions but also guides us toward where additional labeled examples would be most valuable for improving our models.

9.8   Summary

The Bayesian approach to logistic regression addresses a limitation of standard maximum likelihood methods: the tendency to make overconfident predictions in regions of feature space poorly represented by training data. By treating model parameters as uncertain quantities rather than fixed values, we can make predictions that appropriately express our confidence or lack thereof.

The mathematical development required two key approximations to make the problem tractable. First, we used the Laplace approximation to represent the complex, non-Gaussian posterior distribution over weights as a Gaussian centered at the maximum a posteriori (MAP) estimate. This approximation becomes increasingly accurate as we gather more data, thanks to the Bernstein-von Mises theorem, which guarantees that posteriors converge to Gaussian distributions for large sample sizes.

Second, we employed the probit approximation to compute the predictive distribution analytically. By replacing the sigmoid function with a scaled probit function, we could evaluate the integral over parameter uncertainty in closed form. The combination of these approximations yields a practical algorithm that scales well to real astronomical datasets.

The resulting predictive formula contains an uncertainty factor $\kappa(\sigma_a^2) = (1+\pi\sigma_a^2/8)^{-1/2}$ that automatically modulates our confidence based on the distance from training data. This factor has an intuitive interpretation: it dampens predictions in regions where we have little evidence, pushing them toward maximum uncertainty (0.5 probability). Near our training data, where we have more evidence, the uncertainty factor approaches 1, and our predictions resemble standard logistic regression.

This behavior provides exactly what we sought: a classification method that avoids unjustified confidence when encountering novel objects. In astronomical applications, where we frequently classify objects unlike anything in our training set, this appropriate expression of uncertainty helps identify where manual follow-up is needed versus where automated classification is reliable.

The Bayesian approach aligns with broader scientific principles we've encountered throughout this course. Just as Bayesian inference naturally incorporates the principle that extraordinary claims require extraordinary evidence, Bayesian logistic regression embodies the idea that confidence should be proportional to evidence. When we have abundant, relevant training data, the model expresses high confidence. When we venture into unexplored regions of parameter space, it appropriately expresses uncertainty.

This concludes our exploration of supervised learning methods. We have now developed both linear and logistic regression through the lens of Bayesian inference, seeing how principled uncertainty quantification emerges naturally from probabilistic reasoning. These supervised learning techniques—mapping inputs to specific outputs based on labeled training data—represent one major branch of machine learning applications in astronomy.

However, many astronomical problems involve datasets without predefined target variables to predict. We might have measurements of thousands of galaxies without knowing in advance what patterns or groupings exist among them. Or we might have spectra from a survey without predetermined classifications, seeking to discover natural categories within the data.

This leads us to unsupervised learning—the discovery and characterization of struc-

ture within data without the guidance of labels. Rather than learning to map inputs to known outputs, unsupervised methods seek patterns, clusters, and reduced representations that reveal the underlying organization of our observations.

In Chapter 10, we will begin exploring these unsupervised learning methods, starting with Principal Component Analysis (PCA) for dimensionality reduction. This technique helps us identify the most important directions of variation in high-dimensional data, providing both computational advantages and scientific insights. Just as supervised learning proved valuable for classification and regression tasks, unsupervised learning will open new possibilities for exploratory data analysis and discovery in astronomical research.

Further Readings: The Bayesian treatment of logistic regression extends the regression framework through probabilistic modeling of binary outcomes, with Zellner and Rossi [1984] providing analysis of dichotomous quantal response models within the Bayesian paradigm. For readers interested in Bayesian approaches to binary and polychotomous response data, Albert and Chib [1993] develop computational methods including data augmentation techniques for such models. The computational challenge of non-conjugate posteriors in Bayesian logistic regression is addressed through approximation methods, with Tierney and Kadane [1986] offering systematic treatment of the Laplace approximation for posterior moments and marginal densities. The theoretical foundations for Gaussian approximations to posterior distributions build on asymptotic theory, with Walker [1969] examining the behavior of posterior distributions and Le Cam [1986] providing fundamental results including the Bernstein-von Mises theorem. For readers seeking modern machine learning perspectives, MacKay [2003] demonstrates how Bayesian logistic regression integrates with the evidence framework for hyperparameter selection, while Bishop [2006] provides treatment connecting Bayesian methods with contemporary machine learning practice. The broader framework of Bayesian Generalized Linear Models, which encompasses logistic regression as a special case, receives thorough theoretical treatment in McCullagh and Nelder [1989]. Model comparison within the Bayesian framework relies on marginal likelihood computation, with Kass and Raftery [1995] providing review of Bayes factors and computational methods that enable principled selection among competing models.

Chapter 10

Principal Component Analysis

Throughout our exploration of machine learning techniques, we've focused primarily on supervised learning methods—from linear regression to classification algorithms. These approaches all share a common characteristic: they learn to map from input features $\mathbf{x}$ to target outputs $\mathbf{y}$. When we predict stellar ages from spectra or classify galaxies into morphological types, we work with clear target variables that guide our learning process.

But consider the astronomical data we encounter daily. A single stellar spectrum contains measurements at thousands of wavelength bins. A galaxy image consists of millions of pixels. Even a "simple" stellar dataset might include dozens of elemental abundances. Despite this apparent complexity, we often suspect that the underlying physics operates with far fewer parameters than our measurements suggest.

This intuition proves correct remarkably often in astronomy. Stellar spectra, with their thousands of wavelength points, are primarily determined by just a few physical properties: effective temperature, surface gravity, and metallicity. Galaxy morphologies, while visually complex, often reflect a small number of formation and evolution processes. The chemical compositions of stars in a cluster, though measured across many elements, typically follow patterns determined by just a few nucleosynthetic pathways.

This observation raises a natural question: can we automatically discover these underlying patterns? Can we find the small number of parameters that explain most of the variation in our high-dimensional data without knowing the target variables in advance?

This question leads us into unsupervised learning—the discovery and characterization

of structure within data without the guidance of labels. Rather than learning to map inputs to known outputs, unsupervised methods seek patterns, clusters, and reduced representations that reveal the underlying organization of our observations.

Principal Component Analysis (PCA) provides one answer to our question about discovering underlying patterns. PCA seeks to find a lower-dimensional representation of high-dimensional data while preserving as much information as possible. The technique builds upon the same linear algebraic foundations we established in earlier chapters, but applies them to a different problem: identifying directions of maximum variation in our data.

The core insight behind PCA is straightforward. If our high-dimensional data is governed by a smaller number of underlying factors, then most of the variation in our measurements should occur along a few specific directions in the data space. PCA systematically identifies these directions of maximum variation, allowing us to represent our data using far fewer dimensions while retaining most of the original information.

This dimension reduction capability addresses several challenges that arise frequently in astronomical data analysis. High-dimensional data becomes difficult to visualize beyond 2-3 dimensions, making pattern identification through direct inspection nearly impossible. Computational requirements scale dramatically with dimensionality, as processing and analyzing high-dimensional data demands substantial resources. The curse of dimensionality makes statistical inference increasingly difficult as the number of dimensions grows, since available data becomes sparse relative to the volume of the space.

Perhaps most importantly, dimension reduction can reveal the underlying physical parameters that govern complex astronomical phenomena. Rather than working with thousands of spectral measurements, we might discover that just three components capture the essential stellar properties. Instead of analyzing millions of pixels in galaxy images, we might find that a handful of components describe the key morphological features.

In this chapter, we will develop PCA from first principles, showing how it emerges naturally from constrained optimization. We'll discover that principal components are the eigenvectors of the data covariance matrix, ordered by their corresponding eigenvalues. This connection provides both theoretical insight and computational efficiency, especially when we introduce Singular Value Decomposition as an alternative approach for high-dimensional datasets.

Our mathematical journey will reveal that what initially appears as a complex problem—finding optimal lower-dimensional representations—reduces to familiar linear algebra. The eigenvectors that seemed abstract in our mathematical background become the concrete directions of maximum variation in our astronomical data.

10.1   Principal Component Analysis Fundamentals

Principal Component Analysis seeks to find a lower-dimensional representation of high-dimensional data while preserving as much of the original information as possible. To understand the mathematical foundation of this approach, we need to establish what we mean by "information" and how we can systematically identify the most informative directions in our data.

Consider a dataset consisting of N astronomical objects, each characterized by D measurements. We represent this as a data matrix $\mathbf{X} \in \mathbb{R}^{N \times D}$, where each row corresponds to one object and each column corresponds to one measured feature. For stellar spectroscopy, N might represent the number of observed stars while D represents the number of wavelength bins. For galaxy photometry, the features might be magnitudes in different bands.

The central insight behind PCA lies in recognizing that not all directions in this D-dimensional space are equally informative. Some directions exhibit large variations across our sample—these directions reveal how objects differ from one another. Other directions show little variation—these might represent measurement noise, redundant information, or simply aspects of the data that don't distinguish between objects.

Two Perspectives on Dimensionality Reduction   The objective of PCA can be formulated through two complementary approaches that lead to identical mathematical solutions.

Variance Maximization: From this perspective, we seek directions in our high-dimensional space along which our data varies the most. We project our data onto these high-variance directions to create our lower-dimensional representation. The rationale is that directions with greater variance contain more information about the structure of our data.

This approach proves particularly relevant for astronomical applications. In stellar spectroscopy, directions of maximum variance often correspond to physically meaningful variations such as differences in temperature, metallicity, or surface gravity. In galaxy photometry, they might capture variations in mass, star formation rate, or morphology.

Reconstruction Error Minimization: Alternatively, we can view PCA as finding a lower-dimensional representation that, when mapped back to the original space, minimizes the average squared distance between original data points and their reconstructions. This approach focuses on preserving the overall structure of the data cloud.

The mathematical equivalence of these perspectives provides insight into what PCA accomplishes: it finds the most informative lower-dimensional representation possible under linear constraints.

Mathematical Framework   We begin by establishing our notation and making a simplifying assumption that will prove mathematically convenient. Let our dataset consist of samples $\mathcal{X} = \{\mathbf{x}_1, \ldots, \mathbf{x}_N\}$, where each $\mathbf{x}_i \in \mathbb{R}^D$ represents a D-dimensional observation.

To streamline our mathematical development, we assume our data is centered with zero mean:

$$\mathbb{E}[\mathbf{x}] = \overline{\mathbf{x}} = \frac{1}{N} \sum_{i=1}^{N} \mathbf{x}_i = \mathbf{0}. \tag{10.1}$$

In practice, astronomical data rarely has a natural zero point. We center our data by subtracting the sample mean from each observation:

$$\mathbf{x}_i' = \mathbf{x}_i - \overline{\mathbf{x}}. \tag{10.2}$$

This centering step proves crucial because it allows us to interpret variance directly as a measure of information content. With centered data, values represent deviations from the mean, with positive and negative values indicating position relative to the center of the distribution.

Vector Projections and Basis Decomposition   The mathematical foundation of PCA rests on the concept of vector projection. When we project a vector $\mathbf{x}$ onto a unit vector $\mathbf{b}$ in a D-dimensional space, we compute:

$$\widehat{\mathbf{x}} = (\mathbf{x}^T \mathbf{b})\mathbf{b}. \tag{10.3}$$

The scalar value $\mathbf{x}^T \mathbf{b}$ measures how much of vector $\mathbf{x}$ points in the direction of $\mathbf{b}$. When we multiply this scalar by $\mathbf{b}$ itself, we obtain a vector that points in the direction of $\mathbf{b}$ with magnitude proportional to the projection of $\mathbf{x}$ onto that direction.
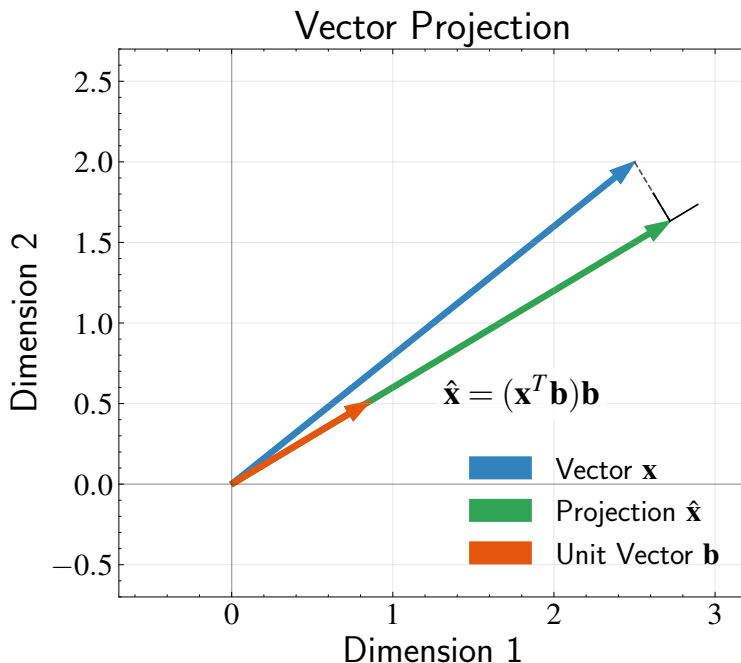
Figure 10.1: Vector projection in 2D space, illustrating a key mathematical concept for PCA. The figure shows an original vector $\mathbf{x}$ (blue), a unit vector $\mathbf{b}$ (red), and the projection $\widehat{\mathbf{x}}$ of $\mathbf{x}$ onto $\mathbf{b}$ (green). The equation $\widehat{\mathbf{x}} = (\mathbf{x}^T\mathbf{b})\mathbf{b}$ shows how we compute this projection: first calculating the scalar projection $\mathbf{x}^T\mathbf{b}$ (which measures how much of $\mathbf{x}$ extends in direction $\mathbf{b}$), then multiplying by $\mathbf{b}$ to get a vector with the appropriate magnitude in the direction of $\mathbf{b}$. The dashed line represents the perpendicular distance from $\mathbf{x}$ to its projection, which is minimized by this projection. This minimization property is crucial to PCA, where we seek basis vectors that minimize the sum of squared projection errors across all data points.

This concept extends to multiple dimensions through basis decomposition. When we have a complete set of orthonormal basis vectors $\{\mathbf{b}_1, \mathbf{b}_2, \ldots, \mathbf{b}_D\}$, we can decompose any vector $\mathbf{x}$ as:

$$\mathbf{x} = \sum_{d=1}^{D}(\mathbf{x} \cdot \mathbf{b}_d)\mathbf{b}_d. \tag{10.4}$$

This decomposition is central to dimensionality reduction. It shows that we can represent any D-dimensional vector using D coefficients, each corresponding to the projection onto one basis vector. In PCA, we seek a special set of orthonormal vectors where most of the variance in our data is captured by projections onto just the first few vectors.

For mathematical convenience, we can express this decomposition in matrix form.

Let $\mathbf{B}_M$ contain the first M basis vectors as columns:

$$\mathbf{B}_M = \begin{bmatrix} \mathbf{b}_1 & \mathbf{b}_2 & \cdots & \mathbf{b}_M \end{bmatrix} \tag{10.5}$$

and $\mathbf{B}_R$ contain the remaining vectors:

$$\mathbf{B}_R = \begin{bmatrix} \mathbf{b}_{M+1} & \mathbf{b}_{M+2} & \cdots & \mathbf{b}_{D.} \end{bmatrix} \tag{10.6}$$

Similarly, we define vectors containing the projection coefficients:

$$\mathbf{z}_M = \begin{bmatrix} \mathbf{x}^T\mathbf{b}_1 \\ \mathbf{x}^T\mathbf{b}_2 \\ \vdots \\ \mathbf{x}^T\mathbf{b}_M \end{bmatrix}, \quad \mathbf{z}_R = \begin{bmatrix} \mathbf{x}^T\mathbf{b}_{M+1} \\ \mathbf{x}^T\mathbf{b}_{M+2} \\ \vdots \\ \mathbf{x}^T\mathbf{b}_D \end{bmatrix}. \tag{10.7}$$

Since $\mathbf{x}$ is a random vector representing our data points, the projection coefficients $\mathbf{z}_M$ and $\mathbf{z}_R$ are also random vectors. Each component $z_i = \mathbf{x}^T\mathbf{b}_i$ represents how much our data varies along direction $\mathbf{b}_i$. Because we have centered our data so that $\mathbb{E}[\mathbf{x}] = \mathbf{0}$, the projections also have zero expectation:

$$\mathbb{E}[z_i] = \mathbb{E}[\mathbf{x}^T\mathbf{b}_i] = \mathbb{E}[\mathbf{x}]^T\mathbf{b}_i = \mathbf{0}^T\mathbf{b}_i = 0. \tag{10.8}$$

This zero-mean property allows us to interpret the variance of these projections directly as a measure of information content.

With this notation, our complete decomposition becomes:

$$\mathbf{x} = \mathbf{B}_M\mathbf{z}_M + \mathbf{B}_R\mathbf{z}_R. \tag{10.9}$$

In PCA, we retain only the first term, giving us our lower-dimensional approximation:

$$\widehat{\mathbf{x}} = \mathbf{B}_M\mathbf{z}_M. \tag{10.10}$$

This approximation introduces a reconstruction error—the difference between the

original data and its approximation:

$$\mathbf{x} - \widehat{\mathbf{x}} = \mathbf{B}_R \mathbf{z}_R. \qquad (10.11)$$
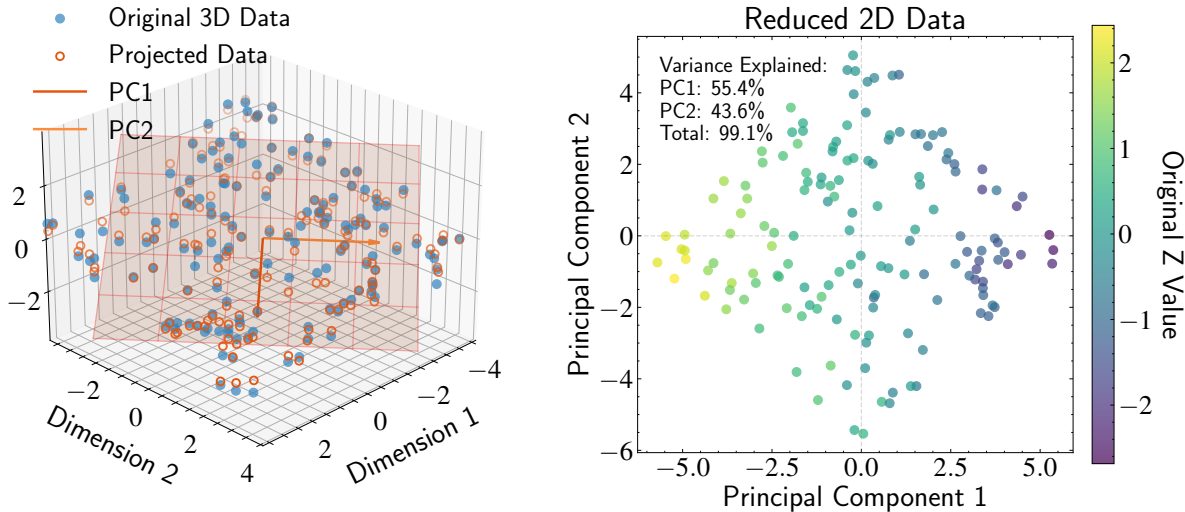
Figure 10.2: Visualization of Principal Component Analysis (PCA) for dimension reduction. **Left panel:** Original 3D data with the principal component plane. Blue points show the original data distributed around a 2D plane in 3D space. Orange arrows represent the first two principal components (PC1 and PC2), which define the optimal projection plane. Dashed lines connect original points to their projections (hollow orange circles) on the PC plane. **Right panel:** The reduced 2D representation of the data after projection onto the principal component plane. Points are colored by their original Z-value in 3D space, showing how the dimensionality reduction preserves the structure of the data. This illustrates how PCA identifies the lower-dimensional manifold that best preserves the information content of high-dimensional data.

Equivalence of the Two Perspectives   The relationship between variance maximization and reconstruction error minimization emerges from considering the total variance in our data. For our centered dataset, the total variance equals:

$$\text{Total Variance} = \mathbb{E}[\|\mathbf{x}\|^2] = \mathbb{E}[\mathbf{x}^T \mathbf{x}]. \qquad (10.12)$$

When we express our data in terms of the orthonormal basis $\{\mathbf{b}_1, \mathbf{b}_2, \ldots, \mathbf{b}_D\}$, the total variance can be written as:

$$\text{Total Variance} = \mathbb{E}\left[\sum_{m=1}^{D} z_m^2\right] = \sum_{m=1}^{M} \mathbb{E}[z_m^2] + \sum_{j=M+1}^{D} \mathbb{E}[z_j^2]. \qquad (10.13)$$

The first term represents the variance captured by our M principal components, while the second term equals the expected reconstruction error. Since the total variance is fixed for any dataset, maximizing the variance captured by our principal components is mathematically equivalent to minimizing the reconstruction error.

10.2   PCA: Mathematical Formalism

Having established that PCA seeks to maximize variance while minimizing reconstruction error, we now formulate this goal mathematically as an optimization problem. Our theoretical framework has shown us what we need to find—the basis vectors $\mathbf{b}_1, \ldots, \mathbf{b}_M$ that capture maximum variance while maintaining orthonormality—but we need a systematic approach to determine these vectors.

Let's begin with the simplest case: finding the first principal component. This single direction should capture more variance than any other possible direction in our data. Once we solve this fundamental case, we can extend our approach to find subsequent components.

Formulating the First Principal Component   Consider the projection of our data onto a unit vector $\mathbf{b}_1$. For any data point $\mathbf{x}_n$, the projection coefficient is $z_{1n} = \mathbf{x}_n^T \mathbf{b}_1 = \mathbf{b}_1^T \mathbf{x}_n$. Our objective is to find the direction $\mathbf{b}_1$ that maximizes the variance of these projection coefficients:

$$\mathrm{Var}[z_1] = \frac{1}{N} \sum_{n=1}^{N} z_{1n}^2. \tag{10.14}$$

To connect this variance to our covariance matrix, we employ the multivariate extension of variance concepts we developed in Chapter 3. Recall that for centered data where $\mathbb{E}[\mathbf{x}] = \mathbf{0}$, the covariance matrix becomes the second moment:

$$\mathbf{S} = \mathrm{Cov}(\mathbf{x}) = \mathbb{E}[\mathbf{x}\mathbf{x}^T] = \frac{1}{N} \sum_{n=1}^{N} \mathbf{x}_n \mathbf{x}_n^T = \frac{1}{N} \mathbf{X}^T \mathbf{X}. \tag{10.15}$$

For the projection $z_1 = \mathbf{b}_1^T \mathbf{x}$, we apply the linear transformation property of variance from Chapter 3. When we transform a random vector $\mathbf{x}$ using a matrix $\mathbf{A}$ to obtain $\mathbf{y} = \mathbf{A}\mathbf{x}$, the covariance of the result is:

$$\mathrm{Cov}(\mathbf{y}) = \mathbf{A} \cdot \mathrm{Cov}(\mathbf{x}) \cdot \mathbf{A}^T. \tag{10.16}$$

In our case, $z_1 = \mathbf{b}_1^T \mathbf{x}$ represents such a transformation with $\mathbf{A} = \mathbf{b}_1^T$. Since z_1 is a scalar, its variance becomes:

$$\mathrm{Var}[z_1] = \mathbf{b}_1^T \cdot \mathrm{Cov}(\mathbf{x}) \cdot \mathbf{b}_1 = \mathbf{b}_1^T \mathbf{S} \mathbf{b}_1. \tag{10.17}$$

This expression connects the variance of our projected data directly to the covariance matrix $\mathbf{S}$. Finding the direction of maximum variance reduces to finding the vector $\mathbf{b}_1$ that maximizes the quadratic form $\mathbf{b}_1^T \mathbf{S} \mathbf{b}_1$.

The Need for Constraints Without constraints, this optimization problem becomes ill-defined. To understand why, consider what happens if we take any vector $\mathbf{b}_1$ and multiply it by a constant $c > 1$. The resulting vector $c\mathbf{b}_1$ would yield a variance of:

$$\mathrm{Var}[z_1'] = (c\mathbf{b}_1)^T \mathbf{S}(c\mathbf{b}_1) = c^2 \mathbf{b}_1^T \mathbf{S} \mathbf{b}_1 = c^2 \mathrm{Var}[z_1]. \tag{10.18}$$

We could make the variance arbitrarily large simply by increasing the magnitude of $\mathbf{b}_1$, without changing its direction. Since only the direction matters for identifying the axis of maximum variation, we need to constrain our search to make the problem well-defined.

The natural constraint requires $\mathbf{b}_1$ to be a unit vector:

$$\|\mathbf{b}_1\|^2 = \mathbf{b}_1^T \mathbf{b}_1 = 1. \tag{10.19}$$

This normalization puts all possible directions on equal footing for comparison. Our optimization problem becomes:

$$\max_{\mathbf{b}_1} \mathbf{b}_1^T \mathbf{S} \mathbf{b}_1 \quad \text{subject to} \quad \mathbf{b}_1^T \mathbf{b}_1 = 1. \tag{10.20}$$

We have arrived at a constrained optimization problem—finding the direction that maximizes variance while having unit length. This type of problem appears frequently across physics, engineering, and economics, and is typically solved using the method of Lagrange multipliers.

10.3   Lagrange Multipliers

Now that we've formulated PCA as a constrained optimization problem, we need a mathematical tool to solve it. The method of Lagrange multipliers provides a systematic approach for finding extrema of a function subject to constraints. This technique transforms what appears to be a difficult constrained problem into a more tractable unconstrained problem.

The Challenge of Constrained Optimization   In unconstrained optimization problems, we find extrema by identifying where the gradient equals zero: $\nabla f(x) = 0$. This approach works because at critical points, the function stops changing in all directions. We applied this technique throughout our course when solving various maximum likelihood estimation problems.

However, in constrained optimization, we are restricted to points that satisfy one or more constraints, typically expressed as $g(x) = 0$. Most practical constraints can be written in this form—for example, a constraint like $h(x) = c$ becomes $g(x) = h(x) - c = 0$. While inequality constraints also exist in optimization problems, they don't concern us for PCA.

Instead of freely exploring the entire domain, we must stay on the "constraint surface" defined by $g(x) = 0$. This changes the nature of the problem fundamentally. In our PCA case, we have the constraint $g(\mathbf{b}_1) = \mathbf{b}_1^T \mathbf{b}_1 - 1 = 0$, which restricts our optimization to unit vectors. This constraint surface is the unit sphere in our parameter space, removing one degree of freedom from our optimization.

Geometric Intuition   To develop intuition for the Lagrange multiplier method, consider a function $f(x, y)$ that we want to maximize, subject to a constraint $g(x, y) = 0$. We can visualize f as a landscape with hills and valleys, while the constraint $g(x, y) = 0$ represents a path on this landscape.

This is a one-dimensional path because the equation $g(x, y) = 0$ removes one degree of freedom from our two-dimensional space. For example, if $g(x, y) = x + y - 1 = 0$, we get a straight line—a one-dimensional object embedded in our two-dimensional space. Our goal is to find where along this constraint path the function f reaches its extremum value.

At a constrained extremum, if we were to move along the constraint path, the function value should not increase or decrease to first order—otherwise, we have not found an extremum. This means that the gradient of f must be perpendicular to the constraint path

at that point.

To understand why, recall that the gradient ∇f points in the direction of steepest ascent of the function. If this gradient had any component tangent to our constraint path, we could move in that direction to increase f while still satisfying the constraint. Since we are at an extremum, no such movement is possible, so ∇f must be perpendicular to the constraint path.

But what direction is perpendicular to the constraint path? Since g is constant (equal to zero) along our constraint path, its gradient must be perpendicular to the path. The gradient ∇g at any point gives the direction of steepest ascent of the function g. If we were to move infinitesimally in the direction of ∇g, we would see the maximum possible increase in the value of g. Conversely, if we move perpendicular to ∇g, the value of g doesn't change to first order.

Therefore, any movement along the constraint path must be perpendicular to the direction that would change g most rapidly (which is ∇g). This is why the gradient ∇g is always perpendicular to the level curves of g, including our constraint path where $g = 0$.

Putting these observations together, we arrive at the key insight of Lagrange multipliers: at a constrained extremum, the gradients of f and g must be parallel to each other. Mathematically:

$$\nabla f(x) = \lambda \nabla g(x), \tag{10.21}$$

where λ is the Lagrange multiplier—a scalar that gives the proportionality between the two gradients.

The Lagrangian Formulation   The Lagrangian approach transforms our constrained optimization problem into an unconstrained one in a higher-dimensional space that includes the Lagrange multipliers. When we have a constraint $g(x) = 0$, we're restricting our search space, effectively reducing the dimensionality of our problem. The Lagrangian formulation introduces an additional parameter λ that acts as a mathematical force keeping our solution on the constraint surface.

To implement this approach, we introduce the Lagrangian function:

$$\mathcal{L}(x, \lambda) = f(x) - \lambda g(x). \tag{10.22}$$
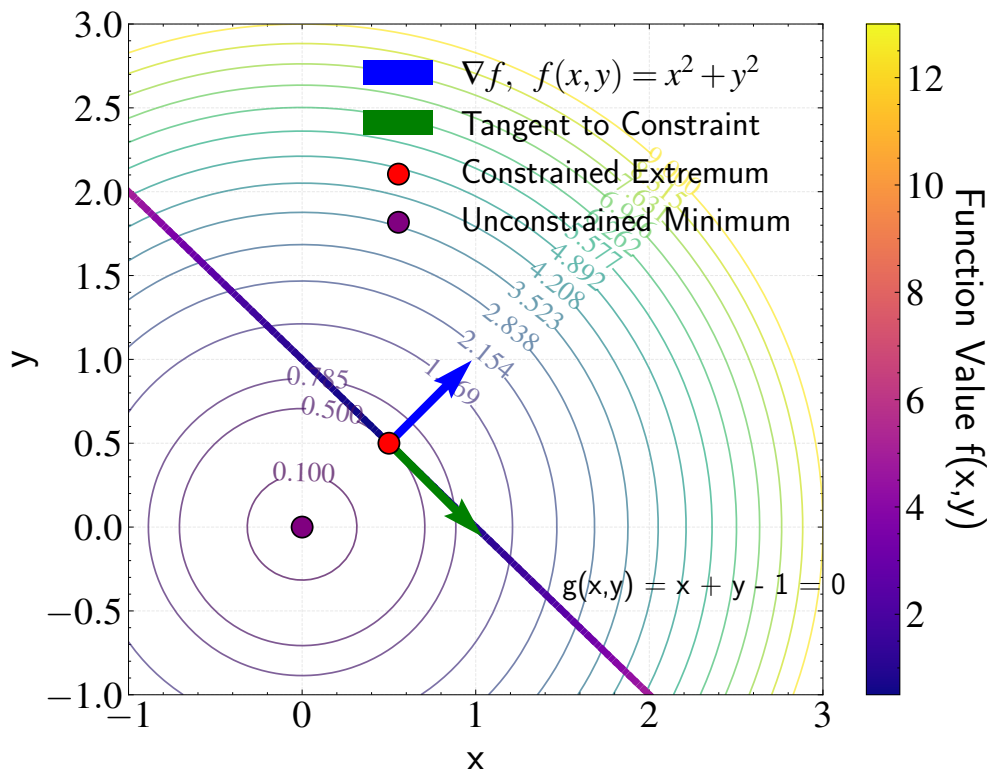
Figure 10.3: Geometric intuition of Lagrange multipliers. The contour lines represent the function $f(x,y) = x^2 + y^2$, with the constraint $g(x,y) = x + y - 1 = 0$ shown as the colored line. Colors along the constraint indicate function values, with warmer colors representing higher values. At the constrained extremum (red dot), the gradient ∇f (blue arrow) is perpendicular to the tangent of the constraint (green arrow). This illustrates a key insight of Lagrange multipliers: at a constrained extremum, moving along the constraint path doesn't change the function value to first order. The figure also shows the unconstrained minimum (purple dot) at the origin, which is inaccessible due to the constraint.

This transformation is powerful because instead of directly solving the difficult constrained problem, we solve an unconstrained problem in a slightly larger space. The critical points of this Lagrangian function correspond precisely to the solutions of our original constrained problem, plus the constraint itself.

To find these critical points, we take partial derivatives with respect to all variables and set them equal to zero. Taking the gradient with respect to x:

$$\nabla_x \mathcal{L} = \nabla f(x) - \lambda \nabla g(x) = 0. \tag{10.23}$$

Rearranging, we get our earlier condition:

$$\nabla f(x) = \lambda \nabla g(x). \tag{10.24}$$

This confirms our geometric intuition that at a constrained extremum, the gradient of the objective function must be parallel to the gradient of the constraint function.
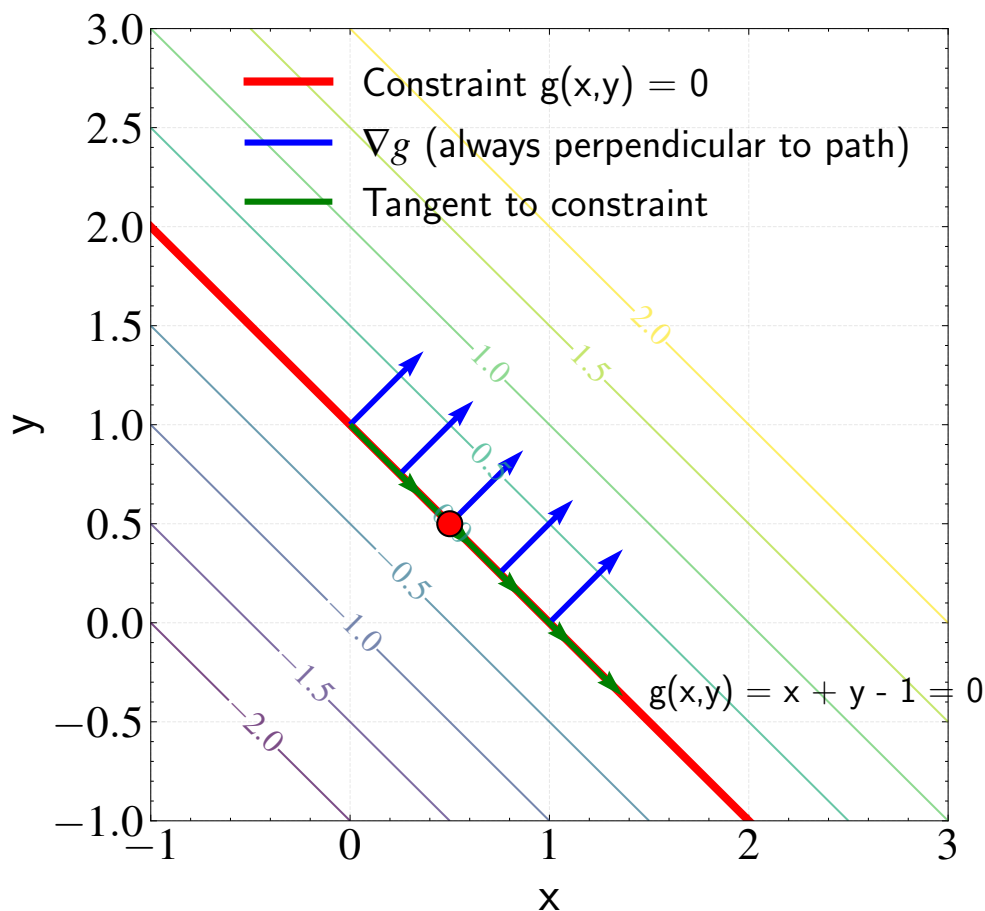
Figure 10.4: Perpendicularity of the constraint gradient. This figure illustrates why the gradient of the constraint function ∇g (blue arrows) is always perpendicular to the constraint path $g(x, y) = 0$ (red line). The contour lines represent different values of the constraint function $g(x, y) = x + y - 1$, with the zero-valued contour highlighted in red. Green arrows show tangent vectors to the constraint path at various points. Because the gradient of any function points in the direction of maximum increase, and the constraint function must remain constant (equal to zero) along the constraint path, the gradient ∇g must be perpendicular to any movement along the constraint. This property explains why, at a constrained extremum, the condition $\nabla f = \lambda \nabla g$ ensures that ∇f is perpendicular to the constraint path, which is necessary for a constrained extremum.

Taking the derivative with respect to λ and setting it to zero:

$$\frac{\partial \mathcal{L}}{\partial \lambda} = -g(x) = 0 \Rightarrow g(x) = 0. \tag{10.25}$$

This simply enforces our original constraint, ensuring that any solution we find satisfies the constraint equation.

By solving the system of equations formed by these conditions, we can identify all critical points that might be constrained extrema of our original problem.

A Simple Example Let's illustrate the Lagrange multiplier method with the example shown in Figure to solidify our understanding. Consider finding the minimum value of $f(x, y) = x^2 + y^2$ subject to the constraint $g(x, y) = x + y - 1 = 0$.

The Lagrangian is:

$$\mathcal{L}(x, y, \lambda) = x^2 + y^2 - \lambda(x + y - 1). \tag{10.26}$$

Taking partial derivatives and setting them to zero:

$$\frac{\partial \mathcal{L}}{\partial x} = 2x - \lambda = 0 \Rightarrow x = \frac{\lambda}{2}, \tag{10.27}$$

$$\frac{\partial \mathcal{L}}{\partial y} = 2y - \lambda = 0 \Rightarrow y = \frac{\lambda}{2}, \tag{10.28}$$

$$\frac{\partial \mathcal{L}}{\partial \lambda} = -(x + y - 1) = 0 \Rightarrow x + y = 1. \tag{10.29}$$

From the first two equations, we see that $x = y$. Substituting into the constraint:

$$x + x = 1 \Rightarrow x = y = \frac{1}{2}. \tag{10.30}$$

The minimum value is $f(1/2, 1/2) = (1/2)^2 + (1/2)^2 = 1/2$.

Note that the Lagrange multiplier method provides necessary conditions for finding constrained extrema—all constrained extrema must satisfy these conditions, but not all points satisfying these conditions are necessarily extrema. In this simple example, we found only one critical point $(1/2, 1/2)$ that satisfies our conditions. Since we know there must be a minimum value of our objective function along the constraint path (which is a bounded line

segment), and we've found only one candidate point, this point must indeed be the minimum we're seeking. In more complex problems with multiple critical points, additional analysis would be required to determine which critical point gives the actual extremum value.

Multiple Constraints   The method extends naturally to multiple constraints. If we have constraints $g_1(x) = 0, g_2(x) = 0, \ldots, g_m(x) = 0$, the condition becomes:

$$\nabla f(x) = \lambda_1 \nabla g_1(x) + \lambda_2 \nabla g_2(x) + \ldots + \lambda_m \nabla g_m(x). \tag{10.31}$$

With multiple constraints, we're restricted to the intersection of all constraint surfaces, which forms a lower-dimensional manifold. At a constrained extremum, the gradient $\nabla f(x)$ must be perpendicular to this manifold. Since any direction tangent to this manifold must be simultaneously tangent to all constraint surfaces, it must be perpendicular to all constraint gradients $\nabla g_i(x)$. Therefore, $\nabla f(x)$ must lie in the span of these constraint gradients.

Mathematically, this means $\nabla f(x)$ can be expressed as a linear combination of the constraint gradients, with the Lagrange multipliers λ_i serving as the coefficients. If this were not true, $\nabla f(x)$ would have a component tangent to the constraint manifold, allowing us to move along the manifold to increase or decrease the function value while still satisfying all constraints.

The Lagrangian formulation captures this relationship:

$$\mathcal{L}(x, \lambda_1, \ldots, \lambda_m) = f(x) - \lambda_1 g_1(x) - \ldots - \lambda_m g_m(x). \tag{10.32}$$

Taking partial derivatives with respect to each variable and setting them to zero yields precisely our constraint equations and the gradient relationship above.

10.4   Solving PCA with Lagrange Multipliers

Having established our constrained optimization problem and introduced the technique of Lagrange multipliers, we can now directly apply this method to find the first principal component. Recall that our objective is to maximize the variance of projected data:

$$\max_{\mathbf{b}_1} \mathbf{b}_1^T \mathbf{S} \mathbf{b}_1 \quad \text{subject to} \quad \mathbf{b}_1^T \mathbf{b}_1 = 1 \tag{10.33}$$

This application will reveal a connection between PCA and linear algebra that makes the method both theoretically elegant and computationally tractable.

Formulating the Lagrangian   To solve this using Lagrange multipliers, we form the Lagrangian function:

$$\mathcal{L}(\mathbf{b}_1, \lambda_1) = \mathbf{b}_1^T \mathbf{S} \mathbf{b}_1 - \lambda_1 (\mathbf{b}_1^T \mathbf{b}_1 - 1). \tag{10.34}$$

Now, we optimize this function by taking partial derivatives with respect to both $\mathbf{b}_1$ and λ_1 and setting them equal to zero.

First, differentiating with respect to λ_1:

$$\frac{\partial \mathcal{L}}{\partial \lambda_1} = -(\mathbf{b}_1^T \mathbf{b}_1 - 1) = 0 \tag{10.35}$$

This simply gives us back our original constraint that $\mathbf{b}_1$ is a unit vector:

$$\mathbf{b}_1^T \mathbf{b}_1 = 1 \tag{10.36}$$

Next, differentiating with respect to $\mathbf{b}_1$. When differentiating vector expressions, we need to be careful with the matrix calculus. For the quadratic form $\mathbf{b}_1^T \mathbf{S} \mathbf{b}_1$ where $\mathbf{S}$ is symmetric, the gradient with respect to $\mathbf{b}_1$ is $2\mathbf{S}\mathbf{b}_1$. Similarly, the gradient of $\mathbf{b}_1^T \mathbf{b}_1$ with respect to $\mathbf{b}_1$ is $2\mathbf{b}_1$. Therefore:

$$\frac{\partial \mathcal{L}}{\partial \mathbf{b}_1} = 2\mathbf{S}\mathbf{b}_1 - 2\lambda_1 \mathbf{b}_1 = 0 \tag{10.37}$$

Rearranging this equation by dividing by 2:

$$\mathbf{S}\mathbf{b}_1 = \lambda_1 \mathbf{b}_1 \tag{10.38}$$

The Eigenvalue Equation   This last equation reveals something remarkable: the critical point $\mathbf{b}_1$ must satisfy a special criterion. When we apply the covariance matrix $\mathbf{S}$ to $\mathbf{b}_1$, the result is proportional to $\mathbf{b}_1$ itself, with λ_1 as the proportionality constant.

In linear algebra, a vector that satisfies this property is called an "eigenvector" of the matrix, and the proportionality constant λ_1 is called the corresponding "eigenvalue." When a matrix transforms an eigenvector, the result points in the same direction as the original

vector—it just gets scaled by the eigenvalue.

The eigenvalue equation $\mathbf{S}\mathbf{b}_1 = \lambda_1\mathbf{b}_1$ is central to understanding PCA. It tells us that the principal components we seek are intimately related to the eigenstructure of our covariance matrix.

Since the covariance matrix $\mathbf{S}$ is a real symmetric matrix, it has several crucial properties that make PCA particularly tractable:

1. All eigenvalues are real numbers

2. Eigenvectors corresponding to distinct eigenvalues are orthogonal to each other

3. The matrix can be diagonalized by an orthogonal matrix composed of its eigenvectors

These properties guarantee that we can find a complete set of orthonormal eigenvectors that span the entire space. This means we can decompose our covariance matrix as $\mathbf{S} = \mathbf{B}\mathbf{\Lambda}\mathbf{B}^T$, where $\mathbf{B}$ is a $D \times D$ orthogonal matrix whose columns are the eigenvectors of $\mathbf{S}$, and $\mathbf{\Lambda}$ is a diagonal matrix containing the eigenvalues. This spectral decomposition is central to PCA and ensures that our principal components will form an orthogonal basis.

Connecting Eigenvalues to Variance   The eigenvectors of a covariance matrix have an important geometric interpretation. When we apply the covariance matrix to vectors on a unit circle, most vectors change both their direction and length. However, eigenvectors maintain their original direction—they're simply scaled by their eigenvalues.

This is precisely what the equation $\mathbf{S}\mathbf{b}_1 = \lambda_1\mathbf{b}_1$ tells us: applying $\mathbf{S}$ to $\mathbf{b}_1$ results in the same vector, just scaled by λ_1. This property makes eigenvectors ideal candidates for our principal components. But the covariance matrix typically has multiple eigenvectors—one for each dimension of our data. Which one should we choose to maximize variance?

To answer this question, let's substitute what we now know about $\mathbf{b}_1$ back into our original variance expression. If $\mathbf{b}_1$ is an eigenvector of $\mathbf{S}$ with eigenvalue λ_1, then:

$$\mathrm{Var}[z_1] = \mathbf{b}_1^T\mathbf{S}\mathbf{b}_1 \tag{10.39}$$

$$= \mathbf{b}_1^T(\lambda_1\mathbf{b}_1) \tag{10.40}$$

$$= \lambda_1\mathbf{b}_1^T\mathbf{b}_1 \tag{10.41}$$

$$= \lambda_1 \tag{10.42}$$
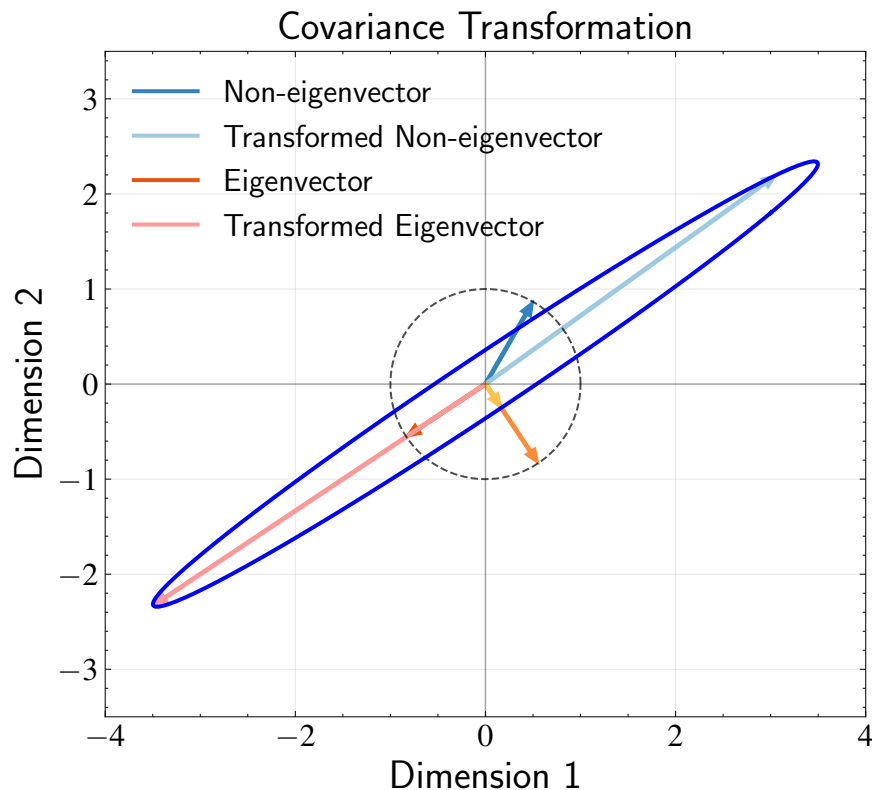
Figure 10.5: Geometric visualization of how eigenvectors maintain their direction under covariance transformation. The figure shows vectors on a unit circle (black dashed line) and their transformation by a covariance matrix, resulting in an ellipse (blue solid line). Eigenvectors (red and orange) preserve their directions exactly when transformed (shown in lighter shades), being scaled by their respective eigenvalues but not rotated. In contrast, non-eigenvectors (blue) change both direction and length when transformed (light blue). This property makes eigenvectors uniquely valuable for PCA: they represent invariant directions in the data space where the covariance transformation produces pure scaling without rotation, corresponding precisely to the principal axes of variation in the data.

In the last step, we used our constraint that $\mathbf{b}_1^T\mathbf{b}_1 = 1$, since $\mathbf{b}_1$ is a unit vector.

This result shows that the variance of our data when projected onto an eigenvector of the covariance matrix equals exactly the corresponding eigenvalue. This connection between statistical variance and algebraic eigenvalues provides a clear mathematical justification for our approach to PCA.

Since we want to maximize variance, we should choose the eigenvector corresponding to the largest eigenvalue. By choosing the eigenvector with the largest eigenvalue, we identify the direction along which our data exhibits the most variation. This eigenvector is what we call the first principal component.
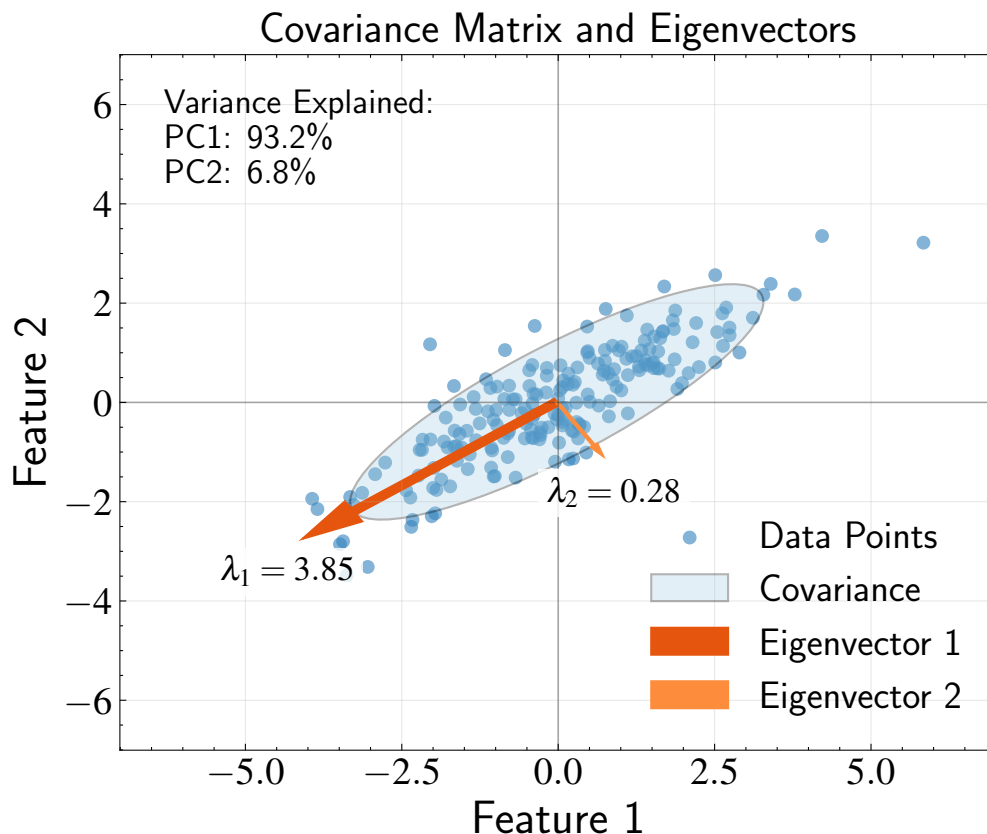
Figure 10.6: Visualization of how PCA identifies principal components using the covariance matrix. The blue points represent the original data, and the light blue ellipse shows the covariance structure (at 2σ). The red and orange arrows represent the eigenvectors of the covariance matrix, with their lengths scaled proportionally to their corresponding eigenvalues (λ_1 and λ_2). The first principal component (red arrow) points in the direction of maximum variance in the data, while the second principal component (orange arrow) is orthogonal to the first and captures the remaining variance. The percentages shown in the figure indicate the amount of total variance explained by each principal component. This illustrates how PCA decomposes the covariance structure of data to find an optimal lower-dimensional representation that preserves maximum variance while reducing dimensionality.

10.5 Higher-Order Principal Components

Now that we've successfully derived the first principal component, we turn our attention to finding additional components. Dimensionality reduction typically requires more than one component to effectively represent high-dimensional data. To build a more complete representation, we need to find additional principal components that capture the remaining variance.

For the second principal component, we seek another direction $\mathbf{b}_2$ that satisfies two

key criteria:

1. It captures the maximum variance in our data that hasn't already been explained by the first principal component

2. It is orthogonal to $\mathbf{b}_1$ (i.e., $\mathbf{b}_1^T \mathbf{b}_2 = 0$), ensuring that it provides new information

The orthogonality constraint represents an inductive bias of PCA. This assumption makes PCA mathematically tractable while ensuring each principal component captures a unique aspect of the data's variation.

Formulating the Second Principal Component   We can formulate this as another constrained optimization problem:

$$\max_{\mathbf{b}_2} \mathbf{b}_2^T \mathbf{S} \mathbf{b}_2 \quad \text{subject to} \quad \mathbf{b}_2^T \mathbf{b}_2 = 1 \quad \text{and} \quad \mathbf{b}_1^T \mathbf{b}_2 = 0 \tag{10.43}$$

To solve this problem, we again use Lagrange multipliers, but now with two constraints. We introduce two Lagrange multipliers: λ_2 for the unit vector constraint and μ for the orthogonality constraint:

$$\mathcal{L}(\mathbf{b}_2, \lambda_2, \mu) = \mathbf{b}_2^T \mathbf{S} \mathbf{b}_2 - \lambda_2(\mathbf{b}_2^T \mathbf{b}_2 - 1) - \mu(\mathbf{b}_1^T \mathbf{b}_2) \tag{10.44}$$

Taking the partial derivative with respect to $\mathbf{b}_2$ and setting it to zero:

$$\frac{\partial \mathcal{L}}{\partial \mathbf{b}_2} = 2\mathbf{S}\mathbf{b}_2 - 2\lambda_2 \mathbf{b}_2 - \mu \mathbf{b}_1 = 0 \tag{10.45}$$

To solve this equation, let's multiply both sides by $\mathbf{b}_1^T$ from the left:

$$\mathbf{b}_1^T(2\mathbf{S}\mathbf{b}_2 - 2\lambda_2 \mathbf{b}_2 - \mu \mathbf{b}_1) = 0 \tag{10.46}$$

Since $\mathbf{b}_1^T \mathbf{b}_2 = 0$ by our orthogonality constraint, and $\mathbf{b}_1^T \mathbf{b}_1 = 1$ since $\mathbf{b}_1$ is a unit vector, this simplifies to:

$$2\mathbf{b}_1^T \mathbf{S} \mathbf{b}_2 - \mu = 0 \tag{10.47}$$

Now, recall that $\mathbf{b}_1$ is an eigenvector of $\mathbf{S}$ with eigenvalue λ_1, so $\mathbf{S}\mathbf{b}_1 = \lambda_1 \mathbf{b}_1$. Taking the transpose of this equation, we get $\mathbf{b}_1^T \mathbf{S} = \lambda_1 \mathbf{b}_1^T$ (since $\mathbf{S}$ is symmetric). Substituting this

into our equation:

$$2\lambda_1 \mathbf{b}_1^T \mathbf{b}_2 - \mu = 0 \tag{10.48}$$

But $\mathbf{b}_1^T \mathbf{b}_2 = 0$ by our orthogonality constraint, so $\mu = 0$. Substituting this back into our derivative equation:

$$2\mathbf{S}\mathbf{b}_2 - 2\lambda_2 \mathbf{b}_2 = 0 \tag{10.49}$$

Simplifying:

$$\mathbf{S}\mathbf{b}_2 = \lambda_2 \mathbf{b}_2 \tag{10.50}$$

This is another eigenvector equation! The second principal component $\mathbf{b}_2$ is also an eigenvector of the covariance matrix $\mathbf{S}$. With the orthogonality constraint, it must be a different eigenvector than $\mathbf{b}_1$.

Following the same reasoning as before, the variance captured by projecting our data onto $\mathbf{b}_2$ is equal to the eigenvalue λ_2. To maximize this variance, we should choose $\mathbf{b}_2$ to be the eigenvector corresponding to the second largest eigenvalue of $\mathbf{S}$.

General Pattern The pattern we've observed extends naturally to all subsequent principal components. For the general case of finding the m-th principal component, we would need to solve:

$$\max_{\mathbf{b}_m} \mathbf{b}_m^T \mathbf{S} \mathbf{b}_m \quad \text{subject to} \quad \mathbf{b}_m^T \mathbf{b}_m = 1 \quad \text{and} \quad \mathbf{b}_i^T \mathbf{b}_m = 0 \quad \text{for all } i < m \tag{10.51}$$

One might imagine that if we were to solve this optimization problem directly for each value of m, we would find that the m-th principal component is the eigenvector of $\mathbf{S}$ corresponding to the m-th largest eigenvalue. This intuition is correct! However, attempting to verify this by explicit calculation for each m would be tedious and impractical.

Instead, we can establish this result rigorously using mathematical induction—a technique for proving statements that hold for all positive integers. This approach allows us to prove our claim once and for all, rather than verifying it separately for each principal component.

10.6   A Proof by Induction

To establish the general result rigorously without resorting to repetitive calculations, we can use mathematical induction—a technique for proving statements that hold for all positive integers. This approach allows us to prove our claim once and for all, rather than verifying it separately for each principal component.

Mathematical induction consists of three key steps:

1. **Base Case:** Prove that the statement is true for the first value (typically $m = 1$).

2. **Inductive Hypothesis:** Assume the statement is true for some arbitrary value $M-1$.

3. **Inductive Step:** Prove that if the statement is true for $M - 1$, then it must also be true for M.

If we can complete these three steps, then by the principle of induction, the statement is true for all positive integers. Intuitively, this is like setting up a row of dominoes: if you ensure the first one falls (base case), and that each falling domino knocks over the next one (inductive step), then all dominoes will eventually fall.

In our PCA context, we've already established that the first principal component corresponds to the eigenvector with the largest eigenvalue of the covariance matrix $\mathbf{S}$. The induction proof will show that if the first $(M - 1)$ principal components correspond to the eigenvectors with the $(M - 1)$ largest eigenvalues of $\mathbf{S}$, then the M-th principal component must correspond to the eigenvector with the M-th largest eigenvalue. Without loss of generality, we assume the eigenvalues of $\mathbf{S}$ are arranged in descending order, $\lambda_1 \geq \lambda_2 \geq \ldots \geq \lambda_D$.

Base Case   We've already proven that the first principal component $\mathbf{b}_1$ is the eigenvector of $\mathbf{S}$ corresponding to the largest eigenvalue λ_1.

Inductive Hypothesis   Assume that for all $m < M$, the m-th principal component $\mathbf{b}_m$ is the eigenvector of $\mathbf{S}$ corresponding to the m-th largest eigenvalue λ_m.

Inductive Step   We need to prove that the M-th principal component $\mathbf{b}_M$ is the eigenvector of $\mathbf{S}$ corresponding to the M-th largest eigenvalue λ_M.

First, let's clarify what we mean by the M-th principal component. Finding the M-th principal component is equivalent to finding the direction of maximum variance in the

residual data that remains after removing the projections onto the first $(M-1)$ principal components.

Let's denote our original data matrix as $\mathbf{X}$, where each row represents a data point and each column represents a feature. The matrix has dimensions $N \times D$, where N is the number of data points and D is the number of features. To find the projection of this data onto the first $M-1$ principal components, we recall that for any unit vector $\mathbf{b}_i$, the projection of a vector $\mathbf{x}$ onto $\mathbf{b}_i$ is given by $(\mathbf{x}^T\mathbf{b}_i)\mathbf{b}_i$. When we apply this projection to each row of $\mathbf{X}$, we get $\mathbf{X}\mathbf{b}_i\mathbf{b}_i^T$, which represents the projection of all data points onto the i-th principal component.

The total projection onto the subspace spanned by the first $M-1$ principal components is:

$$\sum_{m=1}^{M-1} \mathbf{X}\mathbf{b}_m\mathbf{b}_m^T \tag{10.52}$$

The residual data—the part not explained by these components—is:

$$\widehat{\mathbf{X}} = \mathbf{X} - \sum_{m=1}^{M-1} \mathbf{X}\mathbf{b}_m\mathbf{b}_m^T \tag{10.53}$$

This can be written more compactly using matrix notation. Let $\mathbf{B}_{M-1} = [\mathbf{b}_1, \mathbf{b}_2, \ldots, \mathbf{b}_{M-1}]$ be the matrix whose columns are the first $M-1$ principal components. Then:

$$\widehat{\mathbf{X}} = \mathbf{X} - \mathbf{X}\mathbf{B}_{M-1}\mathbf{B}_{M-1}^T \tag{10.54}$$

This expression has an important interpretation: $\mathbf{B}_{M-1}\mathbf{B}_{M-1}^T$ is a projection matrix that projects onto the subspace spanned by the first $M-1$ principal components. When we multiply $\mathbf{X}$ by this projection and subtract from $\mathbf{X}$, we get the component of $\mathbf{X}$ that is orthogonal to this subspace—precisely the residual that we're interested in.

To find the direction of maximum variance in this residual data, we need to compute its covariance matrix:

$$\widehat{\mathbf{S}} = \frac{1}{N}\widehat{\mathbf{X}}^T\widehat{\mathbf{X}} \tag{10.55}$$

Residual Data after Extracting First Principal Component
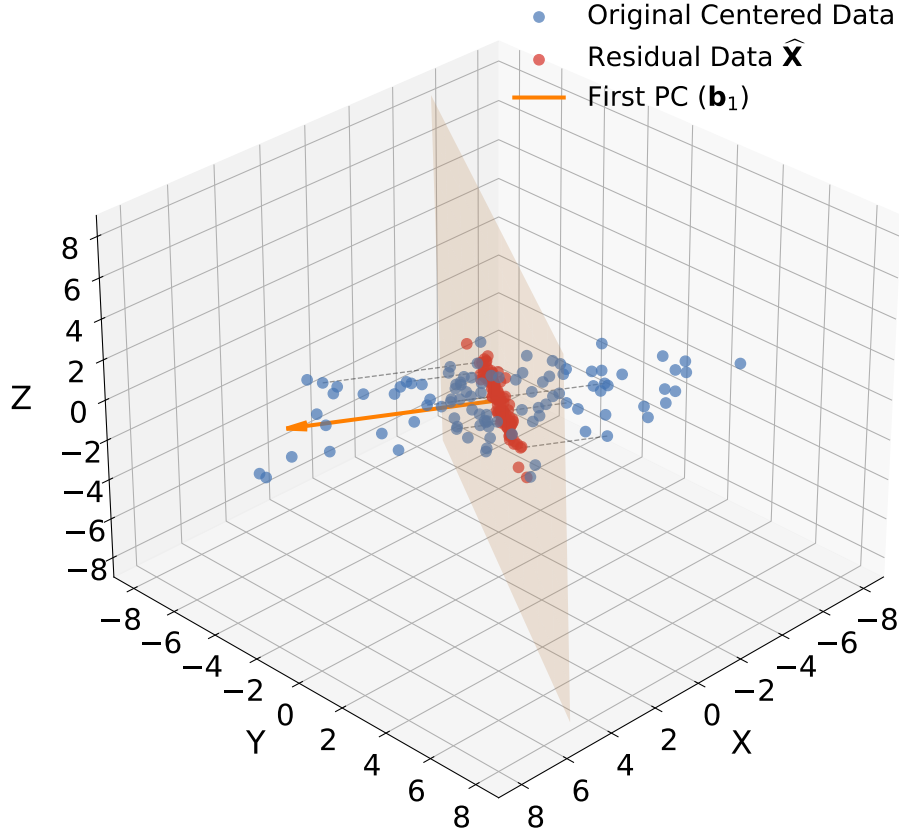
Figure 10.7: Visualization of residual data after extracting the first principal component. Blue points represent the original centered data, while red points show the residual data $\widehat{\mathbf{X}}$ after projecting out the component along the first principal component $\mathbf{b}_1$ (orange arrow). Dashed lines indicate the projection process. The semi-transparent orange plane represents the hyperplane orthogonal to $\mathbf{b}_1$, where all residual data points lie. This illustrates a key concept from the induction proof: after removing the first principal component, the residual data has zero variance in the $\mathbf{b}_1$ direction. The residual covariance matrix $\widehat{\mathbf{S}}$ has the first eigenvector $\mathbf{b}_1$ with eigenvalue zero, while subsequent eigenvectors maintain their original eigenvalues. This demonstrates why the largest eigenvalue of $\widehat{\mathbf{S}}$ corresponds to the second largest eigenvalue of the original covariance matrix, proving that successive principal components are eigenvectors with decreasing eigenvalues.

Substituting our expression for $\widehat{\mathbf{X}}$ and expanding:

$$\widehat{\mathbf{S}} = \frac{1}{N}(\mathbf{X} - \mathbf{X}\mathbf{B}_{M-1}\mathbf{B}_{M-1}^T)^T(\mathbf{X} - \mathbf{X}\mathbf{B}_{M-1}\mathbf{B}_{M-1}^T) \tag{10.56}$$

$$= \frac{1}{N}(\mathbf{X}^T - \mathbf{B}_{M-1}\mathbf{B}_{M-1}^T\mathbf{X}^T)(\mathbf{X} - \mathbf{X}\mathbf{B}_{M-1}\mathbf{B}_{M-1}^T) \tag{10.57}$$

$$= \frac{1}{N}(\mathbf{X}^T\mathbf{X} - \mathbf{X}^T\mathbf{X}\mathbf{B}_{M-1}\mathbf{B}_{M-1}^T - \mathbf{B}_{M-1}\mathbf{B}_{M-1}^T\mathbf{X}^T\mathbf{X} + \mathbf{B}_{M-1}\mathbf{B}_{M-1}^T\mathbf{X}^T\mathbf{X}\mathbf{B}_{M-1}\mathbf{B}_{M-1}^T) \tag{10.58}$$

Recognizing that $\frac{1}{N}\mathbf{X}^T\mathbf{X} = \mathbf{S}$ (our original covariance matrix), we can rewrite this as:

$$\widehat{\mathbf{S}} = \mathbf{S} - \mathbf{S}\mathbf{B}_{M-1}\mathbf{B}_{M-1}^T - \mathbf{B}_{M-1}\mathbf{B}_{M-1}^T\mathbf{S} + \mathbf{B}_{M-1}\mathbf{B}_{M-1}^T\mathbf{S}\mathbf{B}_{M-1}\mathbf{B}_{M-1}^T \tag{10.59}$$

Since $\mathbf{S}$ is symmetric and $\mathbf{B}_{M-1}$ contains the first $M-1$ eigenvectors of $\mathbf{S}$, we can use the relationship $\mathbf{S}\mathbf{B}_{M-1} = \mathbf{B}_{M-1}\mathbf{\Lambda}_{M-1}$, where $\mathbf{\Lambda}_{M-1}$ is a diagonal matrix with the first $M-1$ eigenvalues. After algebraic manipulation using the symmetry of $\mathbf{S}$ and the orthonormality of the eigenvectors, this simplifies to:

$$\widehat{\mathbf{S}} = \mathbf{S} - \sum_{m=1}^{M-1} \lambda_m \mathbf{b}_m \mathbf{b}_m^T \tag{10.60}$$

This calculation demonstrates that the covariance matrix of the residual data $\widehat{\mathbf{S}}$ equals the original covariance matrix $\mathbf{S}$ minus the variance explained by the first $M - 1$ principal components.

To understand the implications of this relationship, let's examine how $\widehat{\mathbf{S}}$ acts on the eigenvectors of the original covariance matrix $\mathbf{S}$. For any of the first $M-1$ eigenvectors (i.e., $\mathbf{b}_k$ for $k < M$):

$$\widehat{\mathbf{S}}\mathbf{b}_k = \mathbf{S}\mathbf{b}_k - \sum_{m=1}^{M-1} \lambda_m \mathbf{b}_m \mathbf{b}_m^T \mathbf{b}_k \tag{10.61}$$

$$= \lambda_k \mathbf{b}_k - \lambda_k \mathbf{b}_k = 0 \tag{10.62}$$

where we used the orthonormality of eigenvectors.

For any other eigenvector of $\mathbf{S}$ (i.e., $\mathbf{b}_j$ for $j \geq M$):

$$\widehat{\mathbf{S}}\mathbf{b}_j = \mathbf{S}\mathbf{b}_j - \sum_{m=1}^{M-1} \lambda_m \mathbf{b}_m \mathbf{b}_m^T \mathbf{b}_j \tag{10.63}$$

$$= \lambda_j \mathbf{b}_j - 0 = \lambda_j \mathbf{b}_j \tag{10.64}$$

We've established two important properties of $\widehat{\mathbf{S}}$:

1. The eigenvectors $\mathbf{b}_1, \mathbf{b}_2, \ldots, \mathbf{b}_{M-1}$ have eigenvalue 0 in $\widehat{\mathbf{S}}$.

2. The eigenvectors $\mathbf{b}_M, \mathbf{b}_{M+1}, \ldots, \mathbf{b}_D$ have the same eigenvalues in $\widehat{\mathbf{S}}$ as they do in $\mathbf{S}$.

The spectrum of $\widehat{\mathbf{S}}$ consists of:

$$\{0, 0, \ldots, 0, \lambda_M, \lambda_{M+1}, \ldots, \lambda_D\} \tag{10.65}$$

where the first $M-1$ eigenvalues are zero, and the remaining eigenvalues retain their original values from $\mathbf{S}$.

Since the M-th principal component is defined as the direction that maximizes variance in the residual data, it must be the eigenvector corresponding to the largest eigenvalue of $\widehat{\mathbf{S}}$. We've just shown that this is $\mathbf{b}_M$, the eigenvector corresponding to the M-th largest eigenvalue of our original covariance matrix $\mathbf{S}$.

This completes our induction proof. We've shown that each principal component, in sequence, is the eigenvector of the original covariance matrix corresponding to the eigenvalue in decreasing order of magnitude.

10.7   Implementing PCA

Having established the theoretical foundation of PCA through our induction proof, we can now turn to its practical implementation. While the mathematical derivation may seem involved, the actual implementation of PCA is straightforward. The process can be distilled into just a few steps:

1. Begin with your centered data matrix $\mathbf{X}$ of size $N \times D$.

2. Calculate the covariance matrix $\mathbf{S} = \frac{1}{N}\mathbf{X}^T\mathbf{X}$.

3. Compute the eigendecomposition of $\mathbf{S}$ to obtain its eigenvectors and eigenvalues.

4. Sort the eigenvectors according to their corresponding eigenvalues in descending order.

5. Select the first M eigenvectors to form your basis matrix $\mathbf{B}_M = [\mathbf{b}_1, \mathbf{b}_2, \ldots, \mathbf{b}_M]$ for the lower-dimensional space.

6. Project your data onto this basis to obtain the lower-dimensional representation $\mathbf{Z} = \mathbf{X}\mathbf{B}_M$, where $\mathbf{Z}$ is an $N \times M$ matrix whose rows correspond to the original data points represented in the new coordinate system.

The matrix $\mathbf{Z}$ contains the coefficients of our data points in the new principal component coordinate system. These coefficients represent our data in the reduced-dimensional space. If needed, we can also reconstruct approximations of the original data using $\widehat{\mathbf{X}} = \mathbf{Z}\mathbf{B}_M^T = \mathbf{X}\mathbf{B}_M\mathbf{B}_M^T$, where $\widehat{\mathbf{X}}$ is the projection of $\mathbf{X}$ onto the M-dimensional subspace spanned by the principal components. This reconstruction allows us to compare our dimensionally-reduced representation with the original data in the D-dimensional observation space, helping us assess how much information is preserved or lost through the dimensionality reduction.

Selecting the Number of Components   While the basic PCA algorithm is straightforward, a crucial question arises: how many principal components should we retain? If we choose $M = D$ (the original dimensionality), we're not reducing dimensions at all. Conversely, if M is too small, we might lose important information from our data. This trade-off between dimensionality reduction and information preservation is at the heart of PCA's practical utility.

Our theoretical analysis provides a natural criterion for selecting M. From our induction proof, we established that each principal component corresponds to an eigenvector of the covariance matrix $\mathbf{S}$, with the variance captured along that component equal to its corresponding eigenvalue. This direct relationship gives us a quantitative way to measure the importance of each component.

Since the variance captured by the m-th principal component equals the m-th eigenvalue λ_m, we can express the total variance in our data as the sum of all eigenvalues:

$$\text{Total Variance} = \sum_{i=1}^{D} \lambda_i \tag{10.66}$$

Similarly, the variance captured by retaining the first M principal components is:

$$\text{Captured Variance} = \sum_{i=1}^{M} \lambda_i \tag{10.67}$$

The fraction of total variance explained by our M-component approximation becomes:

$$\text{Explained Variance Ratio} = \frac{\sum_{i=1}^{M} \lambda_i}{\sum_{i=1}^{D} \lambda_i} \tag{10.68}$$

This ratio provides a quantitative measure of how much information we're retaining
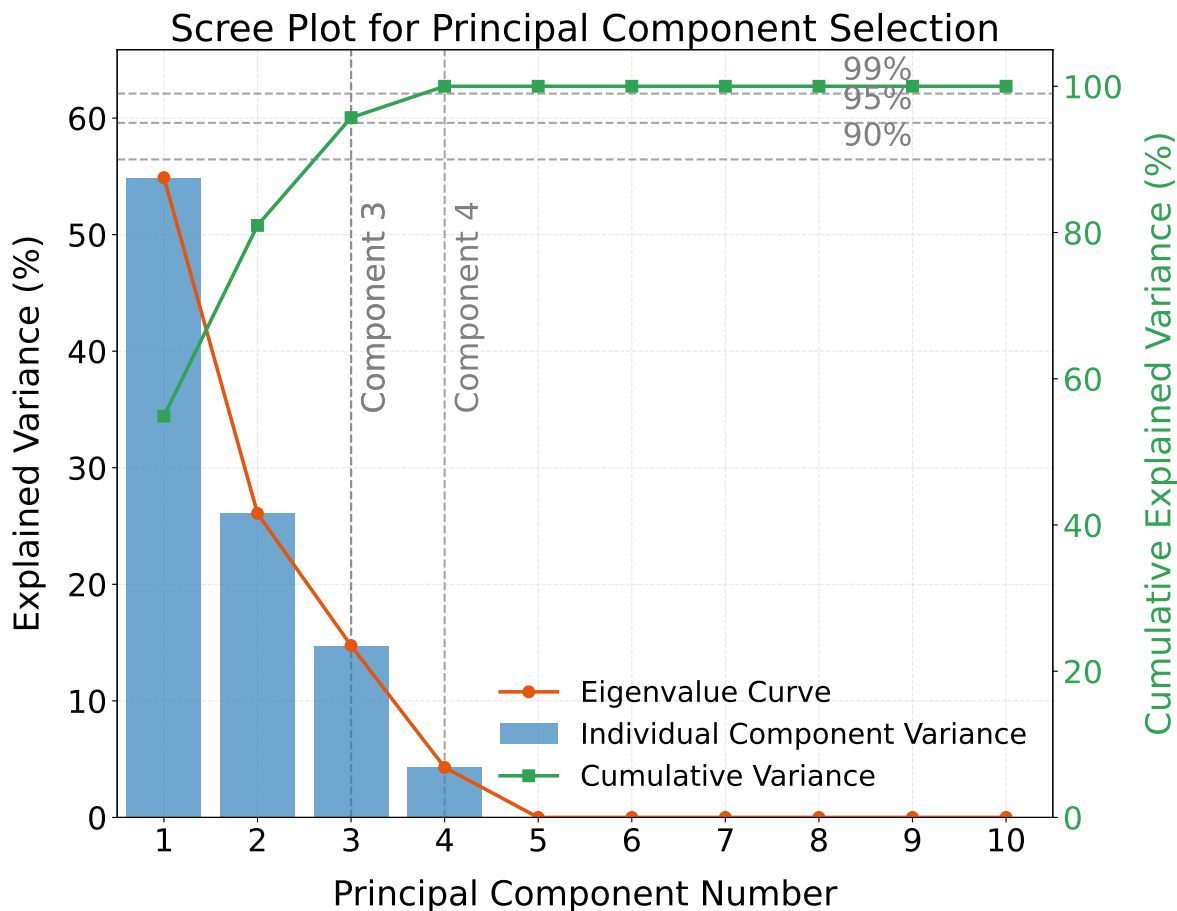
Figure 10.8: Scree plot for selecting the optimal number of principal components. The blue bars and orange line show the individual explained variance percentage for each principal component, demonstrating how the contribution of successive components diminishes. The green line displays the cumulative explained variance, reaching thresholds of 90%, 95%, and 99% (gray horizontal lines) at different component numbers. This visualization guides dimension selection by revealing the trade-off between dimensionality reduction and information preservation. The steep initial decline followed by flattening curve is characteristic of datasets with a few dominant modes of variation, typical in astronomical applications where high-dimensional data often arises from a smaller number of underlying physical processes.

after dimension reduction. When implementing PCA, a common approach is to choose M such that this ratio exceeds a desired threshold, typically 0.90, 0.95, or 0.99, depending on the application's requirements for information preservation.

To visualize this decision process, analysts often use a scree plot, which displays the eigenvalues (or explained variance ratios) against their indices. A typical scree plot shows a steep decline initially, followed by a gradual flattening. The "elbow" in this plot—where the slope changes markedly—can indicate a natural cutoff point for the number of components

to retain.

Physical Interpretation of Components   The output of PCA provides valuable insights beyond mere dimensionality reduction. The eigenvalues tell us how much variance each component captures, allowing us to assess the effectiveness of the reduction and understand the relative importance of different modes of variation in our data.

The eigenvectors (principal components) themselves often admit physical interpretation in terms of the original features. In astronomical applications, examining the principal components can reveal which combinations of measurements contribute most to the observed variation. For stellar spectra, the first principal component might represent the overall flux level or temperature variations, while subsequent components could capture metallicity effects or specific absorption line patterns.

This interpretation capability makes PCA particularly valuable for exploratory data analysis in astronomy. Rather than simply reducing dimensions, PCA can help identify the underlying physical processes that drive the observed variations in our data. When we find that just a few components explain most of the variance, we're discovering that the complex, high-dimensional astronomical phenomena are indeed governed by a smaller number of underlying parameters—exactly what our physical intuition suggests.

10.8   SVD for Efficient PCA

The basic PCA algorithm we've developed works well for datasets with a moderate number of features, but computational considerations become important when dealing with high-dimensional astronomical data. To perform PCA, we need to calculate the data covariance matrix and then diagonalize it. This matrix is $D \times D$, where D is the number of features.

As we've seen, diagonalizing a $D \times D$ matrix has computational complexity of $\mathcal{O}(D^3)$, which becomes prohibitively expensive as D increases. In astronomical applications where D can be extremely large—a single spectrum might have 10,000 wavelength bins, an image from a modern telescope could contain millions of pixels, and time series data might include measurements at thousands of time points—this approach quickly becomes impractical.

For example, diagonalizing a covariance matrix for data with 10,000 features would require on the order of 10^{12} operations, making the computation not just slow but potentially

impossible on standard computing hardware.

In this section, we explore how Singular Value Decomposition (SVD) provides a computationally efficient approach to implementing PCA, particularly for the high-dimensional datasets common in astronomy. SVD produces identical results to standard PCA while dramatically reducing computational complexity.

The SVD Decomposition   The Singular Value Decomposition theorem states that any matrix $\mathbf{X} \in \mathbb{R}^{N \times D}$ can be factorized into the product of three matrices:

$$\mathbf{X} = \mathbf{U}\mathbf{\Sigma}\mathbf{V}^T \tag{10.69}$$

The matrices in this decomposition have specific properties and interpretations:

- $\mathbf{U} \in \mathbb{R}^{N \times N}$ contains orthonormal columns called the left singular vectors. These vectors form an orthogonal basis for the column space of $\mathbf{X}$ and can be interpreted as the principal directions in the sample space. Each column of $\mathbf{U}$ represents a pattern across samples.

- $\mathbf{\Sigma} \in \mathbb{R}^{N \times D}$ is a rectangular "diagonal" matrix with non-negative entries $\sigma_1 \geq \sigma_2 \geq \ldots \geq \sigma_{\min(N,D)} \geq 0$ along its main diagonal, called singular values. These values represent the importance or strength of each corresponding pattern in the data. Larger singular values correspond to directions with greater variance in the data.

- $\mathbf{V} \in \mathbb{R}^{D \times D}$ contains orthonormal columns called the right singular vectors. These vectors form an orthogonal basis for the row space of $\mathbf{X}$ and represent the principal directions in the feature space. Each column of $\mathbf{V}$ describes a pattern of relationships among features.

Geometrically, we can interpret SVD as decomposing any linear transformation into three simpler operations:

1. A rotation or reflection in the input space (represented by $\mathbf{V}^T$)

2. A scaling along coordinate axes (represented by $\mathbf{\Sigma}$)

3. A rotation or reflection in the output space (represented by $\mathbf{U}$)

Computational Efficiency   The computational complexity of calculating the full SVD of a matrix $\mathbf{X} \in \mathbb{R}^{N \times D}$ is approximately $\mathcal{O}(\min(ND^2, N^2 D))$. This complexity depends on the rectangular shape of the matrix:

- When $N > D$ (tall matrix): The complexity is $\mathcal{O}(ND^2)$ operations

- When $N < D$ (wide matrix): The complexity is $\mathcal{O}(N^2 D)$ operations

Modern SVD implementations automatically optimize based on the matrix shape, taking the square of the smaller dimension and multiplying by the larger dimension: $\mathcal{O}((\min(N, D))^2 \cdot \max(N, D))$.

This represents a significant improvement over the $\mathcal{O}(D^3)$ complexity of traditional PCA when dealing with high-dimensional data. For a typical astronomical spectroscopy dataset with $N = 1,000$ spectra and $D = 10,000$ wavelength bins:

- Traditional PCA: $\mathcal{O}(D^3) = \mathcal{O}(10^{12})$ operations

- SVD-based PCA: $\mathcal{O}(N^2 D) = \mathcal{O}(10^{10})$ operations

The advantage becomes even more pronounced with fewer samples. For instance, with only $N = 100$ galaxy spectra and $D = 10,000$ wavelength bins:

- Traditional PCA: Still $\mathcal{O}(D^3) = \mathcal{O}(10^{12})$ operations

- SVD-based PCA: $\mathcal{O}(N^2 D) = \mathcal{O}(10^8)$ operations

This four-order-of-magnitude improvement transforms a calculation that might take days into one that completes in seconds.

Connection to PCA   Let's now see how SVD provides a direct approach to performing PCA. With our centered data matrix $\mathbf{X} \in \mathbb{R}^{N \times D}$, traditional PCA requires calculating the covariance matrix:

$$\mathbf{S} = \frac{1}{N} \mathbf{X}^T \mathbf{X} \tag{10.70}$$

By substituting the SVD decomposition $\mathbf{X} = \mathbf{U\Sigma V}^T$ into this expression, we get:

$$\mathbf{S} = \frac{1}{N}\mathbf{X}^T\mathbf{X} \tag{10.71}$$

$$= \frac{1}{N}(\mathbf{U\Sigma V}^T)^T(\mathbf{U\Sigma V}^T) \tag{10.72}$$

$$= \frac{1}{N}\mathbf{V\Sigma}^T\mathbf{U}^T\mathbf{U\Sigma V}^T \tag{10.73}$$

Since $\mathbf{U}$ has orthonormal columns, $\mathbf{U}^T\mathbf{U} = \mathbf{I}$, allowing us to simplify:

$$\mathbf{S} = \frac{1}{N}\mathbf{V\Sigma}^T\mathbf{\Sigma V}^T \tag{10.74}$$

Note that $\mathbf{\Sigma}^T\mathbf{\Sigma}$ is a diagonal matrix with entries σ_i^2 along the diagonal, where σ_i are the singular values from the diagonal of $\mathbf{\Sigma}$. This is because $\mathbf{\Sigma}$ is a rectangular diagonal matrix where only the diagonal entries are non-zero. Therefore:

$$\mathbf{S} = \mathbf{V}\left(\frac{1}{N}\mathbf{\Sigma}^T\mathbf{\Sigma}\right)\mathbf{V}^T \tag{10.75}$$

$$= \mathbf{V}\left(\frac{1}{N}\mathbf{\Sigma}^2\right)\mathbf{V}^T \tag{10.76}$$

$$= \mathbf{V}\left(\frac{1}{N}\mathrm{diag}(\sigma_1^2, \sigma_2^2, \ldots, \sigma_D^2)\right)\mathbf{V}^T \tag{10.77}$$

This is precisely the eigendecomposition of $\mathbf{S}$, revealing the connection between SVD and PCA:

- The columns of $\mathbf{V}$ are the eigenvectors of $\mathbf{S}$—these are our principal components

- The eigenvalues of $\mathbf{S}$ equal $\lambda_i = \sigma_i^2/N$, where σ_i are the singular values

Most SVD algorithms naturally return the singular values σ_i in descending order, so that $\sigma_1 \geq \sigma_2 \geq \ldots \geq \sigma_D \geq 0$. This ordering corresponds exactly to the ordering of principal components by explained variance, with the first component capturing the most variance, the second component capturing the second most, and so on.

Practical Implementation This relationship allows us to implement PCA using SVD without ever explicitly forming the covariance matrix. The procedure is straightforward:

1. Center the data matrix $\mathbf{X}$

2. Compute its SVD: $\mathbf{X} = \mathbf{U}\boldsymbol{\Sigma}\mathbf{V}^T$

3. Use the columns of $\mathbf{V}$ as our principal components

4. Project the data onto these components to obtain the lower-dimensional representation

For dimensionality reduction, we typically select only the first M principal components, where $M < D$. Let $\mathbf{V}_M$ consist of the first M columns of $\mathbf{V}$. The projection of our data onto this reduced space is:

$$\mathbf{Z} = \mathbf{X}\mathbf{V}_M \tag{10.78}$$

Interestingly, we can compute this projection more efficiently using the SVD components directly. Starting with our projection formula and substituting $\mathbf{X} = \mathbf{U}\boldsymbol{\Sigma}\mathbf{V}^T$:

$$\mathbf{Z} = \mathbf{X}\mathbf{V}_M = (\mathbf{U}\boldsymbol{\Sigma}\mathbf{V}^T)\mathbf{V}_M \tag{10.79}$$

Since $\mathbf{V}$ is orthogonal, $\mathbf{V}^T\mathbf{V} = \mathbf{I}$. When we multiply $\mathbf{V}^T$ by $\mathbf{V}_M$ (the first M columns of $\mathbf{V}$), we get a matrix where the first M diagonal elements are 1 and all other elements are 0. This effectively selects the first M columns of $\mathbf{U}\boldsymbol{\Sigma}$, giving us:

$$\mathbf{Z} = \mathbf{U}_M\boldsymbol{\Sigma}_M \tag{10.80}$$

where $\mathbf{U}_M$ consists of the first M columns of $\mathbf{U}$ and $\boldsymbol{\Sigma}_M$ is the diagonal matrix containing the first M singular values.

This calculation is particularly advantageous when the number of samples N is less than the number of features D (i.e., $N < D$), which is common in astronomical datasets. While both approaches give mathematically equivalent results, using $\mathbf{Z} = \mathbf{U}_M\boldsymbol{\Sigma}_M$ offers computational benefits:

1. When $N < D$, computing $\mathbf{X}\mathbf{V}_M$ requires multiplying an $N \times D$ matrix with a $D \times M$ matrix, resulting in $\mathcal{O}(NDM)$ operations.

2. In contrast, computing $\mathbf{U}_M\boldsymbol{\Sigma}_M$ only requires multiplying an $N \times M$ matrix with an $M \times M$ diagonal matrix, resulting in just $\mathcal{O}(NM)$ operations.

This computational advantage becomes even more important with astronomical data,

where D might represent thousands of wavelength bins in a spectrum or millions of pixels in an image.

Data Reconstruction   A key strength of PCA is that it allows us to reconstruct our original data from the reduced-dimensional representation. This reconstruction follows naturally from the PCA decomposition. If we denote our original data matrix as $\mathbf{X} \in \mathbb{R}^{N \times D}$, the mean-centered data as $\widetilde{\mathbf{X}} = \mathbf{X} - \boldsymbol{\mu}$ (where $\boldsymbol{\mu}$ is the mean vector), and the matrix of principal components as $\mathbf{V}_M \in \mathbb{R}^{D \times M}$ (where M is the number of components we retain), then:

1. The projection onto the principal component space is given by: $\mathbf{Z} = \mathbf{X}\mathbf{V}_M$ (or equivalently, $\mathbf{Z} = \mathbf{U}_M\boldsymbol{\Sigma}_M$)

2. The reconstruction back to the original space is: $\widehat{\mathbf{X}} = \mathbf{Z}\mathbf{V}_M^T + \boldsymbol{\mu} = (\mathbf{U}_M\boldsymbol{\Sigma}_M)\mathbf{V}_M^T + \boldsymbol{\mu}$

To determine the appropriate number of principal components to retain, we can use the singular values to calculate the proportion of variance explained by each component. For the i-th principal component, the proportion of total variance explained is:

$$\text{Explained Variance Ratio}_i = \frac{\sigma_i^2}{\sum_{j=1}^{D} \sigma_j^2} \tag{10.81}$$

This ratio provides the same information as the eigenvalue-based explained variance ratio discussed earlier, but calculates it directly from the singular values. By examining the cumulative explained variance as we add more components, we can determine how many components are needed to capture a desired percentage of the total variance in our data.

This SVD-based approach to PCA is not only computationally efficient but also numerically stable. By avoiding the explicit formation of the covariance matrix, we reduce both the computational complexity and the potential for numerical errors in the eigendecomposition. This makes SVD the method of choice for implementing PCA in practice, especially for the high-dimensional datasets commonly encountered in astronomical research.

10.9   Limitations of PCA

While PCA provides a powerful tool for dimension reduction, it has important limitations that affect its applicability to astronomical data. Understanding these constraints helps determine when PCA is appropriate and when alternative methods might be more suitable.

Orthogonality Constraint   The requirement for orthogonal basis vectors poses challenges for astronomical applications. In reality, physical processes in astronomical phenomena are rarely perfectly orthogonal to each other. For example, in stellar spectra, temperature and metallicity effects can be entangled in complex ways that don't align neatly with orthogonal axes.

This orthogonality constraint means that while the first few principal components capture the maximum variance, they may represent mixtures of physical parameters rather than isolated processes. The principal components might combine effects from multiple physical processes, making direct interpretation challenging. Consequently, astronomers must exercise caution when attempting to assign direct physical meaning to individual principal components, as the orthogonality constraint may force artificial separations between naturally correlated physical processes.

Unimodal Assumption   Another limitation of PCA stems from its reliance on the covariance matrix, which inherently assumes a single mode or unimodal distribution in the data. By optimizing for directions of maximum variance, PCA effectively treats the entire dataset as having a single central tendency. This assumption becomes problematic for astronomical datasets that exhibit multimodal distributions.

Consider galaxy populations that naturally cluster into distinct types (spiral, elliptical, irregular), or stellar populations that form separate groups in parameter space. When applied to such multimodal data, PCA will attempt to find a single set of principal components that spans the entire dataset, potentially missing the natural clustering structure. The resulting principal components may cut across multiple clusters rather than identifying the meaningful differences between them.

This limitation is particularly evident when the variance within clusters is smaller than the variance between clusters. In such cases, the first principal component will primarily capture the separation between clusters rather than the meaningful variation within each cluster. This can obscure important physical relationships that exist within individual populations.

Alternative Approaches   Addressing these limitations often requires more advanced methods. Independent Component Analysis (ICA), which we touched on in our discussions of mutual information in Chapter 9, offers one alternative. Unlike PCA, which uses variance as its optimization criterion, ICA maximizes statistical independence between components,
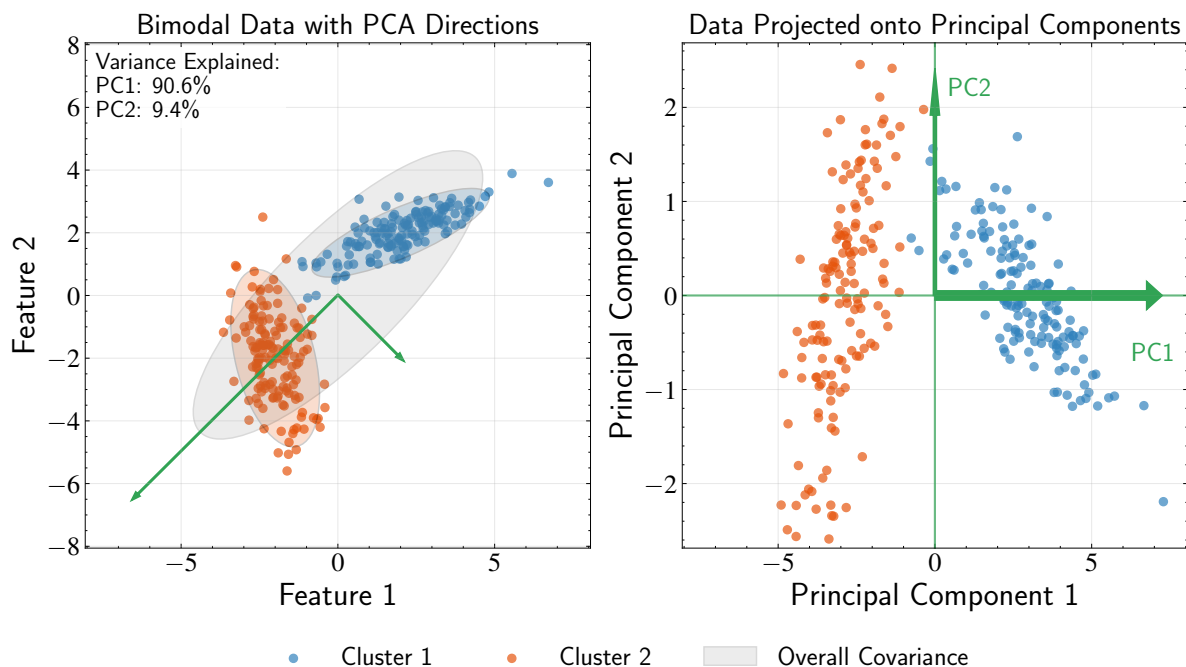
Figure 10.9: Illustration of PCA's limitation with multimodal data. **Left panel:** Bimodal data with two distinct clusters (blue and orange), each with its own internal structure and major axis (shown as dashed arrows). Notice how the first principal component (PC1, green arrow) does not align with the major direction of either cluster. Instead, PC1 points between the clusters to maximize global variance across the entire dataset. This misalignment occurs because PCA treats all data points as samples from a single distribution rather than recognizing the bimodal structure. **Right panel:** Data projected onto the principal components, showing how PC1 primarily captures the between-cluster variation rather than the within-cluster structure. This demonstrates why PCA can be inappropriate for astronomical datasets with natural clustering, such as distinct galaxy types or separate stellar populations. For such multimodal astronomical data, techniques that first identify clusters, as we will discuss in the next chapter, before performing dimensionality reduction often yield more physically meaningful representations.

often yielding more physically interpretable results when underlying processes are truly independent but not necessarily orthogonal. This makes ICA particularly useful for signal separation problems in astronomy, such as disentangling different physical sources in mixed signals.

Neural network autoencoders represent another approach, functioning as nonlinear generalizations of PCA. These techniques relax the orthogonality constraint and can capture more complex relationships in the data, potentially providing more physically interpretable representations. However, they come with their own challenges, including increased computational complexity and potential overfitting.

For astronomical datasets with natural clustering, a two-step approach often proves more effective: first identify distinct populations using clustering methods, then apply dimensionality reduction within each cluster. This approach respects the multimodal nature of astronomical data while still providing the benefits of dimension reduction for analysis within each population.

Sensitivity to Outliers   PCA's reliance on variance maximization makes it sensitive to outliers in the data. A few extreme data points can disproportionately influence the directions of maximum variance, potentially causing the principal components to be dominated by outlier behavior rather than the typical patterns in the data.

In astronomical applications, outliers are common and often scientifically interesting—they might represent rare object types, measurement errors, or genuinely unusual phenomena. However, their presence can skew PCA results, making it important to consider robust variants of PCA or careful outlier treatment before applying standard PCA techniques.

Scale Dependence   PCA is sensitive to the relative scales of different features in the dataset. Features with larger numerical ranges will naturally contribute more to the covariance matrix, potentially dominating the principal components even if they are not the most scientifically important variables.

In astronomical data, different measurements often have vastly different scales — magnitudes might range from 10 to 30, while parallaxes might range from 0.001 to 0.1. Without proper scaling or standardization, the larger-scale features may dominate the principal components, obscuring potentially important relationships in the smaller-scale variables.

10.10   Summary

In this chapter, we have explored Principal Component Analysis as a method for discovering structure in high-dimensional data without target variables. This represents our first step into unsupervised learning, where the goal shifts from predicting outcomes to understanding the patterns hidden within observations.

We began by establishing the central problem: high-dimensional astronomical data often contains redundant information, with most variation occurring along a few key directions. PCA addresses this by finding lower-dimensional representations that preserve

maximum variance while enabling more tractable analysis and visualization.

Our development proceeded through two complementary perspectives that lead to the same mathematical solution. The variance maximization approach seeks directions along which data varies most, while the reconstruction error minimization approach finds representations that best preserve the original data structure when projected back to the full space. The mathematical equivalence of these perspectives provided insight into what PCA accomplishes: it identifies the most informative lower-dimensional representation possible under linear constraints.

The mathematical foundation rested on constrained optimization using Lagrange multipliers. This technique transformed our intuitive goal of finding maximum variance directions into a tractable optimization problem. The solution revealed that principal components are eigenvectors of the data covariance matrix, with the variance along each component equal to its corresponding eigenvalue. This connection between statistical concepts and linear algebra provided both theoretical understanding and computational approaches.

We established this result through mathematical induction, proving that successive principal components correspond to eigenvectors with decreasing eigenvalues. This proof demonstrated that despite the seemingly complex sequential extraction process, the end result reduces to eigendecomposition of the covariance matrix—a single computation that yields all principal components simultaneously.

The computational advantages of Singular Value Decomposition became crucial for high-dimensional astronomical data. SVD avoids explicit covariance matrix formation, reducing complexity from $\mathcal{O}(D^3)$ to $\mathcal{O}(\min(ND^2, N^2D))$. For typical astronomical datasets where features outnumber samples, this often provides orders of magnitude speedup, making PCA practical for modern survey data with thousands or millions of dimensions.

PCA represents more than just a dimension reduction technique; it provides a principled approach to discovering structure in complex data. For astronomical applications where understanding patterns and correlations is crucial for physical insight, PCA offers a mathematically rigorous foundation that connects data analysis to underlying science.

While PCA assumes continuous variation well-captured by linear combinations, clustering explicitly identifies discrete groupings within data. Rather than forcing all data through a single covariance structure, clustering techniques recognize and model the multimodal nature of astronomical phenomena. Together, dimension reduction and clustering

provide comprehensive approaches to discovering structure in astronomical data without pre-determined categories. Chapter 11 will address PCA's limitation with naturally clustered data by exploring clustering as the complementary task in unsupervised learning.

Further Readings: The development of Principal Component Analysis builds upon foundational work in multivariate statistics, with early contributions from Pearson [1901] who investigated methods for finding lines and planes of closest fit to systems of points in space. The formal statistical treatment emerged through the work of Hotelling [1933], with development of principal components as linear combinations of original variables that capture directions of maximum variance within the data. The mathematical connections between PCA and matrix decomposition were illuminated by Eckart and Young [1936], who explored the relationship between principal components and low-rank approximations through Singular Value Decomposition. For readers interested in computational implementation, numerically stable algorithms for SVD computation were developed by Golub and Kahan [1965], with subsequent advances by Golub and Reinsch [1970] that remain influential in modern PCA implementations. The theoretical properties of PCA within multivariate statistical theory are treated in Anderson [1958], while Murtagh and Heck [1987] offers discussion of PCA's role in exploratory data analysis. Jolliffe [2002] provides comprehensive coverage of PCA theory, variants, and applications across diverse fields. For readers interested in addressing PCA's limitations, Comon [1994] offers treatment of Independent Component Analysis as an alternative for non-Gaussian data, while Hinton and Salakhutdinov [2006] explore nonlinear dimensionality reduction through neural network autoencoders that extend beyond PCA's linear assumptions.

Chapter 11

K-means and Gaussian Mixture Models

In our exploration of Principal Component Analysis, we discovered how to identify the most informative directions in high-dimensional data. PCA provided a method for finding continuous lower-dimensional representations that preserve the essential variations in complex datasets.

This success with dimension reduction reveals a broader insight: high-dimensional data often contains structure that can be discovered without labeled examples. The same principle that makes PCA effective—that complex data is often governed by simpler underlying patterns—suggests another type of structure we might seek. Rather than continuous variations captured by PCA, we might want to identify discrete groups within our data.

This leads us to clustering, the second major approach in unsupervised learning. Unlike PCA, which seeks continuous representations, clustering attempts to partition data into discrete groups based on similarity measures.

Unlike the classification methods we studied with logistic regression, clustering operates without labeled training examples. Classification requires known categories and focuses on finding decision boundaries between them. Clustering, by contrast, examines the data itself to discover natural groupings, making it valuable for discovery science where we might not know in advance what categories to expect.

The clustering approach offers several advantages in astronomical research. It al-
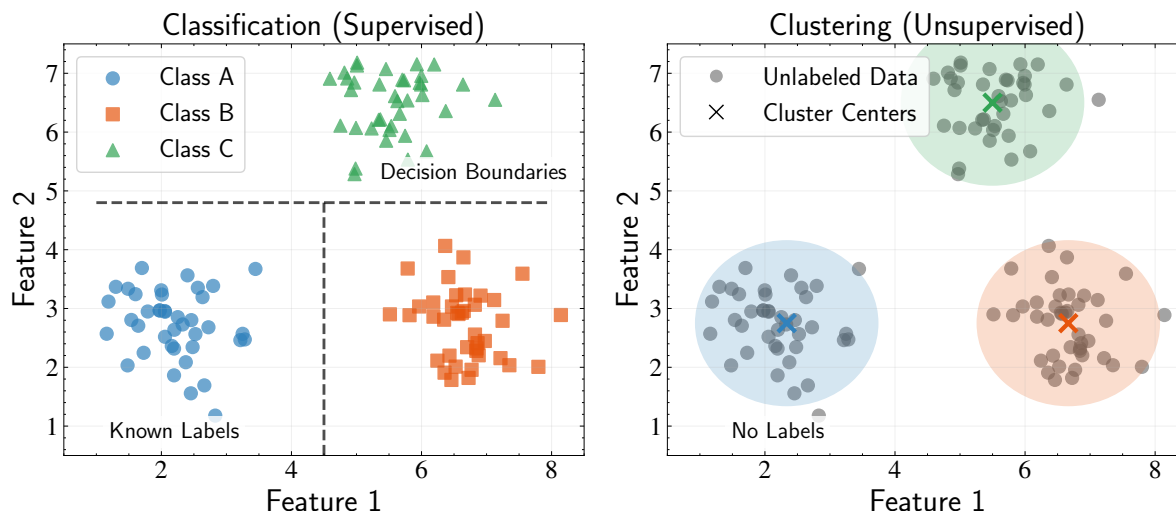
Figure 11.1: Comparison of classification (supervised learning) and clustering (unsupervised learning) approaches in machine learning. **Left panel:** Classification with known labels, where data points are assigned to predefined classes (blue circles for Class A, orange squares for Class B, and green triangles for Class C). Decision boundaries (dashed lines) separate the feature space into regions for different classes based on labeled training data. The horizontal line separates Class C from Classes A and B, while the vertical line separates Class A from Class B. **Right panel:** Clustering without prior labels, where algorithms discover natural groupings in unlabeled data (gray circles). Discovered cluster centers (colored X marks) and their corresponding regions (colored ellipses) emerge from the data's inherent structure rather than predefined categories.

lows exploration of data without preconceived categories, potentially revealing unexpected patterns. Modern surveys generate vast catalogs where manual classification would be impractical, making automated clustering essential. Additionally, clustering can reveal subtle distinctions that might not align with traditional schemes developed through visual inspection.

However, clustering also presents unique challenges. Without ground truth labels, evaluating results becomes more subjective than in supervised learning. Determining the appropriate number of clusters often depends on the scientific question rather than being intrinsic to the data. Different algorithms can produce different results on the same dataset, requiring careful consideration of their underlying assumptions.

At its core, clustering operates on a simple premise: objects that are "similar" to each other likely belong to the same group, while objects that are "dissimilar" likely belong to different groups. However, defining similarity leads to different algorithms suited for different types of data and scientific questions.

In this chapter, we'll explore two complementary approaches that reveal the deep connections between geometric and probabilistic perspectives on clustering. We begin with K-means clustering, which provides a geometric approach that partitions data by minimizing distances between points and cluster centers. This method offers computational efficiency and interpretable results, making it an ideal starting point for understanding clustering concepts.

We then develop Gaussian Mixture Models (GMMs), which reframe clustering as a probabilistic problem. Unlike K-means, GMMs provide probability distributions over cluster assignments and can capture uncertainty in membership—crucial capabilities when dealing with astronomical data where boundaries between populations are often fuzzy rather than sharp.

The progression from K-means to GMMs reveals an important conceptual bridge: K-means can be understood as a special case of GMMs under specific constraints. This relationship creates a natural pathway from geometric intuition to probabilistic sophistication, allowing us to understand both the power and limitations of each approach.

A central challenge in clustering involves determining the optimal number of clusters—the astronomical equivalent of asking how many distinct types of galaxies exist or how many stellar populations are present in a globular cluster. We'll explore principled approaches to this problem through information criteria that balance model fit against complexity, providing mathematical frameworks for choosing between competing explanations of our data.

Together, K-means and GMMs provide a comprehensive toolkit for discovering discrete structure in astronomical data, complementing the continuous representations offered by techniques like PCA and setting the stage for more advanced methods in statistical learning.

11.1   K-means: Mathematical Formalism

To make the clustering problem concrete, we begin with the simplest and most intuitive approach: K-means clustering. The basic idea behind K-means can be stated simply: if we want to divide our data into K groups, we should assign each data point to the group whose center it is closest to.

This intuitive notion leads to a precise mathematical formulation. Let our dataset

consist of N observations $\{\mathbf{x}_1, \mathbf{x}_2, \ldots, \mathbf{x}_N\}$, where each $\mathbf{x}_i$ is a D-dimensional feature vector. For instance, in a study of stellar populations, each $\mathbf{x}_i$ might represent a star with features like metallicity, carbon abundance, nitrogen abundance, and other chemical elements measured from spectroscopy.

The K-means algorithm seeks to find K cluster centers $\{\boldsymbol{\mu}_1, \boldsymbol{\mu}_2, \ldots, \boldsymbol{\mu}_K\}$ and assign each data point to exactly one cluster. We can formalize these assignments using binary indicator variables $r_{ik} \in \{0, 1\}$, where $r_{ik} = 1$ if data point $\mathbf{x}_i$ is assigned to cluster k, and $r_{ik} = 0$ otherwise.

This representation resembles the one-hot encoding we used in logistic regression. For example, if we have $K = 3$ clusters representing different stellar populations and data point $\mathbf{x}_5$ belongs to cluster 2, then $r_{51} = 0$, $r_{52} = 1$, and $r_{53} = 0$. Since each data point must belong to exactly one cluster, we have the constraint $\sum_{k=1}^{K} r_{ik} = 1$ for all i.

The K-means Objective Function   The goal of K-means is to find cluster centers and assignments that make the clusters as "compact" as possible. We measure compactness by the sum of squared distances between each data point and its assigned cluster center:

$$J = \sum_{i=1}^{N} \sum_{k=1}^{K} r_{ik} \|\mathbf{x}_i - \boldsymbol{\mu}_k\|^2. \tag{11.1}$$

Let's understand this expression term by term. The quantity $\|\mathbf{x}_i - \boldsymbol{\mu}_k\|^2$ represents the squared Euclidean distance between data point $\mathbf{x}_i$ and cluster center $\boldsymbol{\mu}_k$. We multiply this distance by r_{ik}, which equals 1 only if point i is assigned to cluster k and 0 otherwise. This means we only count the distance between a point and its assigned cluster center.

The double summation might look complex, but it simplifies due to our binary assignment variables. Since r_{ik} equals 1 for exactly one value of k for each data point i, each data point contributes exactly one distance term to the objective function. Therefore, J simply measures the total squared distance between each data point and its assigned cluster center.

Minimizing J leads to tighter, more well-defined clusters. When J has a smaller value, data points are positioned closer to their assigned cluster centers, resulting in more compact clusters.

The Dual Optimization Challenge The optimization problem becomes:

$$\min_{\{r_{ik}\},\{\boldsymbol{\mu}_k\}} J = \sum_{i=1}^{N} \sum_{k=1}^{K} r_{ik} \|\mathbf{x}_i - \boldsymbol{\mu}_k\|^2 \tag{11.2}$$

subject to $r_{ik} \in \{0, 1\}$ and $\sum_{k=1}^{K} r_{ik} = 1$ for all i.

This optimization presents a challenge we haven't encountered in our previous algorithms. Unlike regression or classification where we optimized a single set of parameters, here we must simultaneously optimize two distinct sets of variables: the cluster centers $\{\boldsymbol{\mu}_k\}$ and the assignments $\{r_{ik}\}$.

The challenge lies in the circular dependency between these two sets of variables. If we knew the optimal cluster centers, determining the best assignments would be straightforward—we would simply assign each point to its nearest center. Conversely, if we knew the optimal assignments, finding the best cluster centers would be easy—each center would be the mean of its assigned points.

This interdependence makes direct optimization difficult. The binary constraint on r_{ik} further complicates matters, introducing a combinatorial aspect to the problem. For a dataset with N points and K clusters, there are K^N possible assignment combinations—a number that grows exponentially with dataset size.

The high dimensionality of this problem—with $N \times K$ binary assignment variables and $K \times D$ continuous cluster center coordinates—makes exhaustive search computationally intractable for any reasonably sized dataset. Standard gradient descent methods also fail because the binary nature of r_{ik} prevents the use of continuous optimization techniques.

These challenges require a specialized approach that can handle the circular dependency between assignments and centers while remaining computationally tractable. This leads us naturally to the Expectation-Maximization algorithm.

11.2 Expectation-Maximization for K-means

The circular dependency between cluster centers and point assignments suggests a natural solution: alternate between optimizing one set of variables while holding the other fixed. This approach, known as the Expectation-Maximization (EM) algorithm, transforms our complex joint optimization into a sequence of simpler problems that can be solved
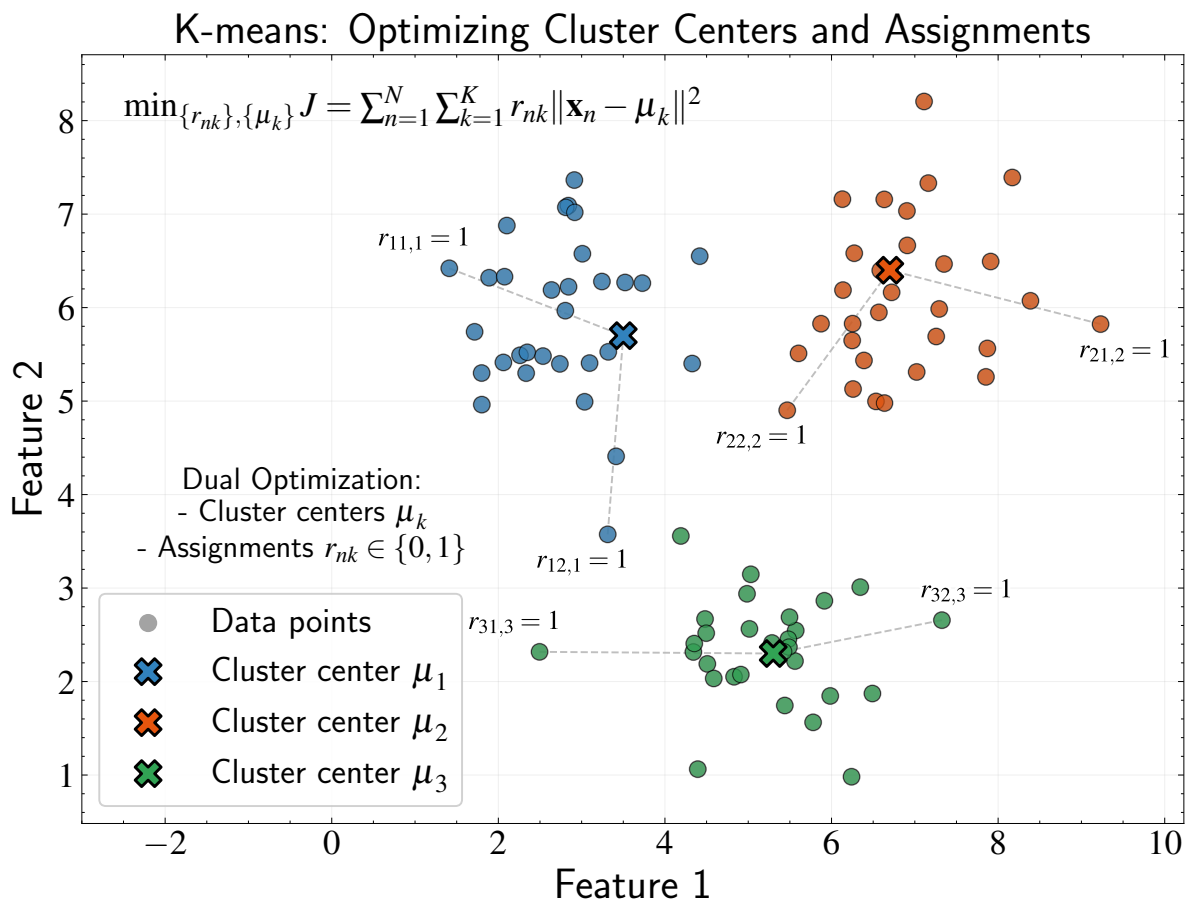
Figure 11.2: Visualization of the dual optimization challenge in K-means clustering. The algorithm simultaneously optimizes two sets of parameters: (1) the cluster centers $\boldsymbol{\mu}_k$ (marked with X symbols) and (2) the binary assignment variables $r_{ik} \in \{0, 1\}$ that assign each data point to exactly one cluster. The objective function $J = \sum_{i=1}^{N} \sum_{k=1}^{K} r_{ik} \|\mathbf{x}_i - \boldsymbol{\mu}_k\|^2$ represents the sum of squared distances between data points and their assigned centers, which the algorithm aims to minimize. Dashed lines connect selected data points to their assigned cluster centers, with $r_{ik} = 1$ indicating that point i belongs to cluster k. This presents a circular dependency in the optimization process: the optimal centers depend on the point assignments, while the optimal assignments depend on the center positions. This interdependence necessitates the iterative Expectation-Maximization approach used in K-means, where we alternate between updating assignments and center positions until convergence.

analytically.

　　The key insight is that while optimizing both $\boldsymbol{\mu}_k$ and r_{ik} simultaneously proves difficult, optimizing one while keeping the other fixed becomes straightforward. We can visualize this as a "coordinate descent" approach through the parameter space, where we alternate between moving along the assignment dimensions and the cluster center dimensions, gradually approaching a minimum of our objective function.

The Basic EM Framework For K-means clustering, the EM algorithm follows a simple iterative pattern:

- **Initialization**: Select K initial cluster centers $\boldsymbol{\mu}_k$. These could be random points from our dataset, though more sophisticated initialization strategies often work better.

- **Expectation Step (E-step)**: Fix the cluster centers $\boldsymbol{\mu}_k$ and find the optimal assignments r_{ik}.

- **Maximization Step (M-step)**: Fix the assignments r_{ik} and find the optimal cluster centers $\boldsymbol{\mu}_k$.

- **Iteration**: Repeat the E-step and M-step until convergence.

Let's work through each step to understand why this approach works and how to implement it.

Expectation Step: Optimal Assignments In the E-step, we assume the cluster centers $\boldsymbol{\mu}_k$ are fixed and solve for the assignments that minimize our objective function:

$$\min_{\{r_{ik}\}} J = \sum_{i=1}^{N} \sum_{k=1}^{K} r_{ik} \|\mathbf{x}_i - \boldsymbol{\mu}_k\|^2 \tag{11.3}$$

subject to $r_{ik} \in \{0, 1\}$ and $\sum_{k=1}^{K} r_{ik} = 1$ for all i.

With fixed centers, this optimization becomes much simpler. For each data point $\mathbf{x}_i$, we need to choose which cluster it belongs to. Since exactly one r_{ik} must equal 1 for each point i, the contribution of point i to the objective function is:

$$\sum_{k=1}^{K} r_{ik} \|\mathbf{x}_i - \boldsymbol{\mu}_k\|^2 = \|\mathbf{x}_i - \boldsymbol{\mu}_{k^*}\|^2 \tag{11.4}$$

where k^* is the cluster to which point i is assigned.

To minimize this contribution, we should choose k^* to be the index of the cluster center closest to $\mathbf{x}_i$. This gives us the optimal assignment rule:

$$r_{ik} = \begin{cases} 1 & \text{if } k = \arg\min_j \|\mathbf{x}_i - \boldsymbol{\mu}_j\|^2 \\ 0 & \text{otherwise} \end{cases} \tag{11.5}$$

This result has an intuitive interpretation: assign each point to its nearest cluster center. The E-step simply implements this nearest-neighbor assignment for all data points.

Maximization Step: Optimal Centers In the M-step, we fix the assignments r_{ik} and solve for the cluster centers that minimize our objective function:

$$\min_{\{\boldsymbol{\mu}_k\}} J = \sum_{i=1}^{N} \sum_{k=1}^{K} r_{ik} \|\mathbf{x}_i - \boldsymbol{\mu}_k\|^2 \tag{11.6}$$

Since the assignments are now fixed, we can rearrange the summation to group terms by cluster:

$$J = \sum_{k=1}^{K} \sum_{i=1}^{N} r_{ik} \|\mathbf{x}_i - \boldsymbol{\mu}_k\|^2 = \sum_{k=1}^{K} J_k \tag{11.7}$$

where $J_k = \sum_{i=1}^{N} r_{ik} \|\mathbf{x}_i - \boldsymbol{\mu}_k\|^2$ represents the contribution from cluster k.

Since each J_k depends only on $\boldsymbol{\mu}_k$, we can optimize each cluster center independently. For cluster k, we minimize:

$$J_k = \sum_{i=1}^{N} r_{ik} \|\mathbf{x}_i - \boldsymbol{\mu}_k\|^2 \tag{11.8}$$

Taking the gradient with respect to $\boldsymbol{\mu}_k$ and setting it to zero:

$$\frac{\partial J_k}{\partial \boldsymbol{\mu}_k} = \sum_{i=1}^{N} r_{ik} \frac{\partial}{\partial \boldsymbol{\mu}_k} \|\mathbf{x}_i - \boldsymbol{\mu}_k\|^2 \tag{11.9}$$

$$= \sum_{i=1}^{N} r_{ik} (-2)(\mathbf{x}_i - \boldsymbol{\mu}_k) \tag{11.10}$$

$$= -2 \sum_{i=1}^{N} r_{ik} \mathbf{x}_i + 2\boldsymbol{\mu}_k \sum_{i=1}^{N} r_{ik} = 0 \tag{11.11}$$

Solving for $\boldsymbol{\mu}_k$:

$$\boldsymbol{\mu}_k = \frac{\sum_{i=1}^{N} r_{ik} \mathbf{x}_i}{\sum_{i=1}^{N} r_{ik}} \tag{11.12}$$

This result also has a clear interpretation: the optimal cluster center is the mean (centroid) of all points assigned to that cluster. The denominator $\sum_{i=1}^{N} r_{ik}$ counts how many points are assigned to cluster k, since r_{ik} equals 1 for assigned points and 0 otherwise.

The Local Minima Problem   While the EM algorithm will always converge to some solution, it typically reaches a local minimum rather than the global minimum of our objective function. This occurs because each step only guarantees improvement given the current state, not global optimality.

The final solution depends critically on initialization. Poor starting positions can trap the algorithm in suboptimal configurations where further improvement through alternating optimization becomes impossible, even though much better solutions exist elsewhere in the parameter space.

This sensitivity to initialization is both a limitation and a motivation for careful algorithm design. Since we often don't know the true cluster structure beforehand, we need initialization strategies that increase our chances of finding good solutions.

The sensitivity to initialization represents both a limitation and an opportunity in K-means. Poor initialization can lead to suboptimal solutions, but good initialization strategies can improve both the quality of results and convergence speed.

Random Initialization   The simplest approach selects K data points uniformly at random as initial cluster centers. While straightforward to implement, this method can lead to poor solutions when centers are initialized too close together or in regions of low data density.

K-means++ Initialization   A more sophisticated strategy, K-means++, addresses the initialization problem through a weighted sampling approach that systematically spreads initial centers. The algorithm provides a principled way to choose starting positions that balance diversity and data density.

The K-means++ algorithm works as follows:

- **Step 1**: Choose the first cluster center $\boldsymbol{\mu}_1$ uniformly at random from the data points:

$$\boldsymbol{\mu}_1 \in \{\mathbf{x}_1, \mathbf{x}_2, \ldots, \mathbf{x}_N\} \text{ with probability } \frac{1}{N} \tag{11.13}$$

- **Step 2**: For each data point $\mathbf{x}_i$, compute $D(\mathbf{x}_i)$, the minimum distance to any existing cluster center:

$$D(\mathbf{x}_i) = \min_{j \in \{1,2,\ldots,m\}} \|\mathbf{x}_i - \boldsymbol{\mu}_j\|^2 \tag{11.14}$$

where m is the number of centers already chosen.
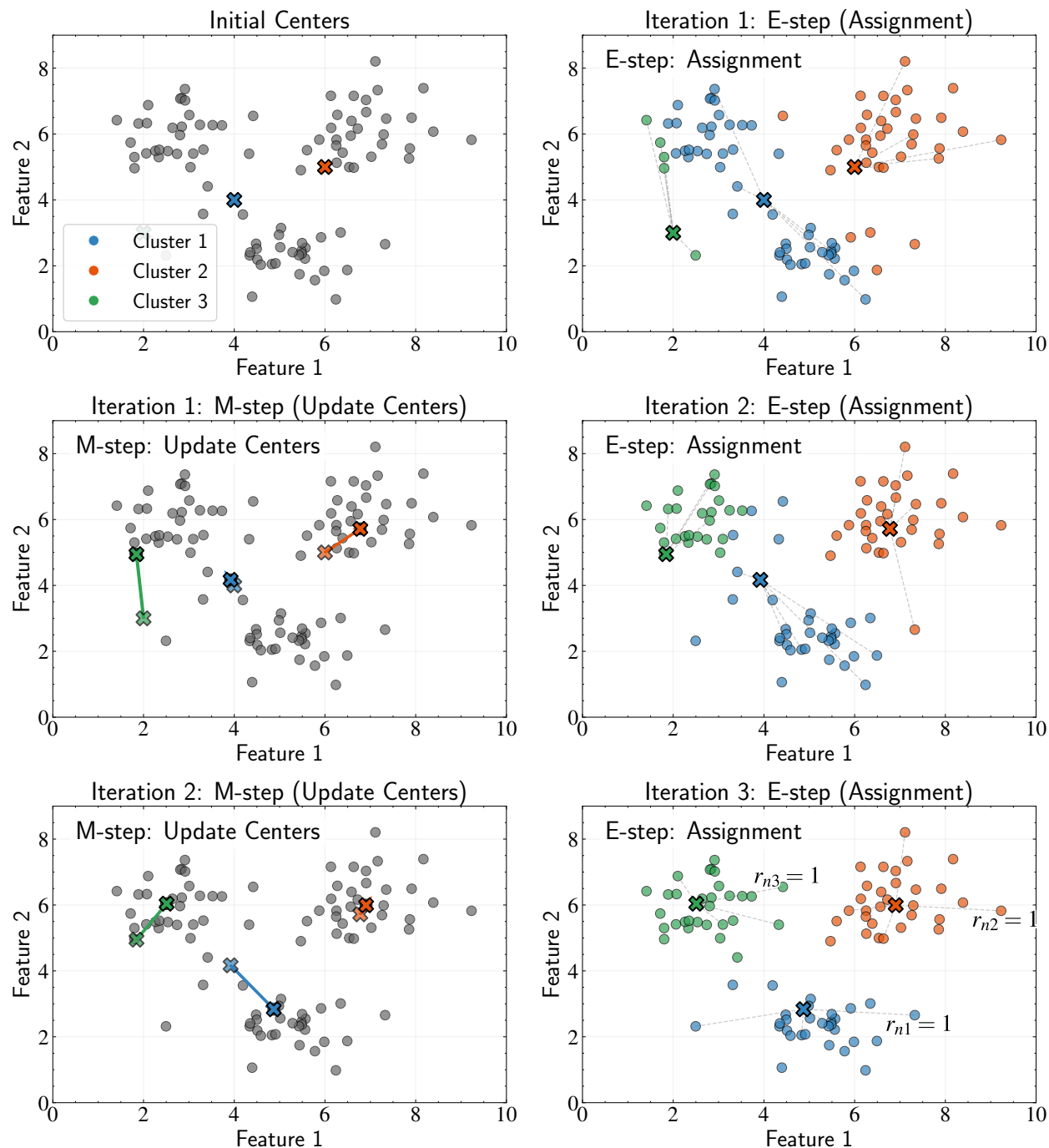
Figure 11.3: Visualization of the Expectation-Maximization (EM) algorithm for K-means clustering across three iterations. **Top row:** Initial centers (left) are chosen arbitrarily, then the first E-step (right) assigns each point to its nearest center (shown by colors and dashed lines). **Middle row:** The first M-step (left) moves each center to the mean of its assigned points, with text showing the exact coordinate transition. The second E-step (right) then reassigns points based on these updated centers. **Bottom row:** The second M-step (left) further refines the centers, followed by the third E-step (right) which shows the final assignments. This demonstrates how K-means resolves the circular dependency between cluster centers and point assignments through iterative optimization.
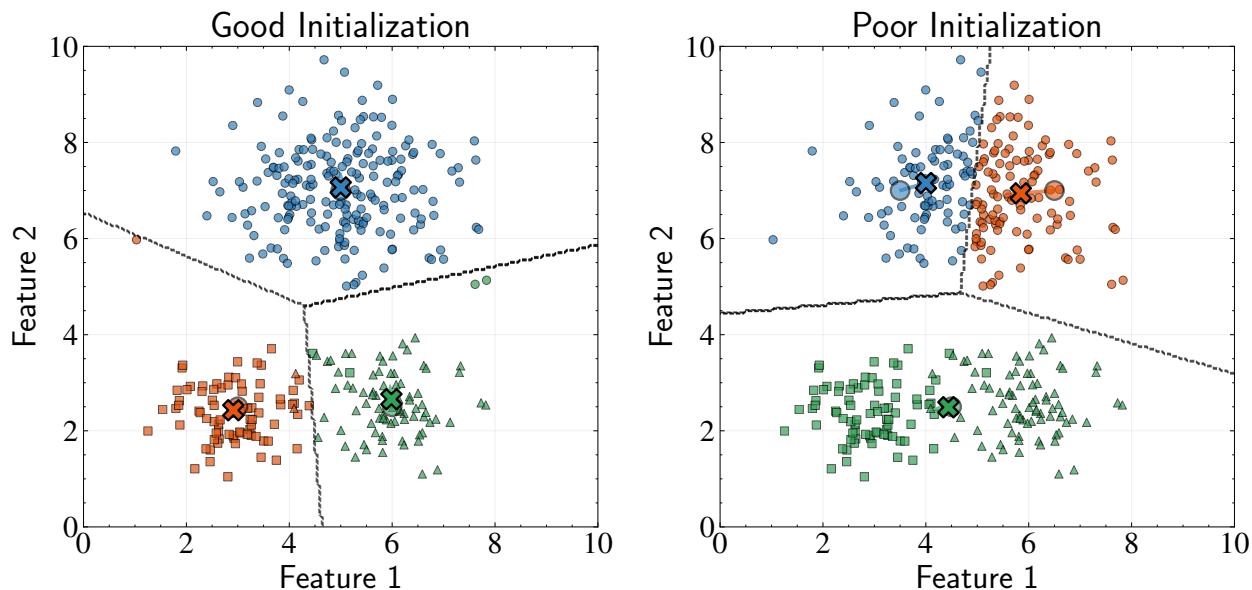
Figure 11.4: Demonstration of K-means sensitivity to initialization. **Left:** Good initialization with centers placed near each true cluster leads to correct identification of all three natural clusters. Initial centers (circles) converge to optimal final positions (X markers). **Right:** Poor initialization with two centers in the top cluster and one center between the bottom clusters results in a suboptimal solution where the large top cluster is incorrectly split while the two smaller bottom clusters are incorrectly merged. This illustrates how K-means can converge to local minima when initial centers are poorly positioned, highlighting why strategies like multiple random initializations or K-means++ are often necessary in practice.

- **Step 3**: Select the next cluster center $\boldsymbol{\mu}_{m+1}$ by sampling from the data points with probability proportional to $D(\mathbf{x}_i)^2$:

$$P(\boldsymbol{\mu}_{m+1} = \mathbf{x}_i) = \frac{D(\mathbf{x}_i)^2}{\sum_{j=1}^{N} D(\mathbf{x}_j)^2} \tag{11.15}$$

- **Step 4**: Repeat Steps 2-3 until all K centers have been chosen.

- **Step 5**: Proceed with the standard K-means EM algorithm using these initial centers.

This initialization strategy optimizes two competing objectives: maximizing the minimum distance between centers to avoid redundant placement within the same natural cluster, and ensuring centers are positioned in regions of high data density. The squared distance weighting in the probability calculation gives higher sampling probability to points that are far from existing centers while still sampling from the actual data distribution.
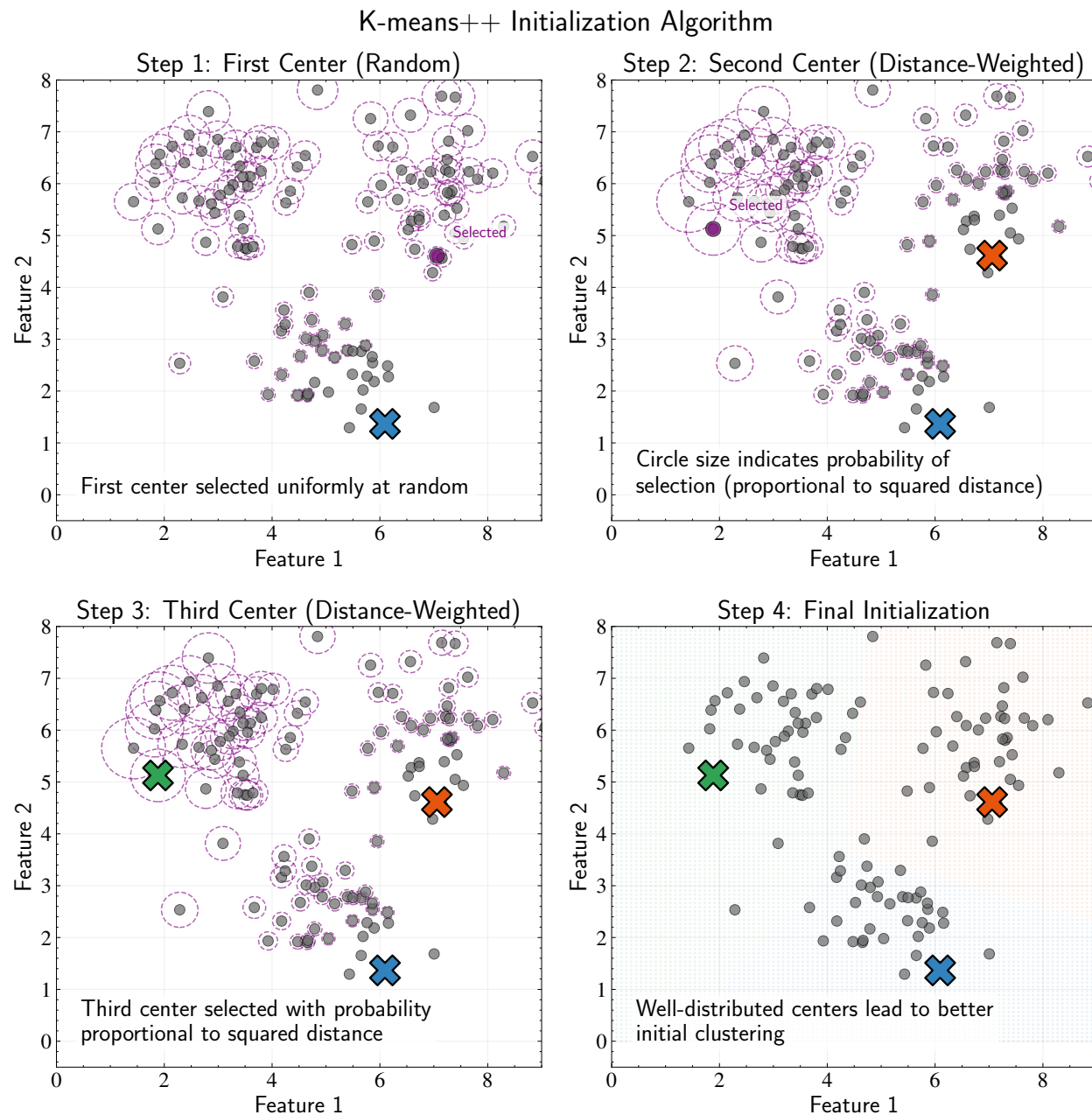
Figure 11.5: Illustration of the K-means++ initialization algorithm. **Step 1 (Top Left):** The first center is chosen uniformly at random from the data points. **Step 2 (Top Right):** The second center is selected with probability proportional to the squared distance from the first center, visualized by circle size. This gives distant points higher probability of selection, encouraging diversity in center placement. **Step 3 (Bottom Left):** The third center is selected with probability proportional to the squared distance from the nearest existing center, again using weighted sampling. **Step 4 (Bottom Right):** The final initialization shows the three centers with their corresponding assignment regions. K-means++ addresses the initialization sensitivity in standard K-means by maximizing the minimum distance between centers, leading to faster convergence and better clustering results compared to random initialization, particularly when distinct cluster structures exist in the data.

The mathematical foundation for K-means++ rests on the observation that good initial centers should be both diverse (far from each other) and representative (located in regions with data). The squared distance weighting achieves this balance by giving higher probability to points that are far from existing centers while still respecting the data distribution.

11.3 Evaluating K-means Clustering

Having established the mathematical foundation and algorithm for K-means, we can now examine its practical performance characteristics. Understanding both the algorithm's strengths and the challenges of applying it to real data will help us use K-means effectively and recognize when alternative approaches might be needed.

Computational Efficiency   One of K-means' primary advantages lies in its computational efficiency. The EM formulation makes the algorithm remarkably scalable for large datasets. Let's analyze the computational complexity of each iteration:

The E-step requires computing distances between each of the N data points and each of the K cluster centers. Since each distance calculation requires $\mathcal{O}(D)$ operations, this gives us $\mathcal{O}(NKD)$ operations total.

The M-step involves updating each of the K centers by averaging the points assigned to that center. Assuming roughly equal-sized clusters, each center is updated using approximately N/K points. Calculating the mean of N/K points in D dimensions requires $\mathcal{O}(ND/K)$ operations per center, giving us $\mathcal{O}(ND)$ operations total for all centers.

The overall complexity per iteration is therefore $\mathcal{O}(NKD)$, since the E-step dominates when $K \geq 1$. This linear scaling with the number of data points, clusters, and dimensions makes K-means feasible for large astronomical datasets with millions of objects and hundreds of features.

Determining the Number of Clusters   While K-means is computationally efficient, it requires us to specify the number of clusters K in advance. This presents a challenge: how do we choose an appropriate value when we don't know the true cluster structure? The optimal K often depends on both the data characteristics and the specific scientific question we're trying to answer.

Inertia and the Elbow Method   The most intuitive approach examines how the K-means objective function changes as we increase K. The within-cluster sum of squares (also called "inertia") measures how tightly clustered our data points are:

$$\text{Inertia} = \sum_{k=1}^{K} \sum_{i \in C_k} \|\mathbf{x}_i - \boldsymbol{\mu}_k\|^2 \tag{11.16}$$

where C_k represents the set of points assigned to cluster k.

As we increase K, the inertia will naturally decrease because clusters become smaller and more homogeneous. The key insight is that if there are K^* natural clusters in the data, then:

- For $K < K^*$: Adding another cluster captures genuine structure, producing large reductions in inertia

- For $K > K^*$: Additional clusters subdivide already coherent groups, yielding diminishing returns

The "elbow" in a plot of inertia versus K—where the slope changes markedly—can suggest an appropriate cutoff point. However, this method can be subjective when no clear elbow exists.

Silhouette Analysis   A more quantitative approach uses the silhouette score, which measures how similar each point is to its own cluster compared to other clusters. For each data point i, the silhouette score is:

$$s(i) = \frac{b(i) - a(i)}{\max\{a(i), b(i)\}} \tag{11.17}$$

where $a(i)$ is the average distance between point i and all other points in the same cluster, and $b(i)$ is the minimum average distance between point i and points in any other cluster.

The silhouette score ranges from -1 to 1:

- $s(i) \approx 1$: Point is well-clustered, far from neighboring clusters

- $s(i) \approx 0$: Point lies near the boundary between clusters

- $s(i) \approx -1$: Point may be assigned to the wrong cluster
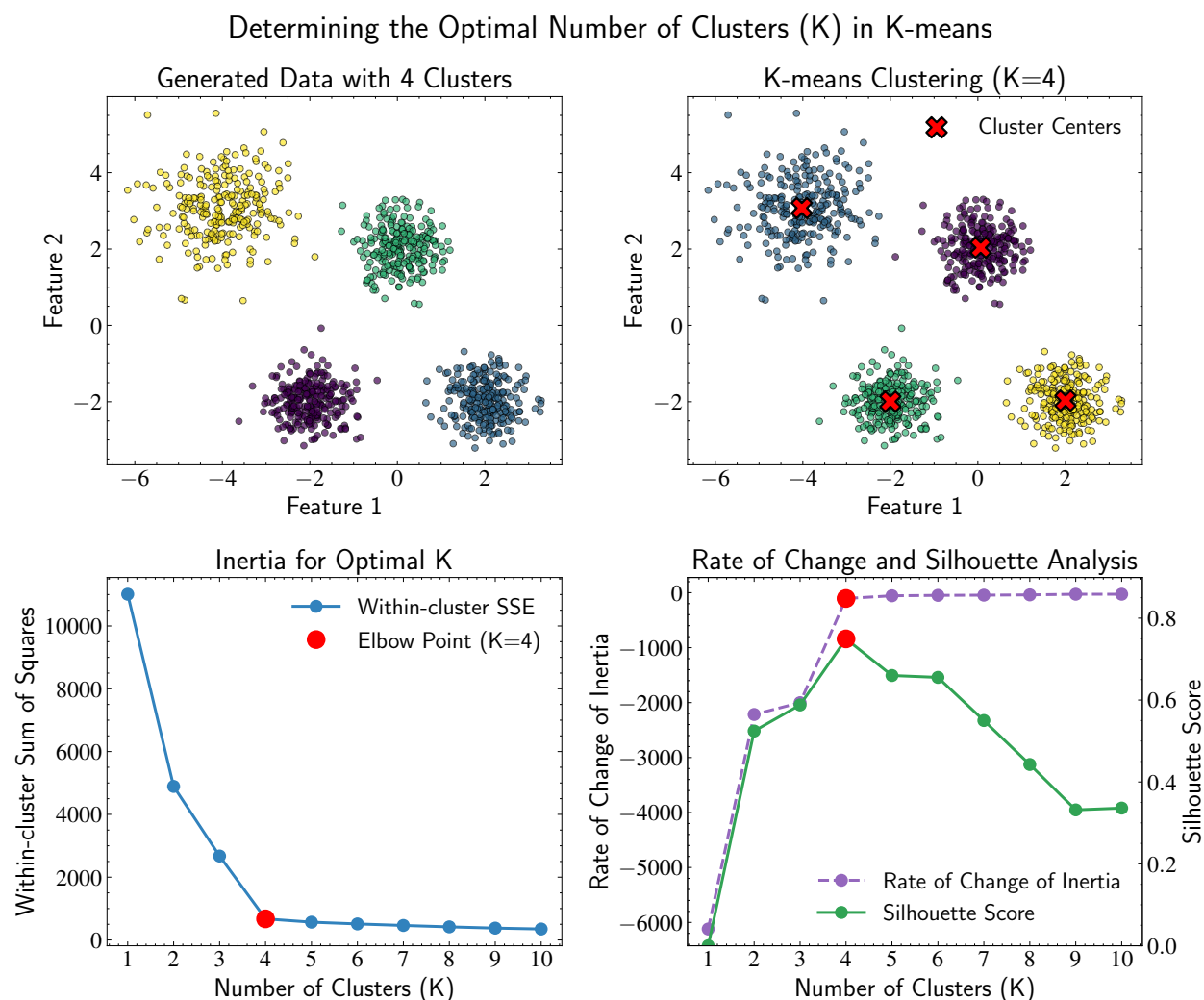
Figure 11.6: Visualization of the elbow method for determining the optimal number of clusters (K) in K-means. **Top Left:** The original dataset with four natural clusters. **Top Right:** K-means clustering results with K=4, showing the identified clusters and their centers (red X markers). **Bottom Left:** The elbow plot showing inertia (within-cluster sum of squares) versus K. The characteristic "elbow" at K=4 indicates the point where adding more clusters yields diminishing returns. This is analogous to the scree plot in PCA for determining the number of components to retain. **Bottom Right:** Additional analysis showing the rate of change of inertia (approximate derivative) and silhouette scores across different K values, both confirming K=4 as optimal. The silhouette score peaks at K=4, indicating that points are well-matched to their own clusters and well-separated from other clusters at this value.

The optimal number of clusters can be identified by the K that maximizes the average silhouette score across all data points.

11.4 K-means as a Generative Model

While we've presented K-means as a geometric optimization problem, there's a deeper statistical perspective that connects it to the broader framework of probabilistic modeling. This connection helps explain both K-means' behavior and points toward more sophisticated clustering methods.

Connecting to Classification Models In our study of logistic regression, we distinguished between discriminative and generative approaches to classification. Discriminative models learn decision boundaries directly, while generative models describe how data is produced within each class. K-means adopts the generative perspective but applies it to the unsupervised setting where class labels are unknown.

From this viewpoint, clustering assumes that our observed data arises from a mixture of different underlying processes. Each cluster represents one such process, and our goal is to identify both the processes (cluster parameters) and which process generated each data point (cluster assignments).

A Probabilistic Data-Generating Story We can formalize K-means through a specific generative model. Imagine that our data points arise from the following process:

- First, nature selects one of K clusters with equal probability $1/K$

- Then, nature generates a data point from that cluster according to a Gaussian distribution centered on the cluster's mean with spherical covariance $\sigma^2 \mathbf{I}$

This gives us the likelihood of observing data point $\mathbf{x}_i$:

$$p(\mathbf{x}_i) = \sum_{k=1}^{K} \frac{1}{K} \mathcal{N}(\mathbf{x}_i | \boldsymbol{\mu}_k, \sigma^2 \mathbf{I}) \tag{11.18}$$

where $\mathcal{N}(\mathbf{x} | \boldsymbol{\mu}, \boldsymbol{\Sigma})$ denotes the Gaussian probability density.

From Soft to Hard Assignments The likelihood expression above describes a "soft" assignment model where each data point has some probability of belonging to each cluster.

However, K-means uses "hard" assignments where each point belongs definitively to exactly one cluster.

We can connect these perspectives by introducing our binary assignment variables r_{ik} into the likelihood. When we make hard assignments, the likelihood becomes:

$$p(\mathbf{x}_i|\{r_{ik}\}) = \sum_{k=1}^{K} r_{ik} \frac{1}{K} \mathcal{N}(\mathbf{x}_i|\boldsymbol{\mu}_k, \sigma^2 \mathbf{I}) \tag{11.19}$$

Since exactly one r_{ik} equals 1 for each data point, this sum reduces to a single Gaussian density term—the one corresponding to the assigned cluster.

For the entire dataset, the log-likelihood becomes:

$$\log L = \sum_{i=1}^{N} \sum_{k=1}^{K} r_{ik} \log \left(\frac{1}{K} \mathcal{N}(\mathbf{x}_i|\boldsymbol{\mu}_k, \sigma^2 \mathbf{I}) \right) \tag{11.20}$$

Deriving the K-means Objective We can now show how maximizing this likelihood leads to the K-means objective function. The Gaussian density for spherical covariance is:

$$\mathcal{N}(\mathbf{x}|\boldsymbol{\mu}, \sigma^2 \mathbf{I}) = \frac{1}{(2\pi\sigma^2)^{D/2}} \exp \left(-\frac{\|\mathbf{x} - \boldsymbol{\mu}\|^2}{2\sigma^2} \right) \tag{11.21}$$

Taking the logarithm:

$$\log \mathcal{N}(\mathbf{x}|\boldsymbol{\mu}, \sigma^2 \mathbf{I}) = -\frac{D}{2} \log(2\pi\sigma^2) - \frac{\|\mathbf{x} - \boldsymbol{\mu}\|^2}{2\sigma^2} \tag{11.22}$$

Substituting into our log-likelihood:

$$\log L = \sum_{i=1}^{N} \sum_{k=1}^{K} r_{ik} \left[\log \frac{1}{K} - \frac{D}{2} \log(2\pi\sigma^2) - \frac{\|\mathbf{x}_i - \boldsymbol{\mu}_k\|^2}{2\sigma^2} \right] \tag{11.23}$$

The first two terms are constants with respect to both the cluster assignments r_{ik} and the cluster centers $\boldsymbol{\mu}_k$. When maximizing the log-likelihood, we can ignore these constants and focus on:

$$\sum_{i=1}^{N} \sum_{k=1}^{K} r_{ik} \left[-\frac{\|\mathbf{x}_i - \boldsymbol{\mu}_k\|^2}{2\sigma^2} \right] \tag{11.24}$$

Maximizing this expression is equivalent to minimizing:

$$\sum_{i=1}^{N}\sum_{k=1}^{K} r_{ik}\|\mathbf{x}_i - \boldsymbol{\mu}_k\|^2 \tag{11.25}$$

This is precisely the K-means objective function! The constant factor $1/(2\sigma^2)$ doesn't affect the optimization since it multiplies all terms equally.

Understanding K-means Assumptions   This derivation reveals that K-means implicitly assumes a specific generative model with restrictive assumptions:

- **Spherical clusters**: All clusters have identical spherical covariance matrices $\sigma^2\mathbf{I}$

- **Equal cluster sizes**: All clusters have equal prior probability $1/K$

- **Hard assignments**: Each data point belongs definitively to one cluster

These assumptions explain both K-means' computational efficiency and its limitations. The spherical assumption makes the algorithm fast but restricts it to finding roughly circular clusters. The equal size assumption works well when clusters naturally have similar populations but fails when cluster sizes vary dramatically. The hard assignment assumption provides mathematical simplicity but loses information about uncertainty in borderline cases.

This probabilistic perspective also reveals a path forward. By relaxing these restrictive assumptions—allowing different covariance matrices, unequal cluster sizes, and soft assignments—we can develop more flexible clustering methods. This leads naturally to Gaussian Mixture Models, which we explore next.

11.5   Gaussian Mixture Models: Mathematical Formalism

Our exploration of K-means revealed both its computational efficiency and its restrictive assumptions. While K-means works well for spherical, well-separated clusters of similar sizes, these assumptions often prove limiting in astronomical applications. Gaussian Mixture Models (GMMs) address these limitations by adopting a fully probabilistic framework that relaxes the key constraints of K-means.

K-means Failure with Non-Convex Clusters
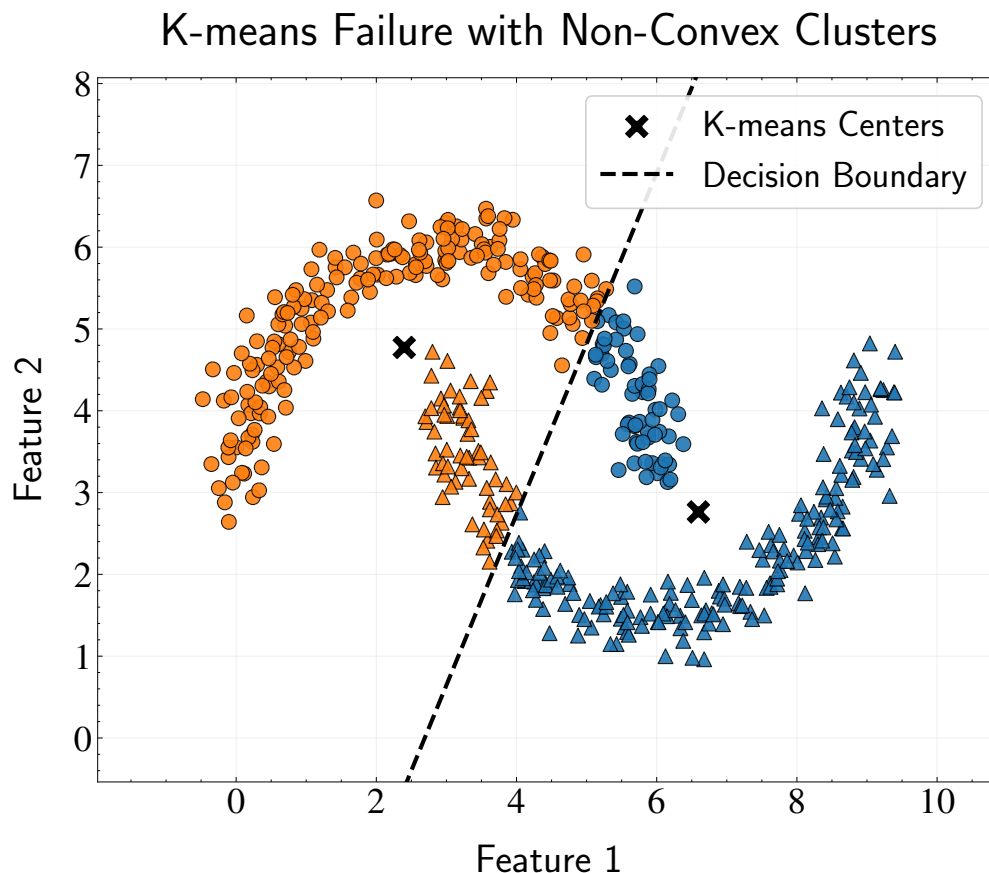
Figure 11.7: Demonstration of K-means clustering limitation with non-convex data structures. The data consists of two half-moon shaped clusters (distinguished by different marker shapes: circles and triangles), but K-means with K=2 creates an inappropriate linear decision boundary (dashed line) that fails to properly separate these naturally curved structures. The colors represent K-means cluster assignments, which clearly cut across the true half-moon patterns rather than respecting their intrinsic shapes. This limitation stems directly from the spherical and convex cluster assumption inherent in K-means, where decision boundaries are always hyperplanes perpendicular to the line connecting cluster centers, similar to logistic regression.

From Hard to Soft Assignments   The most important conceptual shift from K-means to GMMs lies in how we handle cluster membership. K-means forces each data point to belong exclusively to one cluster—a "hard assignment" that provides no information about uncertainty or ambiguity in borderline cases.

GMMs instead use "soft assignments" where each data point has a probability of belonging to each cluster. This probabilistic approach proves particularly valuable in astronomy, where boundaries between different populations are often fuzzy rather than sharp. For example, when studying stellar populations, stars near the boundary between disk and

halo populations might share characteristics of both groups.
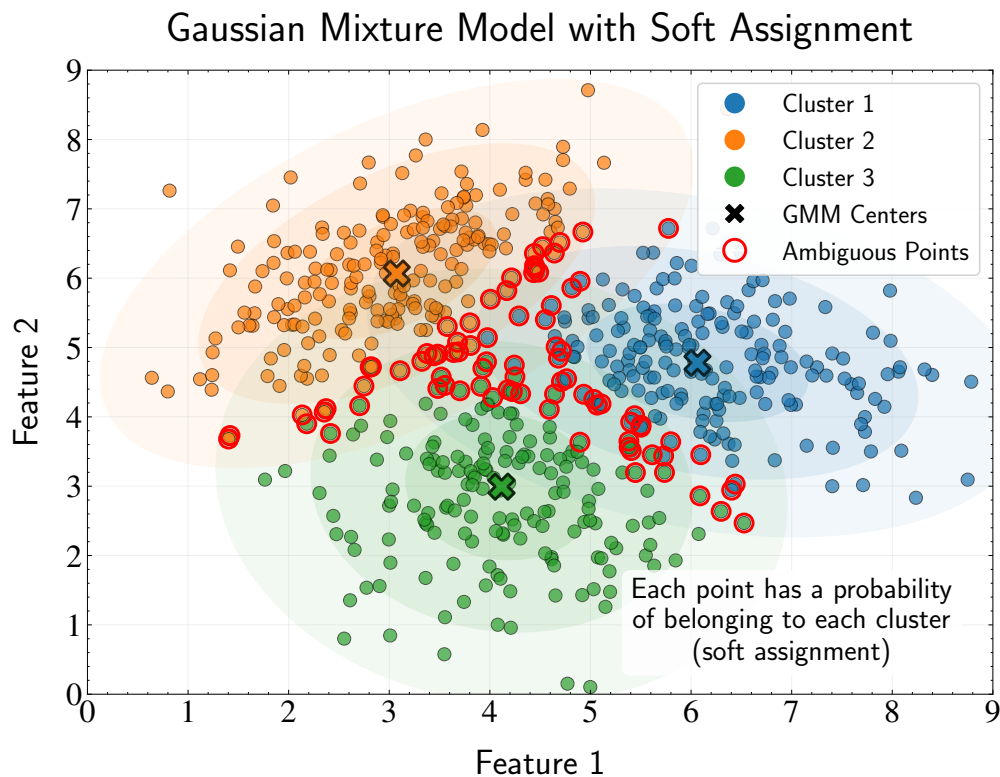
Figure 11.8: Illustration of Gaussian Mixture Models (GMM) with three clusters demonstrating soft assignment. Unlike K-means' hard boundaries, GMM assigns each point a probability of belonging to each cluster. Points are colored according to their most likely cluster assignment, with cluster centers marked by X symbols. The elliptical contours around each center show the 1, 2, and 3 standard deviation boundaries of each Gaussian component, highlighting how GMMs can model clusters with different shapes, sizes, and orientations through their covariance matrices. Red-outlined points indicate ambiguous cases where no single cluster has a dominant ($> 80\%$) probability of membership. This probabilistic framework is a key advantage of GMMs over K-means, allowing them to capture uncertainty in cluster assignments and better represent the underlying data distribution, particularly in regions where clusters overlap.

The Mixture Model Framework Rather than viewing clustering as partitioning data points, GMMs model the entire data distribution as a weighted combination of simpler component distributions. Specifically, we assume that our data points are generated from a mixture of K Gaussian distributions:

$$p(\mathbf{x}) = \sum_{k=1}^{K} \pi_k \mathcal{N}(\mathbf{x}|\boldsymbol{\mu}_k, \boldsymbol{\Sigma}_k) \tag{11.26}$$

This formulation captures a richer view of the data generation process. Let's understand each component:

- $\mathcal{N}(\mathbf{x}|\boldsymbol{\mu}_k, \boldsymbol{\Sigma}_k)$ is the multivariate Gaussian probability density for component k, with mean vector $\boldsymbol{\mu}_k$ and covariance matrix $\boldsymbol{\Sigma}_k$. This represents the probability of observing data point $\mathbf{x}$ if it came from component k.

- π_k is the mixture weight for component k, representing the prior probability that a randomly selected data point belongs to component k. These weights satisfy $\pi_k \geq 0$ and $\sum_{k=1}^{K} \pi_k = 1$.

The mixture weights π_k represent the relative abundance of each component in the overall population. In a galaxy survey, for example, π_1 might represent the fraction of spiral galaxies, π_2 the fraction of ellipticals, and so on.

Increased Model Flexibility   Unlike K-means, which assumes identical spherical covariances for all clusters, GMMs allow each component to have its own covariance matrix $\boldsymbol{\Sigma}_k$. This flexibility enables GMMs to capture clusters with different shapes, sizes, and orientations.

However, this flexibility comes at a cost in terms of model complexity. For a GMM with K components in D dimensions, we need to estimate:

- Mixture weights: $K - 1$ free parameters (due to the constraint $\sum_{k=1}^{K} \pi_k = 1$)

- Mean vectors: KD parameters (each mean has D components)

- Covariance matrices: $K \cdot D(D+1)/2$ parameters (each symmetric matrix has $D(D+1)/2$ free parameters)

This gives a total of $(K-1) + KD + K \cdot D(D+1)/2$ parameters, which grows quadratically with dimension D. This rapid growth can make GMMs computationally challenging in high-dimensional spaces.

Constraining Covariance Complexity   To manage computational complexity, we can impose constraints on the covariance matrices. Common approaches include:

Diagonal covariance: $\boldsymbol{\Sigma}_k = \mathrm{diag}(\sigma_{k1}^2, \sigma_{k2}^2, \ldots, \sigma_{kD}^2)$

This assumes features are uncorrelated within each component, reducing covariance

Gaussian Mixture Model: Mixture Weights
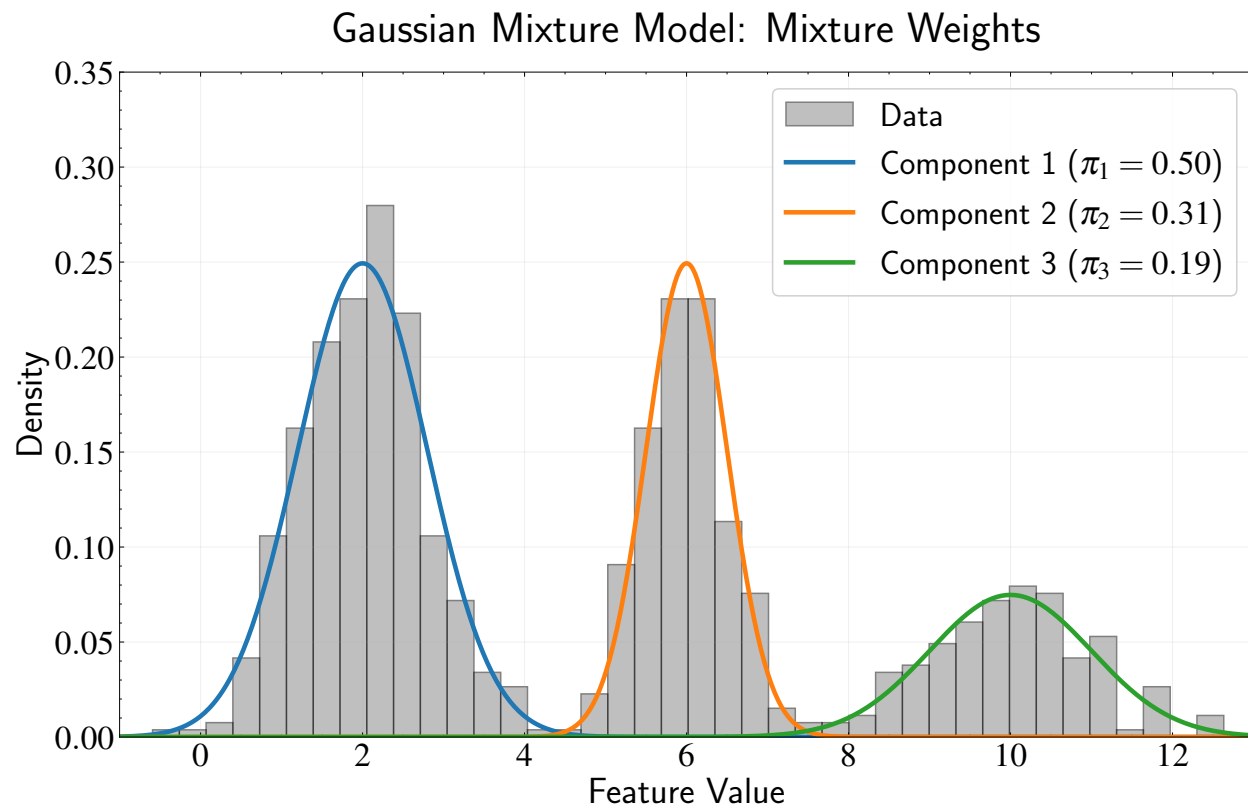
Figure 11.9: Illustration of mixture weights (π_k) in Gaussian Mixture Models. A 1D dataset generated from three Gaussian components with different weights ($\pi_1 = 0.50$, $\pi_2 = 0.31$, $\pi_3 = 0.19$) is shown as a histogram. Each colored curve represents a component density scaled by its corresponding mixture weight. The mixture weights represent the prior probability that a data point belongs to each component before observing its features, and they determine the relative contribution of each Gaussian to the overall mixture. These weights must satisfy $\pi_k \geq 0$ for all k and $\sum_{k=1}^{K} \pi_k = 1$, forming a proper probability distribution over the components.

parameters from $K \cdot D(D + 1)/2$ to $K \cdot D$. While less flexible than full covariance, this constraint still allows elliptical clusters aligned with coordinate axes.

Spherical covariance: $\boldsymbol{\Sigma}_k = \sigma_k^2 \mathbf{I}$

This further constrains each component to be spherical but with potentially different sizes, reducing covariance parameters to just K values. This maintains the probabilistic framework of GMMs while approaching the geometric simplicity of K-means.

The GMM Likelihood Function   To find the optimal parameters for our mixture model, we use maximum likelihood estimation. For a dataset $\{\mathbf{x}_1, \mathbf{x}_2, \ldots, \mathbf{x}_N\}$, assuming indepen-
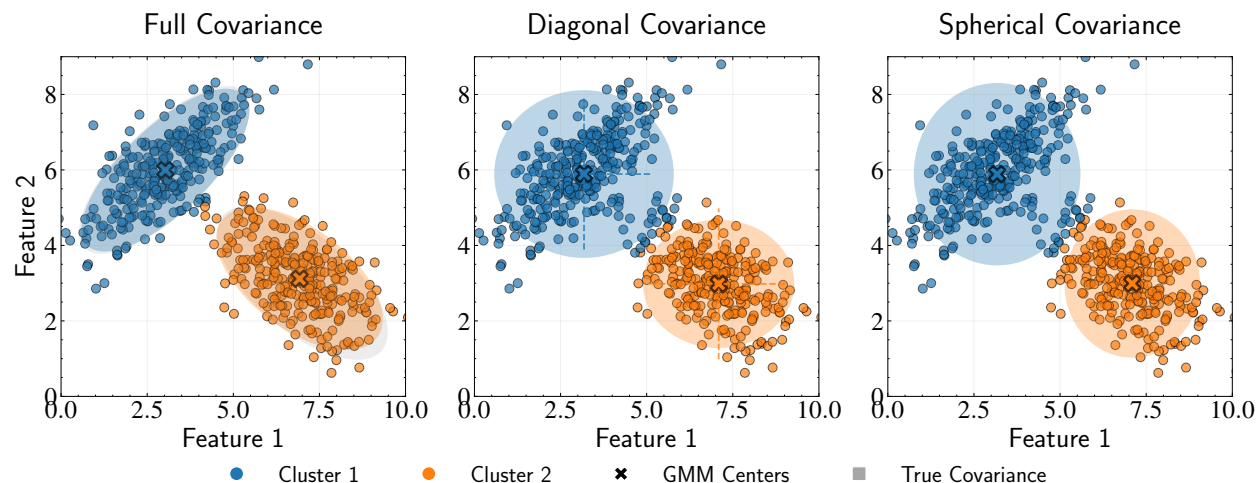
Figure 11.10: Comparison of covariance constraints in Gaussian Mixture Models using the same dataset with correlated features. **Left:** Full covariance matrices ($\mathbf{\Sigma}_k$) with $K \cdot D(D+1)/2$ parameters can capture correlations between features, allowing ellipses of any orientation to accurately model the true cluster shapes. **Middle:** Diagonal covariance matrices ($\mathbf{\Sigma}_k = \mathrm{diag}(\sigma_{k1}^2, \sigma_{k2}^2, \ldots, \sigma_{kD}^2)$) with $K \cdot D$ parameters constrain ellipses to align with coordinate axes, preventing the model from capturing feature correlations. This represents scenarios where different features vary independently within each cluster. **Right:** Spherical covariance matrices ($\mathbf{\Sigma}_k = \sigma_k^2 \mathbf{I}$) with just K parameters constrain clusters to be circular, similar to K-means but maintaining the probabilistic framework. These constraints illustrate the trade-off between model flexibility and computational efficiency.

dence between observations, the likelihood is:

$$L = \prod_{i=1}^{N} p(\mathbf{x}_i) = \prod_{i=1}^{N} \left[\sum_{k=1}^{K} \pi_k \mathcal{N}(\mathbf{x}_i | \boldsymbol{\mu}_k, \mathbf{\Sigma}_k) \right] \tag{11.27}$$

Taking the logarithm to convert the product into a sum:

$$\log L = \sum_{i=1}^{N} \log \left[\sum_{k=1}^{K} \pi_k \mathcal{N}(\mathbf{x}_i | \boldsymbol{\mu}_k, \mathbf{\Sigma}_k) \right] \tag{11.28}$$

This log-likelihood function presents optimization challenges that make direct approaches difficult. The summation inside the logarithm creates a complex, multimodal optimization landscape with many local maxima. Additionally, the interdependence between all parameters—mixture weights, means, and covariances—creates circular dependencies similar to what we encountered in K-means, but more complex.

Consider trying to find the gradient with respect to one of the mean vectors $\boldsymbol{\mu}_k$:

$$\frac{\partial \log L}{\partial \boldsymbol{\mu}_k} = \sum_{i=1}^{N} \frac{1}{\sum_{j=1}^{K} \pi_j \mathcal{N}(\mathbf{x}_i | \boldsymbol{\mu}_j, \boldsymbol{\Sigma}_j)} \cdot \frac{\partial}{\partial \boldsymbol{\mu}_k} \left[\pi_k \mathcal{N}(\mathbf{x}_i | \boldsymbol{\mu}_k, \boldsymbol{\Sigma}_k) \right] \tag{11.29}$$

This expression involves $\boldsymbol{\mu}_k$ in both the numerator and denominator of a complex fraction, making direct optimization extremely challenging. The same complexity arises for the covariance matrices and mixture weights.

These optimization challenges motivate the use of the Expectation-Maximization algorithm, which we can extend from our K-means experience to handle the full probabilistic framework of GMMs.

11.6   Expectation-Maximization for GMMs

The complex optimization landscape of GMM likelihood functions requires a more sophisticated approach than direct gradient methods. Fortunately, we can extend the Expectation-Maximization framework from K-means to handle the full probabilistic setting of GMMs. The key insight remains the same: alternate between estimating cluster memberships and updating model parameters.

Introducing Responsibilities   The central concept in GMM optimization is the "responsibility" that component k takes for explaining data point $\mathbf{x}_i$:

$$\gamma_{ik} = \frac{\pi_k \mathcal{N}(\mathbf{x}_i | \boldsymbol{\mu}_k, \boldsymbol{\Sigma}_k)}{\sum_{j=1}^{K} \pi_j \mathcal{N}(\mathbf{x}_i | \boldsymbol{\mu}_j, \boldsymbol{\Sigma}_j)} \tag{11.30}$$

This responsibility γ_{ik} represents the posterior probability that component k generated data point $\mathbf{x}_i$, given the current model parameters. It serves as the probabilistic analog to the binary assignment variables r_{ik} we used in K-means.

The key difference is that while K-means assignments could only be 0 or 1 (hard assignment), GMM responsibilities can take any value between 0 and 1 (soft assignment). This allows data points to have partial membership in multiple clusters, capturing uncertainty in borderline cases.

For each data point i, the responsibilities sum to 1: $\sum_{k=1}^{K} \gamma_{ik} = 1$. This constraint

ensures that the total "probability mass" for each point is properly distributed across all components.

The EM Algorithm for GMMs The EM algorithm for GMMs follows the same alternating optimization strategy as K-means, but now operates on probability distributions rather than discrete assignments.

Initialization: Choose starting values for the parameters $\{\pi_k\}, \{\boldsymbol{\mu}_k\}, \{\boldsymbol{\Sigma}_k\}$. Common strategies include:

- Using K-means results as initial estimates for means, then setting uniform mixture weights and identity covariances

- Randomly partitioning the data and computing initial statistics from each partition

- Using more sophisticated methods like K-means++ for center initialization

Expectation Step (E-step): Compute the responsibilities using the current parameter values:

$$\gamma_{ik} = \frac{\pi_k \mathcal{N}(\mathbf{x}_i | \boldsymbol{\mu}_k, \boldsymbol{\Sigma}_k)}{\sum_{j=1}^{K} \pi_j \mathcal{N}(\mathbf{x}_i | \boldsymbol{\mu}_j, \boldsymbol{\Sigma}_j)} \tag{11.31}$$

These responsibilities represent our current best estimates of which component generated each data point.

Maximization Step (M-step): Update the parameters using the current responsibilities. This step requires deriving update equations for each parameter type.

Deriving the M-step Updates In the M-step, we treat the responsibilities γ_{ik} as fixed and find the parameter values that maximize the log-likelihood. While the E-step was straightforward (just apply Bayes' rule), the M-step requires careful mathematical derivation for each parameter type. The key insight is that when responsibilities are fixed, we can optimize each parameter set independently.

Updating the Mean Vectors Let's start with the means, since they have the most direct geometric interpretation. For component k, we want to find the mean $\boldsymbol{\mu}_k$ that maximizes the log-likelihood when all other parameters are held fixed.

Starting with our log-likelihood:

$$\log L = \sum_{i=1}^{N} \log \left[\sum_{j=1}^{K} \pi_j \mathcal{N}(\mathbf{x}_i | \boldsymbol{\mu}_j, \boldsymbol{\Sigma}_j) \right] \tag{11.32}$$

Taking the derivative with respect to $\boldsymbol{\mu}_k$:

$$\frac{\partial \log L}{\partial \boldsymbol{\mu}_k} = \sum_{i=1}^{N} \frac{1}{\sum_{j=1}^{K} \pi_j \mathcal{N}(\mathbf{x}_i | \boldsymbol{\mu}_j, \boldsymbol{\Sigma}_j)} \cdot \frac{\partial}{\partial \boldsymbol{\mu}_k} [\pi_k \mathcal{N}(\mathbf{x}_i | \boldsymbol{\mu}_k, \boldsymbol{\Sigma}_k)] \tag{11.33}$$

Using the chain rule and the fact that $\frac{\partial}{\partial \boldsymbol{\mu}_k} \mathcal{N}(\mathbf{x}_i | \boldsymbol{\mu}_k, \boldsymbol{\Sigma}_k) = \mathcal{N}(\mathbf{x}_i | \boldsymbol{\mu}_k, \boldsymbol{\Sigma}_k) \boldsymbol{\Sigma}_k^{-1}(\mathbf{x}_i - \boldsymbol{\mu}_k)$:

$$\frac{\partial \log L}{\partial \boldsymbol{\mu}_k} = \sum_{i=1}^{N} \frac{\pi_k \mathcal{N}(\mathbf{x}_i | \boldsymbol{\mu}_k, \boldsymbol{\Sigma}_k)}{\sum_{j=1}^{K} \pi_j \mathcal{N}(\mathbf{x}_i | \boldsymbol{\mu}_j, \boldsymbol{\Sigma}_j)} \boldsymbol{\Sigma}_k^{-1}(\mathbf{x}_i - \boldsymbol{\mu}_k) \tag{11.34}$$

Recognizing that the fraction is our responsibility γ_{ik}:

$$\frac{\partial \log L}{\partial \boldsymbol{\mu}_k} = \sum_{i=1}^{N} \gamma_{ik} \boldsymbol{\Sigma}_k^{-1}(\mathbf{x}_i - \boldsymbol{\mu}_k) \tag{11.35}$$

Setting this equal to zero and solving for $\boldsymbol{\mu}_k$:

$$\sum_{i=1}^{N} \gamma_{ik} \boldsymbol{\Sigma}_k^{-1}(\mathbf{x}_i - \boldsymbol{\mu}_k) = 0 \tag{11.36}$$

$$\boldsymbol{\Sigma}_k^{-1} \sum_{i=1}^{N} \gamma_{ik}(\mathbf{x}_i - \boldsymbol{\mu}_k) = 0 \tag{11.37}$$

$$\sum_{i=1}^{N} \gamma_{ik} \mathbf{x}_i - \boldsymbol{\mu}_k \sum_{i=1}^{N} \gamma_{ik} = 0 \tag{11.38}$$

$$\boldsymbol{\mu}_k = \frac{\sum_{i=1}^{N} \gamma_{ik} \mathbf{x}_i}{\sum_{i=1}^{N} \gamma_{ik}} \tag{11.39}$$

This result is both mathematically elegant and intuitively sensible: the optimal mean is simply the weighted average of all data points, where the weights are the responsibilities. This directly generalizes the K-means result, where hard assignments $r_{ik} \in \{0, 1\}$ are replaced by soft responsibilities $\gamma_{ik} \in [0, 1]$.

Let's define the effective number of points assigned to component k as:

$$N_k = \sum_{i=1}^{N} \gamma_{ik} \tag{11.40}$$

With this notation, our mean update becomes:

$$\boldsymbol{\mu}_k^{new} = \frac{1}{N_k} \sum_{i=1}^{N} \gamma_{ik} \mathbf{x}_i \tag{11.41}$$

Updating the Covariance Matrices The covariance update is more complex but follows the same principle. We want each component's covariance to reflect the spread of data points that belong to it, weighted by their responsibility values.

The derivation requires matrix calculus, so we'll differentiate with respect to the precision matrix $\boldsymbol{\Sigma}_k^{-1}$ and then invert the result. This approach avoids some technical complications while maintaining mathematical rigor.

First, let's recall the multivariate Gaussian distribution:

$$\mathcal{N}(\mathbf{x}|\boldsymbol{\mu}, \boldsymbol{\Sigma}) = \frac{1}{(2\pi)^{D/2}|\boldsymbol{\Sigma}|^{1/2}} \exp\left(-\frac{1}{2}(\mathbf{x} - \boldsymbol{\mu})^T \boldsymbol{\Sigma}^{-1}(\mathbf{x} - \boldsymbol{\mu})\right) \tag{11.42}$$

Taking the logarithm:

$$\ln \mathcal{N}(\mathbf{x}|\boldsymbol{\mu}, \boldsymbol{\Sigma}) = -\frac{D}{2} \ln(2\pi) - \frac{1}{2} \ln |\boldsymbol{\Sigma}| - \frac{1}{2}(\mathbf{x} - \boldsymbol{\mu})^T \boldsymbol{\Sigma}^{-1}(\mathbf{x} - \boldsymbol{\mu}) \tag{11.43}$$

Since we're differentiating with respect to $\boldsymbol{\Sigma}_k^{-1}$, we rewrite the determinant term using $|\boldsymbol{\Sigma}| = 1/|\boldsymbol{\Sigma}^{-1}|$, giving us $\ln |\boldsymbol{\Sigma}| = -\ln |\boldsymbol{\Sigma}^{-1}|$.

We need two matrix calculus identities:

$$\frac{\partial}{\partial \mathbf{A}} \ln |\mathbf{A}| = \mathbf{A}^{-1} \quad \text{and} \quad \frac{\partial}{\partial \mathbf{A}} \mathbf{x}^T \mathbf{A} \mathbf{x} = \mathbf{x}\mathbf{x}^T \tag{11.44}$$

Following the same pattern as for the means, we compute:

$$\frac{\partial}{\partial \mathbf{\Sigma}_k^{-1}} \ln L = \sum_{i=1}^{N} \frac{1}{\sum_{j=1}^{K} \pi_j \mathcal{N}(\mathbf{x}_i|\boldsymbol{\mu}_j, \mathbf{\Sigma}_j)} \cdot \frac{\partial}{\partial \mathbf{\Sigma}_k^{-1}} [\pi_k \mathcal{N}(\mathbf{x}_i|\boldsymbol{\mu}_k, \mathbf{\Sigma}_k)] \tag{11.45}$$

Using the chain rule:

$$\frac{\partial}{\partial \mathbf{\Sigma}_k^{-1}} [\pi_k \mathcal{N}(\mathbf{x}_i|\boldsymbol{\mu}_k, \mathbf{\Sigma}_k)] = \pi_k \mathcal{N}(\mathbf{x}_i|\boldsymbol{\mu}_k, \mathbf{\Sigma}_k) \cdot \frac{\partial}{\partial \mathbf{\Sigma}_k^{-1}} \ln \mathcal{N}(\mathbf{x}_i|\boldsymbol{\mu}_k, \mathbf{\Sigma}_k) \tag{11.46}$$

Computing the derivative of the log Gaussian:

$$\frac{\partial}{\partial \mathbf{\Sigma}_k^{-1}} \ln \mathcal{N}(\mathbf{x}_i|\boldsymbol{\mu}_k, \mathbf{\Sigma}_k) = \frac{\partial}{\partial \mathbf{\Sigma}_k^{-1}} \left[-\frac{D}{2} \ln(2\pi) + \frac{1}{2} \ln |\mathbf{\Sigma}_k^{-1}| - \frac{1}{2}(\mathbf{x}_i - \boldsymbol{\mu}_k)^T \mathbf{\Sigma}_k^{-1}(\mathbf{x}_i - \boldsymbol{\mu}_k) \right] \tag{11.47}$$

$$= \frac{1}{2}\mathbf{\Sigma}_k - \frac{1}{2}(\mathbf{x}_i - \boldsymbol{\mu}_k)(\mathbf{x}_i - \boldsymbol{\mu}_k)^T \tag{11.48}$$

Substituting back and using responsibilities:

$$\frac{\partial}{\partial \mathbf{\Sigma}_k^{-1}} \ln L = \sum_{i=1}^{N} \gamma_{ik} \left[\frac{1}{2}\mathbf{\Sigma}_k - \frac{1}{2}(\mathbf{x}_i - \boldsymbol{\mu}_k)(\mathbf{x}_i - \boldsymbol{\mu}_k)^T \right] \tag{11.49}$$

Setting equal to zero and solving:

$$\sum_{i=1}^{N} \gamma_{ik} \left[\frac{1}{2}\mathbf{\Sigma}_k - \frac{1}{2}(\mathbf{x}_i - \boldsymbol{\mu}_k)(\mathbf{x}_i - \boldsymbol{\mu}_k)^T \right] = 0 \tag{11.50}$$

$$\frac{1}{2}\mathbf{\Sigma}_k \sum_{i=1}^{N} \gamma_{ik} - \frac{1}{2} \sum_{i=1}^{N} \gamma_{ik}(\mathbf{x}_i - \boldsymbol{\mu}_k)(\mathbf{x}_i - \boldsymbol{\mu}_k)^T = 0 \tag{11.51}$$

$$\mathbf{\Sigma}_k^{new} = \frac{1}{N_k} \sum_{i=1}^{N} \gamma_{ik}(\mathbf{x}_i - \boldsymbol{\mu}_k^{new})(\mathbf{x}_i - \boldsymbol{\mu}_k^{new})^T \tag{11.52}$$

This result again has a clear interpretation: the optimal covariance is the responsibility-weighted sample covariance. This generalizes the standard covariance formula by giving each data point a weight proportional to how much it "belongs" to the component.

Updating the Mixture Weights Finally, we derive the update for mixture weights, which must satisfy the constraint $\sum_{k=1}^{K} \pi_k = 1$. This requires Lagrange multipliers, a technique we've used before for constrained optimization, as we have seen in the last chapter.

We form the Lagrangian:

$$\mathcal{L} = \log L + \lambda \left(1 - \sum_{k=1}^{K} \pi_k \right) \tag{11.53}$$

Taking the derivative with respect to π_k and setting to zero:

$$\frac{\partial \mathcal{L}}{\partial \pi_k} = \sum_{i=1}^{N} \frac{\mathcal{N}(\mathbf{x}_i | \boldsymbol{\mu}_k, \boldsymbol{\Sigma}_k)}{\sum_{j=1}^{K} \pi_j \mathcal{N}(\mathbf{x}_i | \boldsymbol{\mu}_j, \boldsymbol{\Sigma}_j)} - \lambda = 0 \tag{11.54}$$

Multiplying both sides by π_k and summing over all components:

$$\sum_{k=1}^{K} \pi_k \sum_{i=1}^{N} \frac{\mathcal{N}(\mathbf{x}_i | \boldsymbol{\mu}_k, \boldsymbol{\Sigma}_k)}{\sum_{j=1}^{K} \pi_j \mathcal{N}(\mathbf{x}_i | \boldsymbol{\mu}_j, \boldsymbol{\Sigma}_j)} = \lambda \sum_{k=1}^{K} \pi_k = \lambda \tag{11.55}$$

The left side simplifies because the inner sum equals 1 for each data point:

$$\sum_{i=1}^{N} \sum_{k=1}^{K} \frac{\pi_k \mathcal{N}(\mathbf{x}_i | \boldsymbol{\mu}_k, \boldsymbol{\Sigma}_k)}{\sum_{j=1}^{K} \pi_j \mathcal{N}(\mathbf{x}_i | \boldsymbol{\mu}_j, \boldsymbol{\Sigma}_j)} = \sum_{i=1}^{N} 1 = N = \lambda \tag{11.56}$$

Substituting back into our original equation:

$$\sum_{i=1}^{N} \gamma_{ik} = N \pi_k \tag{11.57}$$

$$\pi_k^{new} = \frac{N_k}{N} \tag{11.58}$$

This result is intuitive: the optimal mixture weight equals the average responsibility that component k takes across all data points. Components that explain more data points get higher weights in the mixture.

The Complete Algorithm The complete EM algorithm for GMMs consists of:
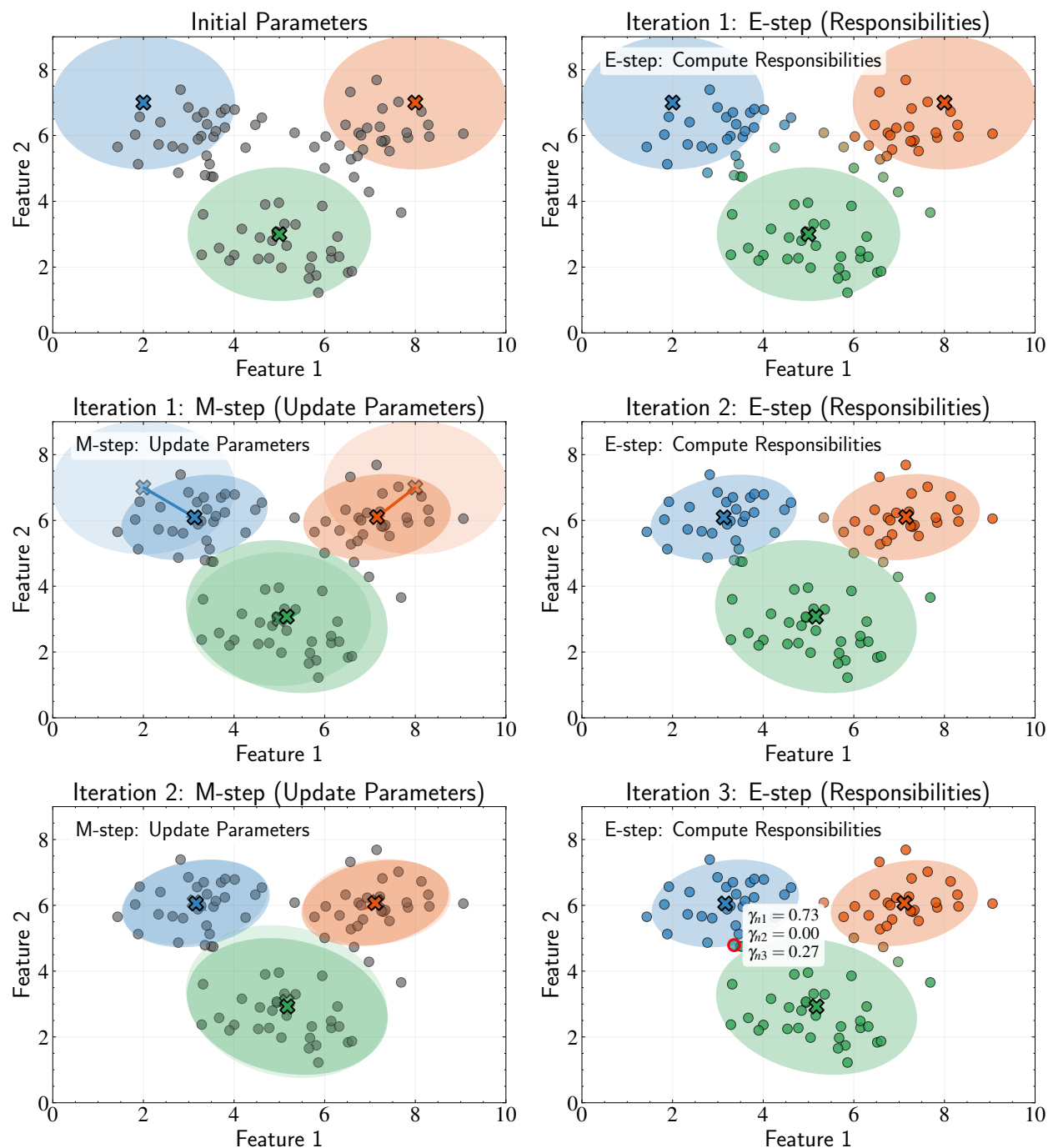
Figure 11.11: Expectation-Maximization (EM) algorithm for Gaussian Mixture Models. **Top row:** Initial parameters with spherical covariances (left) and the first E-step showing responsibilities γ_{ik} as color intensities (right). **Middle row:** First M-step updating means, covariance matrices, and weights (left), followed by the second E-step with refined responsibilities (right). **Bottom row:** Second M-step further refining parameters (left) and final E-step showing a point with membership in multiple components highlighted in red (right). Unlike K-means' hard assignments, GMM uses soft probabilistic assignment through the responsibility values γ_{ik}, capturing clusters with different shapes and orientations through component-specific covariance matrices.

- **Initialize** parameters $\{\pi_k\}, \{\boldsymbol{\mu}_k\}, \{\boldsymbol{\Sigma}_k\}$

- **E-step**: Compute responsibilities

$$\gamma_{ik} = \frac{\pi_k \mathcal{N}(\mathbf{x}_i | \boldsymbol{\mu}_k, \boldsymbol{\Sigma}_k)}{\sum_{j=1}^{K} \pi_j \mathcal{N}(\mathbf{x}_i | \boldsymbol{\mu}_j, \boldsymbol{\Sigma}_j)} \tag{11.59}$$

- **M-step**: Update parameters

$$N_k = \sum_{i=1}^{N} \gamma_{ik} \tag{11.60}$$

$$\boldsymbol{\mu}_k^{new} = \frac{1}{N_k} \sum_{i=1}^{N} \gamma_{ik} \mathbf{x}_i \tag{11.61}$$

$$\boldsymbol{\Sigma}_k^{new} = \frac{1}{N_k} \sum_{i=1}^{N} \gamma_{ik} (\mathbf{x}_i - \boldsymbol{\mu}_k^{new})(\mathbf{x}_i - \boldsymbol{\mu}_k^{new})^T \tag{11.62}$$

$$\pi_k^{new} = \frac{N_k}{N} \tag{11.63}$$

- **Repeat** E-step and M-step until convergence

Convergence and Local Optima Like K-means, the EM algorithm for GMMs guarantees that the likelihood increases (or remains constant) at each iteration. However, it typically converges to a local maximum rather than the global maximum. The final solution depends on initialization, making it common practice to run the algorithm multiple times with different starting points and select the solution with the highest likelihood.

The initialization sensitivity in GMMs is generally more pronounced than in K-means because of the increased parameter space and more complex likelihood surface. Good initialization strategies, such as using K-means results as starting points, can significantly improve both the quality of final solutions and convergence speed.

11.7   Advantages of Gaussian Mixture Models

Having developed the mathematical machinery for GMMs, we can now examine how they address the limitations of K-means while providing additional capabilities. The probabilistic framework of GMMs offers several key advantages that make them particularly well-suited for complex clustering tasks.
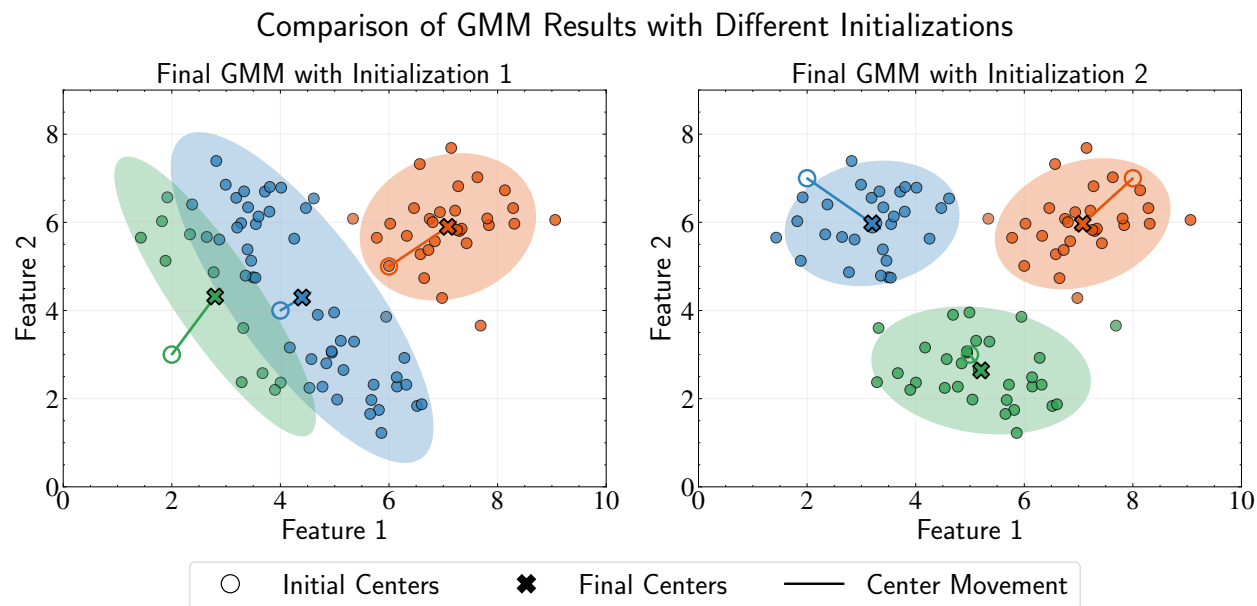
Figure 11.12: Comparison of Gaussian Mixture Model results with different initializations. Initial component centers are shown as hollow circles, final centers as X markers, with arrows indicating movement during EM optimization. **Left:** Poor initialization leading to a suboptimal fit where the algorithm fails to properly identify the true underlying clusters. **Right:** Better initialization resulting in a fit that accurately captures the true cluster structure. The covariance ellipses show the shape and orientation of each Gaussian component. This comparison demonstrates how the EM algorithm for GMMs can converge to different local optima depending on initialization, highlighting the importance of proper starting conditions in mixture modeling.

The Connection to K-means K-means and GMMs are closely related, with K-means being a special case of GMM under specific constraints. We can recover K-means from GMM by imposing three key restrictions:

- **Equal mixture weights**: Set $\pi_k = 1/K$ for all components

- **Identical spherical covariances**: Use $\boldsymbol{\Sigma}_k = \sigma^2 \mathbf{I}$ for all components

- **Hard assignments**: As $\sigma^2 \to 0$, the responsibilities γ_{ik} approach the binary indicators r_{ik} used in K-means

This relationship shows that K-means represents the most constrained version of the GMM framework. As the covariance becomes infinitesimally small, each data point's responsibility becomes concentrated entirely on the closest cluster center, effectively creating hard boundaries between clusters.

Soft Assignment and Uncertainty Quantification Perhaps the most important advantage of GMMs over K-means is their use of soft assignments. The responsibility γ_{ik} represents the probability that data point i belongs to cluster k, providing a natural measure of uncertainty in cluster membership.

This proves crucial in astronomy, where boundaries between different populations are often fuzzy. When trying to separate different stellar populations based on chemical abundances, stars near the boundaries between populations might share characteristics of multiple groups. GMMs acknowledge this uncertainty instead of forcing arbitrary hard assignments.

Flexible Cluster Shapes K-means inherently assumes that clusters are spherical in shape, a consequence of using Euclidean distance and isotropic covariance matrices. GMMs, in contrast, can model clusters with arbitrary elliptical shapes through their component-specific covariance matrices $\mathbf{\Sigma}_k$.

This flexibility allows GMMs to better capture the true structure of astronomical data. The eigenvalues and eigenvectors of the covariance matrices directly characterize the size, shape, and orientation of elliptical clusters, enabling more accurate representation of natural data distributions.

Probabilistic Generative Framework GMMs are probabilistic generative models, meaning they capture the full probability distribution of the data rather than just cluster assignments. This probabilistic foundation provides several powerful capabilities that extend well beyond simple clustering.

Synthetic Data Generation: Once we've fit a GMM to our data, we can generate new synthetic data points that follow the same distribution. The process involves two steps: first, select a component k with probability π_k, then draw a sample from the corresponding Gaussian distribution $\mathcal{N}(\boldsymbol{\mu}_k, \mathbf{\Sigma}_k)$.

This capability proves valuable for creating realistic mock catalogs in astronomy. A GMM trained on observed stellar parameters can generate synthetic stellar populations that preserve the correlations and distributions of the original data, enabling more realistic simulations for testing survey selection functions or understanding observational biases.

Outlier Detection: The generative nature of GMMs allows us to compute the

probability density for any data point:

$$p(\mathbf{x}_*) = \sum_{k=1}^{K} \pi_k \mathcal{N}(\mathbf{x}_* | \boldsymbol{\mu}_k, \boldsymbol{\Sigma}_k) \tag{11.64}$$
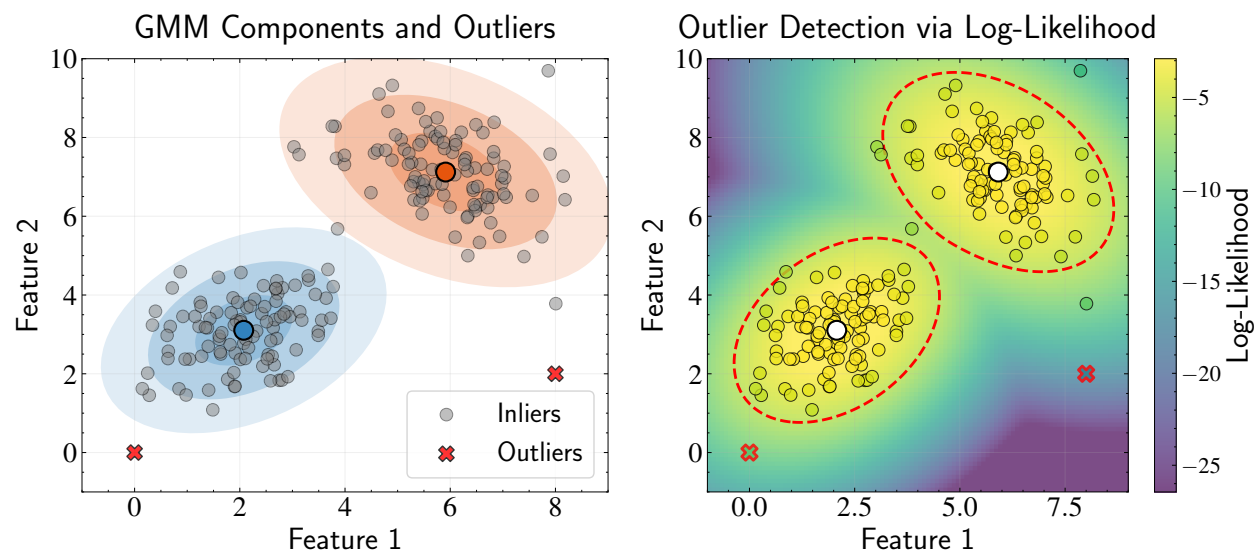
Figure 11.13: Using Gaussian Mixture Models for outlier detection. **Left:** A GMM with two components fitted to data (gray points) with outliers (red X markers) manually added. Ellipses show the 1, 2, and 3 standard deviation contours for each Gaussian component. **Right:** Log-likelihood landscape visualized as a heatmap, where points with low likelihood values (darker colors) are potential outliers. The dashed red contour represents an outlier threshold at the 5th percentile of likelihood values. This demonstrates how the probability density $p(\mathbf{x})$ provided by GMMs can naturally identify data points that lie in low-density regions and are unlikely to have been generated by the estimated model, making GMMs valuable for anomaly detection in astronomical data where outliers often represent scientifically interesting objects.

Data points with low probability density—those that lie far from all cluster centers or in low-density regions where $p(\mathbf{x}) \ll 1$—can be identified as potential outliers. In astronomy, such outliers often represent the most scientifically interesting objects. Stars with unusual chemical abundance patterns might indicate unique nucleosynthetic pathways, while galaxies with atypical properties might challenge our current understanding of galaxy formation.

By quantifying precisely how "unusual" an object is through its probability density, GMMs provide a principled approach to anomaly detection that goes beyond simple distance-based measures. This is particularly valuable in astronomical applications where outliers often represent rare but important phenomena rather than measurement errors.

Density Estimation: GMMs can estimate the probability density function of complex, multimodal data distributions. This allows us to understand not just where clusters are located, but how probability mass is distributed throughout the feature space. Such information can reveal important physical insights about the processes that generate astronomical populations and help identify regions of parameter space that are under-populated or unexplored.

11.8 Model Selection with Information Criteria

Throughout our development of K-means and Gaussian Mixture Models, we have assumed that the number of clusters K is known beforehand. In practice, however, determining this value represents one of the most challenging aspects of clustering analysis. This question reflects the broader statistical problem of model selection—how to choose the model complexity that best explains our data without overfitting.

While we discussed the elbow method and silhouette analysis for K-means, these approaches provide primarily qualitative guidance. For GMMs, we can leverage their probabilistic foundation to apply more principled statistical criteria: the Bayesian Information Criterion (BIC) and the Akaike Information Criterion (AIC).

The Model Selection Challenge Both BIC and AIC address the same fundamental challenge: balancing model fit against model complexity. As we increase the number of clusters K, our model becomes more flexible and can fit the data more closely, with the log-likelihood monotonically increasing. However, improved fit comes at the cost of additional parameters that may capture noise rather than genuine structure.

Taking this to extremes illustrates the problem clearly. With $K = N$ (one cluster per data point), we would achieve perfect "fit" in terms of likelihood but learn nothing about underlying structure. Conversely, with $K = 1$ (all data in one cluster), we would have maximum simplicity but potentially poor representation of heterogeneous data.

Information criteria formalize this trade-off by penalizing the model's likelihood based on its complexity. All such criteria rely on the principle of parsimony, often called "Occam's razor"—when multiple models explain the data equally well, we should prefer the simplest one. This principle helps us avoid overfitting by preventing models from becoming unnecessarily complex.

11.8.1 The Bayesian Information Criterion (BIC)

The Bayesian Information Criterion, introduced by Schwarz (1978), derives from a Bayesian approach to model selection. It approximates the Bayes factor, which compares the posterior probabilities of different models. For a GMM with K components, BIC is defined as:

$$\text{BIC} = -2\ln(\hat{L}) + P\ln(N) \tag{11.65}$$

where $\hat{L}$ is the maximum likelihood of the model, P is the number of free parameters, and N is the number of data points.

For a Gaussian Mixture Model, counting the free parameters requires careful consideration of the covariance structure. For full-covariance GMMs with K components in D dimensions:

$$P = (K-1) + KD + K\frac{D(D+1)}{2} = K\left(1 + D + \frac{D(D+1)}{2}\right) - 1 \tag{11.66}$$

with fewer parameters for diagonal ($P = (K-1) + KD + KD$) or spherical ($P = (K-1) + KD + K$) covariance structures.

Bayesian Foundation of BIC   To understand BIC's theoretical foundation, we need to extend our Bayesian framework to model selection. When comparing different models, we treat the model itself as a variable. Let $\mathcal{M}_K$ denote a model with K components. The posterior for model $\mathcal{M}_K$ given data $\mathbf{X}$ is:

$$p(\mathcal{M}_K|\mathbf{X}) = \frac{p(\mathbf{X}|\mathcal{M}_K)p(\mathcal{M}_K)}{p(\mathbf{X})} \tag{11.67}$$

When we have no prior preference among models ($p(\mathcal{M}_K)$ is uniform), the posterior probability becomes proportional to the marginal likelihood $p(\mathbf{X}|\mathcal{M}_K)$. This marginal likelihood integrates over all possible parameter values:

$$p(\mathbf{X}|\mathcal{M}_K) = \int p(\mathbf{X}|\boldsymbol{\theta}_K, \mathcal{M}_K)p(\boldsymbol{\theta}_K|\mathcal{M}_K)d\boldsymbol{\theta}_K \tag{11.68}$$

This integration automatically implements Occam's razor through a mathematical elegance. To understand this intuitively, consider what happens in parameter space:

A complex model (with many parameters) spreads its prior probability $p(\boldsymbol{\theta}_K|\mathcal{M}_K)$

thinly over a vast parameter space. Imagine this prior as a probability density distributed across all possible parameter combinations. As the number of parameters increases, this density must be spread more thinly to maintain a total probability of 1. In contrast, a simpler model concentrates its prior probability in a much smaller region of parameter space, resulting in higher probability density in that region.

When we integrate the product of the likelihood and prior over the entire parameter space, two scenarios can occur:

- If the complex model doesn't fit the data substantially better than the simpler model, its likelihood won't be high enough to compensate for its thinly spread prior, resulting in a lower marginal likelihood.

- Only if the complex model provides a dramatically better fit (much higher likelihood) across a significant portion of its parameter space will it overcome this inherent disadvantage.

This mathematical behavior naturally favors simpler explanations unless the data strongly supports additional complexity—precisely the principle of Occam's razor implemented through Bayesian integration.

However, this integral is generally intractable for GMMs. The Laplace approximation provides a solution by approximating the posterior distribution around its mode. Let's derive this more explicitly. The key idea is to approximate the logarithm of the integrand at its maximum:

$$\ln[p(\mathbf{X}|\boldsymbol{\theta}_K, \mathcal{M}_K)p(\boldsymbol{\theta}_K|\mathcal{M}_K)] \approx \ln[p(\mathbf{X}|\hat{\boldsymbol{\theta}}_K, \mathcal{M}_K)p(\hat{\boldsymbol{\theta}}_K|\mathcal{M}_K)] - \frac{1}{2}(\boldsymbol{\theta}_K - \hat{\boldsymbol{\theta}}_K)^T\mathbf{H}(\boldsymbol{\theta}_K - \hat{\boldsymbol{\theta}}_K)$$

$$(11.69)$$

Here, $\mathbf{H}$ is the Hessian matrix of the negative log posterior evaluated at $\hat{\boldsymbol{\theta}}_K$. For large sample sizes, the likelihood dominates the prior, making $\mathbf{H}$ approximately equal to the observed information matrix $\mathcal{I}(\hat{\boldsymbol{\theta}}_K) = -\nabla^2 \ln p(\mathbf{X}|\hat{\boldsymbol{\theta}}_K, \mathcal{M}_K)$.

Because the log-likelihood is a sum over N independent observations:

$$\ln p(\mathbf{X}|\boldsymbol{\theta}_K, \mathcal{M}_K) = \sum_{i=1}^{N} \ln p(\mathbf{x}_i|\boldsymbol{\theta}_K, \mathcal{M}_K) \tag{11.70}$$

The Hessian is also a sum over N terms:

$$\mathbf{H} = -\nabla^2 \ln p(\mathbf{X}|\boldsymbol{\theta}_K, \mathcal{M}_K) = -\sum_{i=1}^{N} \nabla^2 \ln p(\mathbf{x}_i|\boldsymbol{\theta}_K, \mathcal{M}_K) \tag{11.71}$$

This means $\mathbf{H}$ scales linearly with N. We can express this as $\mathbf{H} = N \cdot \mathcal{J}(\hat{\boldsymbol{\theta}}_K)$, where $\mathcal{J}(\hat{\boldsymbol{\theta}}_K)$ is the average information matrix per observation.

With this Gaussian approximation, the integral becomes:

$$p(\mathbf{X}|\mathcal{M}_K) \approx p(\mathbf{X}|\hat{\boldsymbol{\theta}}_K, \mathcal{M}_K)p(\hat{\boldsymbol{\theta}}_K|\mathcal{M}_K) \int \exp\left(-\frac{1}{2}(\boldsymbol{\theta}_K - \hat{\boldsymbol{\theta}}_K)^T \mathbf{H}(\boldsymbol{\theta}_K - \hat{\boldsymbol{\theta}}_K)\right) d\boldsymbol{\theta}_K \tag{11.72}$$

$$= p(\mathbf{X}|\hat{\boldsymbol{\theta}}_K, \mathcal{M}_K)p(\hat{\boldsymbol{\theta}}_K|\mathcal{M}_K) \cdot (2\pi)^{P/2}|\mathbf{H}|^{-1/2} \tag{11.73}$$

For the determinant of $\mathbf{H}$, a key property of matrices is that scaling a $P \times P$ matrix by a factor N scales its determinant by N^P:

$$|\mathbf{H}| = |N \cdot \mathcal{J}(\hat{\boldsymbol{\theta}}_K)| = N^P \cdot |\mathcal{J}(\hat{\boldsymbol{\theta}}_K)| \tag{11.74}$$

Taking the negative logarithm of the model evidence and multiplying by 2:

$$-2\ln p(\mathbf{X}|\mathcal{M}_K) \approx -2\ln p(\mathbf{X}|\hat{\boldsymbol{\theta}}_K, \mathcal{M}_K) - 2\ln p(\hat{\boldsymbol{\theta}}_K|\mathcal{M}_K) - P\ln(2\pi) + \ln|\mathbf{H}| \tag{11.75}$$

$$= -2\ln p(\mathbf{X}|\hat{\boldsymbol{\theta}}_K, \mathcal{M}_K) - 2\ln p(\hat{\boldsymbol{\theta}}_K|\mathcal{M}_K) - P\ln(2\pi) + P\ln(N) + \ln|\mathcal{J}(\hat{\boldsymbol{\theta}}_K)| \tag{11.76}$$

Now, it's crucial to understand which terms dominate as N becomes large. Let's analyze the scaling of each term:

- The log-likelihood term $-2\ln p(\mathbf{X}|\hat{\boldsymbol{\theta}}_K, \mathcal{M}_K)$ scales as $\mathcal{O}(N)$ because it sums over all N data points.

- The penalty term $P\ln(N)$ scales as $\mathcal{O}(\ln N)$, growing much more slowly than the likelihood term.

- The remaining terms—the log-prior $-2\ln p(\hat{\boldsymbol{\theta}}_K|\mathcal{M}_K)$, the constant $-P\ln(2\pi)$, and the determinant of the average information matrix $\ln|\mathcal{J}(\hat{\boldsymbol{\theta}}_K)|$—do not depend on N at all, making them $\mathcal{O}(1)$.

When comparing models as $N \to \infty$, the dominant term in the expression is the log-likelihood $-2 \ln p(\mathbf{X}|\hat{\boldsymbol{\theta}}_K, \mathcal{M}_K)$, followed by the penalty term $P \ln(N)$. The other terms become relatively negligible as they don't scale with N. Therefore, as N grows large:

$$-2 \ln p(\mathbf{X}|\mathcal{M}_K) \approx -2 \ln p(\mathbf{X}|\hat{\boldsymbol{\theta}}_K, \mathcal{M}_K) + P \ln(N) + \mathcal{O}(1) \tag{11.77}$$

This asymptotic behavior gives us the BIC formula. We retain the log-likelihood term and the complexity penalty term $P \ln(N)$, as they have the most significant impact on model selection for large datasets, while dropping terms that become relatively insignificant in the asymptotic limit.

BIC Properties and Interpretation BIC has several important properties that make it particularly valuable for model selection:

Consistency: Under regularity conditions, BIC will select the true model as $N \to \infty$, assuming the true model is among the candidates considered.

Stronger penalty: The $P \ln(N)$ penalty grows with sample size, making BIC increasingly conservative as more data becomes available. This reflects the Bayesian philosophy that with more evidence, we should require stronger justification for complex explanations.

When comparing models, we select the one with the lowest BIC value. The BIC difference $\Delta \text{BIC} = \text{BIC}_1 - \text{BIC}_2$ can be interpreted as twice the log Bayes factor, providing a measure of evidence strength for model 2 over model 1.

It's important to emphasize that BIC's validity depends critically on its underlying assumptions. The asymptotic approximation requires large sample sizes relative to the model complexity, well-behaved likelihoods, and appropriately diffuse priors. In astronomical applications, these conditions aren't always met—particularly when dealing with small samples, complex parameter interdependencies, or multimodal distributions. Therefore, while BIC provides valuable guidance, we should not treat it as absolute ground truth but rather as one piece of evidence that requires case-by-case evaluation in conjunction with scientific domain knowledge.

11.8.2 The Akaike Information Criterion (AIC)

The Akaike Information Criterion approaches model selection from information theory rather than Bayesian statistics. AIC connects to concepts of entropy and mutual information,

Model Selection with Information Criteria
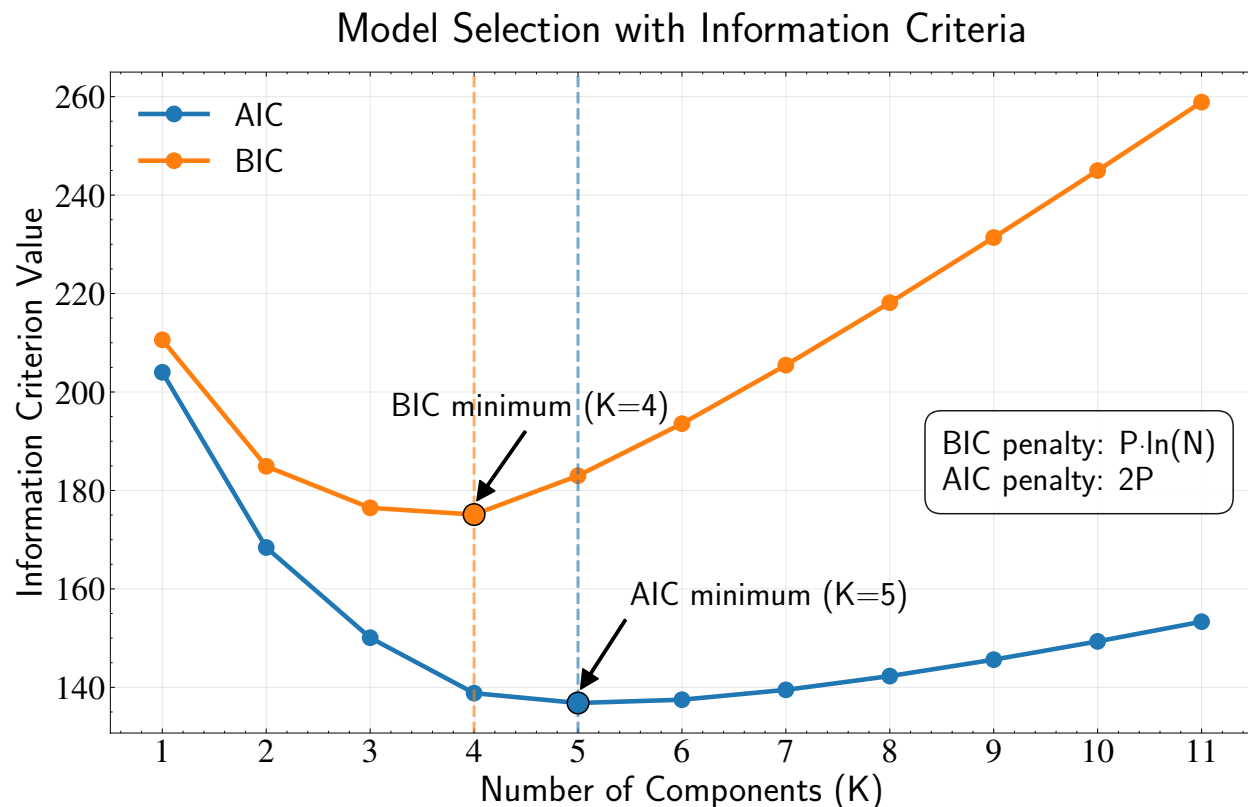
Figure 11.14: Model selection for Gaussian Mixture Models using information criteria. The plot shows how AIC (blue) and BIC (orange) values change as a function of the number of components (K). Both criteria balance the model fit (log-likelihood) against model complexity (number of parameters). The BIC applies a stronger penalty term $P \ln(N)$ compared to AIC's penalty of $2P$, where P is the number of parameters and N is the sample size. Consequently, BIC typically favors simpler models (lower K) than AIC. AIC tends to identify more clusters because it focuses on optimizing prediction accuracy rather than finding the "true" model, making it more willing to accept additional complexity when it offers even modest improvements in fit. The minimum of each curve indicates the optimal number of components according to that criterion. After reaching their minima, both criteria begin to increase as the penalty for additional complexity outweighs the diminishing improvements in fit. This demonstrates how information criteria implement Occam's razor by mathematically formalizing the trade-off between model fit and complexity.

focusing on the model's ability to predict new data rather than identifying the "true" model.

The standard AIC is defined as:

$$\text{AIC} = -2 \ln(\hat{L}) + 2P \tag{11.78}$$

Compared to BIC, AIC has a smaller penalty for model complexity ($2P$ instead of

$P \ln(N)$), meaning it tends to favor more complex models, especially for large sample sizes where $\ln(N) > 2$.

Information-Theoretic Foundation   AIC's foundation rests on information theory and the concept of Kullback-Leibler divergence. Akaike's insight was connecting model selection to the information-theoretic goal of minimizing the distance between our fitted model and the true data-generating process.

When we use the same data to both fit a model and evaluate its performance, we introduce an optimistic bias—we overestimate how well our model will generalize to new data. This bias increases with model complexity because complex models have greater capacity to fit noise rather than signal.

Remarkably, Akaike demonstrated that this bias can be asymptotically approximated by the number of parameters P. Therefore, to estimate how well our model will perform on new data, we subtract this bias from our observed log-likelihood, yielding the AIC formula.

For small sample sizes, a corrected version (AICc) provides better performance:

$$\mathrm{AIC}_c = \mathrm{AIC} + \frac{2P(P+1)}{N-P-1} \tag{11.79}$$

This correction addresses the limitation that standard AIC works well asymptotically but can be biased when sample size is limited relative to model complexity. The correction term increases as either P grows or N shrinks, providing more aggressive penalty for complex models when data is scarce.

Philosophical Differences Between BIC and AIC   The distinction between BIC and AIC reflects different philosophical approaches to model selection:

BIC Philosophy: Assumes one true model exists among the candidates and aims to identify it. BIC is "consistent"—it will select the true model as sample size increases, assuming the true model is in the candidate set.

AIC Philosophy: Acknowledges that all models are approximations and focuses on finding the model that makes the best predictions on new data. AIC is "efficient"—it minimizes expected prediction error even when all candidate models are misspecified.

These philosophical differences manifest practically. BIC tends to select simpler mod-

els than AIC, especially for large datasets. BIC's stronger penalty ($P \ln(N)$ versus $2P$) makes it more conservative about adding complexity.

Practical Application to GMMs   In practice, when applying these criteria to GMMs, we compute the log-likelihood at convergence of the EM algorithm:

$$\ln(\hat{L}) = \sum_{i=1}^{N} \ln \left(\sum_{k=1}^{K} \hat{\pi}_k \mathcal{N}(\mathbf{x}_i | \hat{\boldsymbol{\mu}}_k, \hat{\boldsymbol{\Sigma}}_k) \right) \tag{11.80}$$

where $\hat{\pi}_k$, $\hat{\boldsymbol{\mu}}_k$, and $\hat{\boldsymbol{\Sigma}}_k$ are the maximum likelihood estimates.

When BIC and AIC agree on the optimal number of clusters, we have strong evidence for that choice. When they disagree, examining both solutions often provides deeper insights. The BIC-selected model typically identifies the most prominent, well-separated clusters, while the AIC-selected model might capture more subtle structures that could be scientifically relevant.

This complementary use of both criteria reflects the reality that model selection in clustering often depends on the specific scientific question. For exploratory analysis aimed at understanding broad population structure, BIC's conservative approach may be preferred. For detailed studies where subtle subpopulations might be scientifically important, AIC's willingness to embrace complexity could prove valuable.

The model selection problem in clustering parallels what we encountered with dimensionality reduction in PCA. Both involve determining appropriate model complexity—the number of principal components in PCA or clusters in GMM. Information criteria provide a consistent framework for such decisions across different unsupervised learning tasks, though the specific choice remains context-dependent.

11.9   Summary

In this chapter, we have explored clustering as a powerful approach for discovering structure in unlabeled astronomical data. Our journey began with K-means clustering, a geometric method that partitions data by minimizing the distance between points and their assigned cluster centers. While K-means offers computational efficiency and intuitive results, it comes with important limitations: hard assignments that provide no uncertainty quantification, an assumption of spherical clusters of similar sizes, and sensitivity to outliers.

These limitations naturally led us to Gaussian Mixture Models (GMMs), which address K-means' shortcomings through a fully probabilistic framework. GMMs model data as arising from a mixture of Gaussian distributions, enabling soft assignments where data points can have fractional membership in multiple clusters. This probabilistic foundation allows GMMs to capture uncertainty in cluster assignments, model elliptical clusters with different orientations and sizes, and provide a complete generative model of the data distribution.

The expectation-maximization (EM) algorithm emerged as a powerful framework for optimizing both K-means and GMMs. By alternating between computing cluster assignments (E-step) and updating model parameters (M-step), EM decomposes complex optimization problems into sequences of simpler ones that can be solved analytically. This approach revealed the deep connection between K-means and GMMs: K-means can be understood as a special case of GMMs with equal mixture weights, identical spherical covariances, and hard assignments obtained in the limit of vanishing variance.

Our exploration revealed a progression from geometric intuition to probabilistic sophistication. K-means provides geometric clarity through its direct minimization of within-cluster distances, making it an ideal starting point for understanding clustering concepts. GMMs build upon this foundation by embedding the geometric intuition within a probabilistic framework that can handle uncertainty and complex cluster shapes. This progression connected clustering to the broader theme of generative models that we encountered in classification, where clusters represent distinct populations with their own characteristic distributions.

The generative perspective provides capabilities that extend far beyond simple data partitioning, including synthetic data generation, outlier detection, and probability density estimation. A critical challenge in clustering involves determining the optimal number of clusters. We examined both heuristic approaches (elbow method, silhouette analysis) and principled statistical frameworks through information criteria. The Bayesian Information Criterion (BIC) and Akaike Information Criterion (AIC) formalize Occam's razor by balancing model fit against complexity, though they embody different philosophical approaches.

The progression from linear models through clustering reflects the broader evolution of statistical learning. We began with simple, interpretable models that provide exact solutions but make strong assumptions about data structure, then moved to more flexible approaches like GMMs that relax some assumptions while maintaining analytical tractability.

This recognition points toward the need for even more flexible computational ap-

proaches. In our next chapter, we will shift our focus to sampling and Monte Carlo methods, which provide a computational backbone for complex probabilistic models where analytical solutions are unavailable. These techniques will enable us to work with arbitrary probability distributions, perform inference in high-dimensional parameter spaces, and quantify uncertainty in ways that extend far beyond the analytical frameworks we've explored thus far.

Further Readings: The development of clustering methods builds upon fundamental work in set partitioning and mixture distributions, with early contributions from Steinhaus [1957] who provided mathematical formulations for dividing sets into homogeneous groups and Pearson [1894] whose work on mixture distributions laid groundwork that remains foundational today. For readers interested in K-means clustering, Lloyd [1982] offers the least squares quantization perspective that underlies modern implementations, while MacQueen [1967] provides comprehensive methods for multivariate classification and Hartigan and Wong [1979] presents an algorithmic treatment that became widely adopted. The probabilistic framework of Gaussian Mixture Models is developed in Day [1969] and Wolfe [1970] who extends mixture analysis to multivariate settings. The Expectation-Maximization algorithm, essential for both K-means and GMM optimization, receives definitive treatment in Dempster et al. [1977] whose unified framework encompasses many iterative algorithms, with Redner and Walker [1984] providing an accessible review that connects mixture densities with maximum likelihood estimation. For comprehensive coverage of finite mixtures, Titterington et al. [1985] offers rigorous statistical analysis. Model selection in clustering benefits from information-theoretic criteria developed by Akaike [1974] and the Bayesian perspective of Schwarz [1978], with theoretical extensions explored in Bozdogan [1987]. Readers seeking practical guidance will find Kaufman and Rousseeuw [1990] valuable for its treatment of finding groups in data, while Arthur and Vassilvitskii [2007] addresses the initialization challenge through careful seeding strategies. The connection between hard and soft clustering assignments is illuminated through fuzzy clustering methods in Dunn [1973] and Bezdek [1981], with Selim and Ismail [1984] providing unifying convergence theory. For comprehensive treatments, Hartigan [1975] remains a classic reference on clustering algorithms, while Duda et al. [2001] places these methods within the broader context of pattern classification.

Chapter 12

Sampling and Monte Carlo Methods

In our previous chapters, we have completed our survey of the essential techniques for each of the key tasks of machine learning in astronomy—supervised learning (regression, classification) and unsupervised learning (dimension reduction with PCA, and clustering). While these tasks appear different on the surface, the mathematics behind each follows a remarkably similar pattern—all involving the maximization of likelihood and deriving the posterior of proposed models, though the specific form of these models varies depending on the task at hand.

This chapter marks a transition point in our exploration, shifting from model-specific techniques to general computational methods that apply across different models. The sampling methods we will develop serve as a computational backbone for complex probabilistic models that extends well beyond any single machine learning task.

Consider the progression we have followed throughout this course. When we first introduced linear regression, logistic regression, and other parametric models, we benefited from their mathematical tractability. For simple models like linear regression with Gaussian priors and likelihoods, we could derive closed-form expressions for the posterior distribution. The mathematical tractability of Gaussian distributions allowed us to perform exact calculations without approximation.

However, as our models become more sophisticated—incorporating non-linearities, hierarchical structures, or complex priors—analytical solutions quickly become unavailable. Even modest departures from the simple cases we have studied create substantial computational challenges. From Bayes' theorem, we can always write the posterior distribution

formally as:

$$p(\boldsymbol{\theta}|\mathcal{D}) \propto p(\mathcal{D}|\boldsymbol{\theta}) \cdot p(\boldsymbol{\theta}), \tag{12.1}$$

where $\boldsymbol{\theta}$ represents our model parameters and $\mathcal{D}$ our data.

This formal expression gives us the mathematical form of the posterior, but it's often insufficient for practical use. The key challenge is not obtaining the mathematical form—we already have that—but rather computing expectations with respect to this distribution. Most practical questions in Bayesian inference require computing expectations of the form:

$$\mathbb{E}[f(\boldsymbol{\theta})] = \int f(\boldsymbol{\theta})p(\boldsymbol{\theta}|\mathcal{D})d\boldsymbol{\theta}. \tag{12.2}$$

These integrals arise whenever we want to predict new observations, summarize parameter values, or integrate out nuisance parameters. For the simple models we studied earlier, these integrals could be computed analytically. In Bayesian linear regression, the posterior distribution is Gaussian, allowing us to either use standard packages to generate samples or perform analytical calculations directly.

The mathematical tractability we relied on earlier has guided many of our modeling choices. We often resorted to combinations of Gaussianity and linear transformations because these create models that we can manipulate easily mathematically. However, we have also seen that even slight deviations from these assumptions create substantial difficulties. In logistic regression, the non-linearities made obtaining the posterior considerably more challenging. We managed to proceed by making approximations like the Laplace approximation, or by using the probit function as a substitute for the logistic function.

In Bayesian logistic regression, for example, we could write down the posterior precisely, but we couldn't easily sample from it without approximations. As models grow more complex, these approximation techniques become increasingly inadequate. For many distributions encountered in Bayesian inference—particularly posterior distributions resulting from complex likelihoods or hierarchical models—analytical solutions simply do not exist.

This is where Monte Carlo methods become invaluable. Rather than attempting to solve integrals analytically, we approximate them using samples. The key insight is remarkably simple: if we can generate samples $\boldsymbol{\theta}^{(1)}, \boldsymbol{\theta}^{(2)}, \dots, \boldsymbol{\theta}^{(N)}$ from the distribution $p(\boldsymbol{\theta}|\mathcal{D})$, then

$$\mathbb{E}[f(\boldsymbol{\theta})] \approx \frac{1}{N} \sum_{l=1}^{N} f(\boldsymbol{\theta}^{(l)}). \tag{12.3}$$

We have actually encountered this concept earlier in the course when we used finite samples to estimate summary statistics like means and variances. Those calculations can be viewed as simple Monte Carlo approximations, where we used our observed data samples to estimate population parameters.

The power of Monte Carlo methods lies in their convergence properties—as the number of samples N increases, our approximation becomes increasingly accurate. By the Law of Large Numbers, the approximation converges to the true expectation as $N \to \infty$. Furthermore, the Central Limit Theorem tells us that the error in our approximation decreases at a rate of $\mathcal{O}(1/\sqrt{N})$. This convergence rate applies regardless of the dimensionality of the problem—a crucial advantage when working with high-dimensional parameter spaces common in astronomical applications.

The name "Monte Carlo" originates from the famous casino in Monaco, reflecting the method's reliance on randomness and chance. This naming was coined by scientists working on the Manhattan Project in the 1940s, particularly John von Neumann and Stanislaw Ulam, who used these techniques for nuclear physics calculations.

Monte Carlo approximation allows us to estimate quantities that would otherwise require solving complex, often intractable integrals. The beauty of this approach is that it works regardless of the complexity of the distribution or the dimension of the integration space, provided we can generate samples from the target distribution. However, this power comes with a critical requirement: we need effective methods to generate samples from complex probability distributions.

This chapter explores several approaches to sampling from probability distributions, each with different strengths and limitations. We begin with simple methods that work well for low-dimensional problems and provide important conceptual foundations. The grid approach discretizes continuous distributions into manageable histogram approximations. The inverse CDF method provides exact sampling when analytical inverse cumulative distribution functions are available. Rejection sampling offers a geometric approach that works with any evaluable distribution.

We then examine importance sampling, which shifts the focus from exact sample generation to efficient expectation estimation. This method can estimate expectations without generating exact samples from the target distribution, making it particularly valuable when our primary goal is computing integrals rather than exploring distributions.

While these methods provide valuable tools for simple problems, they reach practical limits with the complex, high-dimensional models common in modern astronomy. The exponential scaling of computational requirements with dimensionality renders these basic techniques impractical for many realistic applications. These limitations motivate more advanced techniques like Markov Chain Monte Carlo methods, which we will explore in the next chapter.

12.1   Historical Context

The concept of using randomness to solve mathematical problems has deep historical roots, predating modern computers by centuries. To understand the principles behind Monte Carlo methods, it's instructive to examine one of the earliest examples: Buffon's needle experiment, first proposed by Georges-Louis Leclerc, Comte de Buffon in the 18th century.

Buffon's experiment demonstrates how physical randomization can be used to estimate mathematical constants—in this case, the value of π. The setup is deceptively simple: drop needles of length L on a floor with parallel lines spaced distance D apart (where $L \leq D$). By counting how many needles cross the lines, we can estimate π without performing any complex mathematical calculations.

To understand why this works, we need to analyze the geometry of the problem. When a needle lands on the floor, its position is characterized by two random variables: the perpendicular distance x from the center of the needle to the nearest line (where $0 \leq x \leq D/2$), and the angle θ between the needle and the lines (where $0 \leq \theta < \pi$).

Both variables are uniformly distributed: x is uniform over $[0, D/2]$ with probability density $2/D$, and θ is uniform over $[0, \pi]$ with probability density $1/\pi$. A needle crosses a line when the perpendicular distance x is less than or equal to half the needle length projected onto the perpendicular direction. This occurs when:

$$x \leq \frac{L}{2}\sin\theta. \tag{12.4}$$

The probability of crossing is then:

$$p(\text{crossing}) = \int_0^\pi \int_0^{\frac{L}{2}\sin\theta} \frac{2}{D} \cdot \frac{1}{\pi} \, dx \, d\theta \tag{12.5}$$

$$= \int_0^\pi \frac{L\sin\theta}{D\pi} \, d\theta \tag{12.6}$$

$$= \frac{L}{D\pi} \int_0^\pi \sin\theta \, d\theta \tag{12.7}$$

$$= \frac{L}{D\pi} \cdot 2 \tag{12.8}$$

$$= 2\frac{L}{\pi D}. \tag{12.9}$$

This result connects the probability of needle crossings to the value of π. If we drop N total needles and observe n crossings, our empirical probability is $\frac{n}{N}$. Setting this equal to the theoretical probability gives us:

$$\frac{n}{N} \approx 2\frac{L}{\pi D} \tag{12.10}$$

$$\pi \approx 2\frac{L}{D}\frac{N}{n}. \tag{12.11}$$

This approach demonstrates several key principles that remain central to modern Monte Carlo methods. First, it shows how random sampling can be used to estimate quantities that would otherwise require complex calculations—in this case, computing π without solving any integrals. Second, it illustrates the characteristic $\mathcal{O}(1/\sqrt{N})$ convergence rate: as we increase the number of needles N, our estimate of π becomes more accurate, but the improvement diminishes with the square root of the sample size.

The connection between Buffon's physical experiment and modern computational sampling is more than historical curiosity. Both rely on the same mathematical principle: using random samples to approximate integrals. While Buffon and his contemporaries used physical randomization out of necessity, we now employ computational random number generators to achieve the same goal with far greater efficiency and precision.

This historical example establishes a crucial insight that underlies all the sampling techniques we will study: random sampling provides a general method for estimating quantities that would otherwise require solving complex, often intractable integrals. The approach works regardless of the complexity of the distribution or the dimension of the integration

Buffon's Needle Experiment
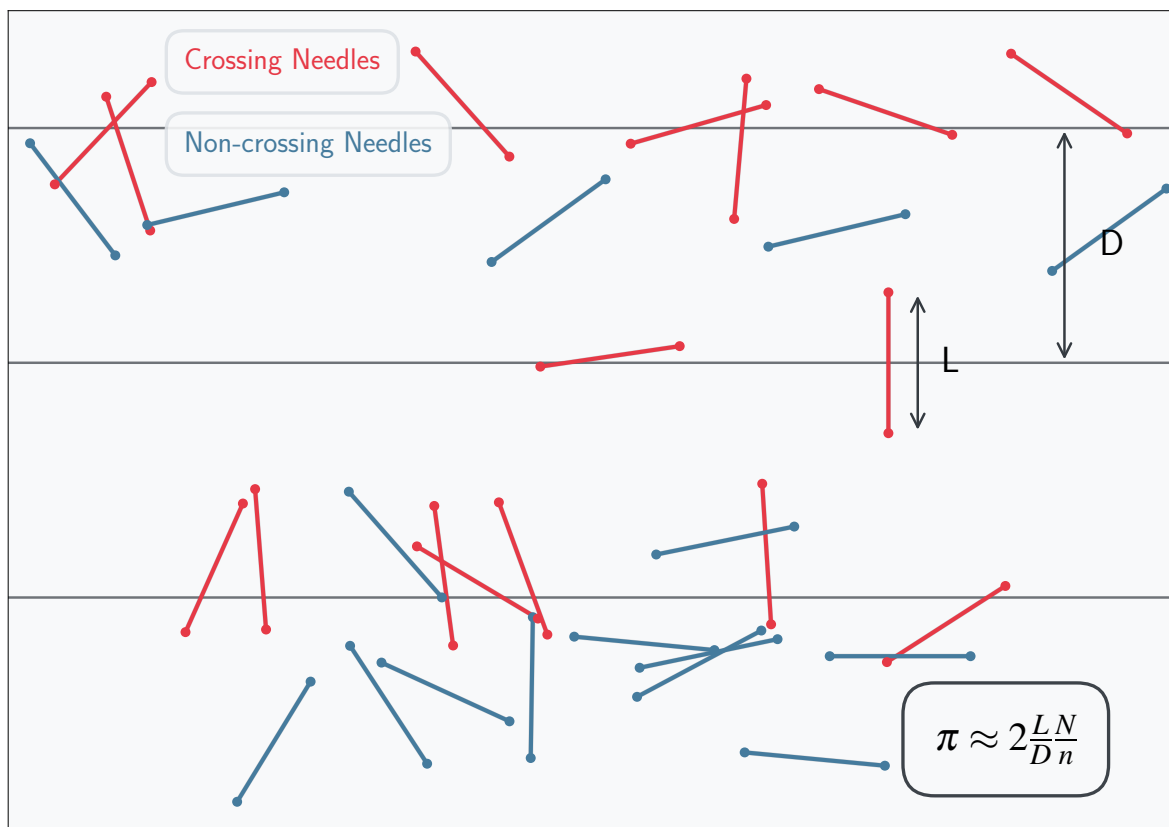
Figure 12.1: Illustration of Buffon's needle experiment, an early example of Monte Carlo methods from the 18th century. The experiment involves randomly dropping needles of length L (shown in vertical orientation) on a surface with parallel lines spaced at distance D. Needles are colored according to whether they cross a line (red) or not (blue). The probability of a needle crossing a line is directly related to π through the formula $\pi \approx 2LN/(Dn)$, where N is the total number of needles dropped and n is the number of needles that cross a line. This physical randomization process provides a method to empirically estimate π without requiring complex mathematical calculations, illustrating the core principle behind modern Monte Carlo integration techniques.

space, provided we can generate samples from the target distribution. This universality makes sampling methods invaluable for modern statistical computation, where we routinely encounter distributions far more complex than those that admit analytical solutions.

12.2 The Grid Approach

We begin our exploration of computational sampling techniques with the grid-based approach, which provides a foundation for understanding more sophisticated methods. This

method directly implements the principle we saw in Buffon's needle experiment: transforming a continuous mathematical problem into a discrete one that we can solve through counting and probability.

A useful analogy for understanding the grid approach is a pinball machine. When a ball drops from the top, it randomly bounces through a series of pegs before landing in one of several bins at the bottom. Each bin collects balls with a frequency proportional to how many paths lead to it. In our sampling context, the "bins" represent discrete grid points, and the "frequency of balls landing in each bin" corresponds to the probability density at each point. Just as the pinball machine converts the complex physics of bouncing balls into a simple counting problem, the grid approach converts continuous probability distributions into discrete sampling problems.

The grid approach converts the challenging problem of sampling from a continuous distribution into the more manageable task of sampling from a discrete histogram. While this introduces approximation, it offers valuable intuition about how sampling methods work and provides exact results as the grid becomes infinitely fine.

The basic strategy is straightforward. Consider a random variable X with probability density function (PDF) $p(x)$ defined on a bounded domain $[a, b]$. To sample from this distribution using the grid approach, we first discretize the continuous domain into n equally spaced grid points:

$$x_i = a + i\Delta x, \quad i = 0, 1, \ldots, n, \tag{12.12}$$

where $\Delta x = (b - a)/n$ represents the grid spacing.

This discretization approximates the continuous distribution with a binned histogram. At each grid point x_i, we evaluate the PDF to obtain $p_i = p(x_i)$, which represents the height of the probability density at that location. Since these values represent unnormalized probability densities, we must normalize them to form a proper probability mass function (PMF). The normalization constant is computed as $Z = \sum_{i=0}^{n} p_i$, allowing us to define the normalized probabilities $\tilde{p}_i = p_i/Z$.

These normalized probabilities $\tilde{p}_i$ can be interpreted as the probability masses associated with each grid point. The entire process transforms our continuous PDF into a discrete histogram approximation, with the approximation quality improving as the number of bins increases.

Once we have discretized the distribution, sampling becomes straightforward. We

need to generate samples from the discrete distribution defined by the probabilities $\tilde{p}_i$ over the grid points x_i. This requires partitioning the unit interval $[0, 1]$ into segments with lengths proportional to the bin probabilities.

We accomplish this by computing cumulative probabilities:

$$s_i = \sum_{j=0}^{i} \tilde{p}_j, \quad i = 0, 1, \ldots, n. \tag{12.13}$$

These cumulative probabilities create a set of thresholds $\{s_0, s_1, \ldots, s_n\}$ with $s_0 = \tilde{p}_0$ and $s_n = 1$. The sampling procedure then becomes:

1. Generate a uniform random number $u \sim \mathcal{U}(0, 1)$

2. Find the interval where $s_{i-1} < u \leq s_i$

3. Return x_i as our sample

This procedure ensures that the probability of sampling any grid point x_i is precisely $\tilde{p}_i$, as required.

Example: Bimodal Gaussian Mixture   To illustrate the grid approach, consider sampling from a mixture of two Gaussians:

$$p(x) = 0.7 \cdot \mathcal{N}(x| - 2, 0.5^2) + 0.3 \cdot \mathcal{N}(x|2, 1^2). \tag{12.14}$$

This distribution exhibits bimodality with a dominant mode centered at $x = -2$ (narrower and taller) and a secondary mode at $x = 2$ (broader and shorter). While conventional sampling from this mixture would require selecting one component according to the mixing proportions and then sampling from the selected Gaussian, the grid approach permits direct sampling from the composite distribution.

The implementation would discretize an appropriate domain, such as $[-5, 5]$, into $n = 1000$ equally spaced points. After evaluating the PDF at each point and normalizing to obtain bin probabilities, we can generate samples using the procedure described above. This approach accommodates the multimodal nature of the distribution effectively, provided the grid resolution adequately captures the distribution's features.
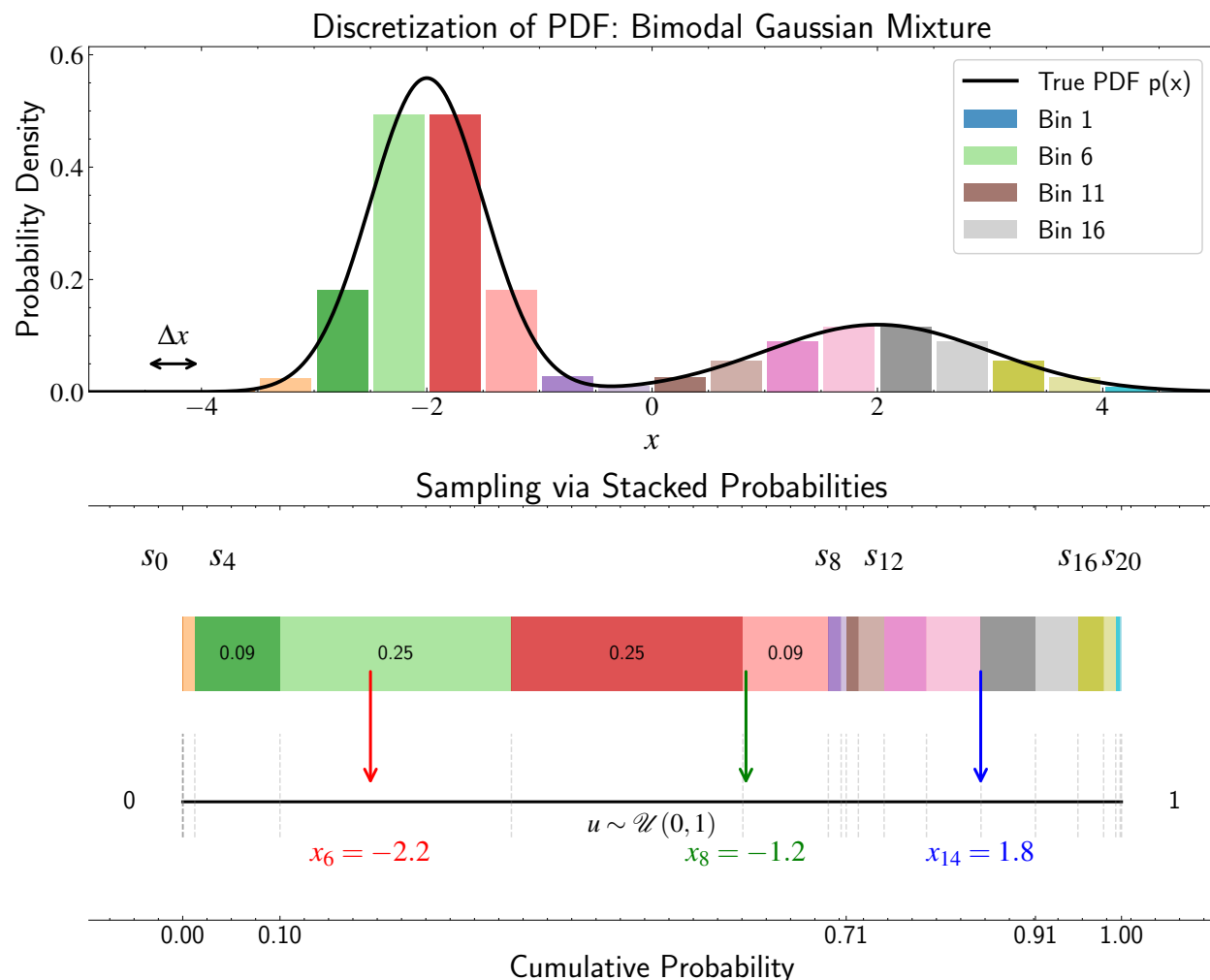
Figure 12.2: Illustration of grid-based sampling for a bimodal Gaussian mixture. **Top panel:** Discretization of the continuous PDF $p(x) = 0.7 \cdot \mathcal{N}(x| - 2, 0.5^2) + 0.3 \cdot \mathcal{N}(x|2, 1^2)$ into equally spaced bins of width Δx, with each bin shown in a different color. The black curve represents the true continuous PDF. **Bottom panel:** The stacked bar representation of bin probabilities, where the width of each colored segment corresponds to the probability mass of the matching bin in the top panel. The thresholds s_i partition the unit interval according to these probabilities. When sampling, a uniform random number $u \sim \mathcal{U}(0, 1)$ maps to the x value from the bin it falls within, as demonstrated by the three colored arrows. This grid-based approach allows direct sampling from complex distributions through discretization and inverse transform sampling.

Extension to Multiple Dimensions   The grid approach extends naturally to multiple dimensions but introduces significant computational challenges. For a d-dimensional random variable $\mathbf{X} = (X_1, X_2, \ldots, X_d)$ with joint PDF $p(\mathbf{x})$, the discretization produces a

d-dimensional grid:

$$\mathbf{x}_{i_1, i_2, \ldots, i_d} = (a_1 + i_1 \Delta x_1, a_2 + i_2 \Delta x_2, \ldots, a_d + i_d \Delta x_d), \tag{12.15}$$

where $i_j \in \{0, 1, \ldots, n_j\}$ for each dimension $j = 1, 2, \ldots, d$.

The joint PDF is evaluated at each grid point and normalized to obtain bin probabilities across the entire grid. The sampling procedure remains conceptually similar to the one-dimensional case, though the implementation complexity increases substantially.

The Curse of Dimensionality   The primary limitation of the grid approach emerges from the curse of dimensionality. With n bins per dimension, the total number of bins scales as n^d, exhibiting exponential growth with dimensionality. This exponential scaling renders the approach computationally prohibitive for high-dimensional problems.

To illustrate this challenge: with 100 bins per dimension, a one-dimensional problem requires 100 bins, a two-dimensional problem requires 10,000 bins, and a five-dimensional problem requires 10 billion bins. At ten dimensions, the required 10^{20} bins exceed practical computational capabilities by several orders of magnitude.

Furthermore, the grid approach introduces discretization error, as samples are constrained to the predefined grid points. This error diminishes with increasing grid resolution but introduces an approximation that may be unacceptable for applications requiring precise sampling from the continuous distribution.

Despite these limitations, the grid approach establishes important concepts that appear throughout sampling theory. The ideas of discretization, probability mass assignment, and cumulative probability sampling will reappear in various forms as we explore more sophisticated techniques.

For low-dimensional problems, particularly in one or two dimensions, the grid approach remains computationally viable and conceptually clear. It provides an ideal starting point for understanding sampling methods before moving to techniques that can handle the high-dimensional distributions common in modern astronomical applications.

The grid approach also illustrates a key trade-off that appears throughout computational statistics: accuracy versus computational efficiency. By making the grid finer, we can achieve arbitrary accuracy in our approximation of the continuous distribution, but at the cost of exponentially increasing computational requirements in high dimensions. This

trade-off motivates the development of more sophisticated methods that can achieve good approximations without exhaustively discretizing the entire probability space.

12.3 Inverse CDF Method

The grid approach introduced the concept of partitioning the unit interval based on probability masses and using uniform random numbers to sample from discrete approximations. We can extend this idea to work directly with continuous distributions by asking: what happens when we take the grid approach to its logical limit and let the bin width approach zero?

The inverse Cumulative Distribution Function (CDF) method provides exactly this limiting case, allowing us to sample from continuous distributions without discretization error. The key insight is that the cumulative probabilities we computed in the grid approach generalize to the cumulative distribution function in the continuous case.

For a random variable X with probability density function (PDF) $p(x)$, the CDF $F(x)$ is defined as:

$$F(x) = \int_{-\infty}^{x} p(t)\, dt. \tag{12.16}$$

This function $F(x)$ represents the probability that the random variable X takes a value less than or equal to x. The CDF possesses several important properties that make it useful for sampling:

- $F(x)$ is non-decreasing: if $x_1 < x_2$, then $F(x_1) \leq F(x_2)$

- $\lim_{x \to -\infty} F(x) = 0$ and $\lim_{x \to \infty} F(x) = 1$

- $F(x)$ is right-continuous

- For continuous distributions, $p(x) = \frac{dF(x)}{dx}$

The CDF acts as a continuous analogue to the cumulative probabilities we computed in the grid approach, providing a mapping between the interval $[0, 1]$ and the support of our target distribution.

The inverse CDF method is remarkably simple in principle. If we can compute the CDF of our target distribution and find its inverse function, we can generate samples by

transforming uniform random numbers:

1. Generate a uniform random number $u \sim \mathcal{U}(0, 1)$

2. Compute $x = F^{-1}(u)$, where F^{-1} is the inverse of the CDF

3. Return x as a sample from the distribution with CDF F

This procedure works because of the probability integral transform theorem, which establishes a connection between arbitrary random variables and the uniform distribution. The theorem states that if we take any random variable and apply its own CDF to it, the resulting transformed variable follows a uniform distribution on $[0, 1]$, regardless of the original distribution.

To understand why this works, consider what a CDF does. In regions where the PDF is high (meaning outcomes are more likely), the CDF rises rapidly. In regions where the PDF is low, the CDF rises slowly. The CDF essentially "stretches" or "compresses" different parts of the domain based on their probability density, ensuring that equal probability mass gets mapped to equal segments of the $[0, 1]$ interval.

More formally, suppose X is a random variable with CDF $F_X(x)$, and define a new random variable $Y = F_X(X)$. We can show that Y follows a uniform distribution on $[0, 1]$ by computing its CDF. For any $y \in [0, 1]$:

$$P(Y \le y) = P(F_X(X) \le y) \tag{12.17}$$

$$= P(X \le F_X^{-1}(y)) \tag{12.18}$$

$$= F_X(F_X^{-1}(y)) \tag{12.19}$$

$$= y \tag{12.20}$$

This is precisely the CDF of a uniform distribution on $[0, 1]$. The inverse CDF method simply reverses this relationship: if $U \sim \mathcal{U}(0, 1)$, then $X = F_X^{-1}(U)$ follows the distribution with CDF $F_X(x)$.

The method has a useful geometric interpretation. When we generate a uniform random number u, we can visualize this as a height on the y-axis of the CDF plot. Finding $F^{-1}(u)$ corresponds to moving horizontally from the point $(0, u)$ until we intersect the CDF curve, and then projecting down to the x-axis to obtain our sample. This geometric perspective explains why the samples match the target distribution: in regions where the PDF $p(x)$
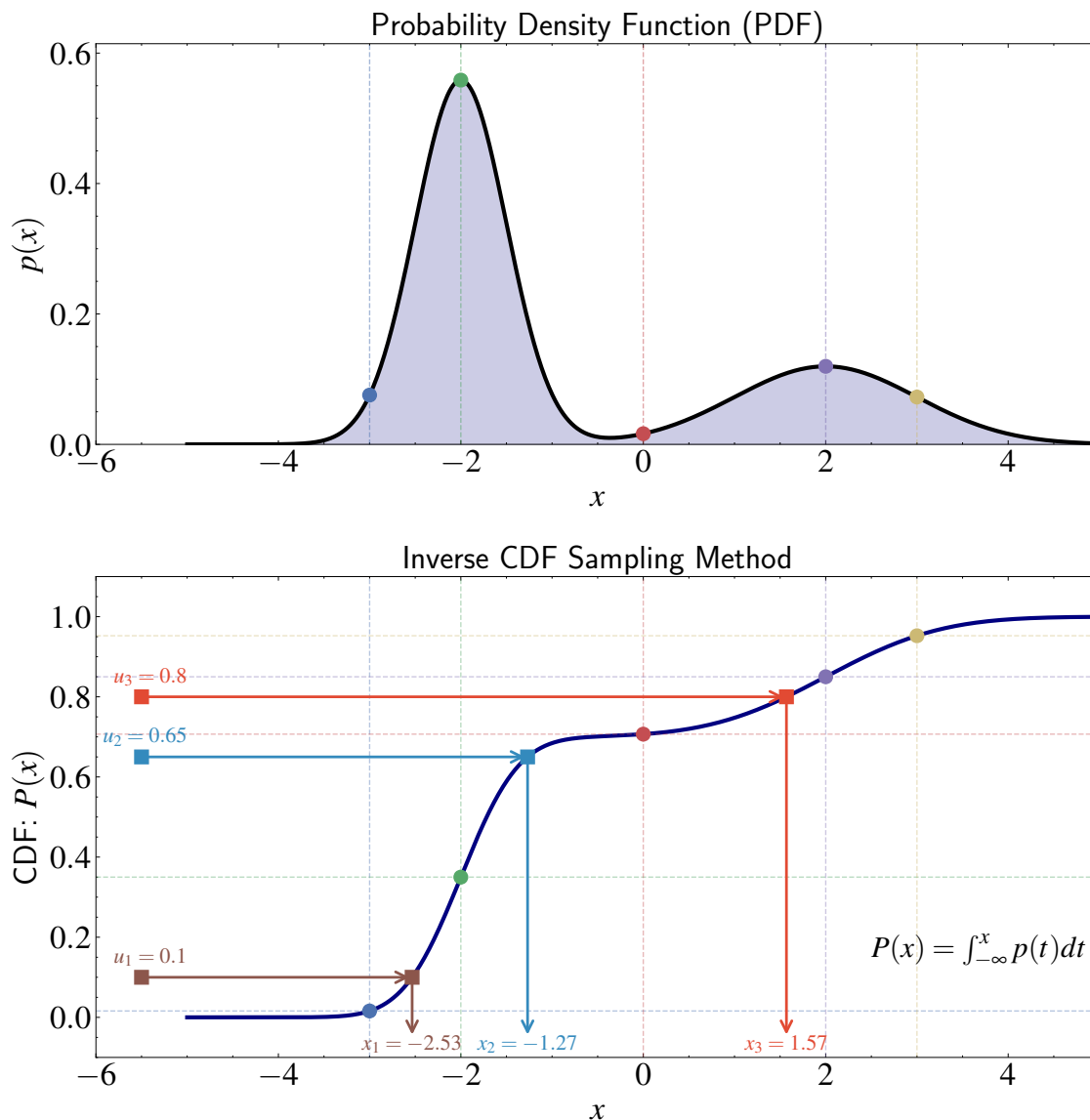
Figure 12.3: Visualization of the inverse CDF method for sampling from a bimodal Gaussian mixture. **Top panel:** The probability density function (PDF) $p(x) = 0.7 \cdot \mathcal{N}(x| -2, 0.5^2) + 0.3 \cdot \mathcal{N}(x|2, 1^2)$, with reference points highlighted in different colors. The navy shaded area represents the total probability mass. **Bottom panel:** The cumulative distribution function (CDF) $F(x) = \int_{-\infty}^{x} p(t)dt$ and illustration of the inverse CDF sampling process. The sampling procedure is demonstrated with three examples: starting with a uniform random number $u \sim \mathcal{U}(0,1)$ on the y-axis, tracing horizontally to the CDF curve, and projecting vertically to the x-axis to obtain the corresponding sample value. This method transforms uniform random numbers into samples that follow the target distribution by leveraging the CDF's property of rising more steeply in high-probability regions and more gradually in low-probability regions.

is high, the CDF $F(x)$ increases rapidly (steep slope), so uniform points along the y-axis get compressed when projected onto the x-axis, resulting in more samples in these high-density regions.

Exponential Distribution For the exponential distribution with PDF $p(x) = \lambda e^{-\lambda x}$ for $x \geq 0$, the CDF is:

$$F(x) = 1 - e^{-\lambda x}. \tag{12.21}$$

Solving for x in terms of $u = F(x)$:

$$u = 1 - e^{-\lambda x} \tag{12.22}$$
$$e^{-\lambda x} = 1 - u \tag{12.23}$$
$$x = -\frac{1}{\lambda} \ln(1 - u) \tag{12.24}$$

Since $1 - u$ is also uniformly distributed on $[0, 1]$ when u is uniform, we can simplify to:

$$x = -\frac{1}{\lambda} \ln(u). \tag{12.25}$$

Power Law Distribution Power law distributions appear frequently in astronomy, governing phenomena such as the mass function of stars, the distribution of galaxy luminosities, and the energy distribution of cosmic rays. For a power law distribution defined on the interval $[x_{\min}, \infty)$ with PDF $p(x) = (\alpha - 1)x_{\min}^{\alpha-1} x^{-\alpha}$ (where $\alpha > 1$), the CDF is:

$$F(x) = 1 - \left(\frac{x_{\min}}{x}\right)^{\alpha-1}. \tag{12.26}$$

Inverting this to find x in terms of $u = F(x)$:

$$u = 1 - \left(\frac{x_{\min}}{x}\right)^{\alpha-1} \tag{12.27}$$
$$\left(\frac{x_{\min}}{x}\right)^{\alpha-1} = 1 - u \tag{12.28}$$
$$x = x_{\min}(1 - u)^{-\frac{1}{\alpha-1}} \tag{12.29}$$

Again using the property that $1 - u \sim \mathcal{U}(0, 1)$ when $u \sim \mathcal{U}(0, 1)$:

$$x = x_{\min} u^{-\frac{1}{\alpha-1}}. \tag{12.30}$$

Advantages and Limitations   The inverse CDF method offers several advantages over the grid approach. Unlike the grid approach, which introduces discretization error, the inverse CDF method generates samples that exactly follow the target distribution. Each sample requires generating only one uniform random number and applying a single function evaluation, making it computationally efficient when the inverse CDF can be calculated analytically. The method is also conceptually straightforward and easy to implement for distributions with known inverse CDFs.

However, the inverse CDF method has important limitations. The primary constraint is that it requires a closed-form expression for the inverse CDF $F^{-1}(u)$, which is not available for many complex distributions. Even when the CDF itself has a closed form, inverting it analytically may be impossible. For distributions where the inverse CDF must be computed numerically, the method can become computationally expensive, potentially requiring numerical root-finding algorithms for each sample.

For multivariate distributions, the inverse CDF method faces additional challenges. In higher dimensions, the CDF becomes significantly more complex, and the many-to-one mapping makes direct inversion impossible. While techniques like the Rosenblatt transformation can address this through conditional distributions, they require knowing all conditional distributions and their inverses, which severely limits practical applicability.

Despite these limitations, the inverse CDF method remains the technique of choice when the inverse CDF is analytically tractable. Modern scientific computing libraries implement this method for standard distributions, often with optimizations that improve numerical stability and computational efficiency. However, for many distributions encountered in Bayesian inference—particularly posterior distributions resulting from complex likelihoods or hierarchical models—the inverse CDF method is not directly applicable, necessitating the alternative approaches we explore next.

12.4   Rejection Sampling

The inverse CDF method provides exact sampling when we can analytically compute and invert the cumulative distribution function. However, this requirement severely limits its applicability—many distributions of interest in Bayesian inference and astronomical modeling do not have tractable inverse CDFs. Rejection sampling addresses this limitation by offering a more versatile technique that can handle any distribution we can evaluate, even when we cannot integrate or invert it analytically.

The core insight behind rejection sampling is geometric. Rather than trying to transform uniform random numbers through mathematical functions, we can think of sampling as a process of accepting or rejecting candidate points based on whether they fall under the target density curve. This transforms the problem from one requiring analytical manipulation to one requiring only function evaluation.

Imagine trying to sample points that lie under a complex curve by throwing darts at a board. If we throw darts randomly at a rectangular region that completely contains our curve, we can keep only those darts that land below the curve and discard the rest. The accepted darts will be distributed according to the shape of the curve—more darts will be accepted in regions where the curve is high, and fewer where it is low. Rejection sampling formalizes this intuitive idea.

Suppose we have a target distribution with PDF $p(x)$ from which we want to draw samples. Rejection sampling employs a proposal distribution with PDF $q(x)$ that satisfies two key requirements:

1. We must be able to efficiently generate samples from the proposal distribution $q(x)$.

2. The proposal distribution must envelope the target distribution when properly scaled — that is, there must exist a constant $M \geq 1$ such that $Mq(x) \geq p(x)$ for all x in the domain.

The second requirement means that our proposal distribution, when scaled by M, must completely envelop the target distribution. This is crucial because it ensures we can use the ratio $p(x)/(Mq(x))$ as a valid acceptance probability, as this ratio will always be between 0 and 1.

The rejection sampling algorithm follows these steps:

1. Generate a sample $x_* \sim q(x)$ from the proposal distribution.

2. Compute the acceptance ratio $\alpha = \frac{p(x_*)}{Mq(x_*)}$.

3. Generate a uniform random number $u \sim \mathcal{U}(0, 1)$.

4. If $u \leq \alpha$, accept x_* as a sample from $p(x)$; otherwise, reject it and return to step 1.

The correctness of this algorithm stems from how the acceptance probability weights different regions of the domain. At each point x_*, we accept it with probability proportional

to the ratio $p(x_*)/(Mq(x_*))$. This means points where $p(x_*)$ is large relative to $q(x_*)$ are more likely to be accepted, while points where $p(x_*)$ is small relative to $q(x_*)$ are more likely to be rejected.

Geometric Interpretation   Rejection sampling has a clear geometric interpretation. We can visualize it as operating in a two-dimensional space—the domain of x and a vertical dimension representing probability density. The proposal distribution, scaled by M, creates an envelope above the target density. When we generate a point $(x_*, uMq(x_*))$, where u is uniform between 0 and 1, we accept it if it falls below the target density curve. Points falling between the target density and the scaled proposal density are rejected.

This geometric view explains why rejection sampling is often described as "sculpting" the proposal distribution. We start with samples from $q(x)$ and selectively keep those that conform to the shape of $p(x)$. The acceptance ratio determines the precise amount of probability mass to "carve away" at each point.

The efficiency of rejection sampling depends critically on the choice of proposal distribution and the scaling factor M. The expected number of iterations required to obtain one accepted sample equals M. Therefore, we want M to be as small as possible while still satisfying the envelope condition.

The optimal proposal distribution would have the same shape as the target distribution, with $M = 1$ and all samples accepted. However, this would require sampling directly from the target distribution, defeating the purpose. In practice, we choose a proposal distribution that balances three considerations: ease of sampling, similarity to the target shape, and sufficient coverage to envelop the target when scaled.

Extension to Multiple Dimensions   Unlike the inverse CDF method, rejection sampling extends naturally to multidimensional distributions. For a d-dimensional target PDF $p(\mathbf{x})$, we use a d-dimensional proposal PDF $q(\mathbf{x})$ and follow the same procedure. One of the most powerful advantages of rejection sampling is its generality—it can work for any distribution whose density we can evaluate, even if only up to a normalizing constant. This makes it particularly valuable for complex distributions that arise in Bayesian inference where we can express the posterior analytically but cannot directly sample from it.

The Curse of Dimensionality   However, rejection sampling faces challenges as dimensionality increases—a manifestation of the curse of dimensionality. To understand this chal-
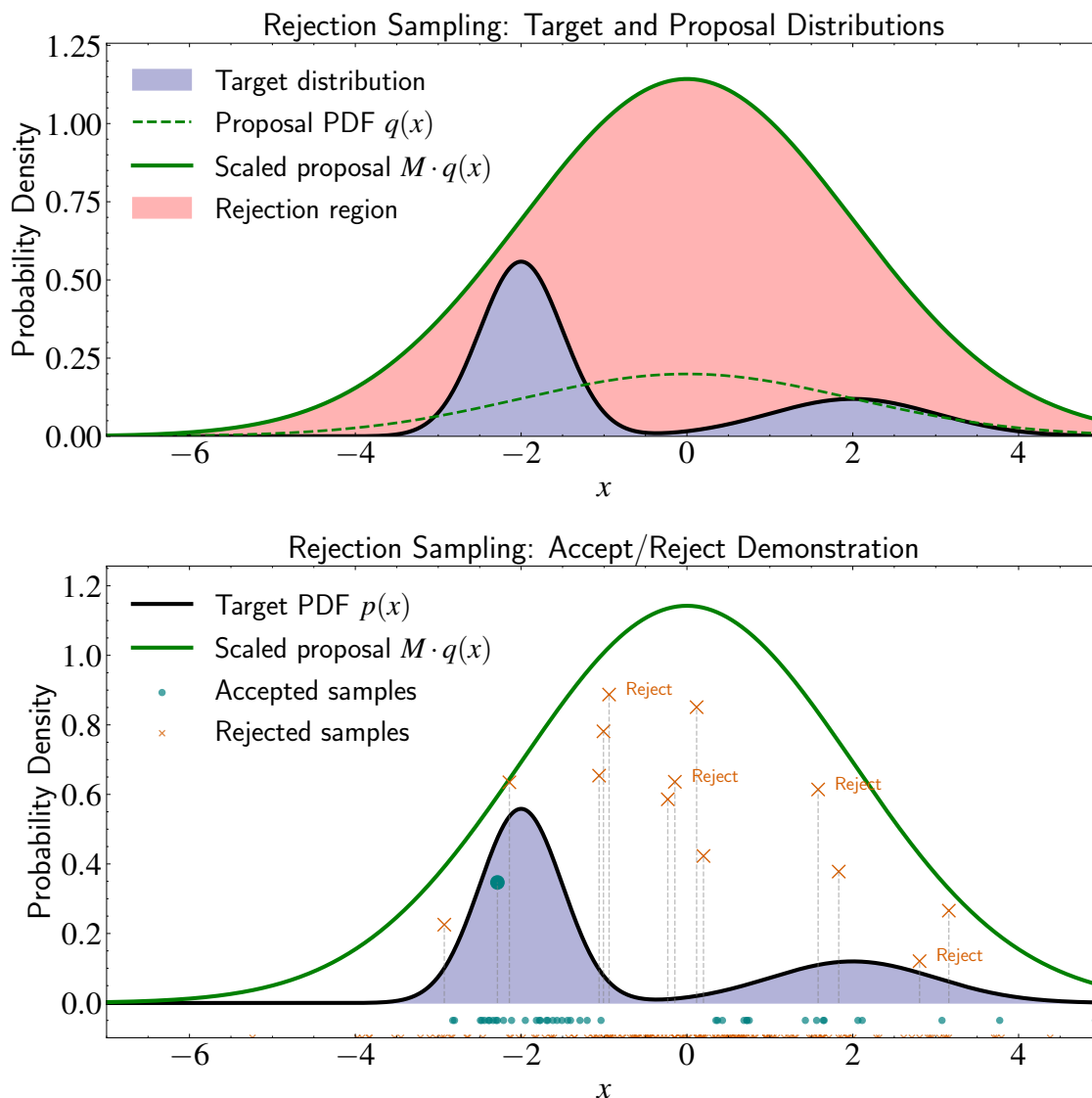
Figure 12.4: Illustration of the rejection sampling method for a bimodal Gaussian mixture distribution. **Top panel:** The target distribution (black curve with navy shading), the proposal distribution $q(x)$ (green dashed line), and the scaled proposal $M \cdot q(x)$ (solid green line). The red shaded area represents the rejection region—points that fall between the target and scaled proposal distributions. **Bottom panel:** Demonstration of the accept/reject mechanism. For each candidate point sampled from the proposal distribution, its vertical position is determined by a uniform random number $u \sim \mathcal{U}(0, 1)$ scaled by $M \cdot q(x)$. Points falling below the target density curve (teal circles) are accepted, while those in the rejection region (orange X marks) are rejected. The scatter plot at the bottom shows the distribution of the resulting samples, illustrating how rejection sampling effectively "sculpts" the proposal distribution to match the shape of the target distribution.

lenge, consider spherically symmetric distributions centered at the origin. If the optimal acceptance region occupies a fraction $c < 1$ of the proposal distribution's mass in one di-

mension, then in d dimensions, the acceptance rate becomes approximately c^d, decreasing exponentially with dimension.

Another limitation arises with heavy-tailed distributions. If the tails of $p(x)$ decay more slowly than those of $q(x)$, the scaling factor M might need to be very large or even infinite. For example, if $p(x)$ has polynomial tails while $q(x)$ has exponential tails, no finite value of M will satisfy the envelope condition everywhere.

Despite these limitations, rejection sampling remains valuable for low-dimensional problems or when the target and proposal distributions are well-matched. It requires minimal assumptions about the target distribution—we only need to evaluate it up to a proportionality constant—making it applicable in many scenarios where the inverse CDF method fails. These limitations motivate the development of more sophisticated techniques like Markov Chain Monte Carlo methods, which we will explore in future chapters, but rejection sampling provides an important stepping stone toward understanding more advanced sampling approaches.

12.5   Importance Sampling

Both the inverse CDF method and rejection sampling aim to generate samples that follow a target distribution exactly. However, in many applications, our primary goal is not to generate samples per se, but rather to estimate expectations with respect to the target distribution. Importance sampling addresses this distinction directly by focusing on efficient expectation estimation rather than exact sample generation.

This shift in perspective opens up new possibilities. While rejection sampling discards candidates that don't meet the acceptance criteria, importance sampling keeps all samples but weights them appropriately to account for the mismatch between the proposal and target distributions. This approach can be more efficient, especially when we only need to compute a few specific expectations rather than explore the entire distribution.

Recall that many problems in Bayesian inference involve computing expectations of the form:

$$\mathbb{E}_p[f] = \int f(x)p(x)dx, \tag{12.31}$$

where $f(x)$ is some function of interest and $p(x)$ is our target probability density function. If we could draw samples $\{x^{(1)}, x^{(2)}, \ldots, x^{(N)}\}$ directly from $p(x)$, we could approximate this

expectation using the Monte Carlo estimator:

$$\mathbb{E}_p[f] \approx \frac{1}{N} \sum_{i=1}^{N} f(x^{(i)}). \tag{12.32}$$

The key insight of importance sampling is that we don't actually need to sample from $p(x)$ to estimate expectations with respect to $p(x)$. Instead, we can sample from a different distribution $q(x)$ that is easier to work with, and adjust our calculations accordingly.

We can rewrite our expectation by introducing a proposal distribution $q(x)$:

$$\mathbb{E}_p[f] = \int f(x)p(x)dx \tag{12.33}$$

$$= \int f(x)\frac{p(x)}{q(x)}q(x)dx \tag{12.34}$$

$$= \mathbb{E}_q\left[f(x)\frac{p(x)}{q(x)}\right]. \tag{12.35}$$

Here, the subscripts p and q in the expectation notation indicate which probability distribution we are taking the expectation with respect to. This mathematical manipulation transforms an expectation with respect to the potentially difficult distribution $p(x)$ into an expectation with respect to the more tractable distribution $q(x)$.

This leads to the importance sampling estimator:

$$\mathbb{E}_p[f] \approx \frac{1}{N} \sum_{i=1}^{N} w(x^{(i)})f(x^{(i)}), \tag{12.36}$$

where $x^{(i)} \sim q(x)$ and $w(x) = p(x)/q(x)$ is called the importance weight.

The importance weight $w(x)$ quantifies how much more (or less) likely each sample point is under the target distribution $p(x)$ compared to the proposal distribution $q(x)$. Points that are more likely under $p(x)$ than under $q(x)$ receive higher weights, while points that are less likely receive lower weights.

Handling Unnormalized Distributions   Like rejection sampling, importance sampling can handle unnormalized distributions, which is crucial for applications in Bayesian inference where the normalizing constant is often unknown. Suppose we only know $p(x)$ up to a

normalizing constant, i.e., $p(x) = \tilde{p}(x)/Z_p$ where $\tilde{p}(x)$ is the unnormalized density and $Z_p = \int \tilde{p}(x)dx$ is the normalizing constant. Similarly, let $q(x) = \tilde{q}(x)/Z_q$.

We can modify our approach to work with unnormalized densities. Starting with our expectation:

$$\mathbb{E}_p[f] = \frac{1}{Z_p} \int f(x)\tilde{p}(x)dx \tag{12.37}$$

$$= \frac{Z_q}{Z_p}\mathbb{E}_q\left[f(x)\frac{\tilde{p}(x)}{\tilde{q}(x)}\right]. \tag{12.38}$$

The key insight is that we don't need to know the normalization constants Z_p and Z_q separately—we only need their ratio, which can be estimated directly from our samples. Consider what the normalization constant Z_p represents:

$$Z_p = \int \tilde{p}(x)dx \tag{12.39}$$

$$= Z_q\mathbb{E}_q\left[\frac{\tilde{p}(x)}{\tilde{q}(x)}\right]. \tag{12.40}$$

This gives us:

$$\frac{Z_p}{Z_q} = \mathbb{E}_q\left[\frac{\tilde{p}(x)}{\tilde{q}(x)}\right], \tag{12.41}$$

which we can estimate using our samples from $q(x)$:

$$\frac{Z_p}{Z_q} \approx \frac{1}{N}\sum_{i=1}^{N}\frac{\tilde{p}(x^{(i)})}{\tilde{q}(x^{(i)})} = \frac{1}{N}\sum_{i=1}^{N}\tilde{w}(x^{(i)}). \tag{12.42}$$

Substituting this back into our expectation formula:

$$\mathbb{E}_p[f] = \frac{Z_q}{Z_p}\mathbb{E}_q\left[f(x)\frac{\tilde{p}(x)}{\tilde{q}(x)}\right] \tag{12.43}$$

$$= \frac{\sum_{i=1}^{N}\tilde{w}(x^{(i)})f(x^{(i)})}{\sum_{i=1}^{N}\tilde{w}(x^{(i)})}. \tag{12.44}$$

This gives us the self-normalized importance sampling estimator, where $\tilde{w}(x) = \frac{\tilde{p}(x)}{\tilde{q}(x)}$ are the unnormalized importance weights. The beauty of this approach is that we never

need to calculate the normalization constants explicitly—they are automatically handled by the ratio of sums in our estimator.

This capability makes importance sampling particularly valuable in Bayesian inference, where the posterior distribution is often only known up to a normalizing constant. The evidence term $p(\mathcal{D}) = \int p(\mathcal{D}|\boldsymbol{\theta})p(\boldsymbol{\theta})d\boldsymbol{\theta}$ in the denominator of Bayes' theorem is typically intractable, but importance sampling allows us to estimate posterior expectations without computing it.

Understanding Efficiency Through Weights   The importance sampling estimator is mathematically valid for any proposal distribution $q(x)$ that covers the support of $f(x)p(x)$ — that is, whenever $f(x)p(x) \neq 0$, we must have $q(x) > 0$. However, its practical effectiveness depends critically on how well $q(x)$ approximates $p(x)$.

To understand this, consider what happens with different proposal choices. When the proposal distribution $q(x)$ perfectly matches the target distribution $p(x)$, all importance weights become equal (constant), and every sample contributes equally to our estimate. When the proposal and target distributions partially match, some weights become larger than others, and fewer samples effectively contribute to our estimate.

The most problematic scenario occurs when the proposal distribution "undershoots" the target—placing too little probability mass in regions where the target has high density. In these regions, the weights $w(x) = p(x)/q(x)$ can become extremely large. These extreme weights can dominate our estimate, effectively reducing it to the contribution from just a few samples, regardless of how many total samples we generate.

This sensitivity to proposal choice motivates careful consideration of how to select $q(x)$ and how to diagnose when our importance sampling scheme is working well. In the next section, we will explore the concept of effective sample size, which provides a quantitative measure of how efficiently our importance sampling estimator is using the available samples.

12.6   Effective Sample Size

The importance sampling estimator is mathematically valid for any proposal distribution $q(x)$ that covers the support of $p(x)$. However, its practical effectiveness depends critically on how well $q(x)$ approximates $p(x)$. This consideration is captured by the concept of effective sample size (ESS), which quantifies how much information our weighted samples

actually contain.

Although we may generate N samples from our proposal distribution, the variance of our estimator might be equivalent to that of a much smaller number of direct samples from $p(x)$. Understanding this relationship is crucial for designing efficient importance sampling schemes and diagnosing when our proposal distribution is inadequate.

Intuitive Understanding   Ideally, we want all our samples to contribute meaningfully to our estimate. This happens when the importance weights are relatively uniform—no single sample dominates the estimate, and no samples are effectively ignored due to negligible weights.

Consider an analogy with voting. If we're trying to estimate public opinion by polling a representative sample, each person's vote should carry roughly equal weight. However, imagine a scenario where a few people's votes count as thousands while most people's votes count as fractions. Even if we poll many people, our estimate would be dominated by just a few individuals, making it unreliable and potentially biased.

Importance sampling faces the same challenge. If a few samples have extremely large weights while most have negligible weights, our estimate is effectively determined by just those few samples. The effective sample size quantifies this phenomenon by asking: "How many direct samples from $p(x)$ would give the same estimation precision as our N weighted samples from $q(x)$?"

The Effective Sample Size Formula   Through variance analysis of the self-normalized importance sampling estimator, we can derive the effective sample size formula:

$$\text{ESS} \approx \frac{(\sum_{i=1}^{N} \tilde{w}(x^{(i)}))^2}{\sum_{i=1}^{N} \tilde{w}(x^{(i)})^2}, \tag{12.45}$$

where $\tilde{w}(x^{(i)})$ are the unnormalized importance weights.

This formula represents the ratio of the squared first moment to the second moment of the weights. We can gain intuition by examining different scenarios:

When the proposal distribution $q(x)$ perfectly matches the target distribution $p(x)$, all weights become equal (constant), resulting in $\text{ESS} = N$—maximum efficiency where every sample contributes equally to our estimate.

When the proposal and target distributions partially match, some weights become larger than others, and the ESS decreases, reflecting that fewer samples effectively contribute to our estimate.

When the proposal distribution "undershoots" the target—placing too little probability mass in regions where the target has significant density—the weights $\tilde{w}(x) = p(x)/q(x)$ can become extremely large. These extreme weights cause ESS to collapse toward 1 and introduce enormous variance in our estimates.

A Concrete Example   To illustrate the impact of proposal distribution choice on effective sample size, consider estimating the mean of a standard normal distribution $\mathcal{N}(0,1)$ truncated to the region $[5, \infty)$. This might represent, for example, the average brightness of the brightest stars in a population where brightness follows a normal distribution.

The target distribution is:

$$p(x) = \frac{\mathcal{N}(x|0,1) \cdot \mathbf{1}(x \geq 5)}{\int_5^\infty \mathcal{N}(t|0,1)dt}, \tag{12.46}$$

where $\mathbf{1}(x \geq 5)$ is an indicator function that equals 1 when $x \geq 5$ and 0 otherwise.

A naive approach would be to use the standard normal distribution as our proposal: $q(x) = \mathcal{N}(x|0,1)$. The unnormalized importance weights would then be:

$$\tilde{w}(x) = \frac{\mathcal{N}(x|0,1) \cdot \mathbf{1}(x \geq 5)}{\mathcal{N}(x|0,1)} = \mathbf{1}(x \geq 5). \tag{12.47}$$

This means we would only use samples that happen to fall in the region $[5, \infty)$. Since the probability of drawing such a sample from a standard normal is approximately 2.87×10^{-7}, we would need millions of samples to get just a few valid ones. With $N = 10^7$ samples, we would expect only about 3 samples to have non-zero weights.

Let's calculate the ESS explicitly for this case. Suppose we generate $N = 10^7$ samples, and $k = 3$ of them fall in the region $[5, \infty)$ and have non-zero weights. The unnormalized weights would be:

$$\tilde{w}(x^{(i)}) = \begin{cases} 1 & \text{for } i \in \{i_1, i_2, i_3\} \text{ (the 3 samples in } [5, \infty)) \\ 0 & \text{for all other } i \end{cases} \tag{12.48}$$

Applying our ESS formula:

$$\text{ESS} \approx \frac{(\sum_{i=1}^{N} \tilde{w}(x^{(i)}))^2}{\sum_{i=1}^{N} \tilde{w}(x^{(i)})^2} \tag{12.49}$$

$$= \frac{(1+1+1)^2}{1^2 + 1^2 + 1^2} \tag{12.50}$$

$$= \frac{9}{3} = 3. \tag{12.51}$$

This confirms our intuition: the ESS equals exactly the number of non-zero weight samples, regardless of how large N is. The effective sample size is severely limited by the rarity of the region we're interested in, making the estimator highly inefficient.

A more effective proposal distribution would concentrate more probability mass in the region of interest. For example, we could use an exponential distribution shifted to start at 5:

$$q(x) = \lambda e^{-\lambda(x-5)} \cdot \mathbf{1}(x \geq 5) \tag{12.52}$$

for some parameter $\lambda > 0$. With this proposal, all samples fall in our region of interest $[5, \infty)$ and have non-zero weights. By choosing an appropriate value of λ (e.g., $\lambda = 1$), we ensure that our proposal has a similar shape to the target distribution in the region of interest. The importance weights remain relatively balanced, and when we apply the ESS formula, we find that approximately 80% of our original samples effectively contribute to our estimate.

This demonstrates a key principle of importance sampling: when the proposal distribution better matches the target distribution in regions of interest, the effective sample size increases dramatically. By focusing our sampling in regions that matter for our target distribution, we achieve estimates with much lower variance for the same computational effort.

Practical Guidelines When selecting a proposal distribution, we should be guided by several key principles:

- The support of $q(x)$ must include the support of $f(x)p(x)$. Mathematically, whenever $f(x)p(x) \neq 0$, we must have $q(x) > 0$.

- Ideally, the proposal $q(x)$ should be proportional to $|f(x)|p(x)$. This minimizes the variance of the importance weights and maximizes the effective sample size.
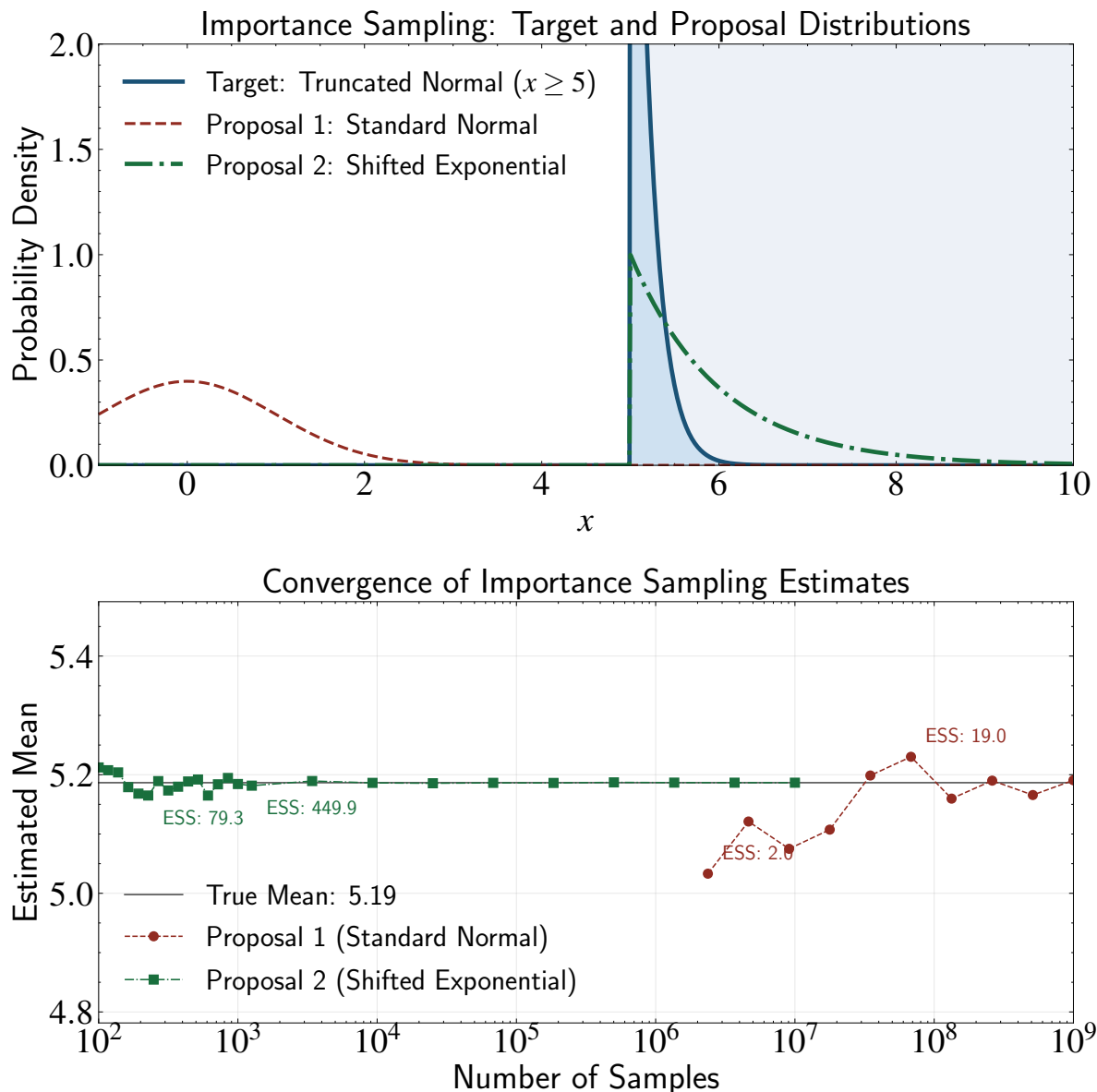
Figure 12.5: Importance sampling example. Top panel: The target distribution (truncated normal for $x \geq 5$) and two proposal distributions: a standard normal distribution (Proposal 1) and a shifted exponential distribution (Proposal 2). The standard normal proposal places very little probability mass in the region of interest, resulting in a very low effective sample size (ESS ≈ 3 for $N = 10^7$ samples). In contrast, the shifted exponential proposal concentrates its probability mass in the region of interest, leading to a much higher effective sample size (ESS $\approx 0.8N$). Bottom panel: Convergence of importance sampling estimates to the true mean as a function of sample size. The shifted exponential proposal (Proposal 2) converges quickly with relatively few samples, while the standard normal proposal (Proposal 1) requires billions of samples to achieve comparable accuracy. The ESS directly impacts the variance of our estimates, with the standard error scaling as $\mathcal{O}(1/\sqrt{\text{ESS}})$.

- $q(x)$ should have heavier tails than $p(x)$ to avoid extreme importance weights in the tails of the distribution, which would reduce the effective sample size.

- $q(x)$ should be easy to sample from and evaluate—after all, if sampling from $q(x)$ were as difficult as sampling from $p(x)$, we would gain little from importance sampling.

When the ESS is small, our estimates suffer from high variance. The standard error of our importance sampling estimate scales as $\mathcal{O}(1/\sqrt{\text{ESS}})$ rather than $\mathcal{O}(1/\sqrt{N})$, highlighting the critical importance of choosing a proposal distribution that yields a high ESS.

Importance sampling is particularly valuable when our primary goal is to estimate expectations of functions with respect to a target distribution, rather than generating samples from that distribution directly. This focus on expectation estimation makes importance sampling especially useful in problems where we need to calculate integrals like posterior means, variances, or other statistical quantities that can be expressed as expectations.

12.7   Summary

Sampling methods form a computational backbone that extends the reach of machine learning and statistical inference far beyond what analytical methods alone can achieve. In this chapter, we have explored several sampling techniques that address the challenge of computing expectations with respect to complex probability distributions where analytical solutions are unavailable.

Our exploration began with historical context through Buffon's needle experiment, which demonstrated how physical randomization can solve mathematical problems that would otherwise require complex calculations. This 18th-century example illustrated the core principle underlying all Monte Carlo methods: using random sampling to approximate integrals, with the characteristic $\mathcal{O}(1/\sqrt{N})$ convergence rate that makes these methods practical for computational applications.

The grid approach provided our entry point into computational sampling methods. By discretizing continuous distributions into histogram approximations, this method transforms the challenging problem of sampling from continuous distributions into the manageable task of sampling from discrete probability mass functions. We used the pinball machine analogy to illustrate how complex continuous processes can be converted into simple discrete counting problems. While the grid approach offers conceptual clarity and works well for low-dimensional problems, it faces the curse of dimensionality—the exponential growth in

computational requirements as the number of dimensions increases makes it impractical for high-dimensional applications.

The inverse CDF method extended the grid approach to its continuous limit, providing exact sampling when analytical inverse cumulative distribution functions are available. We explored concrete examples with exponential and power law distributions that commonly appear in astronomical applications. The method's strength lies in its exactness and efficiency when applicable, but its requirement for closed-form inverse CDFs severely limits its scope. Many distributions encountered in Bayesian inference simply do not have tractable inverse CDFs, necessitating alternative approaches.

Rejection sampling addressed this limitation by offering a geometric approach that works with any evaluable distribution. Using the dart-throwing analogy, we saw how rejection sampling "sculpts" proposal distributions to match target distributions through an accept/reject mechanism. The method requires only the ability to evaluate the target density (even up to a normalizing constant) and works naturally in multiple dimensions. However, it faces efficiency challenges in high-dimensional spaces where acceptance rates can become exponentially small, and it can struggle with heavy-tailed distributions where finding appropriate proposal distributions becomes difficult.

Importance sampling shifted our focus from exact sample generation to efficient expectation estimation. This change in perspective proved valuable because many practical applications in Bayesian inference require computing expectations rather than generating samples. By keeping all samples but weighting them appropriately, importance sampling can be more efficient than rejection sampling, especially when we need only a few specific expectations. The method handles unnormalized distributions naturally through self-normalization, making it particularly valuable for Bayesian applications where posterior distributions are typically known only up to a normalizing constant.

The concept of effective sample size emerged as a critical diagnostic for importance sampling performance. Through the voting analogy, we understood how uneven importance weights can reduce the effective information content of our samples, even when we generate many samples from the proposal distribution. Our concrete example with truncated normal distributions demonstrated how poor proposal choices can yield effective sample sizes orders of magnitude smaller than the actual sample count, while well-chosen proposals can maintain high efficiency.

These methods reveal a progression of increasing sophistication and applicability. The

grid approach provides conceptual foundations but faces dimensionality constraints. The inverse CDF method offers exactness but requires analytical tractability. Rejection sampling provides broad applicability but can suffer efficiency problems. Importance sampling focuses on the practical goal of expectation estimation but requires careful proposal selection to maintain efficiency.

A common theme throughout these methods is the trade-off between accuracy and computational efficiency. Each method represents a different point in this trade-off space, with varying assumptions about what we know about our target distribution and what computational resources we're willing to invest. The grid approach trades accuracy for conceptual simplicity. The inverse CDF method provides perfect accuracy when applicable but fails when analytical solutions don't exist. Rejection sampling trades some efficiency for broad applicability. Importance sampling trades exact sampling for efficient expectation estimation.

Another recurring theme is the curse of dimensionality—the exponential growth of computational requirements as the number of dimensions increases. This challenge affects all the basic sampling methods we studied, though to different degrees. The grid approach faces the most severe dimensionality curse, making it impractical beyond a few dimensions. Rejection sampling faces efficiency challenges in high dimensions due to exponentially decreasing acceptance rates. Even importance sampling can suffer in high dimensions when it becomes difficult to find proposal distributions that adequately cover the target distribution's support.

While the methods covered in this chapter provide valuable tools for low-dimensional problems and establish important conceptual foundations, they reach practical limits with the complex, high-dimensional models common in modern astronomy. Real astronomical applications often involve dozens or hundreds of parameters, making the basic techniques we've studied insufficient for practical use.

These limitations motivate more advanced techniques like Markov Chain Monte Carlo (MCMC) methods, which we will explore in our next chapter. MCMC methods address the dimensionality challenge by generating correlated samples that gradually explore the parameter space according to the target probability distribution. Rather than attempting to sample entire distributions at once, MCMC methods explore the space incrementally through local moves guided by the target distribution itself, focusing computational effort on regions of high probability.

The foundation we've built in this chapter—understanding how sampling can approximate integrals, recognizing the importance of proposal distributions, and appreciating the trade-offs between accuracy and efficiency—will prove essential for understanding the more sophisticated MCMC techniques that have revolutionized computational statistics and enabled practical Bayesian inference for complex models in astronomy and beyond.

12.8 Appendix: Derivation of Effective Sample Size

This appendix provides the detailed mathematical derivation of the effective sample size formula for importance sampling. The derivation uses the delta method to analyze the variance of the self-normalized importance sampling estimator.

We start with our self-normalized importance sampling estimator:

$$\hat{I} = \frac{\sum_{i=1}^{N} \tilde{w}(x^{(i)}) f(x^{(i)})}{\sum_{i=1}^{N} \tilde{w}(x^{(i)})}. \tag{12.53}$$

For clarity, let's define normalized weights:

$$w_i = \frac{\tilde{w}(x^{(i)})}{\sum_{j=1}^{N} \tilde{w}(x^{(j)})}, \tag{12.54}$$

so that $\sum_{i=1}^{N} w_i = 1$. Our estimator becomes:

$$\hat{I} = \sum_{i=1}^{N} w_i f(x^{(i)}). \tag{12.55}$$

For comparison, consider the scenario where we could sample directly from $p(x)$. The variance of such a direct Monte Carlo estimator would be:

$$\text{Var}_{\text{direct}}(\hat{I}) = \frac{\text{Var}_p(f(x))}{N}. \tag{12.56}$$

Variance Analysis Using the Delta Method   Our self-normalized importance sampling estimator can be expressed as a ratio of two random quantities:

$$\hat{I} = \frac{A}{B}, \tag{12.57}$$

where

$$A = \frac{1}{N} \sum_{i=1}^{N} \tilde{w}(x^{(i)}) f(x^{(i)}) \tag{12.58}$$

$$B = \frac{1}{N} \sum_{i=1}^{N} \tilde{w}(x^{(i)}). \tag{12.59}$$

For large N, both A and B will converge to their expected values:

$$\mathbb{E}[A] = \mathbb{E}_q[\tilde{w}(x) f(x)] \tag{12.60}$$

$$\mathbb{E}[B] = \mathbb{E}_q[\tilde{w}(x)]. \tag{12.61}$$

To derive the variance of our estimator $\hat{I} = A/B$, we apply the delta method, which approximates the variance of a function of random variables using a first-order Taylor expansion. Let's expand $\hat{I} = A/B$ around the expected values $\mathbb{E}[A]$ and $\mathbb{E}[B]$:

$$\hat{I} \approx \frac{\mathbb{E}[A]}{\mathbb{E}[B]} + \frac{\partial}{\partial A}\left(\frac{A}{B}\right)\bigg|_{A=\mathbb{E}[A],B=\mathbb{E}[B]} (A - \mathbb{E}[A]) + \frac{\partial}{\partial B}\left(\frac{A}{B}\right)\bigg|_{A=\mathbb{E}[A],B=\mathbb{E}[B]} (B - \mathbb{E}[B]) \tag{12.62}$$

$$= \frac{\mathbb{E}[A]}{\mathbb{E}[B]} + \frac{1}{\mathbb{E}[B]}(A - \mathbb{E}[A]) - \frac{\mathbb{E}[A]}{\mathbb{E}[B]^2}(B - \mathbb{E}[B]). \tag{12.63}$$

Taking the variance of this approximation and noting that $\frac{\mathbb{E}[A]}{\mathbb{E}[B]}$ is a constant:

$$\mathrm{Var}(\hat{I}) \approx \mathrm{Var}\left(\frac{1}{\mathbb{E}[B]}(A - \mathbb{E}[A]) - \frac{\mathbb{E}[A]}{\mathbb{E}[B]^2}(B - \mathbb{E}[B])\right) \tag{12.64}$$

$$= \frac{1}{\mathbb{E}[B]^2}\mathrm{Var}(A) + \frac{\mathbb{E}[A]^2}{\mathbb{E}[B]^4}\mathrm{Var}(B) - 2\frac{\mathbb{E}[A]}{\mathbb{E}[B]^3}\mathrm{Cov}(A, B). \tag{12.65}$$

Recalling that $A = \frac{1}{N}\sum_{i=1}^{N} \tilde{w}(x^{(i)})f(x^{(i)})$ and $B = \frac{1}{N}\sum_{i=1}^{N} \tilde{w}(x^{(i)})$, and that $\frac{\mathbb{E}[A]}{\mathbb{E}[B]} = \hat{I}$, we can express this in terms of the original variables:

$$\mathrm{Var}(\hat{I}) \approx \frac{1}{N}\frac{\mathrm{Var}_q(\tilde{w}(x)f(x)) + \hat{I}^2\mathrm{Var}_q(\tilde{w}(x)) - 2\hat{I}\mathrm{Cov}_q(\tilde{w}(x)f(x), \tilde{w}(x))}{(\mathbb{E}_q[\tilde{w}(x)])^2} \tag{12.66}$$

$$= \frac{1}{N}\frac{\mathrm{Var}_q(\tilde{w}(x)f(x) - \hat{I} \cdot \tilde{w}(x))}{(\mathbb{E}_q[\tilde{w}(x)])^2}. \tag{12.67}$$

The last step follows because $\text{Var}(X - Y) = \text{Var}(X) + \text{Var}(Y) - 2\text{Cov}(X, Y)$, where we set $X = \tilde{w}(x)f(x)$ and $Y = \hat{I} \cdot \tilde{w}(x)$.

This formula captures how the uncertainty in both the numerator and denominator of our estimator contributes to the overall variance. The term $\tilde{w}(x)f(x) - \hat{I} \cdot \tilde{w}(x)$ represents the covariance between the weighted function values and the weights themselves.

For a general approximation, we often simplify by dropping the term $\hat{I} \cdot \tilde{w}(x)$:

$$\text{Var}(\hat{I}) \approx \frac{1}{N} \frac{\text{Var}_q(\tilde{w}(x)f(x))}{(\mathbb{E}_q[\tilde{w}(x)])^2}. \tag{12.68}$$

To find the effective sample size, we set this variance equal to the variance of direct sampling:

$$\frac{\text{Var}_p(f(x))}{\text{ESS}} = \frac{1}{N} \frac{\text{Var}_q(\tilde{w}(x)f(x))}{(\mathbb{E}_q[\tilde{w}(x)])^2}. \tag{12.69}$$

Solving for ESS:

$$\text{ESS} = N \frac{\text{Var}_p(f(x)) \cdot (\mathbb{E}_q[\tilde{w}(x)])^2}{\text{Var}_q(\tilde{w}(x)f(x))}. \tag{12.70}$$

Since we typically don't know $\text{Var}_p(f(x))$ and $f(x)$ may vary across applications, we can derive a function-independent approximation by focusing on the variance of the weights themselves:

$$\text{ESS} \approx N \frac{(\mathbb{E}_q[\tilde{w}(x)])^2}{\mathbb{E}_q[\tilde{w}(x)^2]}. \tag{12.71}$$

Using sample estimates:

$$\text{ESS} \approx N \frac{(\frac{1}{N} \sum_{i=1}^{N} \tilde{w}(x^{(i)}))^2}{\frac{1}{N} \sum_{i=1}^{N} \tilde{w}(x^{(i)})^2} = \frac{(\sum_{i=1}^{N} \tilde{w}(x^{(i)}))^2}{\sum_{i=1}^{N} \tilde{w}(x^{(i)})^2}. \tag{12.72}$$

This formula represents the ratio of the squared first moment to the second moment of the weights, providing a measure of how uniformly distributed the importance weights are across the sample. When all weights are equal, the ESS equals N (maximum efficiency). When the weights are highly variable, the ESS can be much smaller than N, indicating that only a fraction of the samples are effectively contributing to the estimate.

Further Readings: The development of Monte Carlo sampling methods builds upon fundamental work in computational statistics, with early systematic treatment in Von Neumann [1951] who described both the inverse transform method and rejection sampling within a unified computational framework. For the inverse CDF method, Box and Muller [1958] provides an elegant transformation technique for generating normal variates that avoids numerical challenges of the direct approach. The mathematical foundations of rejection sampling are analyzed in Forsythe [1972] who examines von Neumann's comparison method with detailed efficiency analysis. Kinderman and Monahan [1977] presents the ratio-of-uniforms method as a transformation of rejection sampling with improved computational properties, and Marsaglia [1977] introduces squeeze techniques that enhance efficiency through auxiliary bounds. For importance sampling, early applications to particle transport problems appear in Goertzel [1949] and Kahn [1950], with Kahn and Harris [1951] providing accessible exposition for the broader scientific community. The statistical framework for importance sampling as a variance reduction technique is developed in Kahn and Marshall [1953], while Kahn [1955] offers comprehensive treatment of various Monte Carlo sampling techniques within a unified framework. For readers seeking comprehensive coverage, Rubinstein [1981] provides practical treatment bridging theory and applications, Devroye [1986] offers encyclopedic coverage of random variate generation with rigorous mathematical analysis, Kalos and Whitlock [1986] emphasizes variance reduction techniques with physics applications, and Fishman [1996] presents modern computational perspectives with extensive algorithmic coverage and error analysis. These works collectively establish the theoretical foundations and practical implementations of the fundamental Monte Carlo sampling techniques that underpin modern computational statistics.

Chapter 13

Markov Chain Monte Carlo

Chapter 12 introduced us to Monte Carlo methods as computational tools for approximating integrals that lack analytical solutions. We explored how sampling techniques enable Bayesian inference when direct calculation becomes impossible, transforming the challenging problem of computing expectations into the more manageable task of generating samples from target distributions.

The sampling methods we studied—grid approaches, inverse transform sampling, rejection sampling, and importance sampling—provide valuable tools for simple problems and establish conceptual foundations. However, these methods reach practical limits when confronted with the complex, high-dimensional problems common in modern astronomy. Each method suffers from some form of the curse of dimensionality, where computational requirements grow exponentially with the number of parameters.

Consider a typical astronomical inference problem: estimating the physical properties of an exoplanet system from radial velocity and transit data. Such models often involve 10-20 parameters including planetary masses, radii, orbital periods, eccentricities, and stellar properties. The posterior distribution for these parameters exhibits complex correlations and potentially multiple modes representing different valid solutions.

Grid-based methods become prohibitively expensive beyond a few dimensions—with just 10 parameters and 100 grid points per dimension, we would need 10^{20} evaluations. Inverse transform sampling faces a different challenge: computing and inverting the cumulative distribution function becomes analytically intractable for complex posteriors. Rejection sampling suffers from exponentially decreasing acceptance rates as dimensionality increases.

Even importance sampling struggles to find proposal distributions that adequately cover high-dimensional parameter spaces.

This chapter introduces Markov Chain Monte Carlo (MCMC), a family of algorithms that overcome these dimensionality limitations and have revolutionized Bayesian inference in astronomy over the past three decades. Unlike the global approaches from Chapter 12, MCMC methods explore parameter space through sequential, local moves that depend only on the current position—not the entire history of where the chain has been.

The key insight behind MCMC is deceptively simple: instead of trying to sample from the entire posterior distribution at once, we construct a random walk through parameter space where each step depends only on the current location. By carefully designing the rules for this random walk, we can ensure that the chain eventually settles into a pattern that matches our target posterior distribution. The samples generated by this process provide the foundation for all the Bayesian calculations we need to perform.

To build intuition for how MCMC works, imagine an explorer trying to map the population distribution of Columbus, Ohio. Rather than conducting a comprehensive citywide census (analogous to grid methods), our explorer follows a simple strategy: each day, they randomly choose a nearby neighborhood to visit based only on their current location. The key is that they make these choices more often toward neighborhoods with higher population density.

Initially, the explorer might wander somewhat randomly as they learn about the city. However, after many days of exploration, a pattern emerges: they spend more time in densely populated areas like the Short North and less time in sparse suburbs. The frequency with which they visit different neighborhoods eventually matches the true population distribution. By recording their daily locations over many weeks, we obtain a representative sample of Columbus's population density without needing to survey every street systematically.

This exploration strategy captures the essence of MCMC. The "neighborhoods" represent points in our parameter space, the "population density" corresponds to posterior probability, and the "explorer's path" becomes our Markov chain. The sequential nature of the exploration—where each day's destination depends only on today's location—gives the method its name: Markov Chain Monte Carlo.

The advantages of this approach for astronomical applications are substantial. MCMC only requires that we can evaluate the posterior up to a proportionality constant, avoiding

MCMC Sampling of Multimodal Distribution
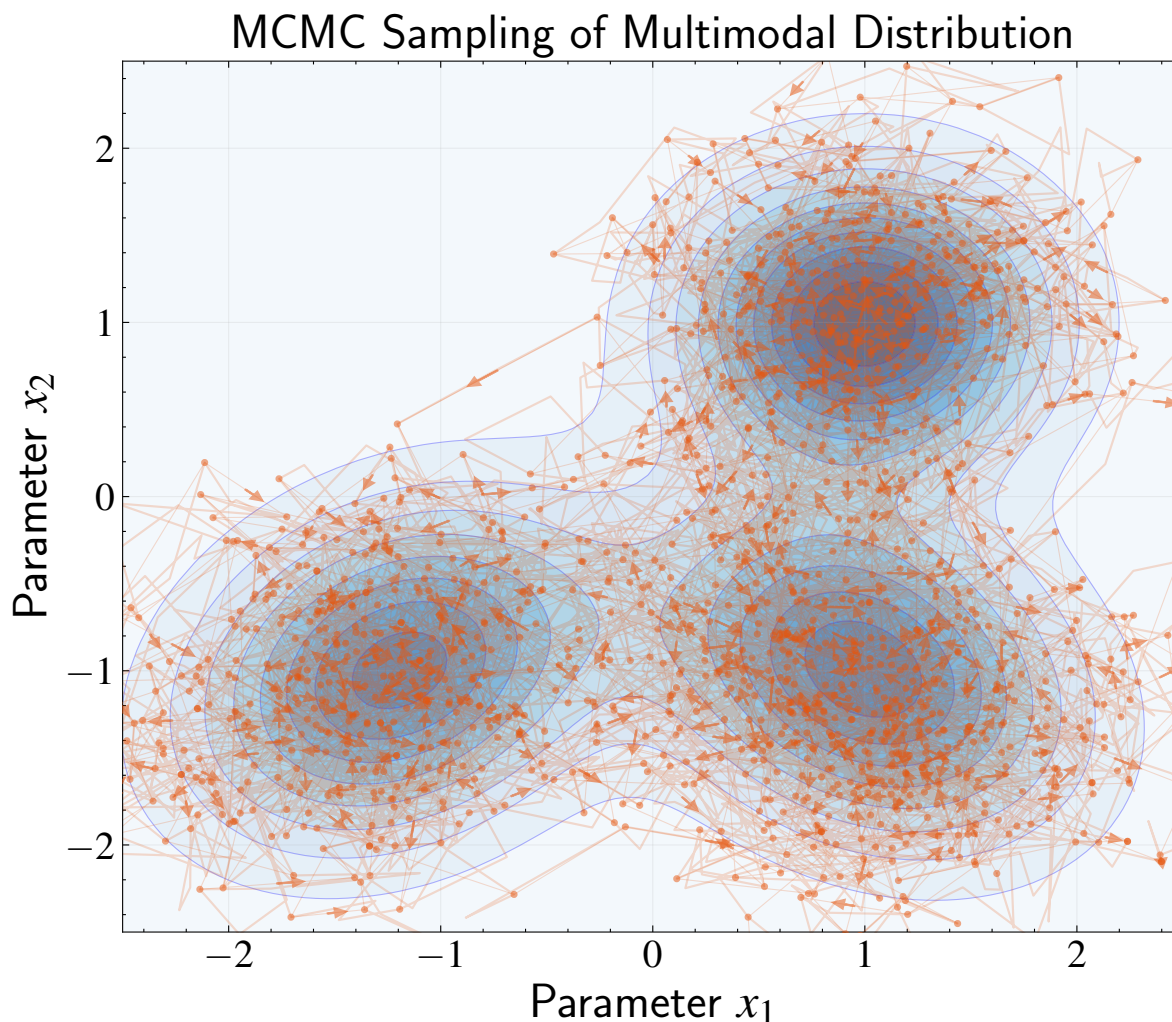
Figure 13.1: Illustration of Markov Chain Monte Carlo (MCMC) sampling on a multimodal posterior distribution. The background contours show the probability density of a complex posterior with three distinct modes. The orange line represents the path of the MCMC chain as it explores the parameter space, with small directional arrows indicating the progression of the chain. The chain continuously navigates through the parameter space, exploring both high and low probability regions, though it naturally spends more time in areas of higher probability density. This sequential exploration strategy transforms an intractable sampling problem into a tractable guided random walk, allowing MCMC to efficiently sample from complex distributions that would be impossible to characterize with simpler methods.

difficult normalization calculations. The method naturally handles correlation structures in complex parameter spaces by exploring them sequentially rather than trying to characterize them globally. It can discover and sample from multiple modes in the distribution when the algorithm is designed appropriately. Most importantly, MCMC scales effectively to high dimensions because it focuses computational effort on regions of high probability rather than

attempting exhaustive exploration.

However, MCMC methods introduce new challenges that don't appear in direct sampling approaches. The sequential nature of the exploration means that successive samples are correlated with each other, reducing their effective information content. Determining when the chain has converged to the target distribution requires careful diagnostics since we cannot directly observe this convergence. The efficiency of exploration depends critically on algorithm design choices, particularly how we propose new moves through parameter space.

This chapter develops these ideas systematically. We begin with the mathematical foundations that ensure MCMC methods work correctly, introducing the concepts of Markov chains, detailed balance, and ergodicity. We then explore practical algorithms, starting with the simple but powerful Metropolis algorithm and progressing to more sophisticated variants. Throughout, we maintain focus on the practical aspects of implementation, including how to tune algorithms for efficiency, diagnose convergence problems, and extract reliable inferences from MCMC output.

The transition from the direct sampling methods of Chapter 12 to the sequential exploration strategies of MCMC represents more than just a computational advancement. It reflects a shift in perspective from trying to characterize entire distributions globally to exploring them locally through guided random walks. This perspective will prove valuable as we encounter increasingly complex models in subsequent chapters, where MCMC provides the computational foundation for advanced techniques like Gaussian processes and neural networks.

13.1   Markov Chains and Monte Carlo: Core Idea

To understand MCMC, we must first grasp what makes a process "Markovian." The term comes from the Russian mathematician Andrey Markov, who studied sequences of events where the future depends only on the present state, not on how we arrived there. This "memoryless" property distinguishes Markov processes from more complex dependencies where the entire history matters.

Let's develop this concept through our Columbus exploration analogy. Each day, our explorer visits a different location—a café, museum, park, or neighborhood. The explorer uses a guidebook that suggests where to go next based solely on their current location. Importantly, the guidebook doesn't care whether they reached the current location from

downtown yesterday or from the suburbs last week. This selective memory defines the Markov property.

Mathematically, if we denote our sequence of locations as $\{X_0, X_1, X_2, ...\}$, then the Markov property states:

$$P(X_{t+1} = x | X_0 = x_0, X_1 = x_1, ..., X_t = x_t) = P(X_{t+1} = x | X_t = x_t) \qquad (13.1)$$

The probability of tomorrow's location depends only on today's location, not on the path taken to reach today's position. This simplification proves computationally powerful because it allows us to characterize the entire system using only the transition probabilities between states.

The transition matrix $T(\mathbf{x}, \mathbf{x}')$ completely characterizes a Markov chain's behavior. This function gives the probability density of moving to state $\mathbf{x}'$ given that the current state is $\mathbf{x}$. In our Columbus analogy, this represents the guidebook that tells our explorer the likelihood of visiting different locations based on where they currently are.

For example, if our explorer is currently in the Short North (a vibrant arts district), the guidebook might suggest:

- 40% chance of staying in the Short North (high local attractions)

- 30% chance of moving to nearby German Village

- 20% chance of visiting downtown

- 10% chance of traveling to more distant neighborhoods

These percentages must sum to 100% since the explorer must go somewhere each day. This constraint—that transition probabilities from any state must sum to 1—represents a requirement for any valid transition matrix.

Now let's expand our perspective beyond a single explorer. Instead of following just one person, imagine we're tracking the entire population of Columbus as they move around the city according to our guidebook's rules. This shift from individual trajectories to population dynamics provides crucial insight into how MCMC works.

Our goal becomes designing a guidebook so that the population distribution across
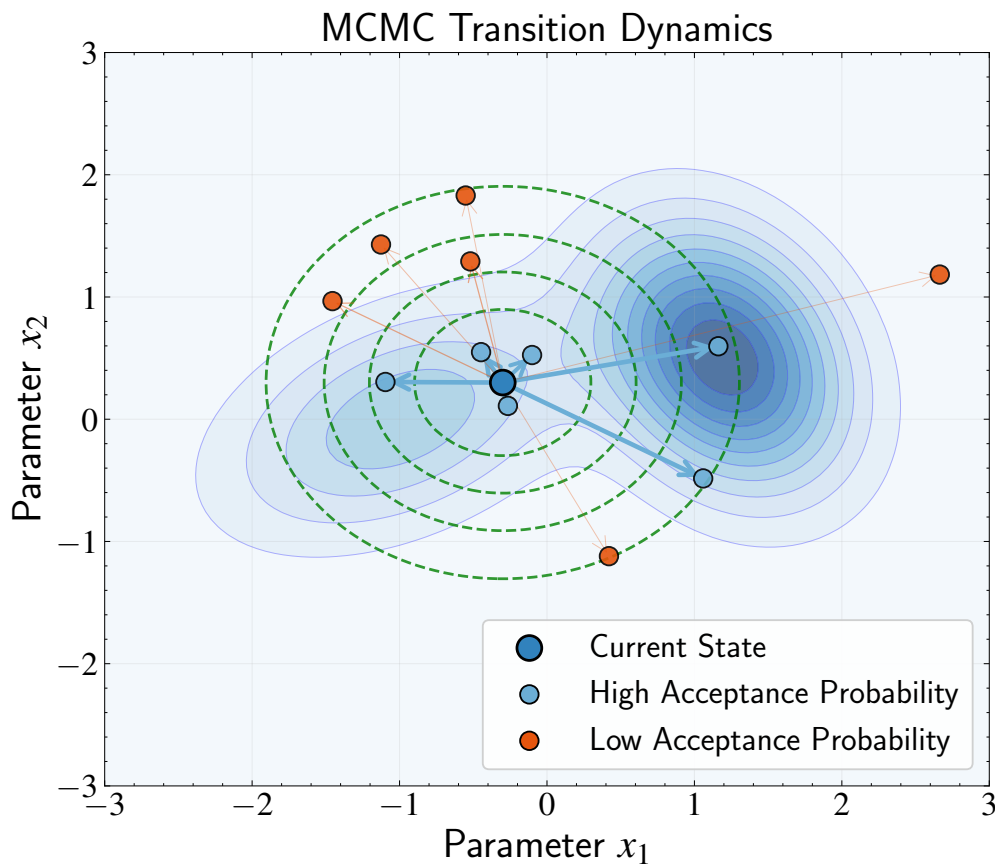
Figure 13.2: Visualization of the transition dynamics in Markov Chain Monte Carlo. The blue contours represent the posterior distribution $p(\mathbf{x}|\mathcal{D})$ that we aim to sample from. The current state (dark blue point) is the center of a transition matrix (green dashed contours) that proposes possible next states. Proposals toward regions of higher posterior density (light blue points) have high acceptance probabilities, indicated by thicker arrows, while proposals toward regions of lower posterior density (orange points) have low acceptance probabilities, shown with thinner arrows. This mechanism ensures that the Markov chain spends more time in high-probability regions while occasionally exploring less probable areas, analogous to our city traveler spending more time in densely populated neighborhoods. Over many iterations, this exploration strategy generates samples that represent the target posterior distribution.

neighborhoods stabilizes to match a specific target distribution—perhaps the actual population density of Columbus. This perspective allows us to view the transition matrix T as an operator that transforms one population distribution into another.

Given a distribution $p(\mathbf{x})$ describing where people are currently located across the city, the transition operator transforms this into a new distribution describing where they'll

be after everyone follows the guidebook for one step:

$$(Tp)(\mathbf{x'}) = \int p(\mathbf{x})T(\mathbf{x}, \mathbf{x'})d\mathbf{x} \tag{13.2}$$

Here, $(Tp)(\mathbf{x'})$ represents the probability density of being at state $\mathbf{x'}$ after applying the transition operator to distribution $p(\mathbf{x})$. The integral sums up all the ways of reaching state $\mathbf{x'}$ from any possible starting state $\mathbf{x}$, weighted by the probability of being at that starting state.

The key question becomes: how do we create a guidebook that leads to our desired distribution? We need a transition matrix that makes the population distribution naturally converge to our target and then remain stable there.

This brings us to the concept of a stationary distribution. A distribution $p(\mathbf{x})$ is stationary with respect to the transition operator T if applying T to p returns the same distribution:

$$(Tp)(\mathbf{x}) = p(\mathbf{x}) \tag{13.3}$$

In our city analogy, if the population is already distributed according to our target distribution, and everyone follows our guidebook's suggestions, the overall population distribution remains unchanged. The stationary distribution represents the equilibrium state of our system.

Consider what this means practically. If we start with any initial distribution of people across Columbus and let them follow our guidebook rules repeatedly, we want the population to eventually redistribute itself to match our target pattern and then stay that way. Once this equilibrium is reached, the flows of people between neighborhoods balance perfectly—as many people move from the Short North to German Village as move in the opposite direction.

The central insight of MCMC emerges from connecting these two viewpoints—the individual explorer and the population distribution. If we design our guidebook so that our target posterior distribution $p(\mathbf{x}|\mathcal{D})$ becomes the stationary distribution of the resulting Markov chain, then a single explorer following this guidebook for a long time will visit different locations with frequencies proportional to their posterior probabilities.

This connection between the population-level equilibrium and individual-level behav-
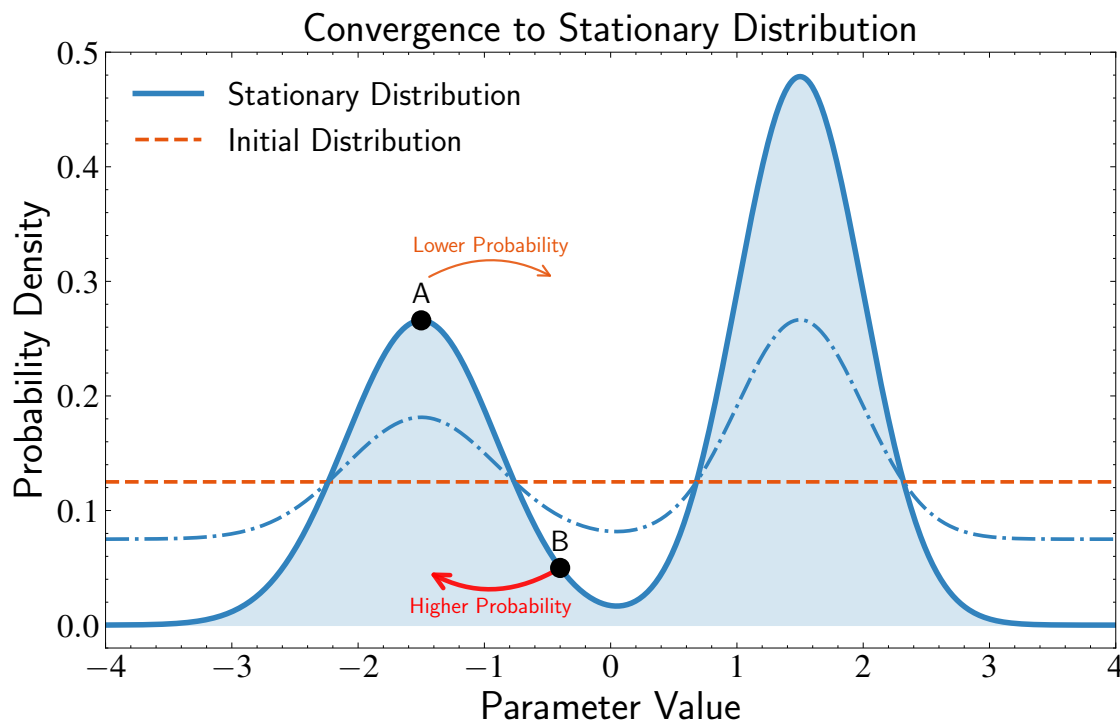
Figure 13.3: Illustration of convergence to the stationary distribution in MCMC. The blue solid curve represents the target stationary distribution, while the orange dashed line shows the initial distribution. The blue dash-dot line depicts an intermediate state during convergence. Before reaching stationarity, there exists a net flow of probability mass toward the target distribution—similar to population migration in our city analogy, with more people moving into densely populated neighborhoods than leaving them. This net flow is driven by asymmetric transition probabilities: transitions from low-probability to high-probability regions (point B to A, thick red arrow) occur with higher probability than transitions from high-probability to low-probability regions (point A to B, thin orange arrow). Once the chain reaches the stationary distribution, these flows perfectly balance each other—the detailed balance principle ensures that for every pair of states, the probability flow in each direction is exactly equal, maintaining the distribution in perfect equilibrium with no further net change. The Markov chain thus first evolves toward the target distribution and then remains there indefinitely.

ior relies on a deep mathematical principle called ergodicity, which we'll explore in detail later. For now, the key insight is that when the population distribution reaches equilibrium, a single traveler's long-term visitation pattern will match this equilibrium distribution.

By recording where our explorer goes over many steps, we effectively sample from the posterior distribution. This gives us the foundation for all the Bayesian calculations we need to perform—computing posterior means, quantifying uncertainties, making predictions, and comparing models.

The beauty of this approach lies in its simplicity: it transforms an intractable sampling problem into a more manageable one of designing a Markov chain with the right properties. We only need to evaluate the posterior at specific points, not normalize it or directly sample from it. This requirement—evaluating rather than integrating—is precisely what makes MCMC practical for the complex posterior distributions encountered in astronomical inference.

This conceptual foundation sets the stage for understanding how to actually construct such transition matrices. The challenge shifts from the impossible task of sampling directly from complex posteriors to the achievable goal of designing random walks with appropriate stationary distributions. In the following sections, we'll explore the mathematical principles that guide this design process.

13.2   Detailed Balance

The previous section established that we need to design a transition matrix so that our target posterior distribution becomes the stationary distribution of the resulting Markov chain. But how do we actually construct such a transition matrix? This is where the concept of detailed balance becomes crucial—it provides a practical condition for ensuring that our Markov chain has the posterior distribution as its stationary distribution.

For clarity, we'll denote our posterior distribution $p(\mathbf{x}|\mathcal{D})$ as $p(\mathbf{x})$, which represents the probability distribution of our model parameters $\mathbf{x}$ given our observed data $\mathcal{D}$. The key insight builds on our Columbus analogy, where we want to achieve a specific population distribution across neighborhoods.

Imagine we want the Short North to have a bustling population while Upper Arlington remains a quieter area. To achieve this distribution, our guidebook needs to encourage more people to move from Upper Arlington to the Short North than vice versa. Over time, the Short North population will build up. However, as more people accumulate in the Short North, the population difference itself creates a counterbalance—there are simply more people in the Short North who might move to Upper Arlington, even if each individual is less likely to make that move.

Eventually, these opposing forces reach equilibrium. The population distribution stabilizes not because people stop moving, but because the flows between neighborhoods balance perfectly. This balance occurs when the number of people moving from the Short

North to Upper Arlington exactly equals the number moving in the opposite direction.

Mathematically, detailed balance expresses this equilibrium condition as:

$$p(\mathbf{x})T(\mathbf{x}, \mathbf{x}') = p(\mathbf{x}')T(\mathbf{x}', \mathbf{x}) \tag{13.4}$$

To understand this equation intuitively, let's interpret each term using our Columbus analogy. The quantity $p(\mathbf{x})$ represents the population of neighborhood $\mathbf{x}$ (the Short North), while $T(\mathbf{x}, \mathbf{x}')$ represents the probability that someone in the Short North will move to Upper Arlington ($\mathbf{x}'$). The left side, $p(\mathbf{x})T(\mathbf{x}, \mathbf{x}')$, therefore represents the "flow" of people from the Short North to Upper Arlington.

Similarly, the right side represents the flow in the opposite direction. Detailed balance says that these flows must be equal for every pair of neighborhoods in our city. This is a strong condition—it requires perfect balance between every pair of states in our system, not just overall balance across the entire city.

The beauty of detailed balance is that it provides us with a concrete way to design our transition matrix. Since we know our target distribution $p(\mathbf{x})$ in advance (it's the posterior we want to sample from), we can use it to construct a guidebook that naturally leads to this distribution. When the flows balance for all pairs of neighborhoods, the overall population distribution remains stable.

Let's prove that detailed balance indeed ensures $p(\mathbf{x})$ is a stationary distribution. We need to show that if detailed balance holds, then $p(\mathbf{x})$ satisfies the stationary distribution equation:

$$p(\mathbf{x}') = \int p(\mathbf{x})T(\mathbf{x}, \mathbf{x}')d\mathbf{x} \tag{13.5}$$

Starting with the detailed balance equation:

$$p(\mathbf{x})T(\mathbf{x}, \mathbf{x}') = p(\mathbf{x}')T(\mathbf{x}', \mathbf{x}) \tag{13.6}$$

We integrate both sides over all possible states $\mathbf{x}$:

$$\int p(\mathbf{x})T(\mathbf{x}, \mathbf{x}')d\mathbf{x} = \int p(\mathbf{x}')T(\mathbf{x}', \mathbf{x})d\mathbf{x} \tag{13.7}$$
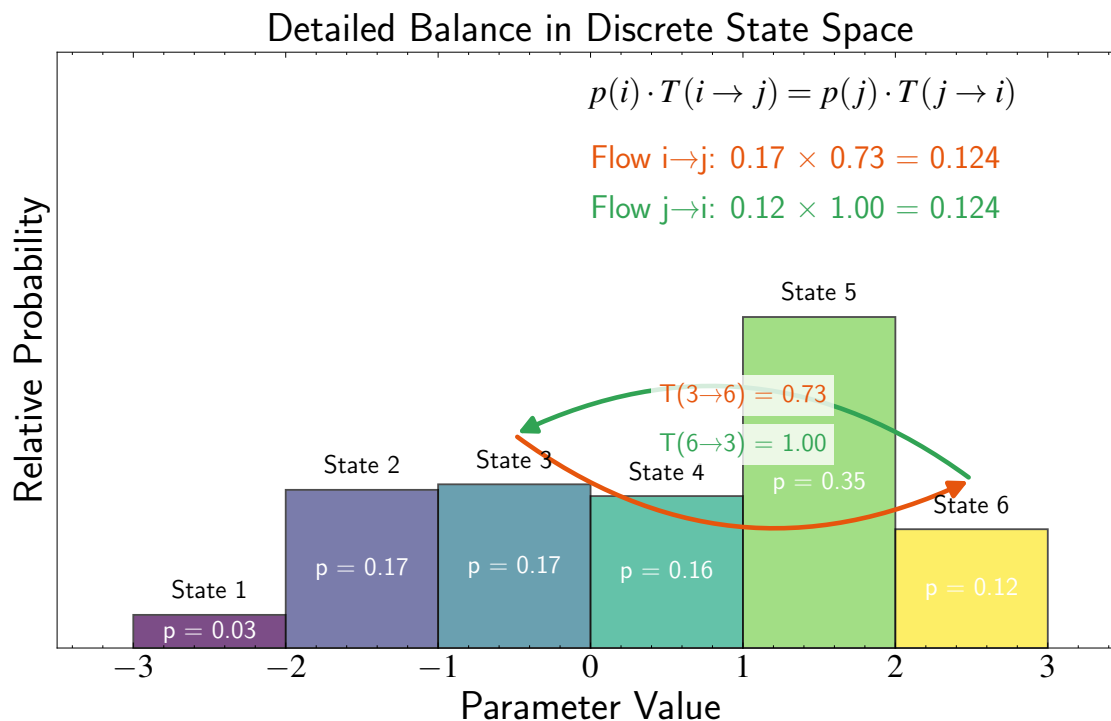
Figure 13.4: Visualization of detailed balance using a discrete state space representation. Each histogram bin represents a state in the Markov chain, with heights proportional to their stationary probabilities $p(i)$. The arrows between states 3 and 6 show transitions in both directions, with their respective transition probabilities $T(i \rightarrow j)$ and $T(j \rightarrow i)$. Detailed balance ensures that the flow from state i to state j equals the flow from j to i: $p(i) \cdot T(i \rightarrow j) = p(j) \cdot T(j \rightarrow i)$. This equality is demonstrated numerically in the figure. When detailed balance holds for all pairs of states, the distribution remains stationary—there is no net change in the probability mass. Moreover, if the system is out of equilibrium, detailed balance actively drives it toward the equilibrium state.

On the right side, notice that $p(\mathbf{x}')$ doesn't depend on $\mathbf{x}$, so we can pull it outside the integral:

$$\int p(\mathbf{x})T(\mathbf{x}, \mathbf{x}')d\mathbf{x} = p(\mathbf{x}') \int T(\mathbf{x}', \mathbf{x})d\mathbf{x} \qquad (13.8)$$

Now, $\int T(\mathbf{x}', \mathbf{x})d\mathbf{x} = 1$ because the total probability of transitioning from state $\mathbf{x}'$ to all possible states must sum to 1. This is a property of transition probabilities—if you're currently in Upper Arlington, the probabilities of moving to all possible neighborhoods (including staying in Upper Arlington) must add up to 100%.

Therefore:

$$\int p(\mathbf{x})T(\mathbf{x}, \mathbf{x}')d\mathbf{x} = p(\mathbf{x}') \cdot 1 = p(\mathbf{x}') \tag{13.9}$$

This is exactly the definition of a stationary distribution. We have proven that if detailed balance holds, then our target distribution $p(\mathbf{x})$ is indeed a stationary distribution of the Markov chain defined by transition matrix T.

Returning to our Columbus analogy, detailed balance ensures that our city's population distribution remains stable over time. If we design our guidebook so that the flow of people between any two neighborhoods is perfectly balanced, then the overall distribution will match our target. The population in each neighborhood stays constant not because people stop moving, but because the inflows and outflows balance perfectly.

This gives us a practical strategy for constructing MCMC algorithms: we need to design transition matrices that satisfy detailed balance with respect to our target posterior distribution. The challenge is no longer the abstract problem of finding stationary distributions, but the concrete task of constructing transition rules that balance flows appropriately. In the next section, we'll see how the Metropolis algorithm provides one such construction.

13.3   The Metropolis Algorithm

Now that we understand detailed balance as a condition for ensuring our target posterior is the stationary distribution of our Markov chain, a natural question arises: How can we actually construct a transition matrix that satisfies this condition? While there are many approaches in the MCMC literature, the Metropolis algorithm provides the simplest and most intuitive solution—demonstrating that such a transition matrix not only exists but can be constructed in a remarkably straightforward way.

The key insight of the Metropolis algorithm is to decompose the transition process into two components: proposing a new state and then deciding whether to accept or reject this proposal. Continuing our Columbus analogy, this is like our traveler first consulting a guidebook that suggests a neighborhood to visit (the proposal), and then making a personal decision about whether to follow that suggestion (the acceptance/rejection step). This two-step process gives us the flexibility needed to design a transition mechanism that satisfies detailed balance.

Mathematically, we can express any transition matrix as:

$$T(\mathbf{x}, \mathbf{x}') = q(\mathbf{x}'|\mathbf{x})A(\mathbf{x}, \mathbf{x}') \tag{13.10}$$

where $q(\mathbf{x}'|\mathbf{x})$ is the proposal distribution—the probability density of suggesting a move to state $\mathbf{x}'$ given that we're currently at state $\mathbf{x}$—and $A(\mathbf{x}, \mathbf{x}')$ is the acceptance probability for that proposed move.

The Metropolis algorithm makes a specific choice for the proposal distribution: it must be symmetric, meaning:

$$q(\mathbf{x}'|\mathbf{x}) = q(\mathbf{x}|\mathbf{x}') \tag{13.11}$$

This symmetry condition simply means that the probability of proposing a move from state $\mathbf{x}$ to state $\mathbf{x}'$ is the same as the probability of proposing the reverse move. In our Columbus analogy, this would mean that the guidebook is equally likely to suggest traveling from the Short North to Upper Arlington as it is to suggest traveling from Upper Arlington to the Short North.

A common example in astronomical applications is a multivariate Gaussian centered at the current position:

$$q(\mathbf{x}'|\mathbf{x}) = \mathcal{N}(\mathbf{x}'|\mathbf{x}, \mathbf{\Sigma}) \tag{13.12}$$

where $\mathbf{\Sigma}$ is the covariance matrix that controls the step size and direction of our proposals. This proposal naturally satisfies the symmetry condition because the distance from $\mathbf{x}$ to $\mathbf{x}'$ is the same as the distance from $\mathbf{x}'$ to $\mathbf{x}$.

With this symmetric proposal distribution, the Metropolis algorithm defines the acceptance probability as:

$$A(\mathbf{x}, \mathbf{x}') = \min\left(1, \frac{p(\mathbf{x}')}{p(\mathbf{x})}\right) \tag{13.13}$$

Let's understand what this acceptance probability means in practice. If the proposed state $\mathbf{x}'$ has higher posterior probability than the current state $\mathbf{x}$ (meaning $p(\mathbf{x}') \geq p(\mathbf{x})$), then the ratio $p(\mathbf{x}')/p(\mathbf{x}) \geq 1$, and we accept the proposal with probability 1—we always move to regions of higher probability.

If the proposed state has lower posterior probability (meaning $p(\mathbf{x}') < p(\mathbf{x})$), then the ratio $p(\mathbf{x}')/p(\mathbf{x}) < 1$, and we accept the proposal with probability equal to this ratio. For example, if the proposed state has 70% of the probability density of the current state, we

accept the move with 70% probability.

Returning to our Columbus analogy, this acceptance rule creates a natural bias toward densely populated neighborhoods. If our explorer is currently in the Short North and the guidebook suggests visiting Upper Arlington, they check the population densities of both neighborhoods. If Upper Arlington is more densely populated, they always go there. If Upper Arlington has only 70% of the population density of the Short North, they have a 70% chance of moving there. If they decide not to go, they stay in the Short North for another day.

Let's verify that this choice of acceptance probability satisfies detailed balance with respect to our target posterior distribution $p(\mathbf{x})$. Recall that detailed balance requires:

$$p(\mathbf{x})T(\mathbf{x}, \mathbf{x}') = p(\mathbf{x}')T(\mathbf{x}', \mathbf{x}) \tag{13.14}$$

Substituting our transition matrix:

$$p(\mathbf{x})q(\mathbf{x}'|\mathbf{x})A(\mathbf{x}, \mathbf{x}') = p(\mathbf{x}')q(\mathbf{x}|\mathbf{x}')A(\mathbf{x}', \mathbf{x}) \tag{13.15}$$

Using the symmetry of our proposal distribution ($q(\mathbf{x}'|\mathbf{x}) = q(\mathbf{x}|\mathbf{x}')$), this simplifies to:

$$p(\mathbf{x})A(\mathbf{x}, \mathbf{x}') = p(\mathbf{x}')A(\mathbf{x}', \mathbf{x}) \tag{13.16}$$

Now, let's consider the two possible cases. If $p(\mathbf{x}') \geq p(\mathbf{x})$, then:

$$A(\mathbf{x}, \mathbf{x}') = \min\left(1, \frac{p(\mathbf{x}')}{p(\mathbf{x})}\right) = 1 \tag{13.17}$$

$$A(\mathbf{x}', \mathbf{x}) = \min\left(1, \frac{p(\mathbf{x})}{p(\mathbf{x}')}\right) = \frac{p(\mathbf{x})}{p(\mathbf{x}')} \tag{13.18}$$

Substituting these into our detailed balance equation:

$$p(\mathbf{x}) \cdot 1 = p(\mathbf{x}') \cdot \frac{p(\mathbf{x})}{p(\mathbf{x}')} \tag{13.19}$$

which simplifies to $p(\mathbf{x}) = p(\mathbf{x})$—clearly true.

If $p(\mathbf{x}') < p(\mathbf{x})$, then:

$$A(\mathbf{x}, \mathbf{x}') = \min\left(1, \frac{p(\mathbf{x}')}{p(\mathbf{x})}\right) = \frac{p(\mathbf{x}')}{p(\mathbf{x})} \tag{13.20}$$

$$A(\mathbf{x}', \mathbf{x}) = \min\left(1, \frac{p(\mathbf{x})}{p(\mathbf{x}')}\right) = 1 \tag{13.21}$$

Substituting these into our detailed balance equation:

$$p(\mathbf{x}) \cdot \frac{p(\mathbf{x}')}{p(\mathbf{x})} = p(\mathbf{x}') \cdot 1 \tag{13.22}$$

which simplifies to $p(\mathbf{x}') = p(\mathbf{x}')$—again clearly true.

Thus, we've verified that the Metropolis algorithm's transition matrix satisfies detailed balance with respect to our target posterior distribution, ensuring that the posterior distribution is a stationary distribution of the chain.

This mechanism creates a natural balance in our system. When the chain has converged to the target distribution, detailed balance ensures that the flows between any two neighborhoods remain equal, maintaining equilibrium. If the chain hasn't yet converged, this mechanism actively drives the population distribution toward equilibrium. Neighborhoods with higher posterior probability gradually accumulate more residents, while areas with lower probability become less populated.

Beyond its theoretical properties, the Metropolis algorithm offers a key practical advantage for Bayesian inference in astronomy: it only requires the ratio of posterior probabilities, not their absolute values. This eliminates the need to calculate the often intractable normalization constant (the Bayesian evidence). Mathematically:

$$\frac{p(\mathbf{x}'|\mathcal{D})}{p(\mathbf{x}|\mathcal{D})} = \frac{p(\mathcal{D}|\mathbf{x}')p(\mathbf{x}')}{p(\mathcal{D})}\frac{p(\mathcal{D})}{p(\mathcal{D}|\mathbf{x})p(\mathbf{x})} = \frac{p(\mathcal{D}|\mathbf{x}')p(\mathbf{x}')}{p(\mathcal{D}|\mathbf{x})p(\mathbf{x})} \tag{13.23}$$

Notice how the evidence term $p(\mathcal{D})$ cancels out completely. This property is invaluable in astronomy, where calculating the evidence becomes practically impossible for complex models with many parameters. The remaining terms are just the likelihood times the prior—expressions we can typically evaluate directly.

The Metropolis algorithm is remarkably simple yet powerful in its capabilities. It

transforms a difficult sampling problem into the much simpler task of evaluating ratios of an unnormalized distribution—a feature perfectly tailored for Bayesian inference. The Metropolis algorithm demonstrates that we can indeed construct transition matrices satisfying detailed balance, providing a concrete foundation for MCMC methods. As we'll see in subsequent sections, understanding when and how well this algorithm converges to the target distribution requires additional theoretical considerations about the properties of Markov chains.

13.4   Convergence and Uniqueness in MCMC

So far, we've shown that the Metropolis algorithm provides a transition matrix that satisfies detailed balance with respect to our target posterior distribution. This is an important first step, but it only ensures that the target distribution is one of the possible stationary distributions of the Markov chain. For practical MCMC applications in astronomy, we need stronger guarantees.

To put this in terms of our Columbus analogy: if the population follows the Metropolis algorithm's rules for movement between neighborhoods, then a population distribution matching the true neighborhood densities is a possible equilibrium state. However, this proof alone is not sufficient for our purposes. When you run an MCMC algorithm in your research, you want confidence not just that you might get the correct posterior, but that you will get the correct posterior.

The detailed balance condition only guarantees that our target distribution could be the stationary distribution of the Markov chain. But this doesn't necessarily mean that the chain will converge, or if it converges, that it will converge to the correct distribution. To ensure reliable MCMC sampling, we need to establish two additional properties: convergence and uniqueness.

Convergence, in the context of MCMC, means that no matter what initial distribution we start with, the chain will eventually settle into a pattern that matches our target posterior distribution. Mathematically, we express this as:

$$\lim_{n \to \infty} T^n \tilde{p}(\mathbf{x}) = p(\mathbf{x}) \tag{13.24}$$

where $\tilde{p}(\mathbf{x})$ is any starting distribution, T is our transition matrix, and $p(\mathbf{x})$ is our target distribution.

In our Columbus analogy, this would be like asking whether, no matter how we initially distribute people across Ohio, they'll eventually redistribute themselves across Columbus neighborhoods according to the true population densities. Imagine we're running an experiment where we've given the Metropolis guidebook to thousands of people distributed in various ways across the city. Convergence means that, given enough time, these people will redistribute themselves to match the true neighborhood densities, regardless of their initial distribution.

Uniqueness ensures that there's only one stationary distribution that our Markov chain can converge to. Mathematically, uniqueness means that if there exist two stationary distributions $p_1(\mathbf{x})$ and $p_2(\mathbf{x})$ such that:

$$(Tp_1)(\mathbf{x}) = p_1(\mathbf{x}) \quad \text{and} \quad (Tp_2)(\mathbf{x}) = p_2(\mathbf{x}) \tag{13.25}$$

then it must be the case that $p_1(\mathbf{x}) = p_2(\mathbf{x})$. This is crucial because we've already shown that our target distribution is a stationary distribution (thanks to detailed balance), but we need to ensure it's the only one.

In our analogy, this is equivalent to ensuring that there's only one possible stable population distribution across Columbus neighborhoods that can result from following our guidebook's rules. Without uniqueness, we might end up with a population distribution that doesn't match the true neighborhood densities, even after running our simulation for a very long time.

Counterexamples to Convergence and Uniqueness   While detailed balance is crucial for MCMC methods, it alone doesn't guarantee that our transition matrix will lead to the desired target distribution. To understand why additional conditions are necessary, let's examine some situations where things can go wrong, even when detailed balance is satisfied.

Consider two examples of problematic transition matrices that fail to produce the sampling behavior we need for Bayesian inference:

First, imagine a guidebook that simply instructs, "always stay where you are." Mathematically, this corresponds to a transition matrix $T = \mathbf{I}$ (the identity matrix). This transition matrix technically satisfies detailed balance with respect to any distribution, because no one ever moves! If we started with everyone in the Short North, they'd all stay in the Short North. If we started with a uniform distribution across Columbus, it would remain uniform forever. While this system instantly "converges" to a stationary distribution,

that distribution depends entirely on our starting point. This violates our requirement for uniqueness—we need our sampling process to converge to the correct posterior distribution regardless of where we start.

For a second example, consider a Columbus with only two neighborhoods: the Short North and German Village. Our guidebook states: "If you're in the Short North today, go to German Village tomorrow. If you're in German Village today, go to the Short North tomorrow." This is represented by the transition matrix:

$$T = \begin{bmatrix} 0 & 1 \\ 1 & 0 \end{bmatrix} \tag{13.26}$$

This transition matrix does have a stationary distribution $p^*(\mathbf{x}) = [0.5, 0.5]$—if we start with exactly half the population in each neighborhood, this will remain true as people swap back and forth. However, for any other starting distribution, the system will never converge. Instead, we get:

$$p^{(t)}(\mathbf{x}) = \begin{cases} \tilde{p}(\mathbf{x}), & \text{if } t \text{ is even} \\ 1 - \tilde{p}(\mathbf{x}), & \text{if } t \text{ is odd} \end{cases} \tag{13.27}$$

If we start with 70% of people in the Short North and 30% in German Village, then the next day it flips to 30% in the Short North and 70% in German Village, continuing this oscillation indefinitely. The system never converges to a single, stable distribution.

These examples illustrate that not all transition matrices will lead to convergence to a unique stationary distribution. Fortunately, most practical MCMC methods, including the Metropolis algorithm we've discussed, have transition matrices designed to avoid these pathological behaviors. They satisfy an additional property called ergodicity, which guarantees both convergence and uniqueness.

The concept of ergodicity provides the theoretical foundation for why MCMC methods work reliably in astronomical applications. In the next section, we'll explore this crucial property that ensures our random walks through parameter space eventually settle into the correct posterior distribution, regardless of where they begin.

13.5 Ergodicity Overview

We've seen that detailed balance alone is insufficient to guarantee that a Markov chain will converge to our target distribution. We need additional conditions to ensure both convergence and uniqueness. This is where the concept of ergodicity comes into play—a property that provides the theoretical foundation for why MCMC methods work in practice.

The term "ergodicity" might sound familiar to those who've studied statistical mechanics in physics, but the concept is more broadly applicable and intuitive than its technical name suggests. In essence, ergodicity means that a system can explore all its possible states over time and reach a stable equilibrium distribution. For our purposes in MCMC, an ergodic Markov chain will converge to a unique stationary distribution, regardless of its starting point—precisely what we need for reliable Bayesian inference.

A Markov chain is considered ergodic if it satisfies three key properties. Let's introduce these conditions intuitively before exploring their mathematical formulations:

Irreducibility: Complete Connectivity The first property is irreducibility. The chain can go from any state to any other state in a finite number of steps. In our Columbus analogy, this means you can travel from any neighborhood to any other neighborhood given enough time. No area of the parameter space is completely isolated or unreachable from other areas. This property prevents the pathological case where our chain gets trapped in one region and never explores the rest of the posterior distribution.

Aperiodicity: Avoiding Cyclic Patterns The second property is aperiodicity. The chain doesn't visit states in a predictable cyclic pattern. This prevents the oscillating behavior we saw in our Short North/German Village example, where people were swapping back and forth endlessly. Aperiodicity ensures that the chain doesn't get trapped in deterministic cycles that prevent convergence to a stable distribution.

Positive Recurrence: Finite Return Times The third property is positive recurrence. The expected time to return to any state is finite. This prevents the chain from wandering off to infinity. In our Columbus analogy, this is like ensuring that travelers will eventually return to neighborhoods they've visited before, rather than continuously exploring new suburbs farther and farther from the city center without ever coming back. Without positive recurrence, our population distribution would never stabilize into the desired equilibrium.
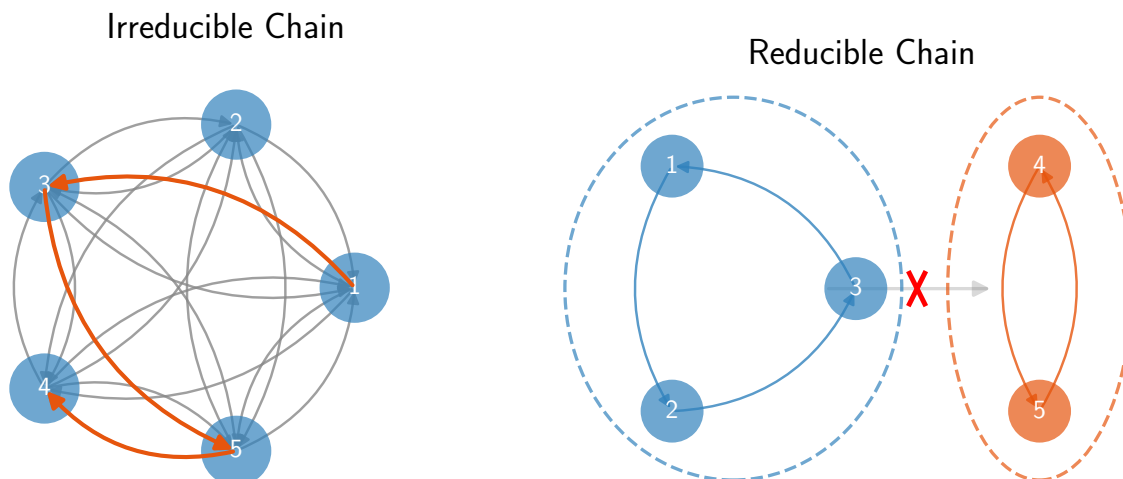
Figure 13.5: Visualization of irreducibility in Markov chains. The left panel shows an irreducible chain where any state can be reached from any other state in a finite number of steps (highlighted path shows one possible route from State 1 to State 4). This property ensures that the chain can explore the entire state space, regardless of the starting point. The right panel illustrates a reducible chain where the state space is disconnected into two separate components: States 1-3 (blue) and States 4-5 (orange). States in one component cannot reach states in the other component, violating irreducibility. In astronomical applications, this would correspond to a posterior distribution with completely separated modes with zero probability between them—for example, two solutions that are equally valid but with no connecting path through parameter space. Such situations violate ergodicity and prevent conventional MCMC methods from correctly sampling the full posterior distribution.

Why These Conditions Matter   These three conditions work together to avoid the pathological cases we discussed earlier. Irreducibility prevents the chain from getting stuck in isolated regions (like the "always stay where you are" example). Aperiodicity eliminates the cyclic oscillations that prevent convergence (like the Short North/German Village swapping). Positive recurrence ensures that the chain doesn't drift away indefinitely without returning to previously visited areas.

When a Markov chain satisfies these three conditions—irreducibility, aperiodicity, and positive recurrence—we can prove two crucial results:

First, a unique stationary distribution exists. This means there's exactly one equilibrium distribution that the chain will settle into, eliminating ambiguity about what distribution we're sampling from.

Second, the chain will converge to this stationary distribution from any starting point.
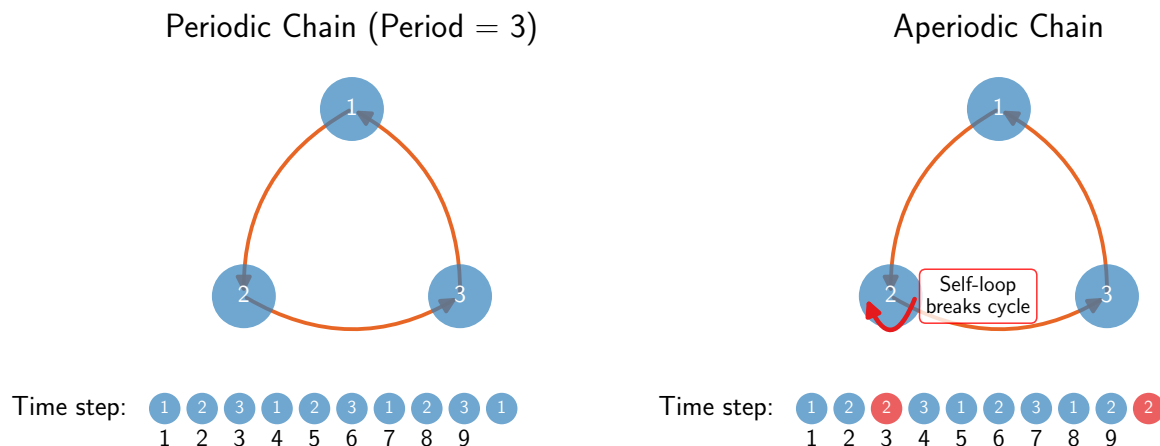
Figure 13.6: Comparison of periodic and aperiodic Markov chains. The left panel shows a periodic chain with period 3, where states must follow a fixed cycle (1→2→3→1...). The sequence below demonstrates how the visitation pattern repeats exactly every three steps, preventing convergence to a stationary distribution. The right panel shows how adding a single self-loop to state 2 breaks this periodicity. Aperiodicity ensures that the chain doesn't get trapped in oscillating patterns, establishing a stable visitation pattern that matches the target distribution.

No matter where we initialize our chain, it will eventually reach the same equilibrium distribution and remain there.

This is precisely what we need for MCMC to work correctly in our astronomical applications. It's analogous to why gas particles in a closed room reach a Maxwell-Boltzmann distribution—they ergodically explore the entire available space until they reach equilibrium.

In practice, most MCMC methods used in astronomy, including the Metropolis algorithm we discussed earlier, are designed to satisfy these ergodicity criteria. However, it's worth being aware of potential pitfalls:

Irreducibility can be violated if your posterior has completely separated modes with zero probability between them. This is like having two separate rooms with a perfect vacuum between them—particles starting in one room can never reach the other. In astronomical applications, this might occur when a parameter space has multiple disconnected high-probability regions separated by regions of essentially zero probability.

Aperiodicity is usually satisfied by default in standard MCMC implementations unless you've explicitly designed a periodic transition scheme. The random nature of the acceptance/rejection step in the Metropolis algorithm typically ensures aperiodicity. This is often
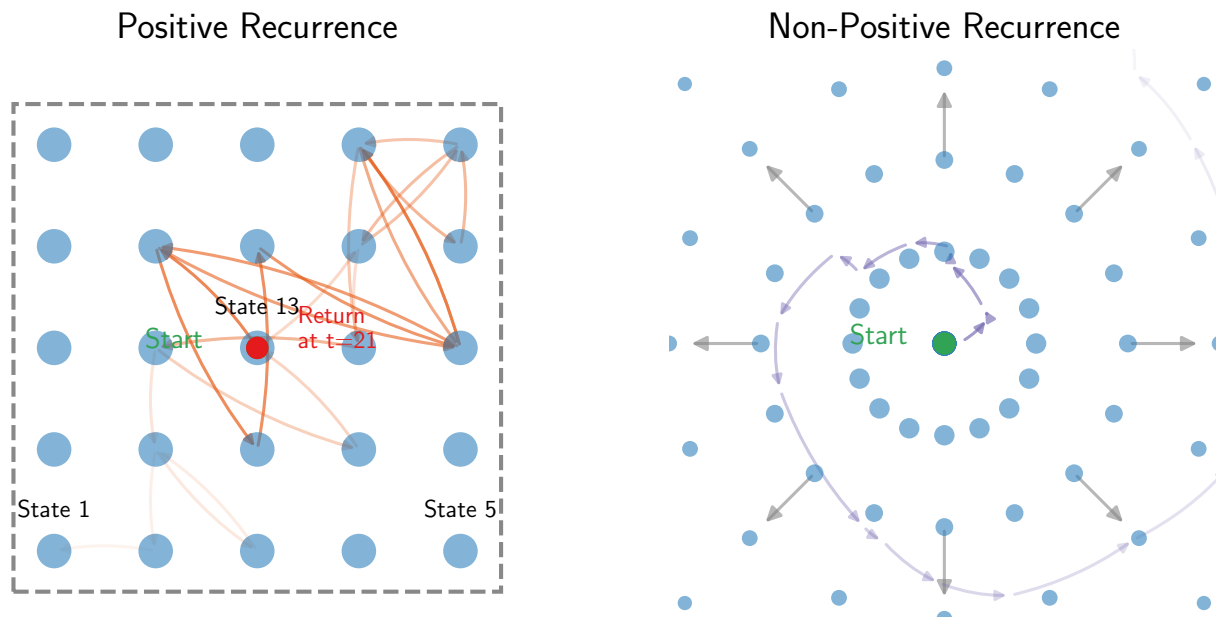
Figure 13.7: Illustration of positive recurrence in Markov chains. The left panel shows a positively recurrent chain in a bounded parameter space where the chain periodically returns to previously visited states (red circles marking returns to the starting state). This property ensures that the expected time to return to any state is finite, allowing the chain to establish a proper stationary distribution. The right panel demonstrates a non-positively recurrent chain in an unbounded parameter space, where the chain can drift away from its starting point. It's important to note that an unbounded space doesn't necessarily imply non-positive recurrence—this is a property of the transition matrix itself, not just the parameter space. Without positive recurrence, a Markov chain cannot establish a stable equilibrium distribution, making it impossible to reliably sample from the target posterior distribution.

achieved through self-loops—the possibility of staying at the current state—which naturally occurs when a proposed move is rejected.

Positive recurrence is typically ensured by setting proper priors that bound your parameter space to a finite region. This is like ensuring your particles are in a finite room rather than an infinite universe where they could wander forever. In astronomical modeling, this usually means choosing priors that reflect physically reasonable parameter ranges.

While astronomers often don't explicitly check for ergodicity in their MCMC implementations, understanding these conditions can help diagnose issues when methods aren't behaving as expected. If multiple chains initialized at different starting points fail to converge to the same distribution despite appearing individually well-mixed, this often indicates a violation of one of the ergodicity conditions, most commonly irreducibility due to disconnected modes in the posterior.

The mathematical details of proving convergence for ergodic chains involve advanced concepts from probability theory that go beyond the scope of this course. However, the intuitive understanding we've developed here provides the conceptual foundation for why MCMC methods work reliably when properly designed. In the following sections, we'll explore more detailed mathematical treatments of these ergodicity conditions and then move on to practical aspects of implementing and diagnosing MCMC algorithms.

13.6   The Uniqueness of the Stationary Distribution

Having established the intuitive understanding of ergodicity, let's explore the mathematical foundations more rigorously. We'll start with uniqueness—proving that an irreducible Markov chain can have at most one stationary distribution. This result is crucial because even though we've shown that our target posterior is a stationary distribution (through detailed balance), we need to ensure it's the only one.

Uniqueness is important because without it, our Markov chain might stabilize to a different distribution than our intended target, even if the chain reaches some equilibrium state. The mathematical condition that guarantees uniqueness is irreducibility—the requirement that the chain can go from any state to any other state in a finite number of steps.

An irreducible Markov chain is one where any state can be reached from any other state via some finite sequence of transitions. Mathematically, we define irreducibility as follows:

$$\forall i, j, \exists t_{ij} \geq 0, \text{ such that } p(\mathbf{x}^{t_{ij}} = j | \mathbf{x}^0 = i) > 0 \qquad (13.28)$$

where i and j represent any two states in the state space, $\mathbf{x}^t$ denotes the state of the chain at step t, t_{ij} is the number of steps needed to go from state i to state j, and $p(\mathbf{x}^{t_{ij}} = j | \mathbf{x}^0 = i)$ is the probability of being in state j after t_{ij} steps, given that we started in state i.

In simpler terms, this equation states that for any two states i and j, there exists some finite number of steps t_{ij} such that the probability of reaching state j from state i in exactly t_{ij} steps is greater than zero. In our Columbus analogy, irreducibility means that from any neighborhood, it's possible to eventually reach any other neighborhood in finite time. There are no isolated regions of the city that are impossible to visit.

The terminology "irreducible" comes from graph theory, where all nodes in the graph are "connected"—there are no isolated regions of the parameter space that the chain cannot access. This connectivity is what allows us to prove uniqueness.

Now, let's prove that irreducibility guarantees uniqueness of the stationary distribution. We'll focus on the finite-dimensional case, though the result extends to general state spaces with appropriate technical conditions.

Since the Markov chain is irreducible, we can go from any state to any other state with non-zero probability. This implies that there exists an integer N such that the composite transition probability matrix:

$$\tilde{T} \equiv \sum_{i=1}^{N} T^i \tag{13.29}$$

has all strictly positive entries. In essence, by considering transitions over multiple steps (up to N), we can reach any state from any other state with positive probability.

For the sake of contradiction, let's assume there are two distinct stationary distributions p and q of our transition matrix T, i.e., $p \neq q$, and:

$$Tp = p, \quad Tq = q \tag{13.30}$$

It follows that these distributions are also stationary with respect to $\tilde{T}$:

$$\tilde{T}p = p, \quad \tilde{T}q = q \tag{13.31}$$

To see why this is true, recall that $\tilde{T} = \sum_{i=1}^{N} T^i$. For any stationary distribution p of T, we have $Tp = p$. This means $T^2 p = T(Tp) = Tp = p$, and by induction, $T^i p = p$ for any positive integer i. Therefore:

$$\tilde{T}p = \sum_{i=1}^{N} T^i p = \sum_{i=1}^{N} p = Np \tag{13.32}$$

Since we're working with probability distributions, we can normalize $\tilde{T}$ by dividing by N, giving us $\frac{\tilde{T}}{N}p = p$. For simplicity, we'll continue using $\tilde{T}$ with the understanding that it's properly normalized. The same logic applies to q, confirming that both p and q are indeed stationary distributions of $\tilde{T}$.

Looking at the first of these equations element-wise:

$$p(\mathbf{x}) = \sum_{\mathbf{y}} \tilde{T}(\mathbf{y}, \mathbf{x}) p(\mathbf{y}) \tag{13.33}$$

Let's define $\mathbf{x}$ to be the state that minimizes the ratio $p(\mathbf{y})/q(\mathbf{y})$ across all states. Since we're in a finite state space, this minimum exists. Now, we can rewrite the equation:

$$p(\mathbf{x}) = \sum_{\mathbf{y}} \tilde{T}(\mathbf{y}, \mathbf{x}) q(\mathbf{y}) \frac{p(\mathbf{y})}{q(\mathbf{y})} \tag{13.34}$$

Since $\mathbf{x}$ minimizes the ratio $p(\mathbf{y})/q(\mathbf{y})$, we know that:

$$\frac{p(\mathbf{y})}{q(\mathbf{y})} \geq \frac{p(\mathbf{x})}{q(\mathbf{x})} \text{ for all } \mathbf{y} \tag{13.35}$$

This gives us:

$$p(\mathbf{x}) = \sum_{\mathbf{y}} \tilde{T}(\mathbf{y}, \mathbf{x}) q(\mathbf{y}) \frac{p(\mathbf{y})}{q(\mathbf{y})} \geq \frac{p(\mathbf{x})}{q(\mathbf{x})} \sum_{\mathbf{y}} \tilde{T}(\mathbf{y}, \mathbf{x}) q(\mathbf{y}) = \frac{p(\mathbf{x})}{q(\mathbf{x})} q(\mathbf{x}) = p(\mathbf{x}) \tag{13.36}$$

For this inequality to be satisfied, it must be an equality, which means:

$$\frac{p(\mathbf{y})}{q(\mathbf{y})} = \frac{p(\mathbf{x})}{q(\mathbf{x})} \text{ for all } \mathbf{y} \text{ where } \tilde{T}(\mathbf{y}, \mathbf{x}) > 0 \tag{13.37}$$

But recall that $\tilde{T}$ has all positive entries (a consequence of irreducibility), so this implies:

$$\frac{p(\mathbf{y})}{q(\mathbf{y})} = \frac{p(\mathbf{x})}{q(\mathbf{x})} \text{ for all } \mathbf{y} \tag{13.38}$$

In other words, the ratio between the two distributions is constant across all states. Since both p and q are probability distributions that sum to 1:

$$\sum_{\mathbf{y}} p(\mathbf{y}) = \sum_{\mathbf{y}} q(\mathbf{y}) = 1 \tag{13.39}$$

The only way for the ratios to be equal while maintaining this constraint is if $p(\mathbf{y}) = q(\mathbf{y})$ for all $\mathbf{y}$. This contradicts our initial assumption that p and q are distinct. Therefore, the stationary distribution must be unique.

This result can also be understood through the lens of linear algebra. According to the Perron-Frobenius theorem, any irreducible non-negative matrix (like our transition probabil-

ity matrix) has a unique largest eigenvalue with a corresponding non-negative eigenvector. When normalized to sum to 1, this eigenvector is precisely the stationary distribution of the Markov chain. This provides an alternative explanation for why irreducibility guarantees uniqueness.

To summarize our result: we've shown that for an irreducible Markov chain with finite states, if two distributions p and q are both stationary, then they must be identical. This means the stationary distribution is unique, which is a property that makes MCMC methods work reliably when the ergodicity conditions are satisfied.

While we've established that an irreducible Markov chain has a unique stationary distribution (if one exists), we haven't yet guaranteed that the chain will converge to this distribution from any starting point. For MCMC methods to be reliable in astronomical applications, we need additional conditions that ensure this convergence. In the next section, we'll explore how the remaining ergodicity conditions—aperiodicity and positive recurrence—provide this guarantee.

13.7　The Convergence of the Stationary Distribution

Having shown that irreducibility guarantees uniqueness of the stationary distribution, we now need to address a more practical concern: will our Markov chain actually converge to this distribution regardless of where it starts? This convergence property is essential for astronomical applications where we need to sample reliably from complex posterior distributions.

Aperiodicity: Breaking Cyclic Patterns　Uniqueness alone isn't sufficient to guarantee convergence. We need additional conditions to ensure that the chain will actually reach its stationary distribution from any starting point. Let's revisit the oscillating example we discussed earlier to understand why.

Consider the simple transition matrix:

$$T = \begin{bmatrix} 0 & 1 \\ 1 & 0 \end{bmatrix} \tag{13.40}$$

This chain alternates deterministically between two states—if we're in state 1, we move to state 2 with certainty, and vice versa. While this chain does have a stationary

distribution $p^*(\mathbf{x}) = [0.5, 0.5]$, it never converges to it unless we happen to start exactly with this distribution.

If we start with everyone in state 1, the entire population moves to state 2 on the next step, then back to state 1, oscillating back and forth indefinitely. The chain exhibits periodic behavior—states can only be revisited at regular intervals (every 2 steps in this case). This observation leads us to the concept of aperiodicity, our second condition for ensuring convergence.

Mathematically, the period k_i of a state i is defined as the greatest common divisor (gcd) of all possible return times:

$$k_i = \gcd\{t : p(z^{(t)} = i | z^{(0)} = i) > 0\} \tag{13.41}$$

where $p(z^{(t)} = i | z^{(0)} = i)$ represents the probability of returning to state i after exactly t steps, given that we started at state i. The period tells us about the cyclical pattern of possible returns to a state.

Let's understand this with our oscillating example. A traveler starting in state 1 can only return after 2, 4, 6, ... steps (even numbers), making the period $k = 2$. This is because:

$$p(z^{(1)} = 1 | z^{(0)} = 1) = 0 \tag{13.42}$$
$$p(z^{(2)} = 1 | z^{(0)} = 1) > 0 \tag{13.43}$$
$$p(z^{(3)} = 1 | z^{(0)} = 1) = 0 \tag{13.44}$$
$$p(z^{(4)} = 1 | z^{(0)} = 1) > 0 \tag{13.45}$$

So the gcd of $\{2, 4, 6, ...\}$ is 2.

A Markov chain is called aperiodic if all states have period 1, meaning they can potentially be revisited at any time step (though not necessarily with high probability). Aperiodicity eliminates the rigid cyclic behavior that prevents convergence. When a chain is aperiodic, the distribution of the chain after many steps becomes less and less dependent on the exact number of steps, allowing it to settle into its stationary distribution.

To understand why aperiodicity is crucial for convergence, consider what happens in a periodic chain. If a chain has period $k > 1$, then after a large number of steps n, the distribution depends critically on whether n is divisible by k. This creates an obstacle to convergence—the chain will cycle through k different distributions rather than settling into

a single stationary distribution. In contrast, when a chain is aperiodic ($k = 1$), this cycling behavior disappears, and the chain can approach a stable distribution as n increases.

One way to make a chain aperiodic is to allow self-loops—transitions from a state back to itself. In our Columbus analogy, this would be like allowing travelers the option to stay in their current neighborhood with some non-zero probability. Even a single self-loop in a chain can break periodicity and help ensure convergence. This is because if a state can transition to itself, then it can be revisited after 1 step, 2 steps, 3 steps, and so on. The gcd of this set $\{1, 2, 3, ...\}$ is 1, making the state aperiodic.

The Metropolis algorithm specifically guarantees self-loops because we do not always accept proposed moves. When a proposal is made to move from the current state $\mathbf{x}$ to a new state $\mathbf{x}'$, we accept this move with probability $A = \min\left(1, \frac{p(\mathbf{x}')}{p(\mathbf{x})}\right)$. Crucially, when this acceptance probability is less than 1, there is a non-zero probability $(1 - A)$ that we reject the proposal and remain at the current state $\mathbf{x}$. This rejection mechanism creates a self-loop in the Markov chain, ensuring that the Metropolis algorithm naturally satisfies the aperiodicity condition.

Positive Recurrence: Preventing Drift to Infinity   So far, we've established two important conditions for Markov chains: irreducibility ensures that the stationary distribution is unique (if one exists), and aperiodicity ensures that the chain doesn't get trapped in cyclic patterns that prevent convergence. However, these two conditions alone don't guarantee that a stationary distribution exists or that the chain will converge to it.

To understand why, we need to introduce a third condition: positive recurrence. This property ensures that the chain doesn't "drift off to infinity" and actually has a well-defined stationary distribution. Consider a simple random walk on integers with the following transition probabilities:

$$T_{ij} = \begin{cases} 1/3, & j \in \{i - 1, i, i + 1\} \\ 0, & \text{otherwise} \end{cases} \tag{13.46}$$

This Markov chain has the following properties. It's irreducible since we can move from any integer to any other integer by taking enough steps (moving one position at a time). It's also aperiodic due to the self-loops—from any state i, we can return to i in 1 step (with probability 1/3), in 2 steps, in 3 steps, etc. The greatest common divisor of these return times is 1.

But does this chain have a stationary distribution? Let's try to solve for it directly. If $\pi = (\pi_0, \pi_1, \pi_2, ...)$ is the stationary distribution, where π_i represents the probability of being in state i after the chain has run for a very long time, then by definition:

$$\pi_i = \frac{1}{3}\pi_{i-1} + \frac{1}{3}\pi_i + \frac{1}{3}\pi_{i+1} \tag{13.47}$$

Rearranging:

$$\pi_{i-1} - 2\pi_i + \pi_{i+1} = 0 \tag{13.48}$$

This is a second-order linear recurrence relation. We can solve it by working out a few terms and discovering that the general solution is:

$$\pi_i = i\pi_1 - (i-1)\pi_0 \tag{13.49}$$

Now let's check if we can satisfy the requirements of a probability distribution. If $\pi_1 = \pi_0 > 0$, then $\pi_i = \pi_0$ for all i, meaning all states have equal probability. This creates a uniform distribution over infinitely many states, giving us $\sum_i \pi_i = \infty$, not 1 as required. If $\pi_1 = \pi_0 = 0$, then $\pi_i = 0$ for all i, giving us $\sum_i \pi_i = 0$, also violating the normalization requirement.

If $\pi_1 > \pi_0$, then π_i grows linearly with i, making $\sum_i \pi_i = \infty$. If $\pi_1 < \pi_0$, then eventually π_i becomes negative for large i, violating the requirement that probabilities be non-negative.

This mathematical contradiction shows that there is no valid stationary distribution for this random walk. The issue is that the chain allows a "drift" to infinity—if we imagine a population of travelers distributed according to any initial distribution, this population would spread out indefinitely over time with no stable configuration.

Unlike our Columbus analogy where the city has finite neighborhoods, this random walk explores an unbounded space with no "gravitational force" pulling the population toward any central region. Each traveler has equal probability (1/3) of moving left, staying put, or moving right at each step. As time progresses, the population disperses more and more widely across the infinite state space. The probability mass continually spreads thinner and thinner, with an ever-expanding frontier of states being populated. This perpetual diffusion prevents the population from settling into any fixed distribution, making a stationary

distribution mathematically impossible.

Ergodicity: The Complete Solution This is precisely why we need the third condition—positive recurrence—to guarantee convergence in Markov chains. Positive recurrence ensures that a chain doesn't "escape" to infinity but instead keeps returning to each state in a finite expected time. A state i is positive recurrent if the expected time to return to that state, starting from that state, is finite:

$$\mathbb{E}[t_i] < \infty, \text{ where } t_i = \inf\{t \geq 1 : z^{(t)} = i | z^{(0)} = i\} \tag{13.50}$$

In our city exploration analogy, positive recurrence means that a traveler, starting from any neighborhood, will return to that neighborhood in a finite expected time. They won't wander further and further away, exploring an ever-expanding periphery without returning to the core areas.

For our random walk on integers, the expected return time to any state is infinite—a traveler can drift arbitrarily far away, making the probability of return vanishingly small. This explains why the chain fails to converge despite satisfying irreducibility and aperiodicity.

The combination of irreducibility, aperiodicity, and positive recurrence defines an ergodic Markov chain. For ergodic Markov chains, we can prove several crucial results:

First, the long-run fraction of time spent in each state converges to a unique stationary distribution, regardless of the starting state. Second, the stationary probability of a state is inversely proportional to its expected return time: $p^*(i) = \frac{1}{\mathbb{E}[t_i]}$. Third, for any initial distribution $\tilde{p}(\mathbf{x})$, repeatedly applying the transition operator will eventually converge to the unique stationary distribution: $\lim_{n \to \infty} T^n \tilde{p}(\mathbf{x}) = p^*(\mathbf{x})$.

These properties translate to an intuitive understanding of our traveler's journey. As the traveler walks through the state space for a long time, their path creates a pattern of visitation across all states. The proportion of time they spend in each state gradually stabilizes, approaching the stationary distribution regardless of where they began. The footprints left by the traveler—marking each location they've visited—would eventually trace out a density map proportional to the stationary distribution, with more frequently visited states showing denser clusters of footprints.

This powerful result forms the foundation for MCMC methods. By carefully designing transition probabilities (as in the Metropolis algorithm) such that our target posterior is

the stationary distribution, we can generate samples from complex distributions simply by running the chain and recording its states.

In practical MCMC applications in astronomy, ensuring ergodicity is typically straightforward. The Metropolis algorithm with a Gaussian proposal naturally satisfies aperiodicity due to its probabilistic acceptance mechanism. Positive recurrence can be guaranteed by using proper prior distributions that bound the parameter space, preventing the chain from wandering indefinitely. However, irreducibility can sometimes fail in astronomical applications when multimodal posterior distributions have widely separated modes, effectively creating a reducible chain that cannot explore the full posterior. Understanding these ergodicity conditions provides us with a diagnostic framework when MCMC chains behave unexpectedly.

13.8 Implementing Metropolis Algorithm

Now that we understand the theoretical foundations of MCMC through detailed balance and ergodicity, we can implement the Metropolis algorithm. The power of MCMC lies in its ability to sample from essentially any distribution, regardless of its complexity or dimensionality. The Metropolis algorithm, through its carefully designed acceptance probability, ensures that detailed balance is satisfied with respect to our target distribution. When combined with ergodicity, which is almost always satisfied in real applications, we have the complete foundation for correctly sampling from our target distribution.

The implementation of the Metropolis algorithm follows these straightforward steps:

1. **Initialize**: Choose a starting point $\mathbf{x}^{(0)}$ in the parameter space.

2. **For each iteration** $t = 1, 2, \ldots, T$:

    (a) **Propose**: Generate a candidate state $\mathbf{x}'$ from a symmetric proposal distribution centered at the current state: $\mathbf{x}' \sim q(\mathbf{x}'|\mathbf{x}^{(t-1)})$, where $q(\mathbf{x}'|\mathbf{x}) = q(\mathbf{x}|\mathbf{x}')$.

    (b) **Compute**: Calculate the acceptance probability: $A(\mathbf{x}^{(t-1)}, \mathbf{x}') = \min\left(1, \frac{p(\mathbf{x}')}{p(\mathbf{x}^{(t-1)})}\right)$

    (c) **Accept/Reject**: Draw a uniform random number $u \sim \mathcal{U}(0, 1)$:

    - If $u \leq A(\mathbf{x}^{(t-1)}, \mathbf{x}')$, accept the proposal: $\mathbf{x}^{(t)} = \mathbf{x}'$

    - Otherwise, reject and stay at the current position: $\mathbf{x}^{(t)} = \mathbf{x}^{(t-1)}$

3. **Return**: The sequence $\{\mathbf{x}^{(0)}, \mathbf{x}^{(1)}, \ldots, \mathbf{x}^{(T)}\}$ as samples from the target distribution (typically discarding some initial portion as burn-in).

This algorithm transforms a difficult sampling problem into the much simpler task of evaluating ratios of an unnormalized distribution—a feature perfectly tailored for Bayesian inference. The remarkable strength of MCMC lies in its universal sampling capability, but practical implementations require careful consideration of several issues that don't appear in direct sampling approaches.

Now that we understand how to construct and implement a Markov chain that samples from our target distribution, we need to consider some practical aspects of MCMC implementation. While the theoretical foundation of MCMC is robust, its practical application requires careful consideration of several challenges.

A key property of Markov chains is that each state depends only on the immediately preceding state, not the entire history. This seemingly simple property leads to two important practical challenges in MCMC:

1. How do we handle samples from the early phase of the chain, when it hasn't yet reached its stationary distribution (the target posterior)?

2. Once the chain has converged, how do we account for the correlation between consecutive samples, which reduces their statistical efficiency?

These questions are critical for obtaining reliable posterior inferences in astronomical applications.

The first challenge relates to the concept of "burn-in." Since our Markov chain starts from an arbitrary position $\mathbf{x}^{(0)}$ that may be far from the high-probability regions of our distribution, the initial samples will reflect this starting position rather than the target distribution. While ergodicity guarantees that the chain will eventually converge to sampling from the target distribution, this convergence isn't instantaneous.

Think of burn-in as the warm-up period for our Markov chain. Imagine Columbus starting his exploration from the outskirts of an unfamiliar city—his initial movements would be spent simply finding the city center before he could begin properly exploring the important areas. Similarly, our chain needs time to find and settle into the high-probability regions of the distribution before it can provide representative samples.
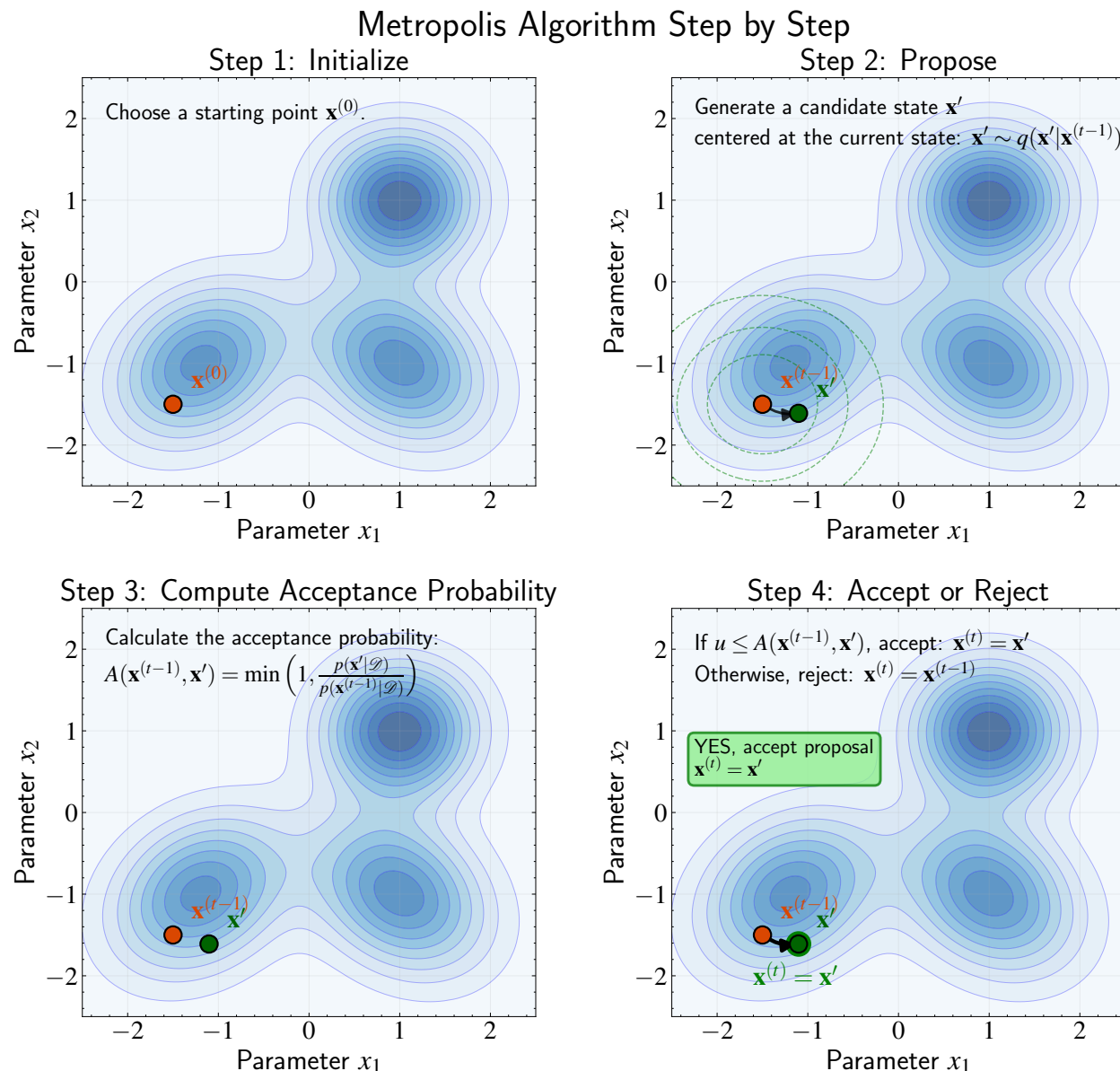
Figure 13.8: Step-by-step illustration of the Metropolis algorithm sampling from a multi-modal distribution. **Step 1 (Initialize):** We choose a starting point $\mathbf{x}^{(0)}$ in parameter space. **Step 2 (Propose):** A candidate state $\mathbf{x}'$ is generated from a symmetric proposal distribution (green dashed contours) centered at the current state. **Step 3 (Compute):** We calculate the acceptance probability as the ratio of densities, $A(\mathbf{x}^{(t-1)}, \mathbf{x}') = \min\left(1, \frac{p(\mathbf{x}')}{p(\mathbf{x}^{(t-1)})}\right)$. **Step 4 (Accept/Reject):** We draw a uniform random number $u \sim \mathcal{U}(0, 1)$ and accept the proposal if $u \leq A$; otherwise, we reject it and stay at the current position. We keep repeating this process for many iterations, which allows the algorithm to explore the parameter space by preferentially moving toward higher-probability regions while occasionally accepting moves to lower-probability regions, ultimately sampling from the target distribution.
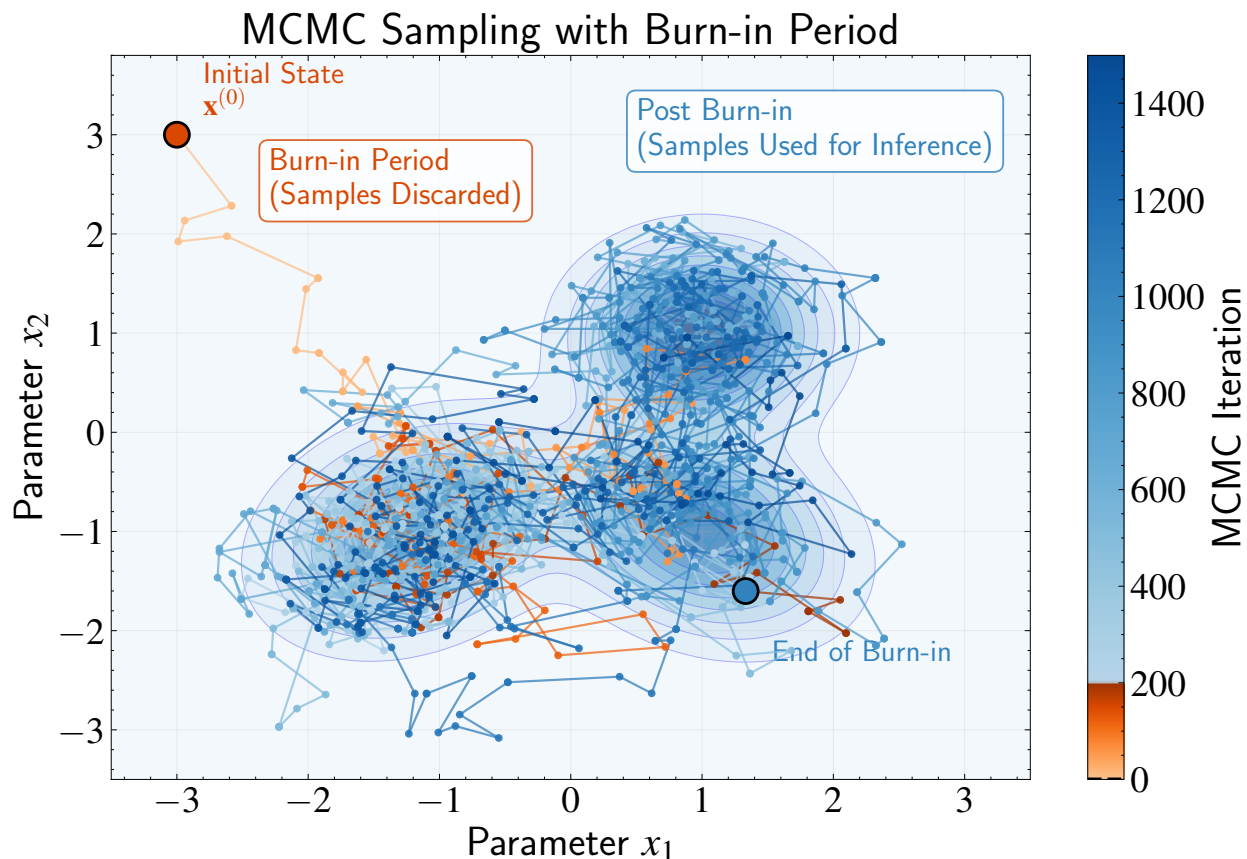
Figure 13.9: Visualization of the burn-in concept in MCMC sampling. The chain starts from a low-probability region (orange point) and initially explores the parameter space inefficiently (orange trajectory). This initial phase constitutes the burn-in period, during which samples are discarded because they reflect the arbitrary starting position rather than the target distribution. After the burn-in period, the chain settles into its stationary distribution and efficiently explores the high-probability modes of the distribution (blue trajectory), providing representative samples for inference. The colorbar shows the progression of iterations with the burn-in cutoff indicated by the horizontal dashed line.

The second challenge concerns computational efficiency. While MCMC can theoretically sample any distribution given sufficient time, the practical reality is that we need algorithms that converge within reasonable timeframes. Even with the minimal assumptions of ergodicity satisfied, the time to convergence could be prohibitively long. In astronomical research, where we face real constraints on computational resources and project timelines, the question shifts from "Can we sample this distribution?" to "How efficiently can we sample it?"

To address these efficiency considerations, we need to understand how MCMC algorithms explore parameter space. While the theoretical foundations guarantee eventual

convergence to the target distribution, practical implementations require careful tuning to achieve efficient sampling. Let's examine key concepts that affect sampling efficiency across MCMC methods.

13.9   Proposal Mechanisms and Sampling Efficiency

The efficiency of MCMC methods is fundamentally tied to how well the chain explores the parameter space. This exploration is governed by the mechanism that proposes new positions for the chain to visit, which varies across different MCMC algorithms but follows similar principles.

The sequential nature of MCMC is both its greatest strength and its primary challenge. This sequential dependency gives MCMC its power to handle complex, high-dimensional problems by transforming difficult sampling tasks into manageable random walks. However, this same property requires us to make careful choices about how these random walks are performed.

In most MCMC algorithms, the transition from one state to another involves some form of proposal mechanism followed by an acceptance/rejection step. While the specific implementation varies between algorithms (including the Metropolis algorithm we have explored above, as well as Metropolis-Hastings and Gibbs sampling that we will introduce later), they all face a common challenge: balancing between local exploration and global coverage of the parameter space.

For the Metropolis algorithm with a symmetric proposal distribution, the transition probability is:

$$T(\mathbf{x}, \mathbf{x}') = q(\mathbf{x}'|\mathbf{x})A(\mathbf{x}, \mathbf{x}') \tag{13.51}$$

where $q(\mathbf{x}'|\mathbf{x})$ is the proposal distribution and $A(\mathbf{x}, \mathbf{x}')$ is the acceptance probability. The specific choice of proposal mechanism critically affects how efficiently we sample from the posterior, regardless of which MCMC variant we use.

For many astronomical applications, proposal distributions based on multivariate Gaussians are common:

$$q(\mathbf{x}'|\mathbf{x}) = \mathcal{N}(\mathbf{x}'|\mathbf{x}, \boldsymbol{\Sigma}) \tag{13.52}$$

where $\boldsymbol{\Sigma}$ is the covariance matrix that determines the scale and orientation of proposals. The choice of $\boldsymbol{\Sigma}$ directly impacts sampling efficiency.

When implementing any MCMC method in practice, we need to balance between making small moves (which are likely to be accepted but explore slowly) and large moves (which explore faster but are more likely to be rejected). This balance affects how quickly our chain converges to the target distribution and how efficiently it samples once converged.

If the proposal mechanism is too conservative, the chain will have a high acceptance rate but will explore the parameter space very slowly. In our Columbus analogy, this would be like taking tiny steps—while you're likely to accept each step (since you're not venturing far from where you are), it would take an impractically long time to explore the entire city. Conversely, if the proposal mechanism is too aggressive, most proposals will land in low-probability regions and be rejected. You would be attempting to take giant leaps across the city, but most would be rejected because they land in unlikely areas, resulting in frequently remaining in the same location.
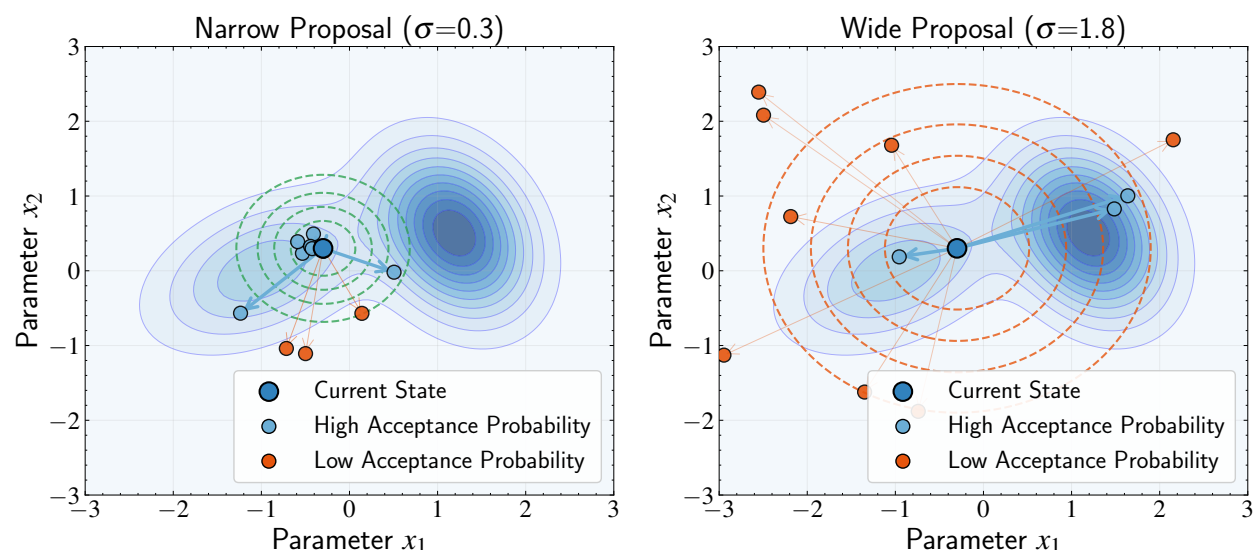
Figure 13.10: Comparison of MCMC performance with different proposal mechanisms. Left panel: A narrow proposal distribution results in a high acceptance rate, as most proposed moves stay within regions of similar posterior probability. Right panel: A wide proposal distribution yields a low acceptance rate, as proposals frequently land in low-probability regions and are rejected. The blue contours represent the target posterior distribution, while dashed contours show the proposal distributions centered at the current state (blue dot). This visualization demonstrates the trade-off in MCMC sampling between small steps (which are readily accepted but explore slowly) and large steps (which explore faster but are more frequently rejected).

The acceptance rate—the proportion of proposed moves that are accepted during sampling—provides a valuable diagnostic for assessing the efficiency of many MCMC algorithms. This simple metric offers immediate insight into how well our chain is exploring the

parameter space.

When the proposal mechanism is too conservative, we observe a very high acceptance rate, often exceeding 90%. While this might initially seem desirable, it actually leads to inefficient sampling. The chain moves through the parameter space in tiny steps, resulting in highly correlated samples. This is analogous to exploring a city by taking baby steps—you'll accept almost every step, but you'll cover very little ground and gather largely redundant information. The chain requires many iterations to explore the full posterior distribution, leading to poor mixing.

Conversely, when the proposal mechanism is too aggressive, the acceptance rate plummets to below 5%. Most proposals jump to regions with much lower posterior probability and are rejected. The chain frequently remains stuck at the same position for many iterations, again resulting in high correlation between samples. This resembles attempting to explore a city by randomly teleporting across vast distances—most attempts land in unlikely or inaccessible areas, so you end up standing still most of the time.

The optimal scenario typically occurs when the proposal mechanism is appropriately tuned to the geometry of the posterior distribution. For many MCMC algorithms, acceptance rates around 20-40% tend to yield the most efficient sampling, though this can vary depending on the specific algorithm and problem. This balance allows the chain to explore efficiently without getting stuck or taking overly timid steps. At this sweet spot, the chain makes moves that are large enough to explore the parameter space effectively, but not so large that most proposals are rejected.

In astronomy, where we often deal with complex models and limited computational resources, properly tuning the proposal mechanism can make the difference between obtaining reliable posterior inferences within days versus weeks or longer. In practice, finding this optimal tuning often requires some experimentation. One might start with an educated guess based on prior knowledge of the problem, then adjust based on the observed acceptance rate during a short pilot run.

While acceptance rates provide a useful rule of thumb for initial tuning, they don't tell the complete story about sampling efficiency. To fully understand how well our chain is exploring the parameter space and how much independent information we're actually obtaining, we need to examine the correlation between successive samples. This leads us to the concept of autocorrelation and effective sample size, which we'll explore in the following sections.

13.10　Autocorrelation in MCMC Sampling

One of the challenges in MCMC is that successive samples are not independent—each new state depends on the previous one. This correlation between samples, known as autocorrelation, reduces the effective information content of our chain compared to truly independent samples. Understanding and quantifying this correlation is crucial for reliable statistical inference.

Recall that when we have N independent and identically distributed (i.i.d.) samples, the standard error of our estimate decreases proportionally to $1/\sqrt{N}$. However, when samples are correlated, this convergence rate is effectively slower. Intuitively, each new correlated sample provides less "new information" about the target distribution than an independent sample would, resulting in less precise estimates for a given number of samples.

For a sequence of samples $\{X_0, X_1, X_2, ...\}$, the autocorrelation at lag k is defined as:

$$R(k) = \frac{\mathbb{E}[(X_t - \mu)(X_{t+k} - \mu)]}{\sigma^2} \tag{13.53}$$

where $\mu = \mathbb{E}[X_t]$ is the mean and $\sigma^2 = \mathbb{E}[(X_t - \mu)^2]$ is the variance of the stationary distribution. This definition should be familiar from our earlier discussions of correlation between random variables. While standard correlation measures the linear relationship between two different variables, autocorrelation measures the relationship between observations of the same variable at different points in the sequence.

To understand autocorrelation in a Markov chain, we need to recognize that values X_t and X_{t+k} can be viewed as different realizations of the same random variable. Once a Markov chain has reached its stationary distribution, each state it visits can be considered a draw from that distribution. The distribution of states at time t and at time $t + k$ are both approximations of the same target distribution, with X_t and X_{t+k} being specific realizations connected by the chain's evolution over k steps.

This perspective is made possible by the ergodic properties of well-designed MCMC algorithms. When the ergodic condition is met, the chain's behavior over time (time average) becomes equivalent to taking multiple independent samples from the target distribution (ensemble average). This equivalence is what allows us to use a single chain to explore and characterize an entire probability distribution.

The inherent dependency between MCMC samples is the trade-off we accept for

being able to sample from complex distributions through random walks. While we still get correct results in the long run, the sampling noise decreases more slowly than the $1/\sqrt{N}$ rate expected with truly independent samples. Understanding this correlation is critical for properly assessing uncertainty in our estimates and determining appropriate chain lengths.
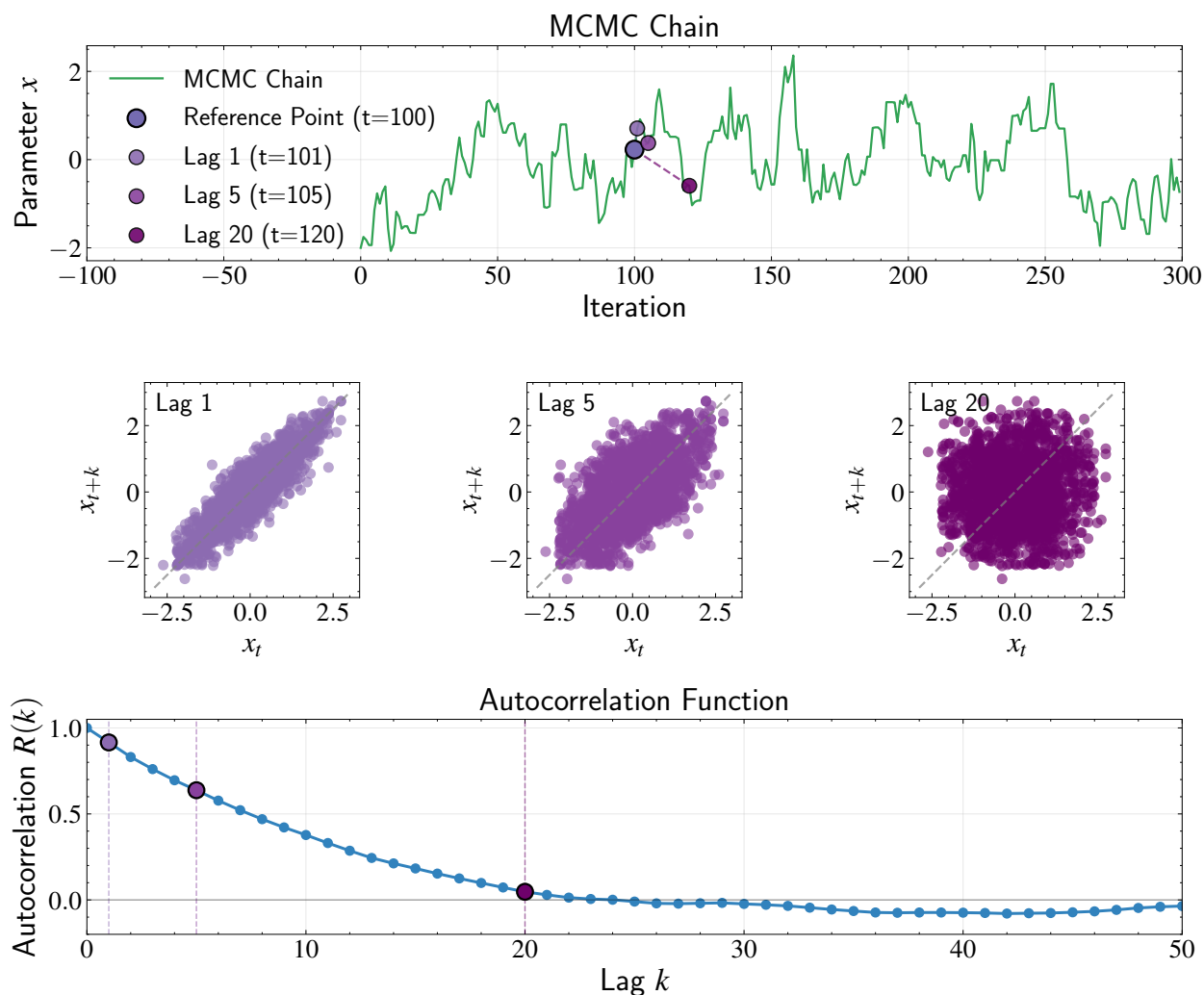
Figure 13.11: Visualization of autocorrelation in MCMC sampling. Top panel: The MCMC chain trace showing a reference point at iteration $t = 100$ (purple) and corresponding points at lags $k = 1$, $k = 5$, and $k = 20$ (different shades of purple). Middle panel: Scatter plots showing the relationship between states x_t and x_{t+k} for different lags. The increasing scatter away from the diagonal as lag increases illustrates decreasing correlation between samples separated by larger intervals. Bottom panel: The autocorrelation function $R(k)$ showing how correlation decays with increasing lag. This progressive decorrelation allows us to treat different points in the chain as approximately independent samples from the target distribution once sufficient lag time has passed, a consequence of the chain's ergodic properties.

To quantify autocorrelation in practice, we need to estimate it from our finite MCMC

chain. The theoretical definition must be adapted to work with the samples we actually have. For a chain of length N, we can estimate the autocorrelation at lag k using:

$$\hat{R}(k) = \frac{\sum_{t=1}^{N-k}(X_t - \bar{X})(X_{t+k} - \bar{X})}{\sum_{t=1}^{N}(X_t - \bar{X})^2} \tag{13.54}$$

where $\bar{X}$ is the sample mean of the chain. This empirical estimator follows naturally from the theoretical definition but uses sample statistics instead of population parameters. The numerator calculates the covariance between samples separated by lag k, while the denominator normalizes by the sample variance to produce a correlation coefficient.

Note that as k increases, we have fewer pairs of points to use in our estimation (only $N - k$ pairs), which is why autocorrelation estimates become less reliable at higher lags. For each lag k, we average over all available pairs of points separated by that lag, which becomes fewer as k increases. This is why the estimation uncertainty grows for larger lag values, and why the autocorrelation estimates become less reliable at high lags.

To develop an intuitive understanding of autocorrelation, let's consider what happens with different proposal mechanisms in MCMC algorithms. When the proposal distribution is too conservative (too narrow), each new sample is very close to the previous one. The chain moves like a cautious explorer taking baby steps, staying in nearly the same location for many iterations. The value at position t is highly predictive of the values at positions $t + 1$, $t + 2$, and so on, resulting in high autocorrelation even at larger lags. Despite having many samples, we're essentially getting the same information repeated with slight variations.

Conversely, when the proposal distribution is too aggressive (too wide), most proposals get rejected because they jump to low-probability regions. The chain frequently stays stuck at the same value for many iterations, creating high autocorrelation through a different mechanism—literal repetition of the same value. When jumps do occur, they can be substantial, but their infrequency limits exploration.

The ideal scenario occurs when the proposal mechanism is well-tuned—a balance that allows enough movement to explore effectively while maintaining a reasonable acceptance rate. In this case, the autocorrelation typically decays more rapidly with lag, indicating each new sample provides more unique information about the target distribution. This balance is what we aim for when tuning MCMC algorithms for efficient sampling.

The autocorrelation function provides insights into the efficiency of our MCMC sam-

pler. In an ideal scenario with completely independent samples, $R(k) = 0$ for all $k > 0$. This is because independent samples, by definition, have no relationship with each other—knowing one value gives no information about any other value. However, in MCMC, we typically observe a decaying autocorrelation as the lag increases.

The rate of this decay directly impacts how efficiently our chain explores the parameter space. A rapidly decaying autocorrelation indicates that the chain quickly "forgets" its starting position and explores the distribution more independently. This faster decay is desirable because it means each new sample provides more unique information about the target distribution, leading to more efficient parameter estimation and uncertainty quantification.

13.11   Effective Sample Size

To quantify the reduction in information content due to autocorrelation, we use the concept of Effective Sample Size (ESS), which represents the equivalent number of independent samples that would provide the same amount of information as our autocorrelated chain. The key insight is that having more samples doesn't necessarily mean we have more useful information if those samples are highly correlated.

To illustrate this concept, imagine an explorer mapping the population distribution of Columbus. If they follow a path with high autocorrelation, they might spend many days revisiting the same neighborhoods or moving in predictable patterns. This behavior would give them a poor understanding of the city's overall population distribution, even after a long exploration. In contrast, a path with low autocorrelation would involve more diverse, seemingly random movements throughout the city, providing a more representative view of Columbus in less time. In MCMC terms, lower autocorrelation means more efficient sampling of the target distribution and a larger effective sample size.

For a parameter of interest in MCMC, the effective sample size (ESS) can be estimated as:

$$\text{ESS} = \frac{N}{1 + 2 \sum_{k=1}^{\infty} R(k)} \tag{13.55}$$

To understand why this specific formula arises, we need to derive the variance of the sample mean estimator for correlated samples. Let's start with the definition of the sample mean for our MCMC chain:

$$\bar{X} = \frac{1}{N} \sum_{i=1}^{N} X_i \tag{13.56}$$

The variance of this estimator is:

$$\text{Var}(\bar{X}) = \text{Var}\left(\frac{1}{N}\sum_{i=1}^{N}X_i\right) = \frac{1}{N^2}\text{Var}\left(\sum_{i=1}^{N}X_i\right) \tag{13.57}$$

For our MCMC chain, we need to account for all possible pairwise relationships between samples. By expanding the variance of the sum, we get:

$$\text{Var}\left(\sum_{i=1}^{N}X_i\right) = \sum_{i=1}^{N}\sum_{j=1}^{N}\text{Cov}(X_i, X_j) \tag{13.58}$$

A key property of a stationary Markov chain is that the covariance between two samples depends only on how far apart they are in the chain (their lag), not on their absolute positions. This directly relates to the ergodicity property we discussed earlier—the time-invariance of the process ensures that statistical properties remain constant regardless of where in the chain we look. After the chain has converged to the stationary distribution, we have:

$$\text{Cov}(X_i, X_j) = \text{Cov}(X_1, X_{1+|i-j|}) = \sigma^2 R(|i-j|) \tag{13.59}$$

where $|i-j|$ is the lag between samples, σ^2 is the variance of each sample, and $R(k)$ is the autocorrelation at lag k. Note that $R(0) = 1$ since a sample has perfect correlation with itself.

We can reorganize the double sum by grouping together all pairs that have the same lag. For example, the pairs $(1,3)$, $(2,4)$, and $(3,5)$ all have a lag of 2. For a chain of length N, there are exactly $(N-k)$ pairs with lag k. Using this counting approach, we can rewrite our variance formula as:

$$\text{Var}(\bar{X}) = \frac{\sigma^2}{N^2}\left[N + 2\sum_{k=1}^{N-1}(N-k)R(k)\right] \tag{13.60}$$

The first term N represents all pairs with lag 0 (i.e., when $i = j$), where $R(0) = 1$. The factor of 2 in the sum appears because for each positive lag k, we're counting both $(i, i+k)$ and $(i+k, i)$ pairs, which have the same autocorrelation due to stationarity.

Dividing both the numerator and denominator by N, we can simplify further:

$$\text{Var}(\bar{X}) = \frac{\sigma^2}{N}\left[1 + 2\sum_{k=1}^{N-1}\left(1 - \frac{k}{N}\right)R(k)\right] \tag{13.61}$$

For large chain lengths N, the term k/N becomes negligible for any fixed lag k, allowing us to approximate:

$$\text{Var}(\bar{X}) \approx \frac{\sigma^2}{N}\left(1 + 2\sum_{k=1}^{\infty}R(k)\right) \tag{13.62}$$

This result reveals that the variance of our sample mean is inflated by a factor of $(1 + 2\sum_{k=1}^{\infty}R(k))$ compared to what we would obtain with independent samples. This inflation factor directly quantifies the information loss due to autocorrelation in our chain.

We can now connect this to our previously defined Effective Sample Size (ESS). For independent samples, the variance would be σ^2/ESS, which we can equate with our MCMC variance:

$$\frac{\sigma^2}{\text{ESS}} = \frac{\sigma^2}{N}\left(1 + 2\sum_{k=1}^{\infty}R(k)\right) \tag{13.63}$$

Solving for ESS gives us:

$$\text{ESS} = \frac{N}{1 + 2\sum_{k=1}^{\infty}R(k)} \tag{13.64}$$

This confirms our earlier definition of ESS. The denominator $1 + 2\sum_{k=1}^{\infty}R(k)$ represents the autocorrelation time—the average number of correlated MCMC samples needed to obtain the equivalent of one independent sample. The factor of 2 in the sum accounts for both positive and negative lags in the autocorrelation function, which are symmetric in stationary processes.

If our samples were completely independent (like in direct sampling methods), all autocorrelations $R(k)$ would equal zero for $k > 0$. In this ideal case, the denominator would equal 1, giving us $\text{ESS} = N$ – meaning all our samples contribute full statistical power. In contrast, when samples are highly correlated, as is typical in MCMC, the autocorrelations $R(k)$ remain positive for many lags. This makes the sum in the denominator large, which in

turn makes the denominator greater than 1, reducing the ESS below N. The stronger and more persistent these autocorrelations are, the smaller the ESS becomes relative to N.

For example, if the autocorrelation time equals 20, it means we need approximately 20 MCMC samples to get the equivalent information of one independent sample. In this case, a chain of 10,000 samples would have an ESS of only about 500, meaning our precision is equivalent to what we would get from just 500 independent samples. This relationship between autocorrelation and ESS helps explain why tuning the proposal distribution is so important. A well-tuned proposal allows the chain to move efficiently through parameter space, reducing autocorrelation and maximizing the ESS for a given computational budget.

The interpretation of ESS is straightforward: it tells us how many truly independent samples our correlated chain is equivalent to. A rule of thumb is to aim for ESS > 100 for reliable posterior estimates, though more demanding applications may require higher values. This threshold ensures that we have sufficient independent information to characterize the posterior distribution and compute meaningful uncertainties on our parameter estimates.

In practice, calculating the autocorrelation function $R(k)$ efficiently is crucial, especially for long chains. A computationally efficient approach leverages the Fast Fourier Transform (FFT). While the details are beyond the scope of this chapter, the key insight is that the autocorrelation function can be calculated by taking the inverse Fourier transform of the power spectrum (which is the squared magnitude of the Fourier transform of the data). This relationship is a consequence of the Wiener-Khinchin theorem, which connects the autocorrelation function to the power spectrum in the frequency domain. This FFT-based method reduces the computational complexity from $O(N^2)$ for direct calculation to $O(N \log N)$, making it practical for the long chains typically generated in astronomical applications.

13.12   Thinning MCMC Chains

Given the autocorrelation in MCMC samples, a common practice is "thinning"—keeping only every k-th sample from the chain to reduce correlation. For example, if we have a chain of 10,000 samples, we might keep only every 10th sample, resulting in a thinned chain of 1,000 samples.

The motivation for thinning stems from the autocorrelation we've just discussed. If successive samples are highly correlated, then keeping every sample may provide redundant

information. By keeping only every k-th sample, we can potentially reduce the correlation between retained samples while decreasing storage and computational requirements for subsequent analysis.
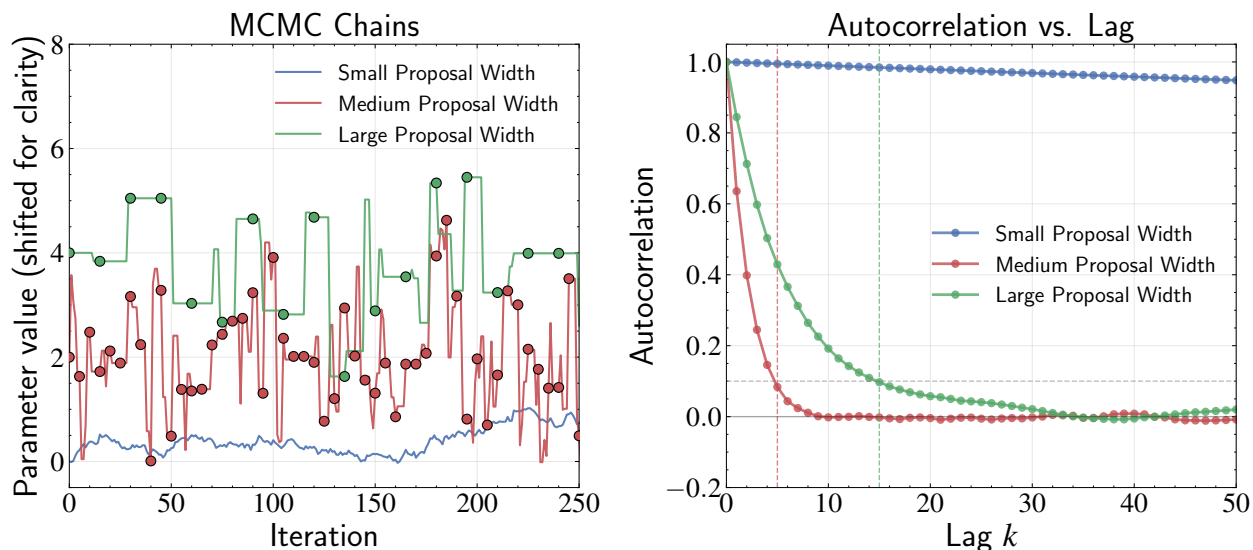
Figure 13.12: Illustration of MCMC thinning based on proposal width and autocorrelation. Left panel: Early iterations of MCMC chains with three different proposal widths (vertically shifted for clarity). The small width chain (blue) makes tiny steps with high acceptance rate but explores the parameter space very slowly. The medium width chain (red) and large width chain (green) show markers indicating which samples would be kept after appropriate thinning, with thinning factors determined by their autocorrelation properties. Right panel: Corresponding autocorrelation functions with vertical dashed lines indicating the thinning factors for the medium and large width chains, chosen where autocorrelation drops below 0.1 (horizontal dashed line). Conversely, an overly large proposal width means that most of the proposed steps are rejected during the chain, resulting in many duplicate samples where the chain remains stuck at the same position, which also reduces efficiency and effective sample size.

Thinning can be beneficial in several contexts. When the cost of storing or processing samples is high, thinning reduces these burdens while maintaining a representative sample of the posterior. When autocorrelation is very strong, thinning can make the data more manageable for analysis and visualization. Additionally, certain Monte Carlo estimators perform better with less correlated samples, making thinning advantageous in those specific applications.

However, it's important to recognize that thinning does discard some information, since correlation between samples is not perfect. For estimating posterior means and quantiles, using the entire chain (after burn-in) will generally provide more precise estimates than

a thinned chain of the same computational cost. This is because even correlated samples contain some independent information about the target distribution.

From a mathematical perspective, we can compare the variance of estimators computed from thinned versus full chains. Consider a chain of length N with autocorrelation function $R(k)$. If we thin by keeping every m-th sample, we obtain a chain of length N/m with a modified autocorrelation structure. The thinned chain has autocorrelation function $R_{\text{thin}}(k) = R(mk)$, since samples separated by lag k in the thinned chain correspond to samples separated by lag mk in the original chain.

The effective sample size of the thinned chain is:

$$\text{ESS}_{\text{thin}} = \frac{N/m}{1 + 2\sum_{k=1}^{\infty} R(mk)} \tag{13.65}$$

Comparing this to the ESS of the full chain reveals the trade-off involved in thinning. While thinning reduces the autocorrelation between consecutive samples in the thinned chain, it also reduces the total number of samples. The net effect on statistical efficiency depends on the specific autocorrelation structure of the original chain.

To understand when thinning might be beneficial, consider two extreme cases. If the original chain has very weak autocorrelation (samples are nearly independent), then $R(k) \approx 0$ for $k > 0$, and the ESS of the full chain is approximately N. Thinning this chain by a factor of m would give us an ESS of approximately N/m, which is clearly worse than using the full chain.

Conversely, if the original chain has very strong autocorrelation that persists for many lags, thinning might remove redundant information without significantly reducing the effective sample size. In this case, the thinned chain might be nearly as informative as the full chain while being much more manageable computationally.

The decision to thin should therefore be based on a balance between computational constraints and statistical precision. In many astronomical applications, where we're primarily interested in posterior summaries and uncertainties, thinning should be applied judiciously rather than as a default practice. When computational resources permit, using the full chain will typically yield more precise estimates.

The balance consideration between storage costs and statistical efficiency becomes

particularly important in astronomical applications where chains may contain millions of samples across hundreds of parameters. In such cases, the computational and storage benefits of thinning may outweigh the loss in statistical precision, especially if the original chain has very high autocorrelation. However, modern computational resources and efficient storage formats often make it feasible to work with full chains, making thinning less necessary than in earlier decades of MCMC applications.

A practical approach to thinning is to base the thinning factor on the autocorrelation length of the chain. If the autocorrelation function drops to negligible values (say, below 0.1) at lag k_0, then thinning by a factor of k_0 will retain samples that are approximately independent. This approach ensures that thinning removes truly redundant information while preserving the statistical content of the chain.

In summary, while thinning can be a useful tool for managing computational and storage requirements, it should be applied thoughtfully. The benefits of reduced storage and computational costs must be weighed against the potential loss in statistical precision. For most modern applications, the default should be to use the full chain when feasible, resorting to thinning only when computational constraints make it necessary or when the autocorrelation structure suggests that little information would be lost.

13.13   Burn-in

Our discussion of autocorrelation and effective sample size assumed that the Markov chain has already converged to its stationary distribution—that is, the chain is sampling from the target posterior distribution we're interested in. However, when we initialize an MCMC algorithm at an arbitrary starting point, the chain doesn't immediately represent samples from the target distribution. The initial portion of the chain, during which it transitions from the starting state to sampling from the stationary distribution, is called the "burn-in" period.

Before convergence, the samples are influenced by the arbitrary starting point and don't represent our target posterior. Using these pre-convergence samples would bias our posterior estimates and lead to incorrect inferences. The challenge lies in determining when the chain has sufficiently converged to begin collecting useful samples.

Determining when a Markov chain has converged to its stationary distribution is a critical challenge in MCMC analysis. To illustrate this concept, let's return to our Columbus

analogy: the burn-in period corresponds to the time it takes our explorer to navigate from their arbitrary starting location (perhaps the outskirts of the city) to the more representative regions where their movement pattern matches the city's population distribution. Any observations made during this initial journey would skew their understanding of Columbus's demographics.

This convergence problem is particularly challenging because the true target distribution is usually unknown—that's why we're using MCMC in the first place! Instead, we must rely on various diagnostics that examine the behavior of the chain itself to determine when burn-in has completed and the chain is sampling from the target distribution.

The simplest and most common approach is visual inspection of trace plots, which show the parameter values at each iteration of the chain. A well-converged chain should exhibit several key characteristics. It should stabilize around a central value, fluctuating around what appears to be a stable mean without obvious drift or trends. It should maintain a consistent spread, with the variability or "width" of the fluctuations remaining relatively constant without systematic changes in the amplitude of oscillations. The chain shouldn't display "stickiness" by getting stuck at particular values for extended periods, which would indicate poor mixing. And it should properly explore the full posterior, visiting all relevant regions of the parameter space with frequencies proportional to their posterior probabilities.

Beyond visual inspection, the effective sample size (ESS) we discussed earlier can serve as another important convergence diagnostic. Since ESS depends on the autocorrelation structure of the chain, monitoring how the ESS changes as we include more samples can provide insights into convergence.

For a well-converged chain, the ESS should grow approximately linearly with the number of samples after burn-in. If we plot the ESS against the number of iterations, we should see an initial nonlinear phase (during burn-in) followed by a roughly linear increase once the chain has converged. A low ESS relative to the chain length might indicate poor mixing and potential convergence issues. However, a high ESS doesn't necessarily guarantee convergence—it's possible for a chain to mix well within a restricted region of the parameter space without fully exploring the target distribution.

Visual inspection and ESS calculations provide useful initial diagnostics, but they become impractical for complex models with many parameters and may miss subtle convergence problems. For more rigorous assessment of convergence, we need quantitative diagnostics that can systematically detect when chains have reached their target distributions. The

following sections explore two such approaches that have become standard tools in MCMC analysis.

13.13.1   Gelman-Rubin Diagnostic

A powerful approach to assessing convergence involves running multiple chains from different starting points and comparing their behavior. If all chains converge to the same distribution, they should, after some burn-in period, be statistically indistinguishable from each other.

The Gelman-Rubin diagnostic formalizes this intuition. For a parameter x, we run M chains (typically at least 3 or 4), each of length $2N$. We consider discarding the first N iterations from each chain as burn-in, then compare the within-chain variance to the between-chain variance. If the chains have converged to the same distribution, these variances should be similar.

Let's denote by x_{ij} the i-th sample of parameter x in the j-th chain (after the burn-in). For each chain j, we compute the mean $\bar{x}_j$ and variance s_j^2:

$$\bar{x}_j = \frac{1}{N} \sum_{i=1}^{N} x_{ij} \tag{13.66}$$

$$s_j^2 = \frac{1}{N} \sum_{i=1}^{N} (x_{ij} - \bar{x}_j)^2 \tag{13.67}$$

The within-chain variance W is the average of these individual variances:

$$W = \frac{1}{M} \sum_{j=1}^{M} s_j^2 \tag{13.68}$$

This represents the average variance we observe within each chain. If the chains have converged, this should directly estimate the true variance of the target distribution σ^2.

Now, we need to compute a measure of the between-chain variance. We first calculate the variance of the chain means:

$$\mathrm{Var}(\bar{x}_j) = \frac{1}{M} \sum_{j=1}^{M} (\bar{x}_j - \bar{x})^2 \tag{13.69}$$
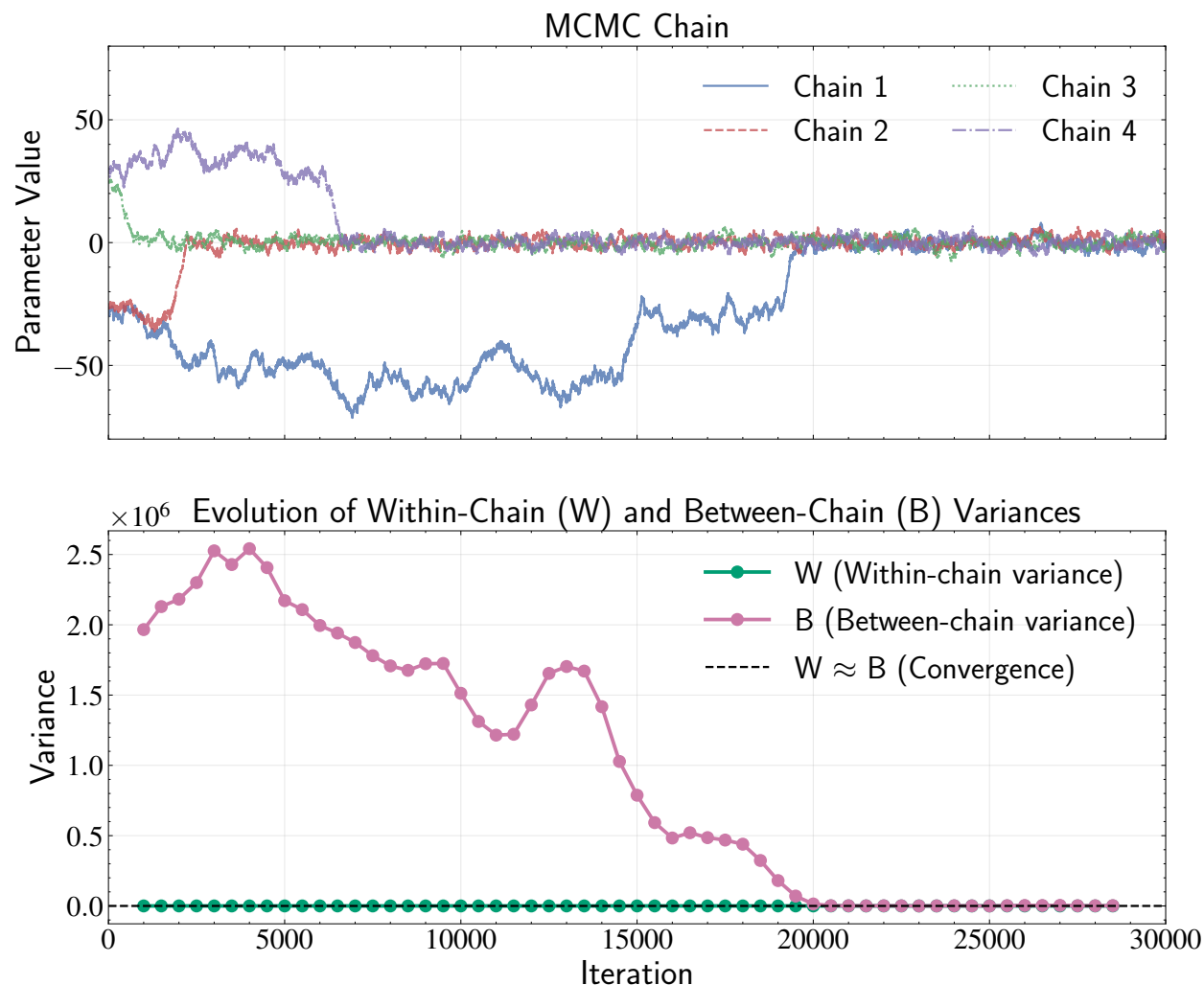
Figure 13.13: Illustration of the Gelman-Rubin diagnostic components and their evolution in MCMC sampling. Top panel: Four chains starting from different widely separated points gradually converge toward the target distribution. The small proposal width deliberately slows convergence to clearly demonstrate the diagnostic process. Bottom panel: Evolution of the within-chain variance (W) and between-chain variance (B) calculated over sliding windows. Initially, B is much larger than W, as chains are exploring different regions of the parameter space. As sampling progresses, B decreases substantially while W stabilizes, indicating chains are mixing across the same regions. Convergence is achieved when B approaches W (dashed reference line), corresponding to chains that are statistically indistinguishable from each other. This visualization demonstrates why the Gelman-Rubin diagnostic is effective at assessing MCMC convergence by comparing variability within chains to variability between chains, without requiring knowledge of the true target distribution.

where $\bar{x} = \frac{1}{M} \sum_{j=1}^{M} \bar{x}_j$ is the overall mean across all chains.

However, this variance of chain means is not directly comparable to W because each

mean $\bar{x}_j$ is based on N samples, which reduces its variance by a factor of N compared to individual samples. From statistical theory, we know that $\text{Var}(\bar{x}_j) = \sigma^2/N$ when the chain has converged to the target distribution.

To make this between-chain variance comparable to the within-chain variance, we define B by multiplying by N:

$$B = N \cdot \text{Var}(\bar{x}_j) = \frac{N}{M} \sum_{j=1}^{M} (\bar{x}_j - \bar{x})^2 \tag{13.70}$$

With this definition, under perfect convergence, we would expect:

$$B \approx W \tag{13.71}$$

This is because when chains have converged to the target distribution with variance σ^2, we have $\text{Var}(\bar{x}_j) = \sigma^2/N$, so $B = N \cdot \sigma^2/N = \sigma^2$. Meanwhile, W directly estimates σ^2 from within-chain variability. Thus, B and W should be approximately equal when the chains have fully converged.

When chains have not converged, they will be exploring different regions of the parameter space, resulting in a between-chain variance that is larger than expected. In this case, B will be larger than W, indicating additional uncertainty due to incomplete convergence.

The Gelman-Rubin statistic $\hat{R}$ quantifies this relationship by forming the ratio:

$$\hat{R} = \sqrt{1 + \frac{B - W}{NW}} \tag{13.72}$$

The numerator represents our estimate of the marginal posterior variance that accounts for both within-chain and between-chain variability. The term $(B-W)/N$ represents the additional variance due to the chains not having fully converged. The division by W then creates a ratio that measures how much larger our total variance estimate is compared to the within-chain variance alone. This normalization makes $\hat{R}$ a dimensionless quantity that can be interpreted consistently across different parameters regardless of their scales.

As the chains converge, B approaches W, causing $\hat{R}$ to approach 1 from above. In practice, values below 1.1 or even 1.05 are often considered acceptable evidence of convergence, while values substantially greater than 1 indicate that the chains have not yet

converged.

To understand this diagnostic intuitively, think of M explorers starting from different parts of Columbus. If they've all learned the city's true population distribution, they should report similar statistics about neighborhood populations (low between-explorer variance). If their reports differ significantly, it suggests they haven't fully explored the city or are still influenced by their starting locations.

The Gelman-Rubin diagnostic is particularly powerful because it doesn't require knowing anything about the true target distribution. It only relies on comparing different chains' behaviors. However, it does require running multiple chains, which increases the computational cost.

The interpretation of $\hat{R}$ is that it measures the factor by which credible intervals might shrink with more sampling. For example, if $\hat{R} = 1.2$, it suggests that credible intervals based on the current chains might be about 20% wider than they would be with perfect convergence.

For practical implementation, the Gelman-Rubin diagnostic should be applied to each parameter separately in multivariate problems. This allows identification of which specific parameters may have convergence issues. However, this approach has limitations: it may miss problems in parameters that aren't explicitly checked, and it cannot detect complex parameter interactions that might indicate convergence problems even when individual parameters appear well-behaved.

The convergence criterion typically used is $\hat{R} < 1.1$ for acceptable convergence, or $\hat{R} < 1.05$ for more stringent requirements. These thresholds represent practical compromises between computational cost and statistical rigor, recognizing that perfect convergence ($\hat{R} = 1$) is rarely achieved in finite sampling.

13.13.2   Geweke Diagnostic

While the Gelman-Rubin diagnostic requires multiple chains, there are situations where running multiple chains may not be feasible due to limited computational resources or other practical constraints. In such cases, we can use the Geweke diagnostic, which assesses convergence using a single MCMC chain.

The Geweke diagnostic is based on a simple but powerful principle: if a Markov chain has converged to its stationary distribution, then different segments of that chain should exhibit similar statistical properties. In particular, the means of different portions

of the chain should be approximately equal, as they're all sampling from the same target distribution.
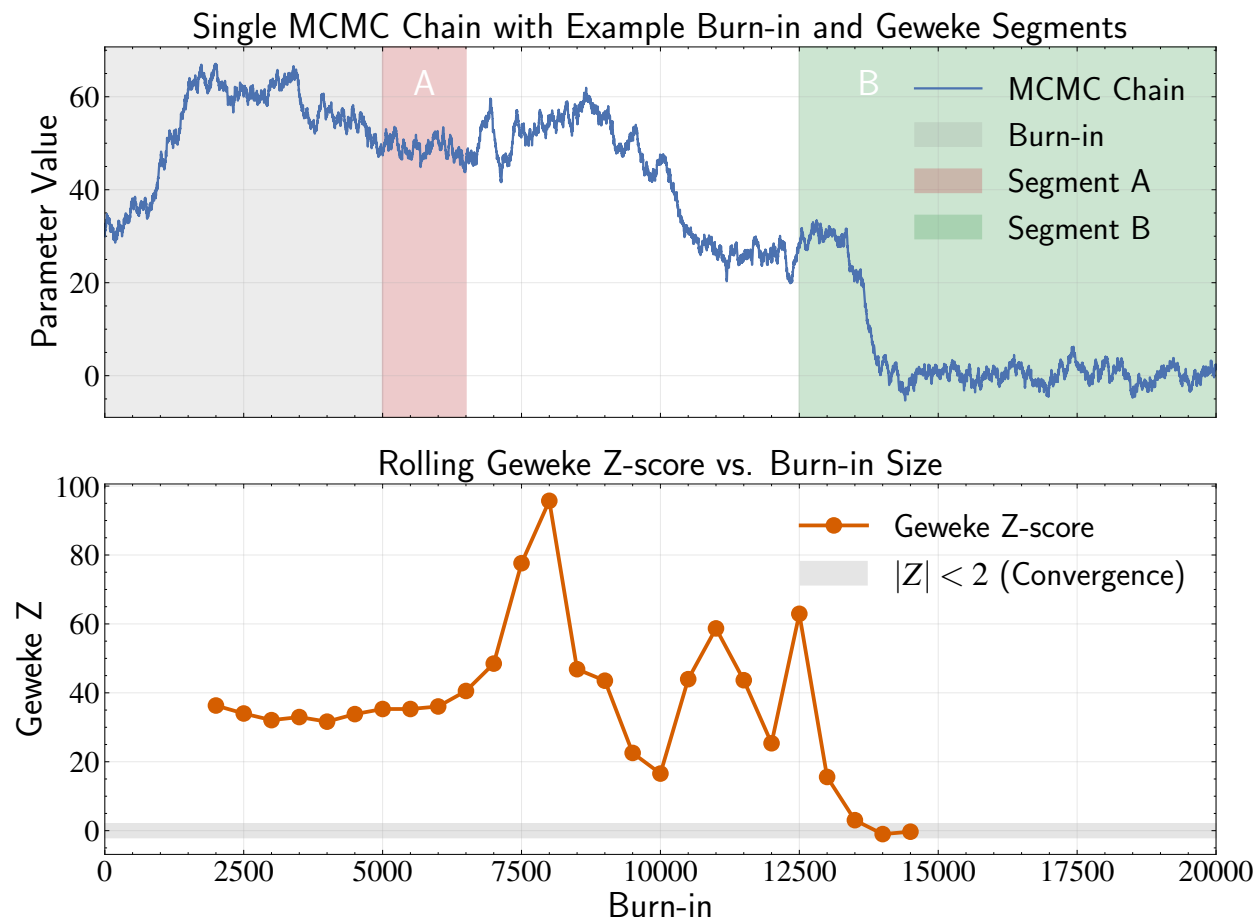
Figure 13.14: Illustration of the Geweke convergence diagnostic for a single MCMC chain. Top panel: A single MCMC chain starting from a point far from the target distribution. The gray shaded area represents a candidate burn-in period, with segments A (first 10% of post-burn-in samples, red) and B (last 50% of post-burn-in samples, green) used for the Geweke test. If the chain has converged, these two segments should have statistically similar means. Bottom panel: Geweke Z-scores computed for different burn-in sizes. The Z-score measures the difference between the means of segments A and B, properly adjusted for autocorrelation. Values within the gray band ($|Z| < 2$) suggest convergence, while values outside indicate that more burn-in may be needed. This diagnostic is particularly valuable when computational constraints limit the ability to run multiple chains for the Gelman-Rubin diagnostic, allowing convergence assessment using a single chain while properly accounting for autocorrelation in the samples.

To implement the Geweke diagnostic, we first run a single chain and discard the initial burn-in period. Then, we compare two specific segments of the remaining chain:

- The mean $\bar{x}_A$ of the first N_A samples (typically the first 10% of the post-burn-in chain)

- The mean $\bar{x}_B$ of the last N_B samples (typically the last 50% of the post-burn-in chain)

These proportions (10% and 50%) are chosen strategically: they provide enough samples in each segment for reliable statistical estimation while ensuring the segments are sufficiently separated in the chain to effectively detect any remaining non-convergence issues.

We calculate these means as:

$$\bar{x}_A = \frac{1}{N_A} \sum_{i=1}^{N_A} x_i \tag{13.73}$$

$$\bar{x}_B = \frac{1}{N_B} \sum_{i=N-N_B+1}^{N} x_i \tag{13.74}$$

If the chain has truly converged, these means should be equal except for random sampling variation. To determine if any observed difference is statistically significant, we need to account for the uncertainty in our estimates of these means.

Here's where MCMC introduces a complication: the samples in our chain are not independent. As we discussed in our section on autocorrelation and effective sample size, consecutive samples in MCMC are correlated, which affects the standard error of sample means. If we were to use the standard formula for independent samples, we would underestimate the true uncertainty, making our test too sensitive.

To address this, we need to properly account for the autocorrelation in our chain when estimating the variance of the sample mean. Earlier, we saw that for autocorrelated samples, the variance of the sample mean is inflated by a factor related to the autocorrelation function:

$$\text{Var}(\bar{x}) = \frac{\sigma^2}{N} \left(1 + 2 \sum_{k=1}^{\infty} R(k) \right) \equiv S \tag{13.75}$$

This expression captures how autocorrelation increases the variance of our mean estimate. The term S represents the attenuated variance, which encapsulates the entire autocorrelation structure's effect on the variance of the sample mean.

In practice, however, we cannot sum an infinite number of autocorrelation terms because we don't have an infinite chain. Additionally, estimates of autocorrelation at high lags become increasingly noisy due to fewer available pairs of observations. To address these

issues, we use a windowed estimator that gives less weight to the higher lags:

$$\hat{S} = \frac{\hat{\sigma}^2}{N}\left(1 + 2\sum_{k=1}^{l} w(k,l)\hat{R}(k)\right) \tag{13.76}$$

where $\hat{\sigma}^2$ is the sample variance of the chain segment, $w(k,l)$ is a window function that decreases with increasing k (like $1 - k/l$), and l is the maximum lag considered. The term $\hat{\sigma}^2$ estimates the marginal variance of the target distribution based on the available samples, while the remaining terms adjust for the autocorrelation structure.

This windowed estimator can be viewed as integrating over a triangular region in lag space. As k increases, the window function $w(k,l)$ decreases linearly, forming a triangle that gives full weight to the first lag and zero weight to lags beyond l. This triangular weighting scheme acknowledges that small lags are more important and reliable in capturing the autocorrelation structure of the chain.

With these attenuated variance estimates $\hat{S}_A$ and $\hat{S}_B$ for the two segments, we can compute the Geweke statistic as a Z-score:

$$Z = \frac{\bar{x}_A - \bar{x}_B}{\sqrt{\hat{S}_A + \hat{S}_B}} \tag{13.77}$$

This Z-score represents the difference between the means, normalized by the standard error of that difference, properly adjusted for autocorrelation. Under the null hypothesis that the chain has converged (meaning both segments are sampling from the same distribution), this Z-score should approximately follow a standard normal distribution. In practice, we typically consider the chain to have converged if the Z-score has magnitude less than 2, corresponding to the 95% confidence interval of the standard normal distribution. Larger Z-scores suggest the chain may not have reached its stationary distribution yet.

Returning to our Columbus analogy, the Geweke diagnostic is like comparing observations made by our explorer during different phases of their journey. If they've truly learned the city's population distribution, their observations from the early part of their exploration (after initial familiarization) and from the end of their journey should yield statistically similar assessments of neighborhood populations.

A key advantage of the Geweke diagnostic is that it can be applied to individual parameters separately, helping identify which aspects of the model might have convergence

issues. In complex astronomical models, some parameters often converge more slowly than others, and the Geweke diagnostic can highlight these problematic parameters.

However, the Geweke diagnostic has limitations. It only compares two specific segments of the chain, potentially missing convergence issues in the middle portions. It also relies on asymptotic properties of autocorrelation, which can be less reliable for shorter chains. Additionally, if the posterior distribution has multiple modes and the chain hasn't explored all of them, the Geweke diagnostic might incorrectly suggest convergence based on exploration of just one mode.

The implementation details of the Geweke diagnostic involve several technical considerations. Spectral density estimation methods are used to compute the windowed variance estimates, with different approaches offering trade-offs between bias and variance. Window function selection affects how much weight is given to different lags in the autocorrelation estimate, with common choices including triangular, rectangular, and Tukey windows.

The advantages of the Geweke diagnostic include its ability to work with a single chain and its established theoretical basis in the Central Limit Theorem for Markov chains. This makes it particularly valuable when computational constraints prevent running multiple chains. However, its limitations include sensitivity to segment choices and the potential to miss multimodality in the posterior distribution.

In astronomical applications where models are computationally expensive, a practical approach is to run a single long chain initially, use the Geweke diagnostic to assess convergence and determine an appropriate burn-in period, and then, if resources permit, run multiple shorter chains from dispersed starting points for the final analysis, verifying convergence with the Gelman-Rubin diagnostic.

13.14   The Metropolis-Hastings Algorithm

As we've established, the theoretical guarantees of MCMC methods rest on two key properties: detailed balance and ergodicity. We've shown how the Metropolis algorithm, with its symmetric proposal distribution, satisfies detailed balance and thus ensures convergence to our target distribution. This algorithm has proven remarkably effective and is widely applied in astronomical research for posterior sampling problems.

However, the symmetric proposal requirement of the Metropolis algorithm, while mathematically elegant, can sometimes limit sampling efficiency in practice. This is partic-

ularly true when the geometry of the posterior distribution is complex—for instance, when parameters have different scales or are strongly correlated. In such cases, we can benefit from a more general framework: the Metropolis-Hastings algorithm.

The Metropolis-Hastings algorithm generalizes the Metropolis method by removing the requirement for symmetric proposal distributions while preserving the detailed balance property that guarantees convergence to the target distribution. In the standard Metropolis algorithm, we're restricted to symmetric proposal distributions where $q(\mathbf{x}'|\mathbf{x}) = q(\mathbf{x}|\mathbf{x}')$, typically implemented as a Gaussian centered at the current position. By allowing asymmetric proposals where $q(\mathbf{x}'|\mathbf{x}) \neq q(\mathbf{x}|\mathbf{x}')$, Metropolis-Hastings offers greater flexibility in exploring the parameter space, which becomes particularly valuable when we have prior knowledge about the geometry or preferred directions of movement within the posterior distribution.
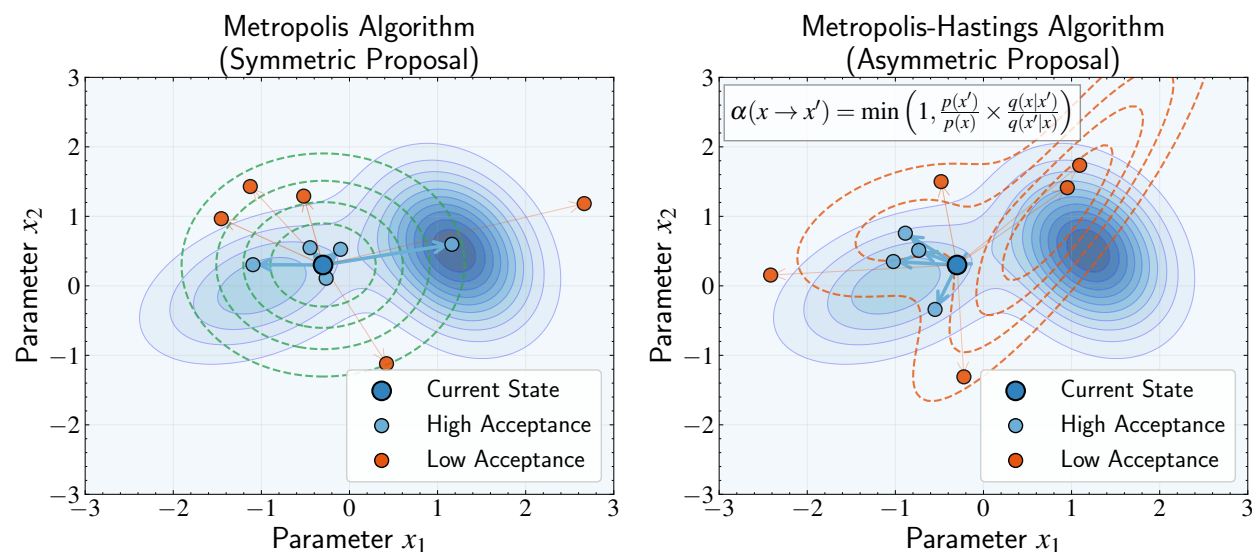
Figure 13.15: Comparison of the Metropolis algorithm (left) versus the Metropolis-Hastings algorithm (right). Both panels show the same bimodal posterior distribution (blue contours) and start from the same current state (blue point). The Metropolis algorithm uses a symmetric proposal distribution (green dashed contours), where the probability of proposing a move from $\mathbf{x}$ to $\mathbf{x}'$ equals the probability of the reverse move. In contrast, the Metropolis-Hastings algorithm uses a highly asymmetric proposal distribution (orange dashed contours), where $q(\mathbf{x}'|\mathbf{x}) \neq q(\mathbf{x}|\mathbf{x}')$. The Metropolis-Hastings algorithm compensates for the proposal asymmetry through the additional correction term $\frac{q(\mathbf{x}|\mathbf{x}')}{q(\mathbf{x}'|\mathbf{x})}$ in the acceptance ratio, maintaining detailed balance despite the directional bias in the proposal mechanism. This generalization allows for more efficient exploration of complex posterior geometries while preserving the theoretical guarantees of convergence to the target distribution, assuming ergodic conditions are met.

To understand the power of asymmetric proposals, consider sampling from a highly

skewed distribution, such as a gamma or log-normal distribution. With a symmetric Gaussian proposal, we would need to take very small steps to maintain a reasonable acceptance rate in the narrow tail region, which would make exploration of the wider region inefficiently slow. An asymmetric proposal could instead adapt to the local geometry, proposing smaller steps in the tail and larger steps in the wider region.

Recall that what we can directly control in MCMC is the transition matrix $T(\mathbf{x}, \mathbf{x}')$. In both the Metropolis and Metropolis-Hastings algorithms, this transition probability is decomposed into two components: the proposal distribution $q(\mathbf{x}'|\mathbf{x})$ and the acceptance probability $A(\mathbf{x}, \mathbf{x}')$:

$$T(\mathbf{x}, \mathbf{x}') = q(\mathbf{x}'|\mathbf{x})A(\mathbf{x}, \mathbf{x}') \tag{13.78}$$

The flexibility to use asymmetric proposal distributions comes with a requirement: we need to adjust our acceptance probability to maintain detailed balance. The acceptance probability for the Metropolis-Hastings algorithm is defined as:

$$A(\mathbf{x}, \mathbf{x}') = \min\left(1, \frac{p(\mathbf{x}')q(\mathbf{x}|\mathbf{x}')}{p(\mathbf{x})q(\mathbf{x}'|\mathbf{x})}\right) \tag{13.79}$$

Notice the addition of the $q(\mathbf{x}|\mathbf{x}')/q(\mathbf{x}'|\mathbf{x})$ term compared to the Metropolis algorithm. This ratio acts as a correction factor for the asymmetry in our proposal distribution, ensuring that detailed balance is maintained despite the non-symmetric proposal mechanism.

To understand this intuitively, consider our Columbus explorer again. In the standard Metropolis algorithm, they were equally likely to propose traveling from the Short North to German Village as from German Village to the Short North. But with Metropolis-Hastings, they might be more likely to propose traveling downhill than uphill, or more likely to propose traveling toward the city center than away from it. The $q(\mathbf{x}|\mathbf{x}')/q(\mathbf{x}'|\mathbf{x})$ term in the acceptance probability compensates for this directional bias, ensuring that the explorer's long-term visitation pattern still matches the population distribution despite their directionally biased proposals.

As with the Metropolis algorithm, the crucial property we need to verify is that the Metropolis-Hastings algorithm satisfies detailed balance. This ensures that our target posterior distribution $p(\mathbf{x})$ is a stationary distribution of our Markov chain. Let's verify this directly:

For detailed balance to hold, we need:

$$p(\mathbf{x})T(\mathbf{x}, \mathbf{x}') = p(\mathbf{x}')T(\mathbf{x}', \mathbf{x}) \tag{13.80}$$

Substituting the transition probability for Metropolis-Hastings, we get:

$$p(\mathbf{x})q(\mathbf{x}'|\mathbf{x})A(\mathbf{x}, \mathbf{x}') = p(\mathbf{x}')q(\mathbf{x}|\mathbf{x}')A(\mathbf{x}', \mathbf{x}) \tag{13.81}$$

The key difference between Metropolis-Hastings and the standard Metropolis algorithm lies in how we handle the proposal distribution. In the Metropolis algorithm, we required $q(\mathbf{x}'|\mathbf{x}) = q(\mathbf{x}|\mathbf{x}')$, which meant the proposal terms would cancel out in our acceptance ratio. However, in Metropolis-Hastings, we allow for asymmetric proposals where $q(\mathbf{x}'|\mathbf{x}) \neq q(\mathbf{x}|\mathbf{x}')$. The correction term in the acceptance probability accounts for any directional bias in our proposal mechanism, ensuring that our chain still converges to the correct posterior distribution despite the asymmetry in how we propose moves.

Let's verify detailed balance by considering two cases:

Case 1: If $\frac{p(\mathbf{x}')q(\mathbf{x}|\mathbf{x}')}{p(\mathbf{x})q(\mathbf{x}'|\mathbf{x})} \geq 1$, then:

$$A(\mathbf{x}, \mathbf{x}') = \min\left(1, \frac{p(\mathbf{x}')q(\mathbf{x}|\mathbf{x}')}{p(\mathbf{x})q(\mathbf{x}'|\mathbf{x})}\right) = 1 \tag{13.82}$$

$$A(\mathbf{x}', \mathbf{x}) = \min\left(1, \frac{p(\mathbf{x})q(\mathbf{x}'|\mathbf{x})}{p(\mathbf{x}')q(\mathbf{x}|\mathbf{x}')}\right) = \frac{p(\mathbf{x})q(\mathbf{x}'|\mathbf{x})}{p(\mathbf{x}')q(\mathbf{x}|\mathbf{x}')} \tag{13.83}$$

Substituting these into our detailed balance equation:

$$p(\mathbf{x})q(\mathbf{x}'|\mathbf{x}) \cdot 1 = p(\mathbf{x}')q(\mathbf{x}|\mathbf{x}') \cdot \frac{p(\mathbf{x})q(\mathbf{x}'|\mathbf{x})}{p(\mathbf{x}')q(\mathbf{x}|\mathbf{x}')} \tag{13.84}$$

$$p(\mathbf{x})q(\mathbf{x}'|\mathbf{x}) = p(\mathbf{x})q(\mathbf{x}'|\mathbf{x}) \tag{13.85}$$

which is true.

Case 2: If $\frac{p(\mathbf{x}')q(\mathbf{x}|\mathbf{x}')}{p(\mathbf{x})q(\mathbf{x}'|\mathbf{x})} < 1$, then:

$$A(\mathbf{x}, \mathbf{x}') = \min\left(1, \frac{p(\mathbf{x}')q(\mathbf{x}|\mathbf{x}')}{p(\mathbf{x})q(\mathbf{x}'|\mathbf{x})}\right) = \frac{p(\mathbf{x}')q(\mathbf{x}|\mathbf{x}')}{p(\mathbf{x})q(\mathbf{x}'|\mathbf{x})} \tag{13.86}$$

$$A(\mathbf{x}', \mathbf{x}) = \min\left(1, \frac{p(\mathbf{x})q(\mathbf{x}'|\mathbf{x})}{p(\mathbf{x}')q(\mathbf{x}|\mathbf{x}')}\right) = 1 \tag{13.87}$$

Substituting these into our detailed balance equation:

$$p(\mathbf{x})q(\mathbf{x}'|\mathbf{x}) \cdot \frac{p(\mathbf{x}')q(\mathbf{x}|\mathbf{x}')}{p(\mathbf{x})q(\mathbf{x}'|\mathbf{x})} = p(\mathbf{x}')q(\mathbf{x}|\mathbf{x}') \cdot 1 \tag{13.88}$$

$$p(\mathbf{x}')q(\mathbf{x}|\mathbf{x}') = p(\mathbf{x}')q(\mathbf{x}|\mathbf{x}') \tag{13.89}$$

which is also true.

Thus, we've verified that the Metropolis-Hastings algorithm satisfies detailed balance with respect to our target posterior distribution. Like the Metropolis algorithm, Metropolis-Hastings requires the same ergodicity conditions we discussed earlier. The chain must be irreducible, meaning it can reach any state from any other state given enough time. It must also be aperiodic, avoiding deterministic cycles that would prevent proper exploration of the parameter space. Finally, it must be positive recurrent, guaranteeing that the chain will return to previously visited states in finite time.

In practice, these conditions are usually satisfied in astronomical applications, but with the same caveats we discussed for the Metropolis algorithm. It's generally advisable to use bounded priors to ensure the chain doesn't wander into regions of parameter space that are physically meaningless or computationally problematic. We should also be careful to avoid regions of zero probability in our parameter space, as these can create barriers that prevent the chain from being truly irreducible. When these conditions are properly addressed, the chain will eventually converge to sampling from our target distribution.

The Metropolis-Hastings algorithm encompasses several special cases that are commonly used in practice. The random walk Metropolis-Hastings uses a proposal of the form $q(\mathbf{x}'|\mathbf{x}) = g(\mathbf{x}' - \mathbf{x})$ for some function g, essentially proposing moves based on the displacement from the current position. The independence sampler uses a proposal that doesn't depend on the current state: $q(\mathbf{x}'|\mathbf{x}) = g(\mathbf{x}')$, which can be effective when we have good prior knowledge about the target distribution. Langevin dynamics incorporates gradient information from the target distribution to propose moves that tend toward higher-probability

regions, making it particularly effective for smooth, differentiable target distributions.

13.15   Gibbs Sampling

After exploring the Metropolis and Metropolis-Hastings algorithms, we now turn to Gibbs sampling—an MCMC technique that offers advantages in certain scenarios. While the previous methods treat the entire parameter vector as a single entity, Gibbs sampling takes a more targeted approach by updating one parameter (or block of parameters) at a time.

In many astronomical applications, we encounter a common scenario: while sampling from the full joint posterior distribution $p(\mathbf{x})$ is challenging, the conditional distributions for subsets of parameters are often tractable. For a parameter vector $\mathbf{x} = (x_1, x_2, \ldots, x_d)$, we can partition it into subdimensions, and the conditional distributions of these subdimensions frequently follow standard forms that we can sample from directly.

This structure creates an opportunity. Even when the joint distribution is complex and difficult to sample from, we can often sample efficiently from the conditional distributions of parameter subsets. Gibbs sampling exploits this by decomposing the high-dimensional sampling problem into a sequence of lower-dimensional sampling tasks—a "divide and conquer" approach that can dramatically improve efficiency when the conditional distributions are well-behaved.

When these subdimensions consist of individual parameters, the Gibbs sampling procedure is straightforward. Starting from an initial state $\mathbf{x}^{(t)} = (x_1^{(t)}, x_2^{(t)}, \ldots, x_d^{(t)})$, one iteration proceeds as follows:

- Sample $x_1^{(t+1)} \sim p(x_1 | x_2^{(t)}, \ldots, x_d^{(t)})$

- Sample $x_2^{(t+1)} \sim p(x_2 | x_1^{(t+1)}, x_3^{(t)}, \ldots, x_d^{(t)})$

- $\vdots$

- Sample $x_i^{(t+1)} \sim p(x_i | x_1^{(t+1)}, \ldots, x_{i-1}^{(t+1)}, x_{i+1}^{(t)}, \ldots, x_d^{(t)})$

- $\vdots$

- Sample $x_d^{(t+1)} \sim p(x_d | x_1^{(t+1)}, \ldots, x_{d-1}^{(t+1)})$

At each step, we focus on a single parameter x_i and sample directly from its condi-

tional distribution. Importantly, we immediately use this newly sampled value when conditioning subsequent parameters. This sequential updating approach transforms a complex joint sampling problem into a series of more manageable one-dimensional tasks.
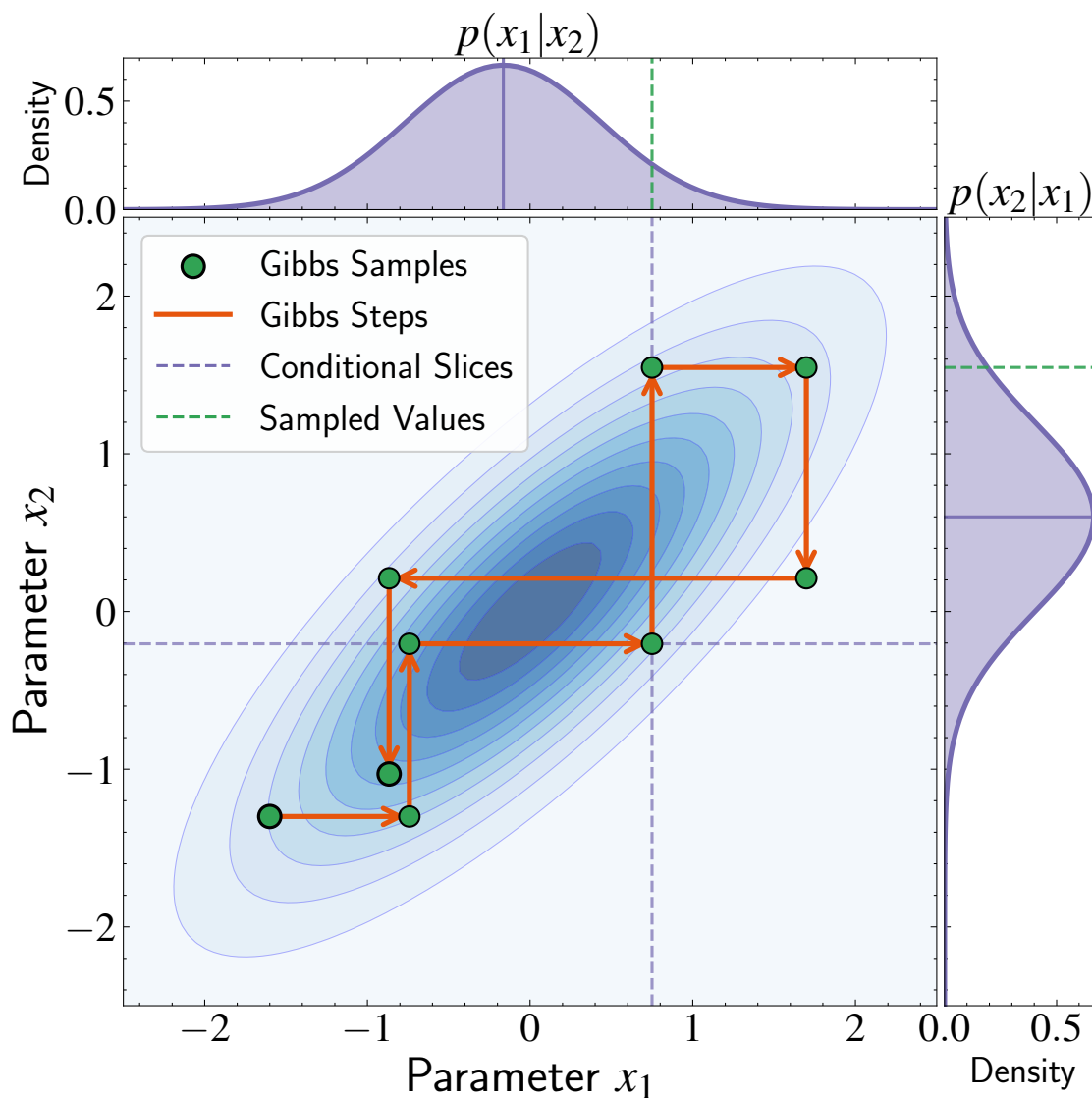
Figure 13.16: Illustration of Gibbs sampling. The main panel shows the joint posterior distribution (blue contours) with the characteristic stair-step pattern of Gibbs sampling. Purple dashed lines indicate the conditional slices where we sample one parameter given the other. Each iteration consists of two steps: first sampling x_1 given x_2 (horizontal movement), then sampling x_2 given the new value of x_1 (vertical movement). The top and right panels show the one-dimensional conditional distributions $p(x_1|x_2)$ and $p(x_2|x_1)$, with purple solid lines marking the modes of these conditionals and green dashed lines showing the actual values sampled. This visual demonstrates how Gibbs sampling decomposes the high-dimensional sampling problem into a series of conditional sampling tasks.

Gibbs sampling offers advantages when the conditional distributions have standard forms (e.g., Gaussian, gamma, beta). In these cases, we can employ efficient exact sampling methods like inverse CDF transformation or specialized random number generators, avoiding the need for proposal distributions and acceptance/rejection steps. Even when some conditional distributions lack standard forms, we can apply MCMC methods just for those specific parameters while directly sampling the others.

Theoretical Foundation: Gibbs as Metropolis-Hastings   Why does Gibbs sampling work? At first glance, it might seem puzzling that we never directly sample from the joint distribution—only from subdimensional conditional distributions. To understand the theoretical foundation, we can show that Gibbs sampling is actually a special case of the Metropolis-Hastings algorithm.

A key distinction from the Metropolis algorithm is that Gibbs sampling doesn't require us to define an arbitrary proposal distribution (like a Gaussian). Instead, it cleverly uses the conditional distributions of the target distribution itself as the proposal mechanism. When updating the i-th component, the Gibbs sampler uses the conditional distribution as the proposal distribution:

$$q_i(\mathbf{x}'|\mathbf{x}) = p(x_i'|x_1, \ldots, x_{i-1}, x_{i+1}, \ldots, x_d) \cdot \prod_{j \neq i} \delta(x_j' - x_j) \qquad (13.90)$$

where δ is the Dirac delta function, ensuring that all components except the i-th remain unchanged. In simpler terms, we're proposing new values only for the i-th component, drawing them directly from its conditional distribution.

This approach might seem unusual at first—we're using the target distribution's own conditional as our proposal. However, this is perfectly valid within the Metropolis-Hastings framework, provided we adjust the acceptance probability accordingly to maintain detailed balance. The key question becomes: what is the appropriate acceptance probability when using conditional distributions as proposals?

To determine this, we need to apply the standard Metropolis-Hastings acceptance criterion:

$$A(\mathbf{x}, \mathbf{x}') = \min\left(1, \frac{p(\mathbf{x}')q(\mathbf{x}|\mathbf{x}')}{p(\mathbf{x})q(\mathbf{x}'|\mathbf{x})}\right) \qquad (13.91)$$

For the Gibbs sampler, we need to carefully analyze this acceptance probability. First, let's note that since we're only updating the i-th component, we have $x_j' = x_j$ for all $j \neq i$.

We can apply the product rule of probability to express the joint distributions:

$$p(\mathbf{x}) = p(x_i | x_1, \ldots, x_{i-1}, x_{i+1}, \ldots, x_d) \cdot p(x_1, \ldots, x_{i-1}, x_{i+1}, \ldots, x_d) \tag{13.92}$$

Similarly for $\mathbf{x}'$:

$$p(\mathbf{x}') = p(x_i' | x_1, \ldots, x_{i-1}, x_{i+1}, \ldots, x_d) \cdot p(x_1, \ldots, x_{i-1}, x_{i+1}, \ldots, x_d) \tag{13.93}$$

Notice that the second term in both expressions is identical because all components except the i-th are the same in $\mathbf{x}$ and $\mathbf{x}'$. Now, let's look at the proposal distributions:

$$q(\mathbf{x}' | \mathbf{x}) = p(x_i' | x_1, \ldots, x_{i-1}, x_{i+1}, \ldots, x_d) \tag{13.94}$$

and

$$q(\mathbf{x} | \mathbf{x}') = p(x_i | x_1, \ldots, x_{i-1}, x_{i+1}, \ldots, x_d) \tag{13.95}$$

For notational convenience, let's define $\mathbf{x}_{-i}$ to represent all components of $\mathbf{x}$ except the i-th component, i.e., $\mathbf{x}_{-i} = (x_1, \ldots, x_{i-1}, x_{i+1}, \ldots, x_d)$. Using this notation, we can write the conditional distributions more compactly as $p(x_i | \mathbf{x}_{-i})$.

Substituting these into our acceptance probability:

$$A(\mathbf{x}, \mathbf{x}') = \min\left(1, \frac{p(\mathbf{x}')q(\mathbf{x}|\mathbf{x}')}{p(\mathbf{x})q(\mathbf{x}'|\mathbf{x})}\right) \tag{13.96}$$

$$= \min\left(1, \frac{p(x_i'|\mathbf{x}_{-i}) \cdot p(\mathbf{x}_{-i}) \cdot p(x_i|\mathbf{x}_{-i})}{p(x_i|\mathbf{x}_{-i}) \cdot p(\mathbf{x}_{-i}) \cdot p(x_i'|\mathbf{x}_{-i})}\right) \tag{13.97}$$

$$= \min(1, 1) = 1 \tag{13.98}$$

The acceptance probability for Gibbs sampling is always exactly 1. This makes intuitive sense: unlike standard Metropolis-Hastings where we use an arbitrary proposal distribution, in Gibbs sampling we're directly sampling from the exact conditional distribution we want. There's no need for rejection because we're already drawing from the correct distribution for each parameter given all others. This is why Gibbs sampling is often described as a "rejection-free" MCMC method.

Since Gibbs sampling is a special case of Metropolis-Hastings, and we've already established that Metropolis-Hastings satisfies detailed balance and converges to the target

distribution (assuming ergodicity), we know Gibbs sampling will also converge to the desired posterior distribution.

However, it's crucial to understand that a perfect acceptance rate doesn't necessarily mean efficient sampling. While every proposal is accepted, the samples can still be highly correlated with each other. The lack of rejection doesn't guarantee that our samples are independent or that they efficiently explore the full posterior distribution.

To understand when Gibbs sampling works well and when it struggles, we need to examine how the structure of the target distribution affects sampling efficiency.

Bivariate Gaussian Example   To better understand both the strengths and limitations of Gibbs sampling, let's examine a concrete and pedagogically rich example: sampling from a bivariate Gaussian distribution. This example is particularly instructive because we can derive the conditional distributions analytically and directly observe how the performance of Gibbs sampling varies with the correlation structure of the target distribution.

Consider sampling from a bivariate Gaussian distribution with zero mean and correlation coefficient ρ:

$$\begin{pmatrix} x_1 \\ x_2 \end{pmatrix} \sim \mathcal{N}\left(\mathbf{0}, \begin{bmatrix} 1 & \rho \\ \rho & 1 \end{bmatrix}\right) \tag{13.99}$$

To implement Gibbs sampling, we need the conditional distributions $p(x_1|x_2)$ and $p(x_2|x_1)$. For a bivariate Gaussian distribution, we can directly apply the standard formula for conditional distributions. If we have a joint Gaussian distribution:

$$\begin{pmatrix} x_1 \\ x_2 \end{pmatrix} \sim \mathcal{N}\left(\begin{pmatrix} \mu_1 \\ \mu_2 \end{pmatrix}, \begin{bmatrix} \Sigma_{11} & \Sigma_{12} \\ \Sigma_{21} & \Sigma_{22} \end{bmatrix}\right) \tag{13.100}$$

Then the conditional distribution of x_1 given x_2 is:

$$p(x_1|x_2) = \mathcal{N}(\mu_1 + \Sigma_{12}\Sigma_{22}^{-1}(x_2 - \mu_2), \Sigma_{11} - \Sigma_{12}\Sigma_{22}^{-1}\Sigma_{21}) \tag{13.101}$$

In our specific case, we have $\mu_1 = \mu_2 = 0$, $\Sigma_{11} = \Sigma_{22} = 1$, and $\Sigma_{12} = \Sigma_{21} = \rho$.

Substituting these values:

$$p(x_1|x_2) = \mathcal{N}(0 + \rho \cdot 1^{-1} \cdot (x_2 - 0), 1 - \rho \cdot 1^{-1} \cdot \rho) \tag{13.102}$$

$$= \mathcal{N}(\rho x_2, 1 - \rho^2) \tag{13.103}$$

Therefore, the conditional distributions are:

$$p(x_1|x_2) = \mathcal{N}(\rho x_2, 1 - \rho^2) \tag{13.104}$$

and by symmetry:

$$p(x_2|x_1) = \mathcal{N}(\rho x_1, 1 - \rho^2) \tag{13.105}$$

These closed-form expressions make this distribution ideal for Gibbs sampling. At each step, we can directly sample from these conditional distributions without needing any rejection steps. The Gibbs sampling procedure would alternate between:

1. Sample $x_1^{(t+1)} \sim \mathcal{N}(\rho x_2^{(t)}, 1 - \rho^2)$

2. Sample $x_2^{(t+1)} \sim \mathcal{N}(\rho x_1^{(t+1)}, 1 - \rho^2)$

Effect of Parameter Correlation   Let's analyze how the correlation coefficient ρ affects the performance of Gibbs sampling in our bivariate Gaussian example.

When $\rho = 0$ (no correlation), the conditional distributions simplify to:

$$p(x_1|x_2) = \mathcal{N}(0, 1) \quad \text{and} \quad p(x_2|x_1) = \mathcal{N}(0, 1) \tag{13.106}$$

In this case, the Gibbs sampler generates independent samples in each dimension. Each conditional sampling step provides a completely new value unrelated to the previous samples, and the chain explores the joint distribution with optimal efficiency. The bivariate Gaussian appears as a circular contour, and the Gibbs sampler moves freely in both dimensions.

As $|\rho|$ increases, the conditional relationship between x_1 and x_2 strengthens. For high correlation (e.g., $\rho = 0.95$), the conditional distributions become:

$$p(x_1|x_2) = \mathcal{N}(0.95x_2, 0.0975) \quad \text{and} \quad p(x_2|x_1) = \mathcal{N}(0.95x_1, 0.0975) \tag{13.107}$$

The means now depend very strongly on the other variable, and the variance is reduced to 0.0975 (which equals $1 - \rho^2$ for $\rho = 0.95$). The Gibbs sampler now shows high autocorrelation between successive samples. The bivariate Gaussian appears as a highly elongated elliptical contour, and the Gibbs sampler moves in a narrow stair-step pattern along this ellipse.

This behavior reveals a limitation of standard Gibbs sampling: it can struggle with strongly correlated parameters, which are common in astronomical models. In such cases, the chain may require many iterations to effectively explore the posterior, resulting in high autocorrelation and a low effective sample size despite the perfect acceptance rate. This example demonstrates that a rejection-free sampling method does not automatically guarantee efficient exploration of the parameter space.

Returning to our Columbus explorer analogy, a Gibbs sampler with highly correlated parameters is like an explorer who can only move north-south or east-west, never diagonally, in a city where all the important pathways run diagonally. Each individual step is valid, but the overall exploration pattern is inefficient.

Block Gibbs Sampling   The challenges posed by correlated parameters naturally lead to several strategies for improving the efficiency of Gibbs sampling. One powerful approach is block Gibbs sampling, where we update groups of correlated parameters simultaneously rather than individually.

In our bivariate Gaussian example, instead of alternating between x_1 and x_2, we could update them jointly—effectively sampling directly from the joint distribution. While this trivializes our specific example, it illustrates an important general principle: by grouping correlated parameters together, we can often sample more efficiently.

Mathematically, if we partition our parameter vector $\mathbf{x}$ into B blocks $(\mathbf{x}_{(1)}, \mathbf{x}_{(2)}, \ldots, \mathbf{x}_{(B)})$, the block Gibbs sampler proceeds as:

1. Sample $\mathbf{x}_{(1)}^{(t+1)} \sim p(\mathbf{x}_{(1)} | \mathbf{x}_{(2)}^{(t)}, \ldots, \mathbf{x}_{(B)}^{(t)})$

2. Sample $\mathbf{x}_{(2)}^{(t+1)} \sim p(\mathbf{x}_{(2)} | \mathbf{x}_{(1)}^{(t+1)}, \mathbf{x}_{(3)}^{(t)}, \ldots, \mathbf{x}_{(B)}^{(t)})$

3. $\vdots$

4. Sample $\mathbf{x}_{(B)}^{(t+1)} \sim p(\mathbf{x}_{(B)} | \mathbf{x}_{(1)}^{(t+1)}, \ldots, \mathbf{x}_{(B-1)}^{(t+1)})$
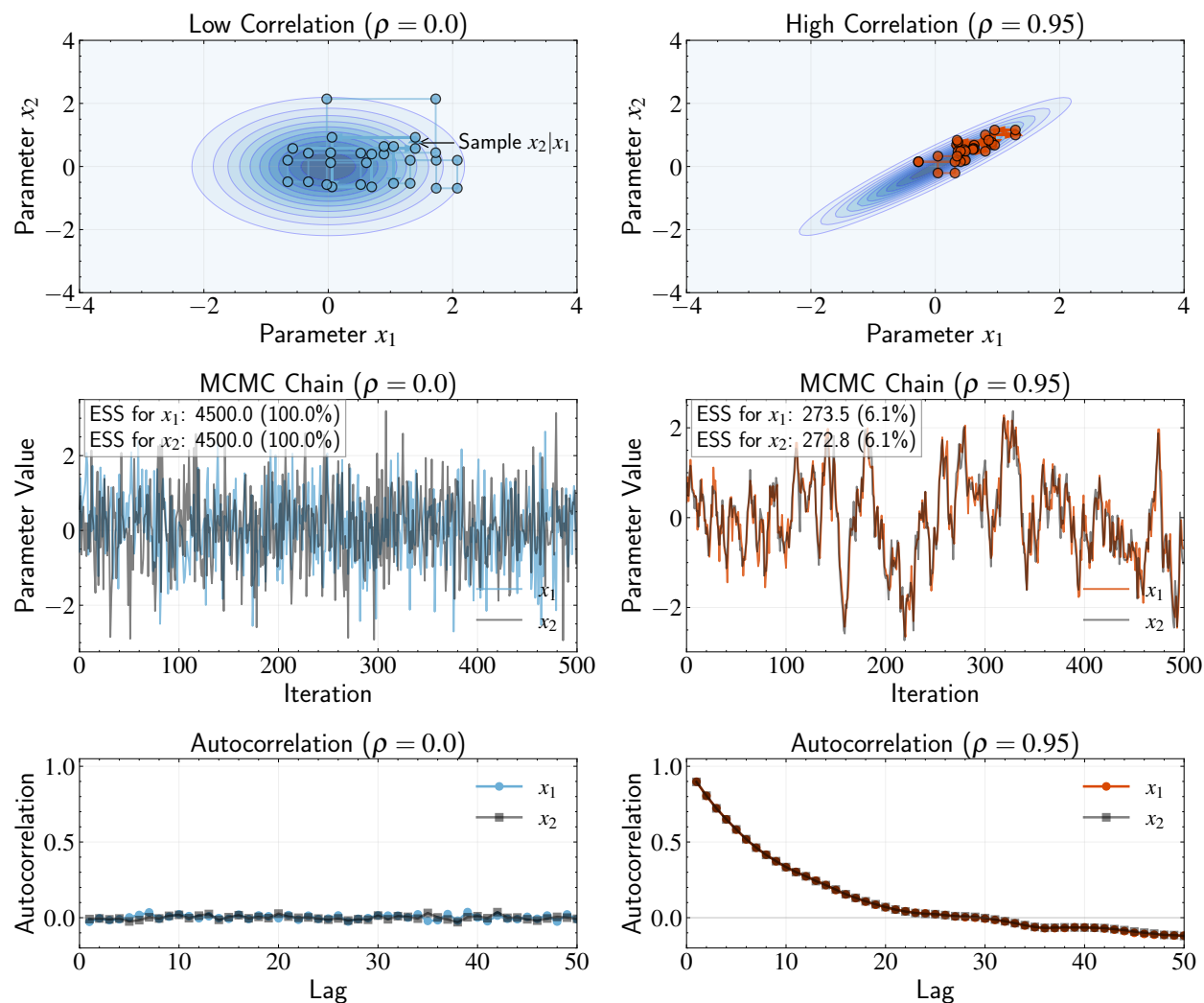
Figure 13.17: Effect of parameter correlation on Gibbs sampling efficiency. **Top row:** Sampling paths in parameter space for bivariate Gaussian distributions with no correlation ($\rho = 0$, left) and high correlation ($\rho = 0.95$, right). The characteristic rectangular pattern of Gibbs sampling becomes increasingly narrow with higher correlation, showing the algorithm's difficulty in exploring the major axis of the distribution. **Middle row:** MCMC chains showing stronger autocorrelation in the high-correlation case. Note the dramatically reduced effective sample size (ESS) percentage when correlation is high. **Bottom row:** Autocorrelation functions for both parameters, demonstrating how autocorrelation decays much more slowly with higher parameter correlation. This example illustrates why Gibbs sampling, despite its rejection-free nature, can be highly inefficient for strongly correlated parameters. While the acceptance rate remains perfect in both cases, the high-correlation scenario requires many more iterations to effectively explore the posterior distribution.

It's worth noting that block Gibbs sampling is also a special case of the Metropolis-Hastings algorithm with an acceptance probability of 1. To see this, consider the proposal

distribution for updating block $\mathbf{x}_{(i)}$:

$$q(\mathbf{x}'_{(i)}|\mathbf{x}_{(i)}, \mathbf{x}_{(-i)}) = p(\mathbf{x}'_{(i)}|\mathbf{x}_{(-i)}) \tag{13.108}$$

where $\mathbf{x}_{(-i)}$ represents all blocks except the i-th. The Metropolis-Hastings acceptance ratio becomes:

$$\alpha = \min\left(1, \frac{p(\mathbf{x}'_{(i)}, \mathbf{x}_{(-i)})}{p(\mathbf{x}_{(i)}, \mathbf{x}_{(-i)})} \cdot \frac{q(\mathbf{x}_{(i)}|\mathbf{x}'_{(i)}, \mathbf{x}_{(-i)})}{q(\mathbf{x}'_{(i)}|\mathbf{x}_{(i)}, \mathbf{x}_{(-i)})}\right) \tag{13.109}$$

$$= \min\left(1, \frac{p(\mathbf{x}'_{(i)}|\mathbf{x}_{(-i)}) \cdot p(\mathbf{x}_{(-i)})}{p(\mathbf{x}_{(i)}|\mathbf{x}_{(-i)}) \cdot p(\mathbf{x}_{(-i)})} \cdot \frac{p(\mathbf{x}_{(i)}|\mathbf{x}_{(-i)})}{p(\mathbf{x}'_{(i)}|\mathbf{x}_{(-i)})}\right) \tag{13.110}$$

$$= \min(1, 1) = 1 \tag{13.111}$$

This shows that the proof of convergence for block Gibbs sampling follows directly from the general Metropolis-Hastings framework. The key insight is that by proposing from the exact conditional distribution, the acceptance ratio simplifies to 1, making the algorithm rejection-free. This generalizes the single-component case we discussed earlier to blocks of arbitrary size, maintaining the perfect acceptance property while potentially improving mixing by updating correlated parameters together.

Applications to Hierarchical Models   The conditional sampling approach of Gibbs sampling makes it particularly well-suited for hierarchical Bayesian models, where parameters are organized in layers, with higher-level parameters (hyperparameters) governing the distributions of lower-level parameters.

For example, consider a model for a population of exoplanets, where we have observations of multiple planetary systems. At the lowest level, we have parameters for individual planets (masses, radii, orbital parameters). At a higher level, we have hyperparameters that describe the population-wide distributions of these properties (e.g., the mean and variance of planetary masses across all systems).

The conditional structure in such models often follows a natural pattern. Given the hyperparameters, the individual planet parameters are conditionally independent of each other, which means we can update each planet's parameters without considering the other planets. Conversely, given the individual planet parameters, the hyperparameters typically have simple conditional distributions that depend only on the collection of individual parameters.

This hierarchical structure is ideal for Gibbs sampling. We can implement an efficient sampling strategy by alternating between two main steps. First, we update all individual planet parameters, potentially in parallel since they're conditionally independent given the hyperparameters. Then, we update the population hyperparameters based on the current values of all the individual parameters. This back-and-forth approach allows us to efficiently explore the joint posterior distribution.

The power of this approach extends to many astronomical applications. In stellar population modeling, individual star properties are governed by cluster-wide hyperparameters, creating a natural hierarchy. Similarly, in galaxy clustering studies, individual galaxy properties depend on their host dark matter halos, forming another hierarchical relationship. Cosmological parameter estimation often combines different observational probes in a hierarchical framework, where Gibbs sampling can efficiently navigate the complex parameter space.

In these contexts, Gibbs sampling offers a natural and efficient approach that respects the inherent conditional independence structure of the model. By exploiting this structure, we can often achieve much more efficient sampling than would be possible with generic Metropolis-Hastings approaches that treat all parameters as a single block.

13.16   Summary

This chapter has introduced Markov Chain Monte Carlo (MCMC) methods as a powerful solution to the high-dimensional sampling problems that arise in Bayesian inference for astronomical applications. We began by establishing the fundamental challenge: while the direct sampling methods from Chapter 12 work well for simple problems, they face the curse of dimensionality that renders them impractical for the complex, multi-parameter models common in modern astronomy.

The central insight of MCMC is to replace global exploration strategies with sequential, local moves through parameter space. Rather than attempting to characterize entire distributions at once, MCMC constructs random walks where each step depends only on the current position. This transformation of an intractable sampling problem into a manageable sequence of local decisions represents one of the most important computational advances in statistical inference.

We developed this concept through the Columbus explorer analogy, where a traveler

following simple local rules eventually produces a visitation pattern that matches the target distribution. This analogy helped illustrate how individual-level behavior (the explorer's path) connects to population-level distributions (the equilibrium pattern), providing intuitive understanding for the mathematical principles that follow.

The theoretical foundation of MCMC rests on two key pillars. Detailed balance provides a sufficient condition for ensuring that our target posterior distribution becomes the stationary distribution of the Markov chain. We showed how this principle naturally balances flows between different regions of parameter space, creating equilibrium when the system reaches the target distribution. Ergodicity guarantees both convergence and uniqueness, ensuring that chains will reach the target distribution from any starting point and that this distribution is the only possible equilibrium.

The Metropolis algorithm provided our first concrete implementation of these principles. By decomposing transitions into proposal and acceptance steps, this algorithm offers a simple yet powerful approach to sampling from complex distributions. The acceptance probability, based on ratios of posterior densities, naturally implements detailed balance while requiring only that we can evaluate the posterior up to a proportionality constant—eliminating the need for difficult normalization calculations.

We then explored the Metropolis-Hastings generalization, which removes the symmetry restriction on proposal distributions. This flexibility allows for more efficient exploration of complex parameter spaces, particularly when we have prior knowledge about the geometry of the posterior distribution. Gibbs sampling introduced a different approach entirely, focusing on conditional distributions rather than joint proposals. When conditional distributions are tractable, this method can be highly efficient, though our analysis revealed that efficiency depends critically on parameter correlations.

Throughout our algorithmic development, we emphasized practical considerations that arise in real implementations. Burn-in periods are necessary because chains must transition from arbitrary starting points to sampling from the target distribution. Autocorrelation between successive samples reduces their effective information content, requiring careful assessment through the effective sample size. The diagnostic tools we developed—particularly the Gelman-Rubin and Geweke tests—provide practical methods for assessing convergence without knowing the true target distribution.

The methods developed in this chapter have revolutionized Bayesian inference in astronomy over the past three decades. Complex problems that were previously intractable—such

as characterizing exoplanet populations, inferring cosmological parameters from multiple observational probes, or modeling stellar evolution with uncertain physics—have become routine applications of MCMC methods.

The transition from direct sampling methods to MCMC represents more than just a computational advancement—it reflects a shift in perspective from trying to solve problems globally to exploring them locally through guided random walks. This perspective proves valuable far beyond the specific algorithms we've studied, providing a general framework for tackling complex inference problems across many domains.

MCMC methods have broad applicability that extends well beyond the scope of this course. They serve as the computational backbone for sophisticated modeling techniques across statistics, machine learning, physics, and many other fields where complex probability distributions arise. However, our journey through statistical methods for astronomy is not complete. While MCMC provides powerful tools for complex inference problems, there remain modeling scenarios where analytical calculations are still possible and often preferable.

In our next chapter, we return to such a scenario as we explore Gaussian processes—an advanced technique that, despite its sophistication, often admits analytical solutions for key quantities like posterior predictions and marginal likelihoods. The journey from the simple grid methods of Chapter 12 to the sophisticated MCMC algorithms of this chapter illustrates a recurring theme in computational statistics: as problems become more complex, we must often abandon exact solutions in favor of approximate methods that scale effectively. Yet as we'll see, the interplay between analytical and computational approaches continues to drive advances in statistical methodology, with each having its place in the modern statistician's toolkit.

Further Readings: The development of Markov Chain Monte Carlo methods builds upon foundational algorithms in computational physics, with early contributions from Metropolis et al. [1953] who developed the algorithm for equation of state calculations, later generalized by Hastings [1970] to accommodate asymmetric proposal distributions. For readers interested in theoretical foundations, Tierney [1994] provides rigorous treatment for general state spaces, while Roberts and Smith [1994] offers practical convergence conditions essential for implementation. The Gibbs sampling approach emerged through work on image restoration by Geman and Geman [1984], with Gelfand and Smith [1990] demonstrating its broader applicability to calculating marginal densities in complex Bayesian models. Earlier

applications to astronomical problems developed through contributions from Christensen et al. [2001] who applied MCMC to cosmological parameter estimation from CMB data, and Lewis and Bridle [2002] whose CosmoMC package became widely adopted for cosmological inference. Verde et al. [2003] presents methodology for analyzing WMAP observations, while Tegmark et al. [2004] demonstrates combined analysis of CMB and large-scale structure data. In exoplanet studies, Ford [2005] addresses uncertainty quantification through MCMC, with Gregory [2005] developing hybrid algorithms for planet detection. Practical implementation concerns are addressed through convergence diagnostics by Gelman and Rubin [1992] and Geweke [1992], with Cowles and Carlin [1996] providing comparative review of available methods. Alternative approaches to posterior sampling emerged through nested sampling introduced by Skilling [2006], with astronomical implementation in MultiNest by Feroz and Hobson [2008] for multimodal distributions. Modern software implementations include emcee by Foreman-Mackey et al. [2013] featuring an affine-invariant ensemble sampler, and PyMC described in Abril-Pla et al. [2023] with advanced algorithms including the No-U-Turn Sampler. For readers seeking comprehensive treatment, Gilks et al. [1996] offers practical guidance, Robert and Casella [1999] provides mathematical foundations, Liu [2001] bridges theory and computational strategies, while Sharma [2017] presents a review focused on astronomical applications and Hogg and Foreman-Mackey [2018] offers practical implementation advice.

Chapter 14

Gaussian Processes

Throughout our exploration of machine learning methods, we have built a foundation spanning linear models, Bayesian inference, and MCMC techniques. Each approach we've studied has offered particular strengths while revealing certain limitations. Linear regression and its Bayesian extensions provide analytical solutions with rigorous uncertainty quantification, but they require us to specify the functional form through careful feature engineering. MCMC techniques can handle arbitrarily complex models, but they become computationally intensive and require careful diagnostics to ensure convergence.

This progression highlights a recurring challenge in statistical modeling: we often face a choice between analytical tractability and modeling flexibility. Simple parametric models give us mathematical convenience but may be too rigid to capture complex relationships. Nonparametric approaches offer flexibility but often sacrifice the clean analytical properties that make inference straightforward.

Consider the challenge of modeling stellar variability from photometric time series data. A linear model could capture this if we carefully design features like polynomial terms, Fourier components, or physical basis functions. But how do we choose the right features? If a star exhibits complex multi-timescale behavior—pulsations on short timescales, rotational modulation on intermediate timescales, and long-term evolutionary changes—designing appropriate features becomes extraordinarily difficult.

We could alternatively use MCMC to fit a complex parametric model incorporating multiple physical processes. But such models require numerous parameters to capture different types of variability, making the sampling computationally expensive and potentially

unstable. We face the classic bias-variance tradeoff: simple models may be too rigid, while complex models may overfit or become intractable.

Gaussian Processes offer a different approach to this tension. Instead of explicitly defining a parametric model, GPs work by specifying properties we expect the underlying function to have and letting the data determine the functional form within these constraints. Rather than choosing between simplicity and flexibility, GPs provide a framework where complexity emerges naturally from the data structure.

The key insight is to move from explicit parametric models to implicit functional models. We specify our beliefs about function properties—smoothness, periodicity, characteristic length scales—through a kernel function rather than through explicit mathematical forms. This approach has proven valuable across diverse astronomical problems where the underlying processes are well-understood qualitatively but difficult to model explicitly.

For stellar variability, we might expect smooth changes on certain timescales combined with periodic modulation, but we don't know the exact functional form. For exoplanet transit analysis, stellar intrinsic variability creates complex patterns that resist simple parameterization. Quasar light curves exhibit stochastic variations driven by chaotic accretion processes that would be extremely difficult to model explicitly.

GPs handle these challenges by using kernels—functions that measure similarity between data points—to encode our beliefs about the underlying process. When predicting stellar brightness at a given time, we base our estimate on observations from nearby times, weighted by their similarity as measured by the kernel function. This assumes smoothness and continuity without requiring us to model the complex physics explicitly.

Two mathematical perspectives illuminate how GPs work. We can derive them by extending linear regression using the kernel trick, showing how GPs connect to familiar models while working in potentially infinite-dimensional feature spaces. Alternatively, we can approach GPs through the function space view, treating them as distributions over functions rather than parameters. Both perspectives lead to identical predictive equations but provide different insights into why and how GPs work.

The practical advantages of GPs for astronomical applications are substantial. They automatically adapt their complexity to the data, becoming more flexible where observations are dense while maintaining appropriate uncertainty where data is sparse. They provide principled uncertainty quantification that accounts for both measurement noise and model

uncertainty. Most importantly, they eliminate the need for explicit feature engineering—we specify similarity through kernels rather than designing transformations of our inputs.

This chapter develops GPs through both mathematical perspectives, showing how the kernel trick connects them to linear models while the function space view provides clean probabilistic interpretations. We then extend the framework from regression to classification, providing a complete treatment of GP methods for supervised learning problems in astronomy.

14.1 The Kernel Trick

Before diving into Gaussian Processes, we need to understand a fundamental concept that underlies many modern machine learning methods: the kernel trick. This idea transforms how we think about modeling complex relationships, shifting from explicit feature engineering to implicit similarity measures. To build this intuition, we'll start with a familiar problem from statistics and show how kernels provide a natural solution.

Kernel Density Estimation: Building Intuition Consider the challenge of estimating probability distributions from data. In many astronomical applications, we encounter datasets where the underlying distribution doesn't follow standard parametric forms. We might have measurements of stellar masses, galaxy luminosities, or exoplanet orbital periods that exhibit complex, multimodal, or skewed distributions that resist simple mathematical description.

The traditional approach offers us a choice between parametric models and histograms. Parametric distributions like Gaussians work well when the data follows familiar patterns, but they fail when the true distribution has complex shapes. Histograms provide flexibility but come with significant drawbacks—they are highly sensitive to bin width choices and produce discontinuous estimates that poorly represent smooth underlying processes.

Kernel Density Estimation (KDE) provides an alternative solution that should be familiar to astronomers. KDE is a non-parametric method that estimates probability distributions without assuming a specific functional form. The approach is intuitive: we place a kernel function (typically Gaussian) at each observed data point and sum their contributions:

$$p(x) = \frac{1}{N} \sum_{n=1}^{N} \frac{1}{(2\pi h^2)^{1/2}} \exp\left(-\frac{\|x - x_n\|^2}{2h^2}\right) \tag{14.1}$$
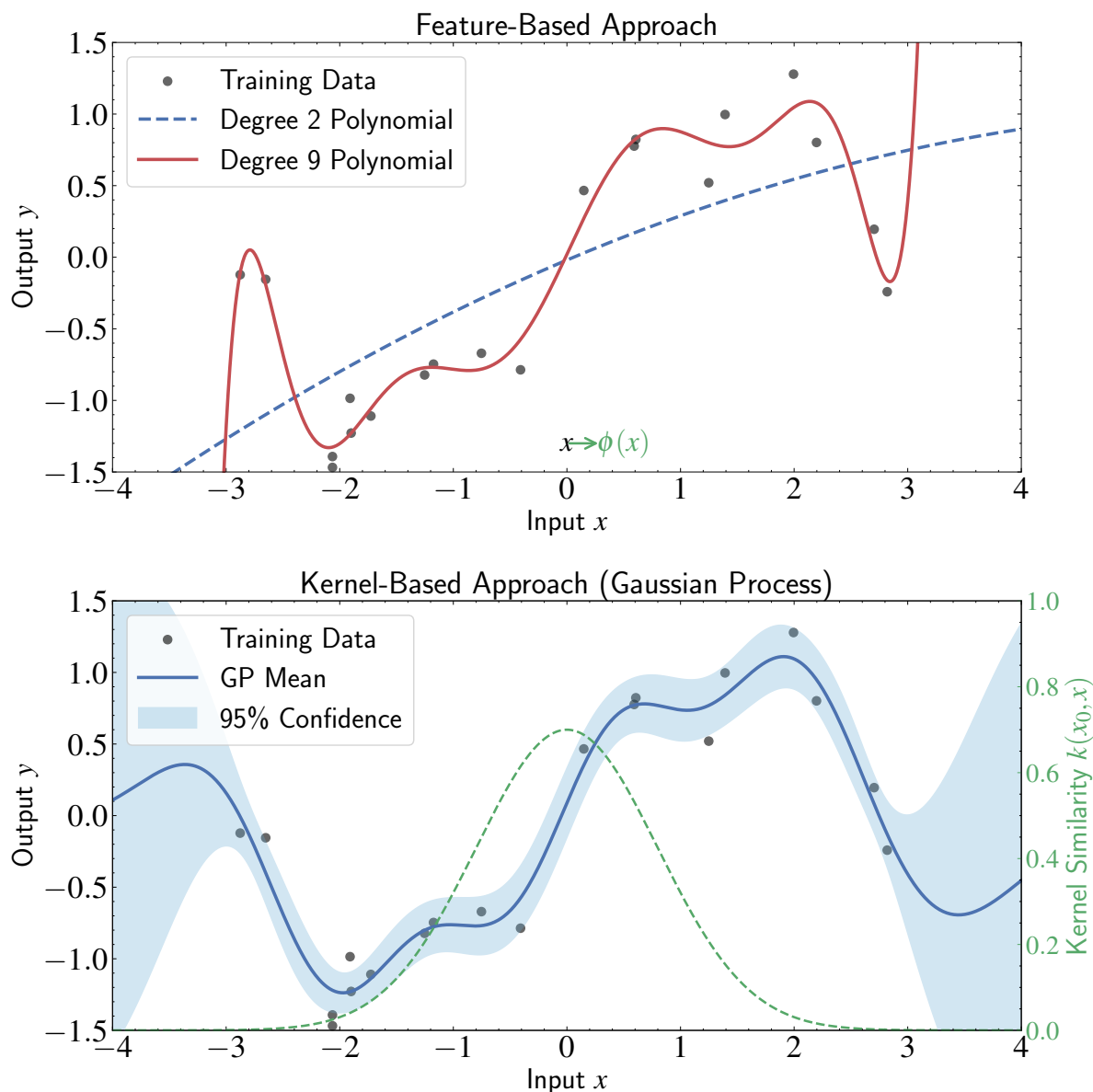
Figure 14.1: Comparison of feature-based and kernel-based approaches for regression tasks. The top panel illustrates the feature-based approach, where inputs x are explicitly mapped to a feature space $\phi(x)$ before applying linear regression. The black points represent training data, while the blue dashed and orange solid lines show predictions from low-degree (underfitting) and high-degree (more flexible) polynomial models, respectively. The bottom panel demonstrates the kernel-based approach using Gaussian Processes, which implicitly works in an infinite-dimensional feature space through the kernel trick. The blue line shows the GP mean prediction with the light blue region indicating the 95% confidence interval, naturally providing uncertainty quantification. The green dashed line (right y-axis) visualizes the kernel similarity function from the reference point $x_0 = 0$, illustrating how Gaussian Processes measure similarity between inputs rather than explicitly defining features.
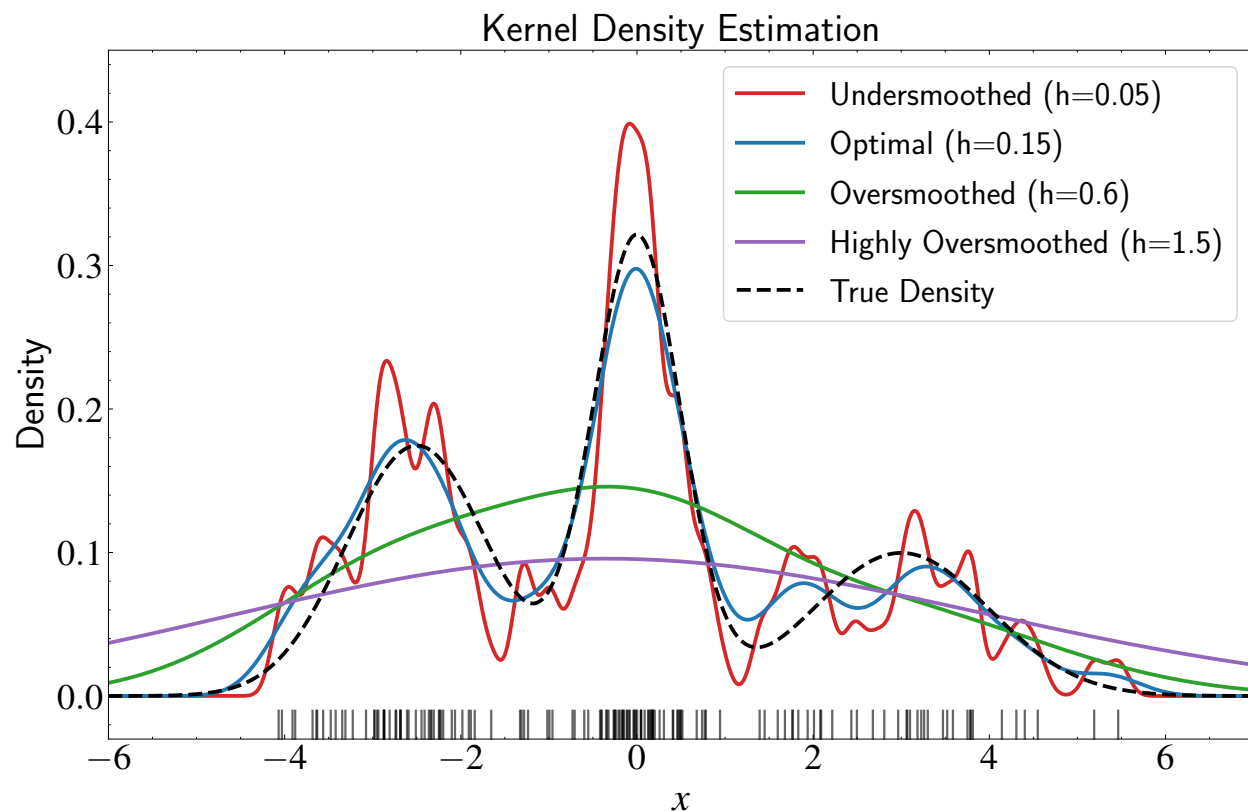
Figure 14.2: Kernel Density Estimation (KDE) illustrating the core concept behind kernel methods. The figure shows how KDE constructs a flexible, non-parametric probability density estimate by placing a kernel function at each observed data point (black tick marks along the x-axis). The overall density estimate is created by summing these kernels, allowing complex functions to emerge from simple building blocks without requiring explicit feature engineering. The bandwidth parameter h controls the smoothness of the estimate, showcasing the bias-variance tradeoff: the red curve (h=0.05) is undersmoothed with high variance but captures fine details, the blue curve (h=0.15) provides optimal smoothing that closely follows the true density, while the green (h=0.6) and purple (h=1.5) curves progressively oversmooth the data. This same principle—using kernels to measure similarity between points—underlies Gaussian Process regression, where inputs with similar features produce similar outputs without requiring explicit feature mappings.

Here, N represents the number of data points, and h is a smoothing parameter (bandwidth) that controls the width of each kernel. This parameter determines how much influence each data point has on its surroundings. For astronomers, this concept should feel familiar from applications like N-body simulations and galaxy density mapping, where similar smoothing techniques are routinely applied.

The key insight of KDE is that we are not specifying a parametric form for $p(x)$. Instead, we let the data speak for itself, with each data point contributing a "bump" to the

overall density. The only parameter we need to specify is h, which controls the smoothness of our estimate. A small h produces a spiky distribution that may overfit to noise, while a larger h gives a smoother distribution that may miss important local variations.

This same principle appears in many computational physics problems familiar to astronomers. In N-body simulations, when calculating gravitational forces or smoothing density fields, kernels distribute the mass or influence of each particle over a finite region, providing continuous approximations to inherently discrete systems. The approach offers several key advantages: there's no need to specify a rigid functional form, the model adapts to the data, and we only need to choose parameters that control smoothness rather than defining exact shapes.

From Density Estimation to Regression The kernel concept extends naturally from density estimation to regression problems. In regression, we have paired data: for each input $\mathbf{x}_i$, we have a corresponding output value y_i. This pairing allows us to leverage similarity in a more directed way, connecting input similarities to output predictions.

A fundamental assumption in many physical systems is that similar inputs should produce similar outputs. This principle appears throughout astronomy: measurements taken at similar times often exhibit similar behavior, observations from nearby spatial regions tend to be correlated, and objects with similar physical properties frequently show comparable observational signatures.

Rather than constructing complex parametric models with carefully engineered features, we can leverage this similarity principle directly. Consider a concrete example from quasar variability analysis. If we want to predict the luminosity at time t_*, we could compute a weighted average of luminosities observed at nearby times:

$$y(t_*) = \frac{\sum_{i=1}^{N} w_i y_i}{\sum_{i=1}^{N} w_i} \tag{14.2}$$

where w_i is a weight that decreases with the temporal distance between t_* and observation time t_i.

This approach assumes continuity in the luminosity function based on temporal proximity, without requiring us to explicitly model the complex accretion physics that drive quasar variability. We're not trying to solve the equations of magnetohydrodynamics around black holes—instead, we're using the empirical pattern that nearby times tend to have similar
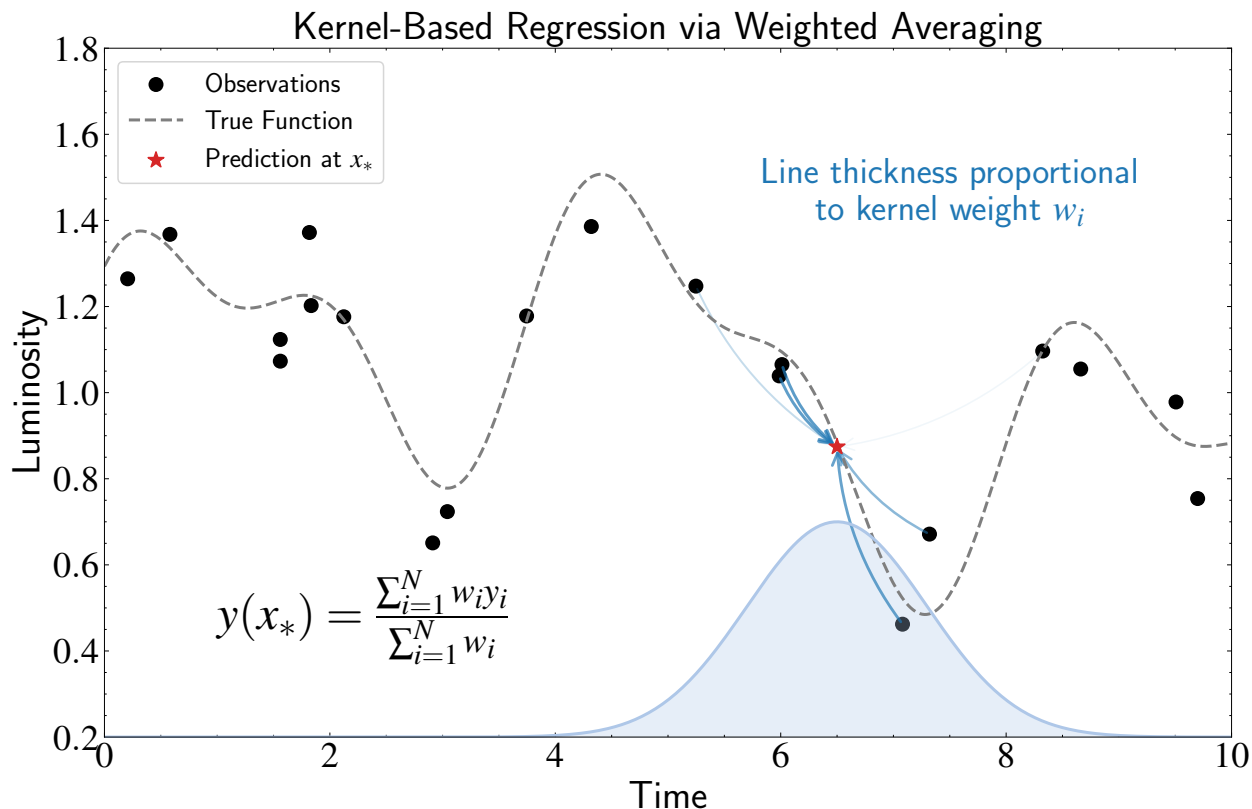
Figure 14.3: Illustration of kernel-based regression through weighted averaging. This figure demonstrates how predictions can be made at a new point x_* (red star) using weighted combinations of existing observations (black dots) without requiring an explicit parametric model. The weights are determined by a kernel function (light blue curve) centered at the prediction point, which assigns higher weights to temporally proximate observations. The thickness of the blue arrows represents the relative contribution (weight) of each observation to the final prediction, with nearby points having stronger influence. Instead of engineering explicit features or constructing a complex physical model, we define similarity between points via the kernel function and let the data speak for itself. The prediction is a weighted average $y(x_*) = \frac{\sum_{i=1}^{N} w_i y_i}{\sum_{i=1}^{N} w_i}$, where weights naturally decrease with distance from the prediction point.

brightness levels.

More generally, we can express kernel-based predictions as:

$$f(\mathbf{x}_*) = \sum_{i=1}^{N} k(\mathbf{x}_*, \mathbf{x}_i)\alpha_i \tag{14.3}$$

where $k(\mathbf{x}_*, \mathbf{x}_i)$ is a kernel function measuring similarity between the prediction point and training point i, and α_i are coefficients determined from the data. The kernel function en-

codes our beliefs about what makes inputs similar, while the data determines the appropriate coefficients.

The Power of Similarity-Based Modeling   This similarity-based perspective represents a shift in modeling philosophy. Instead of asking "What mathematical function describes this relationship?" we ask "How should we measure similarity between observations?" This reframing often proves more intuitive and tractable.

For temporal data like stellar light curves, we might expect that observations close in time should be more similar than those far apart. For spatial data in galaxy surveys, similarity might depend on angular separation. The flexibility to define domain-appropriate similarity measures makes this approach broadly applicable across astronomical problems.

The key insight is that we can often define meaningful similarity measures even when we cannot easily specify explicit functional forms. We might not know the exact equations governing quasar variability, but we have strong intuitions about which observations should be considered similar. This transforms a difficult function specification problem into a more manageable similarity definition problem.

This kernel perspective—using similarity measures rather than explicit functional forms—underlies Gaussian Processes and many other modern machine learning methods. The challenge now becomes: how do we rigorously integrate this similarity-based approach with the statistical frameworks we've developed throughout this course? In the next section, we'll see how this intuitive concept can be formally connected to linear regression, creating a mathematical foundation that maintains statistical rigor while gaining modeling flexibility.

14.2   Kernelizing Linear Regression

Having established the intuition behind kernel methods through density estimation and similarity-based prediction, we now turn to the mathematical framework that makes this approach rigorous. The key insight is that we can reformulate linear regression—a method we understand well—entirely in terms of similarity measures, without ever explicitly computing features. This transformation, known as "kernelizing," bridges the gap between our intuitive similarity-based approach and the statistical rigor of parametric models.

Let us begin with the linear regression framework we have studied throughout this

course. In linear regression, we assume the output y is a linear function of features $\phi(x)$:

$$y(x) = \phi(x)^T \mathbf{w} \tag{14.4}$$

where $\mathbf{w} \in \mathbb{R}^m$ represents the weights, and m is the number of features. For N training data points, we construct a design matrix $\boldsymbol{\Phi} \in \mathbb{R}^{N \times m}$ containing all input features, and a target vector $\mathbf{t} \in \mathbb{R}^N$ for the corresponding outputs.

As we have seen in previous chapters, the maximum likelihood solution for heteroskedastic noise (where each data point has its own noise variance) is:

$$\mathbf{w}^* = (\boldsymbol{\Phi}^T \mathbf{S}^{-1} \boldsymbol{\Phi})^{-1} \boldsymbol{\Phi}^T \mathbf{S}^{-1} \mathbf{t} \tag{14.5}$$

where $\mathbf{S}$ represents the noise covariance matrix. This weighted least squares solution naturally gives more weight to reliable measurements and less influence to noisy data points.

The limitation we identified in the previous section now becomes clear: linear regression requires us to explicitly define the feature mapping $\phi(\cdot)$. In astronomical applications, choosing appropriate features becomes extraordinarily challenging. How do we design features that capture the complex physics of stellar variability, the chaotic dynamics of quasar accretion, or the multiscale structure of galaxy formation? Traditional approaches require us to encode our physical understanding into mathematical transformations—an approach that quickly becomes intractable as system complexity increases.

The Key Mathematical Insight   The breakthrough comes from recognizing that linear regression predictions depend only on inner products between feature vectors. For a new input x_*, the prediction is:

$$y(x_*) = \phi(x_*)^T \mathbf{w}^* = \phi(x_*)^T (\boldsymbol{\Phi}^T \boldsymbol{\Phi})^{-1} \boldsymbol{\Phi}^T \mathbf{t} \tag{14.6}$$

Examining this expression, we see that it depends on two types of inner products:

- $\boldsymbol{\Phi}^T \boldsymbol{\Phi}$ contains all pairwise inner products between training feature vectors

- $\phi(x_*)^T \boldsymbol{\Phi}^T$ contains inner products between the test point and all training points

This observation suggests a different approach. Instead of working with features

explicitly, we can work with these inner products directly. We define a kernel function as:

$$k(x, x') = \phi(x)^T \phi(x') \tag{14.7}$$

This kernel measures similarity between inputs based on their inner product in feature space. The crucial realization is that we can often compute these kernels without ever constructing the feature vectors $\phi(x)$ explicitly.

For our N training data points, we construct an $N \times N$ kernel matrix $\mathbf{K}$:

$$\mathbf{K} = \mathbf{\Phi}\mathbf{\Phi}^T \in \mathbb{R}^{N \times N} \tag{14.8}$$

where each entry $K_{ij} = k(x_i, x_j)$ represents the similarity between training points i and j.

The computational advantage becomes apparent when we consider dimensions. In the original formulation, we invert an $m \times m$ matrix (where m is the number of features). With kernels, we invert an $N \times N$ matrix (where N is the number of training points). When we want flexible models with many features ($m \gg N$), or when m is infinite, the kernel approach becomes not just preferable but necessary.

Deriving the Kernelized Form   To reformulate linear regression in terms of kernels, we need to eliminate explicit dependence on feature vectors. For clarity, we focus on the homoskedastic noise case where $\mathbf{S} = \sigma_n^2 \mathbf{I}$ (constant noise variance). The heteroskedastic case follows the same principles but involves more complex matrix manipulations, which we will address later when we introduce the function space view that handles varying noise more naturally.

With homoskedastic Gaussian noise, the regularized maximum likelihood estimate becomes:

$$\mathbf{w}^* = (\mathbf{\Phi}^T \mathbf{\Phi} + \sigma_n^2 \mathbf{I})^{-1} \mathbf{\Phi}^T \mathbf{t} \tag{14.9}$$

For prediction at x_*:

$$y(x_*) = \phi(x_*)^T (\mathbf{\Phi}^T \mathbf{\Phi} + \sigma_n^2 \mathbf{I})^{-1} \mathbf{\Phi}^T \mathbf{t} \tag{14.10}$$

To kernelize this expression, we apply the Woodbury matrix identity:

$$(A + UCV)^{-1} = A^{-1} - A^{-1}U(C^{-1} + VA^{-1}U)^{-1}VA^{-1} \tag{14.11}$$

Setting $A = \sigma_n^2 \mathbf{I}$, $U = \mathbf{\Phi}^T$, $C = \mathbf{I}$, and $V = \mathbf{\Phi}$, we get:

$$(\mathbf{\Phi}^T\mathbf{\Phi} + \sigma_n^2\mathbf{I})^{-1}\mathbf{\Phi}^T = \frac{1}{\sigma_n^2}(\mathbf{I} - \mathbf{\Phi}^T(\mathbf{\Phi}\mathbf{\Phi}^T + \sigma_n^2\mathbf{I})^{-1}\mathbf{\Phi})\mathbf{\Phi}^T \tag{14.12}$$

$$= \frac{1}{\sigma_n^2}(\mathbf{\Phi}^T - \mathbf{\Phi}^T(\mathbf{\Phi}\mathbf{\Phi}^T + \sigma_n^2\mathbf{I})^{-1}\mathbf{\Phi}\mathbf{\Phi}^T) \tag{14.13}$$

The matrices $\mathbf{\Phi}\mathbf{\Phi}^T$ and $(\mathbf{\Phi}\mathbf{\Phi}^T + \sigma_n^2\mathbf{I})^{-1}$ commute because they share the same eigenvectors. If $\mathbf{v}$ is an eigenvector of $\mathbf{\Phi}\mathbf{\Phi}^T$ with eigenvalue λ:

$$(\mathbf{\Phi}\mathbf{\Phi}^T + \sigma_n^2\mathbf{I})^{-1}\mathbf{v} = (\lambda + \sigma_n^2)^{-1}\mathbf{v} \tag{14.14}$$

$$\mathbf{\Phi}\mathbf{\Phi}^T\mathbf{v} = \lambda\mathbf{v} \tag{14.15}$$

Both products yield the same result for any eigenvector, confirming commutativity.

Continuing the derivation using $\mathbf{I} = (\mathbf{\Phi}\mathbf{\Phi}^T + \sigma_n^2\mathbf{I})(\mathbf{\Phi}\mathbf{\Phi}^T + \sigma_n^2\mathbf{I})^{-1}$:

$$= \frac{1}{\sigma_n^2}\mathbf{\Phi}^T((\mathbf{\Phi}\mathbf{\Phi}^T + \sigma_n^2\mathbf{I} - \mathbf{\Phi}\mathbf{\Phi}^T)(\mathbf{\Phi}\mathbf{\Phi}^T + \sigma_n^2\mathbf{I})^{-1}) \tag{14.16}$$

$$= \frac{1}{\sigma_n^2}\mathbf{\Phi}^T(\sigma_n^2\mathbf{I})(\mathbf{\Phi}\mathbf{\Phi}^T + \sigma_n^2\mathbf{I})^{-1} \tag{14.17}$$

$$= \mathbf{\Phi}^T(\mathbf{K} + \sigma_n^2\mathbf{I})^{-1} \tag{14.18}$$

Define the kernel vector between x_* and all training points:

$$\mathbf{k}_* = [k(x_1, x_*), k(x_2, x_*), \ldots, k(x_N, x_*)]^T = \mathbf{\Phi}\phi(x_*) \tag{14.19}$$

Substituting into our prediction equation:

$$y(x_*) = \phi(x_*)^T(\mathbf{\Phi}^T\mathbf{\Phi} + \sigma_n^2\mathbf{I})^{-1}\mathbf{\Phi}^T\mathbf{t} \tag{14.20}$$

$$= \phi(x_*)^T\mathbf{\Phi}^T(\mathbf{K} + \sigma_n^2\mathbf{I})^{-1}\mathbf{t} \tag{14.21}$$

$$= \mathbf{k}_*^T(\mathbf{K} + \sigma_n^2\mathbf{I})^{-1}\mathbf{t} \tag{14.22}$$

We have successfully kernelized linear regression! The prediction for a new point x_* is now expressed as a weighted sum of training targets, with weights determined by similarities between x_* and training points, modulated by the inverse of the kernel matrix plus noise.

This kernelization transforms our modeling approach fundamentally. We have eliminated the need to explicitly define feature mappings $\phi(x)$. Instead, we work directly with similarity measures between data points. Even when the implicit feature space has infinite dimensions, we perform regression efficiently using only the $N \times N$ kernel matrix.

This mathematical framework provides the foundation for Gaussian Processes. However, we have only shown one direction: starting with features and deriving kernels. The next critical question is: which functions can serve as valid kernels? Not every similarity function corresponds to a legitimate inner product in some feature space. We need mathematical conditions to ensure our kernel defines a valid feature space.

14.3 Mercer's Theorem and Valid Kernels

Up to this point, we have been working in one direction: starting with a feature mapping $\phi(x)$ and deriving a kernel function $k(x, y) = \phi(x)^T \phi(y)$. This approach shows how kernels arise naturally from feature spaces. But the real power of kernel methods comes from working in the opposite direction—defining kernels directly without explicitly specifying features.

This raises a crucial question: When is a function $k(x, y)$ a valid kernel? That is, under what conditions can we guarantee that a function $k(x, y)$ corresponds to some feature mapping ϕ such that $k(x, y) = \phi(x)^T \phi(y)$? Not any similarity function can be expressed as a dot product in some feature space. We have only shown the forward direction: if we have a feature mapping ϕ, then $k(x, y) = \phi(x)^T \phi(y)$ is a valid kernel. But we need the converse direction as well.

This is precisely where Mercer's theorem becomes essential. The theorem states that a function $k(x, y)$ is a valid kernel if and only if it satisfies two key properties:

1. **Symmetry**: $k(x, y) = k(y, x)$ for all x and y in the input space.

2. **Positive semi-definiteness**: For any finite set of points $\{x_1, ..., x_n\}$, the kernel matrix $\mathbf{K}$ with entries $K_{ij} = k(x_i, x_j)$ must be positive semi-definite. In other words, for any vector $\mathbf{u} \in \mathbb{R}^n$, $\mathbf{u}^T \mathbf{K} \mathbf{u} \geq 0$.

Mercer's theorem formally states that if these conditions are met, then there exists a Hilbert space $\mathcal{H}$ and a mapping $\phi : \mathcal{X} \to \mathcal{H}$ such that for all $x, y \in \mathcal{X}$:

$$k(x, y) = \langle \phi(x), \phi(y) \rangle_{\mathcal{H}} \tag{14.23}$$

where $\langle \cdot, \cdot \rangle_{\mathcal{H}}$ denotes the inner product in $\mathcal{H}$.

The proof of Mercer's theorem involves concepts from functional analysis and spectral theory, and lies beyond the scope of this chapter. However, the key insight is that positive semi-definite kernels can be represented through their eigendecomposition. Just as a symmetric matrix can be diagonalized as $\mathbf{A} = \mathbf{Q}\mathbf{\Lambda}\mathbf{Q}^T$, where $\mathbf{\Lambda}$ contains the eigenvalues and $\mathbf{Q}$ the eigenvectors, a kernel function can be decomposed as $k(x, y) = \sum_{i=1}^{\infty} \lambda_i \psi_i(x) \psi_i(y)$, where λ_i are the eigenvalues and ψ_i the eigenfunctions. This decomposition allows us to construct a feature mapping $\phi(x) = (\sqrt{\lambda_1}\psi_1(x), \sqrt{\lambda_2}\psi_2(x), \ldots)$ that reproduces the kernel through the inner product.

The significance of Mercer's theorem for our purposes is this: it provides a mathematical guarantee that if we define a kernel function that satisfies symmetry and positive semi-definiteness, we can be confident that our kernel corresponds to some feature space, even if we never explicitly construct that space. This allows us to design kernels based on our domain knowledge about similarity in a particular problem, without having to worry about finding the corresponding features.

Now that we understand what makes a valid kernel, let us explore some specific kernel functions and their properties. Understanding these common kernels will help us appreciate the power and flexibility of kernel methods in practice.

Linear and Polynomial Kernels   The simplest kernel function is the linear kernel, defined as:

$$k(x_m, x_n) = x_m^T x_n \tag{14.24}$$

This kernel is equivalent to using the identity feature map $\phi(x) = x$. The kernel simply computes the dot product in the original input space. While this might seem trivial, it illustrates the duality: we can either work directly with features or implicitly via kernels, and both approaches are mathematically equivalent.

A natural extension of the linear kernel is the polynomial kernel of degree d:

$$k(x_m, x_n) = (x_m^T x_n + c)^d \tag{14.25}$$

where $c \geq 0$ is a constant that trades off the influence of higher-order versus lower-order terms.

Consider a simple example of a polynomial kernel of degree 2 (quadratic kernel) with $c = 0$:

$$k(x_m, x_n) = (x_m^T x_n)^2 \tag{14.26}$$

For two-dimensional inputs $x = (x_1, x_2)$, this corresponds to the feature mapping:

$$\phi(x) = (x_1^2, \sqrt{2}x_1 x_2, x_2^2) \tag{14.27}$$

You can verify that the dot product of these feature vectors exactly reproduces our kernel:

$$\phi(x_m)^T \phi(x_n) = x_{m1}^2 x_{n1}^2 + 2x_{m1}x_{m2}x_{n1}x_{n2} + x_{m2}^2 x_{n2}^2 = (x_m^T x_n)^2 \tag{14.28}$$

This example illustrates a key point: polynomial kernels implicitly map our data to a higher-dimensional feature space that includes all monomials of degree d or less. For degree 2 in two dimensions, we get three features. But as the input dimensionality or polynomial degree increases, the feature space grows rapidly.

The Gaussian (RBF) Kernel Perhaps the most famous and widely used kernel is the radial basis function (RBF) kernel, also known as the Gaussian kernel:

$$k(x_m, x_n) = \exp\left(-\frac{\|x_n - x_m\|^2}{2\sigma^2}\right) \tag{14.29}$$

This kernel has an intuitive interpretation: it measures the similarity between points x_n and x_m based on their Euclidean distance, modulated by a length scale parameter σ. Points that are close together have kernel values near 1, while points far apart have kernel values approaching 0. The parameter σ controls the "width" of this similarity function—a smaller σ means that points must be very close to be considered similar.

What makes the RBF kernel remarkable is that it corresponds to an infinite-dimensional feature space. We can show this by expanding the kernel using the Taylor series of the ex-

ponential function:

$$\exp(x) = 1 + x + \frac{x^2}{2!} + \frac{x^3}{3!} + \dots \tag{14.30}$$

Applying this expansion to our kernel, we get an infinite series of terms, each corresponding to a different feature in the implicit feature space. This means that using the RBF kernel is equivalent to mapping our data to an infinite-dimensional feature space and performing linear regression there.

The Matérn Kernel Another important generalization of the RBF kernel is the Matérn kernel, which is particularly popular in spatial statistics and Gaussian process modeling. The Matérn kernel is defined as:

$$k(x_m, x_n) = \frac{2^{1-\nu}}{\Gamma(\nu)} \left(\frac{\sqrt{2\nu}\|x_m - x_n\|}{l} \right)^{\nu} K_{\nu} \left(\frac{\sqrt{2\nu}\|x_m - x_n\|}{l} \right) \tag{14.31}$$

where Γ is the gamma function, K_{ν} is the modified Bessel function of the second kind, ν controls the smoothness of the resulting functions, and l is the length scale parameter.

The Matérn kernel is valuable because it allows precise control over the smoothness of functions in the corresponding feature space through the parameter ν. Common choices for ν include $1/2$, $3/2$, and $5/2$, each resulting in functions with different degrees of differentiability. Interestingly, when $\nu \to \infty$, the Matérn kernel converges to the RBF kernel, making the latter a special case of the former.

Combining Kernels An important property of valid kernels is that the sum of valid kernels is also a valid kernel, allowing us to build complex models by combining simpler components. This property follows directly from Mercer's theorem, which states that a kernel function is valid if and only if its corresponding kernel matrix is positive semi-definite for any set of inputs. Since positive semi-definite matrices remain positive semi-definite under addition, the sum of valid kernels must also be valid.

For example, we might model stellar variability using a composite kernel:

$$k(t, t') = \theta_0 \exp\left(-\frac{\theta_1}{2}|t - t'|^2 \right) + \theta_2 + \theta_3 \exp\left(-\frac{2\sin^2(\pi|t - t'|/\theta_4)}{\theta_5^2} \right) \tag{14.32}$$

This kernel combines three components:

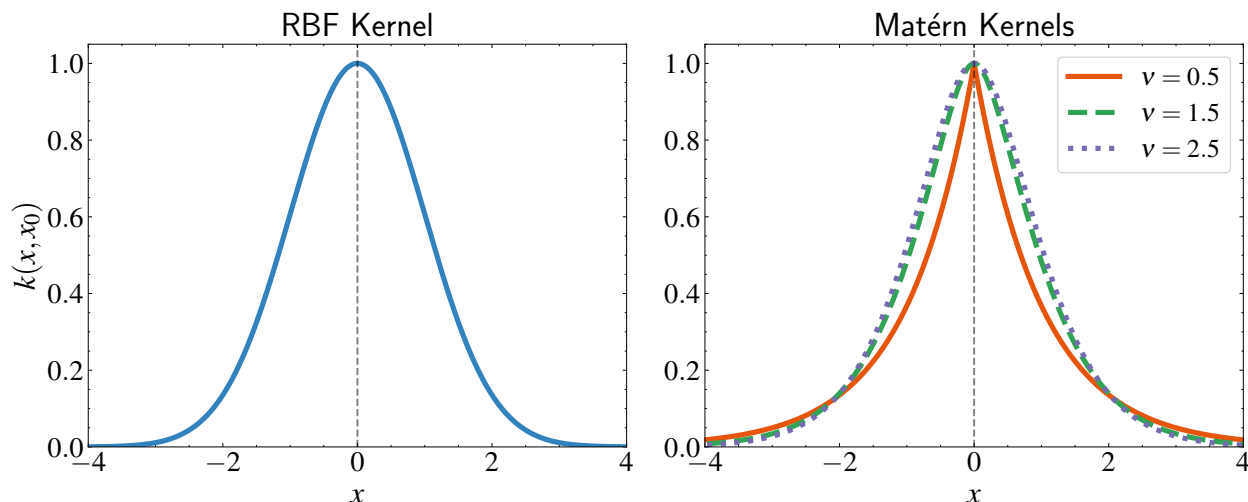1. An RBF component that handles smooth evolution of active regions

Figure 14.4: Comparison of RBF kernel (left) and Matérn kernels with different smoothness parameters (right). Both panels show kernel functions $k(x, x_0)$ centered at the reference point $x_0 = 0$. The RBF kernel exhibits infinite smoothness, decreasing exponentially with squared distance. Matérn kernels demonstrate how the smoothness parameter ν controls function behavior: $\nu = 0.5$ (red) produces continuous but not differentiable functions, $\nu = 1.5$ (green) yields once-differentiable functions, and $\nu = 2.5$ (purple) produces twice-differentiable functions. As ν increases, the Matérn kernel converges to the RBF kernel. This flexibility in controlling function smoothness makes these kernels valuable for modeling astronomical phenomena where different physical processes may exhibit varying degrees of smoothness.

2. A constant component that models baseline brightness level

3. A periodic component that captures rotational modulation

Similarly, we can multiply kernels (the product of valid kernels is valid) or compose them in other ways to create sophisticated models tailored to specific physical processes.

When choosing kernels for astronomical data, we should consider both physical considerations and empirical performance. Physical considerations include the characteristic timescales of the phenomena we are studying, the expected smoothness of the underlying processes, and any known periodicities or trends. For stellar variability, we might expect smooth changes on certain timescales combined with periodic modulation. For quasar variability, we might expect a more irregular, stochastic process with correlations that decay over characteristic timescales.

The practical value of working in these feature spaces without actually computing the features cannot be overstated. Even with infinite-dimensional feature spaces, we only ever need to compute pairwise similarities between our finite set of data points. This makes kernel

methods, and by extension Gaussian Processes, computationally tractable while offering considerable modeling flexibility.

Having established both the intuitive foundation of kernels and the mathematical conditions that make them valid, we can now proceed to develop the full Bayesian framework that transforms kernelized linear regression into Gaussian Processes.

14.4   Kernelizing Bayesian Linear Regression

In our exploration of kernelizing linear regression, we showed how to transform maximum likelihood estimation into a kernel-based framework. This transformation allowed us to work with potentially infinite-dimensional feature spaces while maintaining computational tractability. However, we have only addressed half of the statistical modeling challenge: obtaining point estimates of our predictions.

For astronomical applications, point estimates alone are insufficient. We need rigorous uncertainty quantification to make reliable scientific inferences. When we measure stellar brightness, detect exoplanet transits, or analyze galaxy spectra, understanding the uncertainty in our predictions is as important as the predictions themselves. We need to know not just what we expect to observe, but how confident we should be in that expectation and how this confidence varies across different regions of our input space.

The maximum likelihood approach we kernelized provides no direct mechanism for uncertainty quantification. This limitation motivates our transition to the full Bayesian treatment of kernel methods. In our earlier chapters on Bayesian linear regression, we saw how placing priors over parameters naturally leads to posterior distributions that quantify uncertainty in our predictions. The question now becomes: how can we kernelize this Bayesian framework to obtain the same rigorous uncertainty quantification while working implicitly with complex feature spaces?

Recall from our previous chapters on Bayesian linear regression that with a Gaussian prior $p(\mathbf{w}) = \mathcal{N}(\mathbf{w}|\mathbf{m}_0, \mathbf{S}_0)$ and likelihood $p(\mathbf{t}|\mathbf{X}, \mathbf{w}) = \mathcal{N}(\mathbf{t}|\mathbf{\Phi}\mathbf{w}, \sigma_n^2\mathbf{I})$, the posterior

distribution over weights is:

$$p(\mathbf{w}|\mathbf{X}, \mathbf{t}) = \mathcal{N}(\mathbf{w}|\mathbf{m}_N, \mathbf{S}_N) \tag{14.33}$$

$$\mathbf{S}_N = \left(\frac{1}{\sigma_n^2} \mathbf{\Phi}^T \mathbf{\Phi} + \mathbf{S}_0^{-1} \right)^{-1} \tag{14.34}$$

$$\mathbf{m}_N = \mathbf{S}_N \left(\mathbf{S}_0^{-1} \mathbf{m}_0 + \frac{1}{\sigma_n^2} \mathbf{\Phi}^T \mathbf{t} \right) \tag{14.35}$$

For simplicity, we will use a zero-mean prior $\mathbf{m}_0 = \mathbf{0}$. This is a common choice that reflects our assumption that, before seeing any data, we have no reason to believe the function is biased in any particular direction. While this derivation through the kernel trick involves some mathematical manipulation, many of these concepts will be more intuitively understood when we later introduce the function space view of Gaussian Processes.

With this choice, the posterior mean simplifies to:

$$\mathbf{m}_N = \mathbf{S}_N \frac{1}{\sigma_n^2} \mathbf{\Phi}^T \mathbf{t} \tag{14.36}$$

For a new input x_*, the predictive distribution is:

$$p(f_*|x_*, \mathcal{D}) = \mathcal{N}(f_*|\phi(x_*)^T \mathbf{m}_N, \phi(x_*)^T \mathbf{S}_N \phi(x_*)) \tag{14.37}$$

Our goal is to express this predictive distribution in terms of kernel functions rather than explicit feature mappings. The approach we will take should be reminiscent of our earlier kernelization of the MLE case, but now we need to kernelize both the mean and the variance of our predictions.

Kernelizing the Predictive Mean   Let us start with the predictive mean:

$$\phi(x_*)^T \mathbf{m}_N = \phi(x_*)^T \mathbf{S}_N \frac{1}{\sigma_n^2} \mathbf{\Phi}^T \mathbf{t} \tag{14.38}$$

To kernelize this expression, we need to find a form for $\mathbf{S}_N$ that involves kernel ma-

trices. Similar to the MLE case, we will apply the Woodbury matrix identity:

$$\mathbf{S}_N = \left(\frac{1}{\sigma_n^2} \mathbf{\Phi}^T \mathbf{\Phi} + \mathbf{S}_0^{-1} \right)^{-1} \tag{14.39}$$

$$= \mathbf{S}_0 - \mathbf{S}_0 \mathbf{\Phi}^T (\sigma_n^2 \mathbf{I}_N + \mathbf{\Phi} \mathbf{S}_0 \mathbf{\Phi}^T)^{-1} \mathbf{\Phi} \mathbf{S}_0 \tag{14.40}$$

Substituting this into our expression for the predictive mean:

$$\phi(x_*)^T \mathbf{m}_N = \phi(x_*)^T \left[\mathbf{S}_0 - \mathbf{S}_0 \mathbf{\Phi}^T (\sigma_n^2 \mathbf{I}_N + \mathbf{\Phi} \mathbf{S}_0 \mathbf{\Phi}^T)^{-1} \mathbf{\Phi} \mathbf{S}_0 \right] \frac{1}{\sigma_n^2} \mathbf{\Phi}^T \mathbf{t} \tag{14.41}$$

$$= \frac{1}{\sigma_n^2} \phi(x_*)^T \mathbf{S}_0 \mathbf{\Phi}^T \mathbf{t} - \frac{1}{\sigma_n^2} \phi(x_*)^T \mathbf{S}_0 \mathbf{\Phi}^T (\sigma_n^2 \mathbf{I}_N + \mathbf{\Phi} \mathbf{S}_0 \mathbf{\Phi}^T)^{-1} \mathbf{\Phi} \mathbf{S}_0 \mathbf{\Phi}^T \mathbf{t} \tag{14.42}$$

Let us define our kernel functions in terms of the prior covariance:

$$k(x, x') = \phi(x)^T \mathbf{S}_0 \phi(x') \tag{14.43}$$

Using this definition, we can express the kernel matrix for our training data:

$$[\mathbf{K}]_{ij} = k(x_i, x_j) = \phi(x_i)^T \mathbf{S}_0 \phi(x_j) \tag{14.44}$$

Which means $\mathbf{K} = \mathbf{\Phi} \mathbf{S}_0 \mathbf{\Phi}^T$. We can also define the vector of kernel evaluations between the test point and all training points:

$$\mathbf{k}_* = [k(x_1, x_*), k(x_2, x_*), \ldots, k(x_N, x_*)]^T = \mathbf{\Phi} \mathbf{S}_0 \phi(x_*) \tag{14.45}$$

With these definitions, we can rewrite our expression for the predictive mean:

$$\phi(x_*)^T \mathbf{m}_N = \frac{1}{\sigma_n^2} \phi(x_*)^T \mathbf{S}_0 \mathbf{\Phi}^T \mathbf{t} - \frac{1}{\sigma_n^2} \phi(x_*)^T \mathbf{S}_0 \mathbf{\Phi}^T (\sigma_n^2 \mathbf{I}_N + \mathbf{K})^{-1} \mathbf{K} \mathbf{t} \tag{14.46}$$

This looks complex, but we can simplify it using a matrix identity:

$$(\sigma_n^2 \mathbf{I}_N + \mathbf{K})^{-1} \mathbf{K} = \mathbf{I}_N - \sigma_n^2 (\sigma_n^2 \mathbf{I}_N + \mathbf{K})^{-1} \tag{14.47}$$

Let us prove this identity explicitly. We start by multiplying both sides by $(\sigma_n^2 \mathbf{I}_N + \mathbf{K})$

from the left:

$$(\sigma_n^2 \mathbf{I}_N + \mathbf{K})(\sigma_n^2 \mathbf{I}_N + \mathbf{K})^{-1} \mathbf{K} = (\sigma_n^2 \mathbf{I}_N + \mathbf{K})[\mathbf{I}_N - \sigma_n^2 (\sigma_n^2 \mathbf{I}_N + \mathbf{K})^{-1}] \tag{14.48}$$

$$\mathbf{K} = (\sigma_n^2 \mathbf{I}_N + \mathbf{K}) - \sigma_n^2 (\sigma_n^2 \mathbf{I}_N + \mathbf{K})(\sigma_n^2 \mathbf{I}_N + \mathbf{K})^{-1} \tag{14.49}$$

$$\mathbf{K} = \sigma_n^2 \mathbf{I}_N + \mathbf{K} - \sigma_n^2 \mathbf{I}_N \tag{14.50}$$

$$\mathbf{K} = \mathbf{K} \tag{14.51}$$

Using this identity in our expression:

$$\phi(x_*)^T \mathbf{m}_N = \frac{1}{\sigma_n^2} \phi(x_*)^T \mathbf{S}_0 \boldsymbol{\Phi}^T \mathbf{t} - \frac{1}{\sigma_n^2} \phi(x_*)^T \mathbf{S}_0 \boldsymbol{\Phi}^T [\mathbf{I}_N - \sigma_n^2 (\sigma_n^2 \mathbf{I}_N + \mathbf{K})^{-1}] \mathbf{t} \tag{14.52}$$

$$= \frac{1}{\sigma_n^2} \phi(x_*)^T \mathbf{S}_0 \boldsymbol{\Phi}^T \mathbf{t} - \frac{1}{\sigma_n^2} \phi(x_*)^T \mathbf{S}_0 \boldsymbol{\Phi}^T \mathbf{t} + \phi(x_*)^T \mathbf{S}_0 \boldsymbol{\Phi}^T (\sigma_n^2 \mathbf{I}_N + \mathbf{K})^{-1} \mathbf{t} \tag{14.53}$$

$$= \phi(x_*)^T \mathbf{S}_0 \boldsymbol{\Phi}^T (\sigma_n^2 \mathbf{I}_N + \mathbf{K})^{-1} \mathbf{t} \tag{14.54}$$

$$= \mathbf{k}_*^T (\sigma_n^2 \mathbf{I}_N + \mathbf{K})^{-1} \mathbf{t} \tag{14.55}$$

Note that these kernels are very similar to those in the MLE case, with one key difference: they incorporate the prior covariance $\mathbf{S}_0$ over weights. The kernel definition $k(x, x') = \phi(x)^T \mathbf{S}_0 \phi(x')$ weights the feature inner products according to our prior beliefs about parameter importance. If $\mathbf{S}_0$ has larger values for certain dimensions of the weight space, we expect those corresponding features to potentially have larger coefficients, giving them more influence in determining function similarity. When $\mathbf{S}_0 = \mathbf{I}$ (isotropic prior), this reduces to the standard inner product $\phi(x)^T \phi(x')$ from the MLE case.

Kernelizing the Predictive Variance While the mean prediction formula bears resemblance to the MLE case, a key advantage of the Bayesian approach is that we can also kernelize the predictive variance. This allows us to quantify uncertainty in our predictions, which is crucial for scientific applications. Let us tackle the predictive variance for the latent function:

$$\phi(x_*)^T \mathbf{S}_N \phi(x_*) = \phi(x_*)^T \left(\frac{1}{\sigma_n^2} \boldsymbol{\Phi}^T \boldsymbol{\Phi} + \mathbf{S}_0^{-1} \right)^{-1} \phi(x_*) \tag{14.56}$$

Using our expression for $\mathbf{S}_N$ derived earlier:

$$\mathbf{S}_N = \mathbf{S}_0 - \mathbf{S}_0 \boldsymbol{\Phi}^T (\sigma_n^2 \mathbf{I}_N + \boldsymbol{\Phi} \mathbf{S}_0 \boldsymbol{\Phi}^T)^{-1} \boldsymbol{\Phi} \mathbf{S}_0 \tag{14.57}$$
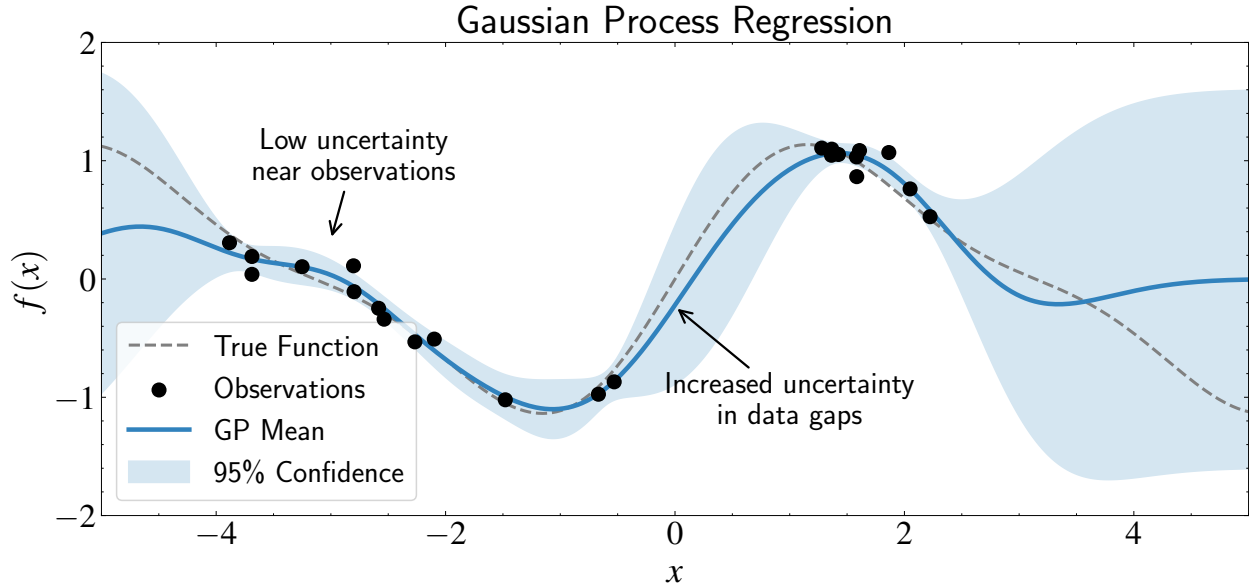
Figure 14.5: Gaussian Process regression demonstrating the key features of the full Bayesian posterior. The figure shows observations (black points), the GP mean prediction (blue line), and 95% confidence intervals (light blue region), along with the true underlying function (dashed gray). Note how the posterior uncertainty varies with data density: it is minimal near observed points and grows in regions where data is sparse or absent. This behavior emerges naturally from the mathematics of GP regression through the posterior variance $\sigma_f^2 = k(x_*, x_*) - \mathbf{k}_*^T (\mathbf{K} + \sigma_n^2 \mathbf{I})^{-1} \mathbf{k}_*$, which decreases when the test point x_* is similar to many training points. This automatic uncertainty quantification makes GPs particularly valuable for astronomical applications with irregular sampling and data gaps, providing principled uncertainty estimates that prevent overconfident conclusions in sparsely observed regions.

Substituting this into our variance expression:

$$\phi(x_*)^T \mathbf{S}_N \phi(x_*) = \phi(x_*)^T \left[\mathbf{S}_0 - \mathbf{S}_0 \boldsymbol{\Phi}^T (\sigma_n^2 \mathbf{I}_N + \boldsymbol{\Phi} \mathbf{S}_0 \boldsymbol{\Phi}^T)^{-1} \boldsymbol{\Phi} \mathbf{S}_0 \right] \phi(x_*) \tag{14.58}$$

$$= \phi(x_*)^T \mathbf{S}_0 \phi(x_*) - \phi(x_*)^T \mathbf{S}_0 \boldsymbol{\Phi}^T (\sigma_n^2 \mathbf{I}_N + \boldsymbol{\Phi} \mathbf{S}_0 \boldsymbol{\Phi}^T)^{-1} \boldsymbol{\Phi} \mathbf{S}_0 \phi(x_*) \tag{14.59}$$

Using our kernel definitions from earlier:

$$\phi(x_*)^T \mathbf{S}_N \phi(x_*) = \phi(x_*)^T \mathbf{S}_0 \phi(x_*) - \phi(x_*)^T \mathbf{S}_0 \boldsymbol{\Phi}^T (\sigma_n^2 \mathbf{I}_N + \mathbf{K})^{-1} \boldsymbol{\Phi} \mathbf{S}_0 \phi(x_*) \tag{14.60}$$

$$= k(x_*, x_*) - \mathbf{k}_*^T (\mathbf{K} + \sigma_n^2 \mathbf{I})^{-1} \mathbf{k}_* \tag{14.61}$$

The Complete Bayesian Predictive Distribution   Having derived both the mean and variance in kernelized form, we now have a complete Bayesian predictive distribution that depends only on kernel evaluations, without requiring explicit feature representations.
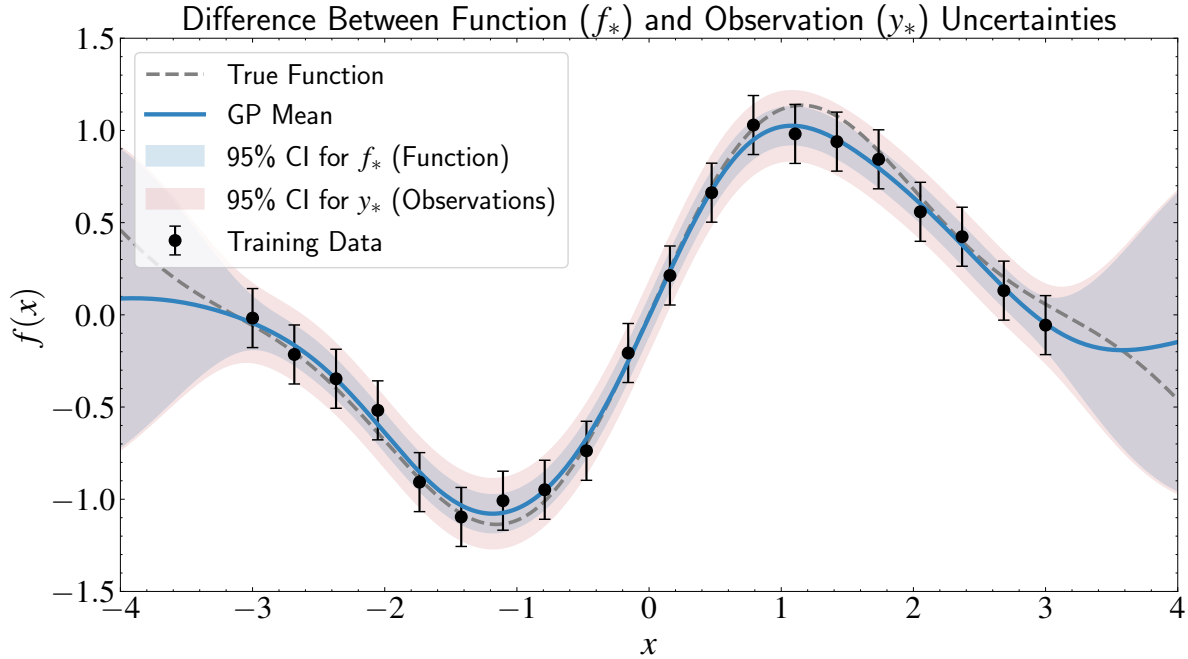
Figure 14.6: Illustration of the difference between latent function values (f_*) and observed outputs (y_*) in Gaussian Process regression. The plot shows training data with error bars representing observation noise (black points), the true function (dashed gray), and GP mean prediction (blue). Two types of uncertainty bands are displayed: the inner blue band shows the 95% confidence interval for the latent function f_* (uncertainty in the underlying pattern), while the outer red band shows the 95% confidence interval for noisy observations y_* (includes both function uncertainty and observation noise). The mathematical relationship between these uncertainties is straightforward: $\mathrm{Var}(y_*) = \mathrm{Var}(f_*) + \sigma_n^2$, where σ_n^2 is the noise variance. When analyzing phenomena like stellar variability or quasar light curves, astronomers are often interested in the latent function f_* to understand the underlying physical processes, while accounting for the total uncertainty including noise when making predictions about future observations y_*.

For the latent function value (without noise):

$$p(f_*|x_*, \mathcal{D}) = \mathcal{N}(f_*|\mu_f, \sigma_f^2) \tag{14.62}$$

where:

$$\mu_f = \mathbf{k}_*^T(\mathbf{K} + \sigma_n^2\mathbf{I})^{-1}\mathbf{t} \tag{14.63}$$

$$\sigma_f^2 = k(x_*, x_*) - \mathbf{k}_*^T(\mathbf{K} + \sigma_n^2\mathbf{I})^{-1}\mathbf{k}_* \tag{14.64}$$

For the observed output (including noise):

$$p(y_*|x_*, \mathcal{D}) = \mathcal{N}(y_*|\mu_f, \sigma_f^2 + \sigma_n^2) \tag{14.65}$$

The distinction between f_* and y_* is important in practice. When we want to understand the underlying pattern in our data, we examine $p(f_*|x_*, \mathcal{D})$. When we want to predict future observations with their associated noise, we use $p(y_*|x_*, \mathcal{D})$. In astronomical applications, this distinction allows us to separate the intrinsic variability of celestial objects from measurement uncertainties.

Let us develop a deeper understanding of each component in these expressions:

- $k(x_*, x_*)$ represents our prior uncertainty about the function value at the test point x_*. This term captures how much variability we expect in the function before seeing any data. For most common kernels (like the RBF), this term equals a constant value for all inputs, reflecting our prior belief about the overall scale of function variations.

- $\mathbf{k}_*^T(\mathbf{K}+\sigma_n^2\mathbf{I})^{-1}\mathbf{k}_*$ quantifies how much uncertainty is reduced by our observations. This term is always non-negative, meaning observations can only decrease our uncertainty. The reduction is greater when the test point x_* is more similar to the training points (i.e., when $\mathbf{k}_*$ has larger values).

- The mean prediction $\mu_f = \mathbf{k}_*^T(\mathbf{K} + \sigma_n^2\mathbf{I})^{-1}\mathbf{t}$ is a weighted sum of the training outputs $\mathbf{t}$. The weight for each training point depends on its similarity to the test point, but crucially, these weights are also influenced by the correlations among training points. If two training points are very similar, they effectively provide less independent information than two dissimilar points would.

- The term $(\mathbf{K} + \sigma_n^2\mathbf{I})^{-1}$ serves dual purposes: it accounts for noise in the observations (through σ_n^2) and it handles redundancy in the training data (through the correlations in $\mathbf{K}$). As noise increases, the influence of the data on our predictions decreases.

- The combined effect produces intuitive behavior: in regions with dense, reliable data, our predictions are confident and closely follow the observations; in regions with sparse or noisy data, our predictions revert toward the prior mean (zero in our case) with increasing uncertainty.

This formulation creates a characteristic pattern in GP uncertainty estimates that

has important implications for scientific applications. In regions densely populated with training data, our uncertainty (given by $\sigma_f^2 = k(x_*, x_*) - \mathbf{k}_*^T(\mathbf{K} + \sigma_n^2\mathbf{I})^{-1}\mathbf{k}_*$) is small. This occurs because when x_* is close to many training points, the vector $\mathbf{k}_*$ contains large values, making the subtraction term $\mathbf{k}_*^T(\mathbf{K} + \sigma_n^2\mathbf{I})^{-1}\mathbf{k}_*$ approach $k(x_*, x_*)$, thus reducing σ_f^2.

As we move away from training data, uncertainty grows smoothly because the elements of $\mathbf{k}_*$ decrease (since kernel functions typically decrease with distance). This makes the subtraction term $\mathbf{k}_*^T(\mathbf{K} + \sigma_n^2\mathbf{I})^{-1}\mathbf{k}_*$ smaller, leaving σ_f^2 closer to the prior variance $k(x_*, x_*)$. The model automatically adapts to varying data density through the matrix $(\mathbf{K} + \sigma_n^2\mathbf{I})^{-1}$, which encodes the information content of the entire dataset.

Unlike parametric models that might overfit sparse data regions, GPs maintain appropriate uncertainty, preventing astronomers from drawing overly confident conclusions from limited data. At the same time, GPs can identify meaningful patterns and correlations at different timescales through the kernel function.

14.5 Gaussian Processes vs. Bayesian Linear Regression

Having explored Gaussian Processes through the kernel trick, we can now examine how GPs relate to the Bayesian linear regression models from earlier chapters. This comparison reveals these approaches as complementary views of the same underlying principles rather than entirely separate techniques.

Both Gaussian Processes and Bayesian linear regression represent Bayesian approaches to function approximation. In Bayesian linear regression, we define a parametric model with fixed basis functions and place a prior distribution over the weights. In Gaussian Processes, we place a prior directly over the space of functions. Despite this apparent difference, we have shown these approaches are mathematically equivalent under certain conditions—specifically, when the GP kernel corresponds to the inner product of feature vectors.

The relationship becomes clear when we recall that a kernel function can be expressed as an inner product in some feature space: $k(x, x') = \phi(x)^T\phi(x')$. For many commonly used kernels, this feature space is infinite-dimensional. The RBF kernel, for example, corresponds to an infinite-dimensional feature space of radial basis functions with all possible length scales.

In Bayesian linear regression, we work explicitly with features by manually designing basis functions $\phi_1(x), \phi_2(x), \ldots, \phi_m(x)$ to transform our inputs. The quality of our model depends critically on our choice of these features—if they fail to capture the underlying patterns, the model will perform poorly regardless of weight optimization. This approach provides direct control and interpretability, as each feature has a corresponding weight that quantifies its importance.

Gaussian Processes operate directly in function space. We define a kernel function that encodes our beliefs about function properties (smoothness, periodicity, etc.) without specifying explicit features. The GP framework automatically handles the mapping from inputs to outputs, adapting its complexity to the data. This offers greater flexibility since we are not restricted to predefined features, though it may provide less direct interpretability regarding which input dimensions are most important.

A critical practical difference lies in computational scaling. In Bayesian linear regression, the computational complexity is dominated by operations involving the feature space dimensionality m. Computing the posterior over weights requires inverting an $m \times m$ matrix with $\mathcal{O}(m^3)$ complexity. Once computed, making predictions requires only $\mathcal{O}(m)$ operations per prediction.

In Gaussian Processes, complexity is dominated by the number of training points N. Computing the predictive distribution requires inverting an $N \times N$ matrix with $\mathcal{O}(N^3)$ complexity. Making a single prediction then requires $\mathcal{O}(N)$ operations for the mean and $\mathcal{O}(N^2)$ for the variance. Bayesian linear regression is generally more computationally efficient than GPs, though GPs offer superior modeling flexibility and automatic complexity adaptation.

The computational cost of GPs comes with an important advantage: automatic complexity adaptation. Model complexity adapts automatically to the data through kernel hyperparameters, with longer length scales leading to smoother functions. This adaptivity makes GPs particularly well-suited to problems where the appropriate complexity is difficult to determine a priori, as often occurs in astronomical data analysis where underlying physical processes may be complex and multiscale.

Bayesian linear regression tends to be preferable when we have strong prior knowledge about the functional form that we can encode directly through feature choice. It excels when interpretability of individual feature weights is important for scientific understanding, as the weights provide direct insight into the importance of different model components. From a practical perspective, Bayesian linear regression is often better for very large datasets where

the $\mathcal{O}(N^3)$ computational complexity of GPs would be prohibitive, and for problems with high input dimensionality that can be effectively modeled using carefully chosen features.

Gaussian Processes excel when the functional form is uncertain or complex. They are particularly valuable when principled uncertainty quantification is critical. GPs work best for datasets that are moderate in size but potentially complex in structure, especially when modeling functions with varying characteristics across the input space—light curves exhibiting multiple timescales of variability, for example. However, they work best when input dimensionality is relatively low, keeping kernel evaluations computationally tractable.

Many modern GP packages implement approximations achieving computational scaling much better than $\mathcal{O}(N^3)$, though usually with trade-offs in exactness or flexibility. Packages like GPyTorch offer specialized implementations that can handle much larger datasets than traditional GP implementations, making them increasingly practical for astronomical applications.

14.6   The Function-Space Perspective

Having explored Gaussian Processes through kernelizing Bayesian linear regression, we now turn to an alternative mathematical perspective: the function-space view. Rather than starting with a parametric model and applying the kernel trick, this approach directly defines a probability distribution over functions. While initially more abstract, it offers remarkable clarity and leads to the same mathematical results with less algebraic manipulation.

Connection to Stochastic Processes   This perspective connects directly to the stochastic processes we encountered in our MCMC chapter. Recall that a stochastic process is a collection of random variables indexed by time or space. In MCMC, we used Markov chains—a type of stochastic process where each state depends only on the previous state. A Gaussian process is another type of stochastic process, but with different properties that make it useful for regression tasks.

This connection is more than terminological. Both MCMC and GPs deal with sequences of random variables, but they serve different purposes in our statistical toolkit. MCMC uses a stochastic process (the Markov chain) as a computational tool to sample from complex distributions, while GPs use a stochastic process as a modeling framework to represent unknown functions. This duality highlights the versatility of stochastic processes

in statistical inference—they can be both computational tools and modeling frameworks.

From Finite to Infinite Dimensions To understand stochastic processes more deeply, let us revisit random variables. In earlier chapters, we dealt with finite-dimensional random variables—vectors like $\mathbf{x} \in \mathbb{R}^d$ with probability distributions $p(\mathbf{x})$. Each element x_i is a single random variable indexed by integers: $x_1, x_2, \ldots, x_d$.

A stochastic process extends this indexing to potentially uncountable sets. Instead of integers, we index random variables by elements of some set $\mathcal{T}$, which might represent time points, spatial locations, or inputs to a function. For each $t \in \mathcal{T}$, we have a random variable X_t. The entire collection $\{X_t : t \in \mathcal{T}\}$ forms a stochastic process.

The indexing differs between our two contexts:

- In MCMC, the index is typically the iteration number or "time step" in our sampling algorithm. We have a sequence $\{X_1, X_2, X_3, ...\}$ where X_t represents the state of our Markov chain at iteration t. The Markov property tells us that $P(X_{t+1}|X_1, X_2, ..., X_t) = P(X_{t+1}|X_t)$—the next state depends only on the current state.

- In Gaussian processes, the index is the input to our function. If we are modeling a function $f : \mathcal{X} \to \mathbb{R}$, then for each $x \in \mathcal{X}$, we have a random variable $f(x)$. The collection $\{f(x) : x \in \mathcal{X}\}$ forms our Gaussian process.

While MCMC indices are typically discrete (iteration numbers), GP indices can be continuous (like spatial coordinates or time). This allows GPs to model smooth functions over continuous domains.

When $\mathcal{T}$ is uncountable (like the real line $\mathbb{R}$), we effectively have an infinite-dimensional random variable. We never need to work with all dimensions simultaneously—just as we can consider marginal distributions of subsets of components in a finite-dimensional vector, we can examine the joint distribution of $\{X_{t_1}, X_{t_2}, \ldots, X_{t_n}\}$ for any finite subset of indices $\{t_1, t_2, \ldots, t_n\} \subset \mathcal{T}$.

This makes stochastic processes tractable: while the full process is infinite-dimensional, any actual computation involves only finite-dimensional marginals. In time series analysis, for instance, we observe the process at discrete time points and make inferences based on these finite observations.

Defining Gaussian Processes   A Gaussian process is a stochastic process where any finite collection of random variables has a joint Gaussian distribution. More formally, a Gaussian process is a collection of random variables $\{f(x) : x \in \mathcal{X}\}$, any finite subset of which follows a multivariate Gaussian distribution.

This definition extends the familiar multivariate Gaussian distribution to infinite dimensions. In our previous work with multivariate Gaussians, we dealt with random vectors $\mathbf{x} \in \mathbb{R}^d$ characterized by:

- A mean vector $\mu \in \mathbb{R}^d$ where $\mu_i = \mathbb{E}[x_i]$

- A covariance matrix $\mathbf{\Sigma} \in \mathbb{R}^{d \times d}$ where $\Sigma_{ij} = \mathbb{E}[(x_i - \mu_i)(x_j - \mu_j)]$

A Gaussian process follows the same principle, but extends it to functions. Instead of discrete indices $i \in \{1, 2, ..., d\}$, we have a continuous index set $x \in \mathcal{X}$. To specify a Gaussian process, we need:

- A mean function $m(x)$ that gives the expected value at each input:

$$m(x) = \mathbb{E}[f(x)] \tag{14.66}$$

- A covariance function (or kernel) $k(x, x')$ that specifies how function values at different inputs relate:

$$k(x, x') = \mathbb{E}[(f(x) - m(x))(f(x') - m(x'))] \tag{14.67}$$

We denote this as:

$$f \sim \mathcal{GP}(m, k) \tag{14.68}$$

The covariance function encodes our assumptions about the function's smoothness, connecting directly to our discussion of autocorrelation in MCMC. Recall that in MCMC, we examined how samples at different lags were correlated, which told us about the "memory" or smoothness of our Markov chain. Similarly, the covariance function in a GP tells us how function values at different inputs relate to each other.

For instance, if $k(x, x')$ decreases rapidly as $|x - x'|$ increases, we are modeling functions that can change quickly—where knowing $f(x)$ tells us little about $f(x')$ when x and x' are far apart. Conversely, if $k(x, x')$ decreases slowly with distance, we are modeling smoother functions where distant points remain correlated. This resembles how a slowly

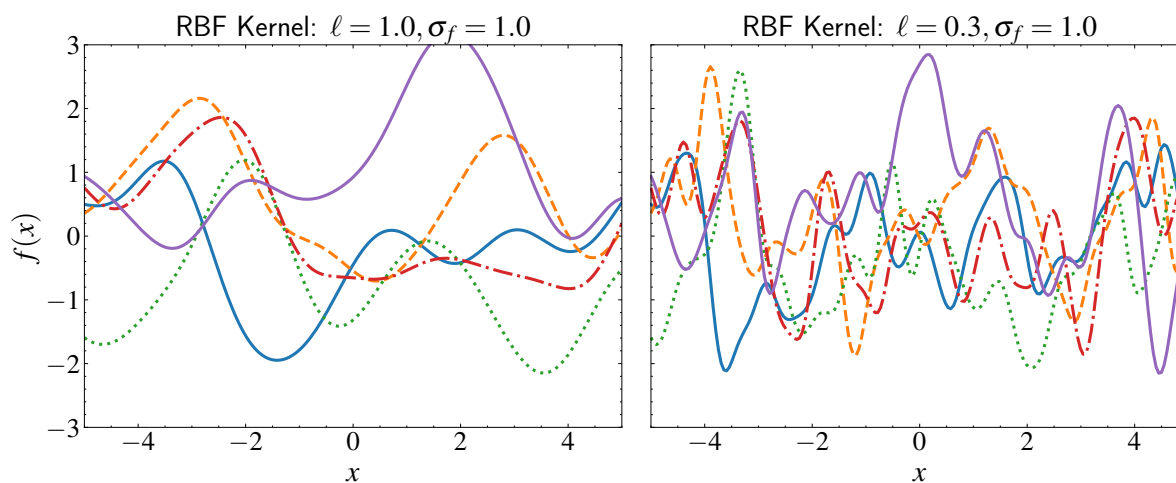decaying autocorrelation function in MCMC indicates a chain that moves slowly through the parameter space.

Figure 14.7: Visualization of function spaces defined by Gaussian Processes with different RBF kernel parameters. Each panel shows five random functions sampled from a GP prior with zero mean and a specified RBF kernel. Left: Functions sampled from a GP with longer length scale ($\ell = 1.0$) exhibit smoother behavior with gradual variations. Right: Functions sampled from a GP with shorter length scale ($\ell = 0.3$) show more rapid fluctuations and can capture finer details. Both GPs use the same amplitude parameter ($\sigma_f = 1.0$) and the same random seeds, isolating the effect of the length scale. This illustrates a key property of the function-space view of Gaussian Processes: the kernel directly determines the properties of functions in the prior distribution.

Finite-Dimensional Projections The key insight that makes Gaussian processes practical is that while the process itself is infinite-dimensional, we only ever need to evaluate it at a finite number of points for any actual computation. For any finite set of inputs $\mathbf{X} = [x_1, x_2, \ldots, x_n]^T$, the corresponding function values follow a multivariate Gaussian:

$$\mathbf{f} = [f(x_1), f(x_2), \ldots, f(x_n)]^T \sim \mathcal{N}(\mathbf{m}, \mathbf{K}) \tag{14.69}$$

where $\mathbf{m} = [m(x_1), m(x_2), \ldots, m(x_n)]^T$ and $\mathbf{K}_{ij} = k(x_i, x_j)$.

While a GP defines a distribution over an infinite-dimensional space of functions, any finite "slice" of this distribution is just a regular multivariate Gaussian. This property—that any marginal distribution of a Gaussian is also Gaussian—makes GPs computationally tractable despite their infinite-dimensional nature.

Mathematically, we can write this marginalization property as:

$$f \sim \mathcal{GP}(m, k) \implies [f(x_1), f(x_2), \ldots, f(x_n)]^T \sim \mathcal{N}(\mathbf{m}, \mathbf{K}) \tag{14.70}$$

This connects directly to astronomical examples. When modeling stellar light curves, we might have observations at a finite set of time points, but we believe there is an underlying continuous process. The GP framework allows us to evaluate this continuous process at our specific observation times through the marginalization property.

But marginalization alone is not enough for practical applications. We need to learn from data. This brings us to the second crucial property of Gaussian distributions: conditioning. Recall from earlier chapters that if a random vector $\mathbf{x} = [\mathbf{x}_A, \mathbf{x}_B]^T$ follows a multivariate Gaussian, then the conditional distribution of $\mathbf{x}_A$ given $\mathbf{x}_B$ is also Gaussian.

This conditioning property is what transforms Gaussian processes from mathematical curiosities into practical modeling tools. Through conditioning, we can update our prior beliefs about functions after observing data, obtaining posterior distributions that reflect both our initial assumptions and the evidence from observations.

14.7　Conditioning the Gaussian Process

We now face the central challenge in Gaussian process modeling: how do we learn from data? We have established that GPs define distributions over functions, and we can extract finite-dimensional marginals for computation. But how do we incorporate observations to update our beliefs about the unknown function?

This is where conditioning becomes crucial. Consider the modeling scenario: we have some noisy observations of an unknown function, and we want to predict what the function looks like at new points. In parametric models like linear regression, we solve this by fitting parameters. In Gaussian processes, we solve it by conditioning our prior distribution on the observed data.

The challenge is more subtle than it first appears. We are not simply fitting a function to data points—we are updating an entire distribution over functions. This requires us to carefully account for the relationship between our prior beliefs, the noise in our observations, and the correlations encoded by our kernel function. The beauty of the GP framework is that this complex updating process reduces to familiar multivariate Gaussian conditioning,

despite the infinite-dimensional nature of function space.

To see how this works, let us build up the conditioning process step by step, starting with the simplest case and gradually adding the complexities that arise in real applications.

The Basic Setup: From Prior to Posterior Suppose we have observed some data points and want to make predictions at new locations. In the GP framework, this means we have a prior distribution over functions, we observe some noisy function evaluations, and we want the posterior distribution over functions given these observations.

The key insight is that we can treat this as a standard multivariate Gaussian conditioning problem. Even though our GP lives in infinite dimensions, we only care about function values at a finite set of points: our training locations and our test location. By focusing on this finite subset, we can apply the conditioning formulas we already know.

To build intuition, let us first consider a simple finite case. Imagine we have a multivariate Gaussian distribution over three variables (x_1, x_2, x_3). If we observe the values of x_1 and x_2, we can use the conditioning property to determine the distribution of x_3 given these observations. This conditional distribution will also be Gaussian, with updated mean and variance that depend on the observed values and the correlations between all variables.

Gaussian processes work in exactly the same way, except that instead of three variables, we are dealing with function values at potentially many input points. Despite this higher dimensionality, whenever we make practical computations, we are always working with finite marginal distributions—precisely the property that makes GPs computationally tractable.

Setting Up the Conditioning Problem Let us now formalize this intuition. Consider a scenario where we have a collection of input-output pairs $\mathcal{D} = \{(\mathbf{x}_i, t_i)\}_{i=1}^n$, which constitute our training data. We assume that the outputs t_i are noisy observations of some underlying function $f(\mathbf{x})$, such that:

$$t_i = f(\mathbf{x}_i) + \epsilon_i \tag{14.71}$$

where $\epsilon_i \sim \mathcal{N}(0, \sigma_n^2)$ is Gaussian noise.

Our goal is to infer the function value at any arbitrary test point $\mathbf{x}_*$. That is, we want to compute $p(f(\mathbf{x}_*)|\mathcal{D})$. This is a classic Bayesian inference problem: we start with a prior over functions and update it to a posterior after observing data.

The power of Gaussian processes is that both the prior and posterior remain Gaussian, allowing for closed-form computations. To see why, we need to construct the joint distribution of all relevant function values and then apply standard Gaussian conditioning.

We begin with a prior Gaussian process over the function:

$$f \sim \mathcal{GP}(m, k) \tag{14.72}$$

For simplicity, we will use a zero-mean prior, setting $m(\mathbf{x}) = 0$, though the derivation extends straightforwardly to non-zero means.

The key step is to construct the joint distribution of the training function values $\mathbf{f} = [f(\mathbf{x}_1), \ldots, f(\mathbf{x}_n)]^T$ and the test function value $f_* = f(\mathbf{x}_*)$. By the definition of a Gaussian process, this joint distribution is multivariate Gaussian:

$$\begin{bmatrix} \mathbf{f} \\ f_* \end{bmatrix} \sim \mathcal{N}\left(\begin{bmatrix} \mathbf{0} \\ 0 \end{bmatrix}, \begin{bmatrix} \mathbf{K} & \mathbf{k}_* \\ \mathbf{k}_*^T & k_{**} \end{bmatrix} \right) \tag{14.73}$$

Here, we have used the following notation:

- $\mathbf{K}$ is the $n \times n$ covariance matrix for the training inputs, with entries $K_{ij} = k(\mathbf{x}_i, \mathbf{x}_j)$

- $\mathbf{k}_*$ is the $n \times 1$ vector of covariances between the test point and all training points, with entries $[\mathbf{k}_*]_i = k(\mathbf{x}_i, \mathbf{x}_*)$

- $k_{**} = k(\mathbf{x}_*, \mathbf{x}_*)$ is the prior variance at the test point

This joint distribution captures all the correlations between function values at different points, as encoded by our kernel function. The matrix $\mathbf{K}$ tells us how training points relate to each other, while $\mathbf{k}_*$ tells us how the test point relates to the training points.

Accounting for Observation Noise   There is one more crucial step before we can apply conditioning. We do not observe the true function values $\mathbf{f}$ directly, but rather noisy observations $\mathbf{t} = [t_1, \ldots, t_n]^T$. This distinction between the latent function and our observations is critical for realistic modeling.

Accounting for the independent Gaussian noise $\epsilon_i \sim \mathcal{N}(0, \sigma_n^2)$, we have:

$$\mathbf{t} = \mathbf{f} + \epsilon, \quad \epsilon \sim \mathcal{N}(\mathbf{0}, \sigma_n^2 \mathbf{I}) \tag{14.74}$$
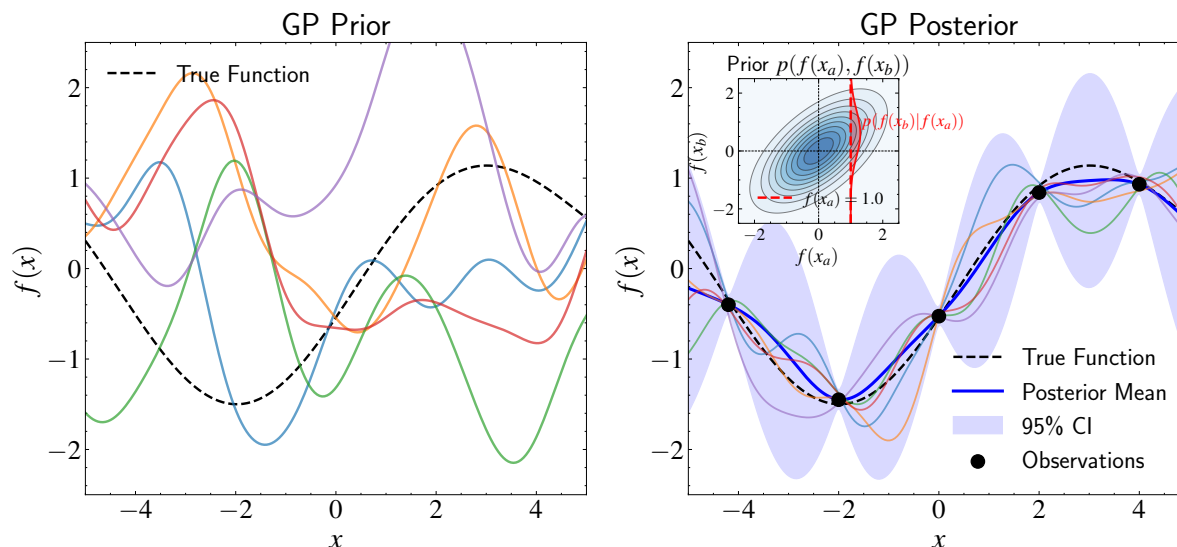
Figure 14.8: Comparison of Gaussian Process prior and posterior, illustrating the connection to conditioning multivariate Gaussians. Left panel: The GP prior shows five random functions sampled from a zero-mean GP with an RBF kernel. This is analogous to sampling from the joint distribution of a high-dimensional Gaussian before conditioning. Right panel: The GP posterior after conditioning on five observations (black points) demonstrates how observing data updates our beliefs. The posterior mean (solid blue line) and 95% confidence interval (light blue region) show reduced uncertainty near observations. The inset plot directly illustrates this conditioning process through a 2D Gaussian representing the joint prior distribution of function values at two arbitrary points (x_a, x_b). The red dashed line shows conditioning on $f(x_a) = 1.0$, while the red curve displays the resulting conditional distribution $p(f(x_b)|f(x_a))$ - a direct visualization of how conditioning one point in a GP affects correlated points based on their distance in correlation space. This reinforces that GP regression applies Gaussian conditioning principles in infinite dimensions.

This means that the joint distribution of the observations $\mathbf{t}$ and the test function value f_* is:

$$\begin{bmatrix} \mathbf{t} \\ f_* \end{bmatrix} \sim \mathcal{N}\left(\begin{bmatrix} \mathbf{0} \\ 0 \end{bmatrix}, \begin{bmatrix} \mathbf{K} + \sigma_n^2 \mathbf{I} & \mathbf{k}_* \\ \mathbf{k}_*^T & k_{**} \end{bmatrix} \right) \tag{14.75}$$

Notice how the noise appears: it adds σ_n^2 to the diagonal of the covariance matrix. This makes intuitive sense—observations at the same point become less perfectly correlated because of measurement noise, but the noise does not affect correlations between different points.

Now we can apply the standard conditioning formula for multivariate Gaussians.

Recall that if a random vector $\begin{bmatrix} \mathbf{x}_A \\ \mathbf{x}_B \end{bmatrix}$ has a joint Gaussian distribution:

$$\begin{bmatrix} \mathbf{x}_A \\ \mathbf{x}_B \end{bmatrix} \sim \mathcal{N}\left(\begin{bmatrix} \mu_A \\ \mu_B \end{bmatrix}, \begin{bmatrix} \mathbf{\Sigma}_{AA} & \mathbf{\Sigma}_{AB} \\ \mathbf{\Sigma}_{BA} & \mathbf{\Sigma}_{BB} \end{bmatrix} \right) \tag{14.76}$$

Then the conditional distribution $p(\mathbf{x}_B | \mathbf{x}_A)$ is also Gaussian:

$$p(\mathbf{x}_B | \mathbf{x}_A) = \mathcal{N}(\mu_B + \mathbf{\Sigma}_{BA} \mathbf{\Sigma}_{AA}^{-1} (\mathbf{x}_A - \mu_A), \mathbf{\Sigma}_{BB} - \mathbf{\Sigma}_{BA} \mathbf{\Sigma}_{AA}^{-1} \mathbf{\Sigma}_{AB}) \tag{14.77}$$

Applying this formula to our case, with $\mathbf{x}_A = \mathbf{t}$ and $\mathbf{x}_B = f_*$, we get:

$$p(f_* | \mathbf{t}) = \mathcal{N}(\mu_{f_*}, \sigma_{f_*}^2) \tag{14.78}$$

$$\mu_{f_*} = 0 + \mathbf{k}_*^T (\mathbf{K} + \sigma_n^2 \mathbf{I})^{-1} (\mathbf{t} - \mathbf{0}) \tag{14.79}$$

$$= \mathbf{k}_*^T (\mathbf{K} + \sigma_n^2 \mathbf{I})^{-1} \mathbf{t} \tag{14.80}$$

$$\sigma_{f_*}^2 = k_{**} - \mathbf{k}_*^T (\mathbf{K} + \sigma_n^2 \mathbf{I})^{-1} \mathbf{k}_* \tag{14.81}$$

These equations give us the posterior distribution of the function value at the test point $\mathbf{x}_*$, conditioned on our observations. Remarkably, these are exactly the same equations we derived earlier using the kernel trick! This confirms that both perspectives—the kernel trick view and the function-space view—lead to identical mathematical formulations.

Extending to General Cases Given this equivalence, one might ask: why not just start with the function-space view and avoid all the matrix manipulations of the kernel trick? The answer lies in understanding the deeper connections between these approaches. While the function-space view provides a more direct route to the final equations, the kernel trick view reveals that Gaussian processes are, at their core, generalized linear models. By working through the kernel trick derivation, we see that GPs are not a completely different approach from the linear models we have studied extensively—they are an extension where we have substituted explicit features with kernels.

This connection is conceptually important. It shows that the seemingly distinct worlds of parametric models (like linear regression) and non-parametric models (like GPs) are actually closely related. Understanding both perspectives gives us a more complete picture: the kernel-trick view connects GPs to our familiar linear models, while the function-space view

provides computational simplicity and intuitive probabilistic interpretations.

While the function-space view might not be as mechanistic as the kernel-trick approach, it offers considerable advantages when extending our model. For instance, in our derivation so far, we have made several simplifying assumptions: we used a zero-mean prior and assumed homoskedastic noise (same noise variance for all observations). Let us now explicitly derive the extensions to non-zero mean functions and heteroskedastic noise.

For a non-zero mean function $m(\mathbf{x})$, we start with a prior Gaussian process:

$$f \sim \mathcal{GP}(m, k) \tag{14.82}$$

The joint distribution of the training function values $\mathbf{f}$ and the test function value f_* is:

$$\begin{bmatrix} \mathbf{f} \\ f_* \end{bmatrix} \sim \mathcal{N}\left(\begin{bmatrix} \mathbf{m} \\ m_* \end{bmatrix}, \begin{bmatrix} \mathbf{K} & \mathbf{k}_* \\ \mathbf{k}_*^T & k_{**} \end{bmatrix} \right) \tag{14.83}$$

where $\mathbf{m} = [m(\mathbf{x}_1), \ldots, m(\mathbf{x}_n)]^T$ and $m_* = m(\mathbf{x}_*)$.

With noisy observations $\mathbf{t} = \mathbf{f} + \epsilon$, the joint distribution becomes:

$$\begin{bmatrix} \mathbf{t} \\ f_* \end{bmatrix} \sim \mathcal{N}\left(\begin{bmatrix} \mathbf{m} \\ m_* \end{bmatrix}, \begin{bmatrix} \mathbf{K} + \sigma_n^2 \mathbf{I} & \mathbf{k}_* \\ \mathbf{k}_*^T & k_{**} \end{bmatrix} \right) \tag{14.84}$$

Applying the conditioning formula for multivariate Gaussians with $\mathbf{x}_A = \mathbf{t}$, $\mathbf{x}_B = f_*$, $\mu_A = \mathbf{m}$, $\mu_B = m_*$, $\boldsymbol{\Sigma}_{AA} = \mathbf{K} + \sigma_n^2 \mathbf{I}$, $\boldsymbol{\Sigma}_{AB} = \mathbf{k}_*$, $\boldsymbol{\Sigma}_{BA} = \mathbf{k}_*^T$, and $\boldsymbol{\Sigma}_{BB} = k_{**}$, we get:

$$p(f_*|\mathbf{t}) = \mathcal{N}(\mu_{f_*}, \sigma_{f_*}^2) \tag{14.85}$$

$$\mu_{f_*} = m_* + \mathbf{k}_*^T (\mathbf{K} + \sigma_n^2 \mathbf{I})^{-1}(\mathbf{t} - \mathbf{m}) \tag{14.86}$$

$$\sigma_{f_*}^2 = k_{**} - \mathbf{k}_*^T (\mathbf{K} + \sigma_n^2 \mathbf{I})^{-1} \mathbf{k}_* \tag{14.87}$$

This formula has an intuitive interpretation: we start with our prior mean at the test point m_* and adjust it based on the deviation of observations from their prior means $(\mathbf{t} - \mathbf{m})$, weighted by the similarity (as measured by the kernel) between the test point and the training points.

For heteroskedastic noise, where each observation has its own noise variance σ_i^2, we

modify our observation model to:

$$t_i = f(\mathbf{x}_i) + \epsilon_i, \quad \epsilon_i \sim \mathcal{N}(0, \sigma_i^2) \tag{14.88}$$

This means the covariance matrix of the noise vector ϵ is now a general covariance matrix $\boldsymbol{\Sigma}_n$ rather than $\sigma_n^2 \mathbf{I}$. While we often assume independent noise (making $\boldsymbol{\Sigma}_n$ diagonal), the formulation works for any positive definite covariance structure. The joint distribution becomes:

$$\begin{bmatrix} \mathbf{t} \\ f_* \end{bmatrix} \sim \mathcal{N}\left(\begin{bmatrix} \mathbf{m} \\ m_* \end{bmatrix}, \begin{bmatrix} \mathbf{K} + \boldsymbol{\Sigma}_n & \mathbf{k}_* \\ \mathbf{k}_*^T & k_{**} \end{bmatrix} \right) \tag{14.89}$$

Applying the conditioning formula again, we get:

$$p(f_*|\mathbf{t}) = \mathcal{N}(\mu_{f_*}, \sigma_{f_*}^2) \tag{14.90}$$

$$\mu_{f_*} = m_* + \mathbf{k}_*^T (\mathbf{K} + \boldsymbol{\Sigma}_n)^{-1}(\mathbf{t} - \mathbf{m}) \tag{14.91}$$

$$\sigma_{f_*}^2 = k_{**} - \mathbf{k}_*^T (\mathbf{K} + \boldsymbol{\Sigma}_n)^{-1}\mathbf{k}_* \tag{14.92}$$

This naturally handles varying noise levels, giving less weight to noisier observations—a critical feature for astronomical applications where measurement uncertainties can vary substantially across different instruments or observing conditions.

So far, we have derived $p(f_*|\mathbf{t})$, the distribution of this underlying function. When predicting a new observation that will include noise, we need $p(y_*|\mathbf{t})$. Since $y_* = f_* + \epsilon_*$ with $\epsilon_* \sim \mathcal{N}(0, \sigma_*^2)$ independent of f_*, we have:

$$p(y_*|\mathbf{t}) = \int p(y_*|f_*)p(f_*|\mathbf{t})df_* \tag{14.93}$$

$$= \int \mathcal{N}(y_*|f_*, \sigma_*^2)\mathcal{N}(f_*|\mu_{f_*}, \sigma_{f_*}^2)df_* \tag{14.94}$$

This is the convolution of two Gaussians, which results in another Gaussian:

$$p(y_*|\mathbf{t}) = \mathcal{N}(y_*|\mu_{f_*}, \sigma_{f_*}^2 + \sigma_*^2) \tag{14.95}$$

The mean remains the same, but the variance increases to account for the additional observation noise.

This distinction is crucial in practice: we use the distribution of f_* when interested in

the underlying physical process (e.g., the intrinsic variability of a star) and the distribution of y_* when predicting future observations with their associated measurement uncertainties (e.g., forecasting what a telescope will actually measure).

Through either derivation approach, we arrive at these predictive equations:

$$\mu_{f_*} = m_* + \mathbf{k}_*^T (\mathbf{K} + \sigma_n^2 \mathbf{I})^{-1} (\mathbf{t} - \mathbf{m}) \tag{14.96}$$

$$\sigma_{f_*}^2 = k_{**} - \mathbf{k}_*^T (\mathbf{K} + \sigma_n^2 \mathbf{I})^{-1} \mathbf{k}_* \tag{14.97}$$

The function-space view provides several insights not apparent from the kernel trick derivation. Most importantly, it shows that Gaussian Process regression emerges naturally from applying standard Gaussian conditioning to infinite-dimensional distributions. The complex matrix manipulations required in the kernel trick become simple applications of familiar conditioning formulas when we work directly in function space.

Additionally, the function-space perspective makes extensions like non-zero means and heteroskedastic noise straightforward—they follow immediately from the conditioning formula without requiring new matrix identities. This view also makes clear why GPs provide such natural uncertainty quantification: the posterior variance automatically reflects both our prior uncertainty and the information gained from observations, with no additional modeling required.

By understanding both the kernel trick and function-space perspectives, we gain a complete view of Gaussian processes: they are both generalized linear models (connecting to our familiar regression framework) and stochastic processes (offering natural probabilistic interpretations). This dual understanding equips us to apply GPs effectively across a range of astronomical problems, from modeling stellar variability to characterizing exoplanet transits, with principled uncertainty quantification at every step.

14.8   Practical Implementation of Gaussian Processes

Having developed the theoretical foundations of Gaussian Processes through both the kernel trick and function-space perspectives, we now face a crucial transition: how do we actually implement these methods for real-world problems? While the mathematics of GPs is elegant, the practical implementation requires careful attention to computational efficiency and numerical stability.

The challenge becomes apparent when we examine our predictive formulas. We have derived beautiful closed-form expressions, but they all depend on computing terms like $(\mathbf{K} + \sigma_n^2\mathbf{I})^{-1}$. For a dataset with N observations, this requires inverting an $N \times N$ matrix—an operation that scales as $\mathcal{O}(N^3)$ and quickly becomes prohibitive for large datasets.

We need computational approaches that maintain the mathematical rigor of our derivations while making the calculations tractable. This is where careful algorithm design becomes crucial for practical GP implementation.

The Computational Challenge   At the core of Gaussian Process implementation is the predictive distribution formula:

$$p(f_*|\mathbf{x}_*, \mathbf{X}, \mathbf{t}) = \mathcal{N}(m_*, \sigma_*^2) \tag{14.98}$$

with mean and variance given by:

$$m_* = m(\mathbf{x}_*) + \mathbf{k}_*^T(\mathbf{K} + \boldsymbol{\Sigma}_n)^{-1}(\mathbf{t} - \mathbf{m}) \tag{14.99}$$

$$\sigma_*^2 = k(\mathbf{x}_*, \mathbf{x}_*) - \mathbf{k}_*^T(\mathbf{K} + \boldsymbol{\Sigma}_n)^{-1}\mathbf{k}_* \tag{14.100}$$

where $\mathbf{t}$ represents our observed target values, $\mathbf{m} = [m(\mathbf{x}_1), \ldots, m(\mathbf{x}_N)]^T$ is the vector of prior mean values, and $\boldsymbol{\Sigma}_n$ is the matrix of observation noise covariances.

The bottleneck is clear: both the mean and variance calculations require the inverse matrix $(\mathbf{K} + \boldsymbol{\Sigma}_n)^{-1}$. For a dataset with N observations, this is an $N \times N$ matrix, and direct inversion requires $\mathcal{O}(N^3)$ operations. In astronomy, where we often work with thousands of data points, this computation can become prohibitively expensive.

Moreover, direct matrix inversion is numerically unstable. When the kernel matrix is poorly conditioned—which can happen when data points are very close together or when the kernel parameters are poorly chosen—small numerical errors can lead to large errors in the final predictions. We need a more robust approach.

The Cholesky Decomposition Solution   Fortunately, we can improve both efficiency and numerical stability using the Cholesky decomposition. This technique is particularly appropriate for our problem because $\mathbf{K} + \boldsymbol{\Sigma}_n$ has a special structure: it is symmetric positive definite. This property is guaranteed by the definition of valid kernels (which ensure $\mathbf{K}$ is positive semidefinite) and the positive definiteness of the noise covariance matrix $\boldsymbol{\Sigma}_n$.

The key insight is that any symmetric positive definite matrix can be decomposed as:

$$\mathbf{K} + \mathbf{\Sigma}_n = \mathbf{L}\mathbf{L}^T \tag{14.101}$$

where $\mathbf{L}$ is a lower triangular matrix called the Cholesky factor. This decomposition offers three key advantages:

1. It requires only $N^3/3$ operations, compared to N^3 for general matrix inversion

2. It provides greater numerical stability, especially for ill-conditioned matrices

3. It enables efficient computation of both predictive mean and variance

While we are still working with $\mathcal{O}(N^3)$ complexity, reducing computation by a factor of three can transform an hour-long calculation into a twenty-minute one—a meaningful improvement during exploratory data analysis. More importantly, the numerical stability improvements can mean the difference between reliable results and numerical garbage.

To understand why the Cholesky decomposition is more stable, consider what happens during direct matrix inversion. The algorithm must compute many divisions by potentially small numbers, each introducing round-off error that can accumulate catastrophically. The Cholesky decomposition avoids this by working with the more stable triangular structure, where operations proceed in a controlled sequence that limits error propagation.

Efficient Implementation Using Cholesky Decomposition   Let us see how we can use the Cholesky factor $\mathbf{L}$ to efficiently compute predictions without explicitly forming the inverse matrix. The key insight is that instead of computing $(\mathbf{K}+\mathbf{\Sigma}_n)^{-1}$ and then multiplying it by vectors, we can solve triangular systems of equations.

For the predictive mean, we need to compute:

$$m_* = m(\mathbf{x}_*) + \mathbf{k}_*^T(\mathbf{K} + \mathbf{\Sigma}_n)^{-1}(\mathbf{t} - \mathbf{m}) \tag{14.102}$$

Instead of directly computing the inverse, we define $\boldsymbol{\alpha} = (\mathbf{K} + \mathbf{\Sigma}_n)^{-1}(\mathbf{t} - \mathbf{m})$ and solve for it using a two-step process. Since $\mathbf{K} + \mathbf{\Sigma}_n = \mathbf{L}\mathbf{L}^T$, we have:

$$\mathbf{L}\mathbf{L}^T\boldsymbol{\alpha} = \mathbf{t} - \mathbf{m} \tag{14.103}$$

We solve this in two stages:

$$\mathbf{L}\mathbf{v} = \mathbf{t} - \mathbf{m} \quad \text{(solve for } \mathbf{v} \text{ using forward substitution)} \tag{14.104}$$

$$\mathbf{L}^T\boldsymbol{\alpha} = \mathbf{v} \quad \text{(solve for } \boldsymbol{\alpha} \text{ using backward substitution)} \tag{14.105}$$

Forward substitution solves a lower triangular system by working from top to bottom. For a system $\mathbf{L}\mathbf{v} = \mathbf{b}$:

$$v_1 = b_1/L_{11} \tag{14.106}$$

$$v_i = \frac{1}{L_{ii}} \left(b_i - \sum_{j=1}^{i-1} L_{ij} v_j \right) \quad \text{for } i = 2, 3, \ldots, N \tag{14.107}$$

Backward substitution solves an upper triangular system by working from bottom to top. For a system $\mathbf{L}^T\boldsymbol{\alpha} = \mathbf{v}$:

$$\alpha_N = v_N/L_{NN} \tag{14.108}$$

$$\alpha_i = \frac{1}{L_{ii}} \left(v_i - \sum_{j=i+1}^{N} L_{ji} \alpha_j \right) \quad \text{for } i = N-1, N-2, \ldots, 1 \tag{14.109}$$

Both operations are $\mathcal{O}(N^2)$, much faster than matrix inversion. Once we have $\boldsymbol{\alpha}$, the predictive mean is simply:

$$m_* = m(\mathbf{x}_*) + \mathbf{k}_*^T \boldsymbol{\alpha} \tag{14.110}$$

For the predictive variance, we follow a similar approach. We need:

$$\sigma_*^2 = k(\mathbf{x}_*, \mathbf{x}_*) - \mathbf{k}_*^T (\mathbf{K} + \boldsymbol{\Sigma}_n)^{-1} \mathbf{k}_* \tag{14.111}$$

We first solve $\mathbf{L}\mathbf{v} = \mathbf{k}_*$ for $\mathbf{v}$ using forward substitution, then compute:

$$\sigma_*^2 = k(\mathbf{x}_*, \mathbf{x}_*) - \mathbf{v}^T \mathbf{v} \tag{14.112}$$

This works because:

$$\mathbf{v}^T\mathbf{v} = \mathbf{k}_*^T(\mathbf{L}^T)^{-1}\mathbf{L}^{-1}\mathbf{k}_* \tag{14.113}$$

$$= \mathbf{k}_*^T(\mathbf{L}\mathbf{L}^T)^{-1}\mathbf{k}_* \tag{14.114}$$

$$= \mathbf{k}_*^T(\mathbf{K} + \boldsymbol{\Sigma}_n)^{-1}\mathbf{k}_* \tag{14.115}$$

The mathematical equivalence ensures we get exactly the same answer as direct matrix inversion, but with better numerical properties and improved computational efficiency.

Complete Implementation Algorithm We can now summarize the complete implementation process for Gaussian Process prediction:

1. **Compute the Cholesky decomposition**: $\mathbf{L} = \text{cholesky}(\mathbf{K} + \boldsymbol{\Sigma}_n)$

2. **For the predictive mean**:

    - Solve $\mathbf{L}\mathbf{v} = \mathbf{t} - \mathbf{m}$ for $\mathbf{v}$ using forward substitution

    - Solve $\mathbf{L}^T\boldsymbol{\alpha} = \mathbf{v}$ for $\boldsymbol{\alpha}$ using backward substitution

    - Compute $m_* = m(\mathbf{x}_*) + \mathbf{k}_*^T\boldsymbol{\alpha}$

3. **For the predictive variance**:

    - Solve $\mathbf{L}\mathbf{v} = \mathbf{k}_*$ for $\mathbf{v}$ using forward substitution

    - Compute $\sigma_*^2 = k(\mathbf{x}_*, \mathbf{x}_*) - \mathbf{v}^T\mathbf{v}$

This approach is both efficient and numerically stable. The computationally intensive Cholesky decomposition is performed just once during training, after which predictions for new points require only $\mathcal{O}(N^2)$ operations for the mean and $\mathcal{O}(N^2)$ for the variance. This efficiency makes it practical to generate predictions across many test points—necessary for visualizing the predicted function or computing derived quantities in astronomical applications.

The algorithm also handles edge cases gracefully. If the kernel matrix is singular or nearly singular (which can happen with poorly chosen hyperparameters), the Cholesky decomposition will fail cleanly rather than producing misleading results. This provides a natural diagnostic for numerical problems and guides hyperparameter optimization.

14.9 Optimizing Hyperparameters in Gaussian Processes

Having established the computational framework for implementing Gaussian Processes, we now encounter another crucial question: how do we select the optimal hyperparameters for our kernel function? Our derivations have assumed these parameters are known, but in practice we must learn them from data.

The choice of hyperparameters has a profound impact on the types of functions our GP can represent. To understand why this matters, consider modeling stellar variability where we might use a composite kernel:

$$k(t, t') = \theta_0 \exp\left(-\frac{\theta_1}{2}|t - t'|^2\right) + \theta_2 + \theta_3 \exp\left(-\frac{2\sin^2(\pi|t - t'|/\theta_4)}{\theta_5^2}\right) \tag{14.116}$$

This kernel combines three components: an RBF term (smooth evolution), a constant term (baseline brightness), and a periodic term (rotational modulation). Each parameter controls different aspects of the function behavior.

The figure illustrates how these specific parameters shape function behavior: θ_0 controls the amplitude of variations, θ_1 determines smoothness, θ_4 sets the periodic spacing, and θ_5 governs how strictly the periodicity is enforced. Different parameter choices produce dramatically different function classes, and some will fit our data much better than others.

When we observe stellar data, we want parameter values that make our observations likely under the resulting function distribution. If our data shows rapid oscillations but we choose parameters that only allow smooth functions, the fit will be poor. Conversely, if we choose parameters that are too flexible for slowly varying data, the GP may overfit to noise.

How do we systematically determine which parameter values best capture the patterns in our data? Gaussian processes offer a principled solution through the marginal likelihood.

The Marginal Likelihood Approach The key insight is to treat hyperparameter selection as a model comparison problem. For any choice of hyperparameters $\boldsymbol{\theta}$, we ask: how probable are our observations under this parameterization? This probability is the marginal likelihood:

$$p(\mathbf{t}|\mathbf{X}, \boldsymbol{\theta}) = \mathcal{N}(\mathbf{m}_{\boldsymbol{\theta}}, \mathbf{K}_{\boldsymbol{\theta}} + \boldsymbol{\Sigma}_n) \tag{14.117}$$
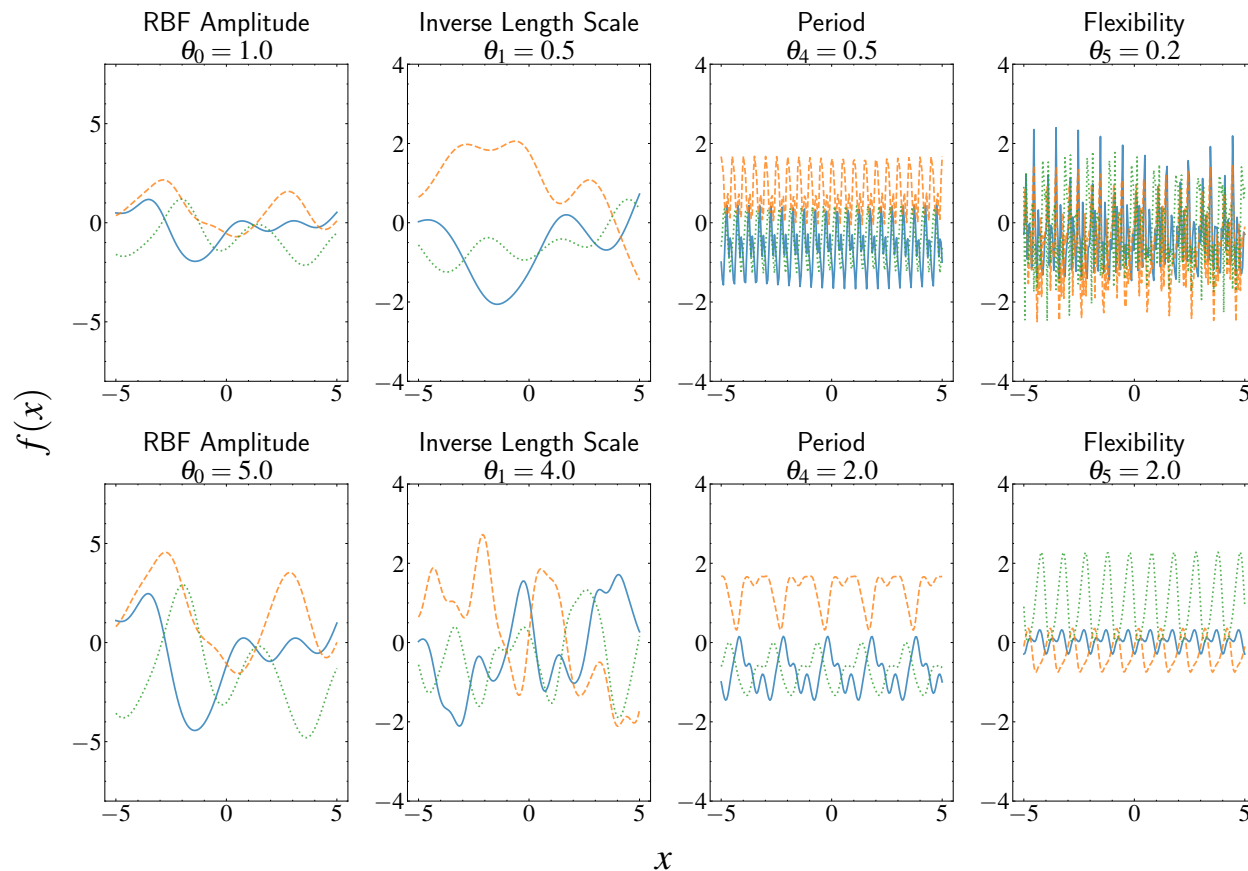
Figure 14.9: Visualization of how different kernel parameters affect functions sampled from Gaussian Process priors. The figure shows random functions drawn from GP priors with varying kernel parameters. Top row: Functions sampled with smaller parameter values; bottom row: Functions with larger parameter values. From left to right: (1) RBF amplitude parameter θ_0 controls the vertical scale of functions, with larger values allowing greater deviations from the mean; (2) Inverse length scale parameter θ_1 determines function smoothness, with smaller values producing smoother functions and larger values allowing more rapid variations; (3) Period parameter θ_4 in the periodic kernel sets the distance between repetitions in the function; (4) Flexibility parameter θ_5 controls how strictly the periodicity is enforced, with smaller values requiring more exact repetition and larger values allowing the periodic pattern to evolve. Each subplot shows three random function samples (in different colors) from the same GP prior to illustrate the characteristic properties induced by each parameter setting. This visualization demonstrates how kernel parameters directly encode prior beliefs about function properties in the GP framework.

where $\mathbf{K}_{\boldsymbol{\theta}}$ indicates the kernel matrix depends on hyperparameters, and $\mathbf{m}_{\boldsymbol{\theta}}$ represents the mean function values.

The term "marginal" means that the latent function values have been integrated out analytically, leaving us with a direct expression for the data probability. This marginal

likelihood automatically balances model fit against complexity.

To see why, examine its logarithm:

$$\log p(\mathbf{t}|\mathbf{X}, \boldsymbol{\theta}) = -\frac{1}{2}(\mathbf{t} - \mathbf{m_\theta})^T (\mathbf{K_\theta} + \boldsymbol{\Sigma}_n)^{-1}(\mathbf{t} - \mathbf{m_\theta}) - \frac{1}{2}\log|\mathbf{K_\theta} + \boldsymbol{\Sigma}_n| - \frac{N}{2}\log(2\pi) \quad (14.118)$$

This expression contains two competing terms:

1. The data fit term $-\frac{1}{2}(\mathbf{t} - \mathbf{m_\theta})^T (\mathbf{K_\theta} + \boldsymbol{\Sigma}_n)^{-1}(\mathbf{t} - \mathbf{m_\theta})$ rewards models that explain the observations well.

2. The complexity penalty $-\frac{1}{2}\log|\mathbf{K_\theta} + \boldsymbol{\Sigma}_n|$ penalizes overly flexible models. When we make the model more flexible (decreasing length scales, for example), the determinant increases, reducing the likelihood.

This automatic balance embodies Occam's razor: we find the simplest model that adequately explains our data.

Efficient Computation   Computing the log marginal likelihood faces the same computational challenges as prediction. We need matrix inversion and determinant calculation, both expensive for large datasets. The Cholesky decomposition again provides the solution.

With $\mathbf{K_\theta} + \boldsymbol{\Sigma}_n = \mathbf{L}\mathbf{L}^T$, we can compute efficiently:

For the data fit term, we reuse $\boldsymbol{\alpha} = (\mathbf{K_\theta} + \boldsymbol{\Sigma}_n)^{-1}(\mathbf{t} - \mathbf{m_\theta})$ from prediction:

$$(\mathbf{t} - \mathbf{m_\theta})^T (\mathbf{K_\theta} + \boldsymbol{\Sigma}_n)^{-1}(\mathbf{t} - \mathbf{m_\theta}) = (\mathbf{t} - \mathbf{m_\theta})^T \boldsymbol{\alpha} \quad (14.119)$$

For the determinant, we use the diagonal elements of the Cholesky factor:

$$\log|\mathbf{K_\theta} + \boldsymbol{\Sigma}_n| = 2\sum_{i=1}^{N} \log L_{ii} \quad (14.120)$$

This gives us the final efficient form:

$$\log p(\mathbf{t}|\mathbf{X}, \boldsymbol{\theta}) = -\frac{1}{2}(\mathbf{t} - \mathbf{m_\theta})^T \boldsymbol{\alpha} - \sum_{i=1}^{N} \log L_{ii} - \frac{N}{2}\log(2\pi) \quad (14.121)$$
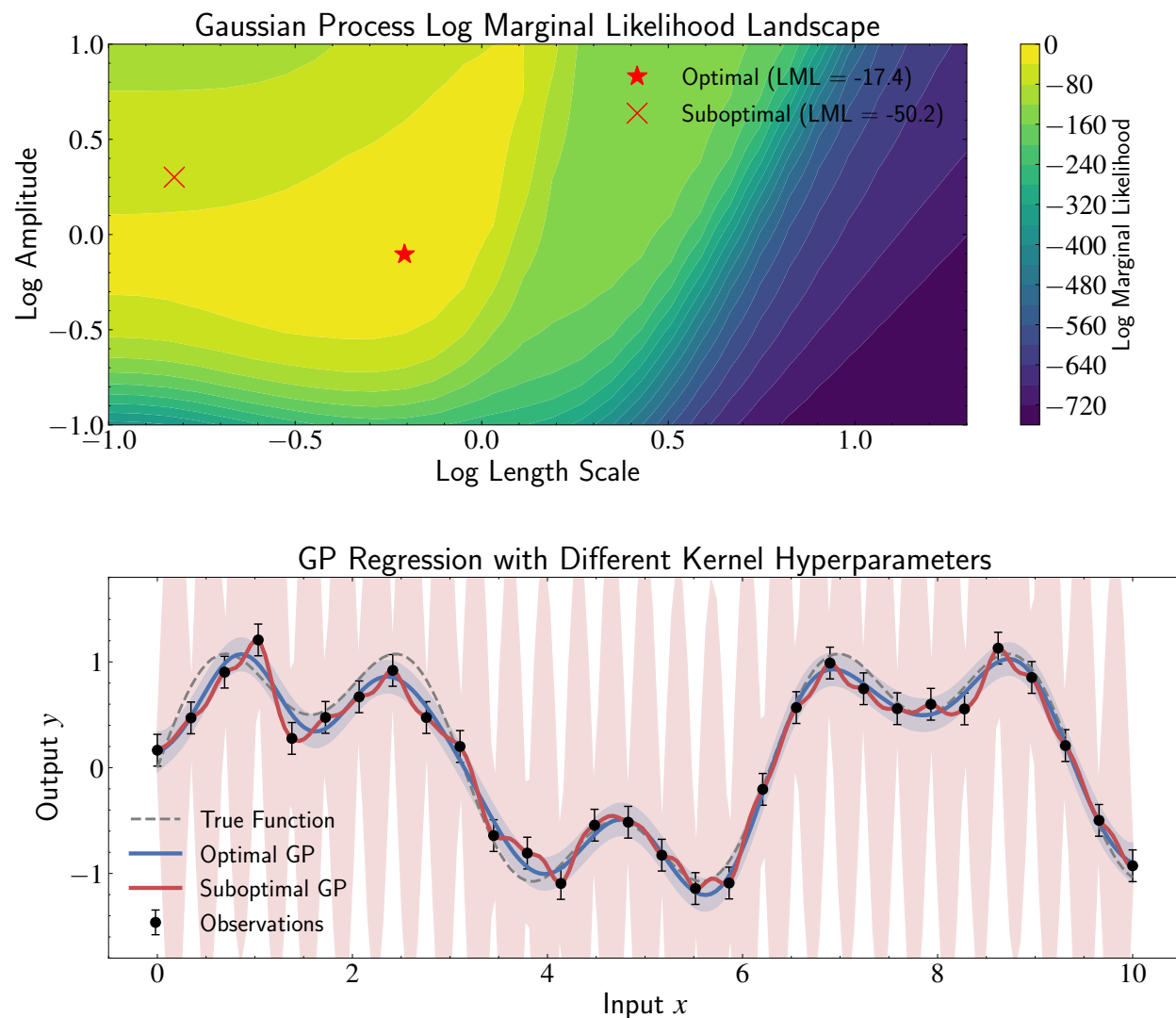
Figure 14.10: Demonstration of hyperparameter optimization in Gaussian Process regression. The top panel shows the log marginal likelihood landscape over a grid of RBF kernel hyperparameters (length scale and amplitude) plotted on logarithmic scales. Brighter regions indicate higher likelihood values, with the optimal hyperparameters (red star) yielding significantly higher likelihood than suboptimal choices (red x). The bottom panel compares GP regression results using optimal versus suboptimal hyperparameters. The optimal model (blue curve) with appropriate length scale and amplitude captures the true underlying function (dashed gray) more accurately, with well-calibrated uncertainty bands (light blue region). In contrast, the suboptimal model (orange) with shorter length scale oscillates unnecessarily between data points, exhibiting overfitting behavior. This figure illustrates how maximizing the marginal likelihood automatically balances model fit and complexity without requiring explicit regularization terms.

Optimization Strategies   With an efficient method for computing the log marginal likelihood, we can optimize it with respect to hyperparameters $\boldsymbol{\theta}$. The choice of optimization

method depends on the dimensionality of the hyperparameter space and the computational resources available.

For low-dimensional hyperparameter spaces (typically 1-3 parameters), grid search provides a straightforward and reliable approach. We evaluate the log marginal likelihood on a predefined grid of hyperparameter values and select the combination yielding the highest value. For example, if our kernel has two hyperparameters—amplitude and length scale—we might evaluate the likelihood on a 20×20 grid, requiring 400 likelihood evaluations.

Grid search offers several advantages: it is simple to implement and parallelize across multiple processors, it provides complete visualization of the likelihood landscape that can reveal important features like multimodality, and it guarantees finding the global optimum within the grid resolution. The visualization aspect is particularly valuable for understanding how different hyperparameters interact and for diagnosing potential problems with the optimization.

However, grid search becomes computationally prohibitive as the number of hyperparameters increases. With d hyperparameters and m grid points per dimension, we need m^d evaluations—an exponential growth that quickly becomes infeasible. For problems with more than three or four hyperparameters, we need more efficient approaches.

For higher-dimensional hyperparameter spaces, gradient-based optimization becomes necessary. The basic approach iteratively updates hyperparameters in the direction of the gradient:

$$\boldsymbol{\theta}^{(t+1)} = \boldsymbol{\theta}^{(t)} + \eta_t \nabla_{\boldsymbol{\theta}} \log p(\mathbf{t}|\mathbf{X}, \boldsymbol{\theta}^{(t)}) \qquad (14.122)$$

where η_t is the learning rate at iteration t. This approach scales much better than grid search, requiring only $\mathcal{O}(d)$ gradient evaluations per iteration regardless of the dimensionality.

Computing the gradient of the log marginal likelihood with respect to hyperparameters can be done analytically for specific kernels, but this becomes tedious for complex composite kernels. Modern implementations increasingly rely on automatic differentiation (autodiff) frameworks to compute these gradients. Autodiff works by tracking all operations during the forward computation and then systematically applying the chain rule during the backward pass.

Libraries like TensorFlow, PyTorch, and JAX provide autodiff capabilities that can automatically compute gradients of arbitrary computational graphs. This eliminates the need for manual gradient derivation and makes it practical to experiment with complex kernel

structures. We will explore automatic differentiation in much greater detail in Chapter 15 when we discuss neural networks, where it plays a central role in training.

Parameter optimization highlights a key advantage of Gaussian processes: the marginal likelihood provides an objective, principled criterion for hyperparameter selection that automatically balances model complexity against data fit. This eliminates the need for ad hoc regularization terms or complex cross-validation procedures that are required by many other machine learning methods.

14.10 Model Selection for Gaussian Process Regression

The previous section addressed hyperparameter optimization within a fixed kernel structure. We now face a more challenging question: how do we choose the kernel structure itself? Should we use a simple RBF kernel, a periodic kernel, or a composite kernel combining multiple components? This kernel selection problem represents a higher level of model choice that goes beyond tuning parameters within a given functional form.

The challenge becomes apparent when we consider real astronomical phenomena. Stellar variability might be driven by multiple physical processes operating on different timescales: pulsations, rotation, magnetic activity, and evolutionary changes. We could model this with a simple RBF kernel and hope it captures the dominant behavior, or we could construct a composite kernel with multiple components. How do we decide which approach is justified by the data?

This question connects directly to the model selection principles we explored in earlier chapters. We need to balance model complexity against explanatory power, avoiding both underfitting (missing important patterns) and overfitting (modeling noise as signal). For Gaussian processes, this challenge has both conceptual and practical dimensions that require careful consideration.

The Kernel Selection Challenge   Unlike hyperparameter optimization, which involves tuning continuous parameters within a fixed functional form, kernel selection involves choosing between fundamentally different model structures. Consider these possibilities for modeling a stellar light curve:

1. Simple RBF kernel: $k(t, t') = \sigma_f^2 \exp\left(-\frac{1}{2l^2}(t - t')^2\right)$

2. Periodic kernel: $k(t, t') = \sigma_f^2 \exp\left(-\frac{2\sin^2(\pi|t-t'|/p)}{l^2}\right)$

3. Composite kernel: RBF + constant + periodic components

4. Matérn kernel with different smoothness parameters

Each choice embodies different assumptions about the underlying physical processes. The RBF kernel assumes smooth, aperiodic variations. The periodic kernel assumes regular repetitive patterns. The composite kernel allows for multiple processes operating simultaneously. These are qualitatively different models, not just different parameter settings.

The selection challenge is compounded by the fact that more complex kernels can always fit the data at least as well as simpler ones. A composite kernel with many components has the flexibility to capture any pattern that a simple kernel could model, plus additional structure. Without proper penalties for complexity, we would always choose the most flexible option, leading to overfitting.

Bayesian Model Comparison Framework   Gaussian processes provide a principled approach to this challenge through Bayesian model comparison. For each candidate kernel structure $\mathcal{M}_i$, we can compute the marginal likelihood:

$$p(\mathbf{t}|\mathbf{X}, \mathcal{M}_i) = \int p(\mathbf{t}|\mathbf{X}, \boldsymbol{\theta}, \mathcal{M}_i)p(\boldsymbol{\theta}|\mathcal{M}_i)d\boldsymbol{\theta} \tag{14.123}$$

where $p(\boldsymbol{\theta}|\mathcal{M}_i)$ represents the prior over hyperparameters for model $\mathcal{M}_i$.

In practice, we typically approximate this integral by using the marginal likelihood at the optimal hyperparameters:

$$p(\mathbf{t}|\mathbf{X}, \mathcal{M}_i) \approx p(\mathbf{t}|\mathbf{X}, \boldsymbol{\theta}_i^*) \tag{14.124}$$

where $\boldsymbol{\theta}_i^*$ maximizes the marginal likelihood for model $\mathcal{M}_i$. This approximation works well when the posterior over hyperparameters is concentrated around the maximum, which is often the case for GP models with sufficient data.

The beauty of this approach is that the marginal likelihood automatically accounts for model complexity through the determinant term we examined earlier. More complex kernels have larger parameter spaces and more flexible covariance structures, which increases the determinant penalty. The model with the highest marginal likelihood represents the best balance between fit and complexity.

This framework treats kernel selection as a natural extension of hyperparameter optimization. Instead of optimizing over a continuous parameter space, we optimize over a discrete set of model structures, using the same objective function that worked so well for parameter tuning.

Information Criteria as Approximations   While the marginal likelihood provides the theoretically correct approach to model comparison, we sometimes want additional safeguards against overfitting or need to work with approximations to the full Bayesian treatment. Information criteria provide valuable alternatives that add explicit penalties for model complexity.

The Bayesian Information Criterion (BIC) and Akaike Information Criterion (AIC) offer simple approaches:

$$\text{BIC} = -2\ln(\hat{L}) + P\ln(N) \tag{14.125}$$

$$\text{AIC} = -2\ln(\hat{L}) + 2P \tag{14.126}$$

where $\hat{L}$ is the maximized likelihood value, P is the number of hyperparameters, and N is the sample size. The model with the lowest criterion value is preferred.

These criteria add explicit penalty terms based on the number of hyperparameters. BIC includes an additional dependence on sample size, making it more conservative for large datasets. Both provide additional protection against overfitting beyond what the marginal likelihood determinant term provides.

For Gaussian processes, these criteria are particularly useful when comparing models with very different numbers of hyperparameters. A simple RBF kernel has 2-3 hyperparameters, while a complex composite kernel might have 10 or more. The explicit counting of parameters in AIC and BIC provides a clear penalty for this additional complexity.

Cross-Validation for Model Assessment   Cross-validation offers another approach that directly measures predictive performance rather than relying on theoretical penalties for complexity. For Gaussian processes, we typically implement K-fold cross-validation, dividing the dataset into K subsets and training on $K - 1$ subsets while testing on the remaining subset.

The negative log predictive density (NLPD) serves as an appropriate performance

metric for GPs:

$$\text{NLPD} = -\frac{1}{|D_{\text{test}}|} \sum_{(\mathbf{x}_i, t_i) \in D_{\text{test}}} \log p(t_i | \mathbf{x}_i, D_{\text{train}}) \qquad (14.127)$$

This metric evaluates both point predictions and uncertainty estimates, making it well-suited for Gaussian processes where uncertainty quantification is a key advantage. A model that makes confident but wrong predictions will be penalized more heavily than one that expresses appropriate uncertainty.

Cross-validation for GPs can be computationally expensive, as each fold requires training a model on approximately $(K-1)/K \times N$ data points. However, it provides direct evidence of predictive performance and can reveal overfitting that might not be apparent from marginal likelihood comparisons alone.

The cross-validation approach is particularly valuable when we want to assess how well different kernel structures generalize to new data. While the marginal likelihood tells us which model best explains the observed data, cross-validation tells us which model is most likely to perform well on future observations.

In practice, effective model selection for Gaussian processes combines multiple approaches. A typical workflow starts with simple kernels (RBF, periodic, linear), compares them using marginal likelihood, then constructs composite models by combining promising components. Cross-validation provides final validation of predictive performance.

For astronomical applications, domain knowledge plays a crucial role in defining the candidate model set. Rather than testing all possible kernel combinations, we focus on those corresponding to plausible physical processes, reducing computational burden while maintaining scientific interpretability.

14.11 Gaussian Process Classification

Throughout our exploration of Gaussian Processes, we have focused exclusively on regression problems—tasks where we predict continuous outputs like stellar brightness or radial velocities. However, many astronomical problems require classification—determining which discrete category an object belongs to. We might want to classify stars by spectral type, distinguish between stars and galaxies in photometric surveys, or identify different types of variable objects.

The success of Gaussian Process Regression naturally leads us to ask: can we extend this framework to handle classification problems? The challenge is that while regression deals with continuous function values that fit naturally into the Gaussian framework, classification involves discrete outcomes that cannot be directly modeled with Gaussian distributions.

This extension parallels our earlier transition from linear regression to logistic regression. Just as we needed special techniques to handle binary outcomes in the linear modeling framework, we now need to adapt our Gaussian process machinery to work with discrete class labels while preserving the benefits of principled uncertainty quantification.

The Challenge of Discrete Outcomes   The fundamental obstacle in extending GPs to classification becomes clear when we examine the nature of the problem. In regression, our observations are continuous values that can be modeled directly as Gaussian random variables (with added noise). We can write $t_i = f(\mathbf{x}_i) + \epsilon_i$ where f is our latent function and ϵ_i represents Gaussian noise.

For classification, our observations are discrete class labels—typically 0 and 1 for binary problems. We cannot simply write $t_i = f(\mathbf{x}_i) + \epsilon_i$ with Gaussian noise, because discrete outcomes cannot arise from adding Gaussian noise to a continuous function. We need a different relationship between our latent function and the observed outcomes.

The solution, familiar from logistic regression, is to introduce a link function that connects continuous function values to class probabilities. Instead of observing the function directly, we assume there is an underlying continuous function $a(\mathbf{x})$ (often called the "logit" or "score" function) that determines class probabilities through a nonlinear transformation.

This approach allows us to maintain the Gaussian process framework for the latent function while handling discrete observations through an appropriate likelihood function. The latent function can take any real value, which fits naturally with Gaussian processes, but these values are converted to probabilities in the $[0, 1]$ range through the link function.

From Linear to Nonlinear Decision Boundaries   To understand the motivation for Gaussian Process Classification, let us first recall the limitations of logistic regression. In logistic regression, we model class probabilities using:

$$p(t = 1|\mathbf{x}, \mathbf{w}) = \sigma(\mathbf{w}^T \phi(\mathbf{x})) \tag{14.128}$$

where $\sigma(a) = \frac{1}{1+e^{-a}}$ is the sigmoid function, and $\phi(\mathbf{x})$ represents our feature mapping.

The key limitation is that the decision boundary—the locus of points where $p(t = 1|\mathbf{x}) = 0.5$—occurs where $\mathbf{w}^T\phi(\mathbf{x}) = 0$. This defines a hyperplane in feature space, restricting us to linear decision boundaries. Even with carefully designed features, many real-world classification problems require nonlinear boundaries that are difficult to capture with explicit feature mappings.
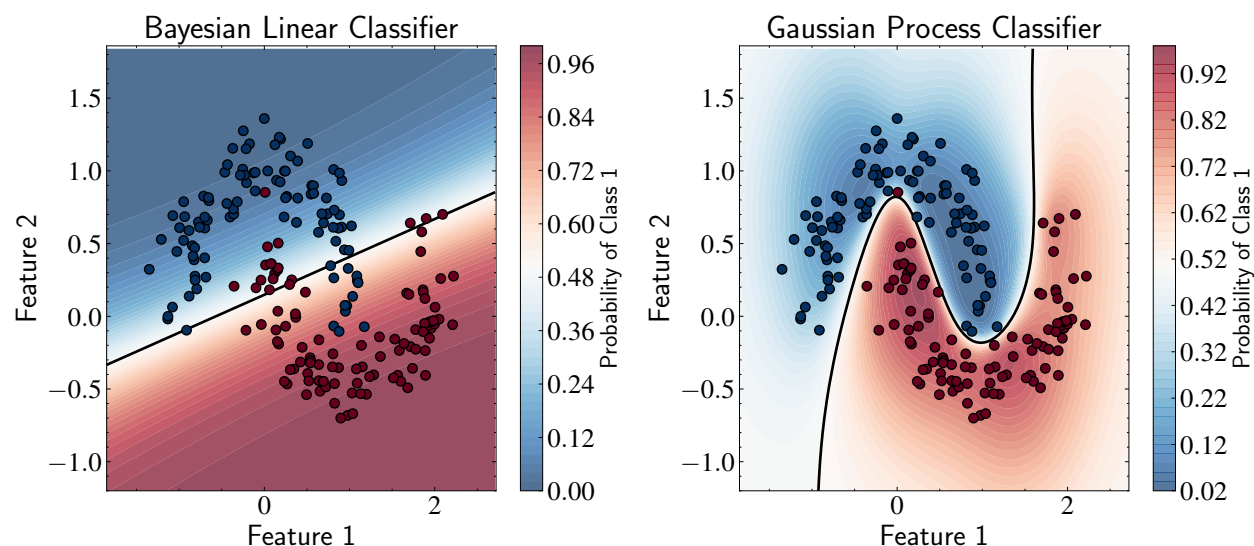

Figure 14.11: Comparison of decision boundaries and predictive uncertainty between Bayesian Linear Classification (left) and Gaussian Process Classification (right) on a synthetic moon-shaped dataset. Colors represent the predicted probability of class membership, with red indicating high probability of class 1 and blue indicating high probability of class 0. The solid black line shows the decision boundary where the class probability equals 0.5. The Bayesian Linear Classifier is limited by its linear nature and cannot capture the moon-shaped structure of the data. In contrast, the Gaussian Process Classifier exhibits both increased uncertainty in sparse data regions and a flexible, nonlinear decision boundary that properly adapts to the data's intrinsic geometry. This comparison illustrates how GPC extends logistic regression beyond linear boundaries while maintaining proper uncertainty quantification—the model becomes appropriately less confident in regions with sparse or no data.

Consider astronomical applications where we need to separate stars from galaxies based on photometric colors. The true boundary between these classes in color space is often curved and complex, depending on redshift effects, stellar populations, and observational selection functions. A linear classifier might capture the gross separation but miss important substructures.

Gaussian Process Classification addresses this limitation by replacing the linear func-

tion $\mathbf{w}^T \phi(\mathbf{x})$ with a more flexible function $a(\mathbf{x})$ that follows a Gaussian process prior:

$$a(\mathbf{x}) \sim \mathcal{GP}(0, k(\mathbf{x}, \mathbf{x}')) \tag{14.129}$$

For simplicity, we use a zero mean function, though this can be generalized. The logit function $a(\mathbf{x})$ can take any real value, which fits naturally with Gaussian processes, while the sigmoid transformation ensures proper probability outputs:

$$p(t = 1|\mathbf{x}, a) = \sigma(a(\mathbf{x})) \tag{14.130}$$

This approach provides the flexibility to learn arbitrarily complex decision boundaries through the kernel function, while maintaining a probabilistic framework that quantifies uncertainty in our classifications.

The Information Flow in GP Classification   To understand how Gaussian Process Classification works, it helps to trace the flow of information through the model. The process involves several stages that connect our input features to final class predictions.

The model works as follows:

1. **Input to latent mapping**: The Gaussian process maps input features $\mathbf{x}_i$ to latent function values $a_i = a(\mathbf{x}_i)$. These latent values can take any real number and represent the "score" for class membership before conversion to probabilities.

2. **Latent to probability transformation**: The sigmoid function converts latent values to class probabilities: $p_i = \sigma(a_i)$. This ensures outputs are properly bounded between 0 and 1.

3. **Probability to class assignment**: We observe discrete class labels t_i that are sampled from Bernoulli distributions with probabilities p_i.

The power of this framework lies in the first step. By using a Gaussian process for the latent function, we can learn complex mappings from inputs to scores without explicitly designing features. The kernel function encodes our assumptions about which inputs should receive similar scores, and the GP automatically adapts the complexity of this mapping to the data.

The uncertainty quantification in GP classification has an interesting property: uncer-
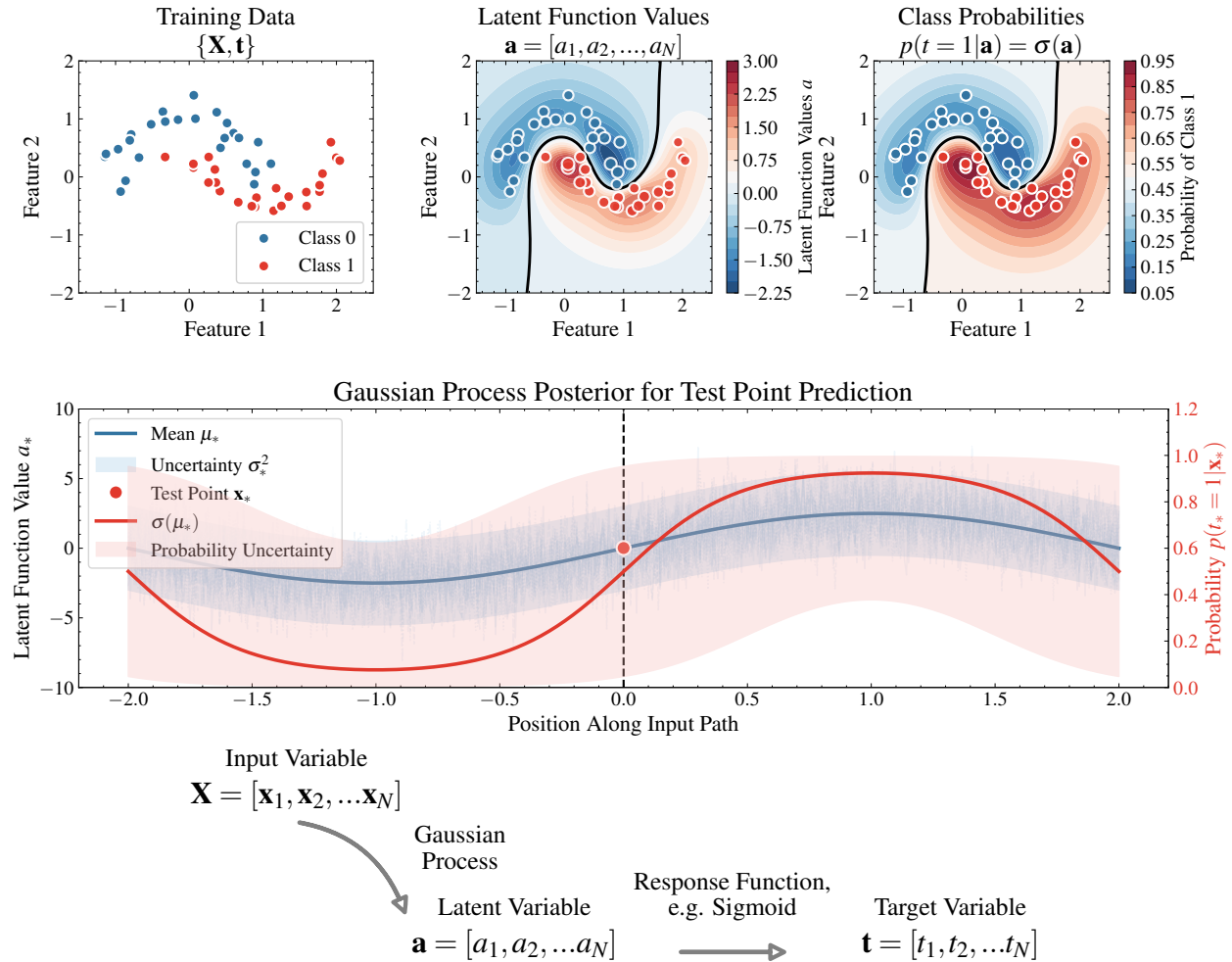
Figure 14.12: Visualization of the information flow in Gaussian Process Classification. The top panels show the progression from training data (left) through latent function values (middle) to class probabilities (right) using moon-shaped data, illustrating how GPC can handle nonlinear decision boundaries. The middle panel demonstrates how uncertainty is propagated from latent space to probability space: the posterior standard deviation in latent space (σ_*) represents our uncertainty about the true latent function value a_* at a test point. When transformed through the sigmoid function, this uncertainty becomes asymmetric in probability space - wider near the decision boundary (where the latent function $a_* \approx 0$) and narrower at the extremes (where $|a_*|$ is large). The bottom diagram shows the core conceptual flow: the Gaussian Process transforms input variables to latent variables (assigning a latent value a_i to each input $\mathbf{x}_i$), then the sigmoid response function converts these latent values to class probabilities. This structure illustrates how GPC extends logistic regression beyond linear boundaries while maintaining proper uncertainty quantification.

tainty in the latent space (represented by the GP posterior variance) translates to uncertainty in probability space through the sigmoid transformation. Near decision boundaries where $a(\mathbf{x}) \approx 0$, small changes in the latent function produce large changes in class probabilities,

so the model appropriately expresses high uncertainty. Far from boundaries where $|a(\mathbf{x})|$ is large, the sigmoid saturates and uncertainty in the latent space has less impact on class probabilities.

This natural uncertainty propagation makes GP classification particularly valuable for astronomical applications where we need to identify objects that are difficult to classify. Rather than forcing a discrete classification, the model can express appropriate uncertainty about ambiguous cases, allowing follow-up observations to be targeted where they will be most informative.

The main challenge in implementing this framework is that the nonlinear link function makes exact Bayesian inference intractable. Unlike GP regression where Gaussian likelihoods preserve conjugacy, the sigmoid function creates a non-Gaussian posterior that requires approximation techniques. This computational complexity is the price we pay for the flexibility of nonlinear decision boundaries.

14.12 The Predictive Distribution in GP Classification

Having established the conceptual framework for Gaussian Process Classification, we now turn to the central computational challenge: how do we actually compute predictions? While the intuition behind GPC is straightforward—use a GP for the latent function and transform through a sigmoid—the mathematical implementation requires careful handling of the nonlinear relationship between latent values and class probabilities.

The challenge stems from the fact that we cannot directly observe the latent function values. We have discrete class labels and need to infer both the latent function and make predictions at new points. This inference problem is more complex than GP regression because the sigmoid likelihood breaks the conjugacy that made GP regression analytically tractable.

Our goal is to compute the predictive distribution for a new test point $\mathbf{x}_*$:

$$p(t_* = 1|\mathbf{x}_*, \mathbf{X}, \mathbf{t}) \tag{14.131}$$

This represents the probability that $\mathbf{x}_*$ belongs to class 1, given our training data $\{\mathbf{X}, \mathbf{t}\}$. Unlike GP regression where we could write down this distribution directly, GPC requires us to carefully handle the latent variables and nonlinear transformations.

The Challenge of Non-Conjugate Likelihoods   To understand why GP classification is more complex than regression, let us trace through the inference process. The complete flow involves several steps that must be handled carefully:

1. **Training data**: We observe inputs $\mathbf{X}$ and discrete class labels $\mathbf{t} \in \{0, 1\}^N$

2. **Latent function inference**: We use this data to infer the distribution of logit values $\mathbf{a}$ at training points

3. **GP prediction**: The trained GP predicts the logit value a_* at test point $\mathbf{x}_*$

4. **Classification**: We convert the predicted logit to a class probability using the sigmoid function

The problem lies in step 2. In GP regression, we directly observed noisy function values, so we could apply standard Gaussian conditioning. In GP classification, we observe discrete labels that are connected to the latent function through the nonlinear sigmoid transformation. This creates a non-Gaussian posterior over the latent function values that cannot be computed analytically.

To formalize this challenge, let us apply the sum and product rules of probability to derive our predictive distribution. Since we do not observe the logit values directly, we must marginalize over all possible values of a_*:

$$p(t_* = 1|\mathbf{x}_*, \mathbf{X}, \mathbf{t}) = \int p(t_* = 1|a_*)p(a_*|\mathbf{x}_*, \mathbf{X}, \mathbf{t})da_* \qquad (14.132)$$

The first term is straightforward: $p(t_* = 1|a_*) = \sigma(a_*)$. The challenge is computing the second term, $p(a_*|\mathbf{x}_*, \mathbf{X}, \mathbf{t})$, which requires us to infer the latent function distribution from discrete observations.

Using the sum rule again:

$$p(a_*|\mathbf{x}_*, \mathbf{X}, \mathbf{t}) = \int p(a_*|\mathbf{a}, \mathbf{x}_*, \mathbf{X})p(\mathbf{a}|\mathbf{X}, \mathbf{t})d\mathbf{a} \qquad (14.133)$$

The first term inside this integral is the standard GP prediction we know how to handle:

$$p(a_*|\mathbf{a}, \mathbf{x}_*, \mathbf{X}) = \mathcal{N}(a_*|\mu_{a_*|\mathbf{a}}, \sigma^2_{a_*|\mathbf{a}}) \qquad (14.134)$$

where the mean and variance follow our familiar GP prediction formulas.

The problematic term is $p(\mathbf{a}|\mathbf{X}, \mathbf{t})$—the posterior distribution of latent function values given the observed class labels. Using Bayes' rule:

$$p(\mathbf{a}|\mathbf{X}, \mathbf{t}) = \frac{p(\mathbf{t}|\mathbf{a})p(\mathbf{a}|\mathbf{X})}{p(\mathbf{t}|\mathbf{X})} \tag{14.135}$$

The prior $p(\mathbf{a}|\mathbf{X}) = \mathcal{N}(\mathbf{0}, \mathbf{K})$ is Gaussian, but the likelihood $p(\mathbf{t}|\mathbf{a}) = \prod_{i=1}^{N} \sigma(a_i)^{t_i}(1 - \sigma(a_i))^{1-t_i}$ involves products of sigmoid functions. When we multiply a Gaussian prior by this non-Gaussian likelihood, the result is no longer Gaussian, preventing analytical computation.

The Laplace Approximation Solution   To make progress, we need approximation techniques that can handle the non-Gaussian posterior. The Laplace approximation, which we introduced in Chapter 9 for Bayesian logistic regression, provides exactly the tool we need. The key idea is to approximate the complex posterior with a Gaussian distribution centered at the posterior mode.

Recall from Chapter 9 that the Laplace approximation works by finding the maximum a posteriori (MAP) estimate of the parameters and then approximating the posterior with a Gaussian based on the local curvature at that point. For GP classification, we apply this same principle to approximate $p(\mathbf{a}|\mathbf{X}, \mathbf{t})$.

The Laplace approximation proceeds in three steps:

1. Find the mode $\mathbf{a}_{\mathrm{MAP}}$ of the posterior distribution

2. Compute the Hessian matrix of the negative log posterior at this mode

3. Construct a Gaussian approximation using the mode and Hessian

To find the mode, we maximize the log posterior:

$$\log p(\mathbf{a}|\mathbf{X}, \mathbf{t}) \propto \sum_{i=1}^{N} [t_i \log \sigma(a_i) + (1 - t_i) \log(1 - \sigma(a_i))] - \frac{1}{2}\mathbf{a}^T \mathbf{K}^{-1}\mathbf{a} \tag{14.136}$$

To find the maximum, we compute the gradient and set it to zero. For the likelihood

term, the partial derivative with respect to each a_i is:

$$\frac{\partial}{\partial a_i}[t_i \log \sigma(a_i) + (1 - t_i) \log(1 - \sigma(a_i))] = t_i \frac{\sigma'(a_i)}{\sigma(a_i)} + (1 - t_i) \frac{-\sigma'(a_i)}{1 - \sigma(a_i)} \tag{14.137}$$

Using the fact that $\sigma'(a_i) = \sigma(a_i)(1 - \sigma(a_i))$, this simplifies to:

$$= t_i \frac{\sigma(a_i)(1 - \sigma(a_i))}{\sigma(a_i)} - (1 - t_i) \frac{\sigma(a_i)(1 - \sigma(a_i))}{1 - \sigma(a_i)} \tag{14.138}$$

$$= t_i(1 - \sigma(a_i)) - (1 - t_i)\sigma(a_i) \tag{14.139}$$

$$= t_i - t_i\sigma(a_i) - \sigma(a_i) + t_i\sigma(a_i) \tag{14.140}$$

$$= t_i - \sigma(a_i) \tag{14.141}$$

Setting the full gradient to zero:

$$\nabla_{\mathbf{a}} \log p(\mathbf{a}|\mathbf{X}, \mathbf{t}) = \mathbf{t} - \boldsymbol{\sigma}(\mathbf{a}) - \mathbf{K}^{-1}\mathbf{a} = \mathbf{0} \tag{14.142}$$

where $\boldsymbol{\sigma}(\mathbf{a}) = [\sigma(a_1), \sigma(a_2), \ldots, \sigma(a_N)]^T$.

This equation has no closed-form solution due to the nonlinearity of the sigmoid function, so we solve it iteratively using gradient-based optimization:

$$\mathbf{a}^{(j+1)} = \mathbf{a}^{(j)} + \eta \left(\mathbf{t} - \boldsymbol{\sigma}(\mathbf{a}^{(j)}) - \mathbf{K}^{-1}\mathbf{a}^{(j)} \right) \tag{14.143}$$

Fortunately, we can prove that this optimization problem is globally concave. The log-likelihood term is concave because the log of the sigmoid function is concave, and the term $-\frac{1}{2}\mathbf{a}^T\mathbf{K}^{-1}\mathbf{a}$ is also concave since $\mathbf{K}$ is positive definite. The sum of concave functions is concave, guaranteeing convergence to a unique global maximum.

The Hessian matrix captures the local curvature of the log posterior. For the diagonal elements:

$$\frac{\partial^2}{\partial a_i^2} \sum_{i=1}^{N} [t_i \log \sigma(a_i) + (1 - t_i) \log(1 - \sigma(a_i))] = \frac{\partial}{\partial a_i}(t_i - \sigma(a_i)) \tag{14.144}$$

$$= -\sigma'(a_i) \tag{14.145}$$

$$= -\sigma(a_i)(1 - \sigma(a_i)) \tag{14.146}$$

For the off-diagonal elements, since each term in the sum depends only on a single a_i, the mixed partial derivatives are zero. The Hessian of the negative log posterior is therefore:

$$\mathbf{H} = -\nabla_{\mathbf{a}}\nabla_{\mathbf{a}}^T \log p(\mathbf{a}|\mathbf{X}, \mathbf{t})|_{\mathbf{a}=\mathbf{a}_{\mathrm{MAP}}} = \mathbf{W} + \mathbf{K}^{-1} \tag{14.147}$$

where $\mathbf{W} = \mathrm{diag}(\sigma(a_1)(1 - \sigma(a_1)), \ldots, \sigma(a_N)(1 - \sigma(a_N)))$ contains the second derivatives of the negative log-likelihood.

The Laplace approximation then gives us:

$$p(\mathbf{a}|\mathbf{X}, \mathbf{t}) \approx \mathcal{N}(\mathbf{a}|\mathbf{a}_{\mathrm{MAP}}, \mathbf{H}^{-1}) \tag{14.148}$$

Deriving the Predictive Distribution With a Gaussian approximation for $p(\mathbf{a}|\mathbf{X}, \mathbf{t})$, we can now tackle the predictive distribution. We need to compute:

$$p(a_*|\mathbf{x}_*, \mathbf{X}, \mathbf{t}) = \int p(a_*|\mathbf{x}_*, \mathbf{X}, \mathbf{a})p(\mathbf{a}|\mathbf{X}, \mathbf{t})d\mathbf{a} \tag{14.149}$$

Substituting our approximations:

$$p(a_*|\mathbf{x}_*, \mathbf{X}, \mathbf{t}) \approx \int \mathcal{N}(a_*|\mathbf{k}_*^T\mathbf{K}^{-1}\mathbf{a}, k_{**} - \mathbf{k}_*^T\mathbf{K}^{-1}\mathbf{k}_*)\mathcal{N}(\mathbf{a}|\mathbf{a}_{\mathrm{MAP}}, \mathbf{H}^{-1})d\mathbf{a} \tag{14.150}$$

This integral has the form of a convolution of two Gaussians, which results in another Gaussian:

$$p(a_*|\mathbf{x}_*, \mathbf{X}, \mathbf{t}) \approx \mathcal{N}(a_*|\mu_*, \sigma_*^2) \tag{14.151}$$
$$\mu_* = \mathbf{k}_*^T\mathbf{K}^{-1}\mathbf{a}_{\mathrm{MAP}} \tag{14.152}$$
$$\sigma_*^2 = k_{**} - \mathbf{k}_*^T\mathbf{K}^{-1}\mathbf{k}_* + \mathbf{k}_*^T\mathbf{K}^{-1}\mathbf{H}^{-1}\mathbf{K}^{-1}\mathbf{k}_* \tag{14.153}$$

These expressions can be simplified using the iterative solution for $\mathbf{a}_{\mathrm{MAP}}$ and matrix identities, yielding:

$$\mu_* = \mathbf{k}_*^T(\mathbf{t} - \boldsymbol{\sigma}(\mathbf{a}_{\mathrm{MAP}})) \tag{14.154}$$
$$\sigma_*^2 = k_{**} - \mathbf{k}_*^T(\mathbf{W}^{-1} + \mathbf{K})^{-1}\mathbf{k}_* \tag{14.155}$$

Converting to Class Probabilities   We now have the distribution of the logit value a_*, but we need the class probability. We must compute:

$$p(t_* = 1|\mathbf{x}_*, \mathbf{X}, \mathbf{t}) = \int \sigma(a_*)p(a_*|\mathbf{x}_*, \mathbf{X}, \mathbf{t})da_* \tag{14.156}$$

This integral does not have a closed-form solution because the sigmoid function does not conjugate with the Gaussian density. However, we can use the probit approximation that we introduced in Chapter 9. Recall that the logistic sigmoid function can be closely approximated by the probit function $\Phi(\lambda a)$, where Φ is the standard normal CDF and $\lambda = \sqrt{\pi/8}$.

Using this approximation and the properties of Gaussian integrals, we get:

$$p(t_* = 1|\mathbf{x}_*, \mathbf{X}, \mathbf{t}) \approx \sigma\left(\frac{\mu_*}{\sqrt{1 + \pi\sigma_*^2/8}}\right) \tag{14.157}$$

This completes our derivation of GP classification predictions. Through the Laplace approximation and probit approximation—both techniques we developed in Chapter 9—we have transformed the intractable exact inference into a practical computational procedure that maintains the probabilistic rigor of the Gaussian process framework.

Interpreting the Predictions   The factor $1/\sqrt{1 + \pi\sigma_*^2/8}$ acts as an uncertainty moderation term—the same mechanism we encountered in Bayesian logistic regression in Chapter 9. When σ_*^2 is large (high uncertainty in the latent function), this factor shrinks μ_* toward zero, pushing the prediction toward $\sigma(0) = 0.5$ (maximum uncertainty).

When the test point is near many training points with consistent labels, σ_*^2 is small, the moderation factor approaches 1, and the prediction is approximately $\sigma(\mu_*)$. When the test point is far from training data or near decision boundaries, σ_*^2 is large, the moderation factor shrinks the effective logit value, and the probability moves toward 0.5.

This automatic uncertainty moderation is a key advantage of the full Bayesian treatment—GP classification naturally becomes more uncertain where it should be, unlike simpler methods that might make overconfident predictions everywhere.

The mean prediction $\mu_* = \mathbf{k}_*^T(\mathbf{t} - \boldsymbol{\sigma}(\mathbf{a}_{\text{MAP}}))$ represents a weighted combination of residuals at training points. When a training point's true label differs significantly from

the model's MAP prediction, it contributes more strongly to predictions at new points. The weights depend on kernel similarities but also account for correlations among training points.

The uncertainty estimate $\sigma_*^2 = k_{**} - \mathbf{k}_*^T(\mathbf{W}^{-1} + \mathbf{K})^{-1}\mathbf{k}_*$ has a structure similar to GP regression, but the matrix $\mathbf{W}$ captures how sensitive each observation is to changes in the latent function. Points near decision boundaries provide the most information about where boundaries lie, having the greatest influence on reducing uncertainty.

14.13   Extending to Multiclass Classification

So far, we have focused on binary classification problems, but many astronomical applications require classifying objects into multiple categories—stellar spectral types, galaxy morphologies, or variable star classifications. The natural question is: can we extend our Gaussian Process Classification framework beyond the binary case?

The challenge goes beyond simply handling more categories. Naive approaches like one-vs-rest can lead to inconsistent decision boundaries and conflicting predictions where different binary classifiers disagree. For astronomical applications requiring principled uncertainty quantification, we need a coherent framework that ensures probabilities sum to one and decision boundaries are consistent across all classes.

The most principled extension uses the multinomial probit model, which models $K-1$ latent functions for a K-class problem (with one function fixed to zero for identifiability). Each function represents the score for class c relative to the reference class:

$$f_c(\mathbf{x}) \sim \mathcal{GP}(0, k_c(\mathbf{x}, \mathbf{x}')) \tag{14.158}$$

We can use the same kernel for all classes or allow different kernels to capture class-specific characteristics. Class assignment follows the simple rule:

$$y = \arg\max_c f_c(\mathbf{x}) \tag{14.159}$$

This creates consistent decision boundaries by design—the boundary between any two classes i and j is defined by the locus of points where $f_i(\mathbf{x}) = f_j(\mathbf{x})$, ensuring the input space is partitioned without gaps or overlaps.

The inference becomes substantially more complex than the binary case. With $K-1$

functions and N training points, we have $(K-1) \times N$ latent variables to infer simultaneously. The likelihood function for a training point $(\mathbf{x}, y = c)$ is:

$$p(y = c|\mathbf{f}(\mathbf{x})) = p(f_c(\mathbf{x}) > f_j(\mathbf{x}) \text{ for all } j \neq c) \tag{14.160}$$

This probability involves integrating over a truncated multivariate Gaussian distribution, which lacks a convenient closed form like the sigmoid function in binary classification. Unlike the binary case where we could use the probit approximation for closed-form solutions, the multiclass setting requires numerical approximation techniques.

The Laplace approximation extends to this setting by finding the mode of the posterior over all $(K-1) \times N$ latent variables and approximating with a Gaussian. However, the optimization problem is much higher-dimensional, and the Hessian matrix grows as $\mathcal{O}((K-1)^2 N^2)$. Even after obtaining the Gaussian approximation, computing predictive probabilities requires additional approximations for the multinomial integrals. For large-scale problems with many classes, the computational burden often becomes prohibitive, with memory requirements scaling as $\mathcal{O}((K-1)^2 N^2)$ and computational complexity increasing correspondingly.

Nevertheless, for moderate-scale astronomical problems where uncertainty quantification is essential, multiclass GP classification provides a principled framework that properly handles relationships between categories while maintaining the rigorous probabilistic foundation we developed for the binary case. The ability to express appropriate uncertainty about class membership—particularly for objects falling between well-defined categories—often justifies the additional computational complexity in scientific applications where misclassification has significant consequences.

14.14   Summary

Throughout this chapter, we have explored Gaussian Processes from multiple perspectives, building a comprehensive framework that extends our statistical toolkit to handle complex, nonlinear modeling problems. Our journey began with a fundamental limitation: while linear regression provides analytical solutions and rigorous uncertainty quantification, it requires explicit feature engineering that becomes intractable for complex astronomical phenomena. Gaussian Processes offer a solution to this dilemma by replacing explicit features with similarity measures encoded through kernel functions.

We developed two complementary views of Gaussian processes. The kernel trick perspective showed how to reformulate Bayesian linear regression entirely in terms of similarity measures, eliminating the need for explicit feature design while maintaining computational tractability. This view revealed that GPs are not fundamentally different from the linear models we studied earlier—they are a natural extension where we substitute kernel evaluations for explicit feature mappings. The function-space view provided a more direct probabilistic interpretation, treating GPs as distributions over functions and using familiar Gaussian conditioning to make predictions.

These perspectives unite in a powerful mathematical framework. Through either derivation path, we arrive at the same predictive equations that provide both point estimates and rigorous uncertainty quantification. The key insight is that we can work with potentially infinite-dimensional feature spaces through finite-dimensional kernel matrices, making flexible modeling computationally feasible.

The practical implementation of Gaussian processes requires careful attention to computational efficiency. The Cholesky decomposition emerged as a crucial technique for handling the matrix operations that dominate GP computations, reducing both computational cost and numerical instability. Hyperparameter optimization through the marginal likelihood provides a principled approach to model selection that automatically balances complexity against data fit, embodying Occam's razor without requiring explicit regularization.

For astronomical applications, Gaussian processes offer several key advantages. They adapt their complexity automatically to the data structure, becoming more flexible where observations are dense while maintaining appropriate uncertainty where data is sparse. This automatic complexity adaptation eliminates much of the manual tuning required by other approaches. Most importantly, GPs provide principled uncertainty quantification that distinguishes between measurement noise and model uncertainty—essential for scientific inference where understanding confidence levels is as important as making predictions.

Our extension to classification demonstrated how the same principles apply beyond regression problems. Through the Laplace approximation and probit function techniques from Chapter 9, we showed how to handle the nonlinear relationship between continuous latent functions and discrete class labels. The resulting framework maintains the flexibility of nonlinear decision boundaries while providing principled uncertainty estimates that help identify ambiguous cases requiring further investigation.

However, we cannot ignore the computational limitations of Gaussian processes. The

$\mathcal{O}(N^3)$ scaling with dataset size restricts direct application to moderate-sized problems, typically those with fewer than several thousand observations. While approximation methods can mitigate this limitation, the computational challenge remains a primary constraint on GP applicability to large-scale astronomical surveys.

Looking forward, this limitation points toward alternative approaches for flexible nonlinear modeling. Chapter 15 will explore neural networks as a different strategy that sacrifices some of the mathematical rigor and automatic uncertainty quantification of GPs in exchange for substantially better computational scalability. Neural networks can handle datasets far beyond the reach of standard GP methods and have revolutionized many areas of machine learning through their ability to learn complex patterns from massive datasets.

The relationship between GPs and neural networks should not be viewed as replacement but rather as complementary strengths. Neural networks excel at discovering complex patterns in large datasets and can scale to problems involving millions of observations. However, they often lack the rigorous uncertainty quantification that makes GPs valuable for scientific applications.

For astronomical applications, both approaches have specific niches. Gaussian processes remain ideal for problems requiring rigorous uncertainty quantification and principled treatment of sparse or irregular data. Examples include modeling stellar variability from ground-based photometry, characterizing exoplanet transit signals, or analyzing spectroscopic time series where understanding uncertainties is crucial for physical interpretation.

Neural networks excel when working with large, regularly sampled datasets where computational efficiency is paramount and when the complexity of underlying patterns exceeds what can be captured by kernel methods. They are particularly powerful for image analysis, large-scale classification problems, and situations where the goal is prediction accuracy rather than physical understanding.

Understanding both approaches—and their connections—provides a complete toolkit for tackling the diverse challenges of astronomical data analysis. As surveys become larger and more complex, the ability to choose the right tool for each problem becomes increasingly important. Gaussian processes represent the pinnacle of classical statistical learning methods, combining mathematical rigor with modeling flexibility. While their computational limitations prevent universal application, they remain invaluable for problems where their strengths align with scientific requirements.

Further Readings: The development of Gaussian Process theory builds upon centuries of advances in stochastic processes and functional analysis, with mathematical foundations provided by Aronszajn [1950] on reproducing kernel Hilbert spaces and connections to spatial statistics through Matheron [1963] and Cressie [1993]. For readers interested in the statistical framework, O'Hagan [1978] provides the Bayesian treatment of curve fitting with GP priors, while Wahba [1990] demonstrates deep connections between splines, smoothing, and Gaussian processes, with theoretical foundations in Kimeldorf and Wahba [1970]. The definitive modern treatment is Rasmussen and Williams [2006], which unifies decades of theory with practical algorithms. Connections between Gaussian processes and neural networks are explored in Neal [1996], revealing GPs as infinite-width limits of neural architectures. For computational efficiency, sparse approximations are developed in Csato and Opper [2002], Quiñonero-Candela and Rasmussen [2005], and Snelson and Ghahramani [2005], with the principled variational framework of Titsias [2009] providing automatic inducing point selection. Classification extensions through approximate inference are treated in Williams and Barber [1998] using Laplace approximation and Minka [2001] for expectation propagation, with comprehensive comparisons in Kuss and Rasmussen [2005]. Readers interested in hyperparameter learning should consult MacKay [1992] on the evidence framework, while Kennedy and O'Hagan [2001] demonstrates GP applications to computer model emulation. For rigorous mathematical treatment of interpolation theory, Stein [1999] provides comprehensive coverage of the Matérn class and theoretical properties.

Chapter 15

Neural Networks

Throughout this course, we have built a comprehensive foundation of statistical techniques, progressing from simple linear models through increasingly sophisticated methods. We began with linear regression and classification, advanced through Bayesian inference and sampling methods, explored Principal Component Analysis and clustering for unsupervised learning, and in the previous chapter examined Gaussian Processes as a powerful nonparametric approach. Neural networks represent the final step in this progression—a shift to the most flexible modeling approach we will cover.

The comparison between Gaussian Processes from Chapter 14 and neural networks reveals complementary strengths and limitations. While GPs provide a mathematically rigorous framework with principled uncertainty quantification and exact Bayesian inference, they face scalability limitations that become prohibitive for large datasets. Neural networks offer greater scalability and flexibility, capable of handling massive datasets and learning complex representations, but often with less formal uncertainty guarantees than Bayesian methods.

Neural networks are not new—the concept was proposed decades earlier before their recent prominence. The perceptron dates to 1958, and multilayer networks were studied in the 1980s. However, theoretical reasons initially suggested they would not work well, and computational limitations hindered their practical application. Their empirical success since around 2012-2013 has revolutionized machine learning, leading to breakthroughs across numerous domains despite incomplete theoretical understanding.

We have purposefully limited our coverage of neural networks in this "classical-centric"

textbook for two primary reasons. First, astronomical data typically exhibits lower complexity than real-life data. As we discussed since the beginning of the course, astronomical phenomena, while fascinating, are usually governed by a few key physical principles, in some cases dominated by gravity itself (for example, large-scale cosmic structures). This means that in many cases, we can achieve excellent results with simpler techniques, focusing on statistical rigor. Second, science requires uncertainty quantification. While progress has been made in neural networks in this regard, a full Bayesian approach—at least at the time of writing—is still not as well established as with classical techniques.

For astronomy, neural networks provide particular value in modeling complex, nonlinear systems where simpler techniques prove insufficient. Many astronomical phenomena exhibit intricate nonlinear relationships—stellar spectra depend nonlinearly on temperature, pressure, and chemical composition; galaxy morphologies form complex manifolds in image space; gravitational dynamics create non-Gaussian structure in the cosmic web. When the linear assumptions of earlier methods break down and the kernel choices for Gaussian Processes become unclear, neural networks offer a path forward.

The key innovation of neural networks lies in their feature learning approach: they discover useful representations directly from data without explicit human design. Instead of requiring astronomers to engineer features manually (as in linear models) or specify kernel functions (as in Gaussian Processes), neural networks automatically learn appropriate transformations through composition of simple nonlinear functions. This capability proves particularly valuable for tasks like galaxy classification or transient detection, where neural networks often discover patterns that human experts might overlook.

While neural networks and deep learning are vast topics deserving of their own dedicated textbook, it's important to provide a foundational understanding even in this classical-focused course. Our approach will be to introduce the essential concepts while drawing connections to the statistical methods we've already covered. We'll keep our discussion focused and practical, covering what you need to know to begin working with neural networks in astronomical applications.

What we'll cover represents just the basics of neural networks rather than the full complexity of modern deep learning. This aligns with our course's philosophy of starting with simpler, statistically rigorous methods before moving to more complex approaches. Given the powerful statistical tools we've already explored, neural networks should often be considered only when simpler methods prove insufficient for particularly complex problems.

Despite their reputation as mysterious "black boxes," neural networks build directly on the statistical principles we've established throughout this course. Their loss functions extend the maximum likelihood principles from our early chapters on regression and classification. Their optimization relies on the gradient-based methods we studied extensively in logistic regression, using the same stochastic gradient descent with enhanced algorithms like Adam. Even their regularization techniques parallel concepts from Bayesian inference—weight decay corresponds exactly to placing Gaussian priors on parameters, connecting to our discussions of ridge regression and Bayesian linear models.

This continuity reveals that neural networks represent natural extensions of familiar statistical methods rather than entirely foreign constructs. The trade-off between Gaussian Processes and neural networks mirrors broader themes in statistical learning: mathematical rigor versus computational flexibility, exact inference versus scalable approximation, interpretable models versus powerful black boxes.

This chapter progresses from basic neural network concepts through specialized architectures and advanced applications. We begin with feedforward networks and backpropagation, explore different architectures and their inductive biases, examine Bayesian approaches to neural networks, and conclude with modern applications including autoencoders, density estimation, and simulation-based inference. Throughout, we emphasize connections to the statistical framework developed in earlier chapters, showing how neural networks extend rather than replace the methods we've studied.

15.1   From Linear Regression to Neural Networks

Throughout this course, we have extensively studied linear models in which the output y depends linearly on some transformation of the input features. For regression tasks, this relationship takes the form $y = \mathbf{w}^T \boldsymbol{\phi}(\mathbf{x})$, while for classification, we employ $y = \sigma(\mathbf{w}^T \boldsymbol{\phi}(\mathbf{x}))$, where σ represents the logistic function.

The primary advantage of linear models lies in their mathematical tractability. For linear regression, we derived closed-form analytic solutions for maximum likelihood estimation, regularized optimization, posterior distributions, and predictive distributions. The optimization landscape is convex, guaranteeing a unique global optimum.

It is important to note that linear models are not limited to strictly linear relationships between input variables and outputs. Through appropriate feature transformations $\boldsymbol{\phi}(\mathbf{x})$, we

can capture various nonlinear patterns. For example, we might transform a single input x into polynomial features $[x, x^2, x^3]$, or create interaction terms like $x_1 x_2$ between inputs. The model remains "linear" because the output y can always be expressed as a linear combination of parameters $\mathbf{w}$:

$$y = \sum_i w_i \phi_i(\mathbf{x}) \tag{15.1}$$

where each $\phi_i(\mathbf{x})$ can be any nonlinear function of the inputs. The linearity refers to how the parameters w_i combine with the features - they only appear as multiplicative coefficients, never inside nonlinear functions like $\sin(w_i)$ or e^{w_i}. This linear parameter structure ensures the optimization problem remains convex, even when the relationship between inputs $\mathbf{x}$ and outputs y is highly nonlinear.

However, these methods share a limitation: they depend critically on our ability to define appropriate feature transformations $\boldsymbol{\phi}(\mathbf{x})$. For complex problems, especially those involving high-dimensional data with nonlinear relationships, manually designing suitable transformations becomes challenging. In essence, we must somehow divine the right nonlinear features before applying our linear model—a task requiring substantial domain expertise and often involving considerable trial and error.

Gaussian Processes, as we discussed in the previous chapter, offered one solution to this challenge by replacing explicit feature engineering with kernel functions. The kernel function implicitly defines features through the similarity measure it computes between data points. This allows GPs to capture complex nonlinear relationships without explicitly constructing features. However, as we discussed earlier, GPs face scalability limitations with large datasets.

Neural Networks as Learned Feature Transformations   Neural networks take a different approach. Instead of using kernels or manually engineered features, they learn the appropriate feature transformations directly from the data through a composition of simple nonlinear functions. This direct learning approach has proven effective, though interestingly, neural networks maintain a deep theoretical connection to Gaussian Processes. Under certain conditions, infinitely wide neural networks converge to Gaussian Processes with specific kernels determined by the network architecture—a relationship formalized in Neural Tangent Kernel theory.

Before we investigate how neural networks achieve this feat, let's first understand why simply composing multiple linear functions isn't sufficient. Consider two successive linear
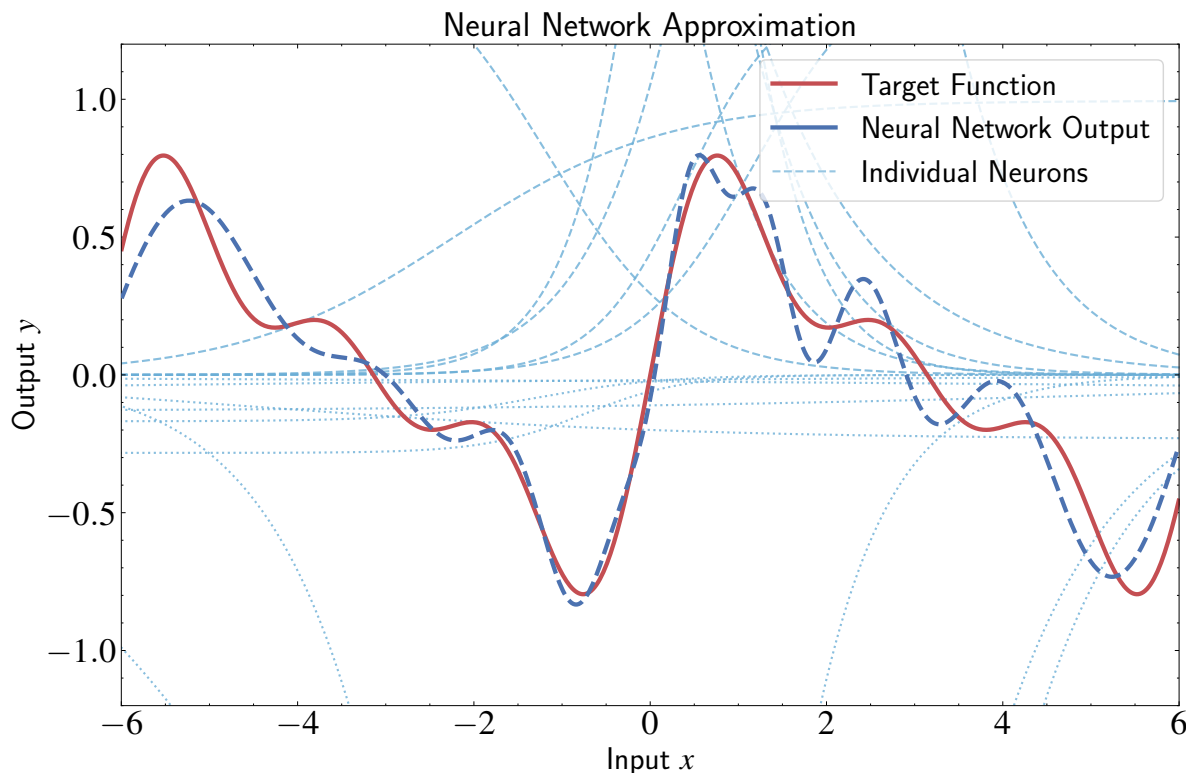
Figure 15.1: Visualization of how neural networks approximate complex functions through composition of simple nonlinear transformations. The figure demonstrates a neural network approximating a target function (red solid line) composed of multiple sine waves of different frequencies. The network output (blue dashed line) closely matches the target pattern by combining multiple sigmoid neurons (light blue lines). Each individual neuron has a simple sigmoidal shape defined by a weight w and bias b as $\sigma(wx + b)$, but when linearly combined with learned coefficients, they form a powerful approximator capable of representing complex nonlinear relationships. This illustrates the principle behind neural networks: while individual neurons perform only simple nonlinear transformations, their composition creates models with extraordinary flexibility. Unlike polynomial regression which requires manual feature engineering, or Gaussian Processes which use kernel functions, neural networks automatically learn the appropriate feature transformations directly from data through the weights and biases of each neuron.

transformations, where w represents weights and b represents bias terms:

$$y^{(1)} = \sum_i w_i^{(1)} x_i + b^{(1)} \tag{15.2}$$

$$y^{(2)} = \sum_j w_j^{(2)} y_j^{(1)} + b^{(2)} \tag{15.3}$$

Substituting the first equation into the second:

$$y^{(2)} = \sum_j w_j^{(2)}(\sum_i w_i^{(1)}x_i + b^{(1)}) + b^{(2)} = \sum_i(\sum_j w_j^{(2)}w_i^{(1)})x_i + (\sum_j w_j^{(2)}b^{(1)} + b^{(2)}) \quad (15.4)$$

This is simply another linear transformation with new weights $w_i = \sum_j w_j^{(2)}w_i^{(1)}$ and bias $b = \sum_j w_j^{(2)}b^{(1)} + b^{(2)}$. No matter how many linear transformations we stack, the result remains a linear combination of the form $y = \sum_i w_i x_i + b$.

The key insight behind neural networks is that we need to introduce nonlinearity between linear transformations. By "sandwiching" nonlinear activation functions between linear layers, we create models that can capture complex, nonlinear relationships. This simple idea—alternating linear transformations with nonlinear activations—forms the core of neural networks and enables them to approximate complex functions when properly structured.

The Artificial Neuron   The basic computational unit of a neural network is the artificial neuron, inspired loosely by biological neurons. In its elementary form, a single neuron applies a linear transformation followed by a nonlinear "activation function" to its inputs. For a neuron receiving inputs $\mathbf{x} = [x_1, x_2, \ldots, x_D]^T$, the output is calculated as:

$$y(\mathbf{x}, \mathbf{w}) = f\left(\sum_{j=1}^{D} w_j x_j + b\right) = f(\mathbf{w}^T\mathbf{x} + b) \quad (15.5)$$

Here, $\mathbf{w}$ is a vector of weights, b is a bias term, and f is the activation function.

The earliest form of artificial neuron, the perceptron, was proposed by Frank Rosenblatt in 1958. The perceptron used a step function as its activation:

$$f(z) = \begin{cases} 1 & \text{if } z \geq 0 \\ 0 & \text{if } z < 0 \end{cases} \quad (15.6)$$

This binary activation was directly inspired by the all-or-nothing firing behavior of biological neurons and aligned with the binary computing paradigms of that era. With this activation function, a single perceptron could classify linearly separable patterns by dividing the input space with a hyperplane.

The initial excitement around perceptrons was tempered by Marvin Minsky and Seymour Papert's 1969 book "Perceptrons," which demonstrated limitations of single-layer perceptrons—notably their inability to learn the XOR function or any other non-linearly

separable pattern. This critique, combined with the limited computing resources of the time, led to a decline in neural network research, often called the "AI winter."

Interest in neural networks resurged in the 1980s with the development of back-propagation, an efficient algorithm for training multi-layer networks. While we'll explore backpropagation in detail later in this chapter, its key innovation was enabling the training of networks with multiple layers, overcoming the limitations of single-layer perceptrons.

These networks replaced the discontinuous step function with continuous, differentiable activation functions, most commonly the sigmoid function:

$$f(z) = \frac{1}{1 + e^{-z}} \tag{15.7}$$

This change was necessary because gradient-based optimization methods require differentiable functions. The sigmoid function connects directly to logistic regression, effectively transforming each neuron into a logistic regression model whose inputs are transformations of the original features. The prevalence of the sigmoid function stems from neural networks' historical roots in classification tasks, following Rosenblatt's original perceptron. While modern neural networks have expanded beyond binary classification to tackle regression, generation, and many other problems, this early focus on classification problems influenced the initial choice of activation functions.

To understand what a single neuron can accomplish, consider astronomical spectroscopy. A single spectrum might contain thousands of wavelength measurements spanning from ultraviolet to infrared. A single neuron could learn to identify specific spectral features like the Balmer series in stellar spectra (Hα at 6563Å, Hβ at 4861Å, etc.), molecular absorption bands in cool stars, or the complex patterns of emission lines in active galactic nuclei. The neuron could also learn to recognize patterns across multiple wavelength regions simultaneously—such as the correlation between the 4000Å break and other metal absorption features that indicate a galaxy's age and metallicity. This ability to process high-dimensional spectral data makes even a single neuron a useful computational unit, capable of extracting astrophysical features that would be difficult to identify with simpler low-dimensional analyses.

Multi-Layer Composition Building on this foundation, the power of neural networks emerges through composition—combining multiple neurons in parallel and across multiple layers. This architecture allows the network to learn increasingly complex representations of
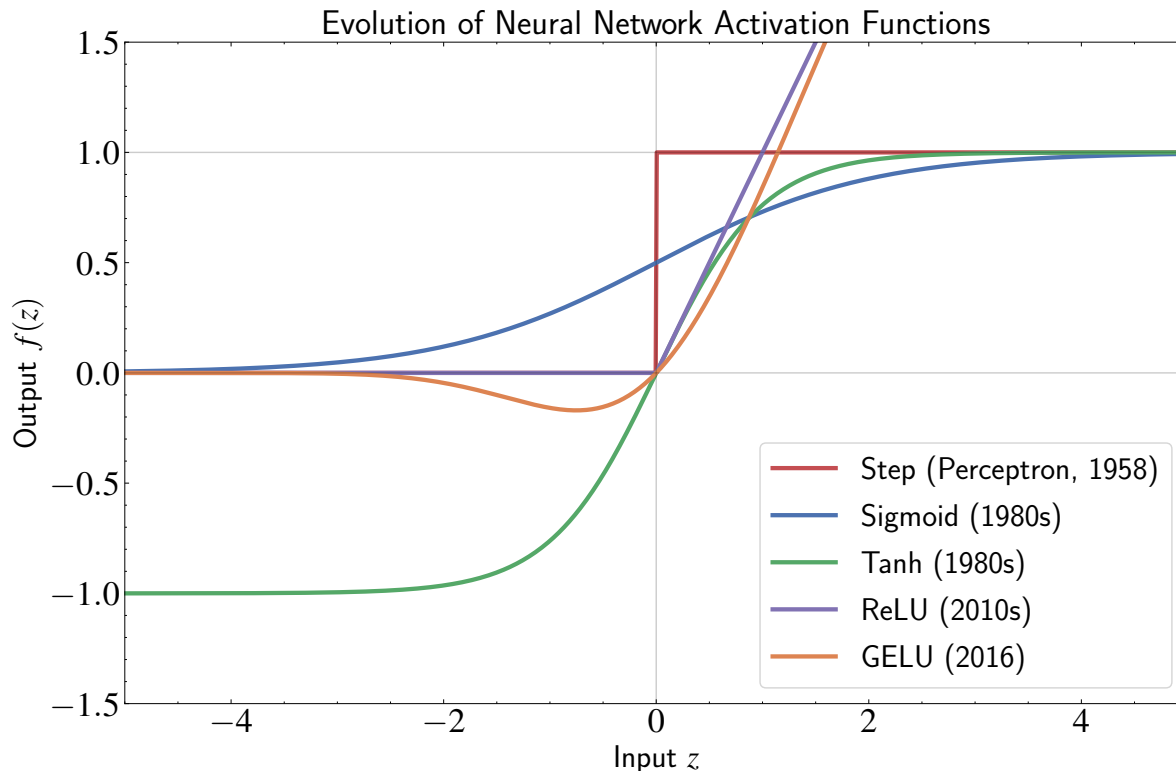
Figure 15.2: Evolution of activation functions in neural networks, highlighting the progression from early discrete models to modern differentiable alternatives. The Step function (red) was used in the original Perceptron (1958), creating a binary output that enabled basic linear classification but prevented gradient-based learning. The Sigmoid function (blue) and Tanh function (green), introduced in the 1980s, enabled backpropagation through their smooth, differentiable nature, though they suffered from vanishing gradient problems in deep networks. ReLU (purple), which became dominant in the 2010s, addressed this issue through its simple piecewise linear form that prevents saturation for positive inputs while providing true sparsity for negative inputs. GELU (orange), introduced in 2016, has become popular in modern transformer architectures, combining the benefits of ReLU with smooth transitions. This evolution reflects the requirement that introduced nonlinearity between linear transformations, which is essential for enabling neural networks to approximate complex functions through composition of simple operations. Each activation function represents a different trade-off between mathematical properties (differentiability, saturation, sparsity), with modern functions optimized for gradient-based learning in deep architectures.

the input data. For a single hidden layer network with M neurons in the hidden layer and a single output, the function becomes:

$$y(\mathbf{x}, \mathbf{W}^{(1)}, \mathbf{W}^{(2)}) = f^{(2)} \left(\sum_{j=1}^{M} w_j^{(2)} f^{(1)} \left(\sum_{i=1}^{D} w_{ji}^{(1)} x_i + b_j^{(1)} \right) + b^{(2)} \right) \qquad (15.8)$$

Here, $\mathbf{W}^{(1)}$ represents the weight matrix for the first layer (with elements $w_{ji}^{(1)}$), $\mathbf{W}^{(2)}$ contains the weights for the output layer, and $b_j^{(1)}$ and $b^{(2)}$ are the respective bias terms.
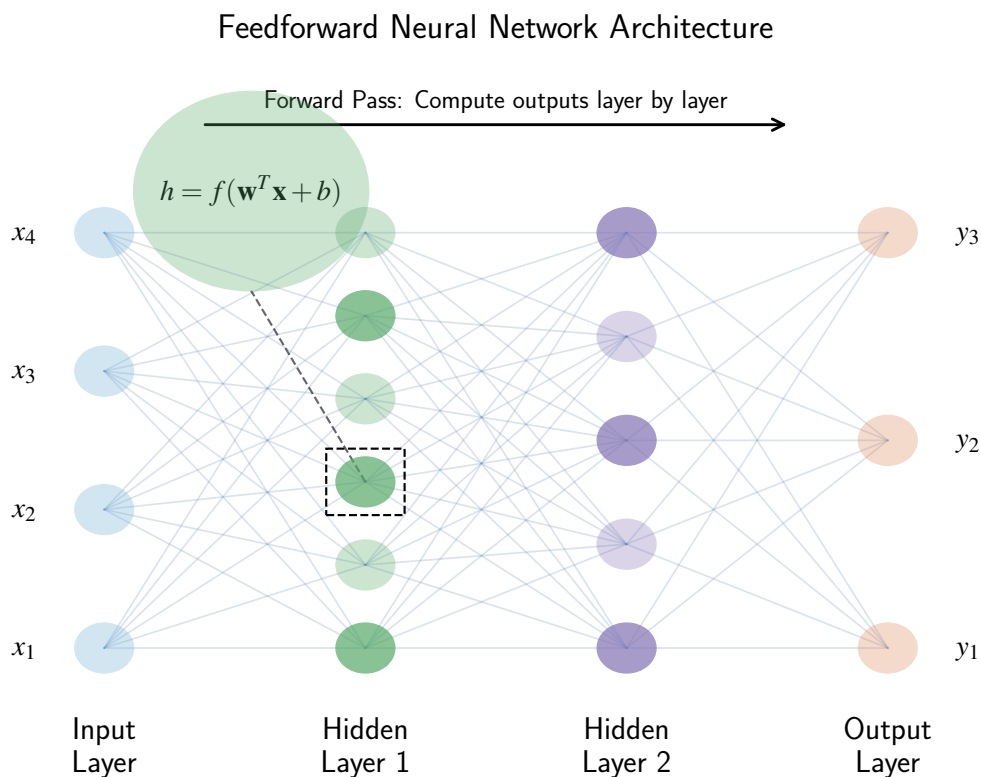

Figure 15.3: Architecture of a fully connected feedforward neural network, also known as a Multi-Layer Perceptron (MLP), with input, hidden, and output layers. Each circle represents a neuron, with connections showing the information flow from inputs (x_i) to outputs (y_j). Every neuron in one layer connects to every neuron in the subsequent layer, creating the "fully connected" structure. The magnified view shows the mathematical operation inside each neuron: a weighted sum of all inputs from the previous layer $(\mathbf{w}^T\mathbf{x}+b)$, passed through a nonlinear activation function f. During the forward pass, information propagates from left to right as each layer transforms the outputs from the previous layer. This composition of simple transformations enables the network to learn complex representations—early layers detect basic features while deeper layers combine these features into higher-level abstractions. The key insight of neural networks lies in this hierarchical composition: by stacking multiple nonlinear transformations, the network can approximate virtually any continuous function to arbitrary precision, as guaranteed by the Universal Approximation Theorem.

We can extend this to networks with multiple outputs and additional hidden layers by further composition. A deep neural network with L layers can be expressed recursively as:

$$\mathbf{h}^{(l)} = f^{(l)}(\mathbf{W}^{(l)}\mathbf{h}^{(l-1)} + \mathbf{b}^{(l)}) \tag{15.9}$$

where $\mathbf{h}^{(0)} = \mathbf{x}$ is the input, $\mathbf{h}^{(L)}$ is the output, and $\mathbf{h}^{(l)}$ represents the activations of the l-th

hidden layer.

This architecture is commonly known as a feedforward neural network, because information flows in one direction from inputs to outputs. These networks are also frequently called Multi-Layer Perceptrons (MLPs), though this is technically a misnomer since they use differentiable activation functions rather than the step function of the original perceptron. The term persists because these networks extend the perceptron concept to multiple layers.

The underlying principle is straightforward: by iteratively applying simple nonlinear transformations, we can approximate complex functions. To understand why this works, consider how each layer transforms the input space. The first layer creates a set of basic nonlinear transformations—essentially carving the input space into regions defined by each neuron's activation boundary. The second layer then combines these regions in new ways, creating more complex patterns. With each additional layer, the network can create increasingly intricate combinations of these patterns, much like how complex shapes can be built by combining simple geometric forms.

15.2   Theoretical Foundations of Neural Networks

Now that we understand how neural networks are constructed through layers of neurons and nonlinear activations, we can explore a mathematical result about their capabilities. While we've seen how these networks can create increasingly complex patterns through layer-wise transformations, you might wonder: just how powerful are they? The answer is quite remarkable and helps explain why neural networks have proven so useful across diverse scientific applications despite their relatively simple building blocks.

The key theoretical result is the Universal Approximation Theorem, which establishes that even a two-layer network with a single hidden layer can, in principle, approximate any continuous function to arbitrary accuracy, given enough hidden units. This property is known as the Universal Approximation Property. While the formal proof involves advanced mathematical concepts beyond the scope of this course, we can understand its significance by drawing parallels to familiar mathematical ideas.

To understand this theorem intuitively, consider how neural networks transform data. Each neuron creates nonlinear boundaries in the input space through its activation function. When we add more neurons, each with its own activation function and different weights and biases, we're adding more building blocks to our approximation. Each neuron contributes its

own "bump" or "edge" to the function space, and by carefully combining these basic shapes—like assembling a complex structure from simple geometric forms—we can construct virtually any continuous function to arbitrary precision.

Those familiar with real analysis might recognize similarities to the Stone-Weierstrass theorem, which shows that any continuous function on a closed interval can be uniformly approximated by polynomials. In physics, we see a similar principle with Fourier series, which allow us to represent any periodic function as a sum of sines and cosines. The universal approximation property of neural networks extends these ideas to a different class of basis functions—the outputs of individual neurons—to build complex approximations.

This property has profound implications for scientific applications. In principle, a neural network could approximate any continuous function in nature—from the gravitational interactions of celestial bodies to the spectral features of distant stars, or even something as complex as human consciousness (assuming, of course, that such phenomena can be represented as continuous functions).

Practical Limitations of the Universal Approximation Theorem   While the universal approximation theorem establishes the theoretical power of neural networks, it comes with important practical limitations. The theorem guarantees that a solution exists but provides no guidance on how to find it efficiently. The appropriate weights are hidden somewhere in a vast, high-dimensional space, making the search for optimal parameters a challenge. Moreover, the theorem only proves the existence of a sufficiently large network without specifying the minimum size needed for any particular problem.

This gap between theoretical capability and practical implementation helps explain the historical skepticism toward neural networks. For decades after their initial proposal, researchers harbored two main concerns. First, the computational demands seemed prohibitive—training even modest networks required computing resources that wouldn't become widely available for many years. Second, the networks' vast number of parameters appeared to invite overfitting, similar to fitting high-degree polynomials to limited data. According to statistical learning theory, models with more parameters than training examples should generalize poorly to new data. Yet intriguingly, neural networks often defied this expectation.

At first glance, neural networks seemed reminiscent of epicycles in astronomy—adding complexity without necessarily improving understanding. Just as epicycles were used to patch the geocentric model of the solar system rather than adopting the simpler heliocentric

view, neural networks appeared to be adding layers of parameters rather than developing better theories. The lack of interpretability further reinforced this perception—unlike linear models where coefficients have clear meanings, neural network parameters often resist straightforward interpretation.

What changed this perspective was the persistence of neural network research coupled with remarkable empirical success across diverse domains, computational advances (particularly GPUs originally designed for video games), and the availability of larger datasets. These successes came as a genuine surprise to many machine learning practitioners who were still pursuing more statistically grounded kernel-based techniques like Gaussian Processes.

Modern Theoretical Understanding Despite their empirical success, some criticisms of neural networks persist, particularly in fields like astronomy. While some criticisms are justified, many are not. A legitimate limitation of neural networks, as we'll see, concerns Bayesian treatment. Although we know how to optimize neural networks (analogous to finding the MLE solution in linear regression), implementing fully Bayesian neural networks remains challenging. This limitation is important for scientific applications where uncertainty quantification is crucial.

However, many common criticisms of neural networks are less well-founded. For instance, they're often dismissed as "black boxes," yet it's important to note that feature engineering in linear regression is often equally non-physical and based on trial and error. Similarly, kernel-based methods can be just as opaque in practice.

It's also worth recognizing that the empirical success of neural networks has spawned entirely new branches of mathematics aimed at understanding their structure and behavior. This situation parallels how we developed steam engines before fully understanding the laws of thermodynamics. And just as thermodynamic theory eventually allowed us to dramatically improve engine efficiency, the emerging "Science of AI" is providing insights that enable more effective neural network applications. While the details of this field are beyond the scope of this introductory course, it's important to recognize that many criticisms of neural networks are being addressed through rigorous theoretical work.

The theoretical developments in understanding neural networks have spawned entirely new branches of mathematics. For example, researchers have discovered phenomena like double descent, which challenges our traditional understanding of model complexity and performance, and the Neural Tangent Kernel, which establishes deep connections between
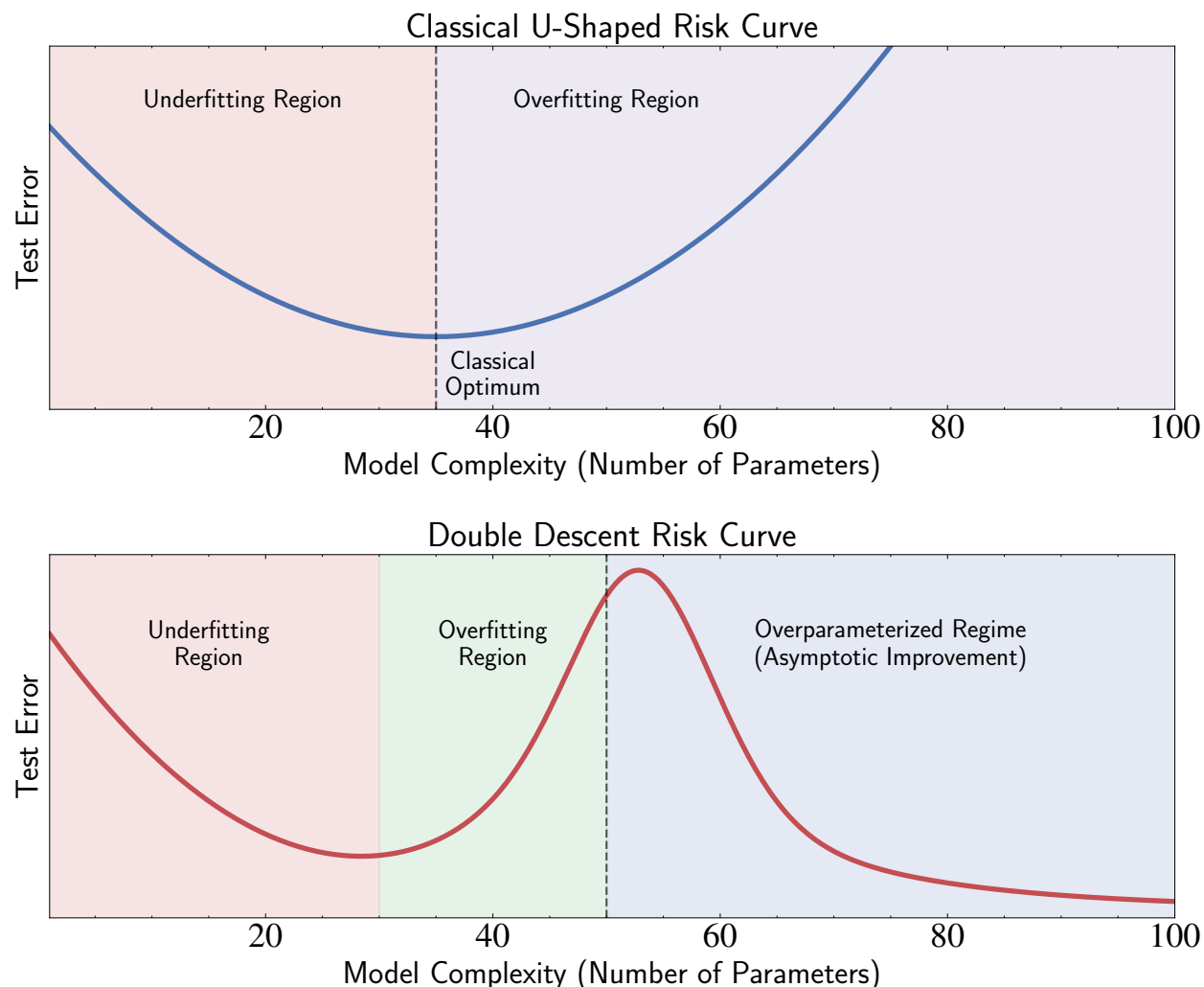
Figure 15.4: Comparison between classical statistical learning theory and the modern double descent phenomenon observed in neural networks. The top panel shows the traditional U-shaped risk curve that has guided model selection for decades. In this classical view, as model complexity increases, test error initially decreases (addressing underfitting), reaches an optimal point, and then increases indefinitely as the model overfits. The bottom panel illustrates the double descent phenomenon, where test error follows a more complex pattern: it first decreases to a local minimum (similar to the classical curve), then increases as the model approaches the interpolation threshold (where parameters equal training samples), but—contrary to classical theory—begins decreasing again in the overparameterized regime, eventually achieving lower error than the first minimum. This unexpected asymptotic improvement in highly overparameterized models helps explain why modern neural networks with millions or billions of parameters can generalize well despite having far more parameters than training examples. This phenomenon has challenged conventional statistical wisdom and sparked new theoretical frameworks to understand the generalization capabilities of deep learning models.

neural networks and the kernel methods we studied with Gaussian Processes. We'll explore these theoretical insights in detail later in this chapter, as they provide important perspectives on why neural networks work so well in practice despite seeming to violate classical statistical wisdom.

In the remainder of this chapter, rather than getting into details of these theoretical aspects, we'll focus on the practical implementation of neural networks, as most practitioners do. We'll explore training methods, particularly backpropagation, which makes efficient optimization of these complex models possible. We'll also examine applications in astronomy, connecting these advanced methods back to the statistical principles we've developed throughout this course.

15.3   Training Neural Networks

Having explored the theoretical foundations of neural networks, let's turn to the practical question of how to train them. While neural networks may seem complex due to their nested structure, we can train them using familiar gradient-based methods that we've studied throughout this course. The key insight is that training neural networks represents a natural extension of optimization principles we already understand.

An advantage of neural networks is their flexibility in handling inputs and outputs of any dimension through matrix multiplication. Unlike simpler models that often require fixed input and output dimensions, neural networks can be designed to map from $\mathbb{R}^D$ to $\mathbb{R}^K$ for any dimensions D and K. This mapping is achieved through a series of matrix multiplications and nonlinear transformations:

$$\mathbf{h} = f(\mathbf{W}\mathbf{x} + \mathbf{b}) \tag{15.10}$$

where $\mathbf{W} \in \mathbb{R}^{M \times D}$ is a weight matrix mapping from D input dimensions to M hidden dimensions, $\mathbf{b} \in \mathbb{R}^M$ is a bias vector, and f is a nonlinear activation function applied element-wise. The input layer accepts a vector $\mathbf{x} \in \mathbb{R}^D$, and through appropriate choice of weight matrices in subsequent layers, eventually produces an output vector in $\mathbb{R}^K$. The hidden layers can have any number of neurons M, with each layer potentially having different dimensions, providing flexible transformations between input and output spaces. This dimensional flexibility through matrix operations is particularly powerful for tasks like multi-class classification, where we need C outputs (one per class) regardless of input dimension.

Loss Functions from Maximum Likelihood Let's begin with the question: what exactly are we trying to optimize? Just as we've done throughout this course, we'll follow the principle of maximum likelihood estimation (MLE) - we want to find parameters that maximize the probability of observing our data. The various loss functions we use for neural networks emerge naturally from this statistical foundation, not as arbitrary choices.

For regression tasks with inputs $\mathbf{x}_i \in \mathbb{R}^D$ and outputs $y_i \in \mathbb{R}$, if we assume homoscedastic Gaussian noise (as we did with linear regression), maximizing the likelihood leads directly to minimizing the mean squared error (MSE):

$$L_{\text{MSE}}(\mathbf{w}) = \frac{1}{N} \sum_{i=1}^{N} (y_i - f_{\mathbf{w}}(\mathbf{x}_i))^2 \tag{15.11}$$

When we have heteroscedastic measurement uncertainties σ_i in our astronomical observations, incorporating these into our likelihood naturally gives us the weighted MSE:

$$L_{\text{weighted MSE}}(\mathbf{w}) = \frac{1}{N} \sum_{i=1}^{N} \frac{(y_i - f_{\mathbf{w}}(\mathbf{x}_i))^2}{\sigma_i^2} \tag{15.12}$$

This is exactly what we derived earlier in the course for linear regression under heteroscedastic Gaussian noise.

The key difference from linear regression is not in the statistical principles, but in the form of $f_{\mathbf{w}}(\mathbf{x}_i)$. Instead of a simple linear function, it's now our neural network's output - a flexible function composed of multiple transformations:

$$f_{\mathbf{w}}(\mathbf{x}) = f^{(L)}(\mathbf{W}^{(L)} f^{(L-1)}(\mathbf{W}^{(L-1)} ... (f^{(1)}(\mathbf{W}^{(1)}\mathbf{x} + \mathbf{b}^{(1)})...) + \mathbf{b}^{(L-1)}) + \mathbf{b}^{(L)}) \tag{15.13}$$

For binary classification, following the same likelihood principles we used in logistic regression, we model the probability of class membership using the sigmoid function:

$$p(y = 1|\mathbf{x}) = \sigma(f_{\mathbf{w}}(\mathbf{x})) = \frac{1}{1 + e^{-f_{\mathbf{w}}(\mathbf{x})}} \tag{15.14}$$

Maximizing the likelihood of our observed binary outcomes leads directly to minimizing the

binary cross-entropy (BCE):

$$L_{\text{BCE}}(\mathbf{w}) = -\frac{1}{N} \sum_{i=1}^{N} [y_i \log(\sigma(f_{\mathbf{w}}(\mathbf{x}_i))) + (1 - y_i) \log(1 - \sigma(f_{\mathbf{w}}(\mathbf{x}_i)))] \tag{15.15}$$

For multi-class problems with C classes, the same maximum likelihood principle applies. We model class probabilities using the softmax function (a generalization of the sigmoid to multiple classes), and maximizing the likelihood gives us the cross-entropy loss:

$$L_{\text{CE}}(\mathbf{w}) = -\frac{1}{N} \sum_{i=1}^{N} \sum_{c=1}^{C} y_{ic} \log(p_{\mathbf{w}}(\mathbf{x}_i)_c) \tag{15.16}$$

where $p_{\mathbf{w}}(\mathbf{x}_i)_c$ is the predicted probability for class c:

$$p_{\mathbf{w}}(\mathbf{x}_i)_c = \frac{e^{f_{\mathbf{w}}(\mathbf{x}_i)_c}}{\sum_{j=1}^{C} e^{f_{\mathbf{w}}(\mathbf{x}_i)_j}} \tag{15.17}$$

It is important to note that these loss functions aren't arbitrary - they're direct consequences of applying maximum likelihood estimation to different types of data. Whether we're using linear regression, logistic regression, or neural networks, we're following the same statistical principle: finding parameters that make our observed data most probable under our model assumptions.

Gradient Descent Optimization   With the loss function defined, the central question becomes: how do we find the weights $\mathbf{w}$ that minimize these potentially complex, non-convex functions? The approach remains gradient descent, a method we've studied extensively in this course. The basic update rule is unchanged:

$$\mathbf{w}^{(t+1)} = \mathbf{w}^{(t)} - \eta \nabla_{\mathbf{w}} L(\mathbf{w}^{(t)}) \tag{15.18}$$

where η is the learning rate and $\nabla_{\mathbf{w}} L(\mathbf{w}^{(t)})$ is the gradient of the loss function with respect to all weights at iteration t.

For neural networks, calculating this gradient becomes more complex than for simpler models. In logistic regression, we derived a compact expression for the gradient using the chain rule. For a single example in binary classification, this was simply:

$$\nabla_{\mathbf{w}} L(\mathbf{w}) = (\sigma(\mathbf{w}^T \mathbf{x}) - y)\mathbf{x} \tag{15.19}$$

For neural networks, while the same chain rule principle applies as in logistic regression, the gradient calculation becomes considerably more complex. We need to propagate derivatives through multiple layers of nonlinear transformations, creating an intricate cascade of derivatives flowing backward through the network. This challenge is solved by the backpropagation algorithm, which we'll examine in detail in the next section.

Before diving into backpropagation, however, let's address another practical challenge in computing gradients. Just as we encountered with logistic regression, calculating gradients over the entire training set for each update would be prohibitively expensive when working with large datasets. To address this, we use Stochastic Gradient Descent (SGD), which we covered in detail earlier in this course. As a reminder, SGD approximates the true gradient using a small random subset or "mini-batch" of training examples:

$$\mathbf{w}^{(t+1)} = \mathbf{w}^{(t)} - \eta \nabla_{\mathbf{w}} L_B(\mathbf{w}^{(t)}) \tag{15.20}$$

where L_B is the loss computed on a mini-batch B of training examples randomly sampled from the full dataset.

As we discussed extensively during our treatment of logistic regression, this stochastic approach offers several critical advantages that make it particularly well-suited for neural network training:

1. **Computational efficiency:** By using mini-batches instead of the full dataset, we can dramatically reduce the computational cost per update. This allows for more frequent parameter updates and faster convergence in terms of wall-clock time.

2. **Implicit regularization:** The inherent noise introduced by sampling different mini-batches acts as a form of regularization. This stochastic behavior helps the optimization process escape shallow local minima and saddle points in the loss landscape, potentially leading to better solutions.

This latter point deserves emphasis. One of the historical criticisms of neural networks was the concern that their non-convex loss landscapes would contain numerous local minima that would trap optimization algorithms. While recent theoretical work suggests that the optimization landscape may be more benign than initially feared, the stochasticity of SGD still provides valuable insurance against potential optimization challenges. By introducing noise into the gradient estimates, SGD helps the optimization process explore the parameter space more thoroughly and avoid getting stuck in suboptimal regions.
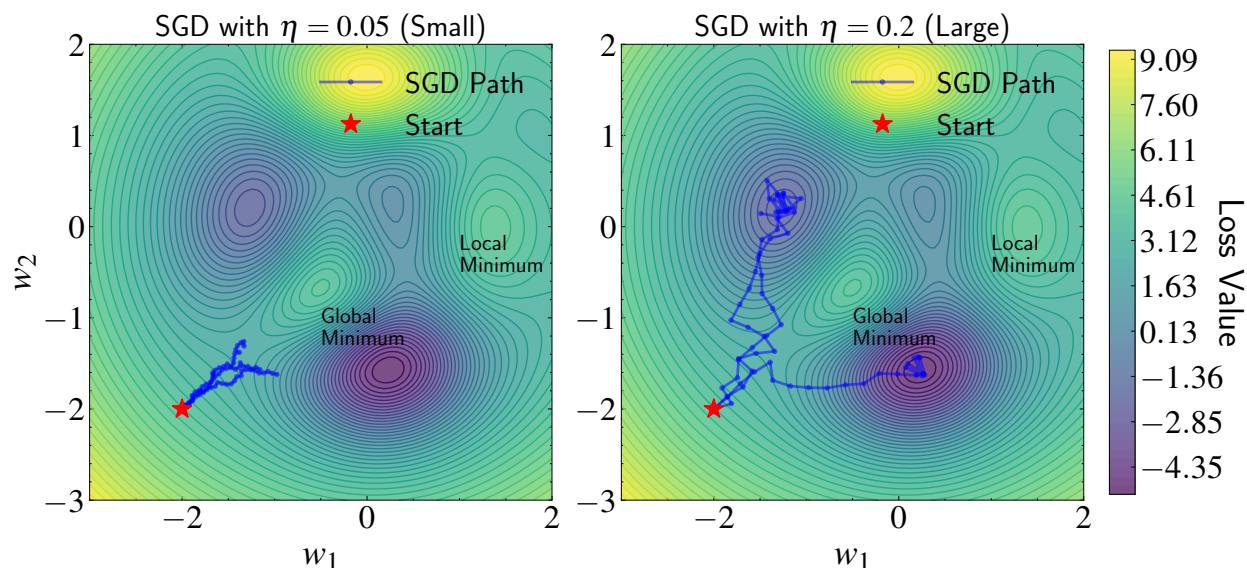
Figure 15.5: Stochastic Gradient Descent (SGD) with different learning rates navigating a non-convex loss landscape. While this visualization was originally introduced in our discussion of logistic regression, the same principles apply directly to neural network training. The contour plots represent a simplified 2D projection of a high-dimensional loss landscape, with darker regions indicating lower loss values. The left panel shows SGD with a small learning rate, which follows the gradient more precisely but may become trapped in local minima. The right panel demonstrates how a larger learning rate enables the optimization to escape shallow local minima, potentially reaching better global solutions. In neural networks, this behavior is particularly important due to the highly non-convex nature of the loss landscapes. The stochasticity introduced by mini-batch sampling—as discussed in the text—provides an additional mechanism that works in concert with the learning rate to help navigate these complex loss surfaces.

The choice of mini-batch size involves a trade-off that can be understood through the analogy of a vehicle navigating a terrain. A large batch size is like a big, heavy vehicle—it moves more precisely along the gradient but may struggle to navigate narrow paths that might lead to better solutions. A small batch size is like a lighter, more agile vehicle—it might not always move in the optimal direction, but its ability to explore more varied paths can sometimes lead to superior final positions. Common batch sizes range from 32 to 256 examples, though the optimal choice depends on the specific problem and available computational resources.

The learning rate η plays a similarly crucial role. Too large a value can cause the optimization to diverge, while too small a value leads to slow convergence. Modern practice typically employs sophisticated learning rate schedules:

1. **Inverse time decay**: The learning rate follows $\eta^{(t)} = \eta_0/(1 + \gamma t)$, where η_0 is the initial learning rate and γ controls the decay speed. Like switching from a large wheel to a smaller one, this schedule enables quick initial progress followed by increasingly precise updates.

2. **Cosine annealing with warm-up**: The learning rate varies according to $\eta^{(t)} = \eta_{\min} + \frac{1}{2}(\eta_0 - \eta_{\min})(1 + \cos(t\pi/T))$. Drawing inspiration from metallurgy, this schedule typically runs for $T/4$ steps before restarting at η_0, creating cycles of exploration (high learning rate) and exploitation (low learning rate) that help escape local minima.
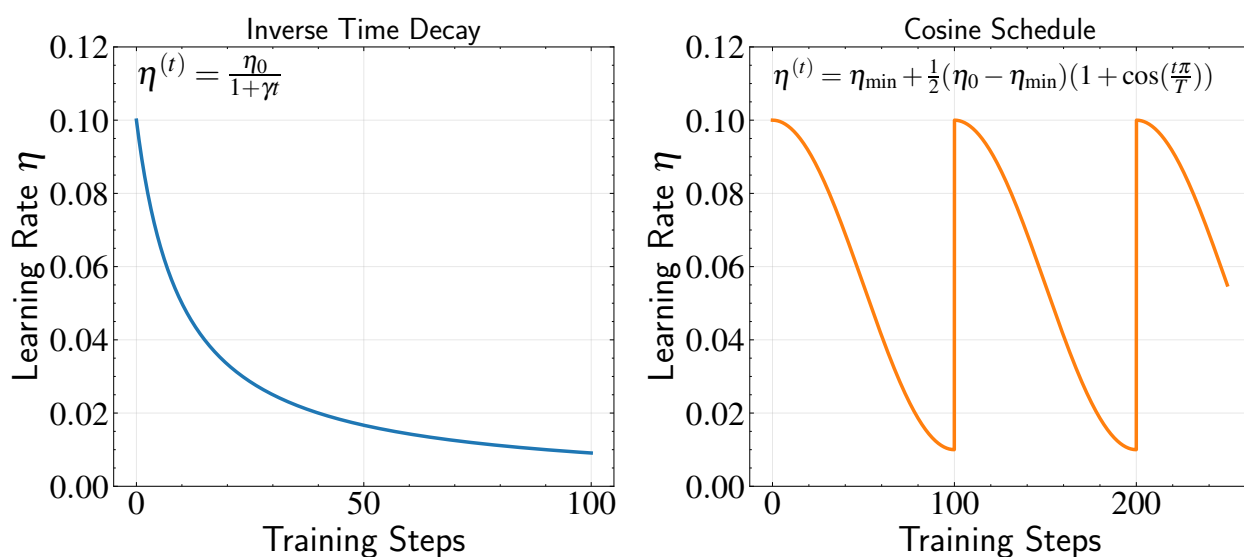

Figure 15.6: Common learning rate schedules used in neural network training. The left panel shows inverse time decay, where the learning rate gradually decreases according to $\eta^{(t)} = \eta_0/(1 + \gamma t)$. This schedule enables larger initial steps for faster progress in early training, followed by progressively smaller steps for fine-tuning. The right panel illustrates cosine annealing with restarts, where the learning rate oscillates according to $\eta^{(t)} = \eta_{\min} + \frac{1}{2}(\eta_0 - \eta_{\min})(1 + \cos(t\pi/T))$. This cyclical approach is particularly effective for neural networks, as it creates alternating phases of exploration (high learning rate) and exploitation (low learning rate), helping the optimization process escape local minima in complex loss landscapes. The restart mechanism, where the learning rate periodically returns to its maximum value, allows the optimizer to explore different regions of the parameter space.

These scheduling techniques have proven particularly important for neural networks, where different layers may benefit from different learning dynamics at various stages of training. The cyclic nature of cosine annealing with restarts is especially effective for navigating the complex loss landscapes characteristic of deep networks.

Advanced Optimization Algorithms   Beyond basic SGD, neural network training has benefited from enhanced optimization algorithms that share interesting parallels with MCMC methods we studied earlier. The most widely used is Adam (Adaptive Moment Estimation), which, like MCMC, generates a sequence of parameter updates that can be viewed as a chain. Similar to how MCMC methods use proposal distributions and acceptance rules to explore parameter space, Adam employs adaptive step sizes and momentum to navigate the loss landscape. The key ideas behind Adam are:

1. **Momentum:** This maintains a moving average of past gradients to continue moving in promising directions, helping the optimization process maintain velocity in productive directions while dampening oscillations.

2. **Adaptive learning rates:** Similar to how adaptive MCMC methods adjust their proposal distributions based on the chain's history, Adam adjusts learning rates for each parameter based on gradient history.

Just as we estimate moments in MCMC by taking running averages over the chain, Adam estimates the first and second moments of the gradients through exponential moving averages:

$$m_t = \beta_1 m_{t-1} + (1 - \beta_1)g_t \tag{15.21}$$

$$v_t = \beta_2 v_{t-1} + (1 - \beta_2)g_t^2 \tag{15.22}$$

where g_t is the current gradient. Here, β_1 and β_2 (typically set to 0.9 and 0.999) act like window sizes for the moving average – larger values give more weight to historical gradients, similar to how we might use longer MCMC chains to get more accurate moment estimates. The exponential decay ensures that recent gradients have more influence, while still maintaining some memory of past updates.

When we initialize these moving averages at zero ($m_0 = 0$ and $v_0 = 0$), they are biased toward zero in the early steps of training. To understand this bias, consider the first moment estimate m_1 after one step: it will be $(1 - \beta_1)g_1$, which is much smaller than the true gradient g_1 since β_1 is close to 1. This bias gradually diminishes as training progresses, but it can slow down early training.
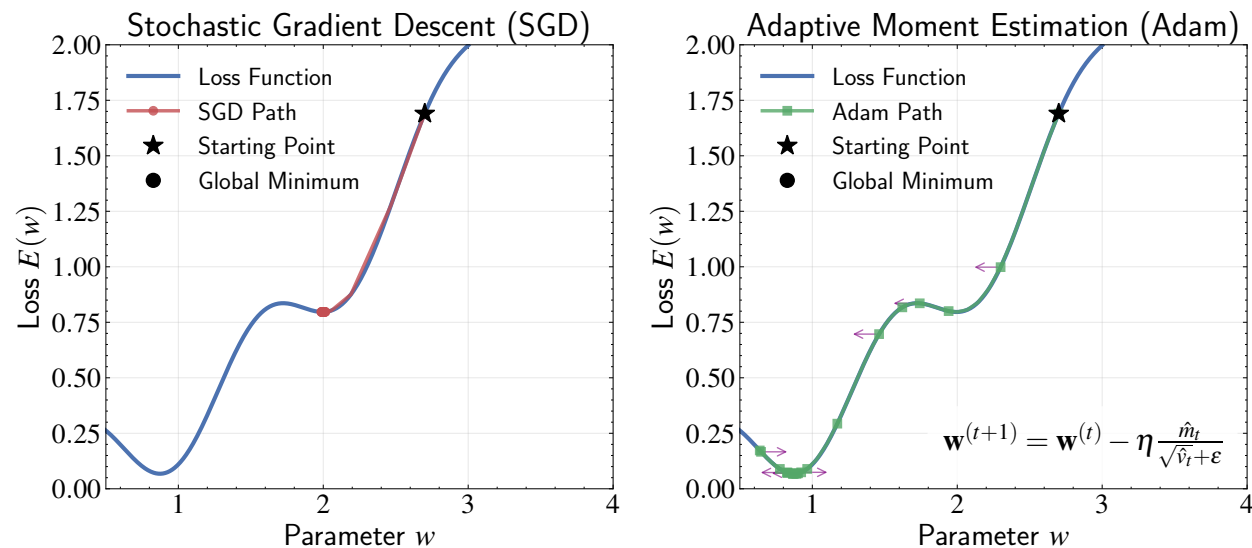
Figure 15.7: Comparison of Stochastic Gradient Descent (SGD, left) and Adaptive Moment Estimation (Adam, right) on a loss landscape with varying curvature. Both optimizers start from the same point (black star) and attempt to find the global minimum (black circle). SGD uses a fixed learning rate that causes oscillatory behavior in regions of high curvature and prevents precise convergence to the minimum. In contrast, Adam combines momentum (shown by purple arrows) with adaptive learning rates to navigate the loss landscape more effectively. The momentum term $\hat{m}_t$ acts as a moving average of past gradients, helping Adam maintain consistent progress through regions with noise or high oscillation. Meanwhile, the second moment term $\sqrt{\hat{v}_t}$ scales each parameter's update according to its gradient history, automatically taking smaller steps in directions with high gradient variance. Dividing the momentum term by the second moment estimate creates these adaptive learning rates, allowing Adam to make rapid progress in flat regions while precisely converging to minima without overshooting.

To correct for this initialization bias, Adam applies a correction factor:

$$\hat{m}_t = \frac{m_t}{1 - \beta_1^t} \tag{15.23}$$

$$\hat{v}_t = \frac{v_t}{1 - \beta_2^t} \tag{15.24}$$

These correction terms account for the number of steps t taken so far. Early in training when t is small, the denominators $(1 - \beta_1^t)$ and $(1 - \beta_2^t)$ are also small, effectively boosting the estimates to compensate for the initialization bias. As training progresses and t increases, these terms approach 1, and the correction becomes negligible.

Finally, these bias-corrected moments determine the parameter update:

$$\mathbf{w}^{(t+1)} = \mathbf{w}^{(t)} - \eta \frac{\hat{m}_t}{\sqrt{\hat{v}_t} + \epsilon} \tag{15.25}$$

The intuition behind Adam connects well with MCMC concepts: just as MCMC methods need to take smaller steps in regions of high curvature and larger steps in flatter regions, Adam automatically adapts its step sizes based on the local geometry of the loss surface. Parameters experiencing consistent gradients (analogous to regions of smooth probability density in MCMC) take larger steps, while those with highly variable gradients (like regions of high curvature in MCMC) take smaller, more cautious steps. This adaptive behavior, reminiscent of the sophisticated proposal mechanisms in modern MCMC methods, has made Adam the optimizer of choice for most deep learning applications.

Regularization Techniques Having explored optimization techniques for neural networks, we now turn to a challenge that should feel very familiar from our earlier discussions: preventing overfitting. For astute readers, you'll notice that many of the techniques we'll discuss here directly parallel the classical statistical methods we covered in previous chapters. This recurring theme—that modern deep learning often rediscovers and builds upon classical statistical principles—continues to prove insightful.

Consider weight decay (or L2 regularization), one of the regularization techniques in neural networks. If this sounds familiar, it should—we encountered this exact same principle when discussing ridge regression. Just as before, we add a penalty term to the loss function that grows quadratically with the magnitude of the weights:

$$L_{\text{reg}}(\mathbf{w}) = L(\mathbf{w}) + \lambda \|\mathbf{w}\|_2^2 \tag{15.26}$$

The gradient update reveals the same intuitive behavior we saw in ridge regression—each weight update includes a decay term:

$$\mathbf{w}^{(t+1)} = \mathbf{w}^{(t)} - \eta(\nabla L(\mathbf{w}^{(t)}) + 2\lambda \mathbf{w}^{(t)}) = (1 - 2\eta\lambda)\mathbf{w}^{(t)} - \eta \nabla L(\mathbf{w}^{(t)}) \tag{15.27}$$

This multiplicative decay factor $(1 - 2\eta\lambda)$ explains the name "weight decay"—as the factor is less than 1, it gradually reduces the magnitude of weights in each training step when there are no opposing gradients. The term "decay" refers to this systematic reduction in weight magnitudes over training iterations. But more importantly, it implements the same principle of parameter shrinkage we studied extensively in our treatment of linear models.

And just as we interpreted ridge regression from a Bayesian perspective, here too we can recognize weight decay as equivalent to placing a zero-mean Gaussian prior on the weights:

$$p(\mathbf{w}) \propto \exp(-\lambda\|\mathbf{w}\|_2^2) \tag{15.28}$$

The primary difference from our earlier encounters with this technique is scale: in neural networks, this regularization affects not just a single layer of weights but propagates throughout the entire network hierarchy. Nevertheless, the principle remains unchanged—we're expressing our preference for simpler models through the same mathematical framework we developed much earlier in this course.

Another common technique in practice is early stopping. Its implementation directly applies the cross-validation principles we established in the first few chapters: during training, we monitor both the training loss and the validation loss (computed on a held-out portion of the data not used for gradient updates). The validation loss typically decreases initially along with the training loss, but as the model begins to overfit, the validation loss will start increasing while the training loss continues to decrease. The principle of early stopping is to save the model parameters at the point of minimum validation loss and terminate training once we've found this minimum.

Early stopping is conceptually identical to the model selection procedures we've used throughout this course. By using the validation set to determine when to stop training, we're effectively using it to select the optimal complexity of our model. While ideally the validation set should be separate from the test set, in practice with limited astronomical data, these sets are sometimes combined. This compromise is not theoretically optimal but represents a practical approach when data is scarce.

Training neural networks can sometimes seem more art than science, given the multitude of choices we need to make—from optimization algorithms to regularization techniques. However, this complexity is not unique to neural networks. Even in linear models, we faced similar challenges in selecting features or kernel functions. The key difference with neural networks lies in the selection of hyperparameters—learning rate, regularization strength, network architecture, activation functions, batch size, and more. While this may seem daunting at first, for many astronomical applications with modest data sizes, a simple grid or random search across the key hyperparameters is often sufficient and practical.

The most important hyperparameters to focus on are typically the learning rate and network architecture (depth and width), which have the largest impact on performance.

Other choices like regularization strength and optimizer selection often have more moderate effects, while parameters specific to optimizers (like momentum values) can usually be set to established defaults.

When simple grid or random search proves insufficient, more sophisticated approaches like Bayesian optimization can be valuable. Bayesian optimization treats the model's performance as a function of its hyperparameters and uses a Gaussian Process to model this relationship, leveraging the GP's uncertainty estimates to guide the search toward promising regions of hyperparameter space. While a detailed treatment is beyond our current scope, it represents a marriage of classical statistical techniques with modern optimization needs.

An encouraging development in the field has been the emergence of certain hyperparameter choices that perform well across a wide range of tasks. For instance, the cosine annealing schedule with warm restarts has proven effective across diverse problems, reducing the need for extensive tuning. These robust settings often provide good starting points for many astronomical applications. While neural networks do introduce additional complexity in terms of hyperparameter selection, the combination of systematic search and cross-validation principles we've discussed throughout this course often provides satisfactory results for most astronomical problems.

15.4   Backpropagation: Efficient Gradient Calculation

Having explored the theory and training approaches for neural networks, we now confront a practical challenge: how do we efficiently calculate gradients in these complex, nested architectures? This question is crucial because gradient computation forms the foundation of neural network training.

Let's start with the basic principle. Neural networks are trained using stochastic gradient descent (SGD), where we iteratively update parameters by taking small steps in the direction that reduces the loss:

$$\mathbf{w}^{(t+1)} = \mathbf{w}^{(t)} - \eta \nabla L(\mathbf{w}^{(t)}) \tag{15.29}$$

While this update rule is simple, it hides a computational challenge: calculating the gradient $\nabla L(\mathbf{w}^{(t)})$ efficiently in a network with potentially millions of parameters.

This computational challenge might seem insurmountable at first. After all, we need to compute how the loss changes with respect to every parameter in the network. However,

a breakthrough algorithm called backpropagation makes this calculation not just possible, but highly efficient. In fact, backpropagation has been so transformative that it's considered one of the most important algorithmic innovations in neural network history.

The key insight behind backpropagation comes from calculus: while our neural networks are complex, they are ultimately just nested compositions of simpler functions. Thanks to the chain rule, we can break down the computation of derivatives in these nested functions into manageable pieces. For a simple composite function $f(g(x))$, the chain rule states:

$$\frac{d}{dx} f(g(x)) = \frac{df}{dg} \cdot \frac{dg}{dx} \tag{15.30}$$

For multivariate functions in neural networks, this extends to partial derivatives and matrix calculus. However, even with this powerful tool, the challenge remains. For even modestly sized networks, manually deriving these gradients would yield expressions spanning many pages, with intricate dependencies between parameters across layers. The sheer number of parameters and the compositional nature of neural networks create a gradient calculation problem that would be practically impossible without computational techniques tailored to this specific structure.

Why Manual Differentiation Fails   To understand the importance of backpropagation, let's first examine how differentiation works and why traditional approaches become impractical for neural networks.

In calculus, we learn rules for differentiating elementary functions: the derivative of x^n is nx^{n-1}, the derivative of $\sin(x)$ is $\cos(x)$, and so forth. For compositions of functions, we apply the chain rule. For example, to differentiate $f(x) = \sin(x^2)$, we can write it as $f(x) = \sin(g(x))$ where $g(x) = x^2$. Then by the chain rule:

$$f'(x) = \frac{d}{dx} \sin(g(x)) = \cos(g(x)) \cdot g'(x) = \cos(x^2) \cdot 2x \tag{15.31}$$

This symbolic approach—deriving explicit formulas using differentiation rules—is what we typically learn in calculus courses and what systems like Wolfram Alpha implement.

However, as functions become more complex with multiple nested compositions, even the chain rule becomes unwieldy to apply manually or symbolically. Consider a moderately

complex neural network with just a few layers:

$$f(x) = W^{(3)}\sigma(W^{(2)}\sigma(W^{(1)}x + b^{(1)}) + b^{(2)}) + b^{(3)} \tag{15.32}$$

Deriving $\partial f/\partial W^{(1)}$ symbolically would require careful application of the chain rule through multiple nested functions, resulting in an expression with numerous terms that grows exponentially as network depth increases. For modern neural networks with dozens of layers and millions to billions of parameters, the resulting symbolic expressions would be impossibly long and computationally inefficient to evaluate. Moreover, we don't actually need the explicit symbolic form of the gradient; we only need its numerical value at specific points for gradient descent updates.

Another approach leverages the definition of derivatives from calculus. Differentiation, at its core, involves taking a limit:

$$\frac{df}{dx} = \lim_{\Delta x \to 0} \frac{f(x + \Delta x) - f(x)}{\Delta x} \tag{15.33}$$

This definition leads directly to numerical approximation through finite differences:

$$\frac{\partial f}{\partial w_i} \approx \frac{f(w_i + \Delta) - f(w_i)}{\Delta} \tag{15.34}$$

For a small but non-zero Δ, this gives an approximation of the derivative. This method has a direct connection to classical numerical methods that have been used extensively in scientific computing, from fluid dynamics simulations to astrophysical modeling.

While conceptually simple, finite differences suffer from numerous drawbacks. For a network with P parameters, we would need at least $P + 1$ forward evaluations to compute the full gradient—one baseline evaluation of $f(w)$ plus one evaluation for each parameter where we perturb that parameter while keeping all others fixed (e.g., $f(w_1 + \Delta, w_2, ..., w_P)$, $f(w_1, w_2+\Delta, ..., w_P)$, and so on). This quickly becomes prohibitively expensive as the number of parameters grows.

Moreover, choosing an appropriate Δ presents a delicate balance: too large, and our approximation becomes inaccurate; too small, and we encounter numerical precision issues due to finite computer arithmetic. For neural networks with millions or billions of parameters, this approach becomes computationally prohibitive, requiring millions or billions of forward passes to compute a single gradient.

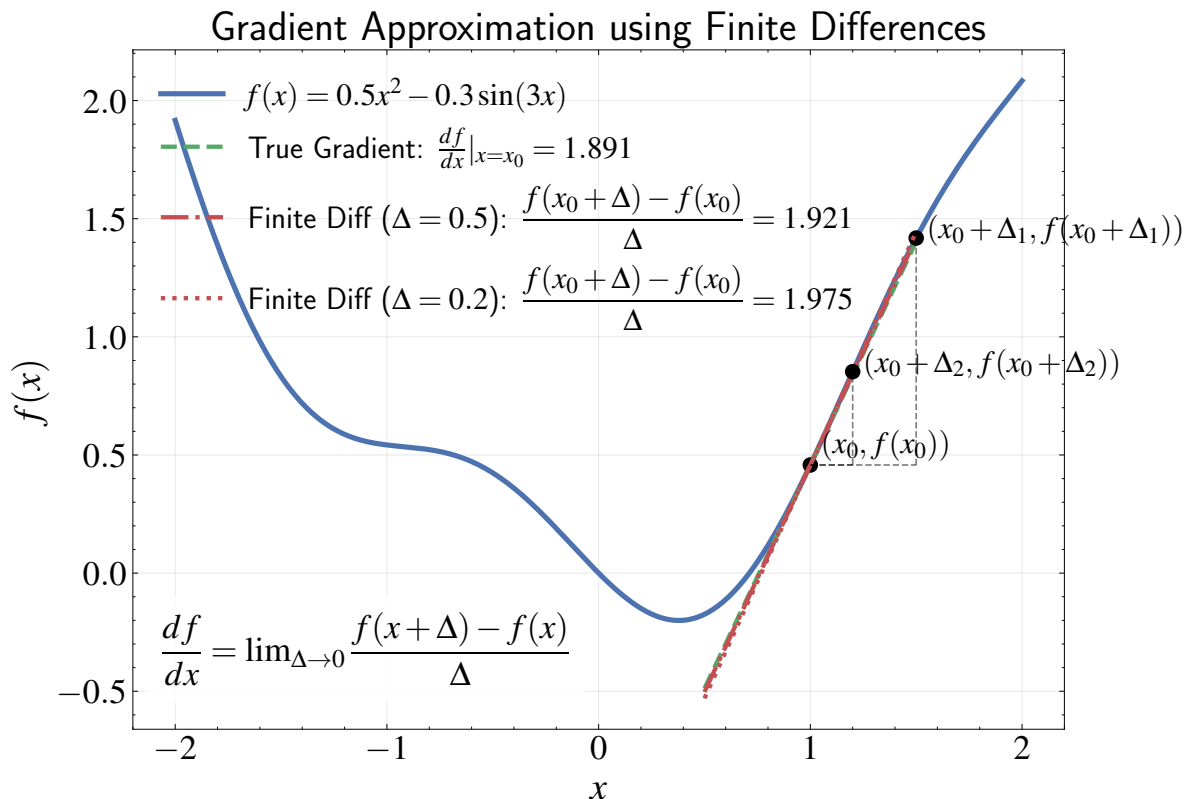## Gradient Approximation using Finite Differences

Figure 15.8: Visualization of gradient approximation using the finite difference method for a one-dimensional function $f(x) = 0.5x^2 - 0.3\sin(3x)$. At the point x_0, the true gradient (green dashed line) is given by the analytical derivative evaluated at that point. The finite difference approximations (red lines) estimate this gradient by computing $\frac{f(x_0+\Delta)-f(x_0)}{\Delta}$ for different values of Δ. As shown, the approximation becomes more accurate as Δ decreases, converging to the true gradient as Δ approaches zero. This illustrates the definition of derivatives: $\frac{df}{dx} = \lim_{\Delta\to 0} \frac{f(x+\Delta)-f(x)}{\Delta}$. While conceptually simple and easy to implement, this approach becomes computationally prohibitive for neural networks with millions of parameters, as it requires a separate function evaluation for each parameter. For a network with P parameters, at least $P + 1$ forward passes would be needed to compute the full gradient vector—one baseline evaluation plus one additional evaluation per parameter. This inefficiency motivates the development of backpropagation, which computes exact gradients more efficiently by applying the chain rule systematically through the computational graph.

Automatic Differentiation This brings us to automatic differentiation, which combines the numerical efficiency of computation with the accuracy of symbolic approaches. Unlike symbolic differentiation, which tries to derive explicit formulas for derivatives, automatic differentiation breaks down complex functions into a sequence of elementary operations (like addition, multiplication, and exponentials) and computes derivatives by applying the chain rule step by step. For example, if we have a function like $f(x) = \sin(x^2)$, instead of deriving the symbolic expression $f'(x) = 2x\cos(x^2)$, automatic differentiation would compute it by

tracking how small changes in x propagate through each operation (x^2 then sin). This approach gives us exact derivatives (not approximations like finite differences) while being computationally efficient.

Automatic differentiation comes in two main forms: forward mode and reverse mode. To understand the difference, imagine computing derivatives through a chain of operations. In forward mode, we start at the inputs and work our way forward, computing how changes in each input affect the intermediate values and final output. Think of it like following a ripple effect from the source. In reverse mode, we first compute the function value, then work backwards from the output to determine how each input contributed to the final result. It's like tracing back the path that led to a particular outcome.

To make this concrete, let's examine a simple neural network layer with a loss function. For a single hidden layer network, we might have:

$$L = E(W, b) = \frac{1}{2}(y - \hat{y})^2 = \frac{1}{2}(y - \sigma(Wx + b))^2 \tag{15.35}$$

where x is the input, W is the weight matrix, b is the bias vector, σ is an activation function like the sigmoid, $\hat{y}$ is the network's prediction, and y is the target value.

This function can be represented as a computational graph—a directed acyclic graph where nodes represent variables (both inputs and intermediate values) and edges represent operations. The computational graph is a powerful conceptual tool that explicitly shows the flow of data and the dependencies between variables.

Each node in this graph stores both the operation and the resulting value when the network is evaluated at specific inputs. The computational graph makes the structure of the calculation explicit, showing how information flows from inputs to outputs during the forward pass, and how gradients flow from outputs back to inputs during backpropagation.

We can decompose this function into a sequence of simpler operations:

$$z = Wx + b \tag{15.36}$$

$$h = \sigma(z) \tag{15.37}$$

$$\hat{y} = h \tag{15.38}$$

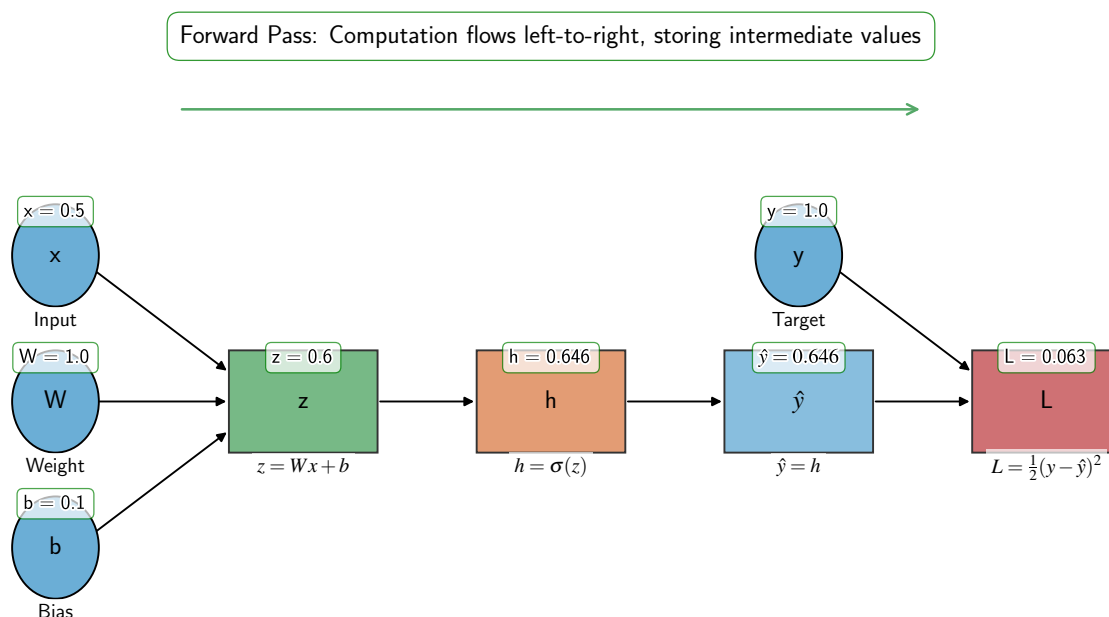$$L = \frac{1}{2}(y - \hat{y})^2 \tag{15.39}$$

Figure 15.9: Computational graph for a simple neural network showing the forward pass with stored intermediate values. The graph represents the function $L = \frac{1}{2}(y - \hat{y})^2 = \frac{1}{2}(y - \sigma(Wx + b))^2$ decomposed into elementary operations. During the forward pass, computation flows left to right through the graph, with each node computing and storing its output value (shown in green boxes). These stored values—such as $z = 0.6$ at the linear computation stage and $h = 0.646$ at the sigmoid activation—are essential for efficient gradient calculation during backpropagation. This example illustrates the first phase of backpropagation, where the model establishes the specific point in parameter space at which gradients will be evaluated. The subsequent backward pass would propagate gradients from the loss node back to each parameter, applying the chain rule at each step to compute partial derivatives like $\frac{\partial L}{\partial W}$ and $\frac{\partial L}{\partial b}$. By structuring computation as a graph with cached intermediate values, backpropagation achieves exact gradient computation with substantially greater efficiency regardless of the number of parameters and exact architecture of the neural network.

To update the weights through gradient descent, we need to compute $\partial L/\partial W$ and $\partial L/\partial b$. Using the chain rule, we can write:

$$\frac{\partial L}{\partial W} = \frac{\partial L}{\partial \hat{y}} \cdot \frac{\partial \hat{y}}{\partial h} \cdot \frac{\partial h}{\partial z} \cdot \frac{\partial z}{\partial W} \tag{15.40}$$

$$\frac{\partial L}{\partial b} = \frac{\partial L}{\partial \hat{y}} \cdot \frac{\partial \hat{y}}{\partial h} \cdot \frac{\partial h}{\partial z} \cdot \frac{\partial z}{\partial b} \tag{15.41}$$

Computing each term at their specific evaluation points:

$$\left.\frac{\partial L}{\partial \hat{y}}\right|_{\hat{y}=\hat{y}^*} = -(y - \hat{y}^*) \tag{15.42}$$

$$\left.\frac{\partial \hat{y}}{\partial h}\right|_{h=h^*} = 1 \tag{15.43}$$

$$\left.\frac{\partial h}{\partial z}\right|_{z=z^*} = \sigma'(z^*) \tag{15.44}$$

$$\left.\frac{\partial z}{\partial W}\right|_{W=W^*,x=x^*} = x^{*T} \tag{15.45}$$

$$\left.\frac{\partial z}{\partial b}\right|_{b=b^*} = 1 \tag{15.46}$$

Therefore:

$$\left.\frac{\partial L}{\partial W}\right|_{W=W^*,x=x^*,z=z^*,\hat{y}=\hat{y}^*} = -(y - \hat{y}^*) \cdot \sigma'(z^*) \cdot x^{*T} \tag{15.47}$$

$$\left.\frac{\partial L}{\partial b}\right|_{b=b^*,z=z^*,\hat{y}=\hat{y}^*} = -(y - \hat{y}^*) \cdot \sigma'(z^*) \tag{15.48}$$

This calculation illustrates the two key ingredients needed for automatic differentiation:

1. Knowledge of how to differentiate each primitive operation

2. Access to the intermediate values (z^*, h^*, $\hat{y}^*$) needed to evaluate these derivatives at specific points

The second point is crucial and often overlooked. Gradients are always evaluated at specific points—they represent the slope of the function at a particular location in parameter space. To compute these gradients, we must first evaluate the function at that point and store all intermediate values. For example, to compute $\partial h / \partial z|_{z=z^*} = \sigma'(z^*)$, we need the specific value z^* from the forward pass. Without storing these intermediate values, we would need to recalculate them during the backward pass, which would be computationally inefficient.

The Two-Phase Algorithm   Backpropagation implements automatic differentiation through two phases:

1. **Forward Pass**: Following the computational graph from inputs to outputs, we com-

pute and store all intermediate values (z^*, h^*, $\hat{y}^*$) by evaluating each operation in sequence. This forward pass establishes the specific point in function space where we'll evaluate gradients, just as we did in our earlier example where we needed z^* to compute $\sigma'(z^*)$ and $\hat{y}^*$ to compute $-(y - \hat{y}^*)$.

2. **Backward Pass**: Propagate gradients backward from the loss function to each parameter, applying the chain rule step by step, effectively traversing the computational graph in reverse. At each node, we compute how changes in that node's output affect the final loss. For example, starting with $\frac{\partial L}{\partial \hat{y}}$, we work backwards through the graph, calculating quantities like $\frac{\partial L}{\partial h} = \frac{\partial L}{\partial \hat{y}} \cdot \frac{\partial \hat{y}}{\partial h}$ and so on.

This two-phase approach is essentially a dynamic programming solution to the gradient calculation problem. By storing intermediate results during the forward pass (like z^*, h^*, and $\hat{y}^*$ in our computational graph), we avoid redundant computations during the backward pass, making the whole process highly efficient. This is particularly evident in our earlier computational graph $x, W, b \to z = Wx + b \to h = \sigma(z) \to \hat{y} = h \to L = \frac{1}{2}(y - \hat{y})^2$, where each node's value is computed and stored once during the forward pass, then reused during backpropagation.

More critically, the computational advantage of backpropagation stems largely from the scalar nature of the loss function. Since our loss function outputs a single scalar, the gradient calculations maintain manageable dimensions as we work backwards. To illustrate this point, let's examine the dimensions of the matrices involved in our earlier calculation. If $x \in \mathbb{R}^D$ (input dimension), $W \in \mathbb{R}^{M \times D}$ (weight matrix for M hidden units), and $z, h \in \mathbb{R}^M$ (hidden layer activations), then:

$$\frac{\partial L}{\partial \hat{y}} \in \mathbb{R} \quad \text{(scalar)} \tag{15.49}$$

$$\frac{\partial \hat{y}}{\partial h} \in \mathbb{R}^{1 \times M} \quad \text{(row vector)} \tag{15.50}$$

$$\frac{\partial h}{\partial z} \in \mathbb{R}^{M \times M} \quad \text{(diagonal matrix)} \tag{15.51}$$

$$\frac{\partial z}{\partial W} \in \mathbb{R}^{M \times (M \times D)} \quad \text{(tensor)} \tag{15.52}$$

Before proceeding, let's clarify what we mean by a tensor. While vectors are one-dimensional arrays and matrices are two-dimensional arrays, tensors are generalizations that can have any number of dimensions. In our case, $\frac{\partial z}{\partial W}$ is a third-order tensor because it represents how each element of z changes with respect to each element of the matrix W.
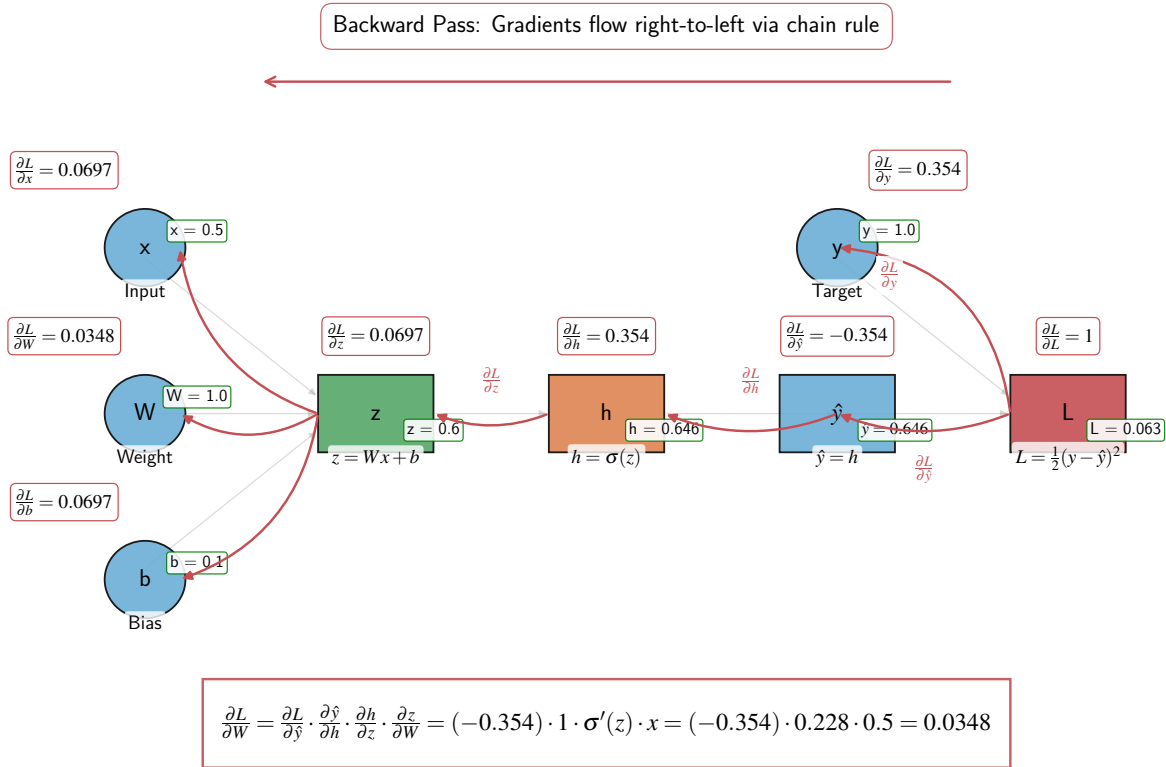
Figure 15.10: Visualization of the backward pass in backpropagation, showing how gradients flow from the loss function back to the network parameters. Following the forward pass (shown with the stored values in green), the backward pass begins at the loss node L with $\frac{\partial L}{\partial L} = 1$ and propagates gradients right-to-left through the computational graph (red arrows). At each node, the incoming gradient is multiplied by the local derivative according to the chain rule. For instance, the gradient at $\hat{y}$ is $\frac{\partial L}{\partial \hat{y}} = -0.354$, which then flows to h with the same value since $\frac{\partial \hat{y}}{\partial h} = 1$. The gradient further propagates to z as $\frac{\partial L}{\partial z} = 0.0697$ after multiplication by $\frac{\partial h}{\partial z} = \sigma'(z) = 0.228$. From z, the gradient branches to compute $\frac{\partial L}{\partial W} = 0.0348$, $\frac{\partial L}{\partial b} = 0.0697$, and $\frac{\partial L}{\partial x} = 0.0697$. The detailed calculation for $\frac{\partial L}{\partial W}$ shown at the bottom illustrates how the full chain rule is applied: $\frac{\partial L}{\partial W} = \frac{\partial L}{\partial \hat{y}} \cdot \frac{\partial \hat{y}}{\partial h} \cdot \frac{\partial h}{\partial z} \cdot \frac{\partial z}{\partial W}$. This systematic backward flow of gradients using stored forward pass values is what makes backpropagation computationally efficient, requiring only one forward and one backward pass regardless of the number of parameters and exact architecture of the neural network.

This creates a three-dimensional structure where each element (i, j, k) represents the partial derivative of the ith element of z with respect to the (j, k)th element of W.

One might wonder, "Why do we need the backward pass? Couldn't we just apply the chain rule in the forward direction?" The answer lies in computational efficiency. Let's

consider what happens if we tried to compute the gradient "forward":

$$\frac{\partial L}{\partial W} = \frac{\partial}{\partial W} \left[\frac{1}{2} (y - \sigma(Wx + b))^2 \right] \tag{15.53}$$

Following the forward chain rule, we would first compute $\frac{\partial z}{\partial W} = x^T$, then $\frac{\partial h}{\partial W} = \frac{\partial h}{\partial z} \cdot \frac{\partial z}{\partial W} = \sigma'(z) \cdot x^T$, and so on. The key problem is that $\frac{\partial h}{\partial W}$ already has dimensions $M \times (M \times D)$, and this grows exponentially as we add more layers. For a deep network, the intermediate Jacobian matrices become intractably large.

In contrast, when we work backwards, we maintain smaller dimensions because we're always multiplying by the gradient of the loss, which is a scalar. This seemingly simple change leads to orders of magnitude faster computation, even though we're performing the same mathematical operations. Consider the calculations:

1. $\frac{\partial L}{\partial \hat{y}} \in \mathbb{R}$ (scalar)

2. $\frac{\partial L}{\partial h} = \frac{\partial L}{\partial \hat{y}} \cdot \frac{\partial \hat{y}}{\partial h} \in \mathbb{R}^{1 \times M}$ (row vector)

3. $\frac{\partial L}{\partial z} = \frac{\partial L}{\partial h} \cdot \frac{\partial h}{\partial z} \in \mathbb{R}^{1 \times M}$ (row vector)

4. $\frac{\partial L}{\partial W} = \frac{\partial L}{\partial z} \cdot \frac{\partial z}{\partial W} \in \mathbb{R}^{M \times D}$ (matrix)

At each step, we're dealing with manageable dimensions, making the computation tractable even for very deep networks. This efficiency gain is dramatic - what might take hours or days to compute in the forward direction can often be completed in seconds or minutes when working backwards.

Another advantage of backpropagation is the reuse of intermediate calculations. Notice that the calculations for $\frac{\partial L}{\partial W}$ and $\frac{\partial L}{\partial b}$ share common terms:

$$\frac{\partial L}{\partial W} = \frac{\partial L}{\partial z} \cdot \frac{\partial z}{\partial W} = \frac{\partial L}{\partial z} \cdot x^T \tag{15.54}$$

$$\frac{\partial L}{\partial b} = \frac{\partial L}{\partial z} \cdot \frac{\partial z}{\partial b} = \frac{\partial L}{\partial z} \cdot 1 \tag{15.55}$$

Once we compute $\frac{\partial L}{\partial z}$, we can reuse it for multiple parameter gradients, further increasing efficiency. This reuse of intermediate calculations is also what we illustrate in the computational graph, where the same gradient information flows backward through shared paths in the network.

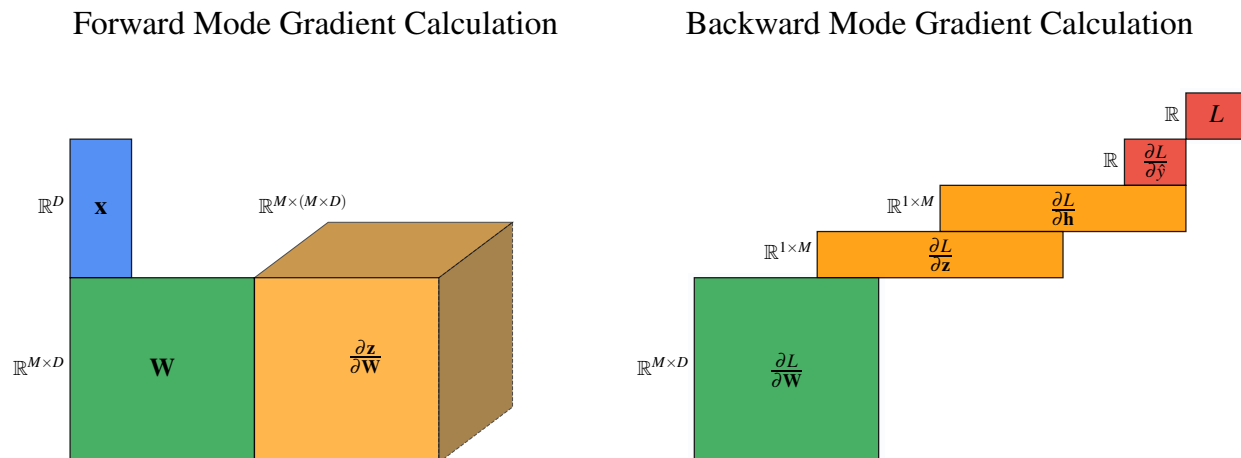Forward Mode Gradient Calculation   Backward Mode Gradient Calculation

Figure 15.11: Comparison of forward mode and backward mode gradient calculation methods, illustrating why backpropagation is computationally efficient. The left panel shows forward mode calculation, where gradient dimensions grow exponentially with network depth, starting from inputs $\mathbf{x} \in \mathbb{R}^D$ and weights $\mathbf{W} \in \mathbb{R}^{M \times D}$. The intermediate tensor $\frac{\partial \mathbf{z}}{\partial \mathbf{W}} \in \mathbb{R}^{M \times (M \times D)}$ rapidly expands in dimension. The right panel demonstrates backpropagation (backward mode), where gradient computation starts from the scalar loss $L \in \mathbb{R}$ and propagates backward through $\frac{\partial L}{\partial \hat{y}}$, $\frac{\partial L}{\partial \mathbf{h}}$, and $\frac{\partial L}{\partial \mathbf{z}}$ to ultimately compute $\frac{\partial L}{\partial \mathbf{W}} \in \mathbb{R}^{M \times D}$. This approach maintains manageable dimensions throughout, resulting in reduced computational complexity.

The efficiency of backpropagation becomes even more apparent when we extend it to deeper networks. For a network with multiple layers, the backward pass simply applies the same chain rule principle recursively through each layer. The gradient "flows" backward through the network, accumulating contributions from each layer.

For instance, in a two-layer network with architecture $x \to z^{(1)} = W^{(1)}x + b^{(1)} \to h^{(1)} = \sigma(z^{(1)}) \to z^{(2)} = W^{(2)}h^{(1)} + b^{(2)} \to h^{(2)} = \sigma(z^{(2)}) \to L$, the gradient of the loss with respect to $W^{(1)}$ would be:

$$\frac{\partial L}{\partial W^{(1)}} = \frac{\partial L}{\partial h^{(2)}} \cdot \frac{\partial h^{(2)}}{\partial z^{(2)}} \cdot \frac{\partial z^{(2)}}{\partial h^{(1)}} \cdot \frac{\partial h^{(1)}}{\partial z^{(1)}} \cdot \frac{\partial z^{(1)}}{\partial W^{(1)}} \tag{15.56}$$

This recursive application of the chain rule through the network layers gives backpropagation its name—gradients propagate backward from the output to the input layer.

It's worth noting that backpropagation's efficiency is particularly well-matched to modern hardware accelerators like Graphics Processing Units (GPUs), which excel at matrix multiplication. There's no inherent reason why GPUs were initially developed for neural

networks—they were primarily created for rendering graphics in video games. These gaming applications demand fast parallel matrix operations for transforming coordinates and computing pixel colors—precisely the same operations needed for neural network training. When researchers discovered that these gaming-oriented processors could accelerate neural network training by orders of magnitude, it catalyzed the deep learning revolution.

This historical accident—that the computational patterns in neural networks perfectly matched existing hardware designed for an entirely different purpose—illustrates how technological progress often depends on such serendipitous alignments. Neural networks, one might say, won the "hardware lottery" by requiring precisely the kind of parallel matrix multiplications that GPUs were designed to accelerate for graphics rendering.

Modern Automatic Differentiation Frameworks What we commonly refer to as "deep learning packages" like PyTorch, JAX, and TensorFlow are, at their core, powerful automatic differentiation frameworks. While they're often described primarily as tools for neural networks, their automatic differentiation capabilities make them valuable for a much broader range of scientific computing applications, from physics simulations to optimization problems in various domains. Their efficiency in handling gradient computation makes them indispensable tools for any application requiring derivatives of complex functions.

In practice, these modern frameworks implement automatic differentiation seamlessly. Researchers can define their models in terms of differentiable operations, and the framework handles the gradient calculations automatically. This abstraction allows for rapid experimentation with complex architectures without manually deriving gradients. This capability has been transformative, enabling the development of sophisticated network architectures that go far beyond simple feed-forward networks.

The term "deep learning" itself stems from this ability to effectively train networks with many layers. While the concept of multi-layer networks existed for decades, it was the combination of automatic differentiation, modern optimization techniques, and architectural innovations that made training such deep networks feasible.

Understanding and Improving Gradient Flow However, being able to write down the model and calculate its gradients does not guarantee successful training or convergence to a good solution. This challenge parallels the historical development of thermodynamics alongside the steam engine—while engineers could build increasingly sophisticated engines, it took the development of thermodynamics to truly understand why and how they worked.

Similarly, while we can construct and compute gradients for increasingly complex neural networks, our theoretical understanding of why they succeed or fail remains incomplete.

Understanding these principles remains crucial for effective neural network development, especially when diagnosing issues like vanishing or exploding gradients. For instance, the vanishing gradient problem—where gradients become extremely small as they propagate backward through many layers—can be understood in terms of the chain rule. If multiple terms in the chain have small derivatives (as with sigmoid activations in their saturated regions), their product can become vanishingly small, effectively stopping gradient flow to earlier layers. This understanding has led to architectural innovations like skip connections and layer normalization that help maintain stable gradient flow through very deep networks.

This understanding of gradient flow has led to numerous innovations in deep learning, such as residual connections (ResNets), which provide shortcuts for gradients to flow through deep networks. Such innovations, while seemingly simple in hindsight, were revolutionary in enabling the training of much deeper networks than was previously possible. While a comprehensive treatment of these advanced techniques is beyond the scope of this chapter, they highlight how the principles of backpropagation continue to inform cutting-edge research in deep learning.

In short, backpropagation represents a synthesis of calculus, dynamic programming, and computational efficiency. It transforms what would otherwise be an intractable gradient calculation into a feasible computation, enabling the training of increasingly complex neural networks. While the mathematical foundation—the chain rule—has been known for centuries, its systematic application through backpropagation has revolutionized machine learning.

15.5   Architectures and Inductive Biases

While we have focused primarily on feedforward neural networks (also called Multi-Layer Perceptrons or MLPs) in this chapter, it's important to recognize that neural networks encompass a much broader family of architectures. Since this textbook concentrates on statistical machine learning principles rather than engineering details, we won't provide comprehensive definitions of these architectures. Nevertheless, understanding the conceptual differences between architectures and their underlying inductive biases is crucial for effective application in astronomical research.

The feedforward neural network we've discussed represents just one architectural pattern—neurons arranged in layers where information flows strictly from input to output without loops or lateral connections. This basic structure, while theoretically powerful due to the universal approximation theorem, is not always the most efficient or effective for specific types of data.

You've likely encountered terms like Convolutional Neural Networks (CNNs) or Transformers in the scientific literature or popular discourse. These architectures all rely on the same backpropagation algorithm we've explored, and benefit from the same theoretical properties like double descent and neural tangent kernels that make neural networks trainable despite their complexity. However, they differ in their structure and the inductive biases they encode.

The concept of inductive bias is central to understanding these architectural choices. As we've emphasized since the first chapter of this textbook, all machine learning methods incorporate some form of inductive bias—assumptions that guide learning when data alone is insufficient to determine the solution. Linear regression assumes relationships are linear in the feature space; logistic regression assumes a linear decision boundary between classes; and Gaussian Processes assume smoothness governed by a specific kernel function.

Neural networks are no exception. While the universal approximation theorem makes MLPs extremely flexible, this flexibility is both a blessing and a curse. Without appropriate inductive biases, a model might require vastly more data and computation to learn patterns that could be more easily discovered with a more constrained architecture. This illustrates a principle: machine learning is always a balance between modeling (incorporating prior knowledge through inductive biases) and learning (extracting patterns directly from data).

Different neural network architectures essentially encode different inductive biases — assumptions about the structure of the data that help the network learn more efficiently. Let's examine some key architectures and their corresponding inductive biases:

Convolutional Neural Networks   Convolutional Neural Networks encode two powerful inductive biases particularly suited to image data: translation invariance and hierarchical local structure. Translation invariance means that a pattern recognized in one part of an image should be recognized regardless of where it appears. Hierarchical local structure means that nearby pixels are more strongly related than distant ones, and these local patterns combine to form increasingly complex features at larger scales.

These inductive biases are implemented through convolutional layers, where small filters (kernels) slide across the input, applying the same transformation at each position. Mathematically, for an input image X and a kernel K of size $k \times k$, the convolution operation at position (i, j) is given by:

$$(X * K)_{i,j} = \sum_{m=1}^{k} \sum_{n=1}^{k} X_{i+m-1,j+n-1} \cdot K_{m,n} \tag{15.57}$$

where $X_{i,j}$ represents the pixel value at position (i, j) in the input image, and $K_{m,n}$ represents the weight at position (m, n) in the kernel. The operation effectively computes a weighted sum of the local neighborhood around each pixel.

This parameter sharing dramatically reduces the number of learnable parameters compared to a fully connected network while encoding the assumption that the same feature detectors should be applied throughout the image. For example, if we have an input image of size $n \times n$ and a kernel of size $k \times k$, a CNN layer requires only k^2 parameters (plus bias), whereas a fully connected layer would require $n^2 \times k^2$ parameters. This reduction in parameters is achieved by reusing the same kernel weights across all positions in the input.

The mathematical foundations of CNNs have led to the development of scattering transforms—a branch of mathematics that provides insights into why these architectures work so well for image data. This mathematical framework helps explain the theoretical underpinnings of CNNs, further illustrating the "Science of AI" we mentioned earlier. Just as thermodynamics emerged to explain the principles behind steam engines, scattering transforms provide a rigorous mathematical foundation for understanding why CNNs are particularly effective for image processing tasks. Notably, scattering transforms have found broad applications in cosmology, where they are used to analyze the large-scale structure of the universe and extract meaningful features from galaxy surveys.

While CNNs excel at image processing, their inductive biases can be counterproductive for many astronomical data modalities. For instance, spectroscopic data and time series often contain critical information in long-range dependencies and global patterns rather than hierarchical local structures. A CNN applied to a stellar spectrum might focus excessively on local spectral features while missing important correlations between widely separated spectral lines that indicate specific physical conditions.

Transformers This limitation of CNNs in handling long-range dependencies led to the development of Transformers, which have become widely used in natural language process-

ing and increasingly other domains as well. Transformers encode a different set of inductive biases compared to CNNs. Rather than assuming locality, Transformers use attention mechanisms that allow direct connections between any elements in a sequence, regardless of their distance. This architecture excels at capturing long-range dependencies and global patterns.
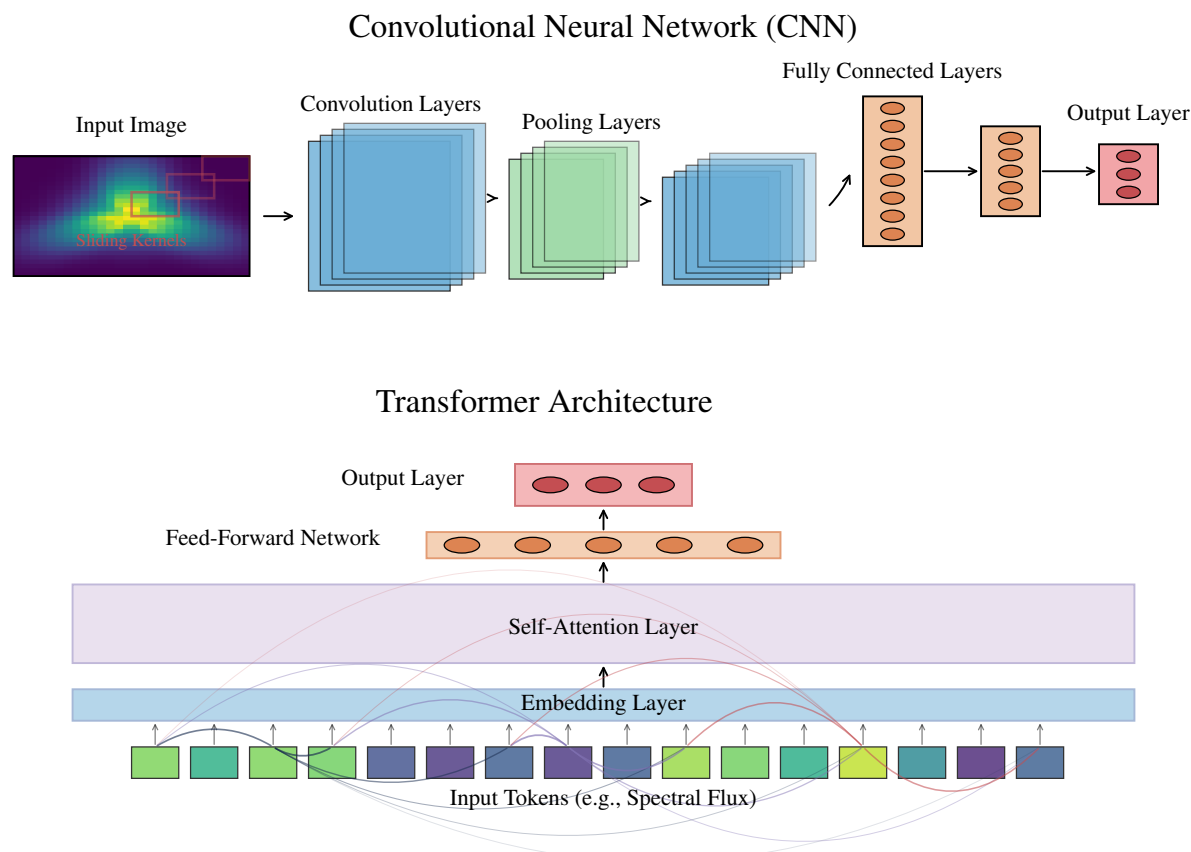

Figure 15.12: Schematic comparison of Convolutional Neural Networks (CNNs) and Transformer architectures, highlighting their distinct structural designs and inductive biases. **Top:** The CNN processes an image through a sequence of specialized layers: convolution layers with sliding kernels detect local features, pooling layers reduce spatial dimensions while preserving important features, and fully connected layers integrate these features for the final output. This architecture encodes translation invariance and hierarchical local structure. **Bottom:** The Transformer processes sequential data through a different approach. Input tokens are embedded into a higher-dimensional space, then processed through a self-attention layer where each token interacts directly with every other token regardless of position (visualized by the curved connections). This global interaction is followed by a feed-forward network and output layer. The self-attention mechanism enables Transformers to capture long-range dependencies, making them particularly effective for data where relationships between distant elements are important, such as spectroscopic data where correlations between widely separated spectral lines can indicate specific physical conditions.

The key innovation in Transformers is the self-attention mechanism, where each element in a sequence is related to every other element through learned attention weights. Mathematically, for a sequence of length n, the attention mechanism computes relationships between all n^2 pairs of elements, allowing the model to learn which elements should influence each other. This enables Transformers to focus on relevant information regardless of position, making them particularly well-suited for data with important long-range dependencies.

For astronomical applications, Transformers are promising. Consider a stellar spectrum: while CNNs might struggle to connect widely separated spectral lines, Transformers can directly model relationships between any wavelengths, regardless of their distance. This capability is crucial for identifying complex patterns that indicate specific stellar compositions or evolutionary states. Similarly, in analyzing light curves, Transformers can capture relationships between events separated by time intervals, potentially revealing subtle periodicities or evolutionary trends that might be missed by other architectures.

The choice of architecture becomes particularly important when working with different types of astronomical data. Each data modality has unique characteristics that make certain architectures more suitable than others. For example, using a CNN for spectral analysis would be inappropriate since spectral data doesn't exhibit the spatial locality that CNNs are designed to exploit. Similarly, using a fully connected network for image classification would be inefficient compared to a CNN, which can leverage the spatial structure of images.

This architectural choice reflects a principle in machine learning: the trade-off between model flexibility and constraints. On one hand, more flexible models can potentially learn more complex patterns, but they require more training data and computational resources. On the other hand, models with appropriate inductive biases can learn effectively from less data, but they might miss patterns that don't align with their built-in assumptions.

While this textbook focuses on core statistical machine learning principles, understanding neural network architectures and their inductive biases is becoming increasingly important for astronomers. We'll explore these concepts in more detail in our upcoming textbook on deep learning for astronomy, where we'll provide practical guidance on selecting and implementing appropriate architectures for different astronomical applications.

The field of neural network architectures is rapidly evolving, with new designs emerging that combine computational principles with domain-specific knowledge. For astronomers, it's essential to stay informed about these developments while carefully evaluating their relevance to specific astronomical problems. This balanced approach ensures that we leverage

the power of neural networks while maintaining scientific rigor in our research.

15.6   Activation Functions

Having explored neural network architectures and their inductive biases, let's return to a more technical aspect of neural networks that we introduced earlier but merits deeper examination: activation functions. While this might seem like a minor implementation detail, the choice of activation function has profound implications for neural network training and performance.

As we described in the beginning of this chapter, the key mathematical property that gives neural networks their expressive power is nonlinearity. Without nonlinear activation functions, composing multiple linear layers would simply result in another linear transformation, regardless of network depth. The universal approximation theorem, which establishes neural networks' theoretical capacity to represent arbitrary continuous functions, critically depends on this nonlinearity.

Given the original focus of neural networks on classification problems, the sigmoid function became a prominent early choice for activation:

$$\sigma(x) = \frac{1}{1 + e^{-x}} \tag{15.58}$$

The sigmoid function maps any real-valued input to the range $(0, 1)$, making it intuitively appealing for representing probabilities or normalized activations. However, despite its historical significance, the sigmoid function is rarely used in modern networks due to limitations that become apparent when we examine its gradient.

Recall from our discussion of logistic regression that the derivative of the sigmoid function is:

$$\frac{d\sigma(x)}{dx} = \sigma(x)(1 - \sigma(x)) \tag{15.59}$$

This derivative has a maximum value of 0.25 at $x = 0$ and approaches zero as $|x|$ increases. This creates problems for gradient-based learning. The vanishing gradient phenomenon occurs when $|x|$ is large, causing the gradient to become extremely small and effectively stopping learning in those regions. Furthermore, the small gradient magnitude provides weak, indecisive signals for parameter updates, slowing convergence considerably.

This indecisiveness in the gradient is analogous to excessive politeness in communica-

tion, where the message becomes too subtle to be effective. In optimization, we often require more decisive signals. The sigmoid's tendency to produce gradients that are neither clearly positive nor negative, but rather ambiguously small, leads to prolonged training times and potential convergence issues.

The limitations of sigmoid functions led to the development of alternative activation functions, most prominently the Rectified Linear Unit (ReLU):

$$\text{ReLU}(x) = \max(0, x) \tag{15.60}$$

With a derivative of:

$$\frac{d\text{ReLU}(x)}{dx} = \begin{cases} 1 & \text{if } x > 0 \\ 0 & \text{if } x < 0 \end{cases} \tag{15.61}$$

ReLU offers several advantages over sigmoid functions. For positive inputs, the gradient is constantly 1, preventing the vanishing gradient problem that plagues sigmoid activations. Additionally, by outputting exactly zero for negative inputs, ReLU creates sparse activations, which can improve computational efficiency and prevent overfitting. Perhaps most practically, both the function and its derivative are extremely simple to compute, making ReLU-based networks faster to train and evaluate.

However, ReLU has its own limitation: the "dying ReLU" problem. When a neuron's weights receive updates that push its pre-activation consistently negative, the gradient becomes zero, and the neuron stops learning entirely—effectively "dying." This led to variants of ReLU that attempt to address this limitation while preserving its advantages.

More recently, the Gaussian Error Linear Unit (GELU) has gained popularity, particularly in transformer architectures:

$$\text{GELU}(x) = x \cdot \Phi(x) \tag{15.62}$$

where $\Phi(x)$ is the cumulative distribution function of the standard normal distribution. GELU smoothly interpolates between passing and blocking signals, avoiding the non-differentiability of ReLU at zero while maintaining its advantages for positive values.

Interestingly, GELU closely approximates ReLU for positive inputs while providing a smooth transition around zero. This similarity to ReLU is not coincidental—it preserves ReLU's beneficial properties like sparse activations and constant gradients for positive in-
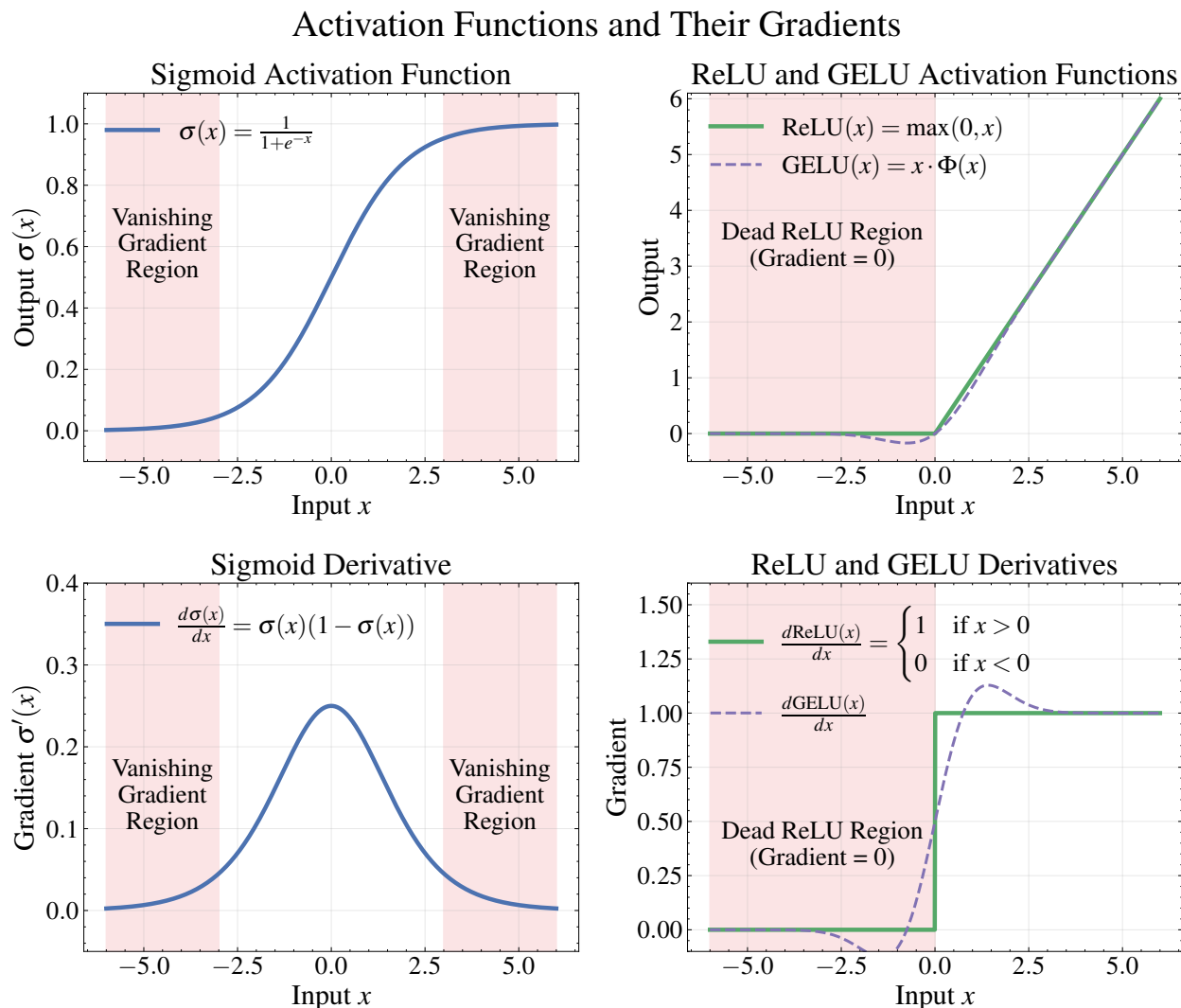
Activation Functions and Their Gradients

Figure 15.13: Comparison of sigmoid and ReLU activation functions and their derivatives. **Top left:** The sigmoid function $\sigma(x) = 1/(1 + e^{-x})$ maps inputs to the range $(0, 1)$, but saturates for large positive or negative inputs (highlighted in red), causing vanishing gradients. **Top right:** The ReLU function $\text{ReLU}(x) = \max(0, x)$ and its smoother variant GELU (dashed purple) provide linearity for positive inputs while creating sparsity for negative inputs. **Bottom left:** The sigmoid derivative $\frac{d\sigma(x)}{dx} = \sigma(x)(1 - \sigma(x))$ rapidly approaches zero in saturation regions, severely limiting gradient flow during backpropagation. **Bottom right:** The ReLU derivative is exactly 1 for all positive inputs, allowing strong and constant gradient flow, while being zero for negative inputs (which can lead to "dying neurons"). GELU provides a smooth transition around zero, addressing ReLU's non-differentiability while maintaining its desirable properties for positive inputs. The vanishing gradient problem with sigmoid activations slows learning in deep networks, while GELU has emerged as a preferred choice in modern neural networks by combining ReLU's advantages with improved smoothness and training stability.

puts, while adding the advantage of smoothness. The connection between GELU and ReLU becomes clear when we note that $\Phi(x)$ approaches 1 for large positive x, making GELU behave nearly identically to ReLU in this regime. This design choice reflects the empirical success of ReLU while addressing its limitations.

The Constraint of Non-Superlinearity   An important observation about all these activation functions is that they are never superlinear—meaning they never grow faster than a linear function as $|x|$ increases. Mathematically, a superlinear function would satisfy:

$$\lim_{|x| \to \infty} \frac{f(x)}{x} = \infty \tag{15.63}$$

This absence of superlinearity is not arbitrary but reflects deep statistical principles. As we discussed in the chapter on summary statistics, higher-order operations—those involving powers greater than 1—are associated with higher sampling variance. To understand why this matters, let's consider a simple example with polynomial functions of increasing order:

$$f_1(x) = x \quad \text{(linear)} \tag{15.64}$$

$$f_2(x) = x^2 \quad \text{(quadratic)} \tag{15.65}$$

$$f_3(x) = x^3 \quad \text{(cubic)} \tag{15.66}$$

When working with noisy data, the variance of our estimates increases dramatically with the polynomial order. Consider a dataset with values around $x = 2$ with a small measurement error of ± 0.1:

- Linear: $2.1 - 1.9 = 0.2$ difference

- Quadratic: $2.1^2 - 1.9^2 = 0.8$ difference

- Cubic: $2.1^3 - 1.9^3 = 2.4$ difference

This example illustrates how each additional power amplifies the impact of measurement errors. The same principle applies to neural networks: superlinear activation functions would amplify small input variations, leading to unstable gradients and numerical problems during training.

By constraining activation functions to be at most linear in their growth, neural net-
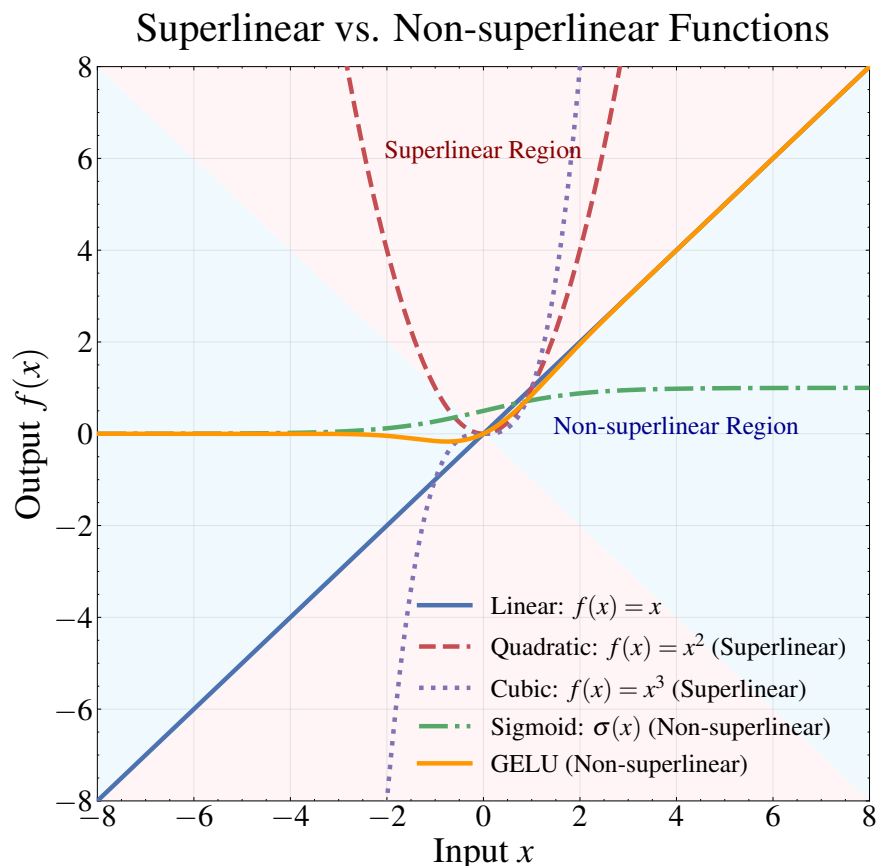
Figure 15.14: Visualization of superlinear versus non-superlinear functions. The light red regions represent superlinear behavior where $|y| > |x|$, while the light blue regions represent non-superlinear behavior where $|y| \leq |x|$. Five functions are displayed: linear ($f(x) = x$), quadratic ($f(x) = x^2$), cubic ($f(x) = x^3$), sigmoid, and GELU. Notably, quadratic and cubic functions quickly enter the superlinear regions, growing much faster than linear as $|x|$ increases. In contrast, neural network activation functions (sigmoid and GELU) remain within the non-superlinear regions—they either saturate to a constant value (sigmoid) or grow at most linearly (GELU). Superlinear functions would amplify small input errors and cause unstable gradients in deep networks, making training difficult or impossible. The non-superlinear constraint represents a careful balance between expressivity and stability in neural network design.

works can build deep representations that extract complex patterns while maintaining stable training dynamics. This design choice allows us to stack many layers without suffering from exploding gradients that would make learning impossible. In essence, the careful calibration of activation function behavior is crucial for balancing expressive power with training stability.

This connection between activation function design and statistical sampling properties reveals an important point about neural networks: while they have advanced properties that

we don't yet fully understand—much like steam engines before thermodynamics—they are not entirely black boxes. Many design choices in neural networks reflect deep statistical and mathematical principles, even if the full theoretical explanation sometimes follows empirical success.

15.7   Bayesian Neural Networks

While backpropagation and stochastic gradient descent provide an efficient way to train neural networks, they only lead to a point estimate of the network parameters—essentially finding the weights $\mathbf{w}$ that minimize the empirical loss:

$$\mathbf{w}^* = \arg \min_{\mathbf{w}} L(\mathbf{w}) \tag{15.67}$$

This is analogous to maximum likelihood estimation in linear regression. Just as with linear regression, this approach gives us the "best fit" model but provides no information about uncertainty in our model parameters. In Bayesian analysis, we aren't merely interested in finding the optimal parameter values, but rather in characterizing the entire posterior distribution of parameters:

$$p(\mathbf{w}|\mathcal{D}) \propto p(\mathcal{D}|\mathbf{w})p(\mathbf{w}) \tag{15.68}$$

Having access to this posterior distribution allows us to make predictions that account for parameter uncertainty by integrating over all possible parameter values:

$$p(y|\mathbf{x}, \mathcal{D}) = \int p(y|\mathbf{x}, \mathbf{w})p(\mathbf{w}|\mathcal{D})d\mathbf{w} \tag{15.69}$$

For astronomical applications, this uncertainty quantification is often as important as the prediction itself. It helps us distinguish between confident predictions based on ample evidence and more speculative ones where the model is uncertain.

One of the key limitations of neural networks compared to the simpler models we've studied is the difficulty of performing rigorous Bayesian inference. For Bayesian linear regression, we derived analytical expressions for the posterior distribution, making Bayesian inference computationally tractable. For neural networks, however, the nonlinear structure and high dimensionality of the parameter space make the posterior distribution intractable to compute exactly. A modern neural network might have millions or even billions of param-

eters, making direct sampling from the posterior distribution computationally prohibitive.

While exact Bayesian inference in neural networks remains challenging, researchers have developed several practical approximations. Among these, dropout stands out as both widely used and theoretically interesting. Originally introduced as a regularization technique, dropout has deep connections to Bayesian methods that make it particularly valuable for uncertainty quantification.

Monte Carlo Dropout Approach The dropout mechanism is simple: during training, each neuron's output is randomly set to zero with probability p. This process involves two key steps:

1. For each forward pass during training, we create a random mask for each neuron i:

$$m_i \sim \text{Bernoulli}(1 - p) \tag{15.70}$$

   Here, $m_i = 1$ means the neuron remains active, while $m_i = 0$ indicates it's temporarily removed. The Bernoulli distribution is a discrete probability distribution that takes only two possible values: 1 with probability $1 - p$ and 0 with probability p. In the context of dropout, this means each neuron has a probability p of being "dropped out" (set to 0) and a probability $1 - p$ of remaining active (set to 1).

2. We then apply this mask to the layer's outputs:

$$\tilde{\mathbf{h}}^{(l)} = \mathbf{m} \odot \mathbf{h}^{(l)}/(1 - p) \tag{15.71}$$

   The $\odot$ symbol represents element-wise multiplication between the mask $\mathbf{m}$ and the layer outputs $\mathbf{h}^{(l)}$. The scaling factor $1/(1-p)$ is crucial: it ensures that the expected output value remains the same during both training and inference, preventing any systematic shift in the network's behavior. This scaling is similar to the bias correction term we saw in the Adam optimizer, where we divide by $(1 - \beta^t)$ to correct for the initialization bias in the moving averages.

Dropout works by randomly deactivating neurons during training, forcing the network to develop redundant pathways and become more robust. This is similar to training a team where members occasionally take sick leave - the team must learn to function effectively even when some members are absent, preventing any single person from becoming a critical bottleneck. This redundancy helps prevent overfitting by ensuring the network doesn't rely

too heavily on any single neuron or pathway.

During standard inference (i.e., when using the trained network to make predictions on new data), dropout is typically turned off to use the full network's capacity. Since the network has already learned to be robust to missing neurons during training, using the complete network generally provides the most accurate predictions.

However, we can also keep dropout active during inference and perform multiple forward passes with different random masks - a technique called Monte Carlo dropout. This approach approximates Bayesian integration, providing not just predictions but also valuable uncertainty estimates. This makes it particularly useful for scientific applications where understanding prediction confidence is crucial.
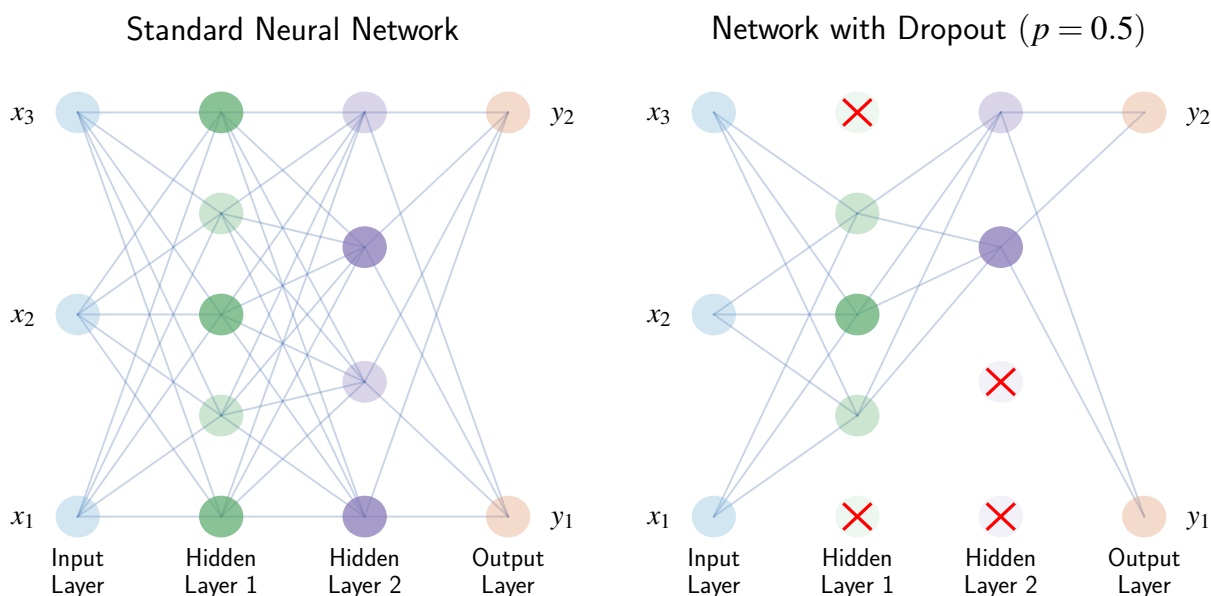

Figure 15.15: Visualization of the dropout technique for neural networks. The left panel shows a standard neural network with fully connected layers, while the right panel demonstrates the same network with dropout applied (probability $p = 0.5$). During training with dropout, neurons are randomly deactivated (marked with red X's) with probability p, and their connections are temporarily removed. This forces the network to develop redundant pathways, preventing overfitting and creating an implicit ensemble of networks. Mathematically, dropout applies a random Bernoulli mask $m_i \sim \text{Bernoulli}(1 - p)$ to each neuron and scales the outputs by $1/(1 - p)$ to maintain consistent expected values. When used during inference (Monte Carlo dropout), this technique approximates Bayesian neural networks by sampling from an implicit posterior distribution over network parameters, enabling uncertainty quantification in predictions.

Monte Carlo dropout is powerful because it allows us to "sample" different possible network configurations during inference. Like a team where different members take sick

leave on different days, Monte Carlo dropout shows how the network's predictions vary when different neurons are temporarily unavailable. This variation provides insight into the network's confidence in its predictions - if the team performs consistently regardless of who's absent, we can be more confident in their collective judgment, while large variations in performance suggest higher uncertainty in their decision-making.

The statistical foundations of dropout can be understood through complementary ensemble learning and Bayesian perspectives, which are more closely connected than they might initially appear.

From the ensemble learning perspective, dropout effectively creates an implicit collection of neural networks. Each time we apply a different dropout mask, we're working with a different "thinned" network—a subnetwork of the original architecture. During training, the network is constantly being reconfigured as different subsets of neurons are randomly dropped, forcing the remaining neurons to compensate. This is conceptually similar to bootstrap aggregating (bagging), where we train multiple independent models on different data subsets and average their predictions to reduce variance and improve generalization.

The ensemble interpretation reveals dropout's effectiveness in preventing overfitting through a mechanism of forced redundancy. By randomly removing neurons during training, the network must develop multiple pathways to process similar information, preventing over-reliance on any single neuron or feature combination. This redundancy becomes particularly valuable for predictions on new data, as it enables effective marginalization over model uncertainty through multiple network configurations.

This ensemble view directly connects to the Bayesian perspective we introduced earlier. When we keep dropout active during inference (Monte Carlo dropout) and perform multiple forward passes with different random masks, we're effectively sampling from an approximate posterior distribution over network functions. Each dropout mask creates a different network configuration, analogous to drawing a sample from the posterior distribution of weights. By averaging predictions from these multiple forward passes:

$$p(y|\mathbf{x}, \mathcal{D}) \approx \frac{1}{T} \sum_{t=1}^{T} p(y|\mathbf{x}, \mathbf{m}_t) \tag{15.72}$$

where T is the number of forward passes with different masks $\mathbf{m}_t$, we obtain an approximation to the predictive distribution that we would ideally compute through Bayesian model

averaging. The variance of these predictions provides a natural measure of uncertainty:

$$\text{Var}(y|\mathbf{x}, \mathcal{D}) \approx \frac{1}{T} \sum_{t=1}^{T} (f(\mathbf{x}, \mathbf{m}_t) - \bar{f}(\mathbf{x}))^2 \tag{15.73}$$

where $\bar{f}(\mathbf{x})$ is the mean prediction across all dropout masks. This uncertainty quantification is particularly valuable for scientific applications like astronomy, where understanding prediction confidence can be as important as the predictions themselves.

The uncertainty captured by Monte Carlo dropout primarily represents model uncertainty (epistemic uncertainty)—uncertainty stemming from the model's lack of knowledge due to limited training data or model capacity. This is distinct from aleatoric uncertainty, which arises from inherent noise in the data itself. Even capturing model uncertainty alone represents an improvement over standard deterministic neural networks, which provide only point predictions with no indication of confidence.

Limitations and Advanced Approaches   While dropout provides a practical approximation to Bayesian inference, it's worth noting that this bagging-like approach is just that—an approximation. Recent research has revealed limitations in Monte Carlo dropout's ability to capture the complete predictive distribution, especially in regions far from the training data or when uncertainty is highly structured. The dropout masks, though they introduce prediction diversity, don't fully explore the parameter space in a way that truly represents the posterior distribution. This has spurred research into more sophisticated approaches to Bayesian neural networks.

Researchers are actively developing more formal approaches to Bayesian neural networks. One direction involves adapting traditional MCMC methods, which we explored earlier in this course, for sampling from the posterior distribution of neural network weights. However, the high dimensionality of the weight space presents computational challenges for these methods.

An alternative approach is to assume a parametric form for the posterior distribution (such as a Gaussian) and optimize the parameters of this distribution rather than sampling directly. This is known as variational inference, which transforms a sampling problem into an optimization problem. While this is a key idea in statistical inference, its detailed application to neural networks involves technical complexities beyond the scope of this introductory textbook.

The contrast between standard neural networks and Bayesian neural networks illustrates a broader theme we've encountered throughout this course: the trade-off between computational efficiency and rigorous uncertainty quantification. Standard neural networks excel in efficiency, leveraging backpropagation and stochastic gradient descent to handle massive datasets and complex function approximation. However, the lack of properly understood (or at least not easily achievable/analytic) uncertainty quantification is, in my opinion, the key limitation of neural networks, rather than just blanket criticisms about their interpretability.

This limitation has led modern research in two promising directions. One approach is to make classical Bayesian models like Gaussian Processes more scalable—for instance, by using neural networks to amortize some computational components while preserving the core Bayesian generalized linear regression framework. The other approach is to develop more rigorous Bayesian methods for neural networks themselves. Both directions have seen progress in recent years.

15.8 Beyond A Fancy Interpolator

Throughout this chapter, we've explored neural networks from both practical and theoretical perspectives. We've seen how backpropagation enables efficient training and how techniques like dropout provide approximations to Bayesian inference. However, a common misconception persists that neural networks are merely "black boxes" or fancy interpolation methods without theoretical grounding. This view not only underestimates the mathematical depth of neural networks but also overlooks theoretical advances that have deepened our understanding of why and how these models work.

While we cannot provide rigorous proofs within the scope of this textbook, it's worth highlighting several key theoretical developments that have reshaped our understanding of neural networks. These insights illustrate that neural networks are far more than just empirical techniques—they have rich mathematical properties that continue to yield insights about learning, generalization, and computation.

Double Descent: One of the most striking phenomena in deep learning, observed consistently since around 2016-2017, is double descent. This phenomenon challenges classical statistical learning theory and our intuitions about model complexity and generalization.

In traditional statistical learning, we expect a U-shaped risk curve: as model complex-

ity increases, performance initially improves as the model captures true patterns in the data, but then deteriorates as the model begins to overfit. This trade-off between underfitting and overfitting is considered a principle in statistical learning theory.

Remarkably, neural networks often violate this classical expectation. Researchers have observed that after the initial overfitting phase, performance often improves again with increased model complexity, creating a double descent pattern in the test error curve. This allows for the effective use of models with far more parameters than training examples—sometimes billions of parameters to fit millions of data points—without the catastrophic overfitting that classical theory would predict. We illustrated this phenomenon earlier in Figure 15.4.

The key insight behind this phenomenon lies in how the solution space evolves as we increase model complexity. In classical optimization, adding more parameters typically creates more local minima, making it harder to find the global minimum. However, in neural networks, there appears to be a phase transition where the solution space undergoes a change. As we increase the dimensionality beyond a certain point, the landscape of possible solutions becomes more connected, creating pathways between what were previously isolated local minima. This means that gradient descent can now navigate between different solutions more easily, gradually finding paths to better minima that might have been inaccessible in lower-dimensional spaces.

This is quite different from the classical notion of local minima, where solutions are typically isolated and optimization can get trapped. In overparameterized neural networks, the solution space becomes more like a connected manifold where optimization can flow between different solutions, allowing the network to find better generalizations even with many more parameters than training examples.

Neural Tangent Kernel: Connecting Deep Learning to Kernel Methods   Another theoretical advance, popularized around 2018-2019, is the Neural Tangent Kernel (NTK) framework. This mathematical construct provides a theoretical bridge between neural networks and kernel methods like the Gaussian Processes we studied earlier in this course.

The key insight of NTK theory is that in the limit of infinite width (i.e., as the number of neurons in hidden layers approaches infinity), the behavior of neural networks during training can be described by a kernel function. This kernel depends only on the network architecture and initialization, not on the specific parameter values during training.

What makes this particularly striking is that it connects directly to the optimization landscape we just discussed. The NTK framework helps explain why gradient descent in overparameterized networks can reliably find good solutions despite the non-convex nature of the loss function. In the infinite-width limit, neural networks' loss landscapes become increasingly benign, with local minima converging toward the global minimum. This helps explain why simple gradient-based methods often work surprisingly well for neural networks, without getting trapped in poor local optima.

In this infinite-width limit, neural networks effectively become kernel machines, with the kernel defined by the architecture rather than chosen a priori as in Gaussian Processes. As we saw in our study of Gaussian Processes, kernel methods are powerful because they implicitly map inputs to infinite-dimensional feature spaces while maintaining computational tractability. The NTK reveals that neural networks implicitly define their own kernels through their architecture, giving them similar expressive power while learning the feature representation directly from data.

The NTK framework also sheds light on why certain neural network architectures work better than others for specific problems. Different architectures induce different kernel functions, which in turn have different inductive biases—implicit preferences for certain types of functions. This perspective allows us to reason about neural network design not just empirically but in terms of the properties of the induced kernel.

From a statistical perspective, the NTK provides a rigorous way to analyze the convergence and generalization properties of neural networks. It helps explain why gradient descent on neural networks, despite operating in a highly non-convex loss landscape, often reliably finds good solutions.

Grokking: Beyond Memorization   A particularly intriguing phenomenon observed in neural networks addresses a question about learning: do neural networks merely memorize training examples, or can they truly "understand" underlying patterns? This phenomenon, termed "grokking" (borrowing from science fiction author Robert A. Heinlein's concept of deep intuitive understanding), provides compelling evidence for the latter.

One definition of true intelligence is the ability to generalize beyond what has been explicitly taught—to extract underlying principles and apply them to novel situations. This generalization capability distinguishes rote memorization from genuine understanding and represents a hallmark of human cognition. The grokking phenomenon suggests that neural

networks can exhibit similar capabilities.

When neural networks are trained on algorithmic tasks, such as modular addition (e.g., $(a + b) \mod c$), they display a striking learning pattern. Initially, these networks appear to simply memorize the training examples, achieving perfect training accuracy but poor generalization to unseen examples. However, with continued training and proper regularization, something remarkable happens—the networks suddenly "grok" the underlying pattern, achieving near-perfect generalization to unseen examples.

What makes this transition particularly revealing is the change in internal representations. When a network merely memorizes, its activation patterns tend to be idiosyncratic and seemingly random. However, when the network "groks" the concept, its activation patterns organize into structured representations that reflect the underlying mathematical properties of the task. For modular arithmetic, these representations capture the inherent periodicity of the operation—a clear indication that the network has discovered the mathematical structure rather than just memorizing individual cases.

This phenomenon occurs even when networks have far more parameters than training examples—a regime where classical theory would predict pure memorization. Yet instead of simply memorizing, these networks eventually discover generalizable patterns, suggesting that neural network learning goes beyond mere interpolation between training points.

The implications of grokking extend far beyond simple arithmetic tasks. We see similar phenomena in large language models, which can generalize in surprising ways. For instance, models trained predominantly on English text can, with relatively few examples, generate coherent responses in languages they were minimally exposed to during training. This suggests these models aren't merely memorizing training data but extracting deeper linguistic patterns that transcend specific languages.

Even more striking is the ability of neural networks to perform counterfactual generalization—combining concepts that never co-occurred in training. Just as humans can easily imagine novel combinations, modern neural networks can generate coherent representations of concepts that never appeared together in their training data. This ability to recombine learned elements in novel ways represents a form of creativity that goes beyond memorization.

These capabilities have important implications for how we use neural networks in scientific applications, including the development of foundation models that we'll explore in
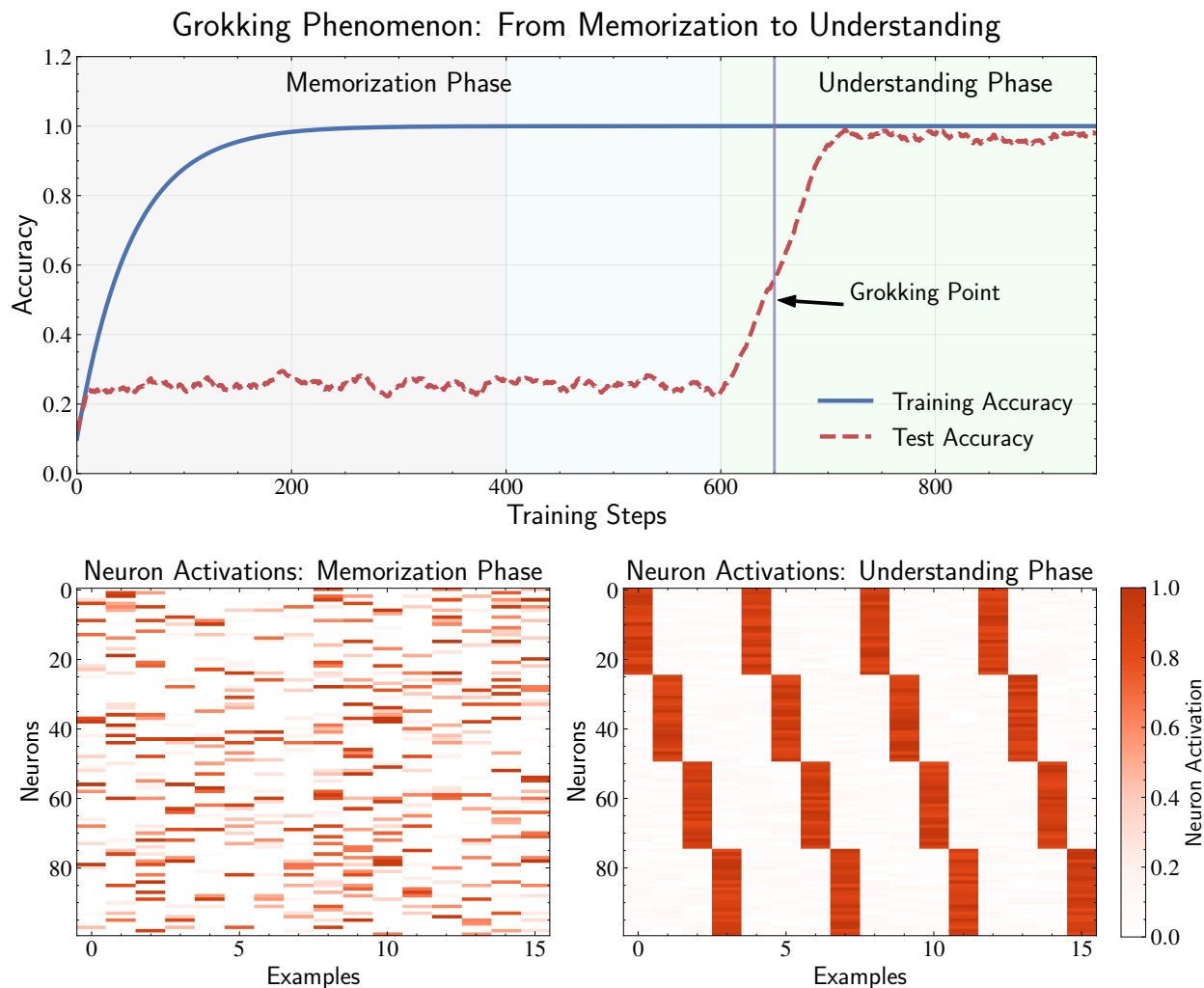
Figure 15.16: Schematic illustration of the "grokking" phenomenon in neural networks. The top panel shows a conceptual representation of accuracy curves: while training accuracy (solid blue) quickly rises as the network memorizes examples, test accuracy (dashed red) remains low for an extended period before suddenly improving at the "grokking point." The bottom panels illustrate the hypothesized transformation in neural representation: during memorization (left), neurons exhibit chaotic, seemingly random activation patterns, while after grokking (right), activations self-organize into structured patterns that reflect the underlying mathematical relationships in the data. This schematic visualization captures the essence of how neural networks can transition from memorizing specific examples to discovering generalizable principles. While simplified, this illustration represents patterns observed in research on neural networks trained on tasks like modular arithmetic, where systematic analysis of internal representations reveals that networks eventually discover compact, generalizable solutions rather than merely interpolating between training examples. This phenomenon challenges the view of neural networks as fancy interpolators and suggests they can develop representations that capture the abstract structure governing the data.

the next section.

In conclusion, phenomena like grokking reveal that neural networks can transcend mere memorization to achieve forms of understanding that capture underlying patterns and principles. Far from being black boxes or fancy interpolation methods, neural networks represent sophisticated learning systems with the capacity to discover and represent complex patterns in data. When applied with theoretical understanding, they offer powerful tools for astronomical research, potentially uncovering patterns and relationships that traditional methods might miss. The ongoing discoveries about how these networks learn and generalize continue to deepen our appreciation of their capabilities and their potential for scientific discovery.
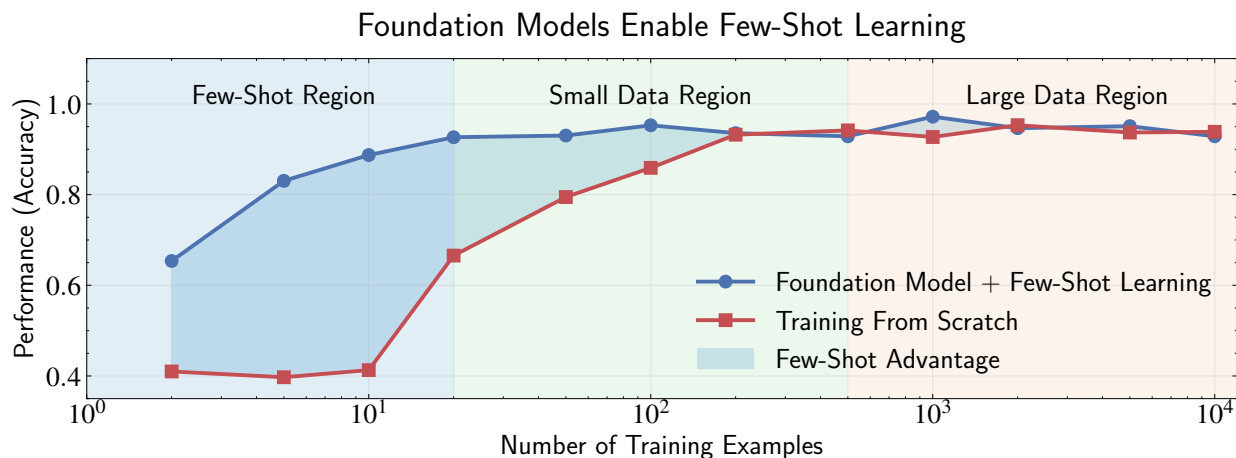
15.9   Foundation Models

The grokking phenomenon described in the previous section points toward a broader shift in how we think about machine learning models. Rather than training specialized networks for each individual task, we can leverage the generalization capabilities that grokking demonstrates by first training large models on diverse, extensive datasets and then adapting them to specific applications with minimal additional training. This approach has given rise to what are known as foundation models.

Foundation models represent a paradigm shift in machine learning: instead of training specialized models for each task from scratch, we first pre-train a general model on diverse, extensive data, then fine-tune it for specific applications. This approach builds directly on the insights from grokking—that neural networks can extract generalizable principles that transcend the specific examples they were trained on.

What makes foundation models particularly interesting is their few-shot learning capability—the ability to perform well on new tasks with very few examples. A model pre-trained on a vast corpus of text and images can rapidly adapt to classify astronomical objects after seeing just a handful of examples from each category. This suggests that during pre-training, these models aren't simply memorizing their training data but are acquiring generalizable knowledge about the structure of data across domains.

The connection between grokking and foundation models is direct. Both phenomena suggest that neural networks can extract generalizable principles from data that enable performance beyond what would be expected from mere memorization. In grokking, net-

Foundation Models Enable Few-Shot Learning

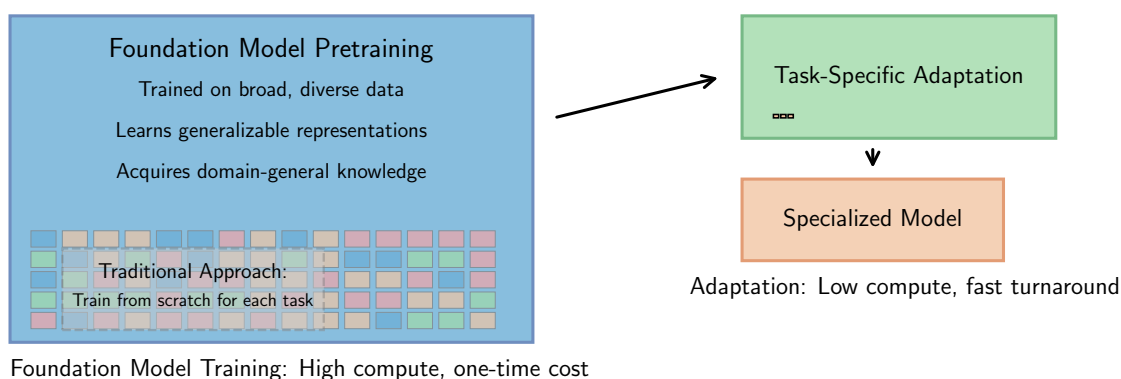## Foundation Model Paradigm vs. Traditional Approach

Figure 15.17: Schematic illustration comparing foundation models with few-shot learning to traditional training approaches. The top panel presents a conceptual performance curve showing how foundation models (blue) achieve high accuracy with very few examples, while models trained from scratch (red) require orders of magnitude more data to reach comparable performance. The shaded blue area highlights the performance advantage of foundation models, particularly pronounced in the few-shot region. The plot demonstrates how performance varies across few-shot, small data, and large data regimes. The bottom panel diagrams the foundation model paradigm: a foundation model is pre-trained once on diverse, extensive data (left blue box), then adapted to specific tasks with minimal examples through fine-tuning (top right green box), resulting in specialized models (right orange box). This approach contrasts with the traditional method of training separate models from scratch for each task (shown in gray). This conceptual diagram illustrates the computational efficiency of the foundation model approach, where the high computational cost of pre-training is incurred only once, while adaptation requires minimal computation and can be performed quickly for new tasks.

works suddenly generalize after extended training on a small dataset; in foundation models, networks leverage broad knowledge acquired during pre-training to quickly adapt to new

scenarios. Both challenge the traditional view of neural networks as simple interpolators.

Transfer Learning in Astronomical Applications   Consider a language model trained on scientific literature that has never seen astronomy datasets. When presented with a few examples of galaxy classification, it can rapidly learn to classify new galaxies by building on its pre-existing knowledge of visual patterns, hierarchical structures, and general scientific concepts. This transfer of knowledge between domains—from general pre-training to specific astronomical applications—suggests that the model has developed representations that capture principles rather than surface-level patterns.

Few-shot learning is particularly valuable in astronomy, where labeled examples of rare phenomena may be scarce. A foundation model pre-trained on broader astronomical data might require only a few examples of a rare event—such as a particular type of stellar explosion or an unusual galaxy merger—to accurately identify other instances. This capability could accelerate the discovery and classification of rare astronomical phenomena from the massive datasets generated by modern observatories.

The practical implications extend beyond simple classification tasks. Foundation models can potentially assist with complex reasoning about astronomical phenomena. For instance, a model trained on diverse scientific texts might help interpret the physical implications of observed spectral features, or suggest follow-up observations based on patterns learned from the scientific literature. This represents a shift from using neural networks merely as pattern recognition tools to using them as scientific reasoning assistants.

Scientific Discovery and Pattern Recognition   In astronomical contexts, foundation models offer intriguing possibilities for scientific discovery. When modeling complex phenomena with neural networks, the goal isn't merely to fit observed data points but to discover the underlying physical laws or patterns. The generalization capabilities demonstrated in grokking suggest that neural networks can potentially discover such patterns, even from limited observations, given sufficient capacity and training.

A neural network trained on limited observational data might, with proper design and training, extract the underlying astrophysical principles rather than just memorizing the training examples. For example, a neural network analyzing spectroscopic data might initially appear to merely interpolate between known stellar spectra, but with sufficient training, it could potentially discover the underlying physics of atomic transitions and stellar atmospheres. Similarly, a network analyzing galaxy morphologies might move beyond

classification based on surface features to discover deeper structural principles governing galaxy formation and evolution.

This potential for discovery extends to cross-domain knowledge transfer. A foundation model trained on diverse scientific data might recognize patterns that connect seemingly disparate phenomena—for instance, identifying similarities between stellar evolution processes and patterns observed in other physical systems. Such connections could lead to new theoretical insights or suggest novel research directions.

For astronomers, this means that neural networks offer more than just efficient data processing—they provide potential windows into physical laws that might be difficult to discern through traditional analysis. By carefully examining what these networks learn—not just their outputs but their internal representations—we might gain new insights into astrophysical phenomena.

Challenges and Considerations While foundation models offer promising capabilities, their application in astronomy requires careful consideration of several factors. The representations learned during pre-training may not always align with the physical principles governing astronomical phenomena. A model trained primarily on our terrestrial generated data might develop biases that are inappropriate for understanding cosmic processes.

Additionally, the scale of computation required for training foundation models raises questions about accessibility and reproducibility in astronomical research. The largest foundation models require computational resources that may be beyond the reach of many research groups, potentially creating disparities in research capabilities.

There are also important questions about interpretability and validation. While foundation models can achieve impressive performance on specific tasks, understanding why they make particular predictions or how their internal representations relate to physical principles remains challenging. For scientific applications, this interpretability gap can be problematic when trying to extract physical insights or validate model predictions against theoretical expectations.

Despite these challenges, foundation models represent an important development in the intersection of artificial intelligence and scientific research. Their ability to transfer knowledge across domains and perform few-shot learning makes them particularly valuable for fields like astronomy, where data may be scarce for rare phenomena but abundant for more common observations. As our understanding of these models improves and computational

resources become more accessible, they are likely to play an increasingly important role in astronomical research and discovery.

15.10   Autoencoders: Nonlinear Dimension Reduction

So far, we have focused on neural networks for supervised learning tasks—primarily regression and classification. In supervised learning, we learn a mapping from input data x to target outputs y, using objective functions like mean squared error (MSE) loss for regression and cross-entropy (CE) loss for classification. These losses provide clear signals for gradient-based optimization, enabling neural networks to learn these input-to-output mappings.

However, neural networks can also be powerful tools for unsupervised learning, where we work with input data x alone, without any target outputs y. Earlier in this course, we explored classical approaches to unsupervised learning, including Principal Component Analysis (PCA) for dimension reduction and K-means clustering and Gaussian Mixture Models (GMMs) for density estimation. These methods provided solutions based on linear algebra and statistical principles but were constrained by their inherent assumptions. Neural networks offer a natural extension to these classical methods, maintaining their conceptual foundations while relaxing their restrictive assumptions.

For dimension reduction, we previously explored Principal Component Analysis (PCA) as a technique for linear dimension reduction. Mathematically, given centered input data $\mathbf{x} \in \mathbb{R}^D$, PCA finds a linear transformation $\mathbf{W} \in \mathbb{R}^{d \times D}$ that maps $\mathbf{x}$ to a lower-dimensional representation $\mathbf{z} \in \mathbb{R}^d$ where $d < D$. This transformation is obtained by identifying the directions of maximum variance through eigendecomposition of the data covariance matrix:

$$\mathbf{\Sigma} = \frac{1}{N} \sum_{n=1}^{N} \mathbf{x}_n \mathbf{x}_n^T \tag{15.74}$$

The resulting projection:

$$\mathbf{z} = \mathbf{W}\mathbf{x} \tag{15.75}$$

preserves as much variance as possible in the lower-dimensional space.

For reconstruction, PCA uses the transpose of the projection matrix:

$$\hat{\mathbf{x}} = \mathbf{W}^T \mathbf{z} \tag{15.76}$$

This gives us the best linear approximation of the original data given the compressed representation. The reconstruction error is then:

$$E = \frac{1}{N} \sum_{n=1}^{N} \|\mathbf{x}_n - \hat{\mathbf{x}}_n\|^2 = \frac{1}{N} \sum_{n=1}^{N} \|\mathbf{x}_n - \mathbf{W}^T \mathbf{W} \mathbf{x}_n\|^2 \tag{15.77}$$

As we have seen in the PCA chapter, this error represents the information lost during the compression process. Minimizing this error is equivalent to maximizing the variance preserved in the low-dimensional space—the two perspectives lead to the same solution.

PCA's strength lies in its closed-form solution through eigendecomposition. However, this mathematical convenience comes at a cost: PCA is constrained to linear transformations. This limitation becomes particularly apparent when our data lies on a nonlinear manifold in the high-dimensional space. The Swiss roll dataset—a two-dimensional sheet curled up in three dimensions—perfectly illustrates this challenge. While PCA would struggle to unfold this structure using only linear projections, an autoencoder can learn to "unroll" the Swiss roll through nonlinear transformations, revealing its true two-dimensional nature.

The Autoencoder Framework Autoencoders address this limitation by replacing PCA's linear transformations with nonlinear neural networks. They preserve the same goal — finding a low-dimensional representation that minimizes reconstruction error—but with the flexibility of nonlinear transformations that can capture complex geometric relationships in the data.

We can formulate the autoencoder approach in direct parallel to PCA. Where PCA performs encoding via $\mathbf{z} = \mathbf{W}\mathbf{x}$ and decoding via $\hat{\mathbf{x}} = \mathbf{W}^T \mathbf{z}$, an autoencoder uses:

1. An encoder function $c(\mathbf{x})$ that maps the input to a low-dimensional representation:

$$\mathbf{z} = c(\mathbf{x}) \tag{15.78}$$

2. A decoder function $f(\mathbf{z})$ that reconstructs the input from this representation:

$$\hat{\mathbf{x}} = f(\mathbf{z}) \tag{15.79}$$

Both functions $c(\mathbf{x})$ and $f(\mathbf{z})$ are implemented as neural networks, though the specific architecture can vary based on the data type and task. While we show a simple fully-

connected network here, in practice we often use specialized building blocks like CNNs for image data or Transformers for sequential data. The choice of architecture reflects the inductive biases we want to encode about our data, but the autoencoder concept remains the same regardless of the specific building blocks used.
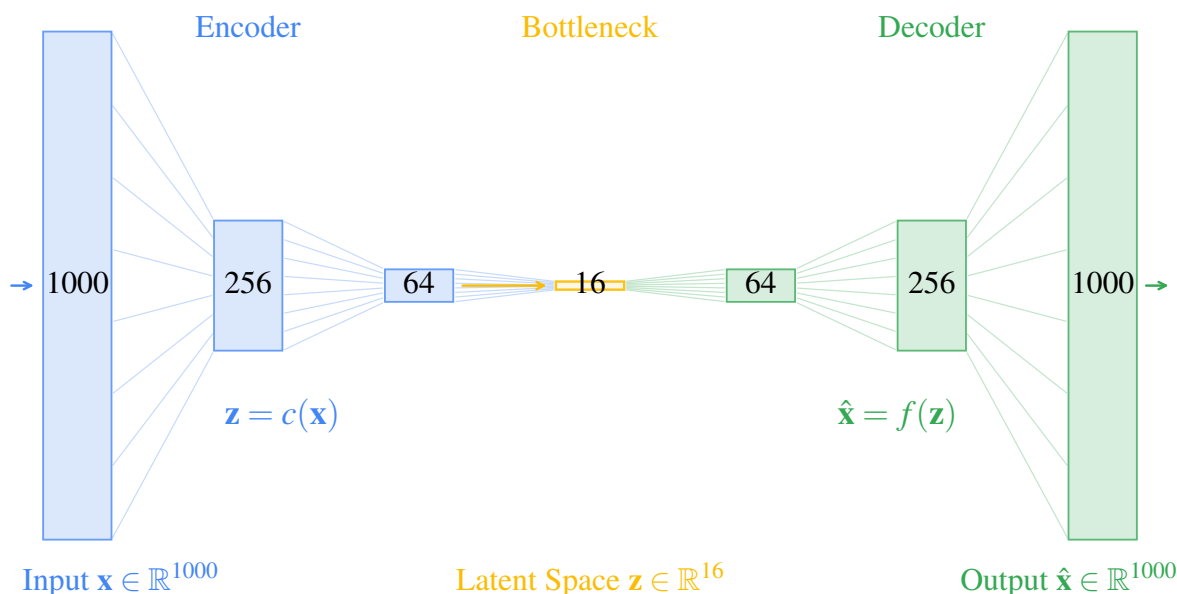

Figure 15.18: Architecture of an autoencoder neural network for nonlinear dimension reduction. The hourglass structure illustrates the compression and reconstruction process: the encoder (blue) progressively reduces input dimensionality from 1000 to 16 through hidden layers of decreasing size (256, 64), while the decoder (green) symmetrically expands from the bottleneck layer back to the original dimensionality. The bottleneck layer (orange) creates an information bottleneck that forces the network to learn efficient representations of the data. During training, the network is optimized to minimize reconstruction error between the input $\mathbf{x}$ and output $\hat{\mathbf{x}}$, encouraging the latent space $\mathbf{z}$ to capture meaningful features. Unlike Principal Component Analysis (PCA) which is limited to linear transformations, autoencoders can model complex nonlinear relationships through their neural network layers.

For illustration, a simple two-layer encoder might look like:

$$c(\mathbf{x}) = \sigma_2(\mathbf{W}_2\sigma_1(\mathbf{W}_1\mathbf{x} + \mathbf{b}_1) + \mathbf{b}_2) \tag{15.80}$$

where σ_1 and σ_2 are nonlinear activation functions like GeLU, and $\mathbf{W}_1$, $\mathbf{W}_2$, $\mathbf{b}_1$, $\mathbf{b}_2$ are the learnable parameters. The decoder $f(\mathbf{z})$ would have a similar structure with its own set of weight matrices and bias vectors. However, this is just one possible implementation - the key is that both encoder and decoder are learnable functions that can capture complex data relationships.

The objective function for training an autoencoder parallels PCA's reconstruction error criterion:

$$\mathcal{L} = \frac{1}{N} \sum_{n=1}^{N} \|\mathbf{x}_n - f(c(\mathbf{x}_n))\|^2 \tag{15.81}$$

This measures the squared distance between the original input and its reconstruction after passing through the encoder and decoder. The parameters we need to optimize include all the weights in both the encoder and decoder networks, regardless of their specific architectural implementation.

Since backpropagation is a general algorithm for computing gradients through any differentiable computation graph, we can use exactly the same mechanism we described earlier to compute gradients of the loss with respect to all these parameters. We then update these parameters using gradient descent, just as we did in supervised learning tasks. The only difference is that here we're optimizing reconstruction error rather than prediction error.

If we constrained the encoder and decoder to be single-layer linear networks with no activation functions:

$$c(\mathbf{x}) = \mathbf{W}_e \mathbf{x} \tag{15.82}$$

$$f(\mathbf{z}) = \mathbf{W}_d \mathbf{z} \tag{15.83}$$

and optimized the reconstruction error, the solution would converge to the PCA projection matrix (up to a rotation). In this sense, a linear autoencoder is equivalent to PCA, and the nonlinear autoencoder represents a natural extension to capture more complex data structures.

Autoencoders employ a distinctive hourglass architecture that mirrors the compression and reconstruction process. The encoder network gradually reduces the input dimensionality through successive layers until reaching the bottleneck layer—the low-dimensional latent space $\mathbf{z}$. The decoder then symmetrically expands back to the original dimensions. The bottleneck layer serves as the crucial constraint that drives meaningful learning. Without this bottleneck, the network could simply learn to copy inputs directly to outputs, failing to extract any useful features. This architectural constraint forces the network to identify and prioritize the most essential aspects of the data needed for accurate reconstruction.

This compression mechanism shares conceptual similarities with PCA's approach to

finding principal components. Just as PCA identifies directions that optimally generate the data, the autoencoder's bottleneck layer captures the most important patterns for reconstruction. However, autoencoders offer greater flexibility through their nonlinear transformations. The latent space dimensions often encode interpretable features because they represent the most efficient pathways for data generation through the decoder network, similar to how PCA vectors capture physically meaningful directions in data space.
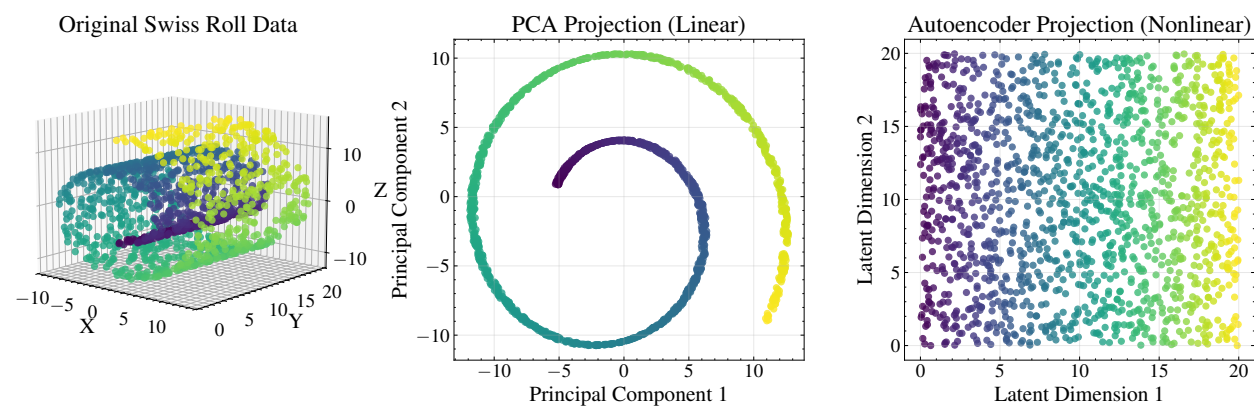

Figure 15.19: Comparison of linear and nonlinear dimensionality reduction techniques using the Swiss roll dataset. The left panel shows the original Swiss roll data—a two-dimensional manifold (sheet) curled in three-dimensional space, with colors indicating positions along the spiral. The middle panel demonstrates Principal Component Analysis (PCA), a linear technique that projects data onto directions of maximum variance. PCA fails to properly unfold the Swiss roll structure because it is constrained to linear transformations, resulting in overlapping points from different parts of the manifold (note the mixing of colors). The right panel illustrates the result of an autoencoder-based dimensionality reduction. By leveraging nonlinear transformations, the autoencoder effectively "unrolls" the Swiss roll, preserving local neighborhood relationships and maintaining the continuous color progression that represents positions along the original manifold.

The resulting compressed representations frequently reveal intuitive features. For example, in face image analysis, the latent dimensions might naturally encode attributes such as pose, lighting, expression, and identity. Similarly, for galaxy images, these dimensions could correspond to physical properties like morphological type, size, orientation, and brightness. These features emerge organically from the network's optimization process rather than through explicit training, as they represent the most efficient encoding paths through the bottleneck.

Applications in Astronomy   Beyond simple dimension reduction, autoencoders have found numerous practical applications in astronomy. One particularly valuable application is denoising. Consider astronomical images corrupted by noise—cosmic rays, readout noise,

or sky background fluctuations. Since noise typically lacks the structured correlations present in the signal, it cannot be efficiently encoded through the bottleneck. When the autoencoder reconstructs the input, it tends to preserve the structured signal while discarding the random noise.

Denoising autoencoders formalize this insight by explicitly training on noisy inputs while targeting clean outputs. If we have pairs of noisy and clean examples (which might be obtained from simulations or controlled observations), we can train:

$$\mathcal{L} = \frac{1}{N} \sum_{n=1}^{N} \|\mathbf{x}_n^{\text{clean}} - f(c(\mathbf{x}_n^{\text{noisy}}))\|^2 \tag{15.84}$$

This encourages the network to learn a mapping that removes noise while preserving the underlying signal.

It's crucial to understand that denoising autoencoders don't actually create new information or "generate more photons" from the observations. From a Bayesian perspective, what they're doing is projecting the noisy data onto a learned prior distribution of what we expect the signal to look like. This prior is encoded in the network's weights through training on similar examples. While this can be extremely useful for visual analysis and pattern recognition, it's important to recognize that the "cleaned" output represents our best guess based on prior knowledge, not additional observational data.

This distinction is particularly important in astronomy, where the temptation to interpret denoised results as "super-resolution" or "enhanced signal-to-noise" can be misleading. The network isn't magically recovering lost information—it's making educated guesses based on patterns it has learned from similar data. This approach has proven effective for cleaning astronomical images, spectra, and time series data, but users must be careful not to overinterpret the results or treat them as if they contained more observational information than the original data.

Autoencoders can also identify anomalies or outliers in data. After training on a dataset of "normal" examples, instances that produce large reconstruction errors are likely outliers—data points that don't conform to the patterns learned by the autoencoder. This technique has been applied to detect unusual astronomical objects, instrument failures, or data quality issues.

For all these applications, the key advantage of autoencoders over PCA is their abil-

ity to capture nonlinear relationships. Astronomical data often exhibits complex, nonlinear structure—the spectrum of a star depends nonlinearly on its temperature, pressure, and chemical composition; galaxy morphologies form complex manifolds in image space; light curves of variable stars display nonlinear patterns across time. By replacing linear transformations with flexible neural networks, autoencoders can discover and leverage these nonlinear patterns, leading to more efficient compression, better denoising, and more accurate anomaly detection.

The success of autoencoders exemplifies a recurring theme in our exploration of neural networks: by relaxing restrictive assumptions of classical methods while preserving their core principles, neural networks offer natural extensions that handle the complexity of real-world data. Just as neural networks extended linear regression to capture nonlinear relationships in supervised learning, autoencoders extend PCA to perform nonlinear dimension reduction in unsupervised learning.

15.11   Encoder-Decoder Architectures

Having explored autoencoders for nonlinear dimension reduction, we now examine a broader class of neural network architectures that extend beyond the self-reconstruction paradigm. While autoencoders learn to map inputs back to themselves through a compressed bottleneck, encoder-decoder architectures can establish more complex relationships between different data domains.

The key insight driving this extension is that an autoencoder's bottleneck layer contains more than just compressed information—it captures meaningful representations of the input data's essential structure. These latent representations abstract away superficial details while preserving the underlying patterns that define the data. If these representations truly encode the "knowledge" or "semantics" of the data, they should prove useful for tasks beyond simple reconstruction.

Mathematically, we can generalize the autoencoder framework by maintaining the encoder structure $c(\mathbf{x}) \to \mathbf{z}$ while introducing flexibility in how we use the latent representation $\mathbf{z}$. Instead of constraining the decoder to reconstruct the original input, we can train it to produce outputs in different domains or modalities. The encoder $c(\cdot)$ and decoder $g(\cdot)$ remain neural networks, but their architectures may be tailored to specific input and output requirements.

This generalized framework enables two particularly powerful capabilities for astronomical research: domain transfer and cross-modal learning.

Domain Transfer   Domain transfer creates mappings between different representations of similar data types. Instead of the autoencoder's $\mathbf{x} \mapsto \mathbf{z} \mapsto \mathbf{x}$ pattern, domain transfer implements $\mathbf{x} \mapsto \mathbf{z} \mapsto \mathbf{y}$, where $\mathbf{x}$ and $\mathbf{y}$ belong to related but distinct domains:

$$\mathbf{z} = c(\mathbf{x}) \tag{15.85}$$

$$\mathbf{y} = g(\mathbf{z}) \tag{15.86}$$

A practical astronomical application involves bridging the gap between simulated and observed data. Consider stellar spectroscopy, where theoretical atmospheric models provide predictions of stellar spectra based on physical parameters like temperature, surface gravity, and metallicity. However, these simulations often fail to capture all physical processes—missing opacity sources, incomplete line broadening mechanisms, or simplified atmospheric assumptions create systematic differences between predicted and observed spectra.

An encoder-decoder network can learn these systematic differences by training on pairs of (simulated, observed) spectra. The encoder extracts the underlying physical information from simulated spectra, while the decoder learns to translate this information into more realistic observed spectra. The latent space $\mathbf{z}$ still encodes the physical parameters, but the decoder $g(\mathbf{z})$ produces outputs that better match observational reality than direct simulation.

This approach acknowledges an important reality in scientific modeling: our simulations represent imperfect approximations of physical processes. Rather than discarding these models, domain transfer allows us to correct for their systematic limitations while preserving their physical basis. The resulting hybrid approach combines the theoretical understanding embedded in simulations with empirical corrections learned from data.

Domain transfer also enables cross-wavelength predictions within astronomy. For example, we might train a network to predict infrared galaxy spectra from optical observations, or to generate radio emission maps from optical images. While these predictions represent educated guesses based on learned correlations rather than new physical information, they can guide observational strategies and help identify promising targets for follow-up studies.

Cross-Modal Learning with Shared Latent Spaces   Cross-modal learning takes a different approach by forcing multiple data modalities to share a common latent representation.

Rather than mapping from one domain to another, this architecture requires different data types to encode into and decode from the same latent space:

$$\mathbf{z}_1 = c_1(\mathbf{x}_1) \tag{15.87}$$

$$\mathbf{z}_2 = c_2(\mathbf{x}_2) \tag{15.88}$$

$$\hat{\mathbf{x}}_1 = g_1(\mathbf{z}) \tag{15.89}$$

$$\hat{\mathbf{x}}_2 = g_2(\mathbf{z}) \tag{15.90}$$

Each modality has its own encoder and decoder, but all share the same latent representation $\mathbf{z}$. The training objective typically involves reconstructing each modality from itself, with the crucial constraint that different modalities must use the same latent space. This forces the network to discover a unified representation that captures information shared between modalities.

Consider a concrete astronomical example: encoding both galaxy images and galaxy spectra into the same latent space. The image encoder c_1 must learn to extract information from morphological features, colors, and spatial structure, while the spectrum encoder c_2 extracts information from spectral lines, continuum shapes, and emission features. The constraint that both encoders map to the same latent space forces the network to identify the underlying physical properties that manifest in both modalities.

This shared representation naturally organizes itself according to physical properties that affect both modalities. For instance, a galaxy's stellar population age influences both its color in images and the strength of specific spectral absorption features. The stellar mass affects both the galaxy's apparent size and its overall spectral energy distribution. By constraining the latent space to represent both modalities, the network discovers these physical relationships without explicit supervision.

The key distinction from domain transfer is that cross-modal learning seeks a common representational space rather than a mapping between spaces. This approach enables several capabilities:

- Self-reconstruction within each modality (preserving the autoencoder property)

- Cross-modal prediction (generating spectra from images or vice versa)

- Discovery of latent variables corresponding to shared physical properties
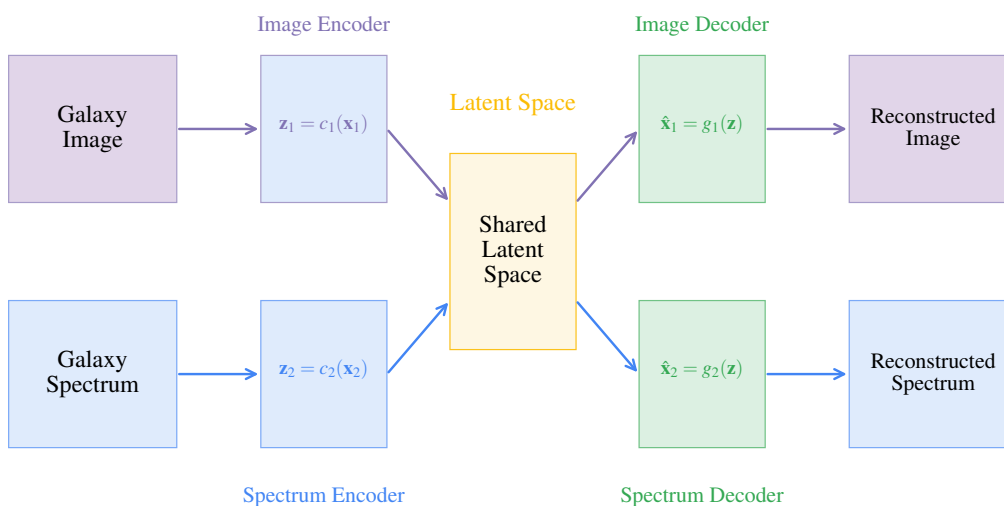
(a) Domain Transfer
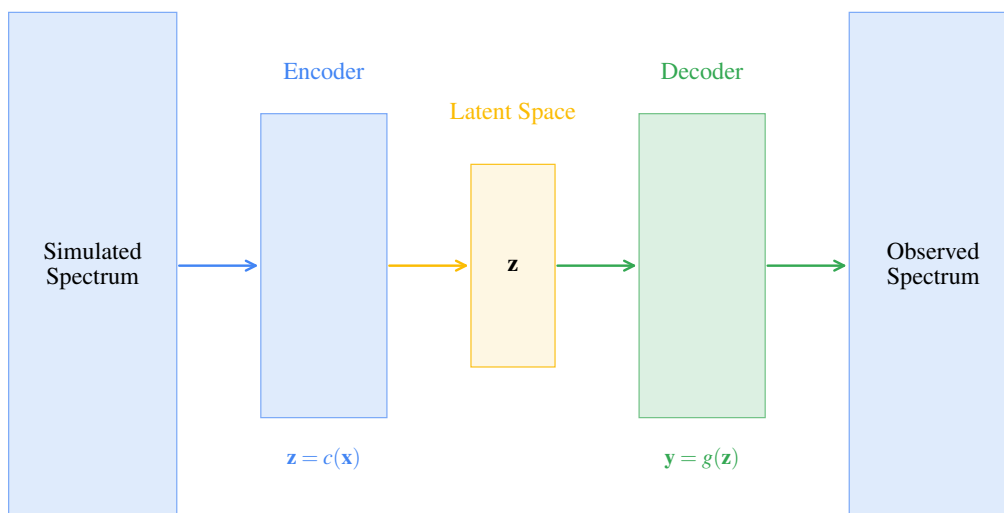
(b) Cross-Modal Learning

Figure 15.20: Encoder-decoder architectures for transformations between data domains. (a) Domain transfer maps data between different representations of the same type, such as converting simulated stellar spectra to match observed spectra. This approach helps bridge the gap between theoretical models and observations by learning systematic differences between simulations and real data. (b) Shared latent space architectures enable integration of different data modalities by mapping them to a common representation. For example, by encoding both galaxy images and spectra into the same latent space, the network learns correlations between visual morphology and spectral features, forcing the network to discover relationships between different data types.

Cross-modal learning proves particularly valuable in astronomy, where objects are routinely observed through multiple instruments and across different wavelength regimes. Large surveys are routinely providing both imaging and spectroscopic data for millions to billions of galaxies, while upcoming facilities will generate multi-wavelength observations across unprecedented scales. By learning unified representations from these diverse observations, we can discover the physical properties that manifest across observational modalities.

The latent representations learned through encoder-decoder architectures often reveal physically meaningful organization, even without explicit training on physical parameters. In galaxy studies, latent dimensions might naturally correspond to properties like stellar age, metallicity, star formation rate, or morphological type. This emergent organization occurs because these physical properties represent the most efficient pathways for encoding information that can successfully reconstruct both modalities.

This capability makes encoder-decoder networks valuable not just for prediction but for scientific discovery. By examining how the latent space organizes itself and what features the network considers important for reconstruction, we can gain insights into the relationships between different observational signatures of the same physical phenomena.

The broader significance of encoder-decoder frameworks lies in their ability to create unified representations from heterogeneous data sources—a persistent challenge in astronomy where observations span multiple instruments, surveys, and wavelength regimes. Rather than analyzing each data type in isolation, these architectures enable integrated analysis that potentially leads to more complete understanding of astronomical objects and phenomena.

15.12   Mixture Density Networks

Having explored encoder-decoder architectures and dimension reduction through autoencoders, we now turn to another application where neural networks extend beyond simple supervised learning: density estimation. This represents a crucial area where neural networks move beyond deterministic curve fitting to model the full probabilistic structure of data.

To understand why density estimation matters, consider a limitation of traditional supervised neural networks. Standard multilayer perceptrons assume a deterministic one-to-one mapping from input $\mathbf{x}$ to output $\mathbf{y}$. However, this assumption frequently breaks down in scientific applications, where one-to-many mappings occur naturally.

The Problem with One-to-Many Relationships   Consider the Swiss roll dataset we encountered earlier, but now applied to a supervised learning task. In this scenario, data points form a complex, folded structure where a single input value x corresponds to multiple distinct output values y. If we train a standard neural network to predict y from x using mean squared error (MSE), the result fails to capture the true data structure.

The network learns to predict the conditional mean $E[y|x]$ at each input point — effectively averaging across all possible outputs for a given input. This averaging smooths out the multimodal nature of the true distribution, producing predictions that may not correspond to any realistic outcome. At an input where three distinct output values are equally likely, the network predicts their average, which might represent an impossible configuration.
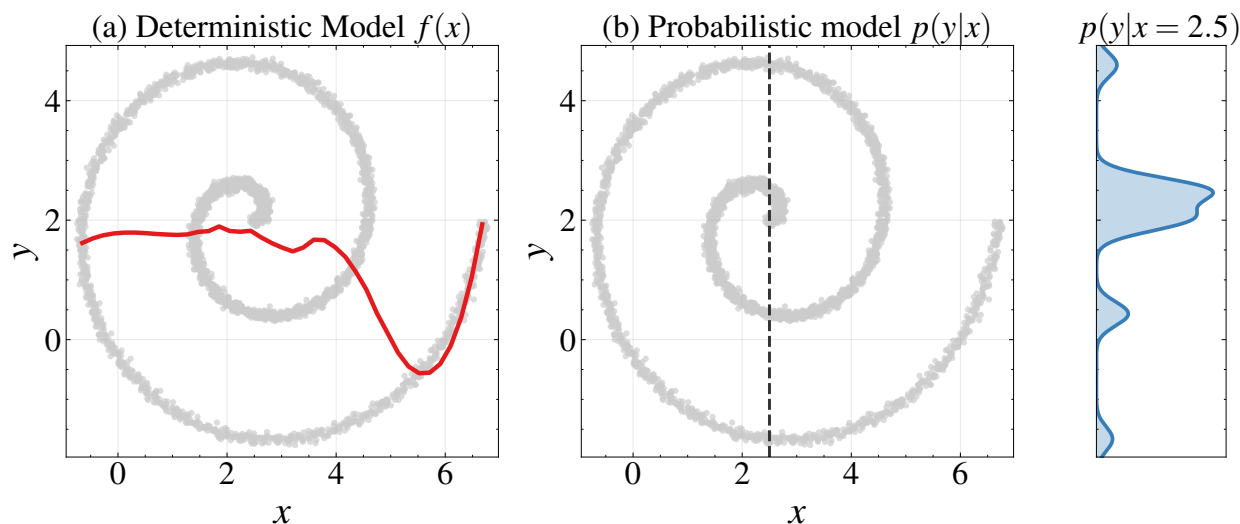

Figure 15.21: Comparing deterministic and probabilistic approaches to modeling one-to-many relationships. Panel (a) shows how a standard neural network trained with mean squared error (red curve) models the Swiss roll dataset. This deterministic approach must predict a single output for each input, effectively averaging across multiple valid solutions at the same x coordinate. Panel (b) shows a probabilistic approach with a vertical dashed line at $x = 2.5$ demonstrating how one input can correspond to multiple possible outputs. The right panel shows the conditional distribution $p(y|x = 2.5)$, with multiple peaks capturing all possible outcomes and their probabilities. Mixture Density Networks model the full conditional distribution $p(y|x)$ that varies smoothly with x, allowing the model to capture how the multimodal nature of the data gradually changes across the input space.

One-to-many relationships pervade astronomy and other scientific fields. When cosmological simulations use identical physical parameters but different random seeds, they produce structurally similar but detailed different realizations of the same underlying physics. Multiple galaxy types might share the same stellar mass while differing in morphology, metal-

licity, or star formation history. These examples highlight that true one-to-one mappings are rare in complex scientific domains.

This reality requires us to move beyond deterministic mappings. Instead of seeking a function $y = f(x)$ that makes single predictions, we need frameworks that model the entire distribution of possible outcomes given an input.

From Unconditional to Conditional Density Estimation   This need brings us to density estimation, which takes two distinct forms. In classical unconditional density estimation, which we explored with Gaussian Mixture Models (GMMs), we learn the probability density function $p(\mathbf{x})$ of our data. For supervised problems with one-to-many relationships, we need conditional density estimation—learning $p(\mathbf{y}|\mathbf{x})$ rather than just $p(\mathbf{x})$.

The distinction is crucial: $p(\mathbf{x})$ describes the general distribution of our data, while $p(\mathbf{y}|\mathbf{x})$ captures how the distribution of $\mathbf{y}$ varies with different values of $\mathbf{x}$. This conditional framework allows us to represent the full range of possible outputs for each input through probability distributions.

This approach aligns with the Bayesian perspective we have emphasized throughout this course. In Bayesian analysis, we routinely work with likelihood functions, which are conditional distributions. The conditional distribution approach acknowledges inherent variability in complex systems—even when underlying physics remains fixed, specific realizations may vary.

Focusing on conditional distributions $p(\mathbf{y}|\mathbf{x})$ rather than joint distributions $p(\mathbf{x}, \mathbf{y})$ also offers computational advantages. Describing the joint distribution for complex structures like the Swiss roll would be extremely challenging. However, if we fix $\mathbf{x}$ and examine the resulting distribution of $\mathbf{y}$, we often find simpler, more tractable structures.

We can draw inspiration from our previous work with Gaussian Mixture Models. GMMs excel at capturing complex, multimodal distributions by representing multiple peaks — precisely the structure we observe in one-to-many mappings. However, standard GMMs have a key limitation: they model a single, static distribution $p(\mathbf{y})$ rather than one that varies with input conditions $p(\mathbf{y}|\mathbf{x})$.

Consider using a single GMM to model $p(\mathbf{y})$ for all values of $\mathbf{x}$ in our Swiss roll example. Such a model would need to represent all possible y values across the entire range of x, effectively averaging out the distinct local patterns that exist at specific x val-

ues. What we need instead is a GMM whose parameters—means, covariances, and mixture weights—change as functions of $\mathbf{x}$.

These parameter changes should be gradual and smooth. When two input values $\mathbf{x}_1$ and $\mathbf{x}_2$ are similar, their corresponding conditional distributions $p(\mathbf{y}|\mathbf{x}_1)$ and $p(\mathbf{y}|\mathbf{x}_2)$ should also be similar. This assumption of local smoothness is both physically reasonable and computationally advantageous.

The Mixture Density Network Framework This insight leads to Mixture Density Networks (MDNs), which combine neural networks with mixture models to perform conditional density estimation. The core idea is straightforward: use a neural network to compute the parameters of a GMM as functions of the input $\mathbf{x}$. The resulting model can capture complex, multimodal distributions that vary smoothly across the input space.

Formally, an MDN models the conditional distribution $p(\mathbf{y}|\mathbf{x})$ as a mixture of Gaussians:

$$p(\mathbf{y}|\mathbf{x}) = \sum_{k=1}^{K} \pi_k(\mathbf{x}) \mathcal{N}(\mathbf{y}|\boldsymbol{\mu}_k(\mathbf{x}), \boldsymbol{\Sigma}_k(\mathbf{x})) \tag{15.91}$$

Here, $\pi_k(\mathbf{x})$ represents the mixture weights, $\boldsymbol{\mu}_k(\mathbf{x})$ the means, and $\boldsymbol{\Sigma}_k(\mathbf{x})$ the covariance matrices—all varying as functions of the input $\mathbf{x}$. For each value of $\mathbf{x}$, we have a different GMM describing the distribution of $\mathbf{y}$.

The innovation of MDNs lies in parameterizing these functions through neural networks rather than specifying explicit functional forms. This leverages the universal approximation capabilities of neural networks to learn complex relationships directly from data without requiring prior knowledge of the true functional forms.

Architecturally, an MDN consists of a neural network that takes $\mathbf{x}$ as input and produces parameters for a GMM as output. For a mixture with K components in a D-dimensional output space, the network must output:

- K mixture weights $\pi_k(\mathbf{x})$ (constrained to sum to 1)

- $K \times D$ mean values $\boldsymbol{\mu}_k(\mathbf{x})$ (one D-dimensional mean vector per component)

- Covariance parameters for each component (often simplified to diagonal matrices)

Training and Implementation Optimization of MDNs follows the maximum likelihood principle we have employed throughout this course. Given a dataset of input-output pairs
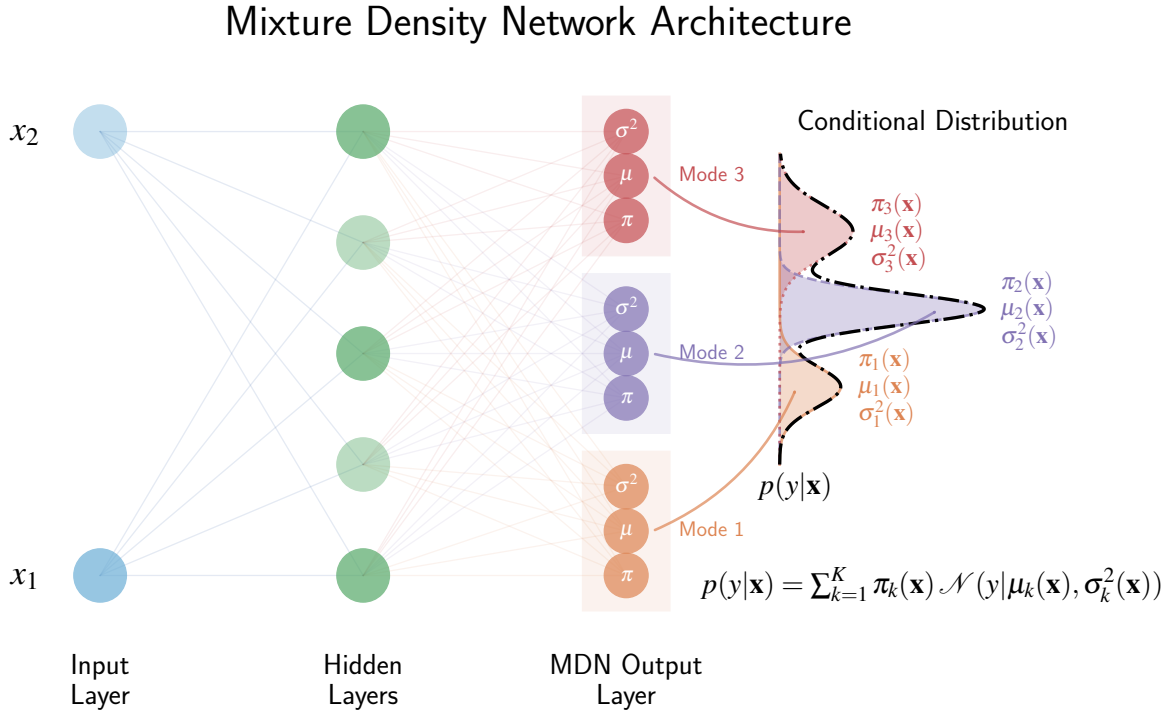
Mixture Density Network Architecture

Figure 15.22: Architecture of a Mixture Density Network (MDN) for modeling conditional probability distributions. The left side shows the neural network structure with input neurons (blue), hidden neurons (green), and output neurons organized by mixture component (orange, purple, red). Each mode has three parameter outputs: mixture weight (π_k), mean (μ_k), and variance (σ_k^2). The right side visualizes the resulting conditional distribution $p(y|\mathbf{x})$ as a mixture of Gaussians, with each colored component corresponding to a mode in the network output. MDNs extend traditional neural networks to model full probability distributions rather than point estimates, making them particularly valuable for problems with one-to-many relationships where a single input can correspond to multiple plausible outcomes. The network learns to output the parameters of a mixture model that varies with the input, effectively implementing the conditional distribution $p(y|\mathbf{x}) = \sum_{k=1}^{K} \pi_k(\mathbf{x})\mathcal{N}(y|\mu_k(\mathbf{x}), \sigma_k^2(\mathbf{x}))$. This approach enables uncertainty quantification and multimodal predictions, addressing a limitation of standard (deterministic) neural networks in scientific applications.

$\{(\mathbf{x}_n, \mathbf{y}_n)\}_{n=1}^{N}$, we maximize the log-likelihood:

$$\mathcal{L}(\mathbf{w}) = \sum_{n=1}^{N} \log p(\mathbf{y}_n|\mathbf{x}_n, \mathbf{w}) = \sum_{n=1}^{N} \log \left[\sum_{k=1}^{K} \pi_k(\mathbf{x}_n)\mathcal{N}(\mathbf{y}_n|\boldsymbol{\mu}_k(\mathbf{x}_n), \boldsymbol{\Sigma}_k(\mathbf{x}_n)) \right] \qquad (15.92)$$

where $\mathbf{w}$ represents the neural network parameters. This optimization uses the same gradient-based methods we have discussed throughout this chapter.

Practical implementation requires attention to constraints. Since mixture weights $\pi_k(\mathbf{x})$ must be non-negative and sum to one, we apply a softmax function to the correspond-

ing network outputs:

$$\pi_k(\mathbf{x}) = \frac{\exp(z_k(\mathbf{x}))}{\sum_{j=1}^{K} \exp(z_j(\mathbf{x}))} \tag{15.93}$$

where $z_k(\mathbf{x})$ are the raw network outputs. To ensure positive variances, we typically apply exponential or softplus functions to the relevant outputs.

Numerical stability requires working with log-probabilities rather than probabilities directly, as products of small probabilities can cause underflow. The objective function becomes the negative log-likelihood, optimized using standard gradient descent methods.

Applications in Astronomy MDNs have found numerous applications in astronomy where one-to-many relationships abound. In stellar parameter inference, the same photometric observations could arise from different combinations of temperature, gravity, and metallicity due to degeneracies and unmodeled effects like extinction. An MDN can provide complete posterior distributions over stellar parameters rather than just point estimates, properly capturing uncertainty and potential multimodality.

Color-magnitude diagrams (CMDs) exhibit complex multimodal distributions due to superposition of different stellar populations and evolutionary stages. MDNs can model these structures, enabling more accurate stellar population analysis and distance determinations.

In cosmological parameter estimation, MDNs can model the conditional distribution of cosmological parameters given summary statistics of observations. This probabilistic approach captures degeneracies and constraints in parameter space, aligning with the Bayesian framework that dominates modern cosmological inference.

These applications represent early examples of simulation-based inference (SBI), where neural networks learn to approximate complex likelihoods or posteriors from simulated data. The ability to model full conditional distributions rather than point estimates makes MDNs particularly valuable for scientific applications where uncertainty quantification is as important as the predictions themselves.

The contrast between standard neural networks and MDNs illustrates a broader theme: the trade-off between computational simplicity and rigorous uncertainty quantification. While standard networks excel in efficiency, MDNs provide the probabilistic framework essential for scientific inference, representing a bridge between deterministic machine learning and the probabilistic methods we have studied throughout this course.

15.13   Modern Neural Density Estimators

While MDNs provide a solid foundation for neural density estimation, they represent just one approach within a broader class of methods that has expanded considerably in recent years. The field of neural density estimators encompasses techniques that use neural networks to estimate probability density functions, whether joint or conditional distributions. These methods address limitations of MDNs while opening new possibilities for modeling complex probabilistic relationships in scientific data.

Understanding these techniques matters beyond simple curve fitting. In many scientific applications, we are not fitting curves at all—instead, we are capturing the full probabilistic relationship between variables, providing crucial information about uncertainty. This capability for uncertainty quantification proves essential in the intersection of artificial intelligence and scientific research.

Limitations of Mixture Models   MDNs, despite their utility, carry an important constraint: they rely on a specific parametric form—the Gaussian mixture model. While GMMs are flexible, they may require many components to approximate complex distributions accurately. Each additional component increases the number of parameters that must be estimated, potentially leading to overfitting with limited data.

More fundamentally, the Gaussian assumption may not match the true structure of scientific data. Consider astronomical observations where measurement errors follow heavy-tailed distributions due to cosmic ray hits, or where physical processes generate distributions with sharp boundaries that Gaussians cannot represent well. In such cases, forcing a Gaussian mixture representation may introduce systematic biases.

These limitations have motivated the development of more expressive neural density estimators that can represent arbitrary distributions without committing to specific parametric families. The key insight unifying these approaches is the recognition that if we can transform a complex distribution into a simple one (like a standard Gaussian), we can perform density estimation by working in reverse—transforming from the simple distribution back to the complex one.

The Transformation Principle   At the heart of modern density estimation lies a mathematical insight: complex probability distributions can be understood through their relationship to simple ones. This principle—transforming between simple and complex distribu-

tions—connects to deep mathematical concepts in optimal transport theory, which studies efficient methods for transforming one distribution into another.

An interesting perspective on this approach comes from cosmology itself. The universe began with nearly Gaussian random fields—effectively a Gaussian Process like those we studied earlier—and through gravitational evolution, developed the complex, non-Gaussian structures we observe today. Neural density estimators essentially attempt to reverse-engineer this process, learning transformations that map complex distributions back to simple ones, or vice versa.

This transformation principle manifests in two main approaches that have gained prominence: normalizing flows and diffusion models. While these methods differ in implementation, both use the same core idea of establishing mappings between simple and complex distributions.

Normalizing Flows Normalizing flows directly implement the transformation approach by learning invertible mappings between a simple base distribution (typically a standard Gaussian) and a complex target distribution. The key requirement is invertibility: we must be able to transform in both directions between the distributions.

The mathematical foundation rests on the change of variables formula from calculus. If we transform a random variable $\mathbf{z}$ with known density $p_Z(\mathbf{z})$ using an invertible function f to obtain $\mathbf{y} = f(\mathbf{z})$, the density of $\mathbf{y}$ is:

$$p_Y(\mathbf{y}) = p_Z(f^{-1}(\mathbf{y})) \left| \det \left(\frac{\partial f^{-1}}{\partial \mathbf{y}} \right) \right| \tag{15.94}$$

The Jacobian determinant term accounts for how the transformation stretches or compresses space, ensuring that probability mass is conserved during the transformation.

By parameterizing f as a neural network while ensuring it remains invertible, we can learn complex distributions directly from data. The network learns to map from a simple base distribution (where we can easily evaluate probabilities and generate samples) to our target distribution (where evaluation and sampling would otherwise be difficult).

What makes normalizing flows particularly useful is their dual capability: they provide both exact density evaluation and efficient sampling. For density evaluation, we transform an observed data point to the base distribution and compute its probability there. For sampling, we draw from the simple base distribution and transform the samples to our
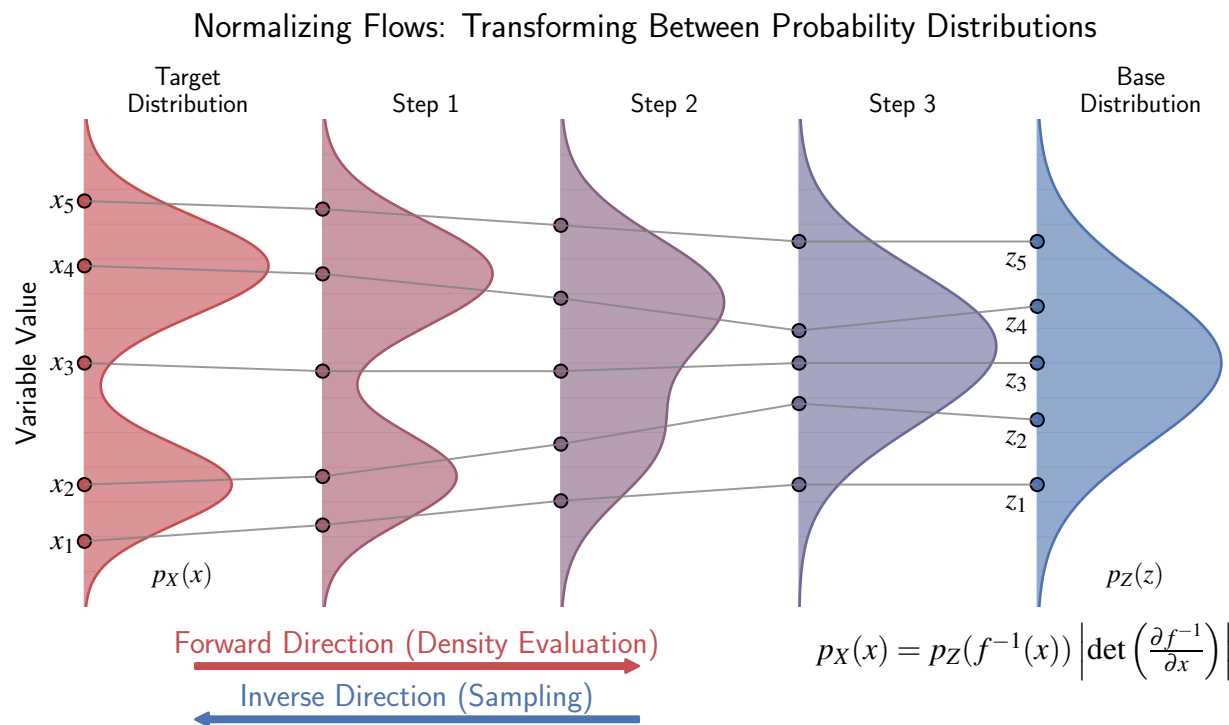
Figure 15.23: Visualization of normalizing flows showing the gradual transformation between probability distributions. The diagram illustrates how a complex bimodal target distribution (left, red) is progressively transformed through intermediate steps into a standard Gaussian base distribution (right, blue). The gray lines track specific points (x_1 through x_5) as they move through each transformation stage, demonstrating how probability mass is transported from one space to another. The forward direction (left to right) enables density evaluation using the change of variables formula shown at the bottom, while the inverse direction (right to left) allows sampling from the complex target distribution. The Jacobian determinant in the formula accounts for how volume elements are stretched or compressed during transformation. Normalizing flows learn this invertible mapping directly from data, providing both precise density estimation and efficient sampling capabilities—a combination that makes them particularly powerful for modeling complex astronomical distributions where analytical forms for likelihoods are often intractable.

target distribution. This bidirectional capability addresses both inference and generation needs.

However, this power comes with constraints. The requirement for invertibility severely limits the types of neural networks we can use. Not all transformations are invertible, and even among those that are, not all have computationally tractable inverses or Jacobian determinants. This forces normalizing flows to use specialized architectures that sacrifice some expressivity to maintain invertibility.

Diffusion Models The limitations of invertibility requirements have motivated an alternative approach: can we achieve the same goal—transforming between simple and complex distributions—without requiring exact invertibility for the entire transformation? This question leads to diffusion models, which offer a different path to the same destination.

Diffusion models work by gradually transforming a complex distribution into a simple Gaussian through many small steps of adding noise. This forward process follows a Markov chain where each step adds controlled amounts of Gaussian noise according to a predefined schedule:

$$x_t = \sqrt{1 - \beta_t} x_{t-1} + \sqrt{\beta_t} \varepsilon \tag{15.95}$$

where x_t is the data at time step t, β_t is the noise schedule (typically increasing from near 0 to near 1), and $\varepsilon \sim \mathcal{N}(0, I)$ is random Gaussian noise.

As t approaches the final time step T, the distribution of x_t approaches a standard Gaussian distribution, regardless of the initial data distribution. The noise schedule is designed so that after sufficient steps, any complex structure in the original data is completely obliterated by accumulated noise.

The neural network is then trained to reverse this process by learning to predict the noise component ε that was added at each step:

$$\hat{\varepsilon}_\theta(x_t, t) \approx \varepsilon \tag{15.96}$$

where $\hat{\varepsilon}_\theta$ is the neural network with parameters θ. By predicting and removing this noise, the model can gradually denoise a pure Gaussian sample back into a sample from the target distribution.

The key insight is that by breaking the transformation into many small steps, we can "Gaussianize" a complex distribution without requiring strict invertibility of the entire transformation. Each step needs only to model the noise component, which can be accomplished using standard neural architectures without invertibility constraints.

This progressive approach offers greater flexibility in architectural choices compared to normalizing flows. Since we only need to model noise components rather than entire invertible transformations, we can use standard neural network architectures. The relationship between original data and noised versions follows well-defined statistical principles, providing a solid mathematical foundation.
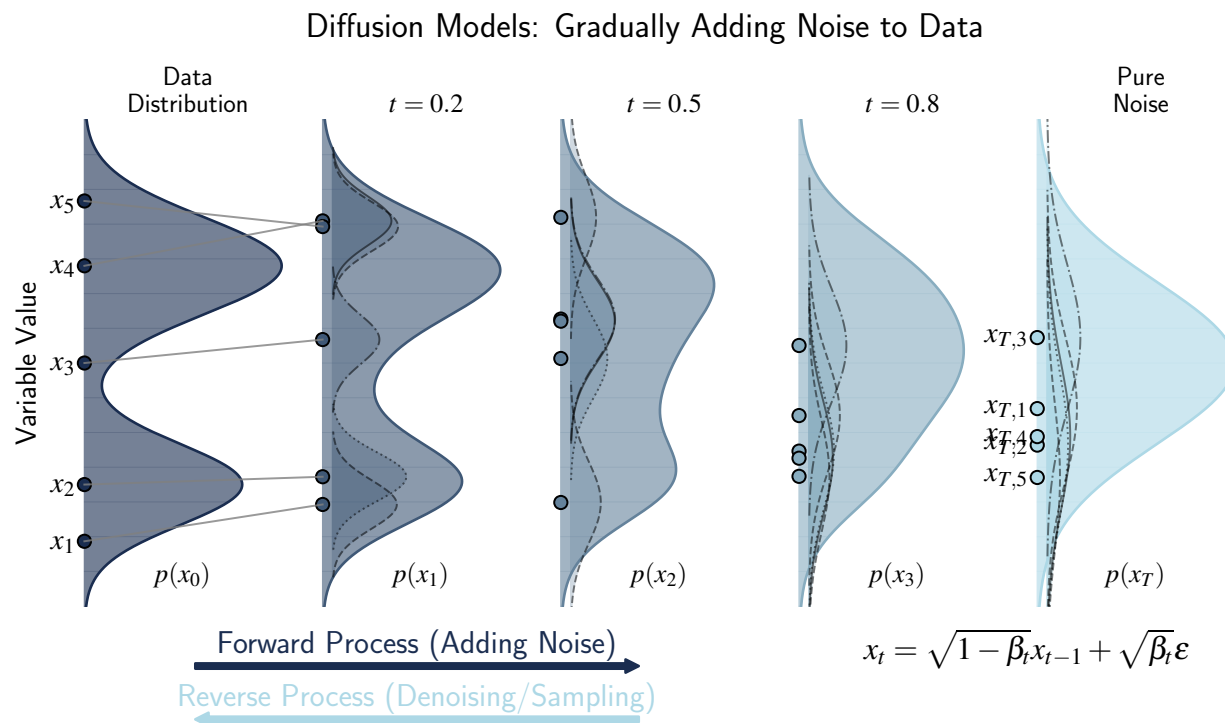
Figure 15.24: Visualization of diffusion models showing the gradual addition of noise to transform data into a standard Gaussian distribution. The diagram illustrates how a complex bimodal data distribution (left, dark blue) progressively absorbs more noise through intermediate time steps ($t = 0.2, 0.5, 0.8$) until reaching pure Gaussian noise (right, light blue). Specific points (x_1 through x_5) are tracked throughout the process, eventually becoming $x_{T,1}$ through $x_{T,5}$ at the pure noise stage. Small 1D Gaussian distributions alongside each point visually represent how noise progressively disperses the data, with the width of these mini-Gaussians increasing with each step to show the growing variance. The forward process (dark blue arrow) follows a Markov chain of noising steps defined by the equation $x_t = \sqrt{1 - \beta_t}x_{t-1} + \sqrt{\beta_t}\varepsilon$, where β_t controls the noise schedule. The learned reverse process (light blue arrow) performs denoising to generate new samples. Unlike normalizing flows which require invertible transformations, diffusion models operate through this progressive noising-denoising approach, allowing them to model complex distributions without architectural constraints. This approach has proven particularly effective for generating high-quality astronomical data where physical consistency and uncertainty quantification are essential.

The trade-off is computational cost. Diffusion models typically require many steps for sampling—often hundreds or thousands of denoising iterations to generate a single sample. This makes them computationally intensive compared to the single-pass transformation of normalizing flows. However, the quality of samples often justifies this expense for many applications.

Connections and Applications   What unites these diverse approaches—MDNs, normalizing flows, diffusion models—is their use of neural networks to model probability distributions, moving beyond the deterministic paradigm that dominated early machine learning. Despite different implementations, they all serve the same goal: enabling both density estimation and sampling from complex distributions.

This probabilistic perspective proves particularly valuable in scientific applications, where quantifying uncertainty often matters as much as making predictions. In astronomy, these methods enable modeling of complex observational processes, accounting for selection effects, and generating synthetic datasets that preserve the statistical properties of real observations.

For example, normalizing flows have been applied to modeling the distribution of galaxy properties in large surveys, capturing complex correlations between mass, color, and morphology that simple parametric models miss. Diffusion models have shown promise for generating synthetic astronomical images that maintain realistic noise properties and preserve subtle correlations across different wavelengths.

These neural density estimators have become increasingly standard in modern astrostatistics, particularly in simulation-based inference applications where complex physical models must be connected with observational data. Rather than reducing observations to simple summary statistics, these methods can work with high-dimensional data directly, potentially extracting more information while maintaining rigorous statistical foundations.

The field continues to evolve rapidly, with new architectures and training methods appearing regularly. However, the core principle remains constant: using neural networks to learn complex probability distributions enables more flexible and powerful approaches to scientific inference than traditional parametric methods, while preserving the probabilistic framework essential for uncertainty quantification in scientific applications.

15.14   Simulation-Based Inference

The neural density estimators we have just explored find their most transformative application in simulation-based inference (SBI), which represents a paradigm shift in how we connect complex scientific theories with observational data. This approach addresses a persistent challenge in modern astronomy: how to perform rigorous Bayesian inference when our theoretical models are so complex that analytical likelihood functions become intractable.

The Likelihood Problem in Modern Astronomy Throughout this course, we have emphasized the Bayesian framework for scientific inference. In its standard form, Bayesian inference requires specifying a likelihood function $p(\mathbf{x}|\boldsymbol{\theta})$ that describes the probability of observing data $\mathbf{x}$ given parameters $\boldsymbol{\theta}$. Combined with a prior $p(\boldsymbol{\theta})$, we compute the posterior distribution:

$$p(\boldsymbol{\theta}|\mathbf{x}) \propto p(\mathbf{x}|\boldsymbol{\theta})p(\boldsymbol{\theta}) \tag{15.97}$$

This framework works well when we can write down explicit expressions for the likelihood function. However, as scientific models become increasingly sophisticated, specifying analytical forms for likelihood functions becomes challenging or impossible. Consider modern cosmological simulations: given cosmological parameters, we can run numerical simulations that generate synthetic observations like galaxy distributions or weak lensing maps, but we typically cannot write closed-form expressions for the probability of obtaining specific observational outcomes.

The core issue stems from dimensionality and distributional complexity. When we observe a phenomenon like a galaxy density field represented as an image, we work with extraordinarily high-dimensional data—a modest 512×512 pixel image lives in a space with over 250,000 dimensions. In such high-dimensional spaces, explicitly characterizing the distribution $p(\mathbf{x}|\boldsymbol{\theta})$ becomes intractable. The distribution itself typically exhibits complex multimodality, strong correlations, and heavy tails that resist simple parametric representation.

The past few decades have witnessed remarkable advancement in our ability to simulate complex physical systems. From cosmological structure formation to stellar evolution, astronomy has developed sophisticated simulation capabilities through high-performance computing and numerical methods. These simulations incorporate increasingly detailed physics and achieve higher resolution. Yet a critical gap has persisted: how to rigorously connect these simulations with observational data in a statistically principled way.

Traditional Approaches and Their Limitations Traditionally, astronomers have addressed this challenge by reducing dimensionality through summary statistics. As we explored in the chapter on summary statistics, this approach offers clear advantages. By condensing high-dimensional observations into low-dimensional summaries like power spectra or correlation functions, we create a more manageable statistical problem. Thanks to the central limit theorem, these summary statistics often have distributions closer to Gaussian, making techniques like the Laplace approximation more applicable.

However, this convenience comes at a substantial cost: information loss. Summary statistics like the power spectrum capture only certain aspects of the data—specifically the second moments of the distribution. For a Gaussian random field, the power spectrum provides a complete statistical description. But cosmic structures and other astronomical phenomena are decidedly non-Gaussian, containing rich information in their higher-order moments and phase correlations that summary statistics discard.

We thus face a classic scientific dilemma: a tension between tractability and completeness. Using full high-dimensional observations preserves all available information but makes likelihood functions effectively incalculable. Reducing observations to summary statistics creates tractable inference problems but potentially sacrifices information. This tension has historically forced astronomers to make pragmatic compromises, typically favoring tractability at the expense of statistical power.

The Simulation-Based Solution   SBI resolves this dilemma by leveraging an asymmetry common to many scientific domains: while the forward problem (generating observations from parameters via simulation) is tractable, the inverse problem (inferring parameters from observations) is challenging. SBI uses neural networks to learn surrogates for key components of the Bayesian inference pipeline directly from simulated data.

The SBI workflow begins with simulation—the one thing we can do reliably regardless of model complexity. Consider a concrete cosmological example: we want to infer parameters like matter density Ω_m, dark energy equation of state w, and amplitude of fluctuations σ_8 from observations of the cosmic web. We generate parameter-observation pairs $\{(\boldsymbol{\theta}_i, \mathbf{x}_i)\}_{i=1}^{N}$ by:

1. Sampling cosmological parameters $\boldsymbol{\theta}_i = (\Omega_m, w, \sigma_8, ...)_i$ from a prior distribution $p(\boldsymbol{\theta})$

2. Running cosmological simulations with these parameters to generate synthetic galaxy density fields $\mathbf{x}_i$

This simulation-first approach sidesteps the need to specify analytical likelihood functions. Instead, we use the simulated data to train neural networks that approximate either the likelihood $p(\mathbf{x}|\boldsymbol{\theta})$ or the posterior $p(\boldsymbol{\theta}|\mathbf{x})$ directly.

Neural Likelihood Estimation   Neural Likelihood Estimation (NLE) represents the most theoretically straightforward approach to SBI. By directly learning the likelihood function $p(\mathbf{x}|\boldsymbol{\theta})$, NLE maintains the structure of traditional Bayesian inference while extending it to
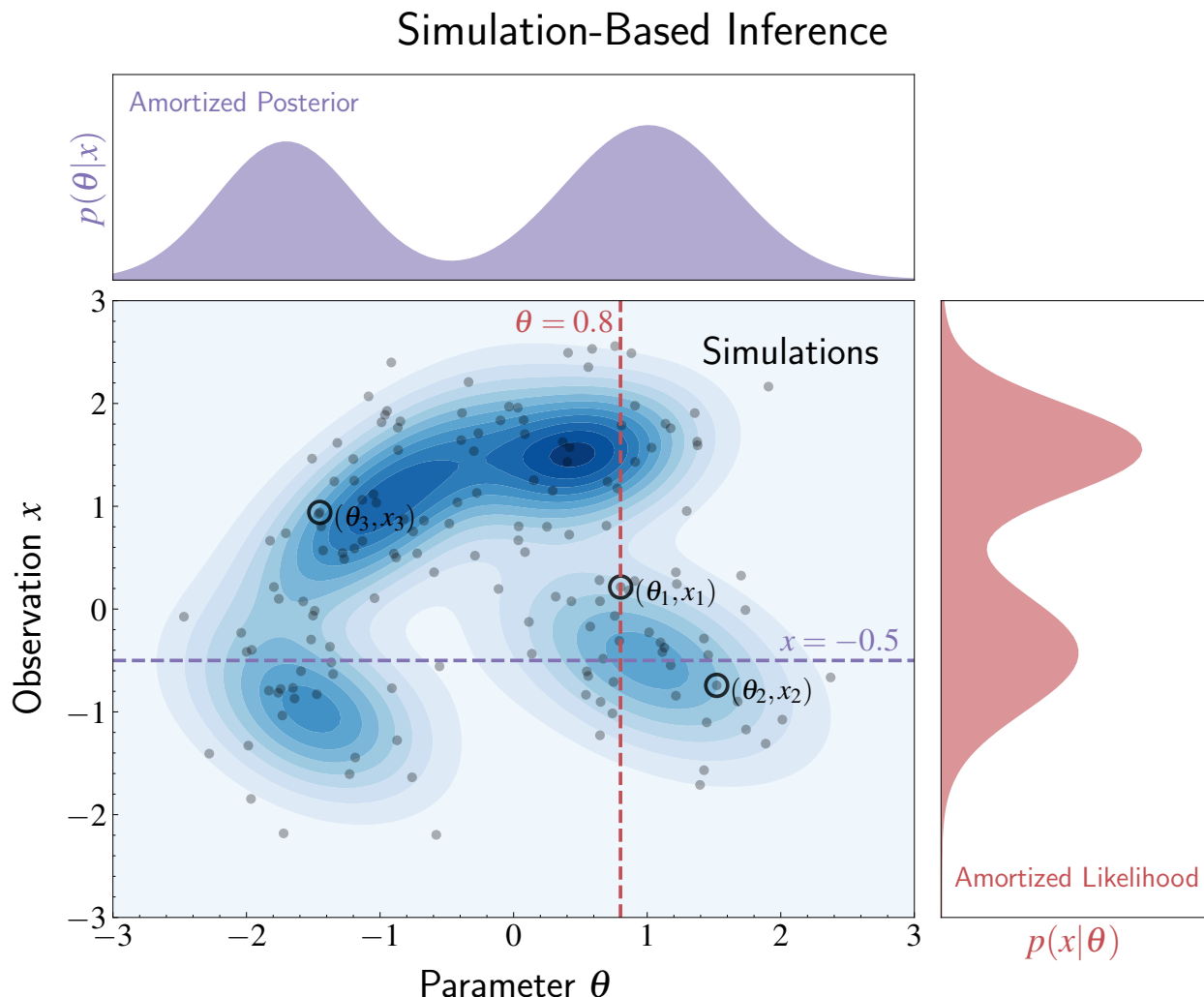
Simulation-Based Inference

Figure 15.25: Visualization of Simulation-Based Inference (SBI) showing the relationship between parameter space and observation space. The central panel shows the joint distribution $p(\theta, x)$ with black dots representing individual simulations (parameter-observation pairs). The top panel displays Neural Posterior Estimation (NPE), showing the posterior distribution $p(\theta|x)$ obtained by conditioning on a specific observation value x (purple horizontal dashed line). The right panel shows Neural Likelihood Estimation (NLE), displaying the likelihood function $p(x|\theta)$ obtained by conditioning on a specific parameter value θ (red vertical dashed line). Both approaches enable amortized inference—once trained, they can rapidly evaluate likelihoods or posteriors for any values without re-running simulations. This visualization highlights how SBI addresses a challenge in astronomical inference: NPE directly learns posteriors in lower-dimensional parameter space (more computationally efficient), while NLE maintains the traditional likelihood-based framework but works with complex simulation-based models. By leveraging neural networks to learn these relationships from simulations, SBI enables Bayesian inference for sophisticated models where analytical likelihoods would be intractable, without sacrificing statistical rigor.

previously intractable problems. The learned likelihood function acts as a drop-in replacement for analytical likelihoods, interfacing seamlessly with the broader Bayesian framework.

We can implement NLE using the neural density estimators discussed in the previous section. For example, using an MDN approach, we model:

$$p(\mathbf{x}|\boldsymbol{\theta}) = \sum_{k=1}^{K} \pi_k(\boldsymbol{\theta})\mathcal{N}(\mathbf{x}|\boldsymbol{\mu}_k(\boldsymbol{\theta}), \boldsymbol{\Sigma}_k(\boldsymbol{\theta})) \tag{15.98}$$

The training process follows standard maximum likelihood principles. Given our dataset of simulated parameter-observation pairs, we maximize:

$$\mathcal{L}(\mathbf{w}) = \sum_{i=1}^{N} \log p(\mathbf{x}_i|\boldsymbol{\theta}_i, \mathbf{w}) \tag{15.99}$$

where $\mathbf{w}$ represents the neural network parameters.

For high-dimensional observations like galaxy density fields, we might use more sophisticated density estimators like normalizing flows or diffusion models instead of MDNs. The key principle remains the same: learning a mapping from parameters to observation distributions, effectively encoding complex physics into a differentiable probabilistic model.

An attractive feature of NLE is that it preserves the modular nature of Bayesian inference. We can change priors, combine with other likelihood terms, or use different sampling methods without retraining the neural likelihood. However, modeling high-dimensional observations presents computational challenges—predicting distributions in 250,000-dimensional observation space requires enormous networks with potentially billions of parameters.

Neural Posterior Estimation   This dimensionality challenge provides strong motivation for Neural Posterior Estimation (NPE), which takes a more direct route by approximating the posterior distribution $p(\boldsymbol{\theta}|\mathbf{x})$ using conditional density estimators. By modeling $p(\boldsymbol{\theta}|\mathbf{x})$ instead of the likelihood, we only need to predict distributions in the much lower-dimensional parameter space.

Consider the dimensional contrast: while $\mathbf{x}$ might be a 512×512 pixel density field (262,144 dimensions), $\boldsymbol{\theta}$ might consist of just 5-10 cosmological parameters. The neural network takes observations $\mathbf{x}$ as input and outputs a distribution over parameters $\boldsymbol{\theta}$, making this approach computationally more efficient and statistically more feasible.

The fundamental difference in what we model:

- NLE asks: "Given parameters $\boldsymbol{\theta}$, what observations $\mathbf{x}$ might we see?"

- NPE asks: "Given observations $\mathbf{x}$, what parameters $\boldsymbol{\theta}$ might have generated them?"

NPE provides posteriors directly without requiring likelihood evaluation and MCMC sampling, making inference extremely fast once the network is trained. However, it comes with an important limitation: the network implicitly incorporates the prior distribution used during training. Exploring different prior assumptions later requires either retraining or applying mathematical corrections through importance sampling.

This trade-off makes NPE particularly suitable for applications where priors are well-established and unlikely to change, or where computational speed at inference time is paramount—such as analyzing millions of galaxy spectra from large surveys.

Amortized Inference Both NLE and NPE enable amortized inference, which changes the computational paradigm of Bayesian analysis. In traditional approaches, we run MCMC algorithms for each new observation, which can be expensive for complex models where each likelihood evaluation requires extensive calculation.

Amortized inference changes this pattern. Once we train a neural network to approximate either the likelihood or posterior, we can reuse this approximation for multiple observations without retraining. For NLE, we still need MCMC for each new observation, but likelihood evaluations become extremely fast—just forward passes through the neural network. For NPE, we get immediate posterior samples without any sampling procedure.

This computational advantage becomes crucial when analyzing large astronomical datasets. Consider a survey with millions of galaxy spectra—running traditional MCMC for each spectrum would be prohibitively expensive. With amortized inference, we pay the computational cost upfront during training and then benefit from rapid inference across the entire dataset.

Historical Context and Modern Developments The concept of performing inference without explicit likelihood functions is not entirely new. Earlier approaches like Approximate Bayesian Computation (ABC) aimed for similar goals by comparing summary statistics of simulated and observed data, accepting parameter values that produce simulations "close enough" to observations. However, these methods struggled with scalability and often re-

quired careful manual design of summary statistics and distance metrics.

What has made modern SBI methods revolutionary is the dramatic advancement in neural density estimation. The same deep learning innovations that transformed generative AI have made it possible to reliably approximate high-dimensional, multimodal distributions at scale. Early neural approaches often suffered from mode collapse—a phenomenon where the network learns to generate samples from only one or a few modes of a multimodal distribution, effectively "forgetting" about other equally valid regions of high probability. For example, when trying to model a distribution with three distinct peaks, a network suffering from mode collapse might only learn to represent one peak while ignoring the others entirely. Modern techniques like normalizing flows and diffusion models largely overcome these limitations through improved architectures and training procedures that better preserve multimodal structure.

SBI applications extend well beyond cosmology to virtually any area with complex forward models but intractable likelihoods. In stellar population synthesis, we can infer stellar population properties from integrated galaxy spectra. In exoplanet characterization, we can determine atmospheric compositions from transmission spectra. In gravitational wave analysis, we can infer properties of merging compact objects from gravitational wave signals.

Challenges and Considerations   While SBI offers transformative capabilities, it carries important caveats. The neural surrogate is only valid within the parameter space used for training, and its accuracy depends on how well training simulations represent reality. As we incorporate more information at all scales, we also include more systematic effects. For example, cosmological simulations may not accurately model baryon physics at all scales, and blindly applying SBI might lead to overconfident inferences that depend on these systematic effects.

However, this challenge affects all simulation-based methods, not just SBI. The solution lies in rigorous testing and validation—generating additional simulations with varied physical assumptions to assess sensitivity to modeling choices. We can train on one set of simulations and test on others, quantifying the impact of systematic effects.

Interestingly, using more information does not necessarily amplify systematic biases compared to summary statistics. In some cases, biases might average out when more information is included. This remains an active research area, but the key point is that addressing these challenges requires careful scientific methodology rather than abandoning the SBI ap-

proach.

A promising development is that modern neural density estimators have matured to the point where approximation errors are often subdominant compared to simulation-based systematics. This allows us to focus on physical questions rather than worrying about neural network reliability. We return to familiar scientific territory—rigorous benchmarking, blind tests, and systematic error analysis—but now with the ability to extract more information from observations while maintaining statistical rigor.

15.15 Summary

Our exploration of neural networks represents a fitting conclusion to our journey through statistical methods in astronomy. This chapter has traced a path from the universal approximation theorem through backpropagation to modern applications like simulation-based inference, revealing how these techniques both extend and build upon the statistical foundations we have established throughout this course.

The structure of this textbook has been deliberately designed to provide the groundwork necessary for understanding neural networks in their proper context. Rather than treating them as fundamentally different from classical approaches, we have emphasized the deep connections between neural networks and the statistical principles developed in earlier chapters.

These connections pervade every aspect of neural network methodology. The loss functions we optimize emerge directly from maximum likelihood principles—mean squared error for Gaussian noise assumptions, cross-entropy for categorical distributions. The optimization techniques build on the gradient descent methods we studied extensively in logistic regression. Regularization approaches like weight decay correspond exactly to placing Gaussian priors on parameters, connecting to our discussions of ridge regression and Bayesian linear models.

Even the architectural choices in neural networks reflect statistical principles. The careful design of activation functions addresses issues of gradient flow and numerical stability. The use of non-superlinear functions connects to our discussions of sampling variance in summary statistics. The inductive biases encoded in different architectures—from CNNs to Transformers—represent explicit assumptions about data structure, much like the kernel choices in Gaussian Processes.

This continuity challenges the common characterization of neural networks as inscrutable "black boxes." Throughout our discussion, we have highlighted how understanding emerges through careful analysis. The emerging science of deep learning reveals insights into phenomena like grokking, Neural Tangent Kernels, and double descent—areas of active mathematical research that continue to deepen our theoretical understanding.

The relationship between neural networks and science mirrors other historical patterns in scientific progress. Just as practical steam engines preceded the formal laws of thermodynamics, neural networks have demonstrated empirical success before their theoretical foundations were fully established. This pattern—where engineering practice leads theoretical understanding—is common in scientific advancement and does not diminish the validity of the approach.

Our deliberate choice not to center this textbook around neural networks stems partly from challenges in their full Bayesian treatment. Despite their capabilities, rigorously quantifying uncertainty in neural network predictions remains difficult compared to the classical methods we studied earlier. Cross-validation provides insight into prediction error but does not fully account for uncertainty in model parameters themselves. This limitation in uncertainty quantification is important for scientific applications where understanding confidence intervals often matters as much as the predictions.

Nevertheless, neural networks have proven useful in practice. Their ability to capture complex nonlinear relationships often results in models where errors from the fitting process become subdominant to other sources of uncertainty—whether statistical noise in observations or systematic effects in underlying simulations. This pragmatic advantage explains their widespread adoption across astronomical applications.

Perhaps nowhere is this practical success more evident than in simulation-based inference, where neural networks have enabled entirely new possibilities for connecting complex theoretical models with observational data. These methods allow rigorous Bayesian inference in contexts where traditional approaches would be intractable, potentially extracting more information from observations while maintaining statistical rigor.

The applications we have explored—from autoencoders for dimension reduction to mixture density networks for modeling one-to-many relationships—demonstrate the breadth of neural network capabilities. Each represents a natural extension of classical methods: autoencoders extend PCA to nonlinear manifolds, mixture density networks extend GMMs to conditional distributions, and encoder-decoder architectures enable cross-modal learning

that would be impossible with traditional approaches.

The field continues to evolve rapidly, with new architectures, training methods, and theoretical insights appearing regularly. Foundation models demonstrate capabilities for few-shot learning and cross-domain transfer that seemed impossible just years ago. Neural density estimators enable sophisticated approaches to probabilistic modeling that maintain the statistical rigor essential for scientific applications.

Our exploration in this chapter provides a foundation for understanding these modern techniques within the broader context of statistical inference. By grounding neural networks in familiar statistical principles, we can approach them not as mysterious algorithms but as natural extensions of methods we already understand. This perspective enables more thoughtful application of these tools while maintaining the scientific rigor that distinguishes astronomy from purely engineering disciplines.

Further Readings: The theoretical foundations of neural networks are explored in McCulloch and Pitts [1943] who examine mathematical models of neural computation, and Rosenblatt [1958] who discusses the perceptron learning algorithm. Analysis of single-layer network limitations can be found in Minsky and Papert [1969]. For readers interested in the backpropagation algorithm, Rumelhart et al. [1986] provides comprehensive treatment with practical examples. Universal approximation properties are investigated in Cybenko [1989] and Hornik et al. [1989], while Vapnik [1995] places neural networks within statistical learning theory. Bayesian perspectives on neural networks are offered by MacKay [1992] discussing connections to Bayesian inference, with Neal [1996] providing full Bayesian treatment and Williams [1996] exploring relationships to Gaussian processes. Important architectural developments include convolutional networks detailed in LeCun et al. [1998], recurrent architectures in Elman [1990], and long short-term memory networks in Hochreiter and Schmidhuber [1997]. For uncertainty quantification methods relevant to scientific applications, Bishop [1994] introduces mixture density networks while Hinton et al. and Srivastava et al. [2014] develop dropout regularization techniques. While neural networks have become ubiquitous in modern astronomy, their application to astronomical problems dates back decades, with Storrie-Lombardi et al. [1992] applying them to galaxy morphology classification, von Hippel et al. [1994] to stellar spectral classification, Lahav et al. [1995] comparing networks with human classifiers, and Bailer-Jones et al. [1998] extending to stellar parameter estimation, demonstrating that astronomers explored these methods well before the current deep learning era. Recent theoretical developments include the double descent phenomenon explored in Belkin et al. [2019], with deep learning evidence provided in Nakkiran et al. and theoret-

ical analysis in Adlam and Pennington. The Neural Tangent Kernel framework developed in Jacot et al. reveals connections between neural networks and kernel methods, with Lee et al. and Matthews et al. establishing links to Gaussian processes. For readers interested in simulation-based inference, Cranmer et al. [2020] offers comprehensive treatment, while neural density estimation approaches are examined in Papamakarios et al., and neural posterior estimation methods are discussed in Greenberg et al. and Gonçalves et al. [2020]. Foundation models and few-shot learning capabilities are explored in Bommasani et al., with Brown et al. demonstrating large language model behaviors, Wei et al. analyzing emergent properties, and Devlin et al. and Raffel et al. [2020] examining pre-training and transfer learning approaches. Modern generative modeling encompasses variational autoencoders by Kingma and Welling, generative adversarial networks by Goodfellow et al., normalizing flows examined in Rezende and Mohamed with further developments in Dinh et al. and Durkan et al., along with diffusion-based approaches including denoising diffusion models by Ho et al. and Song et al..

Chapter 16

Afterword: A Personal Note

The writing of this textbook has been an interesting personal journey, motivated primarily by two experiences that many researchers working at the interface of statistics, AI, and astronomy will recognize. First, I found myself repeatedly engaged in discussions with colleagues about various techniques, often ending up scribbling LaTeX notes to share my thoughts. Over time, these scattered notes not only helped my collaborators but also served as a way for me to organize and clarify my own understanding. There is something about the process of writing that forces clarity of thought in ways that mere conversation cannot achieve.

Perhaps more importantly, I have found myself repeatedly drawn into debates about the utility of machine learning in astrophysics—debates where "machine learning" often means different things to different people. The responses I encounter range from overly pessimistic to unrealistically optimistic, and I often find both positions difficult to defend. These discussions touch on questions that go far beyond technical implementation: What does it mean for a method to be trustworthy? What makes something interpretable? Is deep learning always a black box? Are simpler models morally superior? What is our philosophy of science, and what should be the ultimate goals of scientific inquiry?

I find these conversations fascinating because they reveal how much our methodological choices reflect deeper beliefs about the nature of scientific knowledge itself. Writing this textbook has helped me organize my thoughts on these questions and develop a more coherent perspective on the role of different statistical approaches in astronomical research. The process has been as much about understanding my own views as it has been about

communicating them to others.

The encouragement to undertake this project came partly from an informal poll I conducted on social media, where the overwhelming support from colleagues ultimately convinced me to take on this challenge. However, the transition from scattered notes and lecture materials to a coherent textbook—especially for a non-native English speaker—proved more demanding than I initially anticipated.

When I began this project, I ambitiously planned to cover both classical machine learning and deep learning in equal detail within a single volume. This turned out to be wildly optimistic. The classical foundations alone expanded to fill the current volume, and while I hope I have provided a sufficient introduction to neural networks and deep learning, a comprehensive treatment of these topics will require a separate volume—a project I look forward to tackling once I have recovered from this one.

This has certainly been one of my largest academic undertakings. From conceptualization to writing the first draft, each page required approximately one hour of focused work, sustained by many cups of coffee and the occasional dessert for motivation. The subsequent rounds of editing and revision added another hour per page. For this 650-page volume, the total time investment approached 1,300 hours, consuming most of my non-working time and weekends during the 2024-2025 academic year. This time commitment ultimately reinforced my decision to defer the deep learning volume to the future.

I should acknowledge the role that modern language models have played in making this project feasible. While the preliminary writing, organization, mathematical content, and overall perspective represent years of my own thinking and research, I have relied on LLM assistance primarily for language editing to make the text as readable as possible while hopefully maintaining my professional voice and occasional attempts at humor. Without this support, the language polishing alone would have made this project prohibitively time-consuming for a non-native speaker. The irony is not lost on me that a textbook partly about machine learning was itself enabled by machine learning.

Despite my own research focus on deep learning applications in astronomy, I remain convinced that a solid foundation in classical statistical methods addresses a large portion of the analytical needs in our field. While there are certainly astronomical problems that benefit from deep learning—which is why I find this research area so compelling—the combination of domain knowledge and solid statistical reasoning can solve many problems that might initially seem to require more complex approaches.

The choice between classical and modern methods should be driven by the nature of the problem rather than by fashion or technological enthusiasm. This textbook aims to provide the foundation necessary to make such choices thoughtfully and with full awareness of the trade-offs involved.

Ultimately, as I mentioned in the preface, my hope is that this textbook contributes to a more nuanced understanding of how machine learning techniques have evolved and how they connect to the statistical foundations that astronomers have always relied upon. If this work contributes in any way to more meaningful and informed discussions about the role of these methods in astronomy, then the considerable time investment will have been worthwhile.

When I began this project, I debated whether to pursue traditional publishing or to release the work as an open-access resource. While I was fortunate to receive interest from publishers—and the prospect of a physical textbook remains appealing from a personal standpoint—I ultimately decided to prioritize accessibility. Growing up in Malaysia, where educational resources in specialized fields like statistical astronomy can be limited, I am acutely aware of how access barriers can affect learning opportunities. I have therefore chosen to release this work on arXiv, making it freely available to anyone with an internet connection. The possibility of a traditional published version remains open, potentially through crowdsourced funding for open-access publication costs.

This textbook is dedicated to my family, who have supported my somewhat unusual intellectual trajectory with remarkable patience. My parents endured having a child who was more interested in solving linear algebra problems than playing with friends—my father even resorted to paying me to go outside and play, hoping to encourage more conventional childhood activities. Their tolerance allowed me to explore the mathematical topics that have always fascinated me and ultimately enabled me to develop expertise spanning physics, statistics, and artificial intelligence.

The dedication also extends to my grandmother (Popo), who, despite never having formal education herself, was always amused by my mathematics scribble books. During family visits, while she worked on sewing blankets, I would sit in her back room solving equations, and she would occasionally peek over my shoulder with curiosity and pride. Her quiet support and the warmth of those childhood memories have stayed with me throughout this journey.

Looking back on this project, I realize that writing a textbook is itself an exercise

in the kind of thinking it aims to teach. Like statistical modeling, it requires balancing completeness with clarity, rigor with accessibility, and personal perspective with objective presentation. The process has taught me as much as I hope the final product will teach its readers.

To those who undertake the journey through this material, I hope you find it not just informative but transformative in how you think about the relationship between data and knowledge. The future of astronomy will undoubtedly require increasingly sophisticated statistical thinking, and my hope is that this foundation will serve you well regardless of which specific techniques prove most useful for your particular research challenges.

The conversation about machine learning in astronomy is far from over, and it should continue to evolve as both our computational capabilities and our theoretical understanding advance. What matters most is that this conversation remains grounded in careful thinking about what we are trying to achieve and why particular approaches serve those goals better than others.

Thank you for joining me on this journey through the landscape of statistical machine learning for astronomy. The real work begins when you close this book and start applying these ideas to your own research questions.

Bibliography

O. Abril-Pla, V. Andreani, C. Carroll, and et al. Pymc: a modern, and comprehensive probabilistic programming framework in python. *PeerJ Computer Science*, 9:e1516, 2023.

R. J. Adcock. A problem in least squares. *The Analyst*, 5(2):53–54, 1878.

B. Adlam and J. Pennington. Understanding double descent requires a fine-grained bias-variance decomposition. *arXiv preprint arXiv:2011.03321*.

H. Akaike. A new look at the statistical model identification. *IEEE Transactions on Automatic Control*, 19(6):716–723, 1974.

M. G. Akritas and M. A. Bershady. Linear regression for astronomical data with measurement errors and intrinsic scatter. *The Astrophysical Journal*, 470:706, 1996.

J. H. Albert and S. Chib. Bayesian analysis of binary and polychotomous response data. *Journal of the American Statistical Association*, 88(422):669–679, 1993.

E. L. Allwein, R. E. Schapire, and Y. Singer. Reducing multiclass to binary: A unifying approach for margin classifiers. *Journal of Machine Learning Research*, 1(2):113–141, 2001.

T. W. Anderson. *An introduction to multivariate statistical analysis*. Wiley, 1958.

N. Aronszajn. Theory of reproducing kernels. *Transactions of the American Mathematical Society*, 68(3):337–404, 1950.

D. Arthur and S. Vassilvitskii. k-means++: the advantages of careful seeding. In *Proceedings of the Eighteenth Annual ACM-SIAM Symposium on Discrete Algorithms*, pages 1027–1035. Society for Industrial and Applied Mathematics, 2007.

C. A. L. Bailer-Jones, M. Irwin, and T. von Hippel. Automated classification of stellar spectra – ii. two-dimensional classification with neural networks and principal components analysis. *Monthly Notices of the Royal Astronomical Society*, 298(2):361–377, 1998.

T. Bayes. Lii. an essay towards solving a problem in the doctrine of chances. by the late rev. mr. bayes, f. r. s. communicated by mr. price, in a letter to john canton, a. m. f. r. s. *Philosophical Transactions of the Royal Society of London*, 53:370–418, 1763.

M. Belkin, D. Hsu, S. Ma, and S. Mandal. Reconciling modern machine-learning practice and the classical bias–variance trade-off. *Proceedings of the National Academy of Sciences*, 116(32):15849–15854, 2019.

P. M. Bentler and D. G. Weeks. Linear structural equations with latent variables. *Psychometrika*, 45(3):289–308, 1980.

J. Berkson. Application of the logistic function to bio-assay. *Journal of the American Statistical Association*, 39(227):357–365, 1944.

P. Bevington and D. K. Robinson. *Data reduction and error analysis for the physical sciences*. McGraw-Hill, 1969.

J. C. Bezdek. *Pattern recognition with fuzzy objective function algorithms*. Plenum Press, New York, 1981.

C. M. Bishop. Mixture density networks. Technical Report NCRG/94/004, Neural Computing Research Group, Aston University, Birmingham, UK, 1994.

C. M. Bishop. *Pattern recognition and machine learning*. Springer, 2006.

C. I. Bliss. The method of probits. *Science*, 79(2037):38–39, 1934.

R. Bommasani, D. A. Hudson, E. Adeli, R. Altman, S. Arora, S. von Arx, M. S. Bernstein, J. Bohg, A. Bosselut, E. Brunskill, E. Brynjolfsson, S. Buch, D. Card, R. Castellon, N. Chatterji, A. Chen, K. Creel, J. Q. Davis, D. Demszky, C. Donahue, M. Doumbouya, E. Durmus, S. Ermon, J. Etchemendy, K. Ethayarajh, L. Fei-Fei, C. Finn, T. Gale, L. Gillespie, K. Goel, N. Goodman, S. Grossman, N. Guha, T. Hashimoto, P. Henderson, J. Hewitt, D. E. Ho, J. Hong, K. Hsu, J. Huang, T. Icard, S. Jain, D. Jurafsky, P. Kalluri, S. Karamcheti, G. Keeling, F. Khani, O. Khattab, P. W. Koh, M. Krass, R. Krishna, R. Kuditipudi, A. Kumar, F. Ladhak, M. Lee, T. Lee, J. Leskovec, I. Levent, X. Li, X. Li, T. Ma, A. Malik, C. D. Manning, S. Mirchandani, E. Mitchell, Z. Munyikwa, S. Nair, A. Narayan, D. Narayanan, B. Newman, A. Nie, J. C. Niebles, H. Nilforoshan, J. Nyarko, G. Ogut, L. Orr, I. Papadimitriou, J. S. Park, C. Piech, E. Portelance, C. Potts, A. Raghunathan, R. Reich, H. Ren, F. Rong, Y. Roohani, C. Ruiz, J. Ryan, C. Ré, D. Sadigh, S. Sagawa, K. Santhanam, A. Shih, K. Srinivasan, A. Tamkin, R. Taori, A. W. Thomas, F. Tramèr, R. E. Wang, W. Wang, B. Wu, J. Wu, Y. Wu, S. M. Xie, M. Yasunaga, J. You,

M. Zaharia, M. Zhang, T. Zhang, X. Zhang, Y. Zhang, L. Zheng, K. Zhou, and P. Liang. *arXiv preprint arXiv:2108.07258*.

G. E. P. Box and M. E. Muller. A note on the generation of random normal deviates. *The Annals of Mathematical Statistics*, 29:610–611, 1958.

G. E. P. Box and G. C. Tiao. Bayesian inference in statistical analysis. *International Statistical Review*, 43:242, 1973.

H. Bozdogan. Model selection and akaike's information criterion (aic): the general theory and its analytical extensions. *Psychometrika*, 52(3):345–370, 1987.

T. B. Brown, B. Mann, N. Ryder, M. Subbiah, J. Kaplan, P. Dhariwal, A. Neelakantan, P. Shyam, G. Sastry, A. Askell, S. Agarwal, A. Herbert-Voss, G. Krueger, T. Henighan, R. Child, A. Ramesh, D. M. Ziegler, J. Wu, C. Winter, C. Hesse, M. Chen, E. Sigler, M. Litwin, S. Gray, B. Chess, J. Clark, C. Berner, S. McCandlish, A. Radford, I. Sutskever, and D. Amodei. Language models are few-shot learners. *arXiv preprint arXiv:2005.14165*.

R. J. Carroll and D. Ruppert. The use and misuse of orthogonal regression in linear errors-in-variables models. *The American Statistician*, 50(1):1–6, 1996.

R. J. Carroll, D. Ruppert, L. A. Stefanski, and C. M. Crainiceanu. *Measurement error in nonlinear models: A modern perspective, Second edition*. Chapman and Hall, 2006.

G. Casella and R. L. Berger. *Statistical inference*. Duxbury Press, 2002.

A. L. Cauchy. Méthode générale pour la résolution des systèmes d'équations simultanées. *Comptes Rendus de l'Académie des Sciences de Paris*, 25:536–538, 1847.

N. Christensen, R. Meyer, L. Knox, and B. Luey. Bayesian methods for cosmological parameter estimation from cosmic microwave background measurements. *Classical and Quantum Gravity*, 18(14):2677–2688, 2001.

P. Comon. Independent component analysis, a new concept? *Signal Processing*, 36(3):287–314, 1994.

M. K. Cowles and B. P. Carlin. Markov chain monte carlo convergence diagnostics: a comparative review. *Journal of the American Statistical Association*, 91(434):883–904, 1996.

D. R. Cox. The regression analysis of binary sequences. *Journal of the Royal Statistical Society: Series B (Methodological)*, 20(2):215–232, 1958.

D. R. Cox and D. V. Hinkley. *Theoretical statistics*. Chapman and Hall, 1974.

H. Cramer. *Mathematical methods of statistics*. Princeton University Press, 1946.

K. Cranmer, J. Brehmer, and G. Louppe. The frontier of simulation-based inference. *Proceedings of the National Academy of Sciences*, 117(48):30055–30062, 2020.

N. Cressie. *Statistics for spatial data*. Wiley, 1993.

L. Csato and M. Opper. Sparse on-line gaussian processes. *Neural Computation*, 14(3): 641–668, 2002.

H. B. Curry. The method of steepest descent for non-linear minimization problems. *Quarterly of Applied Mathematics*, 2(3):258–261, 1944.

G. Cybenko. Approximation by superpositions of a sigmoidal function. *Math. Control Signal Systems*, 2:303–314, 1989.

A. C. Davison and D. V. Hinkley. *Bootstrap methods and their application*. Cambridge University Press, 1997.

N. E. Day. Estimating the components of a mixture of normal distributions. *Biometrika*, 56 (3):463–474, 1969.

M. H. DeGroot. *Optimal statistical decisions*. McGraw-Hill, 1970.

W. E. Deming. *Statistical adjustment of data*. Wiley, 1943.

A. P. Dempster, N. M. Laird, and D. B. Rubin. Maximum likelihood from incomplete data via the em algorithm. *Journal of the Royal Statistical Society. Series B (Methodological)*, 39(1):1–38, 1977.

J. E. Dennis and R. B. Schnabel. *Numerical methods for unconstrained optimization and nonlinear equations*. Prentice-Hall, 1983.

J. Devlin, M.-W. Chang, K. Lee, and K. Toutanova. Bert: pre-training of deep bidirectional transformers for language understanding. *arXiv preprint arXiv:1810.04805*.

L. Devroye. *Non-uniform random variate generation*. Springer, 1986.

T. G. Dietterich and G. Bakiri. Error-correcting output codes: A general method for improving multiclass inductive learning programs. In *KDD'91*, pages 572–577. AAAI Press, 1991.

T. G. Dietterich and G. Bakiri. Solving multiclass learning problems via error-correcting output codes. *Journal of Artificial Intelligence Research*, 2(1):263–286, 1995.

L. Dinh, J. Sohl-Dickstein, and S. Bengio. Density estimation using real nvp. *arXiv preprint arXiv:1605.08803*.

R. O. Duda, P. E. Hart, and D. G. Stork. *Pattern classification (2nd ed.)*. Wiley, 2001.

J. C. Dunn. A fuzzy relative of the isodata process and its use in detecting compact well-separated clusters. *Journal of Cybernetics*, 3(3):32–57, 1973.

C. Durkan, A. Bekasov, I. Murray, and G. Papamakarios. Neural spline flows. *arXiv preprint arXiv:1906.04032*.

G. M. Eadie, J. S. Speagle, J. Cisewski-Kehe, D. Foreman-Mackey, D. Huppenkothen, D. E. Jones, A. Springford, and H. Tak. Practical guidance for bayesian inference in astronomy. *arXiv preprint arXiv:2302.04703*.

C. Eckart and G. Young. The approximation of one matrix by another of lower rank. *Psychometrika*, 1(3):211–218, 1936.

B. Efron. The efficiency of logistic regression compared to normal discriminant analysis. *Journal of the American Statistical Association*, 70(352):892–898, 1975.

B. Efron. Bootstrap methods: Another look at the jackknife. *The Annals of Statistics*, 7(1):1–26, 1979.

J. L. Elman. Finding structure in time. *Cognitive Science*, 14(2):179–211, 1990.

S. M. Faber and R. E. Jackson. Velocity dispersions and mass-to-light ratios for elliptical galaxies. *The Astrophysical Journal*, 204:668–683, 1976.

F. Feroz and M. Hobson. Multimodal nested sampling: an efficient and robust alternative to markov chain monte carlo methods for astronomical data analyses. *Monthly Notices of the Royal Astronomical Society*, 384:449 – 463, 2008.

L. Ferrarese and D. Merritt. A fundamental relation between supermassive black holes and their host galaxies. *The Astrophysical Journal Letters*, 539(1):L9–L12, 2000.

D. J. Finney. Probit analysis: A statistical treatment of the sigmoid response curve. *Journal of the Royal Statistical Society*, 110(3):263–266, 1947.

R. A. Fisher. On the mathematical foundations of theoretical statistics. *Philosophical Transactions of the Royal Society of London. Series A, Containing Papers of a Mathematical or Physical Character*, 222:309–368, 1922.

R. A. Fisher. The use of multiple measurements in taxonomic problems. *Annals of Eugenics*, 7(2):179–188, 1936.

G. S. Fishman. *Monte Carlo: concepts, algorithms, and applications*. Springer, 1996.

E. B. Ford. Quantifying the uncertainty in the orbits of extrasolar planets. *The Astronomical Journal*, 129(3):1706–1717, 2005.

D. Foreman-Mackey, D. W. Hogg, D. Lang, and J. Goodman. emcee: the mcmc hammer. *Publications of the Astronomical Society of the Pacific*, 125(925):306, 2013.

G. E. Forsythe. Von neumann's comparison method for random sampling from the normal and other distributions. *Mathematics of Computation*, 26:817–826, 1972.

W. A. Fuller. *Measurement error models*. Wiley, 1987.

J. Fürnkranz. Round robin classification. *Journal of Machine Learning Research*, 2:721–747, 2002.

C. F. Gauss. *Theoria combinationis observationum erroribus minimis obnoxiae*. H. Dieterich, 1823.

K. Gebhardt, R. Bender, G. Bower, A. Dressler, S. M. Faber, A. V. Filippenko, R. Green, C. Grillmair, L. C. Ho, J. Kormendy, T. R. Lauer, J. Magorrian, J. Pinkney, D. Richstone, and S. Tremaine. A relationship between nuclear black hole mass and galaxy velocity dispersion. *The Astrophysical Journal Letters*, 539(1):L13–L16, 2000.

A. E. Gelfand and A. F. M. Smith. Sampling-based approaches to calculating marginal densities. *Journal of the American Statistical Association*, 85(410):398–409, 1990.

A. Gelman and D. B. Rubin. Inference from iterative simulation using multiple sequences. *Statistical Science*, 7:457–472, 1992.

A. Gelman, J. B. Carlin, H. S. Stern, D. B. Dunson, A. Vehtari, and D. B. Rubin. *Bayesian data analysis (3rd ed.)*. Chapman and Hall, 2013.

S. Geman and D. Geman. Stochastic relaxation, gibbs distributions, and the bayesian restoration of images. *IEEE Transactions on Pattern Analysis and Machine Intelligence*, 6(6): 721–741, 1984.

J. Geweke. Evaluating the accuracy of sampling-based approaches to the calculation of posterior moments. *In: J. M. Bernardo, J. O. Berger, A. P. Dawid and A. F. M. Smith, Eds., Bayesian Statistics, Vol. 4, Clarendon Press, Oxford, 1992, pp. 169-193*, 1992.

W. R. Gilks, S. Richardson, and D. J. Spiegelhalter. *Markov chain Monte Carlo in practice.* Chapman and Hall, 1996.

G. Goertzel. Quota sampling and importance functions in stochastic solution of particle problems. *Technical Report ORNL-434*, 1949.

G. Golub and W. Kahan. Calculating the singular values and pseudo-inverse of a matrix. *Journal of the Society for Industrial and Applied Mathematics Series B Numerical Analysis*, 2(2):205–224, 1965.

G. H. Golub and C. Reinsch. Singular value decomposition and least squares solutions. *Numerische Mathematik*, 14:403–420, 1970.

G. H. Golub and C. F. Van Loan. An analysis of the total least squares problem. *SIAM Journal on Numerical Analysis*, 17(6):883–893, 1980.

P. J. Gonçalves, J.-M. Lueckmann, M. Deistler, M. Nonnenmacher, K. Öcal, G. Bassetto, C. Chintaluri, W. F. Podlaski, S. A. Haddad, T. P. Vogels, D. S. Greenberg, and J. H. Macke. Training deep neural density estimators to identify mechanistic models of neural dynamics. *eLife*, 9:e56261, 2020.

I. J. Goodfellow, J. Pouget-Abadie, M. Mirza, B. Xu, D. Warde-Farley, S. Ozair, A. Courville, and Y. Bengio. Generative adversarial networks. *arXiv preprint arXiv:1406.2661.*

D. S. Greenberg, M. Nonnenmacher, and J. H. Macke. Automatic posterior transformation for likelihood-free inference. *arXiv preprint arXiv:1905.07488.*

P. C. Gregory. A bayesian analysis of extrasolar planet data for hd 73526. *The Astrophysical Journal*, 631(2):1198–1214, 2005.

J. A. Hartigan. *Clustering algorithms.* Wiley, 1975.

J. A. Hartigan and M. A. Wong. Algorithm as 136: a k-means clustering algorithm. *Journal of the Royal Statistical Society. Series C (Applied Statistics)*, 28(1):100–108, 1979.

W. K. Hastings. Monte carlo sampling methods using markov chains and their applications. *Biometrika*, 57(1):97–109, 1970.

G. E. Hinton and R. R. Salakhutdinov. Reducing the dimensionality of data with neural networks. *Science*, 313(5786):504–507, 2006.

G. E. Hinton, N. Srivastava, A. Krizhevsky, I. Sutskever, and R. R. Salakhutdinov. Improving neural networks by preventing co-adaptation of feature detectors. *arXiv preprint arXiv:1207.0580.*

J. Ho, A. Jain, and P. Abbeel. Denoising diffusion probabilistic models. *arXiv preprint arXiv:2006.11239*.

S. Hochreiter and J. Schmidhuber. Long short-term memory. *Neural Computation*, 9(8): 1735–1780, 1997.

A. E. Hoerl and R. W. Kennard. Ridge regression: Biased estimation for nonorthogonal problems. *Technometrics*, 12(1):55–67, 1970.

D. W. Hogg and D. Foreman-Mackey. Data analysis recipes: using markov chain monte carlo. *Astrophysical Journal Supplement Series*, 236(1):11, 2018.

K. Hornik, M. Stinchcombe, and H. White. Multilayer feedforward networks are universal approximators. *Neural Networks*, 2(5):359–366, 1989.

H. Hotelling. Analysis of a complex of statistical variables into principal components. *Journal of Educational Psychology*, 24(4):417–441, 1933.

T. Isobe, E. D. Feigelson, M. G. Akritas, and G. J. Babu. Linear regression in astronomy. i. *The Astrophysical Journal*, 364:104, 1990.

A. Jacot, F. Gabriel, and C. Hongler. Neural tangent kernel: convergence and generalization in neural networks. *arXiv preprint arXiv:1806.07572*.

E. T. Jaynes. *Probability theory: The logic of science.* Cambridge University Press, Cambridge, 2003.

I. T. Jolliffe. *Principal component analysis (2nd ed.).* Springer, 2002.

H. Kahn. Random sampling (monte carlo) techniques in neutron attenuation problems, i & ii. *Nucleonics*, 6(5):27–37, 1950.

H. Kahn. Use of different monte carlo sampling techniques. *RAND Corporation Papers*, 1955.

H. Kahn and T. E. Harris. Estimation of particle transmission by random sampling. *National Bureau of Standards applied mathematics series*, 12:27–30, 1951.

H. Kahn and A. W. Marshall. Methods of reducing sample size in monte carlo computations. *Journal of the Operations Research Society of America*, 1(5):263–278, 1953.

M. H. Kalos and P. A. Whitlock. *Monte Carlo methods: Volume I: basics.* Wiley, 1986.

R. E. Kass and A. E. Raftery. Bayes factors. *Journal of the American Statistical Association*, 90(430):773–795, 1995.

L. Kaufman and P. J. Rousseeuw. *Finding groups in data: an introduction to cluster analysis.* Wiley, 1990.

B. C. Kelly. Some aspects of measurement error in linear regression of astronomical data. *The Astrophysical Journal*, 665(2):1489–1506, 2007.

M. G. Kendall and A. Stuart. *The advanced theory of statistics.* C. Griffin, 1977.

M. Kennedy and A. O'Hagan. Bayesian calibration of computer models (with discussion). *Journal of the Royal Statistical Society: Series B (Statistical Methodology)*, 68:425–464, 2001.

R. C. Kennicutt. The global schmidt law in star-forming galaxies. *The Astrophysical Journal*, 498(2):541–552, 1998.

G. S. Kimeldorf and G. Wahba. A correspondence between bayesian estimation and smoothing by splines. *Annals of Mathematical Statistics*, 41(2):495–502, 1970.

A. J. Kinderman and J. F. Monahan. Computer generation of random variables using the ratio of uniform deviates. *ACM Transactions on Mathematical Software*, 3:257–260, 1977.

D. P. Kingma and M. Welling. Auto-encoding variational bayes. *arXiv preprint arXiv:1312.6114.*

S. Kullback and R. A. Leibler. On information and sufficiency. *Annals of Mathematical Statistics*, 22(1):79–86, 1951.

M. Kuss and C. E. Rasmussen. Assessing approximate inference for binary gaussian process classification. *Journal of Machine Learning Research*, 6(57):1679–1704, 2005.

O. Lahav, A. Naim, R. Buta, H. Corwin, G. de Vaucouleurs, A. Dressler, J. Huchra, S. Bergh, S. Raychaudhury, and L. Sodre. Galaxies, human eyes, and artificial neural networks. *Science*, 267:859–62, 1995.

P. S. Laplace. *Théorie analytique des probabilités.* Courcier (Paris), 1820.

L. Le Cam. *Asymptotic methods in statistical decision theory.* Springer, 1986.

Y. LeCun, L. Bottou, Y. Bengio, and P. Haffner. Gradient-based learning applied to document recognition. *Proceedings of the IEEE*, 86(11):2278–2324, 1998.

J. Lee, Y. Bahri, R. Novak, S. S. Schoenholz, J. Pennington, and J. Sohl-Dickstein. Deep neural networks as gaussian processes.

A. Lewis and S. Bridle. Cosmological parameters from cmb and other data: a monte carlo approach. *Phys. Rev. D*, 66(10):103511, 2002.

D. V. Lindley. *Introduction to probability and statistics from a Bayesian viewpoint.* Cambridge University Press, 1965.

J. S. Liu. *Monte Carlo strategies in scientific computing.* Springer, 2001.

S. Lloyd. Least squares quantization in pcm. *IEEE Transactions on Information Theory*, 28 (2):129–137, 1982.

T. J. Loredo. The promise of bayesian inference for astronomy. *Statistical Challenges in Modern Astronomy*, 275:275–297, 1992.

R. D. Luce. *Individual choice behavior: A theoretical analysis.* Wiley, 1959.

R. Lupton. *Statistics in theory and practice.* Princeton University Press, 1993.

D. J. C. MacKay. Bayesian interpolation. *Neural Computation*, 4(3):415–447, 1992.

D. J. C. MacKay. *Information theory, inference, and learning algorithms.* Cambridge University Press, 2003.

J. MacQueen. Some methods for classification and analysis of multivariate observations. *Berkeley Symposium on Mathematical Statistics and Probability*, 1:281–297, 1967.

G. Marsaglia. The squeeze method for generating gamma variates. *Computers & Mathematics with Applications*, 3(4):321–325, 1977.

G. Matheron. Principles of geostatistics. *Economic Geology*, 58(8):1246–1266, 1963.

A. G. de G. Matthews, M. Rowland, J. Hron, R. E. Turner, and Z. Ghahramani. Gaussian process behaviour in wide deep neural networks. *arXiv preprint arXiv:1804.11271*.

P. McCullagh and J. A. Nelder. *Generalized linear models (2nd ed.).* Chapman and Hall, 1989.

W. S. McCulloch and W. A. Pitts. A logical calculus of the ideas immanent in nervous activity. *Bulletin of Mathematical Biophysics*, 5:115–133, 1943.

D. McFadden. Conditional logit analysis of qualitative choice behavior. In *Frontiers in Econometrics*, pages 105–142. 1973.

N. Metropolis, A. W. Rosenbluth, M. N. Rosenbluth, A. H. Teller, and E. Teller. Equation of state calculations by fast computing machines. *Journal of Chemical Physics*, 21(6): 1087–1092, 1953.

T. P. Minka. Expectation propagation for approximate bayesian inference. In *Proceedings of the Seventeenth Conference on Uncertainty in Artificial Intelligence*, pages 362–369, San Francisco, CA, USA, 2001. Morgan Kaufmann Publishers Inc.

M. Minsky and S. Papert. *Perceptrons: an introduction to computational geometry*. MIT Press, 1969.

F. Murtagh and A. Heck. *Multivariate data analysis*. Springer, 1987.

P. Nakkiran, G. Kaplun, Y. Bansal, T. Yang, B. Barak, and I. Sutskever. Deep double descent: where bigger models and more data hurt. *arXiv preprint arXiv:1912.02292*.

R. M. Neal. *Bayesian learning for neural networks*. Springer, 1996.

A. Ng and M. Jordan. On discriminative vs. generative classifiers: A comparison of logistic regression and naive bayes. In T. Dietterich, S. Becker, and Z. Ghahramani, editors, *Advances in Neural Information Processing Systems*, volume 14. MIT Press, 2001.

A. O'Hagan. Curve fitting and optimal design for prediction. *Journal of the Royal Statistical Society: Series B (Methodological)*, 40(1):1–24, 1978.

G. Papamakarios, D. C. Sterratt, and I. Murray. Sequential neural likelihood: fast likelihood-free inference with autoregressive flows. *arXiv preprint arXiv:1805.07226*.

K. Pearson. Iii. contributions to the mathematical theory of evolution. *Philosophical Transactions of the Royal Society of London. A*, 185(1):1–110, 1894.

K. Pearson. Liii. on lines and planes of closest fit to systems of points in space. *The London, Edinburgh, and Dublin Philosophical Magazine and Journal of Science*, 2(11):559–572, 1901.

B. T. Polyak and A. B. Juditsky. Acceleration of stochastic approximation by averaging. *SIAM Journal on Control and Optimization*, 30(4):838–855, 1992.

J. Quiñonero-Candela and C. E. Rasmussen. A unifying view of sparse approximate gaussian process regression. *Journal of Machine Learning Research*, 6(65):1939–1959, 2005.

C. Raffel, N. Shazeer, A. Roberts, and et al. Exploring the limits of transfer learning with a unified text-to-text transformer. *Journal of Machine Learning Research*, 21(140):1–67, 2020.

H. Raiffa and R. Schlaifer. *Applied statistical decision theory*. Wiley, 1961.

C. E. Rasmussen and C. K. I. Williams. *Gaussian processes for machine learning.* MIT Press, 2006.

R. A. Redner and H. F. Walker. Mixture densities, maximum likelihood and the em algorithm. *SIAM Review*, 26(2):195–239, 1984.

D. J. Rezende and S. Mohamed. Variational inference with normalizing flows. *arXiv preprint arXiv:1505.05770.*

H. Robbins and S. Monro. A stochastic approximation method. *Annals of Mathematical Statistics*, 22(3):400–407, 1951.

C. P. Robert and G. Casella. *Monte Carlo statistical methods.* Springer, 1999.

G. O. Roberts and A. F. M. Smith. Simple conditions for the convergence of the gibbs sampler and metropolis-hastings algorithms. *Stochastic Processes and their Applications*, 49(2):207–216, 1994.

F. Rosenblatt. The perceptron: a probabilistic model for information storage and organization in the brain. *Psychological Review*, 65(6):386–408, 1958.

R. Y. Rubinstein. *Simulation and the Monte Carlo method.* Wiley, 1981.

Y. D. Rubinstein and T. Hastie. Discriminative vs informative learning. In *KDD'97*, pages 49–53. AAAI Press, 1997.

D. E. Rumelhart, G. E. Hinton, and R. J. Williams. Learning representations by back-propagating errors. *Nature*, 323:533–536, 1986.

G. Schwarz. Estimating the dimension of a model. *The Annals of Statistics*, 6(2):461–464, 1978.

S. Z. Selim and M. A. Ismail. K-means-type algorithms: a generalized convergence theorem and characterization of local optimality. *IEEE Transactions on Pattern Analysis and Machine Intelligence*, PAMI-6(1):81–87, 1984.

C. E. Shannon. A mathematical theory of communication. *The Bell System Technical Journal*, 27(3):379–423, 1948.

S. Sharma. Markov chain monte carlo methods for bayesian data analysis in astronomy. *Annual Review of Astronomy and Astrophysics*, 55(1):213–259, 2017.

D. S. Sivia and J. Skilling. *Data analysis: A Bayesian tutorial.* Oxford University Press, 2006.

J. Skilling. Nested sampling for general bayesian computation. *Bayesian Analysis*, 1(4): 833–859, 2006.

E. Snelson and Z. Ghahramani. Sparse gaussian processes using pseudo-inputs. In *Advances in Neural Information Processing Systems*, volume 18. MIT Press, 2005.

Y. Song, J. Sohl-Dickstein, D. P. Kingma, A. Kumar, S. Ermon, and B. Poole. Score-based generative modeling through stochastic differential equations. *arXiv preprint arXiv:2011.13456.*

N. Srivastava, G. E. Hinton, A. Krizhevsky, I. Sutskever, and R. R. Salakhutdinov. Dropout: a simple way to prevent neural networks from overfitting. *Journal of Machine Learning Research*, 15(56):1929–1958, 2014.

M. L. Stein. *Interpolation of spatial data: Some theory for kriging.* Springer, 1999.

H. Steinhaus. Sur la division des corps matériels en parties. *Bulletin L'Académie Polonaise des Science*, 4:801–804, 1957.

M. Stone. Cross-validatory choice and assessment of statistical predictions. *Journal of the Royal Statistical Society. Series B (Methodological)*, 36:111–147, 1974.

M. C. Storrie-Lombardi, O. Lahav, L. Sodre, and L. J. Storrie-Lombardi. Morphological classification of galaxies by artificial neural networks. *Monthly Notices of the Royal Astronomical Society*, 259(1):8–16, 1992.

A. Stuart and K. Ord. *Kendall's advanced theory of statistics, Volume 1: Distribution theory.* Edward Arnold, 1994.

J. R. Taylor. *An introduction to error analysis: The study of uncertainties in physical measurements.* University Science Books, 1982.

M. Tegmark, M. A. Strauss, M. R. Blanton, K. Abazajian, S. Dodelson, H. Sandvik, X. Wang, D. H. Weinberg, I. Zehavi, N. A. Bahcall, F. Hoyle, D. Schlegel, R. Scoccimarro, M. S. Vogeley, A. Berlind, T. Budavári, A. Connolly, D. J. Eisenstein, D. Finkbeiner, J. A. Frieman, J. E. Gunn, L. Hui, B. Jain, D. Johnston, S. Kent, H. Lin, R. Nakajima, R. C. Nichol, J. P. Ostriker, A. Pope, R. Scranton, U. Seljak, R. K. Sheth, A. Stebbins, A. S. Szalay, I. Szapudi, Y. Xu, J. Annis, J. Brinkmann, S. Burles, F. J. Castander, I. Csabai, J. Loveday, M. Doi, M. Fukugita, B. Gillespie, G. Hennessy, D. W. Hogg, Ž. Ivezić, G. R. Knapp, D. Q. Lamb, B. C. Lee, R. H. Lupton, T. A. McKay, P. Kunszt, J. A. Munn, L. O'Connell, J. Peoples, J. R. Pier, M. Richmond, C. Rockosi, D. P. Schneider,

C. Stoughton, D. L. Tucker, D. E. van den Berk, B. Yanny, and D. G. York. Cosmological parameters from sdss and wmap. *Physical Review D*, 69(10):103501, 2004.

H. Theil. A multinomial extension of the linear logit model. *International Economic Review*, 10(3):251–259, 1969.

E. Thrane and C. Talbot. An introduction to bayesian inference in gravitational-wave astronomy: Parameter estimation, model selection, and hierarchical models. *Publications of the Astronomical Society of Australia*, 36:e010, 2019.

L. Tierney. Markov chains for exploring posterior distributions. *The Annals of Statistics*, 22 (4):1701–1728, 1994.

L. Tierney and J. B. Kadane. Accurate approximations for posterior moments and marginal densities. *Journal of the American Statistical Association*, 81(393):82–86, 1986.

A. N. Tikhonov. Solution of incorrectly formulated problems and the regularization method. *Soviet Mathematics Doklady*, 4:1035–1038, 1963.

M. Titsias. Variational learning of inducing variables in sparse gaussian processes. In *Proceedings of the Twelfth International Conference on Artificial Intelligence and Statistics*, pages 567–574, 2009.

D. M. Titterington, A. F. M. Smith, and U. E. Makov. *Statistical analysis of finite mixture distributions*. Wiley, 1985.

R. Trotta. Bayes in the sky: Bayesian inference and model selection in cosmology. *Contemporary Physics*, 49(2):71–104, 2008.

R. B. Tully and J. R. Fisher. A new method of determining distances to galaxies. *Astronomy and Astrophysics*, 54:661–673, 1977.

S. Van Huffel and J. Vandewalle. *The total least squares problem: Computational aspects and analysis*. Society for Industrial and Applied Mathematics, 1991.

V. N. Vapnik. *The nature of statistical learning theory*. Springer, 1995.

L. Verde, H. V. Peiris, D. N. Spergel, M. R. Nolta, C. L. Bennett, M. Halpern, G. Hinshaw, N. Jarosik, A. Kogut, M. Limon, S. S. Meyer, L. Page, G. S. Tucker, E. Wollack, and E. L. Wright. First-year wilkinson microwave anisotropy probe (wmap) observations: parameter estimation methodology. *Astrophysical Journal Supplement*, 148:195–211, 2003.

T. von Hippel, L. J. Storrie-Lombardi, M. C. Storrie-Lombardi, and M. J. Irwin. Automated

classification of stellar spectra – part one – initial results with artificial neural networks. *Monthly Notices of the Royal Astronomical Society*, 269(1):97, 1994.

J. Von Neumann. Various techniques used in connection with random digits. *Applied Math Series*, 12:36–38, 1951.

G. Wahba. *Spline models for observational data*. Society for Industrial and Applied Mathematics, 1990.

A. M. Walker. On the asymptotic behaviour of posterior distributions. *Journal of the Royal Statistical Society. Series B (Methodological)*, 31(1):80–88, 1969.

J. V. Wall and C. R. Jenkins. *Practical statistics for astronomers*. Cambridge University Press, 2003.

J. Wei, Y. Tay, R. Bommasani, C. Raffel, B. Zoph, S. Borgeaud, D. Yogatama, M. Bosma, D. Zhou, D. Metzler, E. H. Chi, T. Hashimoto, O. Vinyals, P. Liang, J. Dean, and W. Fedus. Emergent abilities of large language models. *arXiv preprint arXiv:2206.07682*.

C. K. I. Williams. Computing with infinite networks. In *Advances in Neural Information Processing Systems*, volume 9. MIT Press, 1996.

C. K. I. Williams and D. Barber. Bayesian classification with gaussian processes. *IEEE Transactions on Pattern Analysis and Machine Intelligence*, 20(12):1342–1351, 1998.

J. H. Wolfe. Pattern clustering by multivariate mixture analysis. *Multivariate Behavioral Research*, 5(3):329–350, 1970.

A. Zellner. *An introduction to Bayesian inference in econometrics*. Wiley, 1971.

A. Zellner and P. E. Rossi. Bayesian analysis of dichotomous quantal response models. *Journal of Econometrics*, 25(3):365–393, 1984.